Nuclear Dependence of Charged Current Inclusive $\bar{\nu}_\mu - A$ Cross Section Measurements at 6 GeV at MINERvA

THESIS

submitted in partial fulfilment of the requirements

to obtain the degree for

Doctorate of Philosophy in Physics

by

Prameet Kumar Gaur (GH-7805)

under the supervision of:

Prof. Mohammad Sajjad Athar
Aligarh Muslim University, Aligarh
Prof. Deborah Harris
York University, Canada

to

Department of Physics
Aligarh Muslim University
Aligarh -202002, India

September, 2024

Candidate's Declaration

I, Prameet Kumar Gaur, Department of Physics, Aligarh Muslim University, certify that the work embodied in this Ph.D. thesis is my bonafide work carried out by me under the supervision of Prof. Mohammad Sajjad Athar at Aligarh Muslim University, Aligarh and under the co-supervision of Prof. Deborah Harris, Senior Scientist, Neutrino Division at Fermilab and professor at Department of Physics and Astronomy, York University, Toronto, Canada. The matter embodied in this Ph.D. thesis has not been submitted for the award of any other degree.

I have faithfully acknowledged, given credit to, and referred to the research workers wherever their works have been cited in the text and the body of the thesis. I further certify that I have not willfully lifted some other's work, para, text, data, result, etc. reported in the journals, books, magazines, reports, dissertations, thesis, etc., or available at websites and included them in this Ph.D. thesis and cited as my work.

Date: **Signature of the candidate**

Prameet Kumar Gaur

Certificate from the Supervisor/Co-Supervisor

This is to certify that the above statement made by the candidate is correct to the best of our knowledge.

Signature of the Co-Supervisor
Prof. Deborah Harris
Department of Physics and Astronomy
York University, Toronto, Canada

Signature of the Supervisor
Prof. Mohammad Sajjad Athar
Department of Physics
Aligarh Muslim University, Aligarh

(Signature of the Chairman of the Department with seal)

COURSE/ COMPREHENSIVE EXAMINATION/ PRE-SUBMISSION SEMINAR COMPLETION CERTIFICATE

This is to certify that Mr. Prameet Kumar Gaur, Department of Physics, has satisfactorily completed the coursework/comprehensive examination and pre-submission seminar requirement which is part of his Ph.D. program.

Date: ..... **Signature of the Department's Chairman**

COPYRIGHT TRANSFER CERTIFICATE

Title of the Thesis: Nuclear Dependence of Charged Current Inclusive $\bar{\nu}_\mu - A$ Cross Section Measurements at 6 GeV at MINERvA

Candidate's Name: Prameet Kumar Gaur

Copyright Transfer

The undersigned now assigns to the Aligarh Muslim University, Aligarh, the copyright that may exist in and for the above thesis submitted for the award of a Ph.D. degree.

Signature of the candidate

Note: However, the author may reproduce or authorize others to reproduce materials extracted verbatim from the thesis or derivative of the thesis for the author's personal use provided that the source and the University's copyright notice are indicated.

Acknowledgements

This research was funded by the Council of Scientific and Industrial Research (CSIR), New Delhi, by providing PhD research fellowship for five years. I would also like to thank the Indian Institutes Fermilab Collaboration (IIFC) for providing the necessary funding while we stayed at the Fermilab, USA.

First and foremost, I would like to express my deepest gratitude to my supervisor, Prof. Mohammad Sajjad Athar, for his immense support, in every which way possible. He consistently encouraged me, from the time he taught particle physics during my Master's to the years I spent as a PhD student. His sincerity has been exemplary to me. His knowledge, the discussions when we needed answers, and where he shared his expertise have been invaluable in putting together this work. I'm thankful for his patience, support, and belief in me. It kept me going and helped me push through tough times when I felt stuck. His lighthearted banter and humorous comments brought a fun vibe and positive energy to the lab.

I would also like to extend my sincere thanks to Prof. Deborah Harris, whose continuous involvement through regular meetings kept me on track. Her immense expertise in the field and thoughtful feedback were crucial in helping me correct my mistakes and improve the quality of this work. Her sincerity and dedication to the process of research, motivated me to do better towards my development as a physicist.

I would also like to extend my heartfelt thanks to Prof. Jeff Nelson. His leadership during the inclusive meetings provided a platform for insightful feedback that greatly helped me make progress with my research work. Prof. Jeff's detailed comments and expert suggestions were instrumental in ensuring that I made steady progress with my work. His advice on effectively presenting research, how to structure a talk, tell the story, and engage an audience—has helped me become a better researcher overall. I would like to thank Dr. Huma Haider and Dr. Zubair

Ahmad Dar, for helping me while I started the analysis, and making me familiar with the different analysis tools that I had to use.

I am thankful to have fellow scientists, who were very friendly and helpful during this journey, Adrian Lozano, Anežka Klustová, Vaniya Ansari, Maria Mehmood, Daniel Correia, Oscar Moreno, Christian Nguyen, Ben Messerly, David Last, Andrew Oliver, Noah Vaughan, Dan Rutherbories, Kevin McFarland, Rik Gran, Steven Manly, Jorge Morfin and so many others.

I would like to appreciate and thank my dear friend, Sayeed Akhter, who was right beside me, as a source of support and camaraderie throughout the years of my PhD, from the start. We not only tackled academic challenges together but also shared countless moments of fun, whether it was cooking meals, going for a walk, or simply enjoying each other's company. I am deeply grateful for his friendship and support, contributing to both my growth and well-being. We conquered many challenges together while moving towards completing our research work.

I would like to express my sincere appreciation to our senior colleagues Dr. Atika Fatima and Dr. Farhana Zaidi for their support and guidance, both during my time in the lab at Aligarh and here in the USA. Their willingness to help, whether by addressing our questions on weak interaction physics or assisting with various tasks, was truly commendable. I was lucky to have Atika as a senior in the lab during the early years of my PhD. She helped me get started with various tools and software that we had to use during our research. Anytime I ran into trouble, she was right there with a solution, and it made everything so much easier.

I am thankful to my brother, Prateek Gaur, who was always there with me, to talk about and discuss just anything in life (except Physics !).

Last but not least, profoundly grateful to my parents for their unwavering love and support throughout my entire academic journey. I dedicate this thesis to my loving parents.

List of Publications

1. M. V. Ascencio, P. K. Gaur *et al.* [MINERvA], *"Measurement of inclusive charged-current $\nu\mu$ scattering on hydrocarbon at $\langle E\nu\rangle \sim 6$ GeV with low three-momentum transfer,"* Phys. Rev. D **106**, no.3, 032001 (2022) DOI:10.1103/PhysRevD.106.032001.

2. F. Akbar, P. K. Gaur *et al.* [MINERvA], *"Vertex finding in neutrino-nucleus interaction: a model architecture comparison,"* JINST **17**, no.08, T08013 (2022) DOI:10.1088/1748-0221/17/08/T08013.

3. D. Ruterbories, P. K. Gaur *et al.* [MINERvA], *"Simultaneous Measurement of Proton and Lepton Kinematics in Quasielasticlike $\nu\mu$-Hydrocarbon Interactions from 2 to 20 GeV,"* Phys. Rev. Lett. **129**, no.2, 021803 (2022) DOI:10.1103/PhysRevLett.129.021803.

4. A. Bercellie, P. K. Gaur *et al.* [MINERvA], *"Simultaneous Measurement of Muon Neutrino $\nu\mu$ Charged-Current Single $\pi+$ Production in CH, C, H2O, Fe, and Pb Targets in MINERvA,"* Phys. Rev. Lett. **131**, no.1, 1 (2023) DOI:10.1103/PhysRevLett.131.011801.

5. A. Bashyal, P. K. Gaur *et al.* [MINERvA], *"High-Statistics Measurement of Antineutrino Quasielastic-like scattering at $E_\nu \sim$ 6~GeV on a Hydrocarbon Target,"* Phys. Rev. D **108**, no.3, 032018 (2023) DOI:10.1103/PhysRevD.108.032018.

6. A. Olivier, P. K. Gaur *et al.* [MINERvA], *"Measurement of the multineutron $\nu^{-}\mu$ charged current differential cross section at low available energy on hydrocarbon,"* Phys. Rev. D **108**, no.11, 112010 (2023) DOI:10.1103/PhysRevD.108.112010.

7. S. Henry, P. K. Gaur *et al.* [MINERvA], *"Measurement of electron neutrino and antineutrino cross sections at low momentum transfer,"* Phys. Rev. D **109**, no.9, 092008 (2024)
DOI:10.1103/PhysRevD.109.092008.

8. P. K. Gaur [MINERvA], *"Inclusive Charged Current Antineutrino - Nucleus Cross Section Analysis at MINERνA,"* DAE Symp. Nucl. Phys. **67**, 1155-1156 (2024)

9. P. K. Gaur [MINERvA], *"Nuclear Dependence of Charged Current Inclusive $\bar{\nu}_\mu - A$ Cross Section Measurements at 6 GeV at MINERvA "*, **Paper in preparation.**

My contribution to the above listed papers (1-7) is that I was a part of the tuple production team, where we were involved in the production of data structures(tuples) which contain all the information about a scattering event and used by the MINERvA collaboration for performing various analyses. These tuples were produced taking advantage of machine learning algorithms.

The last paper(9) in my current ongoing analysis with the experiment, and is in preparation. We want to make sure we are not making any mistakes and taking additional steps to improve the results if we can, before we move forward towards publishing the paper.

Contents

List of Figures

List of Tables

Chapter 1

Introduction

Neutrinos alone, among all the known particles, have ethereal properties that are striking and romantic enough both to have inspired a poem by John Updike and to have sent teams of scientists deep underground for 50 years to build huge science-fiction-like contraptions to unravel their mysteries [1].

— **Lawrence M. Krauss**
(Canadian-American theoretical physicist)

1.1 Brief History of Neutrinos

Neutrino was first hypothesized by Pauli in 1930 [2] with a letter written to the participants of a nuclear physics conference held in Germany, which he had not attended. In this letter, Pauli proposed the existence of a new neutral particle and called it a "neutron" (now known as neutrino) in order to solve the two outstanding problems of nuclear physics at that time viz., the puzzle of energy conservation in the β-decays of nuclei and the anomalies in understanding the spin-statistics relation in the case of ^{14}N and ^{6}Li nuclei. As mentioned in his letter, Pauli's neutron had the following properties:

- It is a spin $\frac{1}{2}$ particle and is a constituent of nuclei.
- It does not travel at the speed of light.
- Its mass is similar to the electron mass but not larger than 0.01 times the proton mass.
- It has a magnetic moment which is of the order of 10^{-13} cm and is bound in the nucleus by the magnetic forces.
- The neutron shares the available energy with the electron leading to the continuous energy spectrum of β-electrons.

Pauli was too shy to talk about his idea of "neutron" publicly until 1933, though he had talked about his proposal to Fermi privately during a conference in 1931. At that time, he had abandoned the idea that the neutrons are a constituent of the nucleus. Fermi took great interest in Pauli's idea of the neutron, and after the discovery of the present-day neutron by Chadwick in 1932, he rechristened Pauli's "neutron" as "neutrino" (meaning the little neutral one). The theory of β-decay was proposed independently by Fermi [3] and Perrin [4] in 1933, which was the first milestone in the theory of neutrino interactions with matter. This theory describes the β-decay of nuclei in which no change of angular momentum and parity of the nucleus is observed and the interaction takes place at a single point (Fig. 1.1). It was assumed that the electron-neutrino pair is created in the basic transitions of β-decay ($n \to p$) i.e.

$$n \longrightarrow p + e^{-} + \nu \tag{1.1}$$

and interaction Lagrangian was written in analogy with Quantum Electrodynamics (QED) for the process given in Eq. 1.1, as:

$$\mathcal{L} = G\bar{\psi}_p(x)\gamma_\mu\psi_n(x) \;\; \bar{\psi}_e(x)\gamma^\mu\psi_\nu(x) + \text{h.c.}, \tag{1.2}$$

where G is the strength of the interaction and $\psi_p(x)$, $\psi_n(x)$, $\psi_e(x)$ and $\psi_\nu(x)$ are the spin $\frac{1}{2}$ Dirac fields of proton, neutron, electron, and neutrino, respectively and

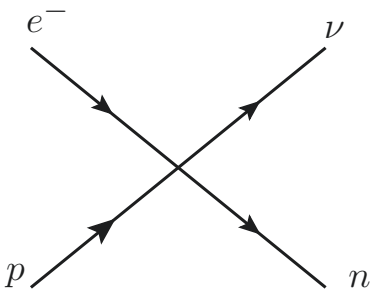

Figure 1.1: Four point Fermi interaction.

γ_μ are the Dirac gamma matrices [5], which implies that the interaction is vector-type in nature. The theory was extended by Gamow and Teller [6], to describe the observation of the nuclear β-decays with change of one unit of angular momentum for the parent and daughter nuclei, and no change in parity. The most general Lagrangian by considering special relativity and Lorentz covariance is given by:

$$\mathcal{L} = \sum_i G_i[\bar{\psi}_p \mathcal{O}_i \psi_n][\bar{\psi}_e \mathcal{O}^i \psi_\nu] + \ h.\ c., \tag{1.3}$$

where G_i is the strength of the interaction corresponding to $\mathcal{O}^i$ form as scalar (I), vector (γ_μ), pseudoscalar (γ_5), axial vector ($\gamma_\mu\gamma_5$), and tensor ($\sigma_{\mu\nu}$) interactions.

Using Fermi's theory of β decay, in 1934, Bethe and Peierls [7] first calculated the neutrino-nucleus cross section and found that the cross section is of the order of 10^{-44} cm^2 for 1 MeV neutrino, which was almost impossible, at that time, to be observed experimentally. Therefore, the attempts to make direct observations of neutrinos and antineutrinos took much longer to succeed experimentally, though there was evidence of the existence of neutrinos by the indirect measurement of the recoil of the daughter nucleus in the nuclear β-decay. With the development of nuclear reactors where the nuclear fusion process leads to the production of very high-intensity flux of electron type antineutrinos, it was suggested by Pontecorvo [8], Alvarez [9] and Fermi [10] that the neutrinos coming from the nuclear reactor may be observed via neutrino-nucleus reactions, despite small neutrino cross sections. In 1953, Reines and Cowan [11, 12] observed the neutrino through the nuclear reaction induced by antineutrinos coming from the reactor by using a

300 L water target mixed with $CdCl_2$ at Hanford reactor, where the liquid scintillator detector was sandwiched between the water tanks. They observed the reaction:

$$\bar{\nu}_e + p \longrightarrow e^+ + n \tag{1.4}$$

by making a coincidence measurement of the photons from particle annihilation $e^- + e^+ \rightarrow \gamma + \gamma$ and a neutron capture $n +^{108}\text{Cd} \rightarrow^{109}\text{Cd} + \gamma$ reaction, a few microseconds later.

In 1956, at the Savannah River reactor, the same group [13, 14] confirmed the observation of neutrino by using a large volume (4200 L) water tank with the same technique as discussed above.

At the same time, i.e. 1956, at the Savannah River reactor, Ray Davis [15] was experimenting using a radiochemical method on the suggestion of Pontecorvo and looking for the electron in the final state

$$\nu +^{37}Cl \longrightarrow e^- +^{37}Ar, \tag{1.5}$$

which was never observed. Therefore, it was concluded that the neutrino that produced a positron in the Reines and Cowan experiment does not produce an electron in the Davis experiment and these two are, thus, different particles.

Since another charged lepton, i.e., muons were discovered in 1936 by Anderson and Neddermeyer [16] while studying cosmic radiation, therefore, with the development of neutrino physics, it was believed that there must be a neutrino associated with it. On the suggestion of Pontecorvo [17], Schwartz [18], Lee and Yang [19] an accelerator was developed to produce pions and kaons in a proton beam, which subsequently decay into a muon and a neutrino and performed experiments using these neutrinos via the following reactions:

$$\nu + n \longrightarrow \mu^- + p \qquad \nu + n \longrightarrow e^- + p \tag{1.6}$$

$$\bar{\nu} + n \longrightarrow \mu^+ + p \qquad \bar{\nu} + n \longrightarrow e^+ + p \tag{1.7}$$

to test whether the neutrinos from pion decays produce muons or electrons through their interaction with matter. The experiments performed at BNL and CERN observed that neutrinos from the pion decays are accompanied by muons and thus it was concluded that these neutrinos (ν_μ) are different from the electron neutrinos as an electron was never produced in the final state, i.e. $\nu_\mu \neq \nu_e$.

In 1975, another heavy-charged lepton τ was discovered by Perl [20]. In analogy with the muon case, it was conjectured that τ has its own associated neutrino ν_τ which is emitted in the τ-decay. The tau neutrino has been directly observed in experiments with accelerator neutrinos by DONUT [21], OPERA [22], and indirectly inferred from experiments like SuperK [23], and IceCube [24].

Thus, the neutrinos were found to exist in three flavours (also known as generations) described as electron neutrinos (ν_e), muon neutrinos (ν_μ) and tau neutrinos (ν_τ). Along with the corresponding leptons, they were grouped into the three doublets under the quantum number I_W called weak isospin i.e.

$$\begin{pmatrix} \nu_e \\ e^- \end{pmatrix}, \quad \begin{pmatrix} \nu_\mu \\ \mu^- \end{pmatrix}, \quad \begin{pmatrix} \nu_\tau \\ \tau^- \end{pmatrix}$$

with similar assignments for their antiparticles *viz.*

$$\begin{pmatrix} e^+ \\ \bar{\nu}_e \end{pmatrix}, \quad \begin{pmatrix} \mu^+ \\ \bar{\nu}_\mu \end{pmatrix}, \quad \begin{pmatrix} \tau^+ \\ \bar{\nu}_\tau \end{pmatrix}.$$

In 1956, in the bubble chamber experiments, two particles were observed and named τ and θ which had almost the same mass, charge, and lifetime, and were considered to be the same particle, except that one of them decayed into two pions and the other into three pion states. The decay of these two particles in different pionic modes implies that one had positive parity (decaying into two pions) while the other one had negative parity (decaying into three pions). To solve the $\tau - \theta$ puzzle, it was suggested that parity may not be conserved in weak interactions [25]. In 1956, Lee and Yang [26, 27], after analyzing many weak interaction processes, argued that parity is not conserved in weak interactions and

these two particles θ and τ are the same, (now known as the K^+). This idea prompted people to look for evidence of parity invariance in weak interactions. The experiment that successfully concluded the test of parity violation in β-decay was performed by Wu et al. [28] using supercooled cobalt nucleus, to achieve a completely polarized target, and observed a large asymmetry of β-electrons concerning the spin direction of the polarized ^{60}Co and by Garwin et al. [29] in pion decay. It was established by 1957, from the studies of various β-decays that parity is violated in weak interactions. Around the same time, the experimental confirmation of the neutrino mass to be almost negligible and the observation of the longitudinal polarization of the electron (positron) to be $-v$ $(+v)$ and the helicities of the neutrino (antineutrino) to be -1 $(+1)$ led to the major developments in the phenomenological theory of weak interactions culminating in the $V-A$ theory of weak interactions, during 1958, which was formulated almost simultaneously by Sudarshan and Marshak [30], Feynman and Gell-Mann [31] and Sakurai [32].

1.2 From the V-A theory of Weak Interactions to the Standard Model

The interaction Hamiltonian H_{int} for the process given in Eq. 1.1, was concluded to have the form:

$$H_{int} = \frac{G_F}{\sqrt{2}} l_\mu J^{\mu\dagger} + h.c., \tag{1.8}$$

where

$$l_\mu = \bar{\psi}_e(x)\gamma_\mu(1-\gamma_5)\psi_\nu(x) \tag{1.9}$$

$$J^\mu = \bar{\psi}_p(x)\gamma^\mu(1-g_A\gamma_5)\psi_n(x) \tag{1.10}$$

where a factor $\frac{1}{\sqrt{2}}$ is introduced in the definition of H_{int} so that the constant G introduced by Fermi (in Eq. 1.2) is consistent with G_F. The theory was extended by Cabibbo [33] to describe the weak interactions of strange particles by adding

a piece involving interactions of the $\Delta S = 1$ hadronic current $J^{\mu}_{\Delta S=1}$, which interacted with the leptonic current with a strength weaker than the $\Delta S = 0$ current of β decays and writing the hadronic current in Eq. 1.8 as

$$J^{\mu} = \cos\theta_C J^{\mu}_{\Delta S=0} + \sin\theta_C J^{\mu}_{\Delta S=1}, \tag{1.11}$$

where $\theta_C = 13.1^{\circ}$ is the Cabibbo mixing angle.

The phenomenological $V-A$ theory when extended to higher energies diverges. For example, the total cross sections for the $\nu_e e^-$ scattering is found to increase with the square of the CM energy (s) i.e. $\sigma(\nu_e e^- \rightarrow \nu_e e^-) = \frac{G^2}{\pi} s$ and would violate the unitarity limit which is given by $\sigma \leq \frac{4\pi}{s}$ for $\nu_e e^- \rightarrow \nu_e e^-$ scattering. To avoid these divergences, intermediate vector bosons (IVB) W were introduced, which mediate the weak interactions, and the interaction Hamiltonian in the IVB model is written as:

$$H^{IVB}_{int} = g_W \left[\bar{\psi}_e \gamma_\mu (1-\gamma_5)\psi_\nu + \bar{\psi}_n \gamma_\mu (1-\gamma_5)\psi_p\right] W^{\mu}. \tag{1.12}$$

where W^{μ} is the vector field.

It was hoped that the momentum dependence of the W_μ propagator, which has spin-1, would resolve the problem of divergence, but it did not. Moreover, the short range of weak interactions implying a large mass of the mediating vector boson created problems with the renormalizability of the theory.

During 1960s, Glashow, Salam, and Weinberg developed the standard model of electroweak interactions, which is one of the most important development in the theory of weak interactions. It unifies the electromagnetic and weak interactions and is based on the principle of invariance under local gauge transformations. It is local, renormalizable, non-abelian gauge field theory based on $SU(2)_L \times U(1)_Y$ gauge symmetry. The left handed leptons and hadrons are assigned to the doublets of the group $SU(2)_L$ and their right handed partners are assigned to a singlet under

$U(1)_Y$ for each flavor like:

$$\begin{pmatrix}\nu_e\\ e^-\end{pmatrix}_L, \begin{pmatrix}\nu_\mu\\ \mu^-\end{pmatrix}_L, \begin{pmatrix}\nu_\tau\\ \tau^-\end{pmatrix}_L, \begin{pmatrix}u\\ d'\end{pmatrix}_L, \begin{pmatrix}c\\ s'\end{pmatrix}_L, \begin{pmatrix}t\\ b'\end{pmatrix}_L.$$

These left-handed doublets form the basic representation of $SU(2)$ and their right-handed partners like

$$e_R, \quad \mu_R, \quad \tau_R, \quad u_R, \quad d'_R, \quad c_R, \quad s'_R, \quad t_R, \quad b'_R$$

form the singlet representation under $U(1)_Y$.

The standard model reproduces the essential features of the phenomenological weak interactions like parity violation, two-component neutrino, and the massive $W^\pm$ bosons mediating the weak charged current interactions, as well as the massless photon (γ) mediating the electromagnetic interaction. In addition, it predicts a new massive neutral gauge boson Z^0 implying neutral currents. The model introduces a new scalar field called Higgs boson to generate the masses of the gauge bosons $W^\pm$ and Z^0 and also their couplings to the leptons are predicted in terms of g_W, the weak coupling of $W^\pm$, e the electromagnetic coupling of the photon and a free parameter θ_W called the weak mixing angle to be determined from the experiments. The mass and the coupling of the Higgs boson remain undetermined in the model. The standard model was first proposed for the leptons and was later extended to the quark sector including strange quarks following the GIM (Glashow-Iliopoulos-Maiani) mechanism [34].

The Standard Model Lagrangian describing the interaction of leptons with gauge bosons is given by

$$\begin{aligned} L_I &= -e\Bigg[\frac{1}{2\sqrt{2}\sin\theta_W}\left(j_\mu^{CC}W^{\mu+} + h.c.\right) + \frac{1}{2\sin\theta_W\cos\theta_W}j_\mu^{NC}Z^\mu \\ &+ j_\mu^{EM}A^\mu\Bigg], \end{aligned} \tag{1.13}$$

where $W_\mu^\pm$, Z_μ and A_μ are the charged, neutral and electromagnetic gauge fields

and

$$j_\mu^{CC} = \sum_{l=e,\mu,\tau} \overline{\psi}_l \gamma_\mu (1-\gamma^5) \psi_{\nu_l} \tag{1.14}$$

$$j_\mu^{NC} = \sum_{l=e,\mu,\tau} \left[\overline{\psi}_l \gamma_\mu (g_V^l - g_A^l \gamma^5) \psi_l + \overline{\psi}_{\nu_l} \gamma_\mu (g_V^{\nu_l} - g_A^{\nu_l} \gamma^5) \psi_{\nu_l} \right] \tag{1.15}$$

$$j_\mu^{EM} = \sum_{l=e,\mu,\tau} \overline{\psi}_l \gamma_\mu \psi_l, \tag{1.16}$$

with $\sin\theta_W = \frac{e}{g}$, $g_V^l = -\frac{1}{2} + 2\sin^2\theta_W$, $g_A^l = -\frac{1}{2}$, $g_V^{\nu_l} = \frac{1}{2}$ and $g_A^{\nu_l} = \frac{1}{2}$, where $e = \sqrt{4\pi\alpha}$, α is the fine structure constant.

In analogy with the Lagrangian for the weak interaction for the leptons, the most general Lagrangian for the weak charged current interaction, for the 4-quark favor, is written as:

$$\mathcal{L}_{cc}^{int}(\text{quarks}) = -\frac{g}{\sqrt{2}} \sum_q \left(\bar{q}_L \gamma^\mu \tau^+ q_L W_\mu^+ + \bar{q}_L \gamma^\mu \tau^- q_L W_\mu^- \right) \tag{1.17}$$

$$= -\frac{g}{2\sqrt{2}} \left[\left(\bar{u} \gamma^\mu (1-\gamma^5) d' + \bar{c} \gamma^\mu (1-\gamma^5) s' \right) W_\mu^+ + h.c. \right]. \tag{1.18}$$

Similarly, the neutral current weak interaction Lagrangian for the quarks is written as:

$$\mathcal{L}_{int}^{NC} = -j_\mu^{NC}(\text{quark}) Z^\mu, \tag{1.19}$$

$$\text{with} \qquad j_\mu^{NC}(\text{quark}) = \frac{e}{2\sin\theta_W \cos\theta_W} \sum_q \bar{q} \gamma^\mu (g_V^q - g_A^q \gamma_5) q, \tag{1.20}$$

$$\text{where} \quad g_V^q = \frac{1}{2}\tau_3^q - 2\sin^2\theta_W Q_q \quad \text{and} \tag{1.21}$$

$$g_A^q = \frac{1}{2}\tau_3^q. \tag{1.22}$$

The values of g_V and g_A for u and d quarks are given in Table-1.1.

States	g_V	g_A
u	$\frac{1}{2} - \frac{4}{3}\sin^2\theta_W$	$1/2$
d	$-\frac{1}{2} + \frac{2}{3}\sin^2\theta_W$	$-1/2$

Table 1.1: Couplings of the quarks(u, d) to Z_μ field.

The success of the standard model of particle physics is startling and various predictions of the model were experimentally observed to a very high accuracy. The last and the most important missing piece in the puzzle of the standard model, known by the name Higgs boson, is the carrier particle of the Higgs field, a field that permeates space and endows all elementary subatomic particles with mass through its interactions with them, was discovered in 2012 by ATLAS and CMS experiments at CERN [36]. We heard this news globally, where newspaper headlines read "Scientists discover the god particle !"

1.3 Sources of Neutrinos: Accelerator neutrinos in focus

Neutrinos are produced by a variety of phenomena, including the neutrinos produced in the early universe after the Big Bang, in the core of the sun and other stars, in the earth's core, in the atmosphere of the earth during the decay of secondary cosmic ray particles, to count a few cosmological sources. Neutrinos are also produced in nuclear reactors, particle accelerators, etc. The neutrinos emitted and produced from these various sources have different distributions of energies. This energy range starts from a few μeV for the cosmological neutrinos to more than EeV for cosmogenic neutrinos, which can be observed from the spectrum shown in Fig. 1.2. Broadly, neutrino production sources can be classified into two broad categories viz. natural and man-made sources.

- **N**atural sources: Relic neutrinos/Cosmic neutrino background, solar neutrinos, atmospheric neutrinos, supernova neutrinos, geoneutrinos, ultra-high energy cosmic neutrinos or neutrinos from the extra-galactic sources, etc.

- **M**an-made sources: Reactor antineutrinos, accelerator neutrinos, neutrinos from the decay of particles at rest, neutrinos from muon storage rings, etc.

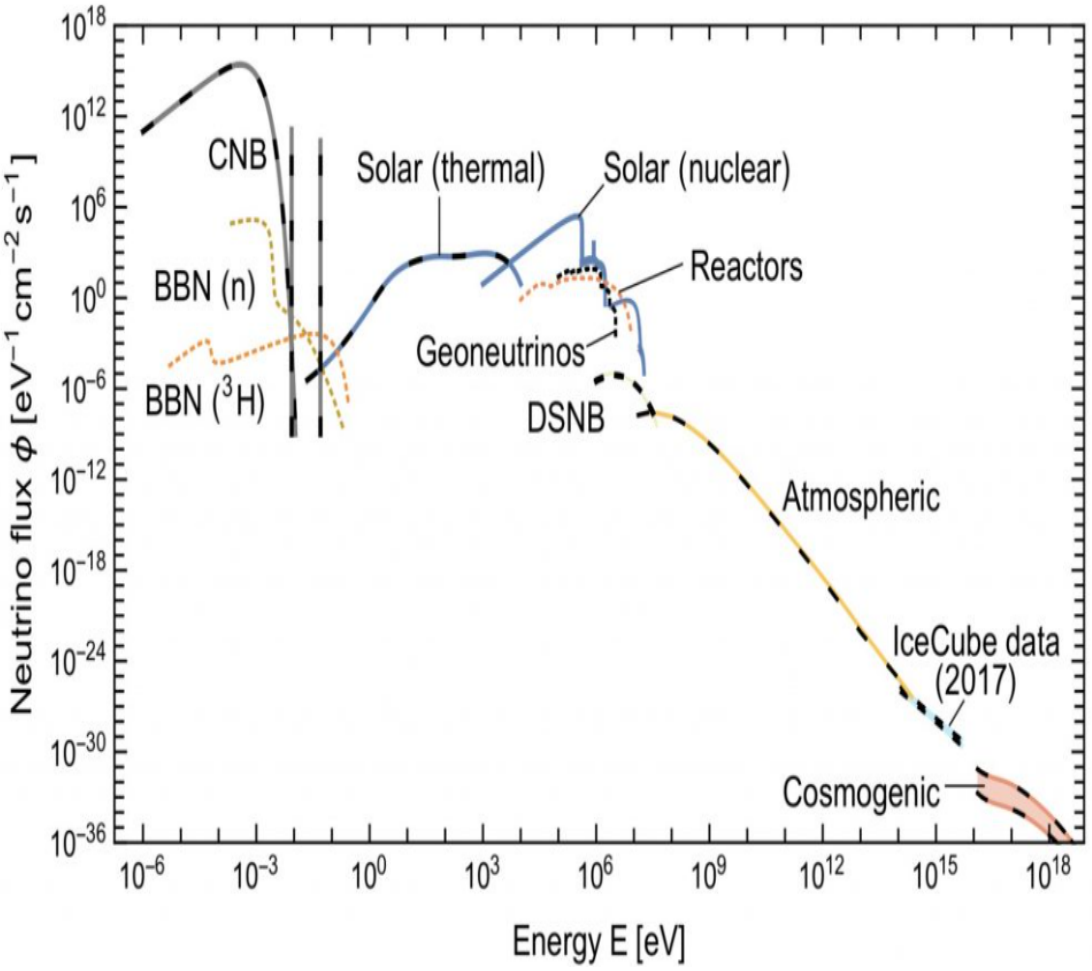

Figure 1.2: Flux of different neutrino sources. Figure has been taken from Ref. [35].

With the development of neutrino physics and the realization that natural sources like solar and atmospheric neutrinos have limitations of beam intensity, energy, etc., it was realized that one should go for accelerator neutrinos. In 1960, Schwartz published the first realistic scheme of a neutrino beam for the study of weak interactions using accelerator sources. The very first neutrino beams were created in 1962 at Brookhaven using a 15 GeV AGS accelerator proton beam striking a beryllium target, primarily generating pions and a small number of kaons. Since then, neutrino beams have been extensively utilized in particle physics research at facilities such as CERN in Europe, ANL, BNL, Fermilab in the USA, and J-PARC in Japan. To obtain the neutrino beam at the accelerators, first,

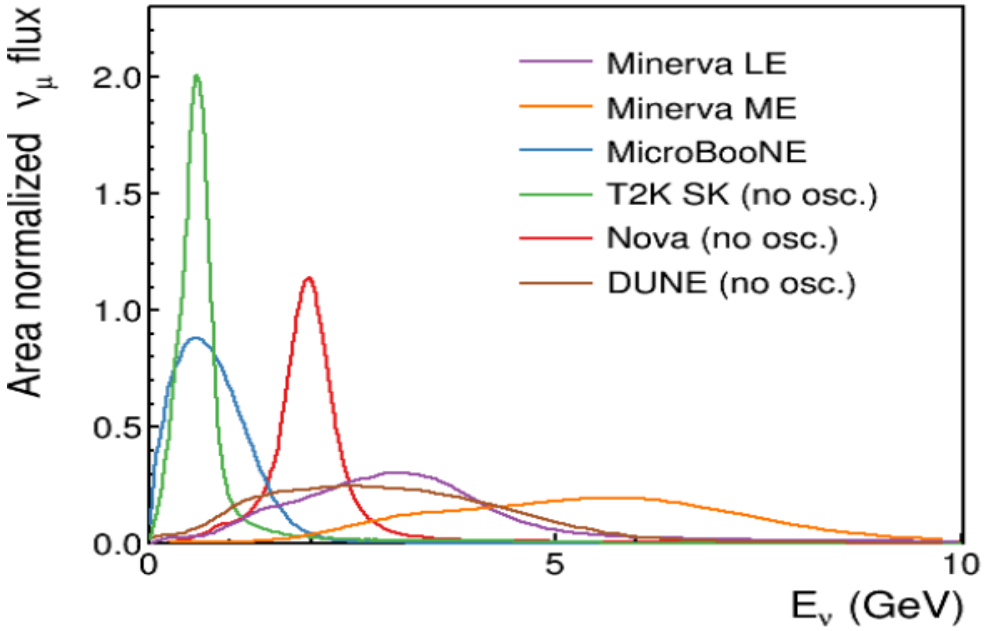

Figure 1.3: Area normalized ν_μ flux as a function of neutrino energy for MINERvA low and medium energy run, MicroBooNE, T2K, NOvA and DUNE experiment. Figure taken from Ref. [37].

the particle accelerators are used to accelerate the protons to very high energies close to the speed of light. Then these highly energetic protons are smashed onto a target like graphite or any other material capable of withstanding very high temperatures. When a proton traveling near the speed of light hits a target, it slows down and the proton's energy is used to produce a jet of hadrons, which consists mainly of pions and kaons. These charged pions and kaons are unstable and decay mainly into muons and neutrinos. Magnetic horns are used to collimate the charged pions and kaons, allowing for the production of either neutrinos or antineutrinos by adjusting the magnetic field direction. Thus, to get a neutrino beam in a certain direction, one focuses the pion/kaon beam in that direction.

In Fig. 1.3, we have shown a typical flux spectrum for the accelerator neutrinos (ν_μ) presently being used or planned to be used like the MINERvA low and medium energy run, MicroBooNE, T2K, NOvA, and DUNE neutrino fluxes. Accelerators generally produce broad neutrino energy beams. For a wide band beam,

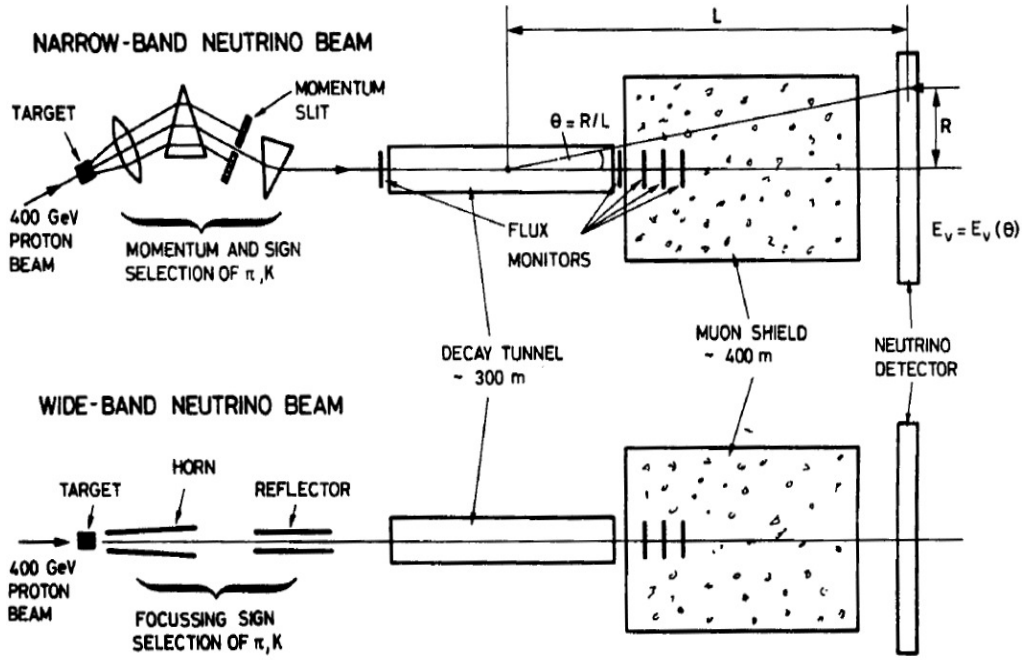

Figure 1.4: Narrow (top) and wide (bottom) band neutrino beam setup. Figure taken from Ref. [38].

a cylindrical target is aligned with the decay tunnel, and magnetic horns focus the mesons (see Fig. 1.4). The mesons decay in the decay pipe, producing an neutrino beam with a broad energy range. The main challenge with wide-band beams is the difficulty in accurately estimating the energy spectrum and the relative proportions of different neutrino species. In contrast, a narrow-band neutrino beam can be achieved by only selecting mesons within a specific energy interval. Here, the cylindrical target is not aligned with the decay tunnel, and additional dipole magnets and momentum slits are used to select mesons of the desired energy (see Fig. 1.4). The neutrino beam so obtained has a narrow band of neutrino energies. For oscillation experiments, using an off-axis setup yields a narrower energy band beam, though this comes with reduced neutrino flux. For this setup, the detector is placed off the beam-axis to obtain a narrow-band of neutrino energies. An example of this is the T2K experiment which uses the off-axis setup for neutrino

oscillation studies, as represented in Fig. 1.5.

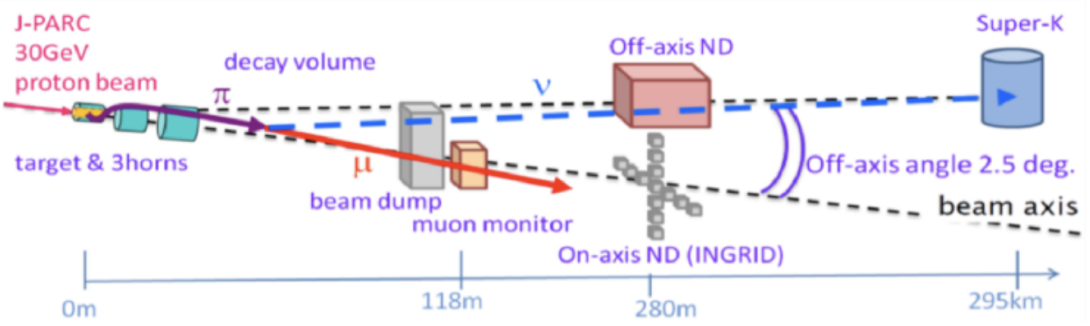

Figure 1.5: Off-axis beam setup at the T2K experiment. Figure taken from Ref. [39].

1.4 (Anti)neutrino Oscillation

Now, let us discuss the (anti)neutrino oscillation phenomena in brief. The neutrino oscillation is purely a quantum mechanical phenomena where the neutrinos oscillate from one flavor, say ν_α, to another flavor, say ν_β, where $\alpha, \beta = e, \mu, \tau$; and $\alpha \neq \beta$, while traversing distance. The neutrino oscillation phenomena implies that neutrinos have non-zero mass and the flavor eigenstates of neutrinos are different from their mass eigenstates. As we have discussed earlier, various neutrino experiments have already confirmed the phenomena of neutrino oscillation in solar, atmospheric, reactor and accelerator neutrinos. Here, for completeness, we are discussing the two flavor neutrino oscillation in vacuum, which can be generalized to three flavor oscillation.

In order to study neutrino oscillation, we have to take into account the non-zero mass of neutrino and thus, the flavor and mass eigenstates of neutrinos are different from one another. Assume that the flavor states ν_e and ν_μ participating in the weak interactions are an admixture of the mass eigenstates ν_1 and ν_2 and this mixing between flavor and mass eigenstates is described by a unitary mixing

matrix U, which is represented in the two-dimensional space as

$$U = \begin{pmatrix} \cos\theta & \sin\theta \\ -\sin\theta & \cos\theta \end{pmatrix} \tag{1.23}$$

such that

$$\nu_{l=e,\mu} = \sum_{i=1,2} U_{li}\nu_i. \tag{1.24}$$

The unitarity of the U matrix requires that in 2-dimensional space it is described by one parameter which is generally chosen to be θ (mixing angle) such that

$$|\nu_e > \;=\; \cos\theta|\nu_1 > + \sin\theta|\nu_2 >, \tag{1.25}$$

$$|\nu_\mu > \;=\; -\sin\theta|\nu_1 > + \cos\theta|\nu_2 > . \tag{1.26}$$

As pure beam of ν_e at $t = 0$ propagates, the mass eigenstates would evolve according to

$$|\nu_1 > \;=\; \nu_1(0)e^{-iE_1 t} \tag{1.27}$$

$$|\nu_2 > \;=\; \nu_2(0)e^{-iE_2 t} \tag{1.28}$$

where same momentum states for E_1 and E_2 are considered, $E_1 = \sqrt{p^2 + m_1^2} = p + \frac{m_1^2}{2p}$ and $E_2 = \sqrt{p^2 + m_2^2} = p + \frac{m_2^2}{2p}$, $p \approx E$ in the highly relativistic limit, being the common momentum of neutrinos with energy E_1 and E_2 and m_1 and m_2 are the mass of $|\nu_1 >$ and $|\nu_2 >$ states, respectively. After a time t, the $|\nu_e(t) >$ will be a different admixture of $|\nu_1 >$ and $|\nu_2 >$.

The probability of finding ν_μ in the beam of ν_e at a later time t is given by

$$P(\nu_e \to \nu_\mu) = \sin^2 2\theta \sin^2\left(\frac{\Delta m^2}{2E}L\right). \tag{1.29}$$

Thus, we see that for $P(\nu_e \to \nu_\mu) \neq 0$ we need $\Delta m^2 \neq 0$ and $\theta \neq 0$ i.e. we need the mass difference between the neutrinos mass eigenstates to be non-zero implying that at least one of them is massive and the mixing angle θ to be non-zero.

The three flavor neutrinos, viz. ν_e, ν_μ, ν_τ, while propagating in space, travel as some admixture of three neutrino mass eigenstates viz. ν_i $(i = 1, 2, 3)$ with

masses m_i, which are related by a 3×3 unitary matrix

$$|\nu_\alpha\rangle = \sum_{i=1}^{3} U_{\alpha i} |\nu_i\rangle \quad (\alpha = e, \mu, \tau)\,. \tag{1.30}$$

$$\begin{pmatrix} \nu_e \\ \nu_\mu \\ \nu_\tau \end{pmatrix} = \begin{pmatrix} U_{e1} & U_{e2} & U_{e3} \\ U_{\mu 1} & U_{\mu 2} & U_{\mu 3} \\ U_{\tau 1} & U_{\tau 2} & U_{\tau 3} \end{pmatrix} \begin{pmatrix} \nu_1 \\ \nu_2 \\ \nu_3 \end{pmatrix}. \tag{1.31}$$

The lepton mixing matrix U_α, in the above expression, is given by Pontecorvo-Maki-Nakagawa-Sakata [40, 41] (PMNS) mixing matrix as:

$$\begin{aligned} U &= \begin{pmatrix} 1 & 0 & 0 \\ 0 & c_{23} & s_{23} \\ 0 & -s_{23} & c_{23} \end{pmatrix} \begin{pmatrix} c_{13} & 0 & s_{13} e^{-i\delta_{CP}} \\ 0 & 1 & 0 \\ -s_{13} e^{i\delta_{CP}} & 0 & c_{13} \end{pmatrix} \begin{pmatrix} c_{21} & s_{12} & 0 \\ -s_{12} & c_{12} & 0 \\ 0 & 0 & 1 \end{pmatrix} \qquad (1.32) \\ &= \begin{pmatrix} c_{12}c_{13} & s_{12}c_{13} & s_{13}e^{-i\delta} \\ -s_{12}c_{23} - c_{12}s_{13}s_{23}e^{i\delta_{CP}} & c_{12}c_{23} - s_{12}s_{13}s_{23}e^{i\delta_{CP}} & c_{13}s_{23} \\ s_{12}s_{23} - c_{12}s_{13}c_{23}e^{i\delta_{CP}} & -c_{12}s_{23} - s_{12}s_{13}c_{23}e^{i\delta_{CP}} & c_{13}c_{23} \end{pmatrix}, \qquad (1.33) \end{aligned}$$

where $s_{ij} = \sin\theta_{ij}$ and $c_{ij} = \cos\theta_{ij} (i, j = 1, 2, 3)$. In this parameterization of the mixing matrix, the mixing parameters can take values in the ranges $0 \leq \theta_{ij} \leq \frac{\pi}{2}$ $(i, j = 1, 3; i \neq j)$ and a $\delta_{CP} \neq 0, \pi$ would lead to CP violation. CP violation refers to the phenomenon that particles and antiparticles behave differently under the combined transformations of charge conjugation (C) and parity (P). In the (anti)neutrino oscillation context, this means that the oscillation probabilities for neutrinos and antineutrinos differ. δ_{CP} affects the probability that a neutrino of one flavor will transform into another flavor over a given distance and energy.

The parameters of the matrix are determined in the neutrino oscillation experiments.

In general, the transition probability of oscillation from ν_α to ν_β is given by

$$\begin{aligned} P(\nu_\alpha \to \nu_\beta) &= \delta_{\alpha\beta} - 4 \sum_{i>j} Re\left(U^*_{\alpha i} U_{\beta i} U_{\alpha j} U^*_{\beta j}\right) \sin^2\left(\frac{\Delta m^2_{ij} L}{4E}\right) \\ &+ 2 \sum_{i>j} Im\left(U^*_{\alpha i} U_{\beta i} U_{\alpha j} U^*_{\beta j}\right) \sin\left(\frac{\Delta m^2_{ij} L}{2E}\right), \end{aligned} \tag{1.34}$$

where $\Delta m^2_{ij} = m^2_i - m^2_j$, with $m_{i,j}; (i, j = 1, 2, 3)$ being the mass of the neutrino mass eigenstates. Using the above expression in two dimensions would lead to the oscillation probability obtained in Eq. 1.29.

The experimental evidence for neutrino oscillations implies that neutrinos are massive and that mixing angles and charge-parity (CP) phase, (δ_{CP}) exists in the lepton sector. Moreover, in matter, the oscillation probabilities of neutrinos and antineutrinos change differently due to the differences in coherent forward scattering off electrons in the earth known as the Mikheyev–Smirnov–Wolfenstein (MSW) effect [42, 43]. Let us first understand the CP violating phase δ_{CP}.

Neutrino oscillation experiments are being performed using detectors having moderate to heavy nuclear targets like ^{12}C, ^{16}O, ^{40}Ar, ^{56}Fe, ^{208}Pb, etc. to get a reasonably good number of events. Many current neutrino experiments are collecting data in the few GeV energy ranges ($1 \leq \mathrm{E}_\nu \leq 10$ GeV) for both neutrinos and antineutrinos. This energy region is crucial for studying neutrino oscillation parameters and gaining insight into CP violation in the lepton sector. This is the energy region which is most intriguing (see Fig. 1.6) as it receives contributions from the Quasielastic Scattering (QE), Inelastic Scattering(IE), Shallow Inelastic Scattering (SIS) and Deep Inelastic Scattering (DIS) processes [44].

1.5 (Anti)neutrino Scattering Theory

In the nuclear targets, the interaction takes place with a bound nucleon, where

(i) nucleon being a hadron has a structure, composed of quarks. Theoretically, these structures are understood in terms of form factors. Since neutrino interactions have contributions from both the vector and axial vector part, therefore, we have both vector form factors (the information about which is

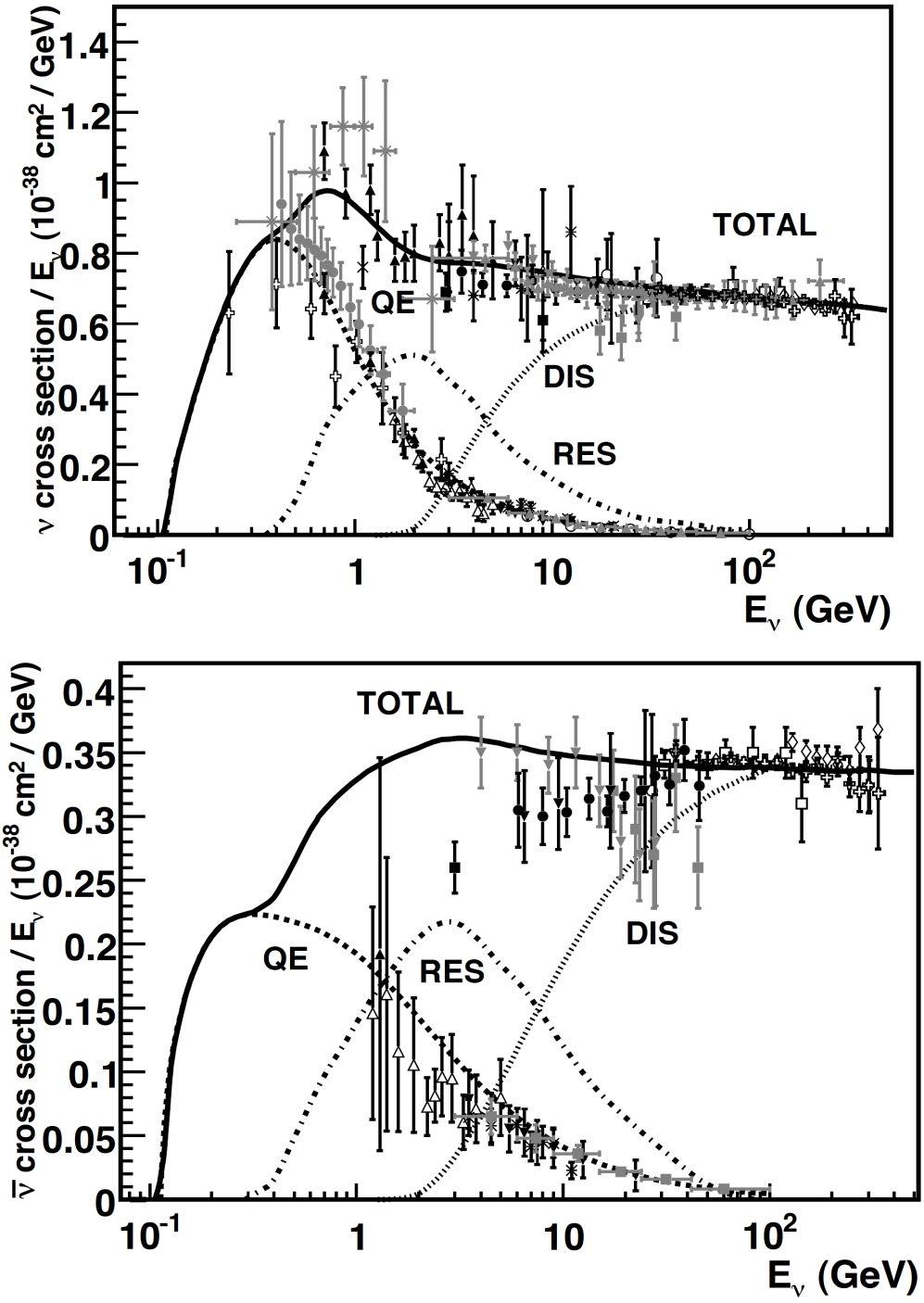

Figure 1.6: Total scattering contribution from the neutrino (upper panel) and antineutrino (lower panel) induced reactions. Figure has been taken from Ref. [45].

obtained from electromagnetic interactions assuming conserved vector current hypothesis) as well as axial vector form factors which have considerable

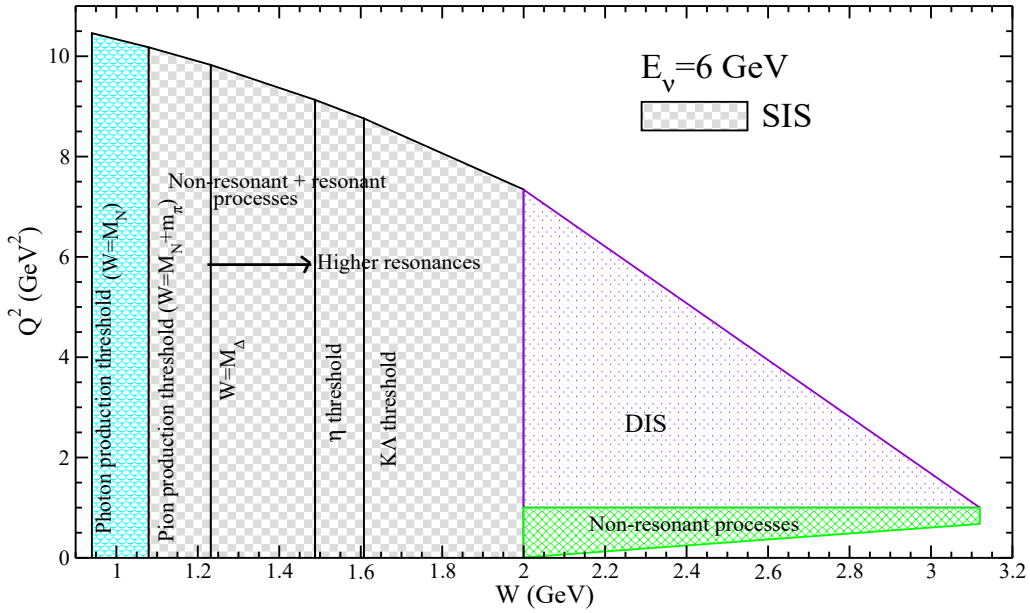

Figure 1.7: Q^2, W plane depicting neutrino-nucleon scattering at two representative laboratory neutrino energies, where $Q^2 \geq 0$ is the negative of the four momentum transfer squared $q^2(\leq 0)$ and W is the center of mass (CM) energy.

uncertainty even at the nucleon level, as the older experiments performed at ANL [46] and BNL [47] to determine axial vector form factors using deuterium targets have large statistical and systematic uncertainties.

(ii) When the nucleons are bound inside the nucleus, nuclear medium effects become important. For example Fermi motion, Pauli blocking, nucleon correlations, final state interaction, etc.

A significant portion of the uncertainty in the systematics arises due to the lack in understanding of these nuclear medium effects. Let us discuss the effects of the presence of a nuclear medium.

1.5.1 Nuclear Medium Effects

Since the (anti)neutrino interactions examined in this thesis occur with nucleons bound within a nucleus, the influence of the surrounding nuclear medium becomes

significant. These medium effects impact both the initial state of the interacting nucleon within the nucleus and the outgoing products of the neutrino interaction as they exit the nucleus. We will first discuss the nuclear medium effects that affect the initial state of nucleons inside the nucleus.

Fermi motion

The most simple and most widely used model that modern-day generators use is the Smith-Monitz Fermi Gas Model [48], where the nucleons inside the nucleus are considered to be non-interacting and are constantly in motion with a momentum $\vec{p}$. These nucleons (fermions) are assumed to move in a constant potential generated due to the presence of other surrounding nucleons and are constrained to have a maximum momentum value of p_F, which can be given in terms of the nuclear density(ρ) as:

$$p_F = (3\pi^2\rho)^{\frac{1}{3}} \tag{1.35}$$

The momentum of a particular nucleon inside the nucleus is defined by using the collective momentum distribution of the nucleons inside the nucleus and is given in terms of a spectral function. The spectral function is obtained by using the wave function of the nucleon in the momentum space $\psi(\vec{p})$, given as:

$$S(\vec{p}, E) \propto \theta(p_F - p)\delta(E - \sqrt{p^2 + m^2} + \epsilon) \tag{1.36}$$

where ϵ is the separation energy and is related to $|\psi(\vec{p})|^2$. Thus, the cross section obtained from the scattering from a nucleon is convoluted with the spectral function. As a result, the scattering peak is not only shifted but also smeared.

Pauli Blocking

In the picture of the nucleus that the Fermi Gas Model takes, all the quantum energy states in the nucleus are occupied from the lowest available state up to the

energy level corresponding to the maximum allowed momentum p_F. This has been depicted in Fig. 1.8. As a result, no interaction is possible with the scattering nucleon in the final state having an energy lower than p_F, because all the lower states are filled, obeying Pauli's exclusion principle, called **Pauli blocked** states. This effect, thus leads to the reduction in the cross section for low momentum transfer scattering regions.

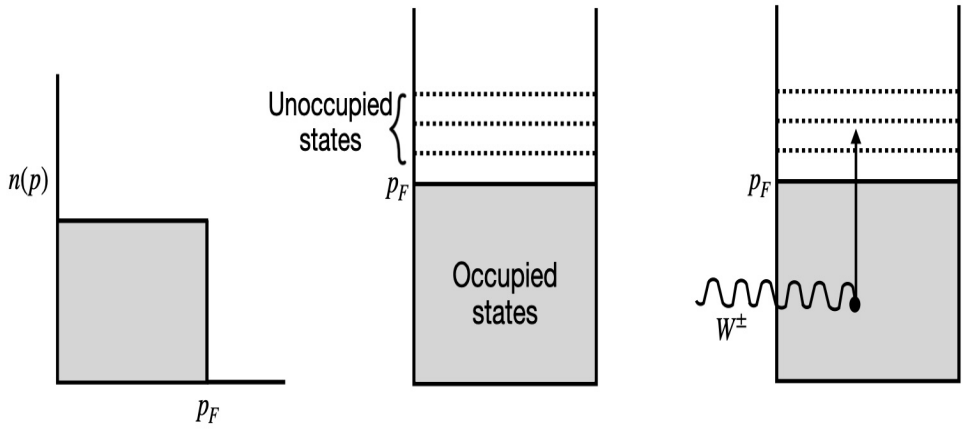

Figure 1.8: Diagram depicting Pauli blocking in the Fermi Gas Model. Reproduced from Ref. [49].

Meson exchange currents (MEC)

Inside the nuclear medium, virtual mesons like $\pi, \rho,\ \eta$ are exchanged between the nucleons. The probes of an interaction viz. photons, W bosons interact with these mesons in flight, which they are being exchanged, giving an additional contribution to both the vector and axial-vector components of the matrix element thus altering the cross section. These are called Meson exchange current (MEC) effects.

Short-range and long-range correlation effects

Due to the constant exchange of the mesons between the nucleons inside the nucleus, the nucleons are correlated. Exchange of heavy mesons like ρ, η, etc.

leads to short-range correlations and the exchange of pions mostly leads to long-range correlation effects. Long-range correlations are handled through the random phase approximation (RPA).

From Fig. 1.8, when an incoming (anti)neutrino interacts with a nucleon in the Fermi sea, it creates a hole in the Fermi sea, and an excited particle above the Fermi sea is created. This is called 1p-1h (one particle-one hole). Similarly, we can have 2p-2h (two particle-two hole) creations during (anti)neutrino interactions with the nucleus. The 2p-2h excitations play a significant role in (anti)neutrino scattering with heavy nuclei, as will be shown in the presented work in this thesis. The 2p2h interaction is said to be present between the quasielastic and the resonant production kinematic region. The 2p2h correlation has been depicted in Fig. 1.9.

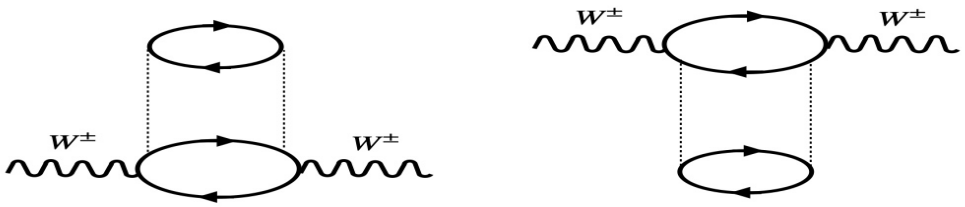

Figure 1.9: Diagram depicting 2p-2h contributions arising due to N-N correlations. Solid(dashed) lines represent nucleon(pion) propagators. Reproduced from Ref. [49].

Let us now discuss the effects of the nuclear medium that alter the final state of the (anti)neutrino nuclear interactions, termed Final state interaction effects (FSI).

Final state interactions

After the (anti)neutrino interacts within the nuclear medium, the final state particles must pass through and exit the nucleus. These outgoing particles can get re-scattered in the process or get absorbed emitting a particle different from the

original particle emitted at the interaction vertex. These effects, called final state interaction effects can alter both the kinematics as well as the multiplicity of the particles in the final state. When talking of these final state effects, we are generally referring to the hadrons in the final state. The first example is a "Quasielastic-like" interaction, where a pion is produced in the final state (through the production of a resonance), but the pion gets absorbed in the nucleus giving a nucleon in the final state, thus mimicking a quasielastic interaction. Thus, it is almost impossible to determine the primary interaction channel, because of the absorption of the pion. The effect increases with the increase in number of atomic nuclei, such that more nuclei are available to absorb the pion. We also call such events as $CC0\pi$ instead of pure $CCQE$ (charged current quasielastic).

Furthermore, the pion can re-scatter (elastically and inelastically) or undergo a charge exchange reaction. Although modeling these effects is very difficult, most generators use the intranuclear cascade model for the simulation of these final-state interaction effects. This has been discussed briefly in Chapter 5.

I have performed an **inclusive** cross section measurement on various nuclear targets at the MINERvA experiment for the analysis presented in this thesis, so let us briefly describe the Quasielastic Scattering (QE), Inelastic Scattering(IE), Shallow Inelastic Scattering (SIS) and the Deep Inelastic Scattering (DIS) processes. The combined contribution of all these channels constitutes an inclusive measurement. To understand the significance of the different processes contributing to the total cross section, in Fig. 1.7, I have shown the different (Q^2, W) regions at the incident neutrino energies of 6 GeV, corresponding to the peak energy of the medium energy mode of the MINERvA experiment.

The Feynman diagrams corresponding to the processes discussed above are shown in Fig. 1.10.

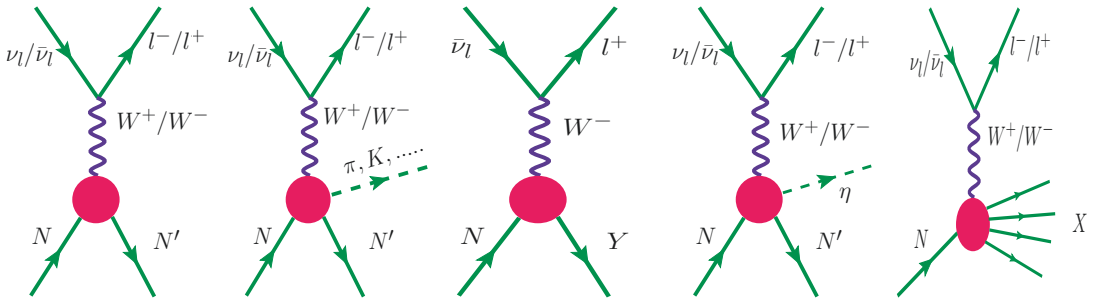

Figure 1.10: Feynman diagram representing(Left to Right) quasielastic scattering process, one pion production, one kaon production, single hyperon production, eta production, and deep inelastic scattering process.

- **Strangeness conserving ($\Delta S = 0$) quasielastic scattering process**
  In the low energy region of neutrinos and antineutrinos (from 0.1 GeV to ~ 1 GeV), the major contribution to the total scattering cross section comes from the quasielastic scattering (see Fig 1.6, $N, N' = n$ or p) where an incoming neutrino or antineutrino interacts with a nucleon and in the final state, a charged lepton, and a nucleon are produced:

$$\nu_l + n \to l^- + p \qquad \text{and} \qquad \bar{\nu}_l + p \to l^+ + n \tag{1.37}$$

- **Strangeness changing ($|\Delta S| = 1$) quasielastic scattering process**
  The antineutrino-induced quasielastic scattering also receives a contribution from the $|\Delta S| = 1$ processes where in the final state a hyperon (Λ, Σ^0 or Σ^-) and an antilepton are produced:

$$\bar{\nu}_l + p \to l^+ + \Lambda \qquad \bar{\nu}_l + p \to l^+ + \Sigma^0 \qquad \bar{\nu}_l + n \to l^+ + \Sigma^-. \tag{1.38}$$

  The $\Delta S = 1$ processes are forbidden in the case of neutrino induced channel due to the $\Delta S \neq \Delta Q$ rule.

- **Inelastic processes**
  As the energy of the incoming (anti)neutrino increases, the four-momentum and energy transferred to the hadronic system increases, which leads to the inelastic scattering resulting not only in the production of a single pion (πN)

in the final state but also to multiple pions $m\pi N$, $m = 2, 3, ..,$ and many other processes like γN, ηN, ρN, KN, $\bar{K}N$ KY, ... in the final states. At low energy transfer i.e. close to the threshold, elementary amplitudes are constrained by the approximate chiral symmetry of QCD, however, as we move away from the threshold region, most of these reactions are dominated by the nucleon and delta resonances, although a significant contribution also comes from non-resonant amplitudes and their interference with the resonant counterpart. For example, in the case of single pion production, $P_{33}(1232)$ (more commonly known as the Δ resonance) has the dominant contribution, however, in the literature, $P_{11}(1440)$, $D_{13}(1520)$, $S_{11}(1535)$, $S_{11}(1650)$, and $P_{13}(1720)$ resonances are also considered [50]. For ηN production, the nucleon resonances which contribute significantly are $S_{11}(1535)$, $S_{11}(1650)$ [51]. For ΛK production, $S_{11}(1650)$, $P_{11}(1710)$, $P_{13}(1720)$, $P_{11}(1880)$, $S_{11}(1895)$, and $P_{13}(1900)$ resonances are dominant [52]. A list of the different nucleon and delta resonances along with their properties like mass, decay width, spin, isposin, branching ratio to the different meson-baryon channel, contributing to the inelastic processes is given in Tables 1.2 and 1.3.

The **Shallow Inelastic Scattering** refers to the processes, dominated by non-resonant contributions, in the kinematic region where Q^2 is small and the invariant mass of the hadronic system, W, is above the pion production threshold. As W increases above the baryon-resonance-dominated region, non-resonant meson production begins to play a significant role. Moreover, with the increase in Q^2, one approaches the onset of the DIS region. This SIS region is poorly understood both theoretically as well as experimentally as this intriguing region encompasses the transition from interactions described in terms of hadronic degrees of freedom to interactions with quarks and gluons described by perturbative QCD. A significant number of events in the MINERvA, NOvA, and the planned DUNE experiment is expected to get a contribution from this region.

We are describing below, in brief, some of the inelastic processes:

Resonance	M_R (GeV)	Γ (GeV)	$I(J^P)$
$P_{11}(1440)$	1.370 ± 0.01	0.175 ± 0.015	$1/2(1/2^+)$
$S_{11}(1535)$	1.510 ± 0.01	0.130 ± 0.020	$1/2(1/2^-)$
$S_{31}(1620)$	1.600 ± 0.01	0.120 ± 0.020	$3/2(1/2^-)$
$S_{11}(1650)$	1.655 ± 0.015	0.135 ± 0.035	$1/2(1/2^+)$
$P_{11}(1710)$	1.700 ± 0.02	0.120 ± 0.040	$1/2(1/2^+)$
$P_{11}(1880)$	1.860 ± 0.04	0.230 ± 0.050	$1/2(1/2^+)$
$S_{11}(1895)$	1.910 ± 0.02	0.110 ± 0.030	$1/2(1/2^-)$
$P_{33}(1232)$	1.210 ± 0.001	0.100 ± 0.002	$3/2(3/2^+)$
$D_{13}(1520)$	1.510 ± 0.005	$0.110 \pm^{0.010}_{0.005}$	$1/2(3/2^-)$
$D_{33}(1700)$	1.665 ± 0.025	0.250 ± 0.05	$3/2(3/2^-)$
$P_{13}(1720)$	1.675 ± 0.015	$0.250 \pm^{0.100}_{0.150}$	$1/2(3/2^+)$
$P_{13}(1900)$	1.920 ± 0.02	0.150 ± 0.05	$1/2(3/2^+)$

Table 1.2: Properties of the spin 1/2 and 3/2 resonances available in the PDG [53], with Breit-Wigner mass M_R, the total decay width Γ, isospin I, spin J, and parity P.

Resonance	Branching Ratios (in %)				
	$N\pi$	$N\eta$	$K\Lambda$	$K\Sigma$	$\pi\pi N$
$P_{11}(1440)$	65	< 1	-	-	34
$S_{11}(1535)$	42	42	-	-	8
$S_{31}(1620)$	30	-	-	-	67
$S_{11}(1650)$	60	25	10	-	22
$P_{11}(1710)$	10	30	15	< 1	-
$P_{11}(1880)$	6	30	20	17	55
$S_{11}(1895)$	10	25	18	13	-
$P_{33}(1232)$	99.4	-	-	-	-
$D_{13}(1520)$	60	-	-	-	30
$D_{33}(1700)$	15	-	-	-	32
$P_{13}(1720)$	11	3	4.5	-	70
$P_{13}(1900)$	10	8	11	5	60

Table 1.3: The central value of the branching ratio of the various nucleon resonances into different meson-baryon like $N\pi$, $N\eta$, $K\Lambda$, $K\Sigma$ and $\pi\pi N$.

i. **One pion production**

At neutrino energies of $\sim$ 1 GeV, the single pion production channel makes a significant contribution to the cross section for charged lepton production and are important processes to be considered in the analysis of oscillation experiments in the few GeV energy region which select charged current inclusive events as signal.

The various possible reactions that may contribute to the single-pion production either through a charged current or neutral current (anti)neutrino-induced reaction on a nucleon target are the following:

Charged current (CC) induced processes:

$$\begin{aligned} &\nu_l p \to l^- p\pi^+ && \bar{\nu}_l n \to l^+ n\pi^- \\ &\nu_l n \to l^- n\pi^+ && \bar{\nu}_l p \to l^+ p\pi^- \\ &\nu_l n \to l^- p\pi^0 && \bar{\nu}_l p \to l^+ n\pi^0 \qquad ;\ l = e, \mu \end{aligned} \tag{1.39}$$

and neutral current (NC) induced processes:

$$\begin{aligned} &\nu_l p \to \nu_l n\pi^+ && \bar{\nu}_l p \to \bar{\nu}_l p\pi^0 \\ &\nu_l p \to \nu_l p\pi^0 && \bar{\nu}_l p \to \bar{\nu}_l n\pi^+ \\ &\nu_l n \to \nu_l n\pi^0 && \bar{\nu}_l n \to \bar{\nu}_l n\pi^0 \\ &\nu_l n \to \nu_l p\pi^- && \bar{\nu}_l n \to \bar{\nu}_l p\pi^-. \end{aligned} \tag{1.40}$$

Moreover, in experiments that select the quasielastic production of charged leptons as the signal for the analysis of oscillation experiments, single pion production channel gives rise to background contribution. For example, neutral current-induced neutral pion production contribute to the background in ν_e-appearance oscillation experiments, while charged current events producing charged pions, contribute to the background in $\nu_\mu-$disappearance experiments. When these processes take place in a nuclear target, the pion events get reduced considerably due to the nuclear medium effects (due to pion absorption in the nuclear medium), or change its identity through the

rescattering processes like $\pi^- p \to \pi^o n$, etc. Due to the pion absorption in the nuclear medium, the events mimic quasielastic reactions, thus, known as quasielastic-like events.

ii. **Multiple pion production**

Instead of a single pion, multiple pions may also be produced in (anti)neutrino induced processes, for example:

$$\nu_l(\bar{\nu}_l) + N \to l^-(l^+) + N' + m\pi, \quad \text{where} \quad m = 2, 3, .. \tag{1.41}$$

iii. **Kaon production**

The primary reactions for the (anti)neutrino induced charged current kaon production are:

$$\begin{aligned} \nu_l + p &\to l^- + K^+ + p & \bar{\nu}_l + p &\to l^+ + K^- + p \\ \nu_l + n &\to l^- + K^0 + p & \bar{\nu}_l + p &\to l^+ + \bar{K}^0 + n \\ \nu_l + n &\to l^- + K^+ + n & \bar{\nu}_l + n &\to l^+ + K^- + n\ . \end{aligned} \tag{1.42}$$

iv. **Eta production**

The fundamental reaction for CC (charged current) eta production induced by (anti)neutrinos is:

$$\nu_l + n \to l^- + \eta + p \qquad \bar{\nu}_l + p \to l^+ + \eta + n \tag{1.43}$$

v. **Associated particle production**

The primary reactions for (anti)neutrino-induced associated particle production are:

$$\begin{aligned} \nu_l + n &\to l^- + K^+ + \Lambda & \bar{\nu}_l + p &\to l^+ + K^0 + \Lambda \\ \nu_l + p &\to l^- + K^+ + \Sigma^+ & \bar{\nu}_l + p &\to l^+ + K^0 + \Sigma^0 \\ \nu_l + n &\to l^- + K^+ + \Sigma^0 & \bar{\nu}_l + p &\to l^+ + K^+ + \Sigma^- \\ \nu_l + n &\to l^- + K^0 + \Sigma^+ & \bar{\nu}_l + n &\to l^+ + K^0 + \Sigma^-, \end{aligned} \tag{1.44}$$

where a strange meson and a strange baryon are produced with opposite strangeness.

- **Deep inelastic scattering process**

  In a DIS process, the energy and Q^2 transferred to the target are large, such that the nucleon loses its identity, and a jet of hadrons is produced. In DIS, a neutrino interacts with a quark inside a bound nucleon producing a charged lepton and multiple hadrons, instead of a nucleon in the final state. Thus, the interaction is described in terms of quarks and gluons using perturbative QCD.

An (anti)neutrino-induced inclusive scattering process on a free nucleon target can be described by the reaction:

$$\nu_l(k)/\bar{\nu}_l(k) + N(p) \rightarrow l^-(k')/l^+(k') + X(p') \quad l = e, \mu \tag{1.45}$$

where k and k' are the four momenta of incoming and outgoing lepton, p and p' are the four momenta of the target nucleon and particle(s) in the final state, respectively.

The process given in Eq. 1.45 is mediated by the W-boson ($W^{\pm}$) and the invariant matrix element corresponding to the reaction given in Eq. 1.45 is written as:

$$-i\mathcal{M} = \frac{iG_F}{\sqrt{2}}\, l_\mu \left(\frac{M_W^2}{q^2 - M_W^2}\right) \langle X|J^\mu|N\rangle \,, \tag{1.46}$$

where G_F is the Fermi coupling constant, M_W is the mass of W boson, and $q^2 = (k - k')^2$ is the four momentum transfer square. l_μ is the leptonic current and $\langle X|J^\mu|N\rangle$ is the hadronic current for the neutrino-induced reaction (shown in the rightmost part of Fig. 1.10).

The four momentum transfer squared $Q^2 = -q^2 \geq 0$ is expressed in terms of the energy of the incoming neutrino (E_ν), the energy of the outgoing muon (E_μ), and the angle of the outgoing muon (θ_μ) as:

$$Q^2 = 4E_\nu E_\mu sin^2\frac{\theta}{2}, \quad q^2 = -Q^2. \tag{1.47}$$

Also, the invariant mass of the hadronic system can be written in terms of the

four-momentum of the particles involved as:

$$W^2 = p_X^2 = (k + p - k')^2$$

which in the lab frame is written as:

$$W^2 = 2M_N E_{had} + M_N^2 - Q^2.$$

or

$$W = \sqrt{2M_N E_{had} + M_N^2 - Q^2} \tag{1.48}$$

The other kinematical variables relevant for an inclusive scattering process are the energy transfer to the hadronic system, ν defined as

$$\nu = E_\nu - E_\mu, \tag{1.49}$$

the bjorken variable x, which is the fraction of the proton momentum carried by the struck quark

$$x = \frac{Q^2}{2M_N \nu}, \tag{1.50}$$

and the inelasticity y, given by

$$y = \frac{\nu}{E_\nu}. \tag{1.51}$$

The variables x and y are dimensionless, and, therefore are known in the literature as the scaling variables.

1.6 Motivation: Why (Anti)neutrino Cross Sections?

Neutrino physics has made significant progress, yet there are still challenges that remain. The primary focus in the field today is on accurately measuring neutrino oscillations. (Anti)neutrino cross section measurements are crucial in mitigating the outstanding challenges in the field of (anti)neutrino oscillation physics, leading to the precise determination of neutrino oscillation parameters. Let us see how cross section measurements can help.

1. **Reducing systematic uncertainties**

   Since the (anti)neutrino oscillation experiments rely on precise predictions of the (anti)neutrino interactions in the detector, any uncertainties in the neutrino interaction model propagate into the uncertainties in the oscillation parameter measurements. A large portion of the systematic uncertainties in the determination of these parameters, comes from cross section uncertainties. These uncertainties in the cross section come from the underlying interaction models that the neutrino generators implement. Inclusive cross section measurements offer a more comprehensive understanding of total interaction rates, which in turn can help refine interaction models, by reducing biases in the interaction models, thereby lowering the systematic uncertainties.

2. **Better understanding of nuclear effects**

   Nuclear medium effects, including the short-range nucleon-nucleon correlations and the final state interaction effects (FSI), contribute significantly to the uncertainty in the (anti)neutrino-nucleus interaction cross section. Nuclear medium effects can alter the final state particles seen in the detector. Inclusive cross section measurements, sum over all the possible final states, and hence provide a direct way to quantify the overall impact of these nuclear effects. In contrast to exclusive analyses, which look at a specific interaction channel, inclusive analysis provides a more stable reference for adjusting underlying models to account for these nuclear medium effects. The upcoming (anti)neutrino oscillation experiment DUNE, will be using liquid argon, and hence the nuclear medium effects due to the presence of heavy nuclei will be relevant.

   The cross section measurement at the MINERvA experiment, presented in this thesis aims to measure the nuclear dependence of the (anti)neutrino interactions, using nuclear targets of different sizes, viz. iron, carbon, lead, and scintillator, in the same (anti)neutrino beam, thus giving a direction quantification of these effects with reduced detector and flux uncertainties.

3. **Improving neutrino energy reconstruction**

   Oscillation experiments need an accurate reconstruction of the energy of (anti)neutrinos but need models for that process. Also, not all particles produced in an (anti)neutrino interaction, leave energy in the detector. The reconstruction of the initial state interaction (anti)neutrino energy becomes complicated due to the above-mentioned nuclear effects, such that the outgoing particle does not always correlate with the initial (anti)neutrino energy. Data from inclusive cross section measurements can be used to benchmark and improve the models used for the prediction of the (anti)neutrino interactions. This improvement directly translates to the mitigation of energy reconstruction errors in the neutrino oscillation experiments as well.

4. **Model validation and constraint**

   Inclusive cross section measurements serve as a robust benchmark for the validation and refinement of interaction models across the entire kinematic range accessible in a given neutrino experiment. Inclusive cross section measurements presented in this thesis, provide data in the $\langle 6\ GeV \rangle$ average (anti)neutrino energy region, on various nuclear targets like iron, carbon, lead, and hydrocarbon (scintillator). The data from the cross section measurement can be used as a constraint to tune the interaction models, which can be used by future neutrino experiments. Inclusive measurement in particular helps in the way that future neutrino experiments, with diverse detection strategies, can use these tuned models with the assurance that the model prediction remains consistent across different kinematic regions.

Various (anti)neutrino oscillation parameters like CP violating phase (δ_{CP}), mixing angle θ_{23}, and mass squared splitting Δm^2_{31} or Δm^2_{32}, which have not been determined precisely so far, are sensitive to the energy region in which we make our cross section measurement. Overall, inclusive (anti)neutrino-nucleus cross section measurements will act as a cornerstone of neutrino oscillation physics.

MINERvA was a dedicated neutrino and antineutrino cross section measurement experiment and used (anti)neutrino beams in the two energy runs *viz.* the low energy run (the peak of which lies $\sim$ 3 GeV) and the medium energy run (the peak lies at $\sim$ 6 GeV). The analysis presented here used the medium energy dataset. The main advantage of the MINERvA detector is that it uses several nuclear targets like ^{4}He, ^{12}C, ^{16}O, ^{56}Fe and ^{208}Pb in the same neutrino beam. This is advantageous because these different nuclear targets in the same beam will help in the direct measurement of nuclear effects with reduced flux and detector uncertainties. MINERvA aims to perform EMC (European Muon Collaboration experiment using charged lepton beam on several nuclear targets) kind of measurements to understand the nuclear medium effects in both the neutrino as well as antineutrino modes in the wide region of bjorken scaling variable x, and the four-momentum transfer squared Q^2, covering the quasielastic, inelastic, and the deep inelastic scattering regions. In the medium energy mode, of $\langle E_\nu \rangle \sim 6$ GeV, MINERvA has very high statistics for cross section measurements on different nuclear targets in the same neutrino beam, one of the highest in all the accelerator-based neutrino experiments around the globe. The details of the experimental setup have been discussed in Chapter 2.

The plan for this thesis is discussed below:

In Chapter 2, we introduce the experimental setup of the MINERvA detector, by first introducing the Fermilab's NuMI (Neutrinos at the Main Injector) beam which is a source of neutrinos and antineutrinos to the MINERvA, MINOS, and NOvA detectors for the cross section and oscillation measurements. We then discuss in detail the MINERvA detector and how the different aspects of physics, electronics, engineering, and computing come together to make the experiment possible.

In Chapter 3, we discuss how the different interactions that happen inside the MINERvA detector are converted to actual physical observables from the

electronic signal that the MINERvA detector records. The chapter also discusses the simulation used to predict the (anti)neutrino interactions inside the detector volume.

Chapter 4 explains the details of the analysis procedure, and how the cross section is extracted for the antineutrino interactions inside the MINERvA detector with the various nuclear targets and the scintillator material. All the different steps that are involved including the selection of desired events, subtraction of background events, correction for acceptance in the MINOS near detector (of the muon), unfolding the distribution to minimize event smearing, and then finally extracting the cross section, are discussed.

In Chapter 5, we have discussed in detail the various sources of systematic errors in the analysis.

Chapter 6 discusses the measured cross section results and concludes the presented analysis.

Chapter 2

The MINERvA experiment

Dare I say that experimental physicists will not have sufficient ingenuity to make neutrinos? Whatever I may think, I am not going to be lured into a wager against the skill of experimenters under the impression that it is a wager against the truth of a theory. If they succeed in making neutrinos, perhaps even in developing industrial applications of them, I suppose I shall have to believe—though I may feel that they have not been playing quite fair [54].

— **Sir Arthur Stanley Eddington**

(One of the first to suggest (1917) conversion of matter into radiation powered the stars)

When Pauli initially proposed the neutrino, he said it is "a particle that can't be detected" [2]. The assumption is reasonable, as the neutrino is extremely tiny (100,000s of times smaller than an electron [55]) and electrically neutral. Even when it required building colossal detectors and venturing deep underground to shield the experiment from cosmic noise, the human quest for knowledge has been relentless, undeterred by these challenges. Despite its ghost-like nature, scientists around the globe have harnessed their collective ingenuity to indirectly detect these enigmatic particles. One such collaborative effort is the MINERvA experiment.

MINERvA (Main INjector ExpeRiment: ν-A) is a dedicated (anti)neutrino scattering experiment using a fine-grained on-axis detector, in the NuMI beamline (discussed in the following section), sitting 100 meters underground on-site at Fermilab in Batavia, Illinois. The primary goals of the experiment are (anti)neutrino cross section measurements and probing nuclear medium effects essential to present and future neutrino experiments. Firstly, we will examine how the (anti)neutrinos are produced.

2.1 The NuMI beamline

Several different sources of (anti)neutrinos are used for different experiments around the globe. These include solar neutrinos, produced by nuclear fusion reactions inside the sun, and atmospheric neutrinos which are produced when cosmic rays (high energy atomic nuclei) interact with earth's atmosphere producing mesons which then decay to give neutrinos. Antineutrinos are produced in fission reactions inside nuclear reactors. Another way to produce (anti)neutrinos is by using particle accelerators, which has been done for this analysis. The NuMI (Neutrinos at the Main Injector) [56, 62] beam consisting of accelerator neutrinos, utilizes the Main Injector accelerator at Fermilab. This beam is used by the oscillation experiments MINOS [58, 59] and NOvA [60] as well as MINERvA. To make the beam of (anti)neutrinos, 120 GeV protons from the Fermilab's Main Injector accelerator are bombarded onto a narrow 1-meter-long graphite target. Fig. 2.1 and 2.2 show a comprehensive illustration of the beamline facility at Fermilab.

2.1.1 The Proton Beam

To make the 120 GeV proton beam, a series of accelerators are used consecutively, which increase the energy of the beam. The process starts with hydrogen gas, which is ionized using a high-voltage arc to produce H^- ions. These H^- ions

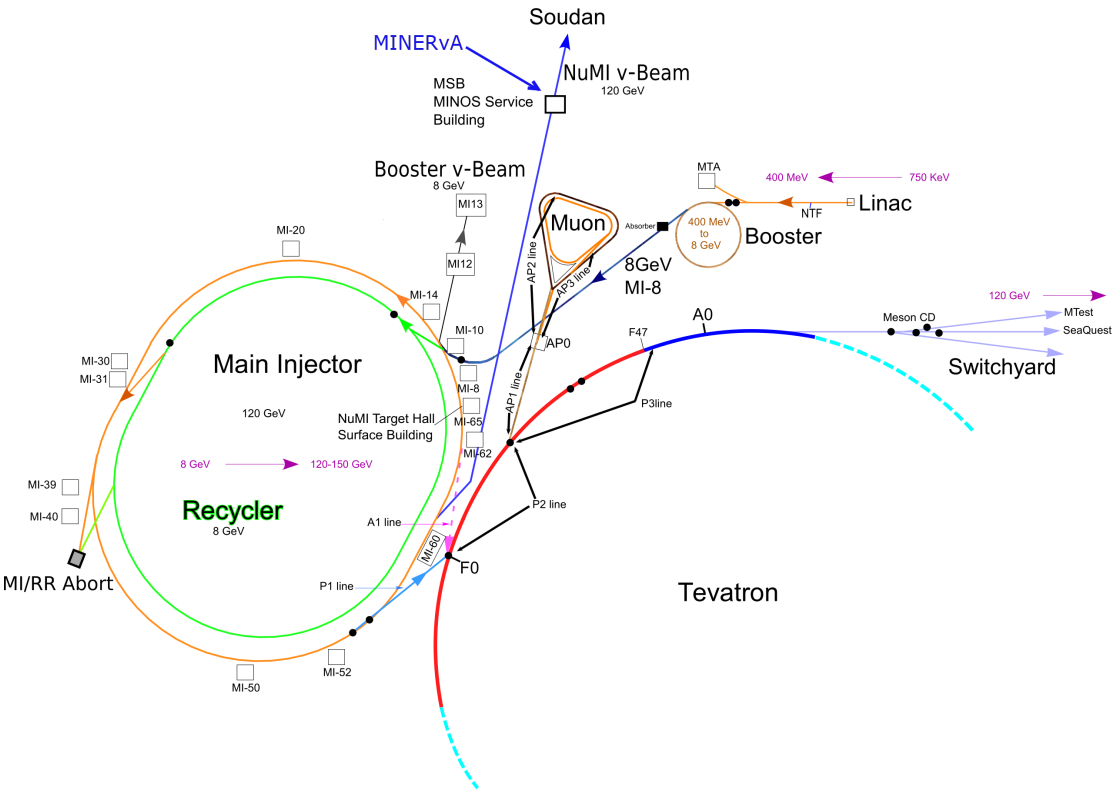

Figure 2.1: A bird's eye view schematic of the Fermi National Accelerator complex, where MINERvA is located near the MINOS service hall. Figure taken from Ref. [62].

are injected into the linear accelerator (Linac) where they are accelerated to 400 MeV [62]. From here, the ions are delivered to the Booster synchrotron having a radius of about 75 metres, where a carbon foil strips off the extra electrons and a proton beam is formed. The booster accelerates the protons to 8 GeV, which are separated into 84 bunches. Each of these bunches contains about 3^{10} protons and is separated by 53 MHz (19 ns). These proton batches from the Booster are then injected into the Recycler, 7 times in circumference than that of the booster. It can hold up to 7 bunches of protons, with six being filled up and one left empty for proton injection. In the medium energy era, which this analysis is based on, a process called "split stacking" was employed in which two proton batches were clubbed into a single batch space, which doubles the proton intensity. After undergoing this process of split stacking, the proton batches are

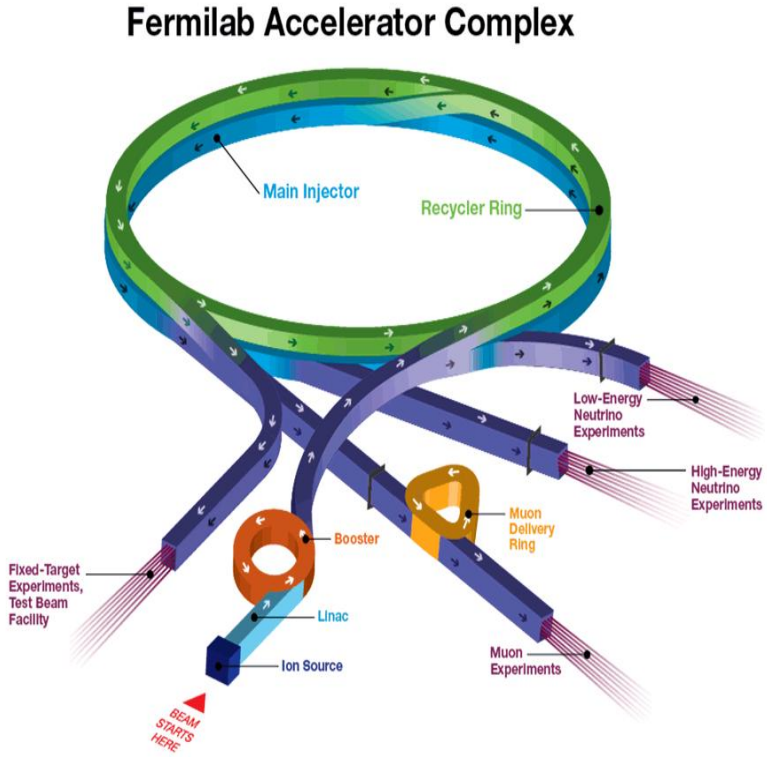

Figure 2.2: The Fermilab accelerator complex depicting the relevant components for the NuMi beamline. Figure taken from Ref. [61].

injected into the main injector, where they are accelerated from 8 GeV to 120 GeV. A *spill* of protons, corresponding to 5-6 of these proton bunches (depending on what other experiments are running at the time) is extracted and spilled onto a graphite target in the NuMI target hall, located 41m underground at Fermilab, every 2.2 seconds. The beam is oriented downwards at an angle of 3.343^0 to the horizontal. This is to align the beam to the MINOS far detector, 734 km away in the Soudan mine in Minnesota, half a mile underground. This induces a 3.343^0 discrepancy between the MINERvA detector axis and the beam. The schematic diagram of the NuMI beam is shown in Fig. 2.3.

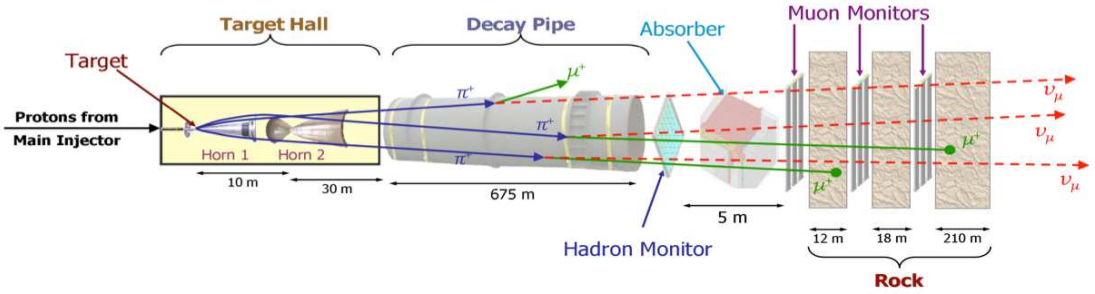

Figure 2.3: Schematic of the NuMI beam. Reprinted from Ref. [62].

2.1.2 NuMI Target [62]

This 400 kW power beam has the potential to destroy expensive components inside the NuMI target hall, if not steered correctly. This is taken care of by a device called the baffle, a narrow tube that can degrade the beam if it is misaligned. It can withstand the full intensity of the beam for short periods, thus protecting components like the target and horn 1 which are most vulnerable. Fig. 2.4 shows the different components of the NuMI baffle. The left figure shows the components of the baffle and the right one shows the Baffle, cooling systems, and the target in place.

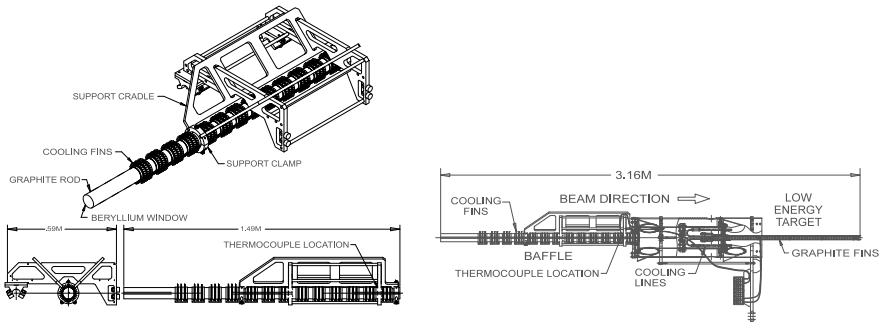

Figure 2.4: Different components of the NuMI baffle. Reproduced from Ref. [62].

The medium energy (ME) NuMI target is made using 24x63x7.4 mm fins, each 0.5 mm apart. The interaction of protons with the graphite fins induces hadronic production, mostly mesons which decay to give neutrinos. The number of protons

striking the graphite target is referred to as "protons on target" (POT) and the number of neutrinos produced is proportional to the POT. This small size of the target limits meson re-scattering, which could increase the uncertainty in how well we know our (anti)neutrino flux. The position of the target with respect to the focusing horn can be changed, using the target carrier system.

Magnetic horns are used to focus negatively or positively charged decay products (mostly pions) to selectively produce a beam of neutrinos or antineutrinos when these mesons further decay, as can be seen from the decay reactions in Table 2.1.

2.1.3 Focusing Horns

The mesons (pions and kaons) thus produced are focused using a pair of aluminum horns, each 368 cm long. Horn 1 has an outer diameter of 35 cm and Horn 2 has an outer diameter of 79 cm. As shown in Fig. 2.5, these magnetic horns are funnel-shaped and their narrowest opening is called the neck of the horn. The

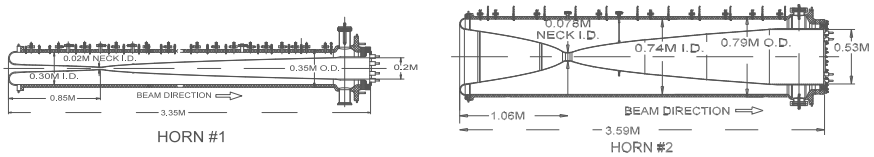

Figure 2.5: Schematic of the magnetic horns. Taken from Ref. [62].

horns comprise concentric inner and outer conductors made of aluminum. The horns are pulsed with a 200 kA half sinusoidal current at the outer conducting surface, producing a toroidal magnetic field of up to 3T between inner and outer conductors, perpendicular to the direction of the beam. The direction of the current can be changed to produce the forward horn current (FHC) or the reverse horn current (RHC) configuration, which selectively focuses positively charged

particles (π^+), producing neutrino beam and negatively charged particles (π^-) producing antineutrino beam, respectively.

It is important to note that particles passing inside the inner conductor experience no magnetic field, and hence will remain in the beam leading to contamination. These are mostly particles that are highly energetic, with large forward momenta. This implies that the wrong-sign (neutrinos in an antineutrino sample) contamination is the highest at high energies. This issue is more prominent in the antineutrino beam since the interaction of the proton colliding with graphite produces more π^+ than π^-. Thus at higher energies, there is a lot of wrong sign contamination in our beam, and is a source of systematic uncertainty in the cross section measurement at the MINERvA experiment. This analysis utilizes the reverse horn configuration (RHC) to obtain an antineutrino ($\bar{\nu}_\mu$) beam.

2.1.4 Meson Decay

The bombardment of the protons onto the graphite target produces mostly pions and kaons. After passing through the horns, these particles (mostly pions, some kaons, residual protons) then move to a 675-meter-long decay pipe, 2 meters in diameter, as shown in Fig. 2.3. It is filled with helium gas at atmospheric pressure, to protect against corrosion. This length is sufficient for accommodating the decay of a 10 GeV pion. The various decay modes of these pions and kaons are shown in Table 2.1. These mesons dominantly decay to give muon type (anti)neutrinos, with a slight component of electron type (anti)neutrinos, coming from kaons (K^+ and K^0 decays) and tertiary muon decays. 97% of muon (anti)neutrinos come from pion decays and the rest from kaon decays. As can be seen from Table 2.1, the mesons decay to give us a beam of (anti)neutrinos. This beam still has contamination in the form of undecayed particles and muons, which need to be absorbed to give us a pure beam of muon-type (anti)neutrinos.

Decay	Channel	Branching Ratio (%)
1	$\pi^{\pm} \rightarrow \mu^{\pm} + \nu_{\mu}(\bar{\nu}_{\mu})$	99.9877
2	$\pi^{\pm} \rightarrow e^{\pm} + \nu_{e}(\bar{\nu}_{e})$	0.0123
3	$K^{\pm} \rightarrow \mu^{\pm} + \nu_{\mu}(\bar{\nu}_{\mu})$	63.55
4	$K^{\pm} \rightarrow \pi^{0} + e^{\pm} + \nu_{e}(\bar{\nu}_{e})$	5.07
5	$K^{\pm} \rightarrow \pi^{0} + \mu^{\pm} + \nu_{\mu}(\bar{\nu}_{\mu})$	3.353
6	$K^{0}_{L} \rightarrow \pi^{\pm} + e^{\mp} + \nu_{e}$	40.55
7	$K^{0}_{L} \rightarrow \pi^{\pm} + \mu^{\mp} + \nu_{\mu}$	27.04
8	$\mu^{\pm} \rightarrow e^{\pm} + \nu_{e}(\bar{\nu}_{e}) + \bar{\nu}_{\mu}(\nu_{\mu})$	100.0

Table 2.1: Dominant decay modes of the particles produced from the proton spill onto the graphite target. The branching ratio gives the probability that a decay happens through that channel. Reproduced from Ref. [63].

2.1.5 Absorption

The hadron absorber lies downstream of the decay pipe, as shown in Fig. 2.3. It is made up of aluminum steel and concrete and removes undecayed pions and kaons as well as non-interacting protons from the beam. (Anti)muons and (anti)neutrinos pass through unaffected. 80 cm upstream of the absorber, sits the hadron monitor. It monitors the hadronic content of the beam, and hence the status of the NuMI target (which needs to be replaced multiple times due to radiation damage). Downstream of the absorber, muons are absorbed by 240 m of dolomite rock. Different chambers have been carved in these rocks, and contain muon monitors, to check the muon content in the beam. Each of these monitors is 2.3 m square, consisting of a 9x9 array of ionizing chambers. Different energy muons range out at different lengths inside the rock.

The (anti)neutrino beam can produce (anti)muons after interacting with the rock and these muons can enter the MINERvA detector along with the (anti)neutrino beam. These are called rock muons. The veto walls in front of the MINERvA

detector take care of these rock muons.

Fig. 2.6 shows the fluxes for (anti)neutrinos in the low energy (LE) and the medium energy (ME) era. It can be seen from the figure that there was a significant jump in the statistics (roughly 10 times) when MINERvA moved from the LE to the ME beam.

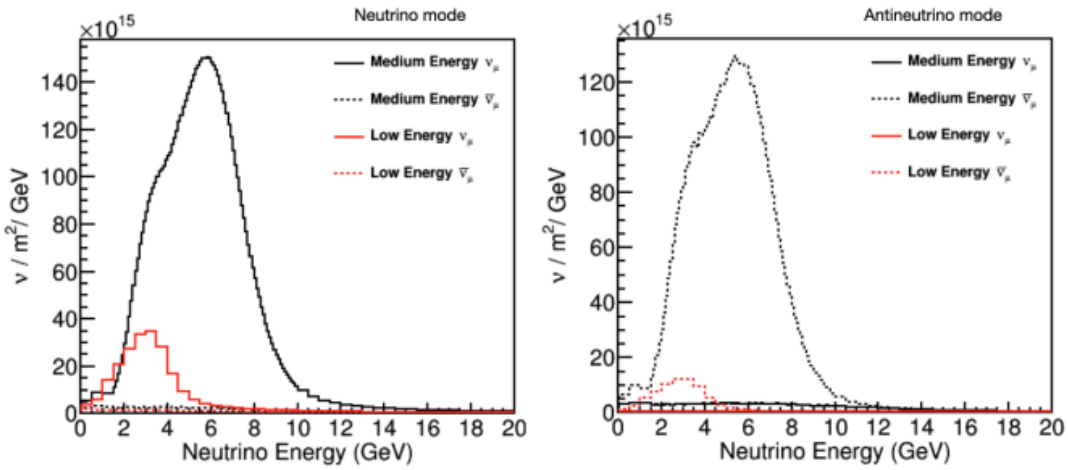

Figure 2.6: FHC (left) and RHC (right) fluxes, for the LE and ME beams for MINERvA experiment. Figure taken from Ref. [64].

2.2 The MINERvA detector

To understand the workings of the MINERvA detector, let us take a simple analogy.

Let us consider we are in a dark room. We have a unique sheet of paper coated with a special paint that glows when it is touched by invisible particles, like tiny, magical fireflies. These fireflies represent high-energy particles that we can't see with our eyes, which move extremely fast.

In this dark room, every time one of these magical fireflies lands on the painted paper, it makes a small spot of light. This glowing spot is extremely brief but

bright enough for you to notice and record. The paper acts like a canvas capturing the arrival of each firefly. Extending this analogy:

- **Scintillator Detector:** The special paint on the paper is like the scintillating material in the detector. When high-energy particles (like the magical fireflies) pass through the scintillator, it emits light (just like the glowing spots on the paper).
- **Photomultiplier Tubes (PMTs):** Consider we have a super-sensitive camera that can see even the faintest glows on the paper. This camera represents the photomultiplier tubes. Now, if this camera is set for long exposure, it amplifies the faintest glows of light produced by the painted paper. This is similar to how the PMTs amplify the signals captured by the scintillator.
- **Electronics and Data Recording:** After your camera captures the glowing spots, a computer records the time and position of each spot, just like how the electronics in a scintillator detector record the events.
- **Particle Identification:** By analyzing the pattern and intensity of the glowing spots, you can figure out how many fireflies landed on the paper, how energetic they were, and what different breeds of fireflies landed on the paper, some more massive than the others (different particles being identified in the detector). Similarly, in a scintillator detector, MINERvA analyzes the light signals to identify and measure the energy of the particles that pass through.

MINERvA experiment is the first of its kind, in the sense that it measures cross section on different nuclear targets like iron, carbon, lead, and water in the same (anti)neutrino beam. Targets with a wide range of nucleon numbers (A) have been chosen to study the nuclear dependence of (anti)neutrino interactions. MINERvA aims at reducing uncertainties in cross section measurements which can help future neutrino oscillation experiments and help benchmark future neutrino models.

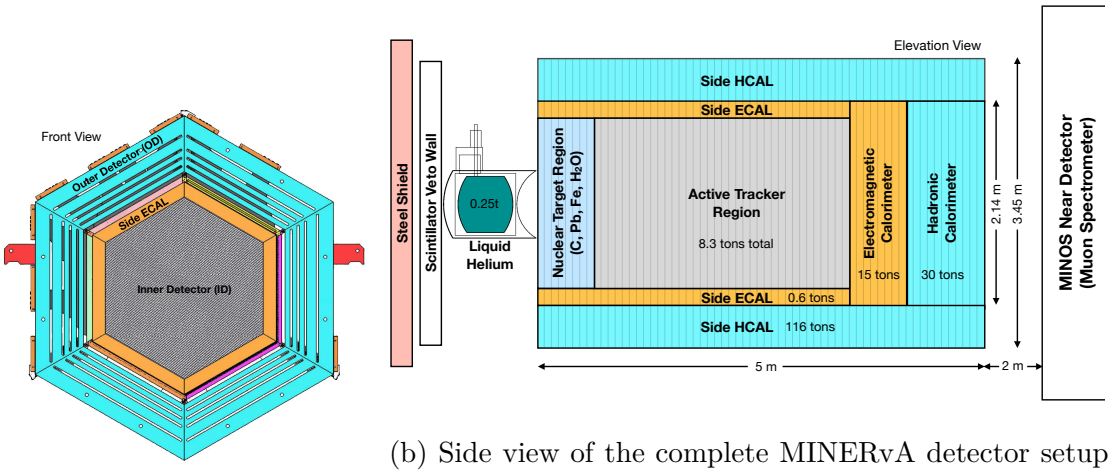

(a) Top View: Single module of the MINERvA detector

(b) Side view of the complete MINERvA detector setup showing the nuclear targets, tracker region and the calorimeter regions.

Figure 2.7: Schematic of the MINERvA detector. Taken from Ref. [65]. The beam enters from the left side of Fig. 2.7(b).

Up to two planes of scintillator are mounted on a frame to constitute a "module", as shown in Fig. 2.7(a). 120 such modules come together to constitute the MINERvA detector, as shown in Fig. 2.7(b). Each module is composed of an inner detector (ID) and an outer detector (OD). The ID is composed of an initial section with active scintillator planes alternating with passive nuclear targets. This is followed by a tracking region made purely of scintillator planes. The active tracker region consists of 62 modules in total. After that, there's a downstream electromagnetic calorimeter (ECAL), and finally, a hadronic calorimeter (HCAL). The OD primarily consists of a heavy steel frame, integrated with scintillator planes, functioning both as a calorimeter and as a support structure for the detector. As shown in Fig. 2.7(b), upstream of the main detector lies the steel shield, veto wall, and a liquid helium target. The helium target was not used for this analysis. 2 m downstream of the MINERvA detector is the MINOS near detector, which functions as a muon spectrometer. The beam enters the detector from the left side in Fig. 2.7(b) and traverses towards MINOS.

The center of the hexagonal modules is treated as the center for MINERvA co-

ordinate system and the z-axis is horizontal, pointing downstream towards MINOS near detector, along the detector axis in Fig. 2.7(b). The downstream surface of the veto wall is located at z = 4 cm and the front face of MINOS is located at z = 1200 cm. The x-axis is horizontal, pointing right to left and the y-axis is vertical, pointing up along the hexagonal cross section of each module as shown in Fig. 2.7(a). As mentioned earlier, there is a 3.343^0 offset between the beam axis and z-axis of MINERvA.

2.2.1 Scintillator Mechanism and Setup

A total of 127 "strips" of polystyrene scintillator with a triangular cross-section, doped with PPO (2,5-diphenyloxazole) and POPOP (1,4-bis(5-phenyloxazol-2-yl)-benzene) each coated with titanium dioxide (TiO_2) constitute a scintillator plane. The TiO_2 coating is reflective and has a high refractive index. Hence, by scattering and reflecting the scintillator light, it helps improve the overall light collection efficiency of the scintillator. PPO acts as the primary fluor in the scintillator. When a high-energy charged particle interacts with the polystyrene matrix, it excites the polystyrene molecules. These molecules then transfer their excitation energy to the PPO molecules. The excited PPO molecules return to their ground state by emitting light in the ultraviolet (UV) region (357 nm). This initial light emission is a key step in the scintillation process. POPOP functions as a secondary fluor or wavelength shifter. The UV light emitted by the excited PPO molecules is absorbed by POPOP molecules. POPOP re-emits the absorbed light at a longer wavelength, typically in the violet region (410 nm) of the visible spectrum. This wavelength shift to the violet region (longer wavelength) reduces the likelihood of reabsorption in the polystyrene matrix thereby increasing the light collection efficiency and overall light yield. The strips vary from 122 to 245 cm in length, depending on their position in the plane. The scintillator strips are interlocked in an alternating arrangement as shown in Fig. 2.8. This makes sure that the charged particle passes through at least two scintillator strips when passing through a

plane and improves position resolution for each plane. Epoxy is used to glue the strips together to form a scintillator plane. The scintillator planes have elemental compositions of 7.42% H, 87.6% C, 3.18% O, 0.26% Al, 0.27% Si, 0.55% Cl, and 0.69% Ti.

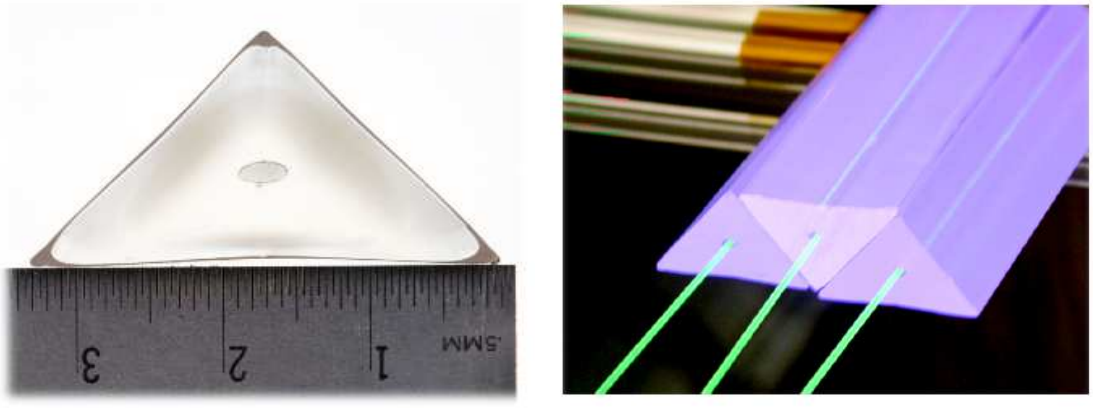

Figure 2.8: Scintilltor strips at MINERvA and their arrangement to constitute a plane, reprinted from Ref. [65].

The scintillator strips in different planes are placed in three different orientations, namely X, U, and V. The X orientation is vertical, parallel to the y-axis and the U and V configurations have a 60^0 offset in the clockwise and anticlockwise direction, respectively, along the vertical axis. These orientations are shown in Fig. 2.9. This helps MINERvA to reconstruct three-dimensional tracks of particles traversing the detector. A module that contains two planes of scintillator, can have them in either UX or VX configuration. The active tracker region consists of 62 modules in total. The outer edges of each scintillator plane are covered by a 2 mm thick lead collar labeled side ECAL in orange color in Fig. 2.7(a). It is used to contain the electromagnetic showers produced by particle interactions inside the detector.

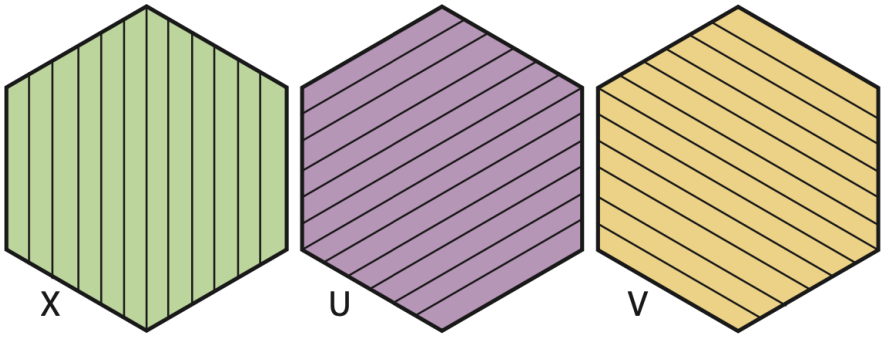

Figure 2.9: A demonstration of the X, U, and V orientations of scintillator strips in the ID (inner detector) x-y plane. Figure taken from Ref. [67].

2.2.2 Photomultiplier Tubes (PMTs): light flashes to electric signals

In the center of each scintillator strip, a wavelength shifting (WLS) fiber is placed, as shown in Fig. 2.8. These are optical fiber cables doped with wavelength-shifting molecules. These molecules have a high absorption coefficient for the near UV and blue light produced by the scintillators and get excited to higher energy states upon absorption. These molecules return to the ground state re-emitting longer wavelengths (typically light in the green region of the visible spectrum). This light gets trapped inside the fiber, by total internal reflection and travels toward the other end of the fiber. The WLS fibers are connected to a photomultiplier tube, with the help of clear optical fibers. MINERvA uses *multi anode* Hamamatsu H8804MOD-2 photomultiplier tubes (PMTs). This PMT was chosen because a timing resolution better than ≈ 5 ns is required to distinguish overlapping events within a single spill of NuMI beam and measure the time of flight and decay times of muons produced in neutrino interactions. PMTs are shielded from the ambient magnetic fields produced from the magnetic coil at the MINOS detector, by housing them in steel cylinders, 2.36 mm in thickness. A typical PMT used by the MINERvA detector can be seen in Fig. 2.10. Each PMT can read out 64 fibers

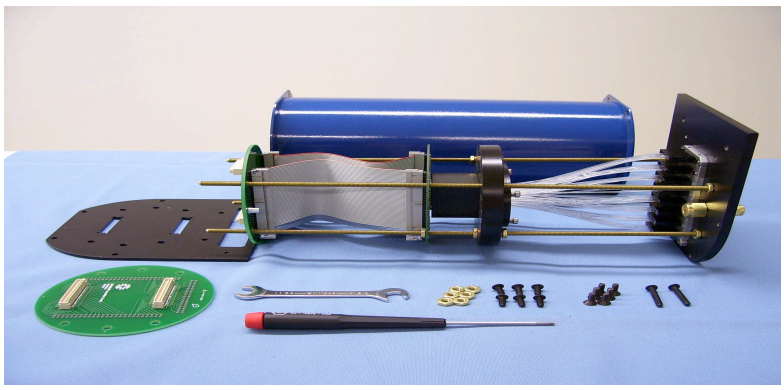

Figure 2.10: PMTs used by the MINERvA detector along with its various components. Figure taken from Ref. [65].

at once, through an array of 8x8 anodes (pixels). Hence, the optical fibers must come into close contact before the light is converted to electrical signals. These optical fibers are mounted onto a cookie in a weave pattern, where adjacent fibers are placed far apart so that light from neighbouring fibers is not read by a neighbouring PMT anode, to reduce the effect of electronic cross-talk between channels. This is shown in Fig. 2.11. With the weave-shaped arrangement, there still is light leakage from one fiber to its adjacent PMTs, but it appears as an isolated energy deposit during reconstruction and can be disregarded. Had it not been a weave pattern, it would have been very difficult to isolate this leakage, as it would have looked like a true physics effect on the event display after reconstruction. The weave-shaped arrangement leads to a fractional cross-talk energy deposited of less than 4%. The PMTs work on the principle of the photoelectric effect. Light fed through the fibers strikes a photocathode, releasing photoelectrons. These photoelectrons are accelerated through a chain of 12 dynodes, releasing further electrons at each dynode. This happens because a high electric field is maintained inside the PMT, creating a high potential difference between dynodes and the photocathode. With a net gain of around half a million electrons per photoelectron, the electrons are collected at the anode. MINERvA uses a total of 507 PMTs.

Fig. 2.12 shows the journey of an event signal, starting from a flash of light, getting converted to an electrical signal, and subsequently into an ADC count.

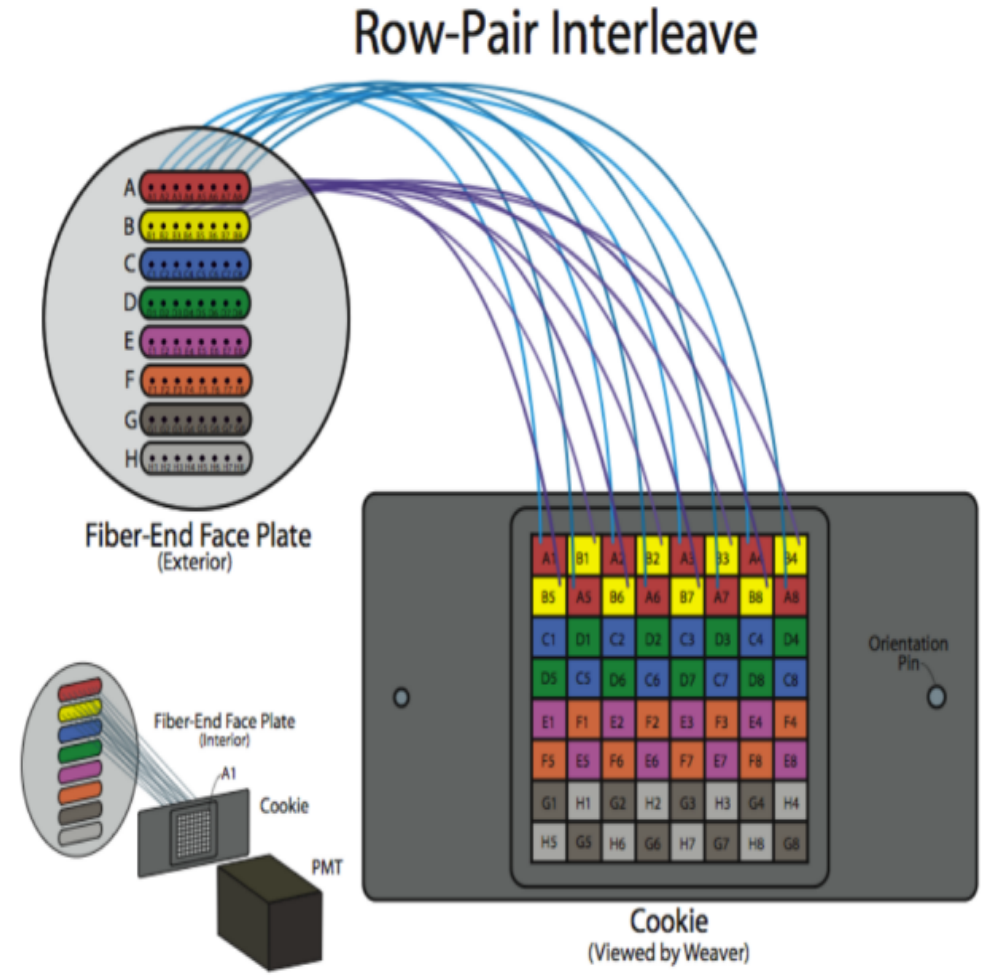

A1	B2	A3	B4	A5	B6	A7	B8
B1	A2	B3	A4	B5	A6	B7	A8

Figure 2.11: Weave shaped arrangements of fibers when fed to PMTs at MINERvA. This helps identify cross-talk. Reprinted from Ref. [65].

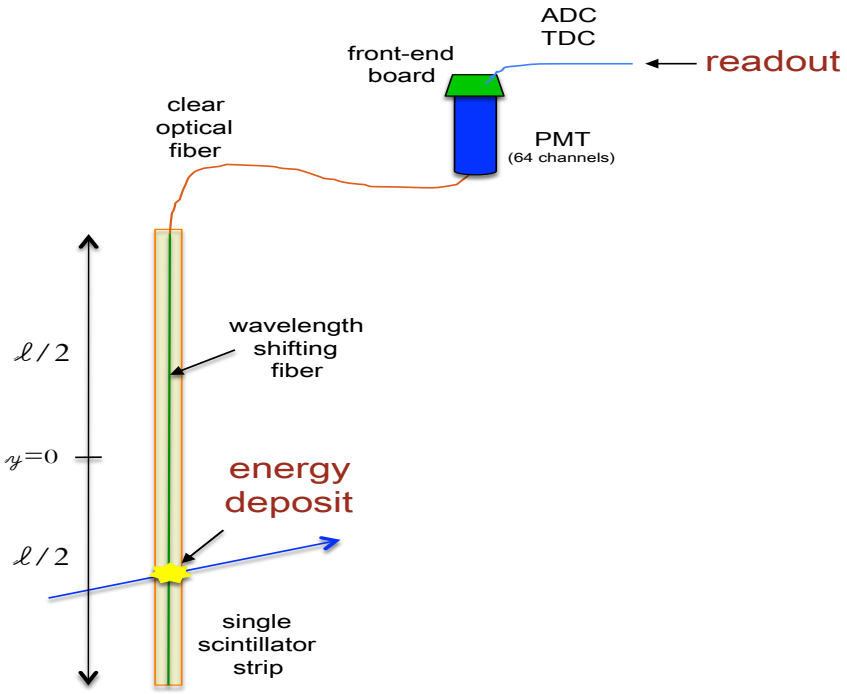

Figure 2.12: A schematic to represent data readout channel at the MINERvA experiment. Figure taken from Ref. [65].

2.2.3 Data Readout Electronics

PMTs store information in the form of current as a function of time. This must be converted to computer-readable digital signals. The analog output from the PMTs is read out by the front-end boards (FEBs). These FEB circuitry, based on D0 TriP-t chips [68], amplify and digitize the timing and pulse-height signals, converting them to ADC counts. This process takes about 151 ns. For about 188 ns, a reset phase takes place, for which, no data can be recorded by the FEBs. This period is called *dead time*. Multiple FEBs are connected using ethernet cables, to readout the entire detector at once, into a readout *chain*. This readout chain is connected to a CROC-E controller (Chain ReadOut Controller - Ethernet). Each CROC-E can support four chains and stores data "frames" from the FEBs on these chains, for short periods. As mentioned in Section 2.1, every 2.2 seconds, NuMI beams deliver neutrinos for a 10 μs spill. A readout gate takes data, 500

ns before the beam is expected and closes 5.5 μs after it ends. Hence, it is a total of $\approx$ 16 μs, accounting for delayed interactions in the detector. A gate is said to be "open" when data is being read and collected. These are called beam gates. Additionally, other gates can be opened for detector calibration purposes. MINERvA triggers beam-off data every $\approx$ 1500 spills, for measuring beam-off backgrounds and calibration purposes. For calibration, light injection (LI) gates are opened where PMTs are exposed to an LED to map its light response as a function of time. Also, pedestal gates are opened, during which, in the absence of the beam, background noise from the electronics is measured. How much energy was deposited and in which scintillator strip (where in the detector), is read and stored during an open gate in the form of "hits". These "hits" help in particle reconstruction, which will be discussed later, in the next chapter. On the software side of things, MINERvA has 3 computers running its data acquisition software (DAQ). The DAQ software is written in C++ and the machines run on Scientific Linux 7. Data from the FEBs are written to a binary file on disk at the end of each subrun. This data is read from the DAQ by the nearline monitoring system and each event is processed from binary format to raw digits format, compatible with ROOT [117]. These ROOT files are stored as raw digits files, on Fermilab's dCache [70]. Nearline machines process this data to also produce monitoring plots and event displays, which are displayed in the control room system, where the shifter at MINERvA can monitor the detector. Further details on the data readout process are provided in Ref. [65].

2.2.4 The Nuclear Target Region

Upstream of the MINERvA detector, lies the passive nuclear target region which comprises 5 different hexagonal nuclear targets, along with a water target. These targets have Fe, Pb, and C as target materials, used to test the dependence of the neutrino interaction cross section on nuclear mass. Fig. 2.13 depicts this region. Targets 1, 2, and 5 have iron and lead sections. Target 3 contains iron, lead, and

carbon, and Target 4 is made entirely of lead. Table 2.2 summarises the different material compositions and the thickness of the targets. The water target was not used for this analysis. These differences in how the materials are arranged in the x-y axes help us account for the difference in the acceptance of the different regions of the target, as the neutrino flux can differ in different regions of the detector. As shown in Fig. 2.13 (bottom), there are four scintillator modules upstream and downstream of each nuclear target 1, 2 and 3. There are 2 scintillator modules downstream of target 4 and upstream of target 5. The nuclear target region contains 22 modules in total. The z-axis starts from the veto wall such that the downstream surface of the veto wall is located at z = 4 cm and z = 1200 cm in at the front face of the MINOS near-detector.

Target	Z position (cm)	Thickness (cm)	Material	Mass (kg)
1	452.5	2.6	Iron	322
			Lead	263
2	470.2	2.6	Iron	321
			Lead	263
3	492.3	2.6	Iron	158
			Lead	107
			Carbon	160
Water	528.4	17-24	Water	452
4	564.5	0.8	Lead	225
5	577.8	1.3	Iron	162
			Lead	134

Table 2.2: Nuclear targets with their z position, thickness, and material composition by mass, within the hexagonal apothem of 85cm [65].

2.2.5 Electromagnetic and Hadronic Calorimeters

Downstream of the active tracker region, is the electromagnetic calorimeter (ECAL). 10 scintillator modules constitute the ECAL region, except that each scintillator plane is covered with a 2 mm thick sheet of lead. This is used to contain electromagnetic showers, as the lead sheet increases the likelihood of photon and electron

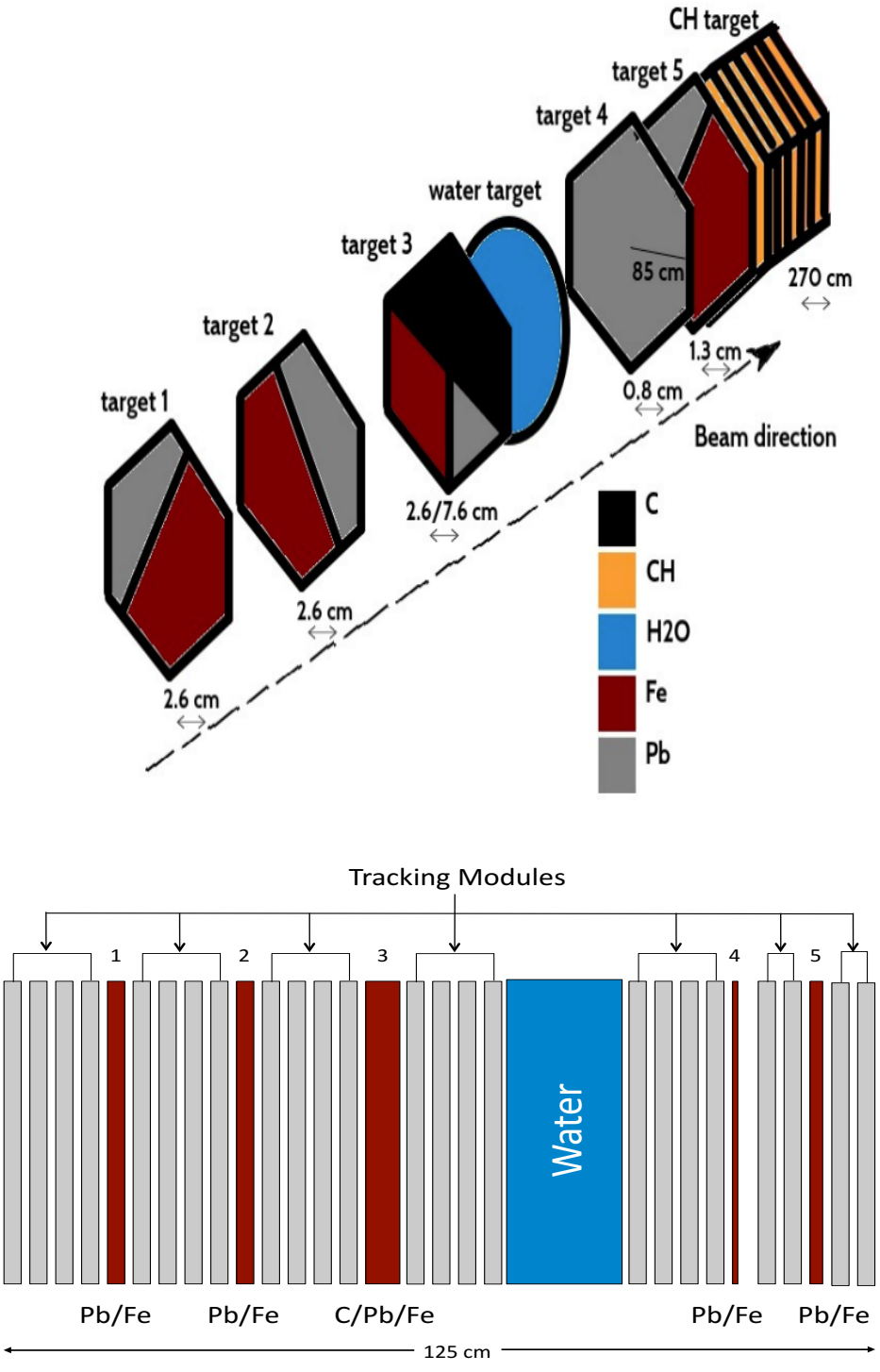

Figure 2.13: Top: Cartoon depicting the nuclear target region of the MINERvA detector, how are different materials arranged in the hexagonal modules, along with the thickness of each target and the total number of different nuclei. **Bottom**: Side view of the nuclear target region. Top figure reproduced from Ref. [71].

interactions. As we already discussed, a side ECAL is also used in each module using a 2 mm lead collar on the outer edges of each module to contain electromagnetic showers exiting from the sides of the detector.

In the most downstream region of the MINERvA detector, is found the hadronic calorimeter (HCAL) region, made up of 20 modules alternating between one plane of scintillator and one plane of 2.54 cm thick steel, to induce hadronic interactions. This region is used to contain hadronic showers exiting the detector.

Another important part of the MINERvA detector setup is the *veto walls*, located upstream of the helium target, which look to record the presence of muons produced in the interaction of the (anti)neutrino beam with the dolomite rock upstream of the target. The veto walls consist of alternating planes of steel and scintillator to help identify muons that might enter our detector. These muons can otherwise be misidentified as the muons produced in the (anti)neutrino-charged current interactions in the first planes of the MINERvA detector.

2.3 The MINOS Near Detector

The Main Injector Neutrino Oscillation Search (MINOS) [72], is a neutrino oscillation experiment in the NuMI beamline, aimed at measurement of θ_{23} through $\nu_\mu(\bar{\nu}_\mu)$ disappearance channel and θ_{13} through the $\nu_e(\bar{\nu}_e)$ appearance channel. Located 2.1 m downstream of MINERvA, it serves as a muon spectrometer to the MINERvA experiment and helps in the measurement of energy and momentum of the muons created by (anti)neutrino interactions inside the MINERvA detector. The 1 kTon MINOS detector is made up of steel plates interspersed with scintillator planes. Fig. 2.14 shows the schematic of the MINOS detector. The MINOS detector is magnetized to a 1.3 T toroidal magnetic field. This magnetic field causes charged particles to curve and the direction and radius of the curve helps determine the charge and the momentum of the particle, respectively. The

momentum of a particle can be identified using both the measurement of the radius of the curvature of the particle, as well as its range if it ranges out inside the MINOS. Muons with kinetic energy less than about 10 GeV will be contained inside the MINOS and their momentum is measured using the radius of curvature as well as the range of the tracks. Muons with kinetic energy greater than 10 GeV, will not be contained within MINOS and range measurements are out of the question. Muons with kinetic energy less than 2 GeV can't be constructed correctly, so they are not reported. Uncertainty in the reconstruction and simulation of muons in the MINOS contributes to MINERvA's systematic uncertainty on the muon energy scale. Requiring that an event from MINERvA must be charge matched in

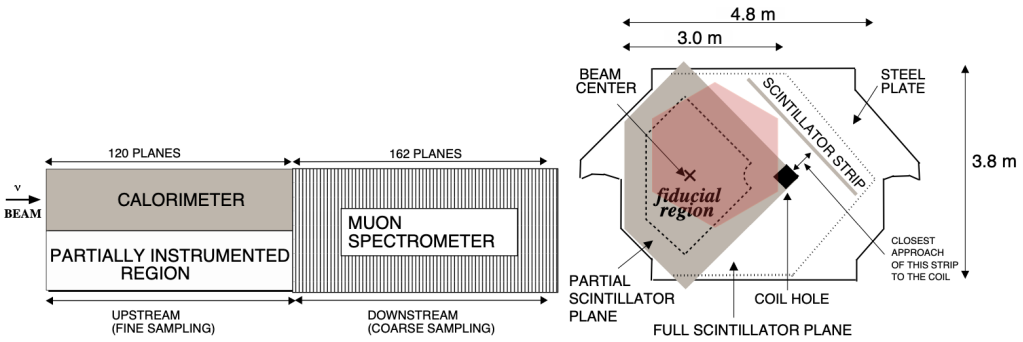

(a) Overhead view (b) Front view

Figure 2.14: Schematic of the MINOS near detector. The red-shaded region is where the MINERvA inner detector is with respect to the MINOS detector. Figure taken from Ref. [73].

the MINOS provides an excellent advantage of removing the wrong sign component from our selected events. One major drawback of using the MINOS for muon measurements is the limited angular acceptance of the MINOS ND (near detector) when used with MINERvA. Since the muon must be matched in MINOS, it must have an angle no more than 17^0 with respect to the (anti)neutrino beam direction. As a result, events happening more downstream of MINERvA, closer to MINOS are more likely to be matched in MINOS as compared to events that happen upstream in MINERvA and have to travel larger distances before getting matched

in MINOS. In summary, the restriction that we impose for MINOS matching is muon energy greater than 2 GeV and muon angle less than 17^0 with respect to the beam direction.

2.4 Detector Calibration

The information collected in the form of optical signals using the MINERvA scintillator strips, electrical signals in the PMTs and converted into ADC counts at the FEBs, must be converted to known units of energy for physical interpretation of the measurements done by the MINERvA detector. Each step of this way, also represented in Fig. 2.12, must be calibrated to convert the ADC counts generated from the FEBs into energy deposited in a given scintillator strip i. This is done using the following formula [65]:

$$E_i = [C(t) \cdot S_i(t) \cdot \eta_i^{att} \cdot e^{i_i/\lambda_{clear}} \cdot G_i(t) \cdot Q_i(ADC)] \times ADC_i \tag{2.1}$$

where:

- $C(t)$ is the overall energy scale constant for the entire detector
- $S_i(t)$ is the relative energy scale correction for scintillator strip i
- η_i^{att} corrects for the attenuation within strip i
- $e^{l_i/\lambda_{clear}}$ accounts for the attenuation in the clear optical fiber cable of length l_i
- $G_i(t)$ is the gain of the PMT from channel (pixel) i corresponding to strip i
- $Q_i(ADC)$ corresponds to ADC to charge conversion factor from the FEB channel corresponding to scintillator strip i

Ex-situ calibrations were done before the assembly and in-situ calibrations were done periodically post the detector assembly, between various data-taking periods. The ex-situ calibrations included measuring the responses of the FEBs, PMTs, and the scintillator strips. The attenuation constant for each scintillator strip, inside a module of the MINERvA detector was measured by an apparatus called module mapper. The test was done using two ^{137}Cs radioactive sources, which were moved in a predefined pattern over the entire module. The response for each strip as a function of position was measured, to determine the attenuation factor, η_i^{att} for each strip. The attenuation constant λ_{clear} for clear optical fibers was measured using a dedicated test stand. The optical fiber cables were connected to a LED source on one end and a readout was done at the other end, measuring their response to known amounts of light. λ_{clear} was measured to be 7.83 m. All the FEBs were tested before installation, for measurement of their response to charge. Each FEB has three different ADC channels with low, medium, and high gain. The response of the FEBs was plotted against the known input charge, for the three channels. A trilinear fit was applied to the response of the three channels. Fig. 2.15 is a typical fit. Baseline ADC counts, involving sources such as cosmic

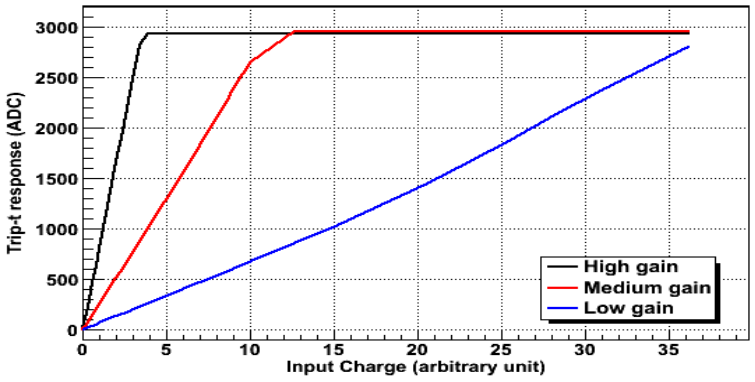

Figure 2.15: Trilinear fit for the FEB response to input charge in high, medium, and low gain ADC channels for MINERvA FEBs during testing. Figure taken from Ref. [65].

ray muons, radioactivity, and noise from detector electronics were measured after detector installation, between beam-on periods. This was done periodically every

10.5 hours. This average baseline ADC count was then subtracted later from the counts measured during beam time.

The gain of a PMT is the number of electrons collected at the anode for every photoelectron (PE) generated at the cathode. Over time, the gain of a PMT increases, as illustrated in Fig. 2.16. Note that $G_i(t)$ in Eq. 2.1 is a function of time, and this factor takes into account the changes in the gain of the PMTs over time. A light injection system, using calibrated LEDs is used for this purpose. LI system is triggered after every beam spill and measures the gain of the PMTs. After each beam gate, this new gain measurement from the LI gate is used for the next beam gate, such that we are looking to use the latest measurement of the gain. The method to calculate gain has been discussed in detail in Ref. [65]. "Rock muons", produced when the neutrinos in the NuMI beam interact with the

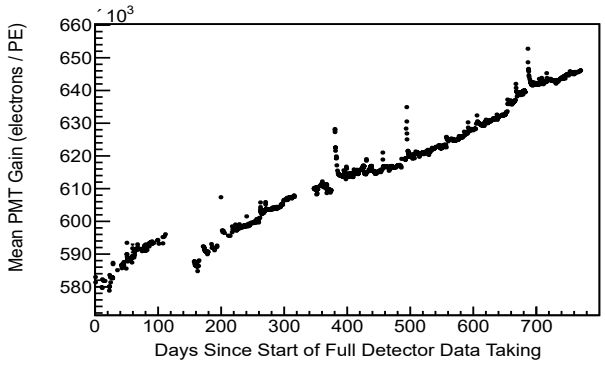

Figure 2.16: Mean PMT gain per photoelectron over a period of two years. The sharp peaks occur when the high voltages to the PMTs are reset. Figure reprinted from Ref. [65].

dolomite rock before entering the MINERvA detector, play a significant role in the calibration of the detector. They were used to correct from scintillator plane alignment, for strip-to-strip calibration for relative energy scale correction in each strip, and also for the absolute energy scale of the MINERvA detector.

The calibration for plane alignment inside the detector is performed over long

periods, typically months, because we need to gather enough rock muon data to perform the calibration. The scintillator strips constituting a plane might be misaligned in two ways - that they can be misaligned by translation such that they are displaced longitudinally or by rotation along the z-axis. Assuming the normal incidence of the rock muons as they travel in the direction of the beam, the energy deposited by the muons in the scintillator strips is proportional to the amount of material they travel inside the strip. Hence, the distribution of energy deposited against the base position of the triangular scintillator strip should be maximum at the triangle's point and should linearly reduce to zero as we move towards the edges. An offset in this distribution can point us to the fact that the plane has been misaligned. This is depicted in the left plot of Fig. 2.17. There is a misalignment of the plane by about 3 mm to the left of its designated position. Making a 2D distribution of energy deposit against the base position as well as the longitudinal position gives us information, on whether the plane got rotated about the z-axis, as shown in the right panel of Fig. 2.17. Rock muons

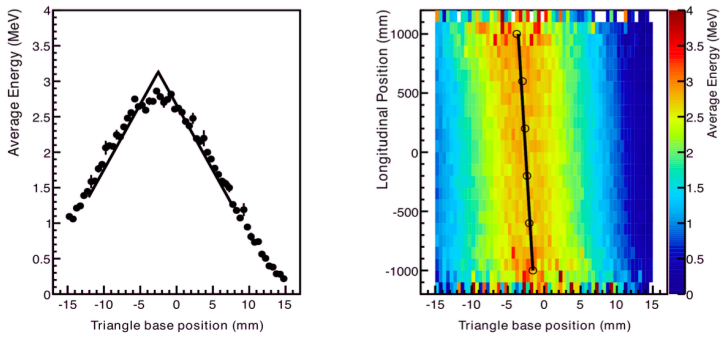

Figure 2.17: Left: The offset of the energy deposit from the triangle base position shows a translational misalignment of the plane. Right: Misalignment of the plane due to rotation along the z-axis, as the plotted line is not vertical. Figure reproduced from Ref. [65].

are used for calibration of differences in the light yields from strip to strip. This can be caused by differences in the relative composition of scintillator strips, air bubbles in the epoxy which is used to glue the strips together and fill the hole for

fiber, and coupling between the fibers and the PMTs. This correction is applied by calculating a multiplicative factor (constant) for each scintillator strip. Peak energy deposited by rock muons passing through the scintillator is used to extract these constants. The constant is normalized such that the average constant over the entire detector is 1. In Eq. 2.1, this constant is the factor $S_i(t)$.

The absolute energy scale of the MINERvA detector is measured in "muon equivalent units" or MEU. Rock muons are used for this calibration whose tracks from the MINERvA have been matched in MINOS. The energy of these muons is calculated after range and curvature measurements in the MINOS detector after corrections for the energy loss in the MINERvA detector are applied. Starting with a trial MEU factor, the energy of each reconstructed energy cluster (details in section 3.4.2) from the muon tracks is plotted in both the data and the simulation. A fifth-degree polynomial is used to fit the peak region for each case. These fitted distributions are used to extract an improved MEU. The uncertainty plane thickness is the primary source of uncertainty ($\approx 2\%$) in the calculation of the MEU. This goes into the Eq. 2.1 as $C(t)$.

It is also crucial to calibrate the timing information for the MINERvA. Time slewing is caused by the fact that scintillators undergo several energy level decays before the light can finally reach the PMTs. Also, timing offset in FEB daisy chains causes channel-to-channel timing differences. Once again, rock muons are used to iteratively calibrate time slewing and channel-to-channel timing differences. The delay caused by the propagation time of light in the fibers is simply accounted for by measuring the length of the fibers and the speed of light inside the fiber.

Chapter 3

Simulation and Reconstruction

It is going to be necessary that everything that happens in a finite volume of space and time would have to be analyzable with a finite number of logical operations. The present theory of physics is not that way, apparently. It allows space to go down into infinitesimal distances, wavelengths to get infinitely large, terms to be summed in infinite order, and so forth; and therefore, if this preposition (that physics is computer-simulatable) is right, physics law is wrong [74].

— **Richard P. Feynman**

(1965, Nobel Prize in Physics, development of quantum electrodynamics)

So far, we have learned how the MINERvA experiment is able to record energy deposits for particle interactions in the MINERvA detector. This recorded data must now be used to reconstruct particle tracks and these particle tracks are interpreted to identify the nature of interaction that has occurred. To do so, based on the interactions and behavior of various particles obtained from physics experiments done around the globe, combined with the predictions of various theoretical models for particle interactions, certain Monte Carlo (MC) simulation models are used to simulate the interactions of (anti)neutrinos and the particles produced by their interaction. We discussed the NuMI beamline in Section 2.1 of

the previous chapter. To determine the energy spectrum of the (anti)neutrinos in the NuMI beamline, we must perform simulations on the NuMI beam to determine the (anti)neutrino flux.

3.1 NuMI Flux Simulation

The first thing that is to be simulated is the production of hadrons from the proton collision with the NuMI graphite target. This is done using the PPFX (Package to Predict the FluX) package, which is based on GEANT4 [75]. It uses the FTFP_BERT hadron shower model [76] (FRITIOF Precompound - Bertini cascade). Data from the CERN experiment NA49 [77] is used to constrain the predicted hadron production at the NuMI target and cross-checked with lower energy experiment NA61 [79]. Since NA49 used a 158 GeV beam and NuMI had a 120 GeV beam, and the sizes of the targets are different for the two experiments, the data from NA49 was rescaled using FLUKA monte carlo simulation, using the Feynman scaling technique [80, 81]. The simulation is reweighted as a function of pion kinematics. Details of the reweighting procedure are provided in Ref. [82]. The PPFX package, originally released using the LE era and later extended to the ME era, is used to perform the above reweighting. It includes the uncertainties on the hadron production cross sections, and attenuation of pions, kaons, and protons due to re-interaction in the target, or with materials of the horn and decay pipe. Additionally, there is a contribution to uncertainty due to K^0 production and from the contribution of isoscalar conjugate of the interaction $pC \to \pi X$ i.e. $nC \to \pi X$.

Another important aspect to model here is the focusing of these hadrons produced at the NuMI target. The horn system for the NuMI beamline is modeled using GEANT4 package [75], using the g4numi package. Parameters that affect beam focusing include horn transverse offset, with a 0.3 mm uncertainty on horn 1 position and 0.5 mm on horn 2. There is a 0.25% uncertainty for the beam to scrape the baffle walls. There is a 2% uncertainty on the POT (protons on

target) counting at NuMI target. Additionally, there is 1% uncertainty on the current delivered to horns. There is also an uncertainty due to modeling the horn inner conductor shape and the magnetic field inside the inner conductor. All these parameters contribute to measuring uncertainties in the simulation.

3.1.1 Constraining the Flux

Electrons are point-like particles, which reside outside the nuclear medium and do not experience complex nuclear effects like the nucleons in the nucleus. As a result, the cross section of the (anti)neutrino scattering off an electron can be precisely measured. Hence, measurement of neutrino-electron scattering cross section ($\nu_\mu(\bar{\nu}_\mu)+e^- \rightarrow \nu_\mu(\bar{\nu}_\mu)+e^-$) can help better estimate the NuMI (anti)neutrino flux. MINERvA measures the event rate for (anti)neutrinos scattering off electrons. Discrepancies between measured and predicted event rates can be attributed to mis-modeling of flux distribution. In LE mode, the neutrino electron scattering constraint is done using the FHC beam, while in the ME mode, the measurements from FHC and RHC for (anti)neutrino-electron scattering are combined together with a further constraint from the inverse muon decay ($\nu_\mu + e^- \rightarrow \mu^- + \nu_e$) to produce a joint fit. Inverse muon decay is used to constrain the high energy tail of our flux [83]. The ME $\nu_\mu(\bar{\nu}_\mu)$ beam's uncertainty in flux is reduced from 7.6% (7.8%) to 3.3% (4.7%) after applying these constraints. Fig. 3.1, 3.2 and 3.3 highlight the effect of the neutrino electron scattering constraint on the antineutrino NuMI beam.

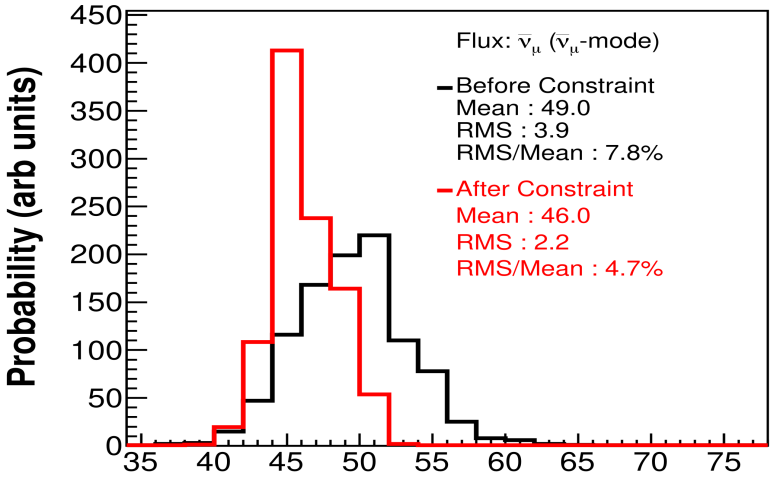

Figure 3.

constrainir

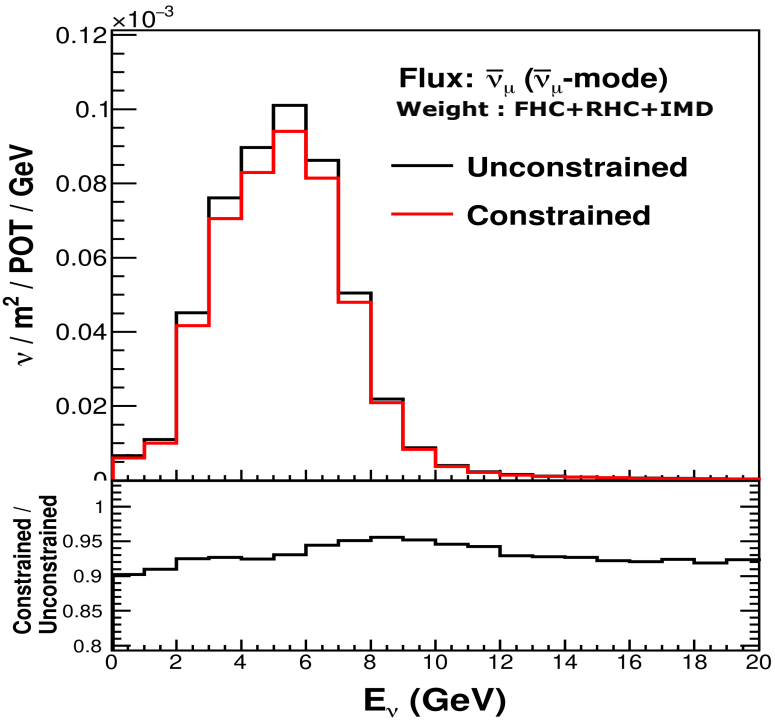

Figure 3.2: Predicted $\bar{\nu}_\mu$ RHC flux in bins of neutrino energy, before and after constraining the model using neutrino electron scattering data [84].

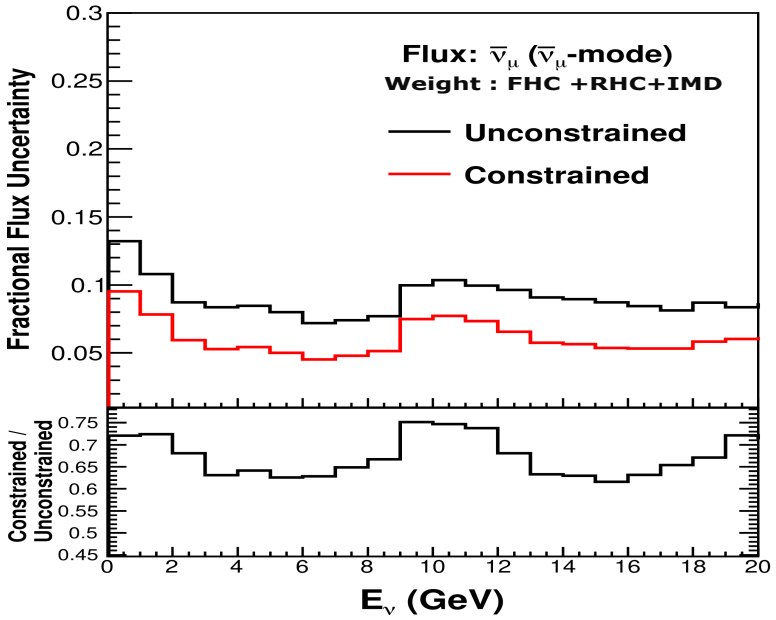

Figure 3.3: Fractional uncertainties on the predicted $\bar{\nu}_\mu$ RHC flux in bins of neutrino energy, before and after constraining the model using neutrino electron scattering data [84].

3.2 Antineutrino Simulation: GENIE Monte Carlo Generator

When (anti)neutrinos interact with the detector, this can lead to a variety of physics processes. These processes are modeled by using the GENIE (Generates Events for Neutrino Interaction Experiments) event generator [86, 87] version 2.12.6 at MINERvA. This code was developed as a result of the Soudan experiment [88]. GENIE works for a variety of nuclear targets and neutrinos of all flavors ranging from MeV to PeV scales of energy, but it focuses on the few-GeV range which is relevant for the current and future accelerator-based neutrino experiments.

We need to model a variety of phenomena, as the (anti)neutrino-nucleus interaction involves a large variety of processes, to get an accurate description of the experimental signature of a detector and its components. This can be broadly

divided into three models: nuclear physics models, cross section models, and hadronization models. Hence, many models need to come together for the working of the GENIE generator. Taking input from the neutrino flux distribution, GENIE generates random numbers to simulate (anti)neutrinos in the MINERvA's energy spectrum and then uses the underlying physics models, which tell the generator how probable a particular process is, to occur, to simulate the interaction of these (anti)neutrinos.

3.2.1 Nuclear Model

In GENIE, nuclear effects are modeled by the relativistic Fermi gas model (RFG) [48]. This defines the initial state of the nucleus before any interactions, characterized by the distribution of energy and momentum among its constituent nucleons. In the RFG model, the nucleons inside the nuclear radius are treated as independent particles, which is also called impulse approximation. The nucleons are considered to have a momentum distribution ranging from 0 to p_F in the ground state and having binding energy E_B, which is the amount of energy required to separate a nucleon bound inside the nucleus. All the ground state energy states inside the nucleus, up to the momentum value p_F are filled. Nucleons being fermions obey Pauli's exclusion principle, and hence in a quasielastic scattering, the final state nucleon must have a momentum greater than p_F, as all the states up to momentum value of p_F are already occupied called Pauli blocked states. This Pauli blocking effect, as a result, significantly reduces the cross section at low values of Q^2. In GENIE, the RFG model has been modified to include nucleon-nucleon correlations, using the Bodek-Ritchie high momentum tail [89]. For Carbon, the Fermi momentum is taken to be $p_F = 0.221$ GeV. Short-range correlations (SRC) are also taken into account, where the SRC effect is represented using the meson exchange currents (MEC), where an intermediate virtual meson cloud is responsible for coupling between nucleons.

3.2.2 Cross section model

GENIE must model the different possible channels of interactions, for example, quasielastic (QE) scattering, resonance production, deep inelastic scattering (DIS), and charged current 2p2h interactions. Quasielastic interactions are simulated using Llewellyn-Smith's (LS) prescription [90], where the cross section as a function of four-momentum transfer squared is parameterized by nucleon form factors, where electromagnetic vector form factors are modeled using the BBBA2005 [91]. For axial vector form factors, a dipole form with the axial dipole mass value of $M_A = 0.99$GeV is used in GENIE [86]. Resonance production is simulated by GENIE using the Rein-Sehgal model [132]. DIS interactions are modeled using the Bodek and Yang model [136], with a low-Q^2 modification. Hadronic showers are modeled by the AGKY model [94]. 2p2h interactions are modeled by the Valencia model [95, 96, 97].

3.2.3 Final State interaction model

In addition, to model final state interaction effects, GENIE simulates the rescattering of pions and nucleons inside the nucleus using the INTRANUKE-hA package [98]. In this package, the progress of the particle is tracked every 0.05 fm. Every step of the way, the mean free path of the hadron inside the nucleus is calculated based on the local nucleon density $\rho_N(r)$ and the energy of the hadron E_h and its interaction cross section σ_{hN}:

$$\lambda(r, E_h) = \frac{1}{\sigma_{hN} E_h \rho_N(r)} \tag{3.1}$$

This gives the probability for interaction for the simulated particle at the step and final state particles are generated if the interaction takes place at this step. At most, one rescattering is allowed per interaction before absorption inside the nucleus or exiting the nucleus.

3.3 MINERvA specific reweights to GENIE

Some of the models used by GENIE are reweighted at MINERvA. These reweights are better supported by the experimental results that have been obtained or are driven by predictions from theoretical models. These reweights are referred to as "tunes", where MC is tuned in a certain way to better agree with the data. The primary set of tunes that MINERvA uses over GENIE prediction are together called **MINERvA tune V1**, with three different reweights: suppression of non-resonant pion production, 2p2h enhancement, QE suppression at low four-momentum transfer squared (Q^2). The first reweight comes from the re-analysis of the deuterium bubble chamber pion production data at the Argonne National Laboratory (ANL) and Brookhaven National Laboratory (BNL) [99]. A significant reduction for the GENIE predictions of non-resonant single pion production was required to explain the bubble chamber data [100] from the ANL and BNL. MINERvA tune V1 suppresses the GENIE predictions for non-resonant pions by a factor of 0.43, i.e. 43% of the original prediction from GENIE is taken.

The second reweight comes to the 2p2h prediction from the Valencia model [96, 97, 101]. A previous measurement from the MINERvA collaboration, [102], was made in low three momentum transfer with LE MINERvA data. This chosen variable can help identify the transition region from the QE to the resonance production channel, where the 2p2h interactions are expected to be dominantly present in the in-between region. However, underprediction of 2p2h interaction was observed in Ref. [102], in the transition region, from QE to delta resonance production region. Hence, for better agreement between observed data and simulation, the prediction of the rate of 2p2h interactions was enhanced using an extra Gaussian weight function in Ref. [102]. This reweight was done on a neutrino event sample. When the reweight was independently applied to the antineutrino sample, it improved the data MC agreement there as well [103].

The next reweight that MINERvA applies is to the low four-momentum transfer squared (Q^2) QE events, where the cross section gets suppressed due to long-range nucleon-nucleon correlation effects, modifying the free electroweak coupling. The reweight is applied to GENIE predictions using the random phase approximation (RPA) effect for low Q^2 events, from the Valencia group [104].

All the above reweights in combination are termed as *MINERvA tuneV1* at MINERvA.

One more reweight that has been used in this analysis is the reweight to the pion production model of GENIE, using reanalysis of bubble chamber deuterium scattering data from ANL/BNL experiments [105], where the values of the parameter **MaRES** has been changed from 1.12 ± 20 % to 0.94 ± 5% and parameter **NormCCRES** has been changed from 1.0 ± 20% to 1.15 ± 7%. These parameters are discussed in Chapter 5. Along with this new reweight, the central value for the Monte Carlo prediction used in this analysis is called **MINERvA tune V4**.

MINERvA uses GEANT4 [75] to simulate how the particles generated by GENIE simulation propagate through the detector. GEANT4 simulates a detailed model of the detector geometry, including all the scintillator material, nuclear targets, and ECAL and HCAL. Optical and electronic systems are also simulated, converting energy depositions into simulated readouts.

3.4 Event Reconstruction

The MINERvA experiment collects data on (anti)neutrino interactions by recording energy deposits ("hits") in various regions of the detector, which is also simulated by MC. A reconstruction algorithm processes this data to track particles and identify interaction vertices. The steps in this reconstruction process are detailed

in the following sections.

3.4.1 Time Slicing

The NuMI beam delivers (anti)neutrinos in 10 μs spills. As discussed in Section 2.1, to account for delayed neutrino interactions within the detector, the data acquisition gate remains open for a total of 16 μs. To handle multiple neutrino interactions during this window and mitigate pile-up, the gate is subdivided into smaller intervals known as time slices. A time slice is generated when a threshold of 10 photoelectrons is reached within a 25 ns window. This time-slicing process helps group hits that occur around the same moment, corresponding to a single interaction.

3.4.2 Clusters

Hits in the scintillator strips adjacent to each other form a cluster. Clusters corresponding to the same time slice are characterised based on the amount of energy deposited and topology:

1. **Low energy**: less than 1 MeV total energy deposited from the adjacent strips of scintillator.
2. **Trackable**: energy deposit of 1-12 MeV, with a maximum of four hits, having adjacent hits with more than 0.5 MeV each.
3. **Heavily ionising**: energy is deposited into two or more scintillator strips and a total energy deposit of at least 1 MeV.
4. **Supercluster**: Broad energy range hits, more than 1 MeV, distributed across four or more hits. These clusters are utilized in the reconstruction of electromagnetic showers.

5. **Crosstalk cluster**: These hits are generated by optical or electronic crosstalk and not by an actual physical particle in the detector. This has been discussed in Section 2.2.3 of the previous chapter.

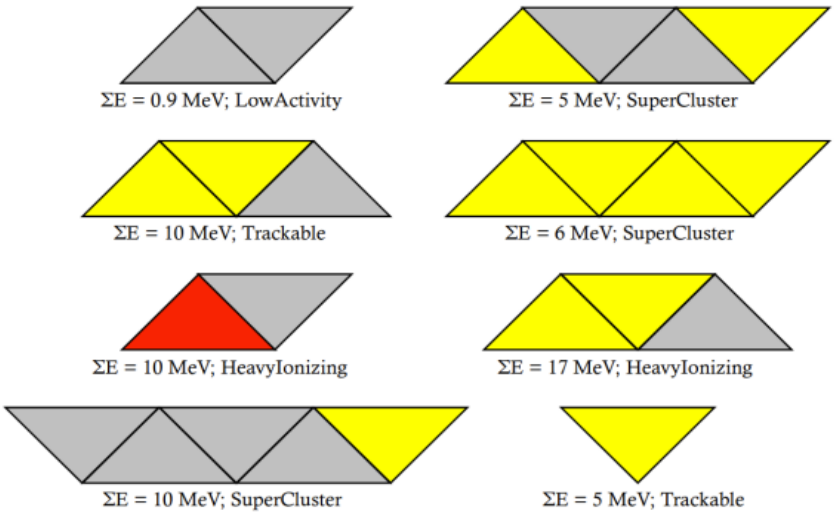

Figure 3.4: MINERvA's different topologies of energy clusters. Grey clusters correspond to less than 1 MeV energy, yellow clusters correspond to 1-8 MeV, and red ones correspond to 8+ MeV energy deposited. Reprinted from an internal MINERvA presentation by Gabe Perdue [66].

These cluster groups have been illustrated in Fig. 3.4. Once these different clusters have been identified, they are joined together to form tracks.

3.4.3 Track Reconstruction

For inclusive analysis, we only need to identify and reconstruct the track of (anti)muons. For the sake of simplicity, we will refer to both muons and antimuons as "muons" in this and the following sections. The first step in the track reconstruction process is to combine the clusters from a time slice into "seeds". Seeds are formed using only trackable and heavily ionising clusters, when three

of these clusters are found consecutively, in a straight line, in the same plane orientation (X, U, V). A track candidate contains multiple seeds in the same plane orientation, having a common cluster, with not more than one cluster in the same plane, and satisfying a fit along a two-dimensional line. Once a track candidate has been identified by merging two seeds together, the algorithm looks for more candidates to merge based on the same criteria. A track candidate is shown in Fig. 3.5. A given seed can only be contained in one track candidate. When all

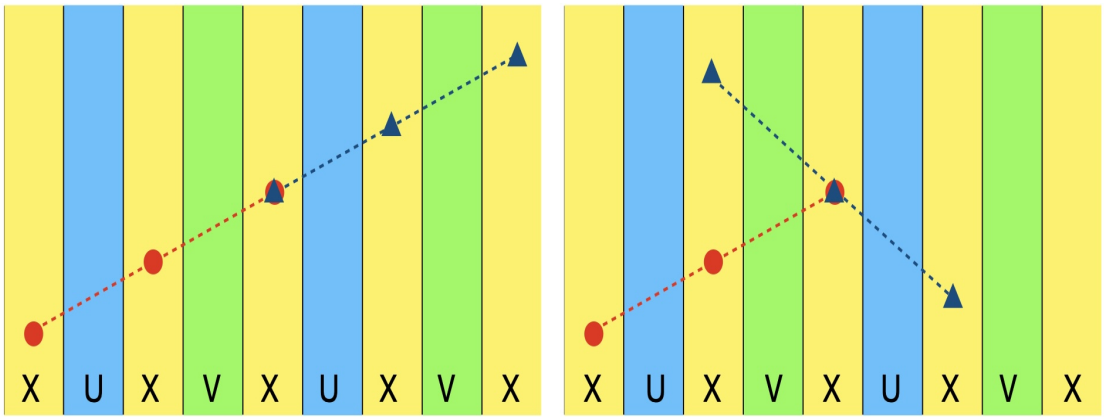

Figure 3.5: *Left:* Two seeds in the same plane orientation form a track candidate. *Right:* Because two clusters are present in the same plane for two different seeds despite having a common cluster, a track candidate is not formed. Figure reproduced from Ref. [67].

track candidates have been built, they are merged using the same algorithm as the seeds, having consistent fitted slopes and intercepts and not containing different clusters in the same plane. Shared clusters are not mandatory for track candidates and they may contain gaps. Hence, the particle trajectory is followed disregarding the dead regions in the detector.

When all the track candidates of a plane are formed, A three-dimensional track is formed using the following algorithms. Firstly, one track from each plane orientation (X, U, V) is chosen to form a three-track combination, which overlaps along the z-axis and falls along the same direction in the 3-dimensional line. The requirement of a track candidate in each view limits the shortest possible track

that can be formed to 11 planes (or 5 modules) long. Secondly, all the remaining candidates that have not yet been used to make a track, are used to form possible combinations of two track candidates, coming from different plane orientations (X/U, X/V or U/V). If they overlap along the z direction, three-dimensional line is constructed from these candidates. These lines are then filled with untracked clusters and if sufficient clusters fit the line, it is promoted to a track. This algorithm is able to construct shorter tracks (9 planes) and also tracks that are obscured in one of the three plane orientations.

All the 3D tracks when identified, are fit by a Kalman filter routine [106]. At this point, the filter is used to add additional untracked clusters from the nearby planes, including superclusters, to the tracks. In situations where two tracks intersect the same supercluster, multiple tracks are allowed to claim a fraction of the energy of the cluster. Tracks are extrapolated and allowed to intersect into areas of high activity such as hadronic showers.

Now the track containing at least 25 clusters is designated as the 'anchor track'. The starting point of this track is considered the (anti)neutrino interaction location in the detector called the primary vertex. The algorithm now looks for unused clusters and tracks emerging from the primary vertex are identified and based on this, the location of the primary vertex is re-estimated. Tracks that are not consistent with emerging from the primary vertex are deleted. Particle trajectories that abruptly change direction due to secondary interactions are identified to be coming from the primary vertex. This procedure is illustrated in Fig. 3.6.

The next step is called 'cleaning' the track, where the anchor track, identified as a muon track is checked to emulate the behavior of a muon. Anchor tracks are expected to deposit energy as minimum ionising particles (muons). If energy deposited near the vertex is inconsistent with a minimum ionising muon or superclusters are present, this extra energy is removed from the track. This reconstructed muon track in the MINERvA detector must now be matched to

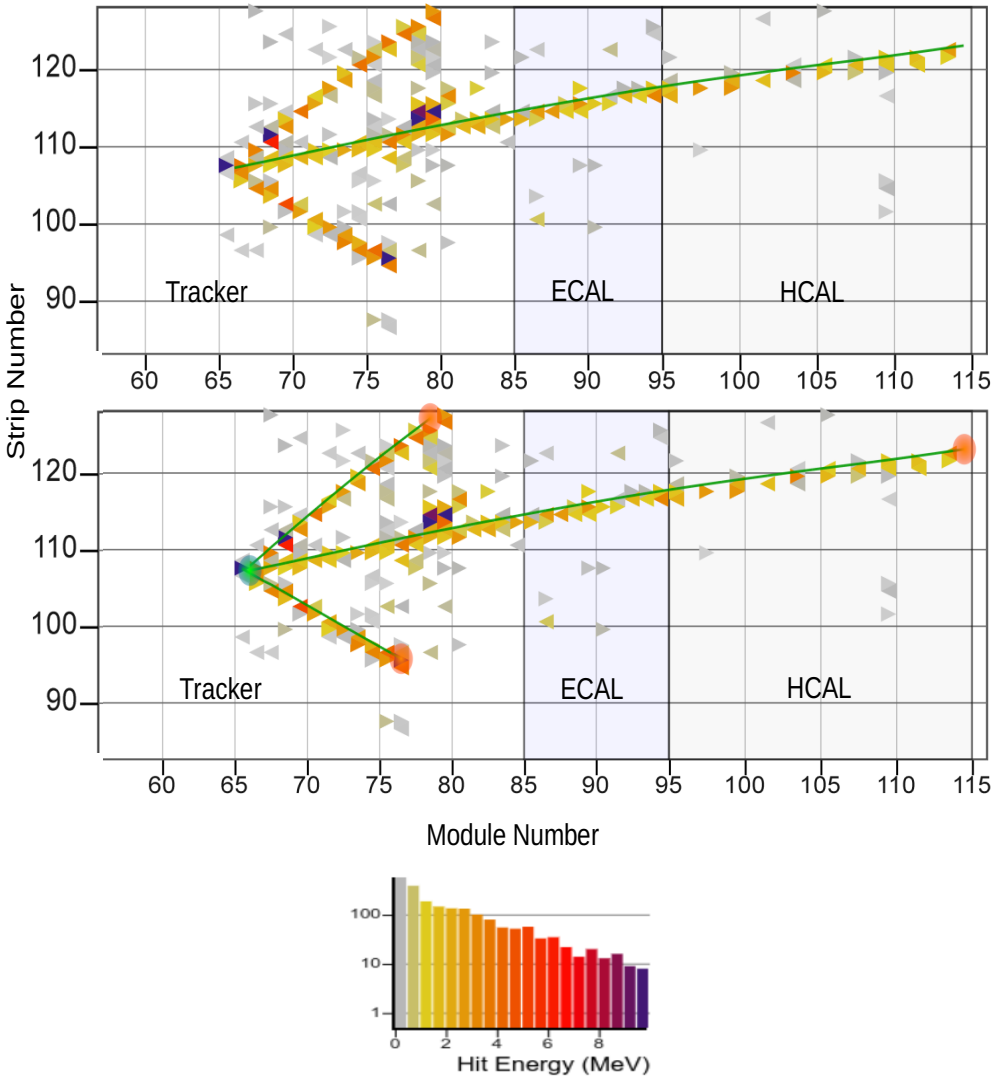

Figure 3.6: Event display from the X view of neutrino interaction in data at the MINERvA detector. The triangles on the plot represent an energy deposit (hit) corresponding to a single scintillator strip. Tracks reconstructed are shown using green lines superimposed on the display. The longest track is first identified to be an muon track and called the anchor track (upper panel). The primary vertex is hence identified using the starting point of this track. Additional tracks coming from the vertex are searched for (bottom panel). In this event, two additional hadronic tracks can be seen to be originating from the primary vertex (short green lines). This way, the primary vertex is further constrained.

MINOS.

The above-discussed method of track-based reconstruction of interaction vertex works well in the active tracker region where we have large volumes of detector material. In the nuclear target region though, a small imprecision in the reconstruction of the event vertex can change the material in which we reconstruct the event. Machine learning (ML) techniques [107] are used to precisely reconstruct the interaction vertex in the nuclear target region [108, 110]. As shown in Fig. 3.6, events inside the MINERvA detector can be shown in the form of images. A deep convolutional neural network can be trained to take these images as input and work on identifying the plane of interaction in the detector. Ref. [109, 110] discuss this procedure in great detail. The betterment in the identification and hence reconstruction of the vertex in the nuclear target region is illustrated in Fig. 3.7.

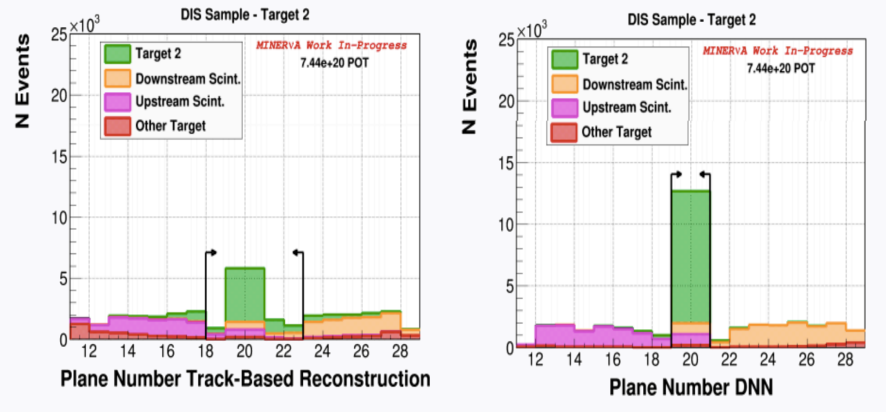

Figure 3.7: Track based vertexing (TBV) (*left*) compared to machine learning vertexing (*right*) for events in the target 2. The colors represent the reconstructed location of the true interaction vertex. A wider range of target 2 planes was chosen for TBV (planes 18 to 22) as compared to ML vertexing (planes 19 and 20), which shows an increase in precision when ML vertexing is used. Figure from Ref. [110].

3.4.4 Matching track in MINOS

As explained in Section 2.3, downstream of the MINERvA detector sits the MINOS near detector, which is used for energy and charge identification of the muon, created by the interaction of the (anti)neutrinos in the MINERvA detector. For the tracks to be matched between the two detectors, the first requirement is that they must occur within 200 ns of each other. The muon tracks in MINOS are reconstructed in a similar manner to the MINERvA detector. The track must end in the last 5 downstream modules of the MINERvA and must begin in the first 4 upstream planes of the MINOS ND. The track from MINERvA is extrapolated forward to the MINOS planes, to see where it would intercept the MINOS and similarly the MINOS track is extrapolated backwards to the MINERvA planes. If the two extrapolated tracks intercept within 30 cm, the tracks are considered to be a match. Muons with energy less than 10 GeV, can be contained within the MINOS ND using the steel walls of the detector to stop the muons.

The measurement of the energy of the muon that enters the MINOS ND, can be done by how far it travels inside the detector volume i.e. 'range' measurement. Energy of the muon is also estimated using the 'curvature' method, where the curvature of the track is calculated in the MINOS magnetic field. Range measurement leads to a scale uncertainty of 2% on the momentum and is the highest precision method of measurement of momentum. If the muon does not range out within the MINOS ND detector volume, the muon momentum must be measured using the radius of curvature of its track (R) in the magnetic field:

$$\frac{1}{R(cm)} = \frac{0.3B}{p_\mu} \tag{3.2}$$

where B is the MINOS magnetic field in kGauss and p_μ is the component of muon momentum perpendicular the magnetic field, in MeV. The curvature method is less precise and adds an additional 0.6% energy scale or momentum uncertainty to the range method.

Chapter 4

Double Differential Cross Section Extraction

Tapestries are made by many artisans working together. The contributions of separate workers cannot be discerned in the completed work, and the loose and false threads have been covered over. So it is in our picture of particle physics [85].

— **Sheldon L. Glashow**
(1979, Nobel Prize in Physics, theory of electroweak interactions)

4.1 Inclusive Analysis

So what does "inclusive" mean in the context of experimental neutrino physics, where we are studying the interaction of neutrinos with atomic nuclei?

As the word suggests, inclusive analysis sums over all the possible final states. This means counting all the events when a neutrino interacts with the nucleus, producing any combination of final states. The inclusive analysis does not require

full reconstruction or identification of all the particles produced in the final state. This contrasts with other "exclusive" analyses that are conducted at MINERvA, where several final state particles are identified and studied. The only requirement for the inclusive $\bar{\nu}_\mu$ charged current analysis is the detection of the charged antimuon in the final state. As a result, inclusive analysis has higher event rates, leading to a more robust statistical analysis. The main processes that contribute to the inclusive cross section are the quasielastic scattering channel, the resonance production channel, and the deep inelastic scattering channel, depicted in the Fig. 4.1.

$$\bar{\nu}_\mu + N \rightarrow \mu^+ + N' \text{ (Quasielastic)} \tag{4.1}$$

$$\bar{\nu}_\mu + N \rightarrow R^* \rightarrow \mu^+ + \pi^- + N \text{ (Resonant pion)} \tag{4.2}$$

$$\bar{\nu}_\mu + N \rightarrow \mu^+ + X \text{ (Deep Inelastic)} \tag{4.3}$$

However, the physics of (anti)neutrino scattering off nucleons is not as straightforward as it appears from the three Feynman diagrams shown in Fig. 4.1. The situation gets complicated by the final state interaction effects, where for example, a nucleon in the final state (n,p), after initial interaction with the (anti)neutrino, can re-interact while exiting the nucleus to produce a pion in the final state. Also, a pion produced by a resonance scattering channel can re-interact within the nuclear medium and get absorbed within the nucleus, thus mimicking a quasielastic-like scattering in the final state produced after such interaction. Also, the effects of the nuclear medium (discussed in Chapter 1) can alter the measured cross section. Hence, in our cross section measurement, the nuclear medium effects and the final state interaction effects are modeled in the MC generated by GENIE.

4.2 Cross Section Extraction at MINERvA

The goal of the analysis presented in this dissertation is to measure double differential charged current antineutrino nucleus scattering cross section for the inclusive

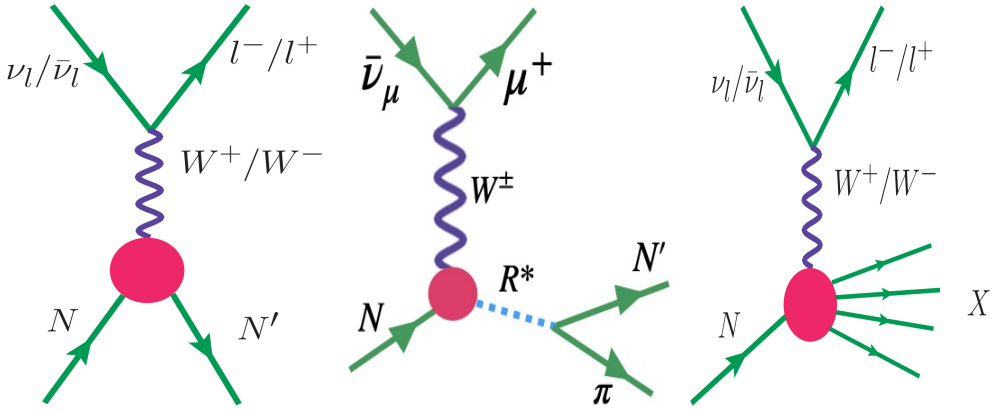

Figure 4.1: Feynman diagrams representing a (a) quasielastic, (b) resonance production(R^*) leading to a pion in the final state and (c) a deep inelastic scattering process, with a jet of hadrons (X) in the final state.

channel. This measurement has been done as a function of the variables bjorken x and Q^2 and W and Q^2 as well as antimuon longitudinal and transverse momentum, p_z and p_t. The mathematical definitions of these variables were provided in Chapter 1.

The double differential cross section as a function of bjorken x and Q^2 is given by:

$$\left(\frac{d^2\sigma}{dxdQ^2}\right)_{ij} = \frac{\Sigma_{\alpha\beta}U_{\alpha\beta ij}(N_{\text{data},\alpha\beta} - N^{\text{bkgd}}_{\text{data},\alpha\beta})}{\epsilon_{ij}(\Phi T)(\Delta x_i)(\Delta Q^2_j)} \tag{4.4}$$

where,

- $N_{\text{data},\alpha\beta}$ are the data events reconstructed in bin (α, β).
- $N^{\text{bkgd}}_{\text{data},\alpha\beta}$ are the events that do not pass the signal definition, identified as background events reconstructed in the bin (α, β).
- $U_{\alpha\beta ij}$ is the migration matrix element mapping the reconstructed bin (α, β) to the true bin (i, j). It accounts for mis-reconstruction due to detector

effects.

- ϵ_{ij} is the correction factor which is a product of the reconstruction efficiency and detector acceptance for the events in true bin (i, j). This is the percentage for signal events out of all identified signal events that are selected in each bin (i, j). Determining this efficiency correction is simulation-driven.

- Φ is the flux of the incoming antineutrinos in the beam

- T is the total number of target nucleons in the detector volume available for scattering

- Factors Δx_i and ΔQ_j^2 are the widths of bin i and bin j and take into account the bin width normalisation for the chosen variables of interest bjorken x and Q^2.

The same formula is used to extract double differential cross sections in bins of $W - Q^2$ and antimuon momenta variables $p_z - p_t$.

Ntuples: Events for data and simulation

The data recorded by the MINERvA detector in the ME mode, and the simulated events generated by the GENIE MC generator [86] are stored in the ROOT file format. Tree like data structures in these files called "ntuples" store all the information about the (anti)neutrino interactions. There are three main type of ntuples:

- **Data ntuples**: These contain information about the actual interactions that took place in the detector, when the detector was exposed to the (anti)neutrinos from the NuMI beam in the medium energy (ME) mode.

- **Reconstructed MC ntuples**: These contain information about the simulation generated events from MINERvA tuned GENIE.

- **Truth ntuples**: These contain all the interaction that the simulation generator predicted. These include the events that we could not reconstruct. This is like a superset of the events in the reconstructed MC ntuples.

It is important to note here that the reconstructed and the true quantities might differ from each other, because of the detector resolution and complex algorithms used for reconstruction. We store both true and reconstructed quantities in the ntuples. These can later be compared among themselves to apply for corrections in our data. MINERvA took data for the medium energy (ME) mode, with $\langle E_\nu \rangle \sim 6$ GeV from July 2013 to February 2019. The ME beam provided a statistical gain of 8 (low W) to 15 (high W) for neutrinos and by factors of 20 to 40 for antineutrinos, compared to the low energy (LE) mode where $\langle E_\nu \rangle \sim 3$ GeV. A total of $12{\times}10^{20}$ protons were delivered on target (POT) in neutrino and antineutrino mode.

4.3 Event Selection

For all analyses performed at MINERvA, the first step of the analysis is to select the desired events from the ntuples, for the chosen channel. This is done using a series of selection "cuts". MINERvA analysis tool is built around GAUDI software architecture [111]. These cuts can select events from a particular kinematic region, can select events from only a particular reconstructed energy of the antimuons, can select events from a specific region of the detector say iron in target 3, etc.

Signal Definition and Selection

For the inclusive analysis, we need all the antineutrino-induced charged current interactions ($\bar{\nu}_\mu$ CC), which produce an antimuon (μ^+) in the final state. Only the detection of this single antimuon as a product of the antineutrino interaction in the detector volume is sufficient to conduct the inclusive analysis. The second

requirement is that this (anti)muon must enter the MINOS ND, where its sign (whether it is a muon or an antimuon) and momentum can be determined based on range and curvature measurements. So, the requirement for event selection is that the (anti)muon must be matched in MINOS ND. This adds another constraint. Since MINOS ND sits 2 m downstream of the MINERvA detector, for the (anti)muon to be matched in the MINOS ND, it must be "forward going", such that all the muons should be within 17^0 of the (anti)neutrino beam direction. The summary of selection cuts used in the analysis presented in this thesis is as follows:

- **Heliicity cut**: The helicity of the selected event is checked to be left-handed for neutrinos or right-handed for antineutrinos. This is done by applying a cut on the charge of the outgoing muons. All events with positive muon charge (μ^+) are selected and rest are rejected.

- **Fiducial volume cut**: The events are checked to be within the fiducial volume of the detector and all the events which are outside the fiducial volume are rejected. For events in the active tracker region, the reconstructed interaction vertex must be within a hexagon of 850 mm apothem.

- **Z distance cut**: The z distance of the event in consideration is checked to be within the detector. The z coordinates of the detector are defined to be between 4290 mm to 6000 mm, for the nuclear target region, based on where the planes of the detector start and end. For the events in the active tracker region, all the events lying between scintillator modules 27 to 80 are selected.

- **Distance to division cut**: This cut is applied to make sure the reconstructed event vertex is far enough from the material lining that separates different nuclear targets as shown in Fig. 2.13. It is only used for the nuclear targets.

- **Dead time cut**: As discussed in Section 2.2.3, MINERvA experiences some dead time, when no event can be recorded. This happens during the beam

spill, while the charge is being read out. The consequence of this is that, during the dead time, the scintilators were not measuring any interaction and were dead and as the particle moves forward, its track is recorded in the downstream part of the detector when the dead time was over. Hence, the upstream part of a particle track could not be recorded. This is particularly challenging, as the rock muon events can be misidentified as CCQE (charged current quasielastic) events, because of the missing upstream track. The way to get around this problem is that the muon track is projected upstream by two modules and a check is placed on these two modules for if they were experiencing dead time. If two or more strips were in dead time, the event is rejected.

- **MINOS coil and curve cut**: The MINOS curve cuts identify the event to be an antineutrino or a neutrino event based on the curvature of the (anti)muon in the MINOS magnetic field. The antimuon detected in the MINOS ND must have a positive curvature, making sure the antimuon was produced from a $\bar{\nu}_\mu$ interaction in the MINERvA detector i.e. $q/|p| > 0$, where q and p are respectively the charge and momentum of the antimuon. The curvature method of antimuon reconstruction applies an additional constraint that the antimuon must have a curvature significance of at least 5σ to reduce the tails of the antimuon energy resolution spread [112] i.e. $(q/|p|)/\sigma_{q/p} \geq 5$, $\sigma_{q/p}$ being the error on the curvature measurement.

  The coil cut checks if the track of the (anti)muon ended within the MINOS coil or outside of it, such that the event must fall within the radial distance 210 mm $< R_{\text{event}} <$ 2500 mm [112, 113]. We use range and curvature measurements both for the energy reconstruction of the (anti)muon.

- **TargetID and Material Cut**: This cut is for the event vertex in the passive nuclear target region. Events are selected from different targets using the targetID cut, where different nuclear targets have been assigned different "targetIDs" as shown in Fig. 2.13 in Chapter 2. Using the material cut, one

of the different materials in the different targets is chosen to select events using the "targetZ" index, which corresponds to the atomic number of the different materials present in the target. To select events from the tracker region we use z-vertex between 5980 mm to 8422 mm.

- **Machine learning probability**: If the highest probability for the vertex reconstruction from the machine learning is less than 20 %, the event is excluded.

- **Muon energy cut**: Events corresponding to (anti)muon energy greater than 2 GeV and less than 20 GeV are selected and all the other ones are rejected. For the events below 2 GeV, they are not likely to traverse through the MINERvA detector, reach the MINOS detector and form a track in the MINOS ND. The upper limit of 20 GeV is applied because of the lack in understanding of the flux modeling in this energy region.

These cuts were used to select the desired inclusive event sample. All the events that pass these cuts are defined as "signal" candidates. Hence, for the inclusive analysis, **signal** is defined as *all antineutrino charged current events, with a* μ^+ *in the final state having interaction vertex within the fiducial volume of the detector, with energy* E_μ *between 2 and 20 GeV and scattering angle* $\theta_\mu < 17^0$. *There is no constrain on the number or type of particles in the final state except for an antimuon which has been matched in MINOS ND.*

The central value (CV) for MC simulation used is **MINERvA tune V4** as discussed in section 3.3. Table 4.1 summarizes the number of events selected for different materials inside the detector along with their *purity*.

In high-energy physics experiments, purity is defined as the ratio of the number of reconstructed signal events to the total number of selected (reconstructed) events (including background events). This is predicted using the MC sample.

$$\text{Purity} = \frac{N_{\text{signal}}}{N_{\text{total reconstructed}}} \tag{4.5}$$

Target	Material	Number of data events	Estimated purity
2	Iron	75760	83.8 %
	Lead	68544	86.1 %
3	Carbon	56742	81.3 %
	Iron	36634	83.4%
	Lead	22799	86.5 %
4	Lead	65445	75.5 %
5	Iron	52227	78.3 %
	Lead	35055	81.1 %
2+3+5	Combined Iron	245692	81.9 %
2+3+4+5	Combined Lead	249207	81.6 %
Tracker	CH (scintillator)	1822956	98.5%

Table 4.1: Number of antineutrino events reconstructed in data, for the inclusive sample, for different regions of the detector in different materials at MINERvA. The fourth column shows the estimated purity of the selected sample, predicted using MC.

It is interesting to note here that for the inclusive analysis, at MINERvA, we have such a high purity for the event sample in the tracker region ($\approx$ 99 %). The average purity for the nuclear target region is around 82 %. It must be also noted the number of selected events is (are) a high number(s) for the neutrino community. The numbers given in Table 4.1 are among the highest number of antineutrino events, on different nuclear targets in the same antineutrino beam analysed to date.

In Fig. 4.2 through 4.9, I have shown the selected event distribution in bins of $x - Q^2$, $W - Q^2$ and $p_z - p_t$ for carbon (target 3), combined Iron (target 2, 3 and 5), combined lead (target 2, 3, 4 and 5), and the tracker region breaking them down based on interaction channel. It is important to note here that we have not taken the contribution from iron and lead in target 1. Target 1 has been excluded because it is the most upstream target and has high rock muon contamination. This rock muon contamination becomes significant for the inclusive analysis. The selected inclusive events is the term $N_{\text{data},\alpha\beta}$ in Eq. 4.4.

These event distributions have been bin width normalised. So, to read the actual number of events in a given bin from the plot, we read the event rate from the y-axis (scaled by a factor of 10^{-4}) and multiply by the width of the bin to get the actual number of events in that given bin. The legend *other* refers to interaction channels like coherent pion production and others that could not be classified among the given categories on the legend. These plots for the different materials in individual targets have been given in Appendix A.

The bin edges for the different combinations of variables of our interest ($x - Q^2$, $W - Q^2$, and $p_z - p_t$) were chosen after constructing migration matrices, mapping the events in the reconstructed space to the truth space. For choosing the bin edges, we look for more than 50% diagonalization in our migration matrices mapping the reconstructed space to the true space. Until we achieve a diagonalized matrix, we keep changing the binning for the chosen combination of variables. This has been discussed in Section 4.5.1.

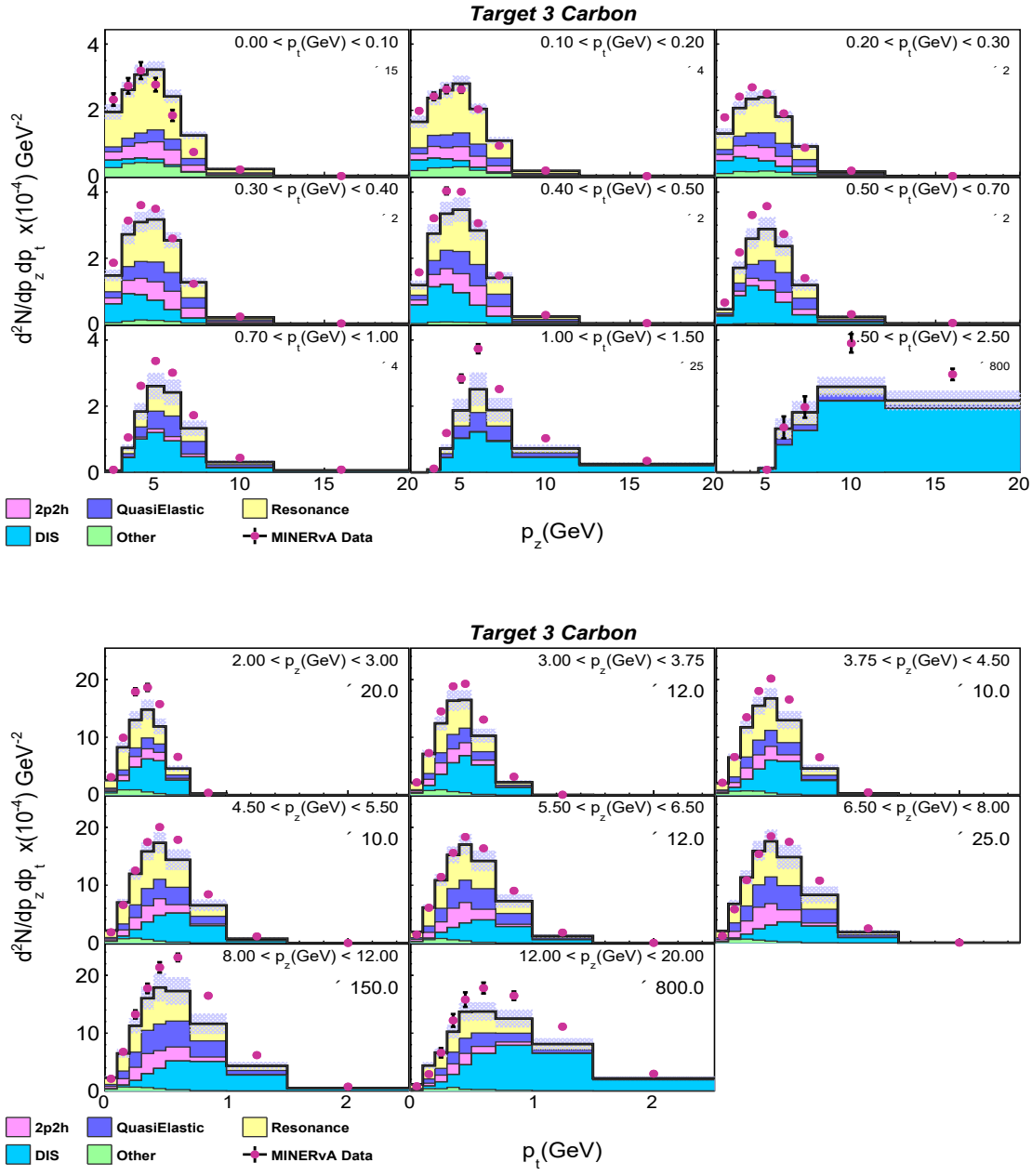

Figure 4.2: Selected inclusive double differential event distributions for carbon in antimuon longitudinal and transverse momentum bins. Top: Antimuon longitudinal momentum is on the x-axis, with each panel showing a different transverse momentum bin. Bottom: The axes are reversed, with transverse momentum on the x-axis. Data points (dark pink) include statistical errors, while stacked MC events are color-coded. Multipliers indicate scaling, with larger values for fewer events. Shaded blue bars show total MC errors (statistical and systematic).

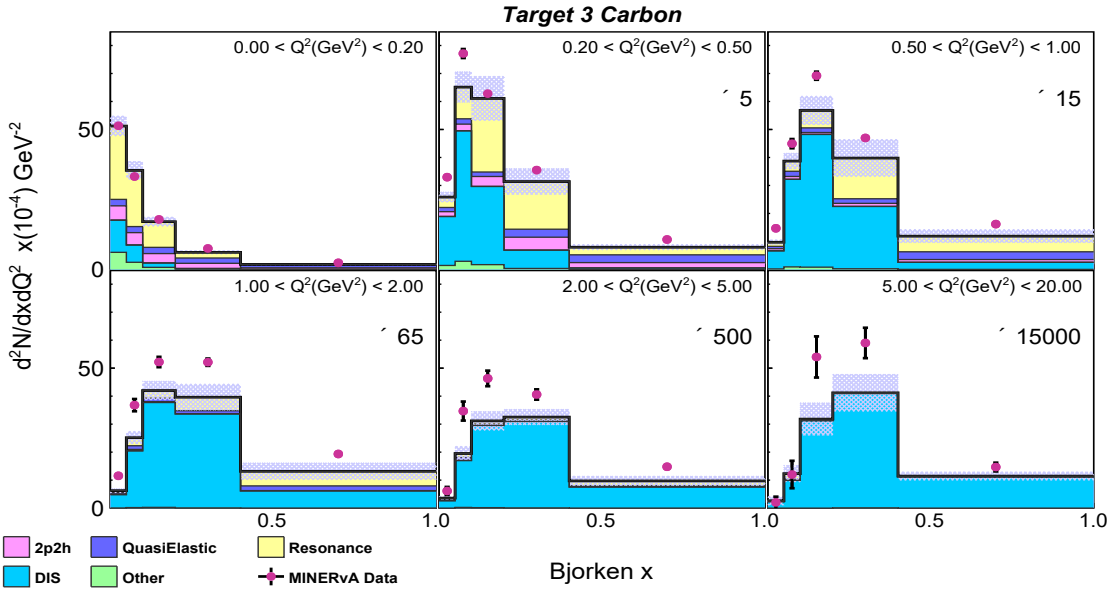

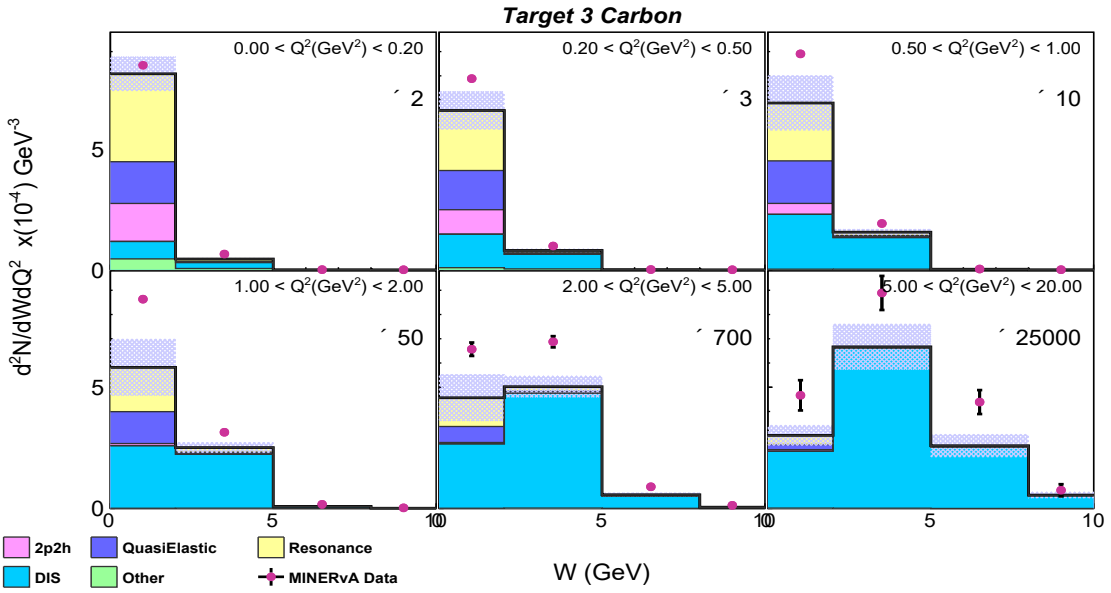

Figure 4.3: Selected inclusive double differential event distributions for carbon in bins of (top) bjorken x vs. Q^2 and (bottom) invariant mass W vs. Q^2. The x-axis shows bjorken x (top) and W (bottom), with each panel representing different Q^2 bins. Data points (dark pink dots) include statistical error bars, and MC events are stacked by channel in different colors. Multipliers indicate event scaling, with larger values corresponding to fewer events. Shaded blue bars represent total systematic and statistical errors on the MC.

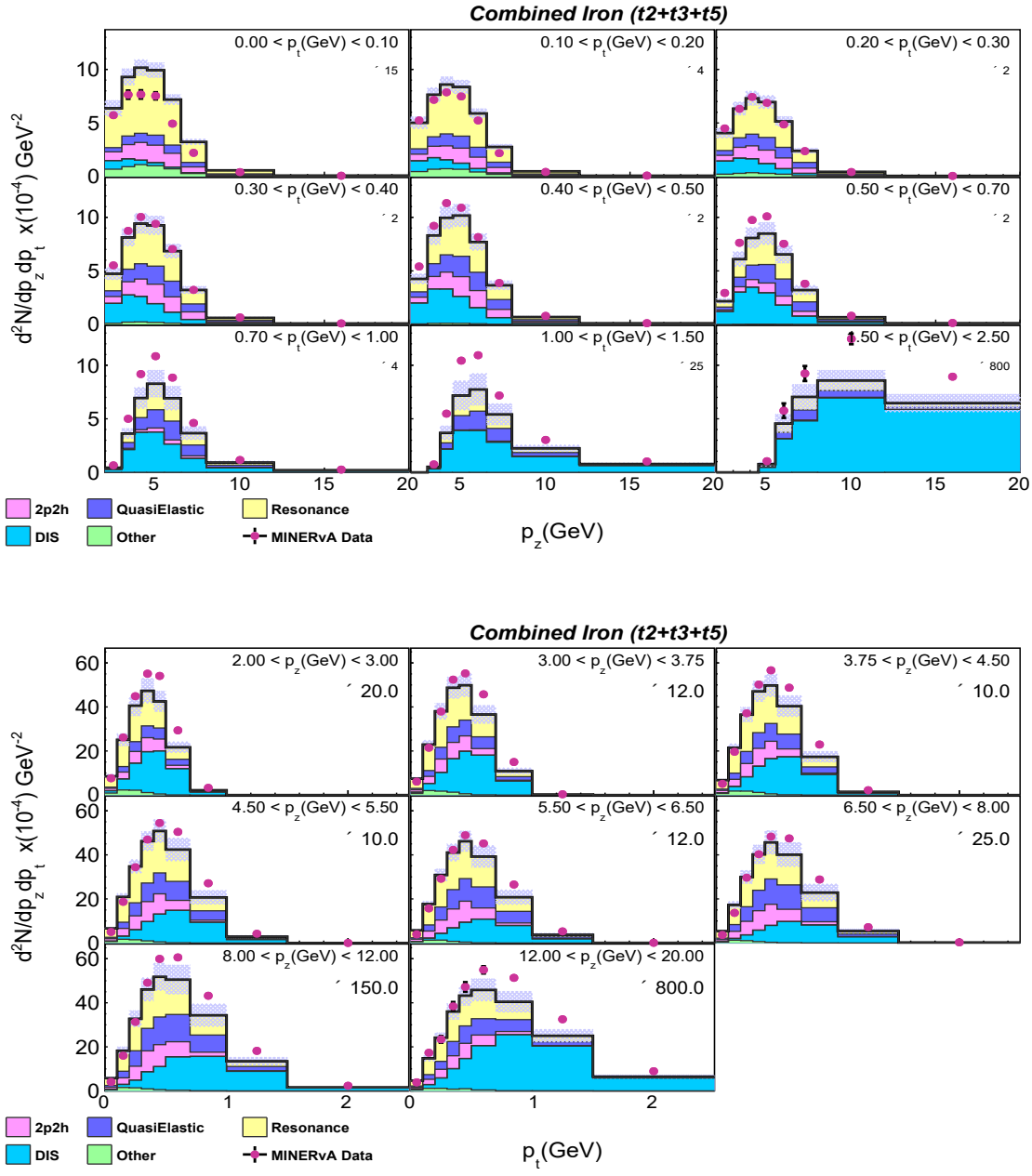

Figure 4.4: Selected inclusive double differential event distribution for combined iron in antimuon longitudinal and transverse momentum bins. Top: The x-axis shows antimuon longitudinal momentum, with panels representing transverse momentum bins. Bottom: The axes are reversed, with transverse momentum on the x-axis and longitudinal momentum across panels. Data points (dark pink) include statistical errors, while MC events are stacked by channel in different colors. Multipliers indicate event scaling, and shaded blue bars show total MC errors (statistical and systematic).

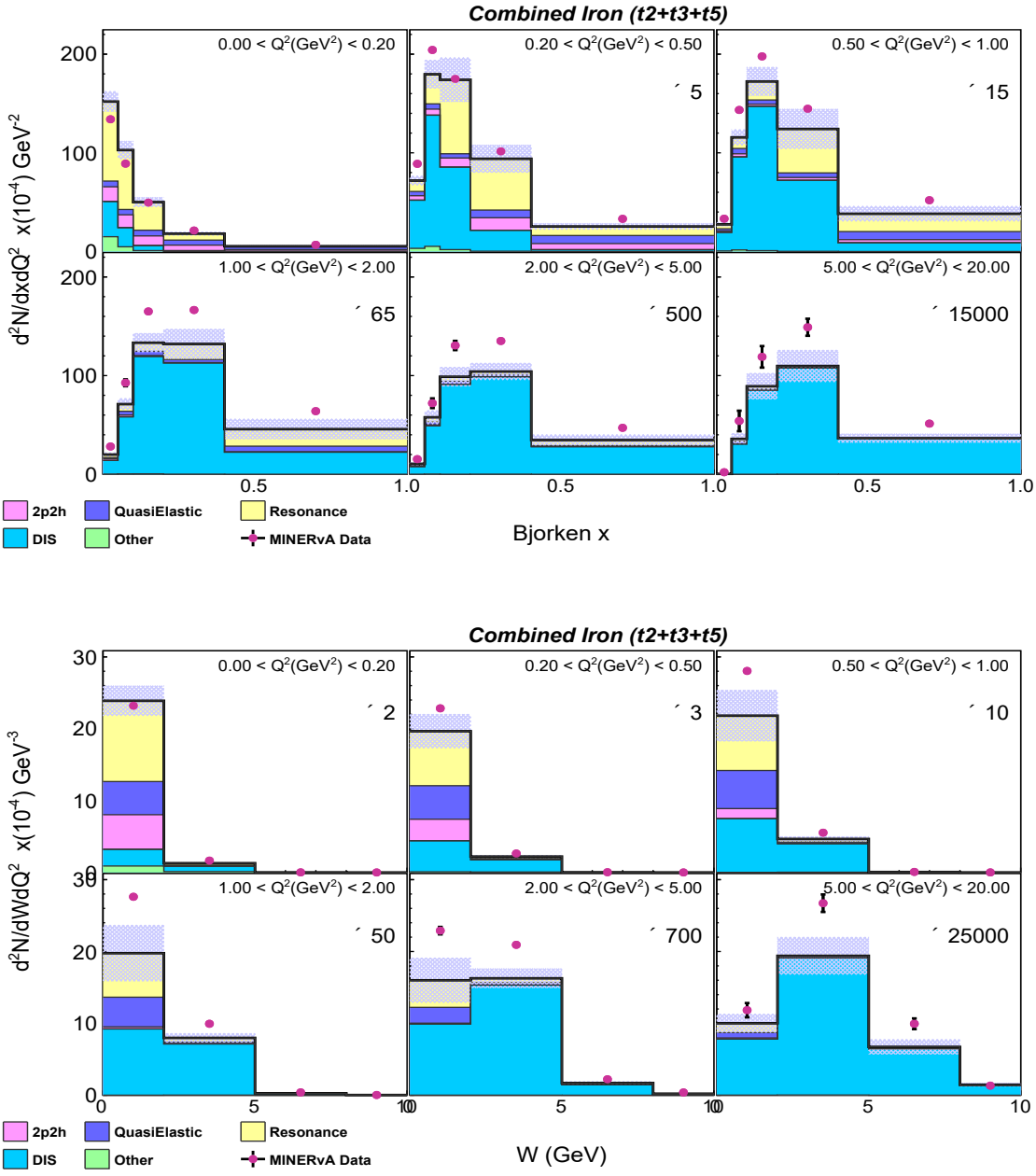

Figure 4.5: Selected inclusive double differential event distribution for combined iron in bins of bjorken x and Q^2, and W and Q^2. Top: The x-axis shows bjorken x, with panels representing Q^2 bins. Bottom: The x-axis shows invariant mass (W), with Q^2 bins across panels. Data points (dark pink) include statistical errors, and MC events are stacked by channel in different colors. Multipliers indicate event scaling, and shaded blue bars represent total MC errors (statistical and systematic).

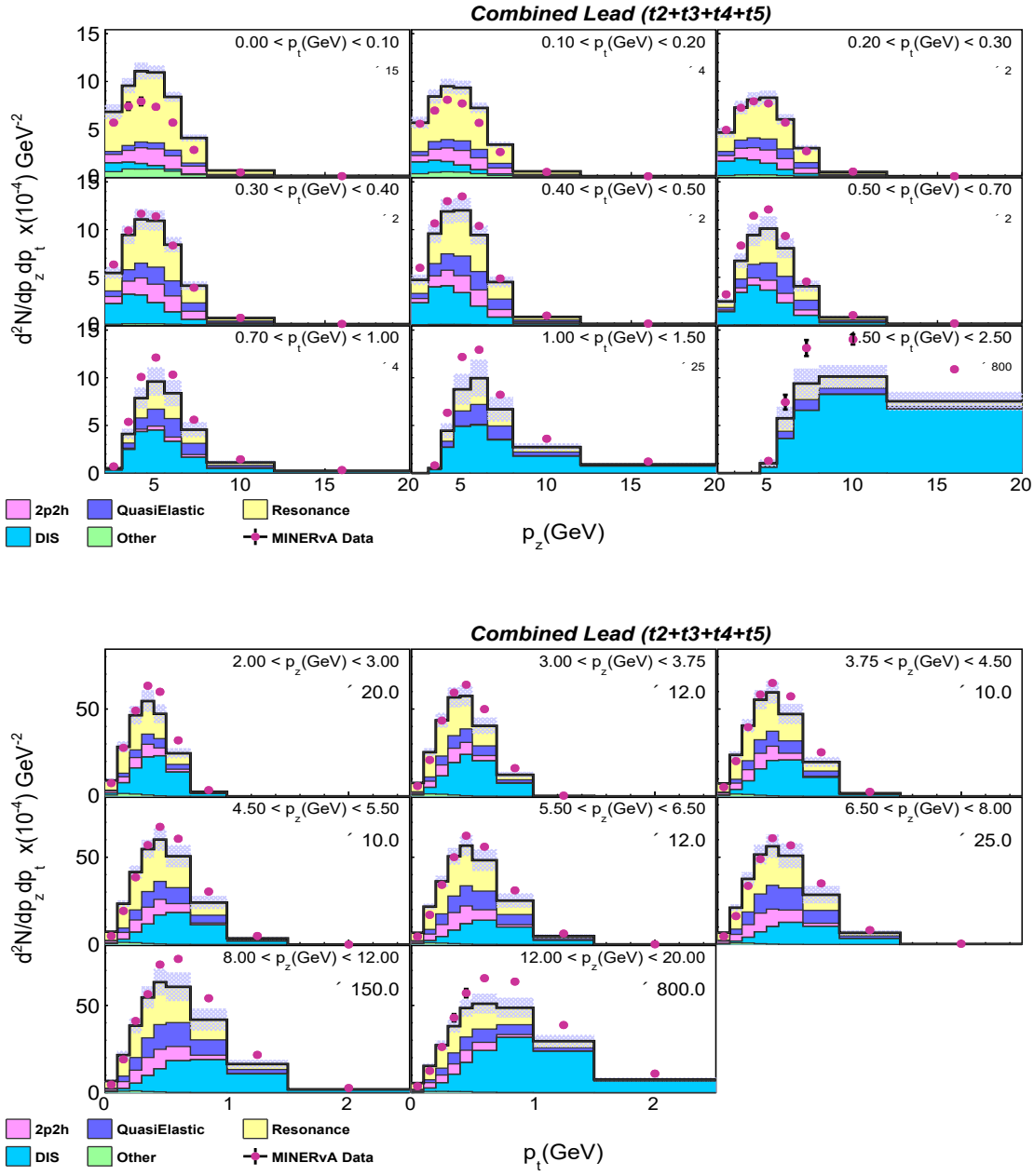

Figure 4.6: Selected inclusive double differential event distribution for combined lead in bins of antimuon longitudinal and transverse momentum. Top: The x-axis shows longitudinal momentum, with panels for transverse momentum bins. Bottom: The x-axis shows transverse momentum, with panels for longitudinal momentum bins. Data points (dark pink) include statistical errors, and MC events are stacked by channel in different colors. Multipliers indicate event scaling, and shaded blue bars show total MC errors (systematic and statistical).

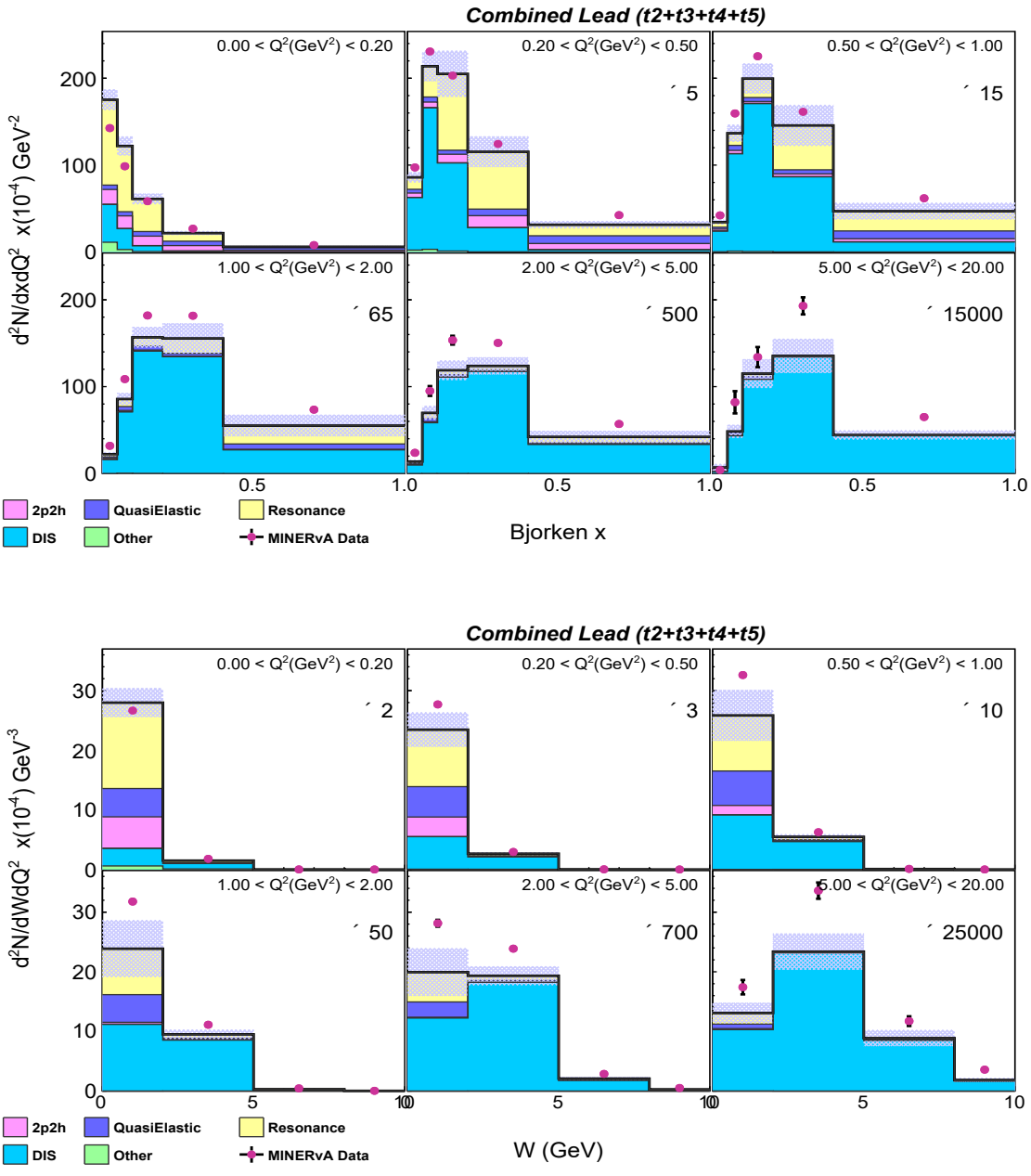

Figure 4.7: Selected inclusive double differential event distribution for combined lead in bins of bjorken x and four-momentum transfer squared, and W and Q^2. Top: The x-axis shows bjorken x, with panels representing different bins of Q^2. Bottom: The x-axis shows invariant mass (W) with panels for Q^2. Data points (dark pink dots) include statistical error bars, while MC events are stacked by component channel in different colors. Multipliers indicate event scaling, and shaded blue bars represent the total systematic and statistical errors on the MC.

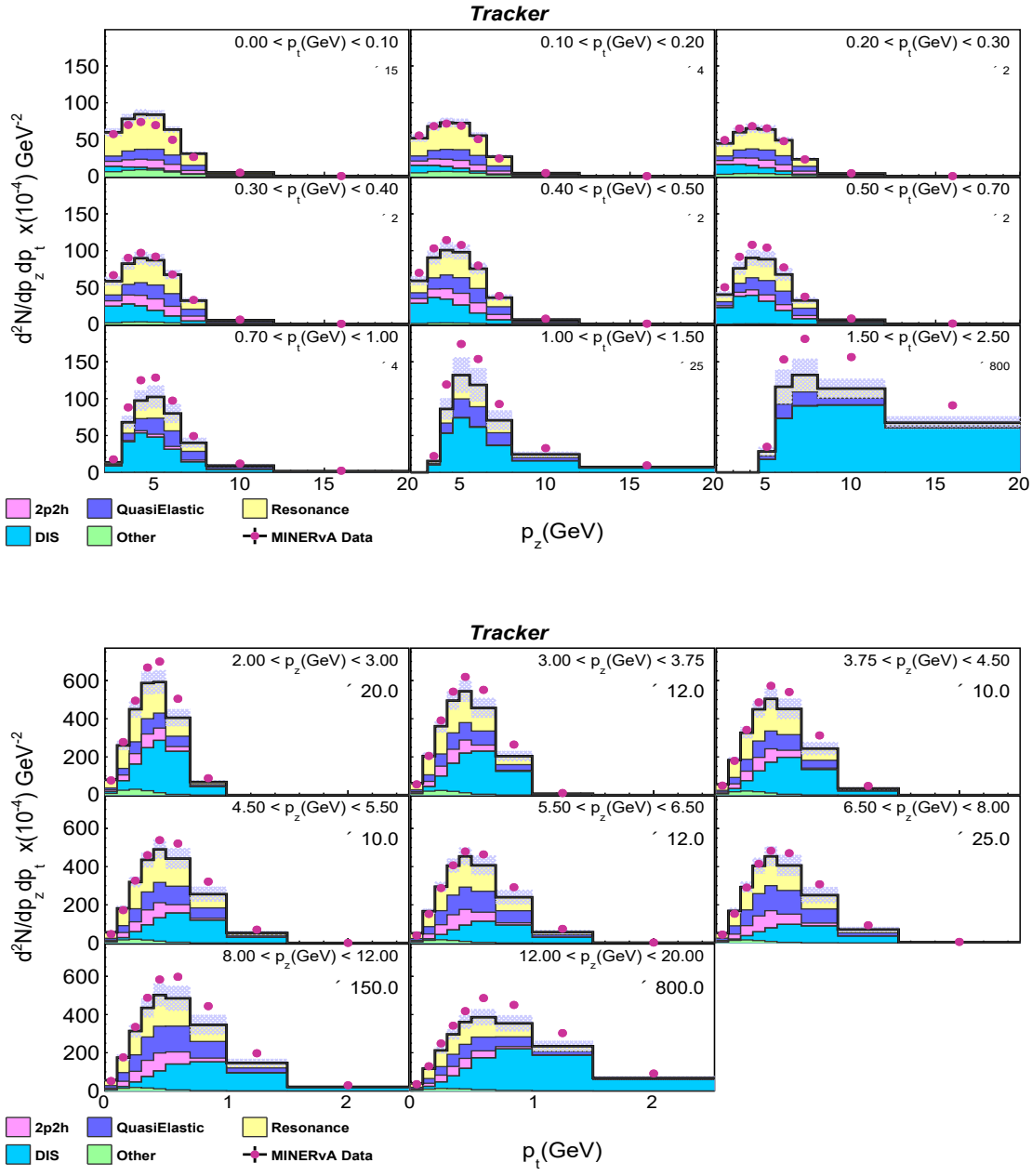

Figure 4.8: Selected inclusive double differential event distribution for the tracker in bins of antimuon longitudinal and transverse momentum. Top: The x-axis shows antimuon longitudinal momentum, with panels representing transverse momentum bins. Bottom: X-axis shows antimuon transverse momentum, with panels representing longitudinal momentum bins. Data points (dark pink dots) include statistical error bars, and MC events are stacked by component channel in different colors. Multipliers indicate event scaling, and shaded blue bars represent the total systematic and statistical errors on the MC.

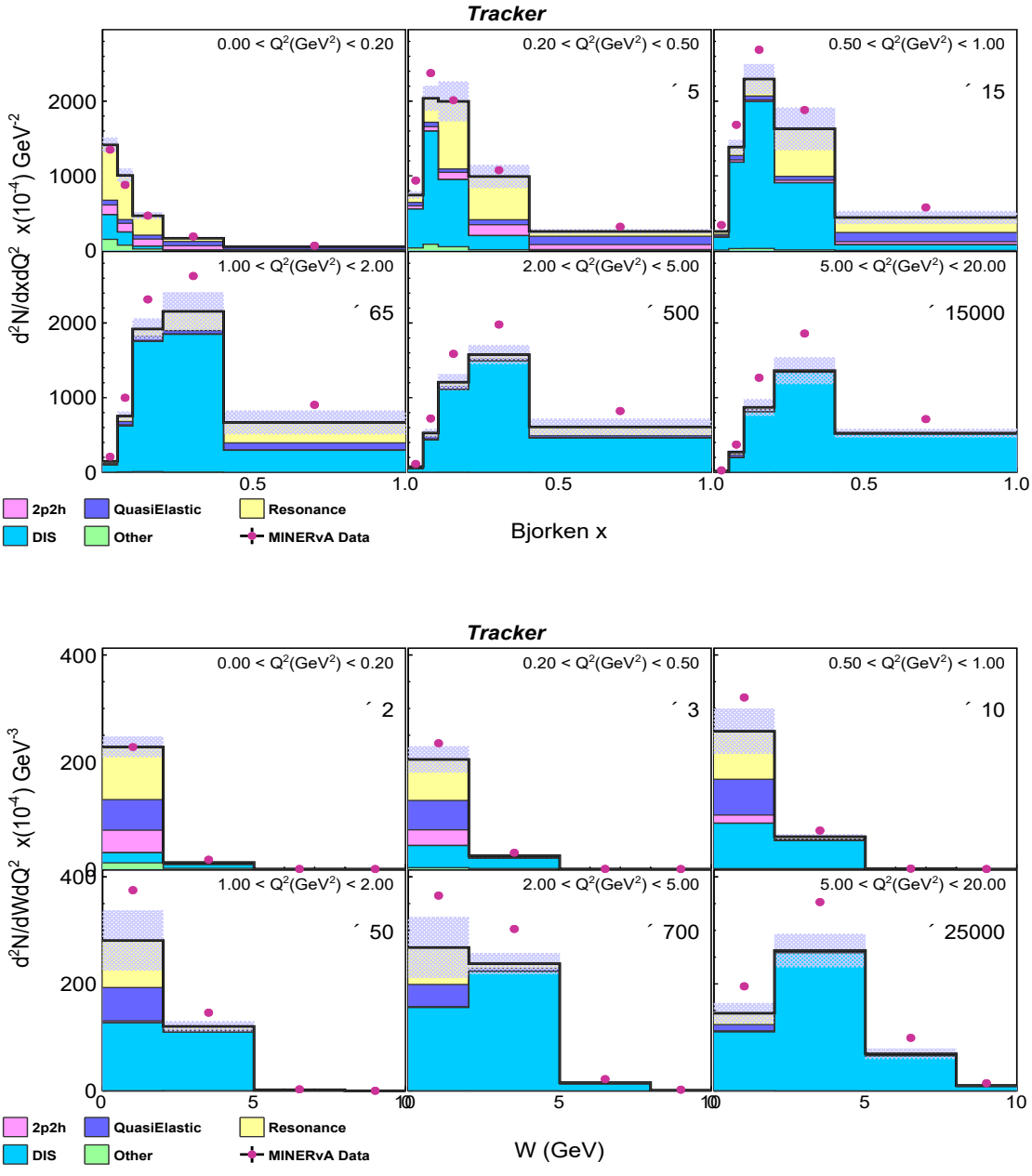

Figure 4.9: Selected inclusive double differential event distribution for the tracker in bins of bjorken x and four-momentum transfer squared, and invariant mass (W) and Q^2. Top: The x-axis shows bjorken x, with panels representing Q^2 bins. Bottom: The x-axis shows invariant mass (W), with panels representing Q^2 bins. Data points (dark pink dots) include statistical error bars, and MC events are stacked by component channel in different colors. Multipliers indicate event scaling, and shaded blue bars represent the total systematic and statistical errors on the MC.

As indicated by the purity numbers in the Table 4.1, some of the events may get misidentified as signal events passing our selection cuts, and need to be subtracted. We use information from the known simulation to estimate these events in data, called background events. The background events include events from plastic scintillators in the neighbourhood of nuclear targets, both upstream and downstream, shadowing the target in the $x - y$ plane. Backgrounds also have wrong sign events i.e. neutrino events in the antineutrino sample and neutral current (NC) events, which are events from a Z^0 exchange at the interaction vertex. There is also a slight contribution to the background from the events that do not pass the muon energy cut in the true space. Let us discuss how we dealt with these backgrounds in the following section.

4.4 Backgrounds

Now, we are dealing with the second term in the bracket of the numerator of Eq. 4.4, which is $N^{\text{bkgd}}_{\text{data},\alpha\beta}$. The main background in the inclusive analysis in the nuclear target region is the events from the neighbourhood scintillator (plastic) that got mis-reconstructed into the nuclear target region. In the simulation we can identify and categorise these background events into events from plastic, both in the upstream and downstream regions of the nuclear target. We also identify the wrong sign and neutral current events as mentioned earlier. A slight contribution to the background comes from the events that do not pass the antimuon energy cut ($2 < E_\mu < 20$GeV). Fig. 4.11 - 4.17 show the breakdown of background events in the bins of the chosen combination of variables, for carbon, combined iron, and combined lead, in the form of stacked plots. These plots for individual targets have been given in Appendix A. It must be noted that the y-axis on all of these background distribution plots, in Fig. 4.11 - 4.17 has been scaled by a factor of 10^{-4} and the events on the y-axis have been normalised by the width of the bins of chosen variables.

Since, the events from the plastic scintillators contaminate the nuclear target region, hence when compared to the tracker region, the purity of the sample is not as high as the tracker region, as seen from Table 4.1. As a result, the model dependence of the background must be accounted for and minimized by constraining the background in the MC sample to the data. Let us understand this. The background estimated by the MC is reliant on the theoretical prediction of the underlying models that the MC simulation is using, i.e. the underlying physics models that the GENIE MC generator is using. These predictions may not fully capture the neutrino interactions or flux. The inaccuracies in the prediction of the backgrounds by the models can be minimized by constraining them, using control samples which are background-enhanced regions in the detector, typically referred to as sidebands, where the signal is virtually absent.

This makes sure that the background subtraction reflects actual data recorded by the experiment, rather than a potentially flawed underlying model from the MC event generator. By this method, the prediction is aligned more closely with the data, reducing the impact of the model-dependent systematic uncertainties, and leading to a more robust measurement. For the above-stated constraining of the background, the idea that we use is to look for event distribution in background-enhanced regions called **sidebands**.

The sideband region has been depicted in Fig. 4.10, namely the upstream and the downstream sideband. Each sideband region has been defined to be constituted of six planes. It is important to note that the immediate neighbouring module (one module consists of two planes) to the nuclear target has been excluded from the sideband region because there can be significant mis-reconstruction of the target (signal) events in these scintillator planes. Because the sideband region is enhanced in background events, with a minimal number of signal events, looking at the event distribution in this region is a good estimate of the nature of the background distribution in the actual signal region i.e. the nuclear target.

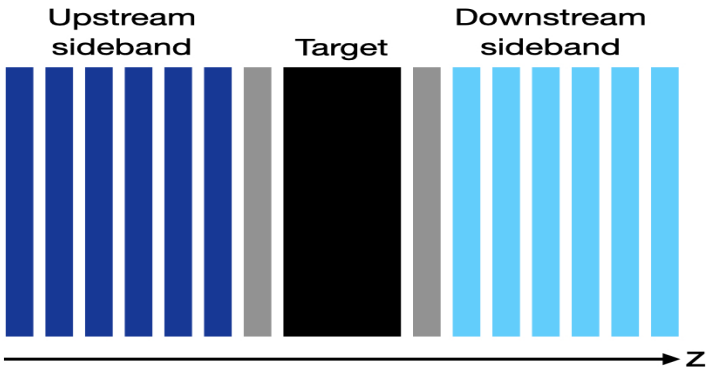

Figure 4.10: Schematic diagram representing the upstream (navy) and downstream (light blue) sideband regions, where 3 modules (6 scintillator planes) are included and the modules immediately next to the nuclear target (black) shown in gray are excluded from the definition of sideband region.

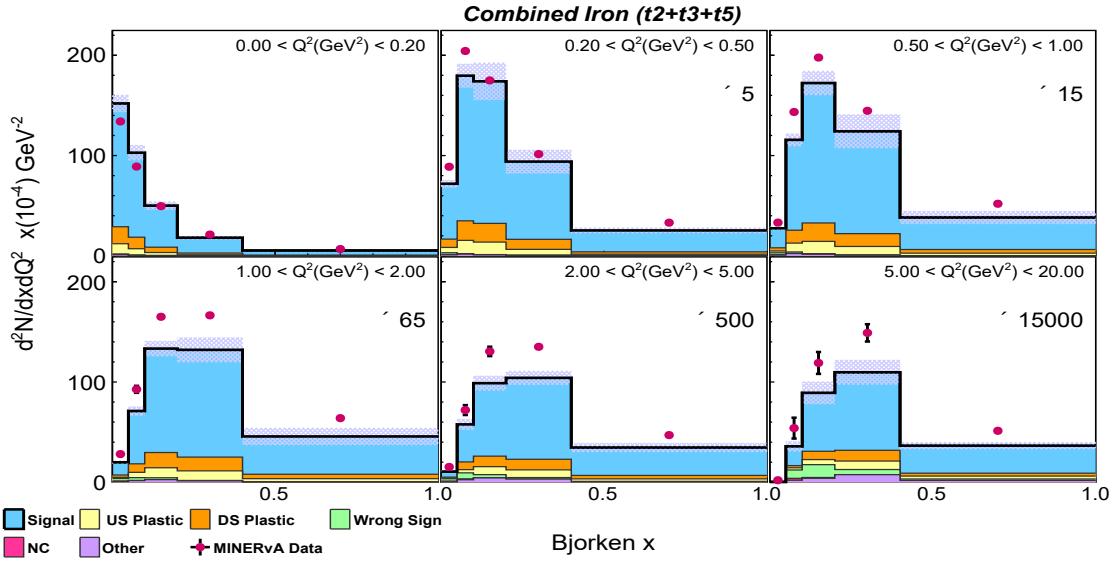

Figure 4.11: Selected inclusive double differential event distribution for iron in bins of bjorken x and four-momentum transfer squared (Q^2), depicting the contribution from background events in different colors as stacked histograms. Data points are shown in dark pink colored dots with statistical error bars. The multiplier numbers is each panel represent the amount of times the events in that panel were scaled, for better visibility on the plot. The shaded purple bars on the MC represent the total systematic and statistical error on the MC.

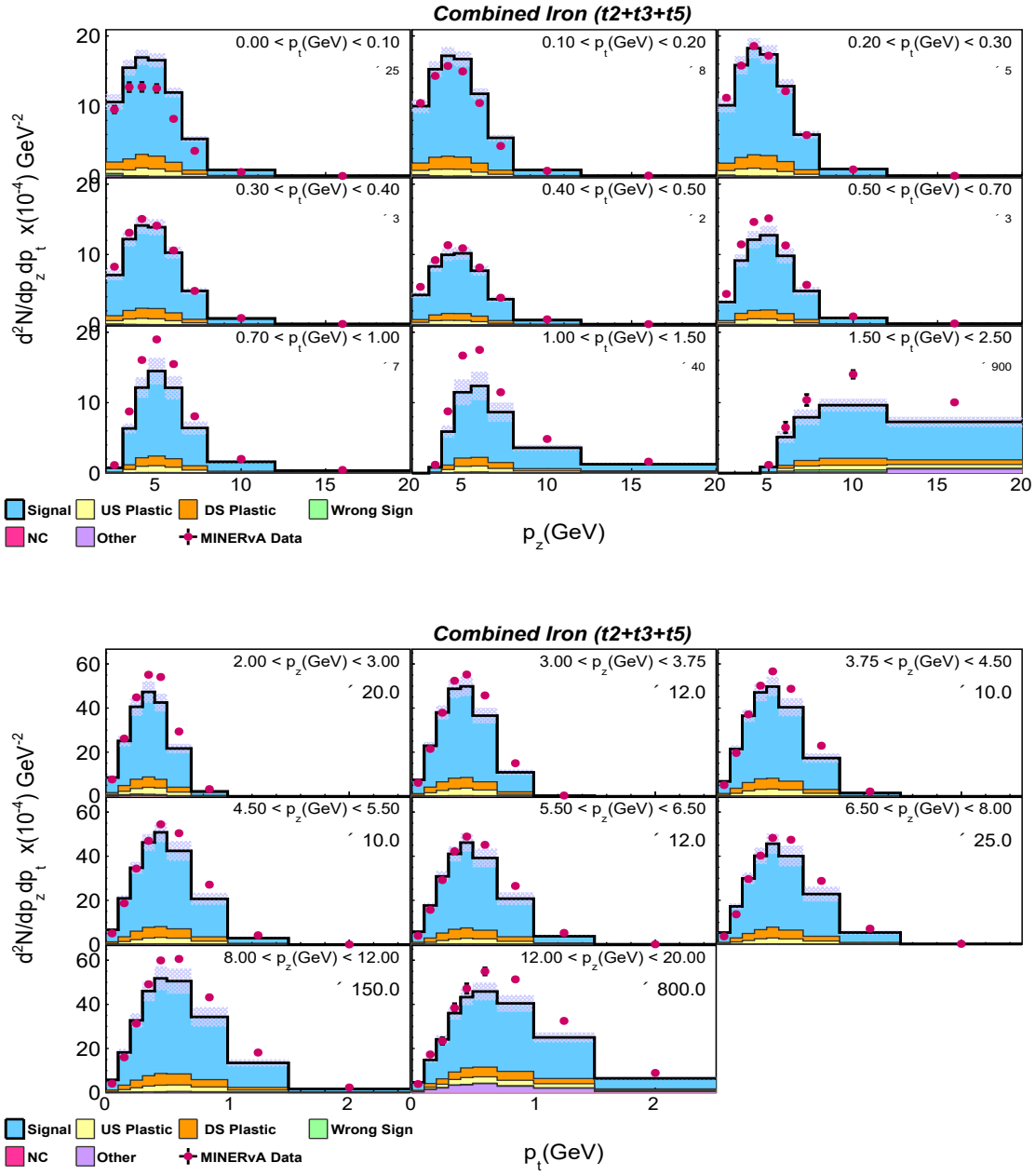

Figure 4.12: Selected inclusive double differential event distribution for iron in bins of antimuon momenta. Top: The x-axis shows antimuon longitudinal momentum panels representing transverse momentum bins. Bottom: The axes are reversed, displaying transverse momentum on the x-axis and longitudinal momentum in the panels. Stacked histograms in various colors represent background contributions, while dark pink dots indicate data points with statistical error bars. Multipliers show scaling for visibility, and shaded purple bars illustrate total systematic and statistical errors on the MC.

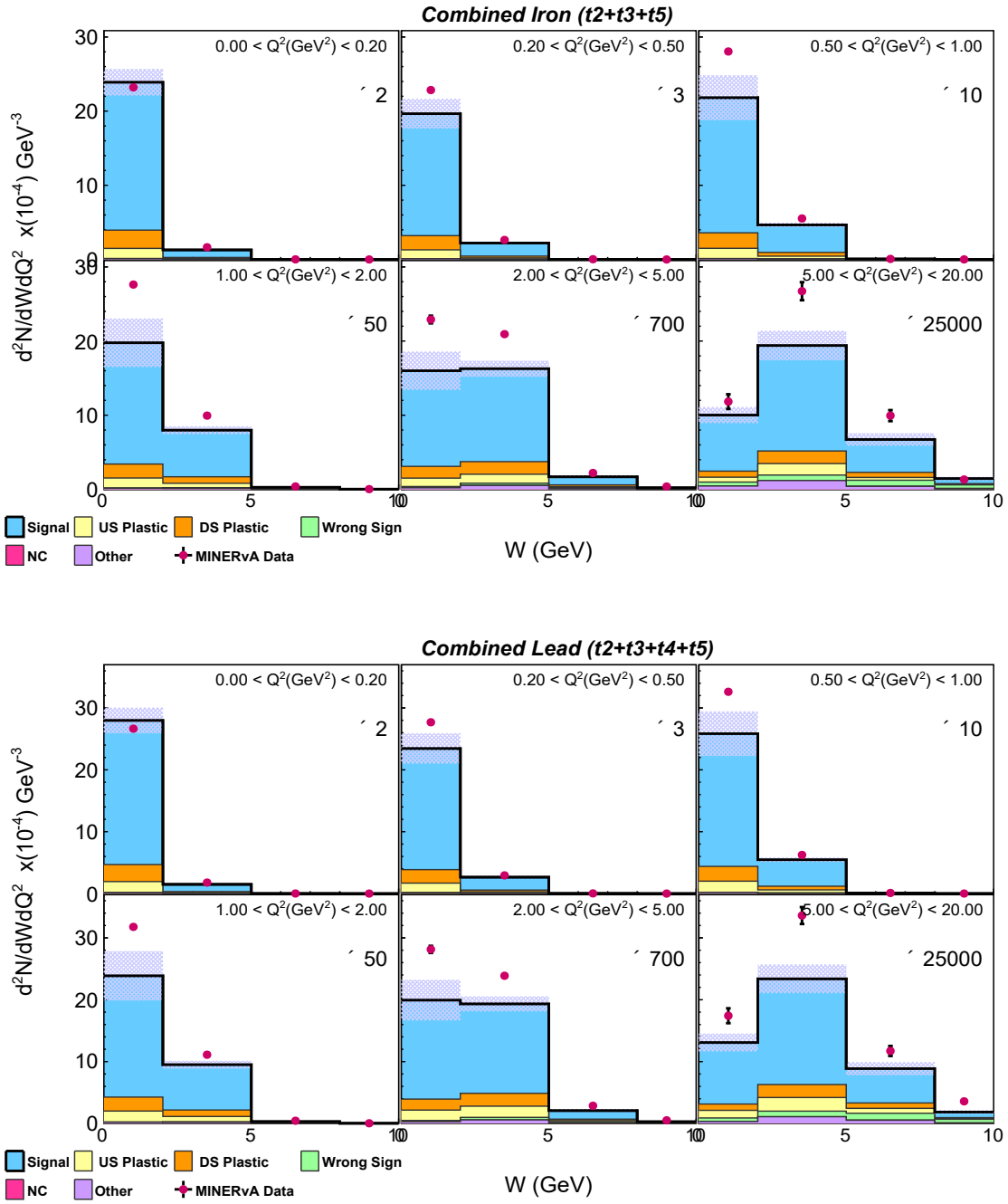

Figure 4.13: Selected inclusive double differential event distribution for iron and lead in bins of W and Q^2. Top: For iron, the x-axis shows invariant mass W bins. Bottom: The same distribution for lead. Background contributions are stacked in various colors, while data points are dark pink dots with statistical error bars. Multiplier numbers indicate scaling, and shaded purple bars represent total systematic and statistical errors.

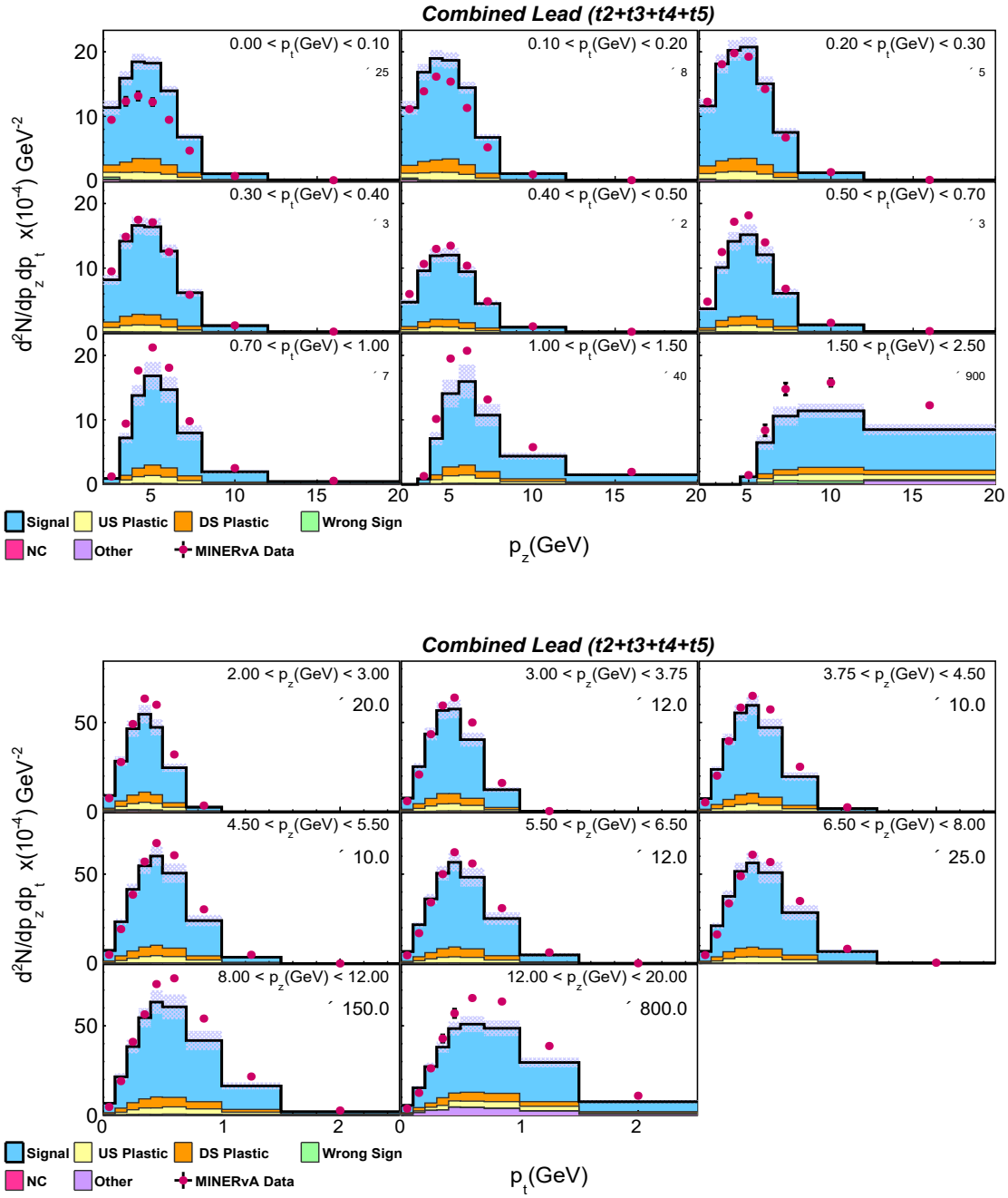

Figure 4.14: Selected inclusive double differential event distribution for lead in antimuon momentum bins. Top: The x-axis shows antimuon longitudinal momentum with panels for transverse momentum bins. Bottom: The x-axis represents transverse momentum, and panels depict longitudinal momentum bins. Histograms are stacked.

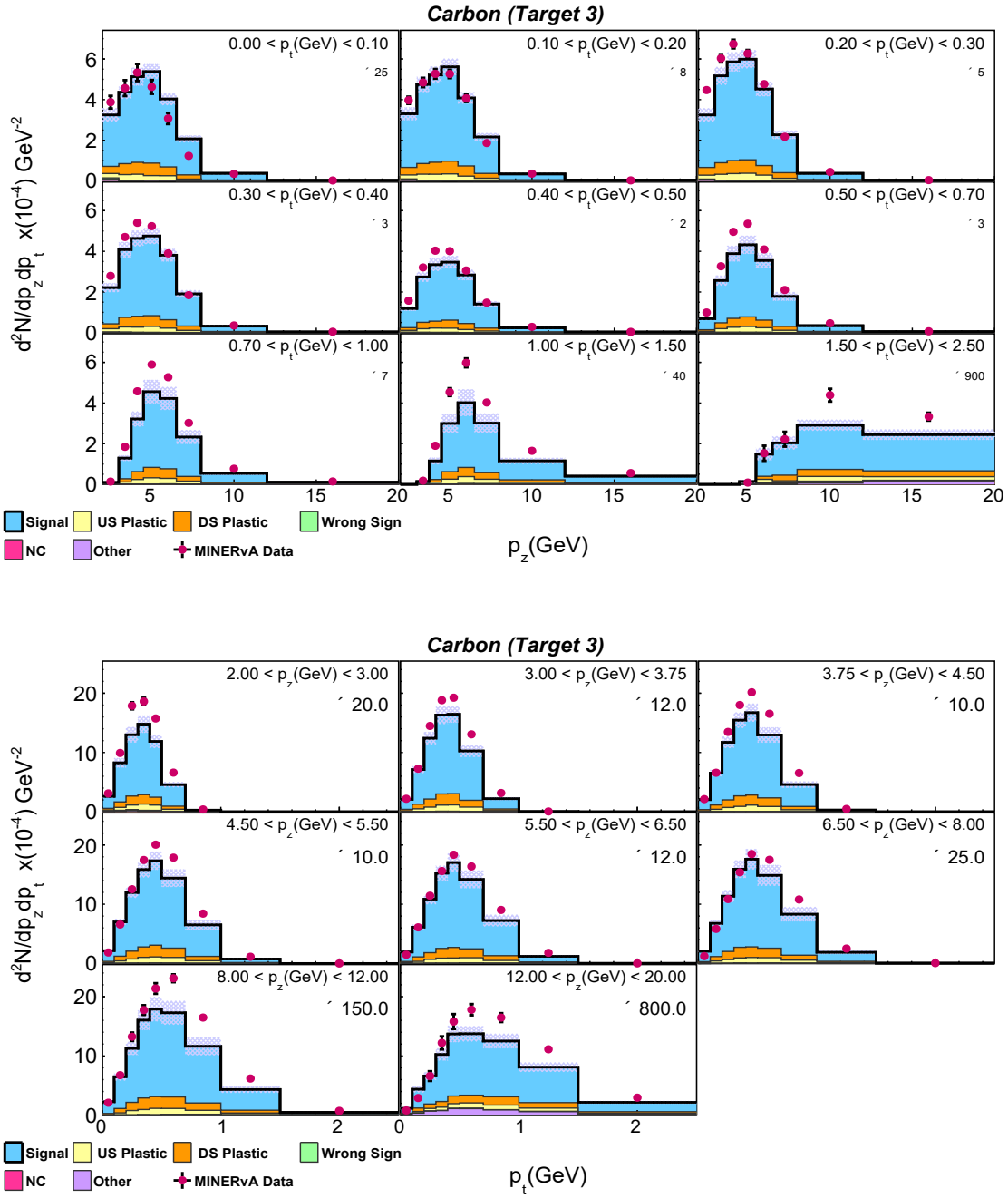

Figure 4.15: Selected inclusive double differential event distribution for carbon in bins of antimuon momenta. Top: The x-axis shows the antimuon longitudinal momentum, with panels representing different bins of transverse momentum. Bottom: The x-axis displays transverse momentum, with panels showing different bins of longitudinal momentum. Background contributions are depicted as stacked histograms in various colors.

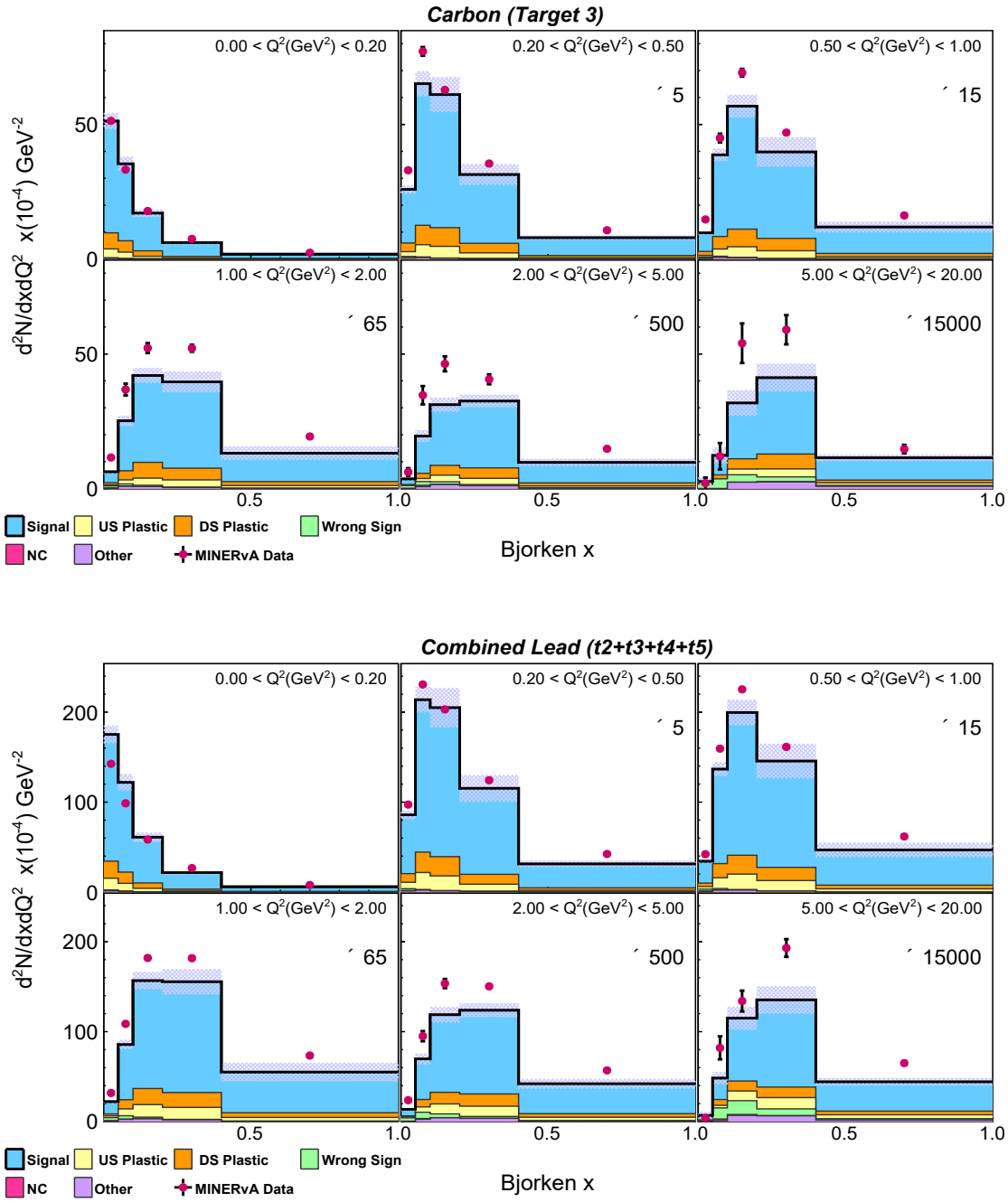

Figure 4.16: Selected inclusive double differential event distribution in bins of $x - Q^2$. The x-axis shows bjorken x with panels representing different bins of Q^2 for (top) carbon and (bottom) lead, depicting the contribution from background events in different colors as stacked histograms.

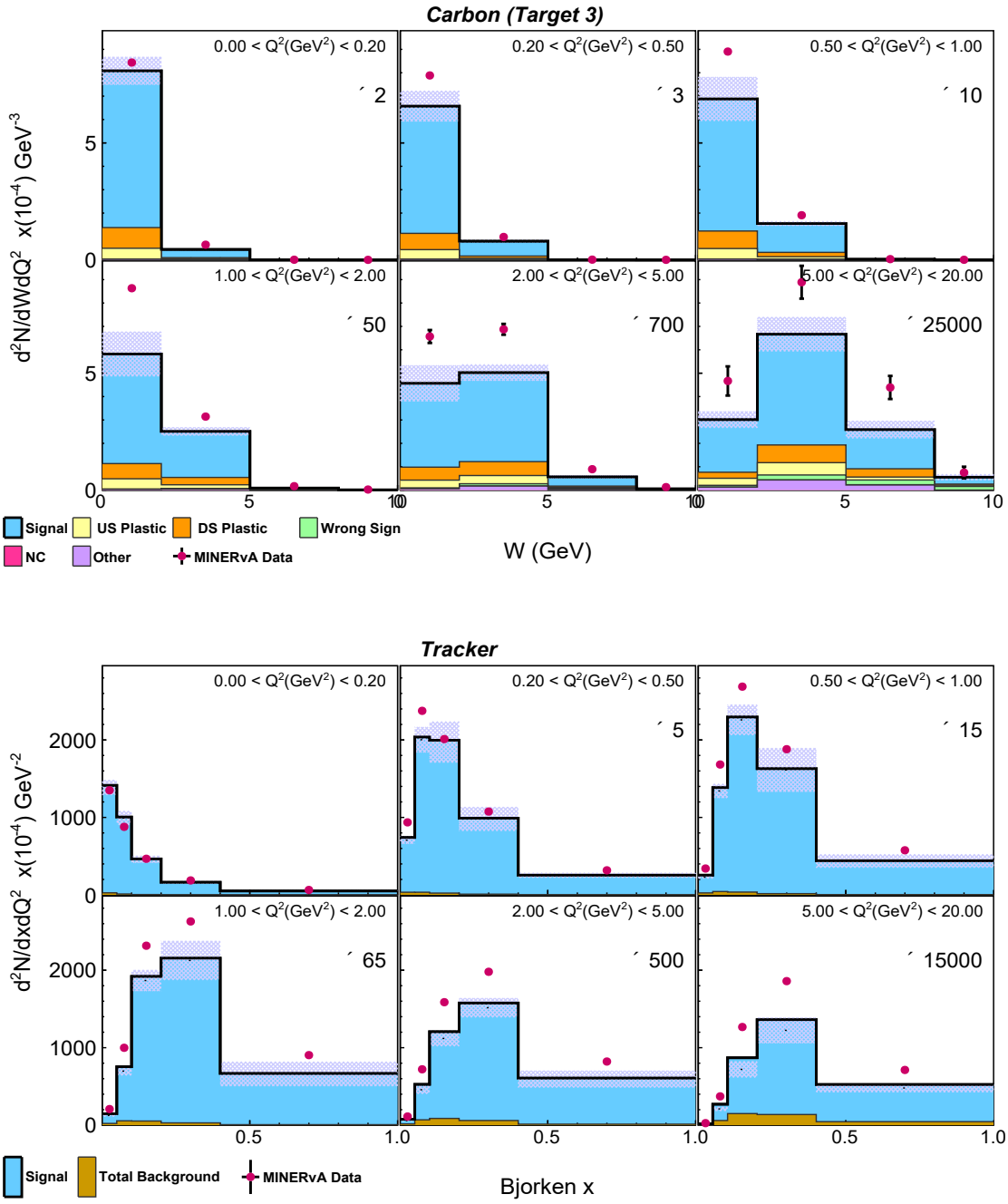

Figure 4.17: Selected inclusive double differential event distribution for (top) carbon in bins of $W-Q^2$ and (bottom) tracker in bins of $x-Q^2$. The x-axis shows (top) invariant mass W, (bottom) bjorken x, with panels representing different bins of Q^2, depicting the contribution from background events in different colors as stacked histograms. Data points are shown in dark pink colored dots with statistical error bars.

We have not shown here, the background events in the tracker scintillator as a function of $p_z - p_t$ and $W - Q^2$ because the purity of the tracker sample is high and contribution to background events comes mainly from wrong sign events, which is pretty low, as indicative from Fig. 4.17 bottom plot.

4.4.1 Background subtraction procedure: Plastic Sidebands

The distribution of events in the background-enhanced plastic sideband regions is used to constrain the MC background prediction to data in the nuclear target region. Based on selection cuts on different materials, and z position, event distribution is obtained in the sidebands for both the upstream and downstream of a particular nuclear target. It is important to note that the upstream region for target 1 was not used for the upstream (US) sideband region, because of potential high rock antimuon contamination in this region.

We construct two templates, one each for the upstream (US) and the downstream (DS) sideband region. These consist of the sum of all the events where the interaction vertex is reconstructed either in the upstream (US template) or the downstream (DS template) plastic region shadowing the nuclear target. A χ^2 minimization technique, using the ROOT Minuit2Minimizer function is used to fit the data to the MC in both the US and DS sideband templates, in each bin i of one of the two chosen variables of interest, for example, we performed the fit in bins of Q^2 for the combination $x - Q^2$ and $W - Q^2$ and in bins of p_t for the combination $p_z - p_t$. This minimization is performed by extracting a scaling factor per bin of our fitting variable (Q^2 and p_t), to obtain the best fit between data and MC, such that χ^2 between data and MC is minimized (closer to 1). Once we obtain these scaling factors, the MC backgrounds in the nuclear target region are scaled in each bin of the chosen combination of variables using the values of the scaling factors extracted in each bin of the fitting variable. Since we extracted the scaling factors, by tuning the MC to the data in a background-enhanced region (sideband), using

these same scaling factors to constrain the MC background in the signal region to obtain the background estimate in data, is a sensible approach, as mentioned earlier. Graphical representation of the extracted scaling factors per bin, for the upstream and downstream sideband templates has been shown in Fig. 4.18 and 4.19.

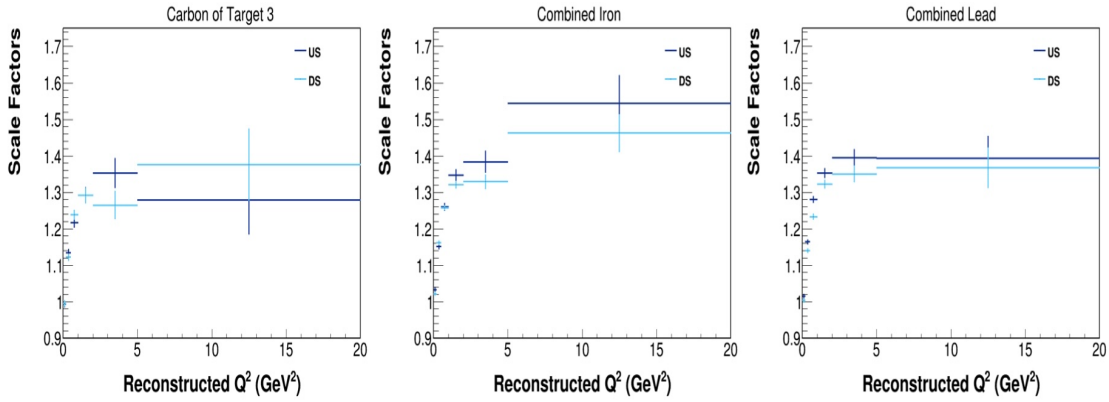

Figure 4.18: Scaling factors for carbon, combined iron and combined lead, in bins of four-momentum transfer squared (Q^2).

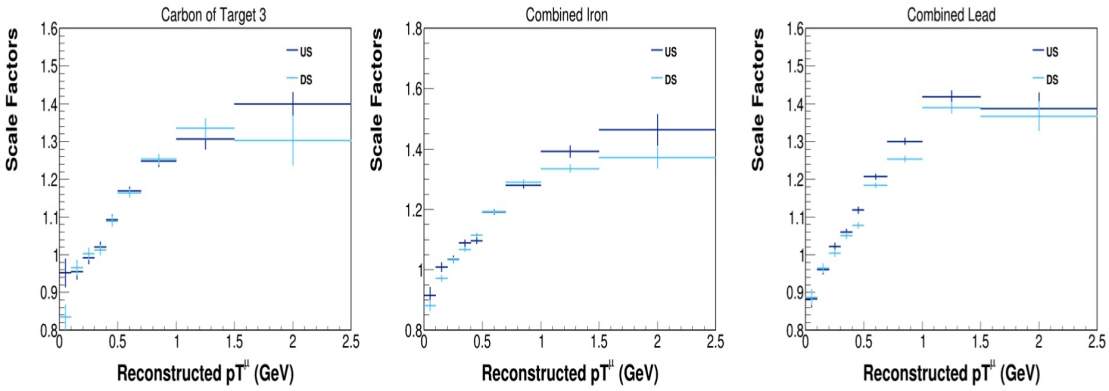

Figure 4.19: Scaling factors for carbon, combined iron and combined lead, in bins of antimuon transverse momentum (pT^{μ}).

In Table 4.2 and 4.3, we have shown the values of the scaling factors extracted per bin of Q^2 with systematic and statistical errors in the upstream and downstream sidebands, respectively. These scaling factors were applied to the two-dimensional distributions in bins of $x - Q^2$ and $W - Q^2$.

Q^2 **bin** (**GeV**^{2})	**US Scaling Factors** (±**stat.** ± **syst.**)		
	Carbon	**Iron**	**Lead**
0-0.2	0.994 ± 0.009 ±0.086	1.033 ±0.006 ±0.091	1.015 ± 0.006 ±0.096
0.2-0.5	1.133 ±0.01 ± 0.129	1.151±0.007 ±0.133	1.164±0.006 ±0.141
0.5-1.0	1.216 ±0.013 ±0.171	1.261±0.01 ±0.179	1.281 ±0.008 ±0.186
1.0-2.0	1.292 ±0.021 ±0.189	1.347±0.015 ± 0.203	1.353±0.013 ±0.206
2.0-5.0	1.353 ± 0.041 ±0.159	1.384±0.029 ±0.163	1.394±0.024 ±0.172
5.0-20.0	1.278 ±0.094 ± 0.166	1.544±0.077 ±0.197	1.393±0.061 ±0.183

Table 4.2: Scaling factors (with statistical and systematic uncertainties) extracted per bin of Q^2 for different nuclear targets in the upstream sideband

Q^2 **bin** (**GeV**^{2})	**DS Scaling Factors** (±**stat.** ± **syst.**)		
	Carbon	**Iron**	**Lead**
0-0.2	0.995 ± 0.009 ±0.086	1.022 ±0.004 ±0.089	1.003 ± 0.005 ±0.095
0.2-0.5	1.122 ±0.01 ± 0.127	1.161±0.005 ±0.133	1.139±0.006 ±0.137
0.5-1.0	1.238 ±0.013 ±0.174	1.258±0.007 ±0.176	1.233 ±0.008 ±0.178
1.0-2.0	1.291 ±0.021 ±0.19	1.321±0.011 ± 0.196	1.322±0.012 ±0.196
2.0-5.0	1.264 ± 0.038 ±0.15	1.329±0.019 ±0.158	1.35±0.022 ±0.16
5.0-20.0	1.376 ±0.098 ± 0.169	1.462±0.051 ±0.184	1.368±0.055 ±0.171

Table 4.3: Scaling factors (with statistical and systematic uncertainties) extracted per bin of Q^2 for different nuclear targets in the downstream sideband

In Table 4.4 and 4.5 we have given the scaling factors extracted in bins of the antimuon transverse momentum, used to tune the two-dimensional distributions in $p_z - p_t$. As an example, of how these scaling factors tune the MC to the data in the sideband region, the sideband event distribution in the downstream sideband for combined iron material has been shown in Fig. 4.20 and Fig. 4.21.

p_t **bin** (**GeV**^{2})	**US Scaling Factors** (±**stat.** ± **syst.**)		
	Carbon	**Iron**	**Lead**
0-0.1	0.952 ± 0.037 ±0.067	0.916 ±0.026 ±0.066	0.882 ± 0.021 ±0.068
0.1-0.2	0.954 ±0.02 ± 0.077	1.01±0.015 ±0.083	0.961±0.012 ±0.084
0.2-0.3	0.991 ±0.016 ±0.085	1.035±0.012 ±0.092	1.022 ±0.010 ±0.096
0.3-0.4	1.02 ±0.013 ±0.095	1.088±0.011 ± 0.103	1.06±0.009 ±0.107
0.4-0.5	1.093 ± 0.014 ±0.112	1.096±0.011 ±0.113	1.118±0.009 ±0.123
0.5-0.7	1.168 ±0.011 ± 0.142	1.091±0.008 ±0.146	1.206±0.007 ±0.153
0.7-1.0	1.248 ±0.014 ± 0.187	1.281±0.011 ±0.194	1.30±0.009 ±0.201
1.0-1.5	1.306 ±0.027 ± 0.205	1.392±0.019 ±0.225	1.418±0.016 ±0.235
1.5-2.5	1.40 ±0.069 ± 0.174	1.463±0.051 ±0.183	1.387±0.042 ±0.178

Table 4.4: Scaling factors (with statistical and systematic uncertainties) extracted per bin of antimuon transverse momentum (p_t) for different nuclear targets in the upstream sideband

p_t **bin** (**GeV**^{2})	**DS Scaling Factors** (±**stat.** ± **syst.**)		
	Carbon	**Iron**	**Lead**
0-0.1	0.834 ± 0.033 ±0.059	0.882 ±0.017 ±0.063	0.887 ± 0.021 ±0.066
0.1-0.2	0.965 ±0.02 ± 0.077	0.971±0.01 ±0.078	0.964±0.012 ±0.084
0.2-0.3	1.002 ±0.016 ±0.087	1.033±0.008 ±0.089	1.003 ±0.009 ±0.094
0.3-0.4	1.012 ±0.013 ±0.094	1.067±0.007 ± 0.10	1.05±0.008 ±0.105
0.4-0.5	1.089 ± 0.014 ±0.111	1.115±0.007 ±0.114	1.078±0.008 ±0.117
0.5-0.7	1.163 ±0.011 ± 0.141	1.193±0.006 ±0.144	1.184±0.007 ±0.149
0.7-1.0	1.253 ±0.014 ± 0.187	1.291±0.007 ±0.193	1.253±0.008 ±0.191
1.0-1.5	1.334 ±0.026 ± 0.212	1.335±0.013 ±0.214	1.389±0.015 ±0.226
1.5-2.5	1.303 ±0.066 ± 0.16	1.371±0.034 ±0.17	1.367±0.038 ±0.173

Table 4.5: Scaling factors (with statistical and systematic uncertainties) extracted per bin of antimuon transverse momentum (p_t) for different nuclear targets in the downstream sideband

Fig. 4.20 shows the distribution of plastic sideband events before the extracted scaling factors given in Table 4.3 were applied to the sideband distribution called untuned distribution. In contrast, Fig. 4.21 shows the distribution of the downstream sideband events after the extracted scaling factors from Table 4.3 were applied to tune the MC to data, now referred to as tuned distributions.

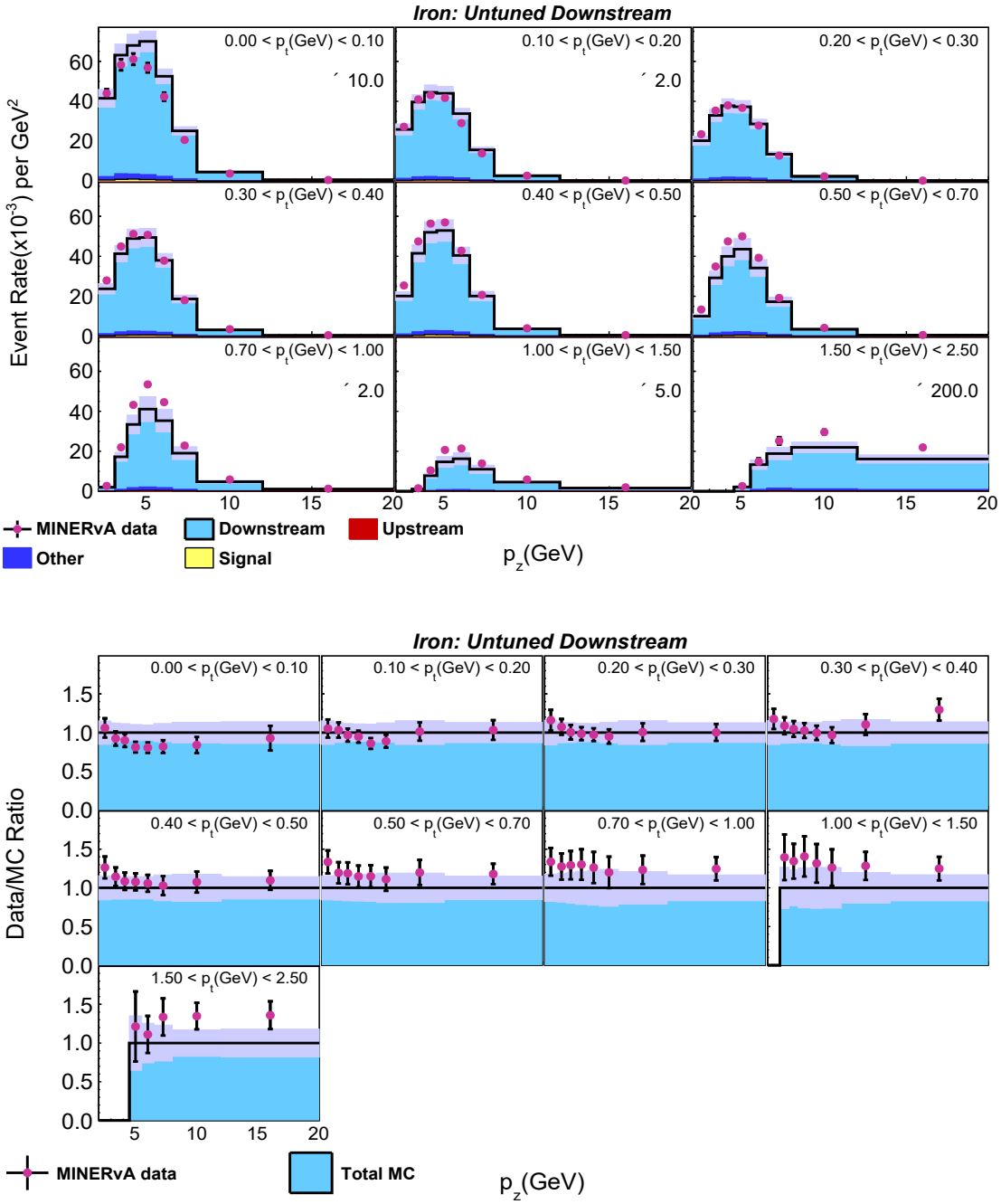

Figure 4.20: Top: Distribution of plastic events downstream of iron before scaling, shown in bins of antimuon momenta ($p_z - p_t$) as a stacked plot. The legend defines "Downstream" as events from the downstream sideband region, "Upstream" as events from upstream reconstructed in the downstream sideband, "Signal" as iron events in the downstream plastic sideband, and "Other" as events from carbon and lead in the same region. Bottom: Ratio of data to total MC in the downstream plastic sideband, with pink bands indicating total uncertainty (statistical + systematic) on the MC.

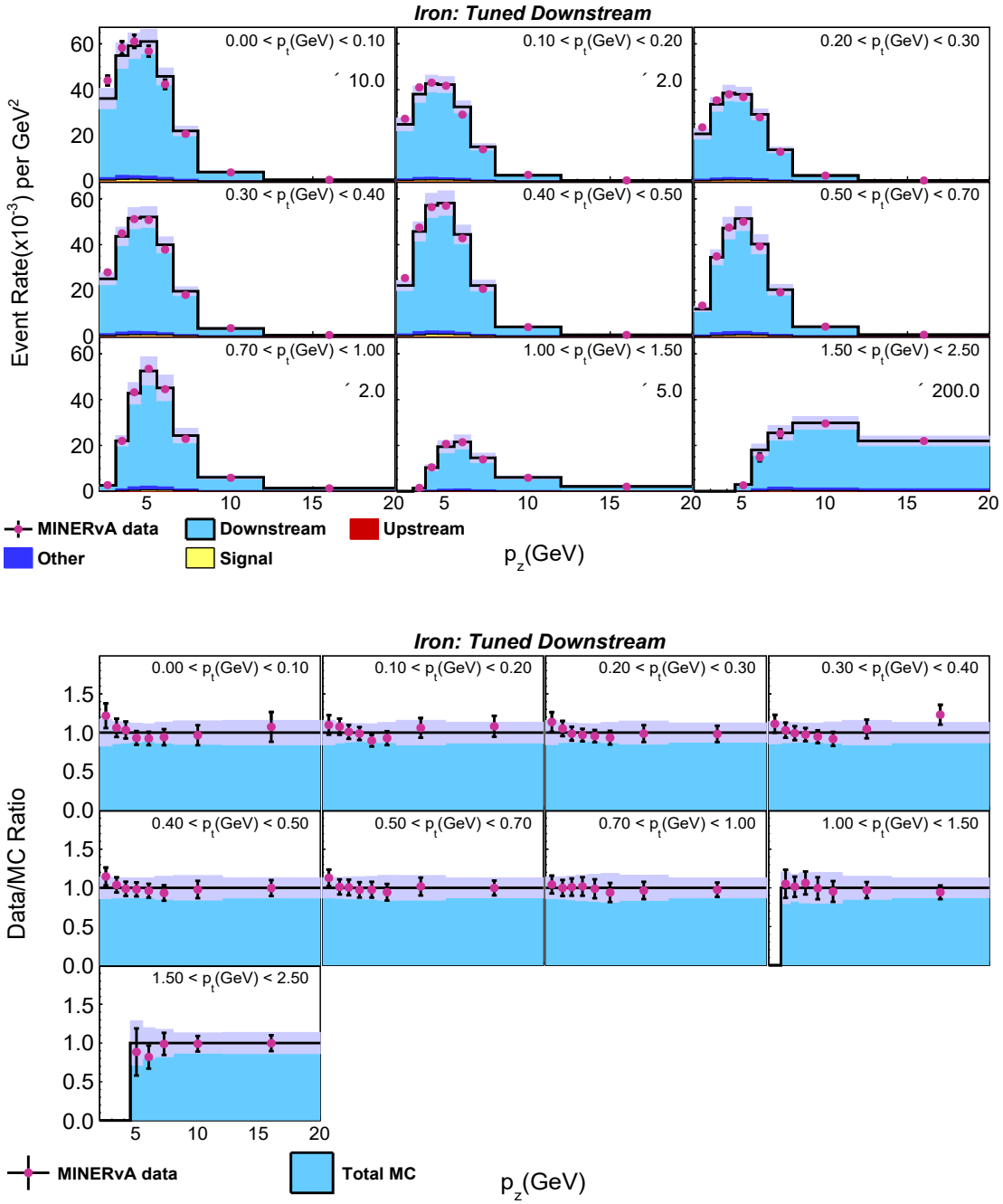

Figure 4.21: Top: Distribution of plastic events downstream of iron after applying scaling factors, shown in bins of antimuon momenta ($p_z - p_t$) as a stacked plot. The legend indicates "Downstream" as events from the downstream sideband region, "Upstream" as events from upstream reconstructed in the downstream sideband, "Signal" as iron events in the downstream plastic sideband, and "Other" as events from carbon and lead in the same region. Bottom: Ratio of data to total MC in the downstream plastic sideband, with pink bands showing the total uncertainty (statistical + systematic) on the MC.

We have also shown in these figures, the ratio of the data to the MC in the sideband region before and after the tuning using the extracted scaling factors. More sideband tuning results have been given in Appendix B. The extracted scaling factors from the sideband study, given in Table 4.2, 4.3, 4.4 and 4.5 were used to tune the MC predicted background to obtain the data constrained background prediction, in the nuclear target region. The MC background was first scaled to data POT and then the scaling factors were applied to obtain the background prediction in data.

Once we have obtained the background prediction on data, we can simply subtract these events from the data, and the MC background that we had all along is simply subtracted from the MC to obtain background-subtracted distributions for both MC and data. At this step, it is important to note that the systematic uncertainties from MC first get propagated to the data.

In Fig. 4.22, we have shown the MC background prediction, the total signal, data, and the data-constrained background prediction obtained using the sideband study, for carbon in $x-Q^2$ and p_z-p_t bins. The data-constrained background prediction was obtained by scaling the MC plastic backgrounds in the upstream and downstream region using the scaling factors obtained using the sideband studies, as given in tables 4.5, 4.4, 4.3 and 4.2. Similar plots were obtained for combined iron, combined lead, tracker and for individual iron and lead in different targets which have been given in Appendix B.

It must be noted that for the tracker, we do not have to perform any sideband study as the entire tracker region is made of plastic scintillator, and the background in data is extracted by simply scaling the MC background to the dataPOT. The background percentage in the tracker region is really low, as we discussed earlier, and the tracker event sample is a very high-purity sample. This is reflected in Fig. 4.23.

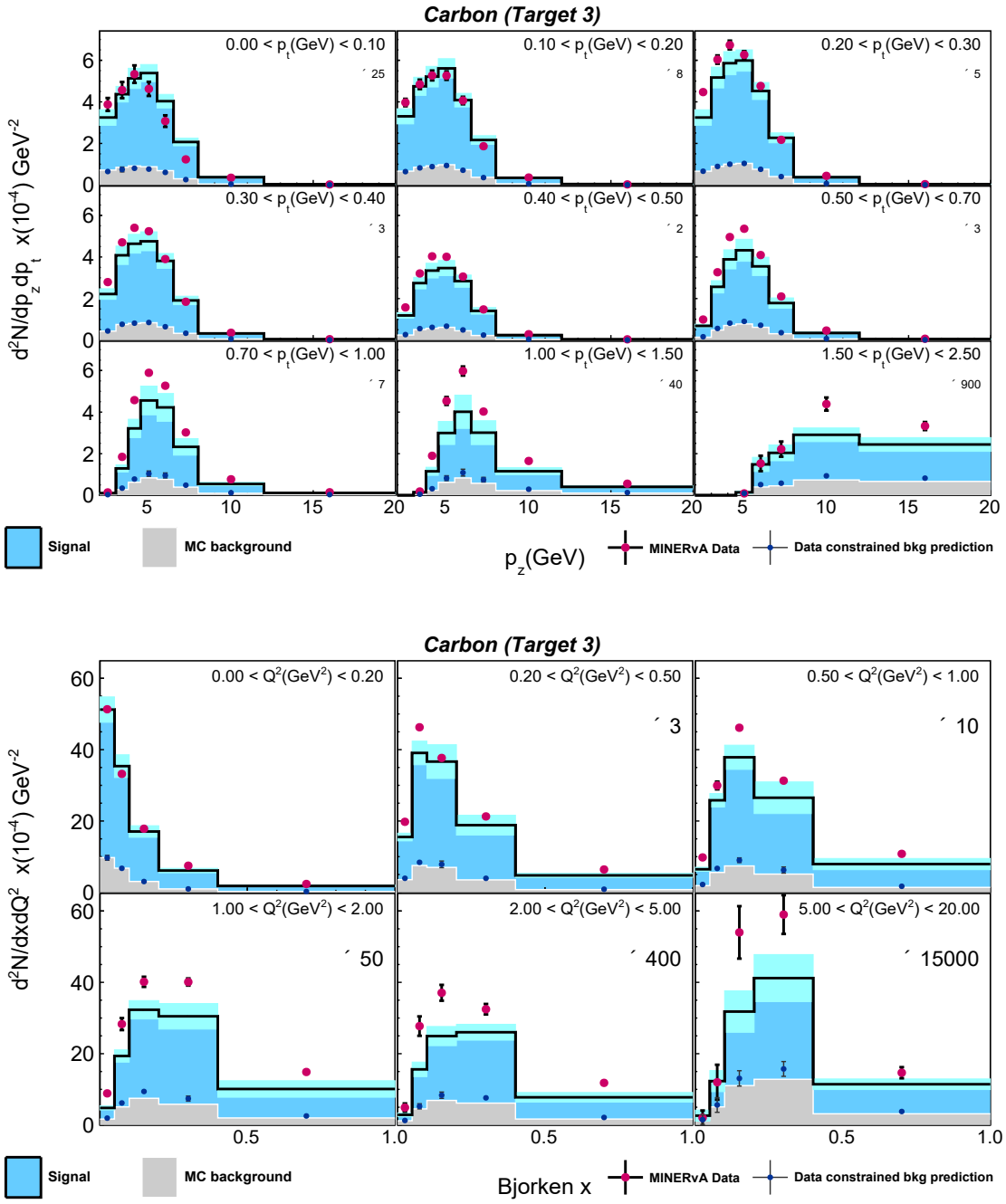

Figure 4.22: Distribution of MC signal, data, mc background and data constrained background prediction for carbon in bins of $p_z - p_t$ (top) and $x - Q^2$ (bottom) in the form of stacked plot. Light blue shows the total signal events predicted by MC and gray represents MC prediction of total background. Red dots represent data along with error bars. Blue dots represent the data constrained background prediction obtained using sideband study. Cyan bands represent the total uncertainty (stat. + syst.) on MC.

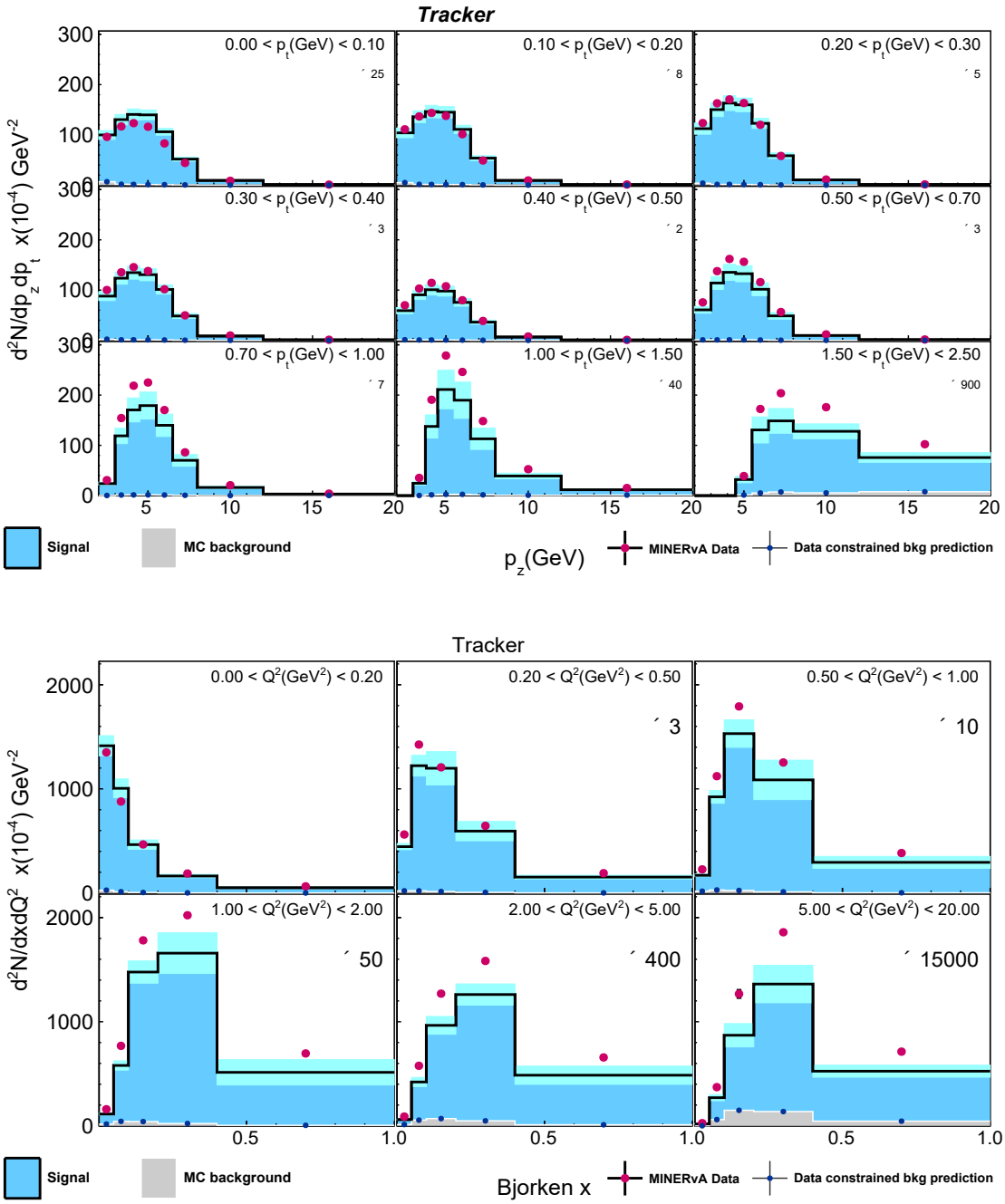

Figure 4.23: Distribution of events from MC signal, data, MC background and data constrained background prediction for tracker in bins of $p_z - p_t$ (top) and $x - Q^2$ (bottom) in the form of stacked plot. Light blue shows the total signal events predicted by MC and gray represents MC prediction of total background. Red dots represent data along with error bars. Blue dots represent the data constrained background prediction obtained using sideband study. Cyan bands represent the total uncertainty (stat. + syst.) on MC.

The background predictions in data and MC, as shown in Fig. 4.22 for carbon, were subtracted off to obtain the background subtracted distribution. A similar procedure was performed for iron and lead. In Fig. 4.24, - 4.29 we have shown the background subtracted distribution for carbon, combined iron, and combined lead in bins of p_z-p_t and $x - Q^2$. Distribution for single target iron, lead, and tracker and distributions in $W - Q^2$ bins have been given in Appendix B.

Systematic uncertainties were propagated to data at the background subtraction step. As an example, the propagated systematic uncertainties (as a fraction) in background subtracted data from combined lead, in p_z-p_t bins has been shown in Fig. 4.30. Fractional uncertainties for carbon, combined iron, combined lead, and tracker, in the variables of interest have been given in Appendix B.

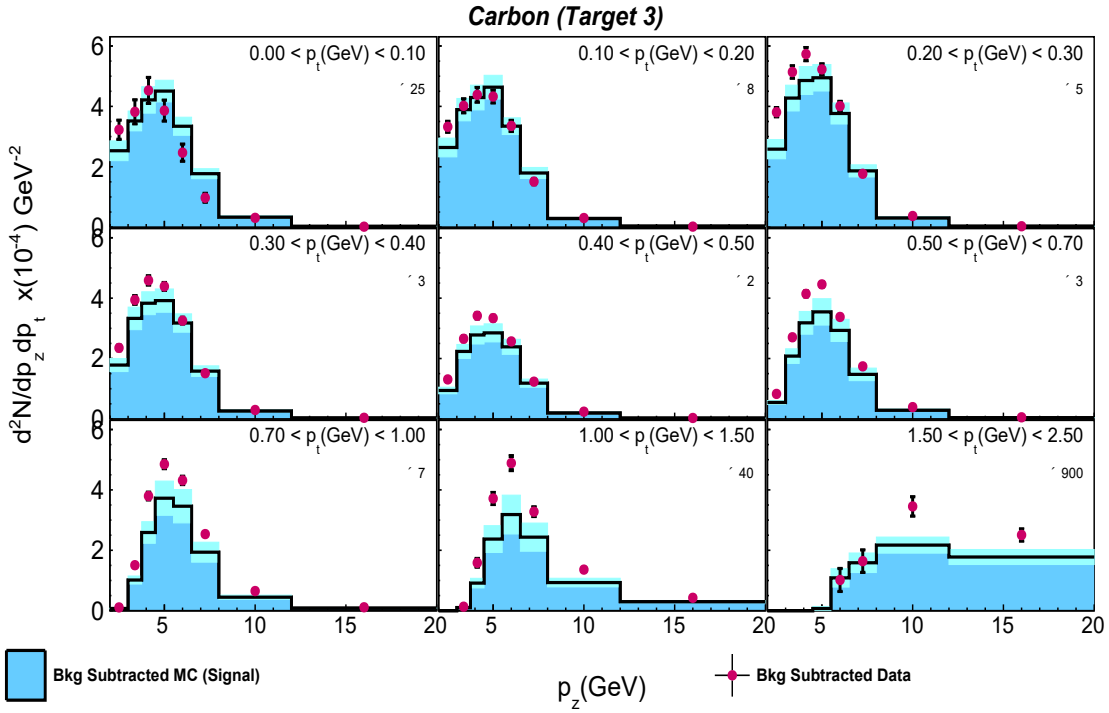

Figure 4.24: Background subtracted event distributions in bins of $p_z - p_t$ for carbon. Light blue shows the MC prediction of signal (background subtracted MC) events. Red dots represent background subtracted data along with error bars containing statistical and systematic uncertainties both. Cyan bands represent the total uncertainty (stat. + syst.) on MC.

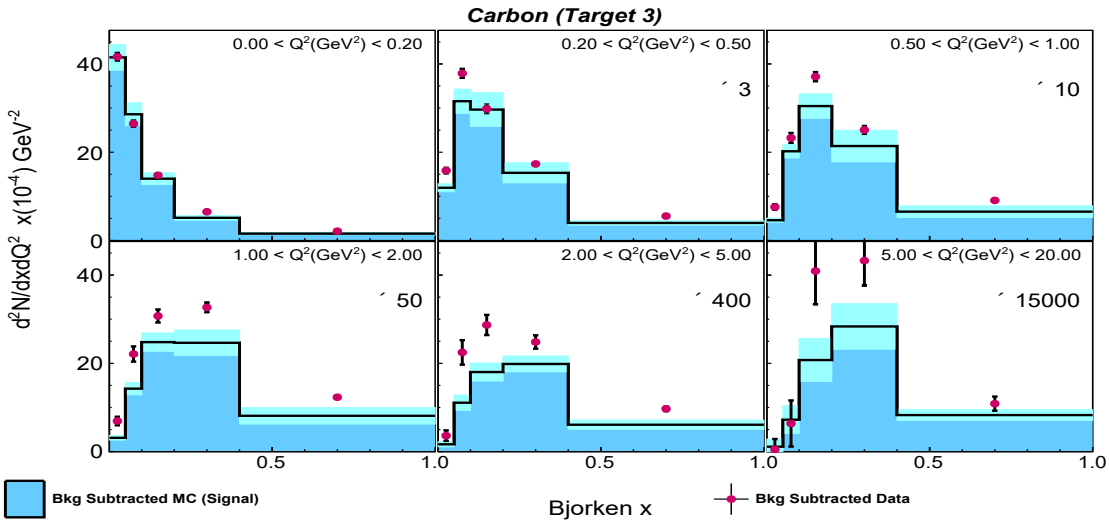

Figure 4.25: Background subtracted event distributions in bins of $x - Q^2$ for carbon. Light blue shows the MC prediction of signal (background subtracted MC) events. Red dots represent background subtracted data along with error bars containing statistical and systematic uncertainties both. Cyan bands represent the total uncertainty (stat. + syst.) on MC.

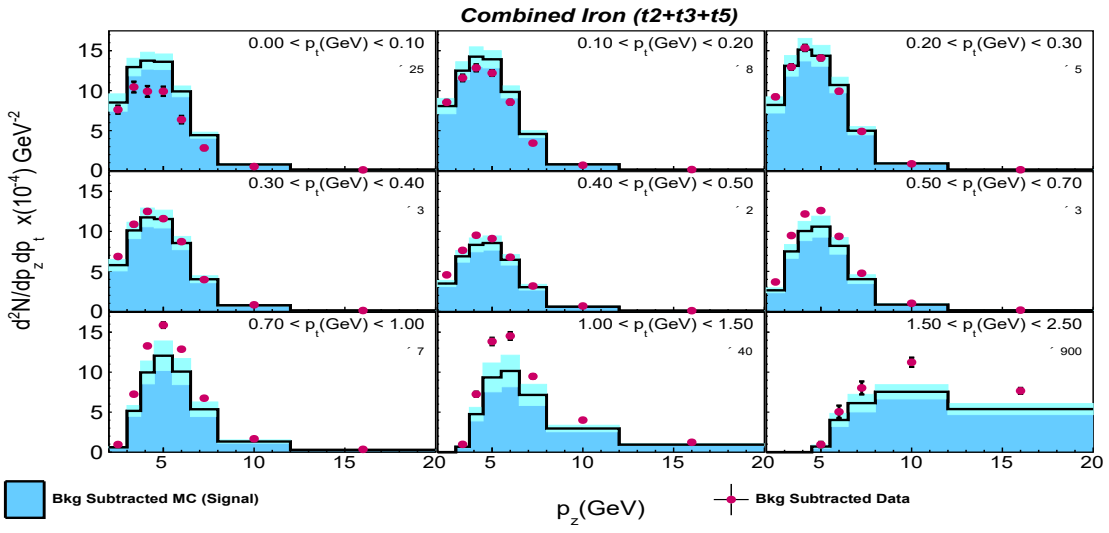

Figure 4.26: Background subtracted event distributions in bins of $p_z - p_t$ for combined iron. Light blue shows the MC prediction of signal (background subtracted MC) events. Red dots represent background subtracted data along with error bars containing statistical and systematic uncertainties both. Cyan bands represent the total uncertainty (stat. + syst.) on MC.

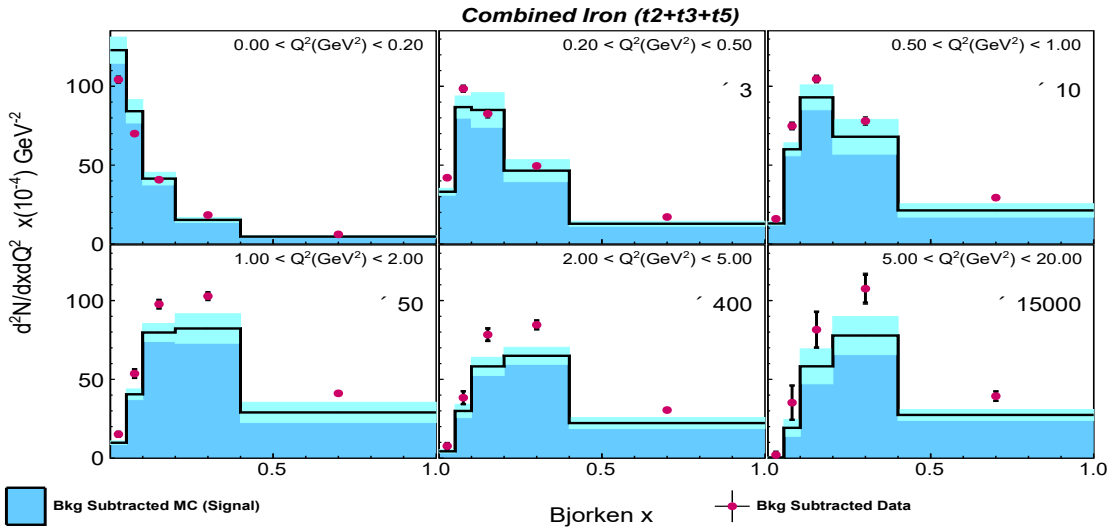

Figure 4.27: Background subtracted event distributions in bins of $x - Q^2$ for combined iron. Light blue shows the MC prediction of signal (background subtracted MC) events. Red dots represent background subtracted data along with error bars containing statistical and systematic uncertainties both. Cyan bands represent the total uncertainty (stat. + syst.) on MC.

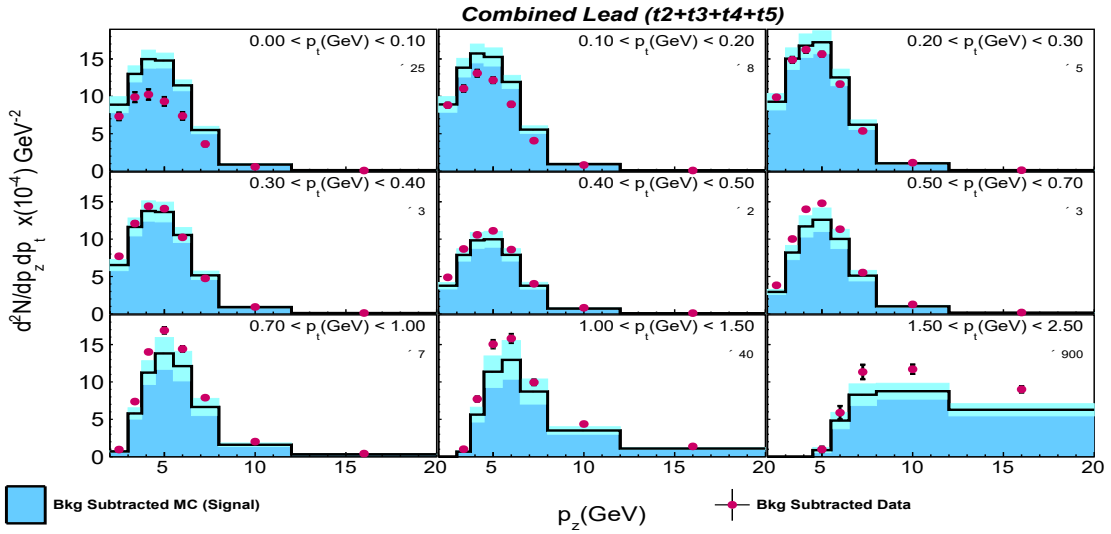

Figure 4.28: Background subtracted event distributions in bins of $p_z - p_t$ for combined lead. Light blue shows the MC prediction of signal (background subtracted MC) events. Red dots represent background subtracted data along with error bars containing statistical and systematic uncertainties both. Cyan bands represent the total uncertainty (stat. + syst.) on MC.

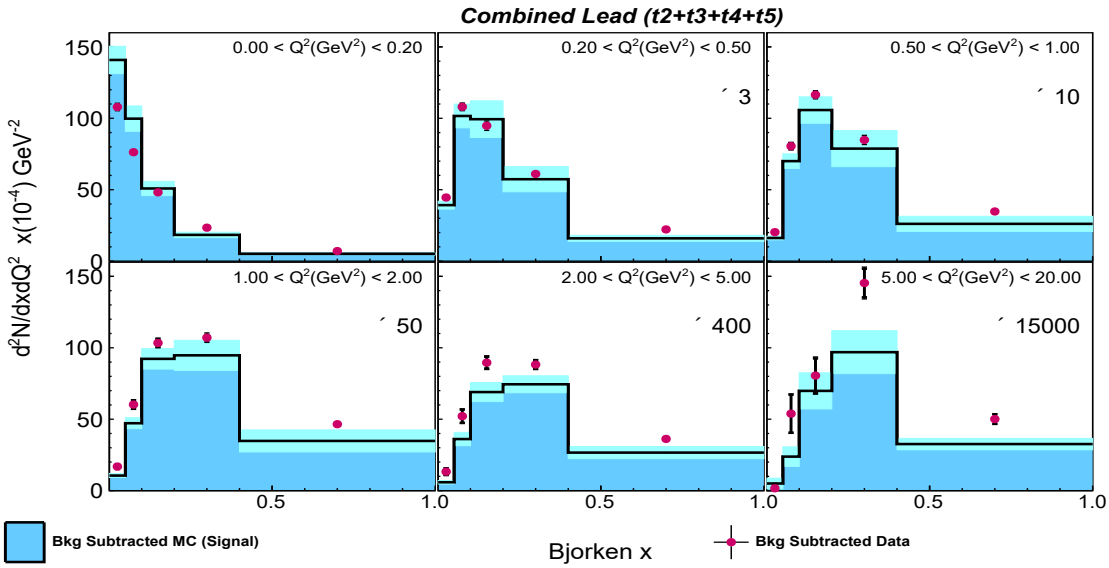

Figure 4.29: Background subtracted event distributions in bins of $x - Q^2$ for combined lead. Light blue shows the MC prediction of signal (background subtracted MC) events. Red dots represent background subtracted data along with error bars containing statistical and systematic uncertainties both. Cyan bands represent the total uncertainty (stat. + syst.) on MC.

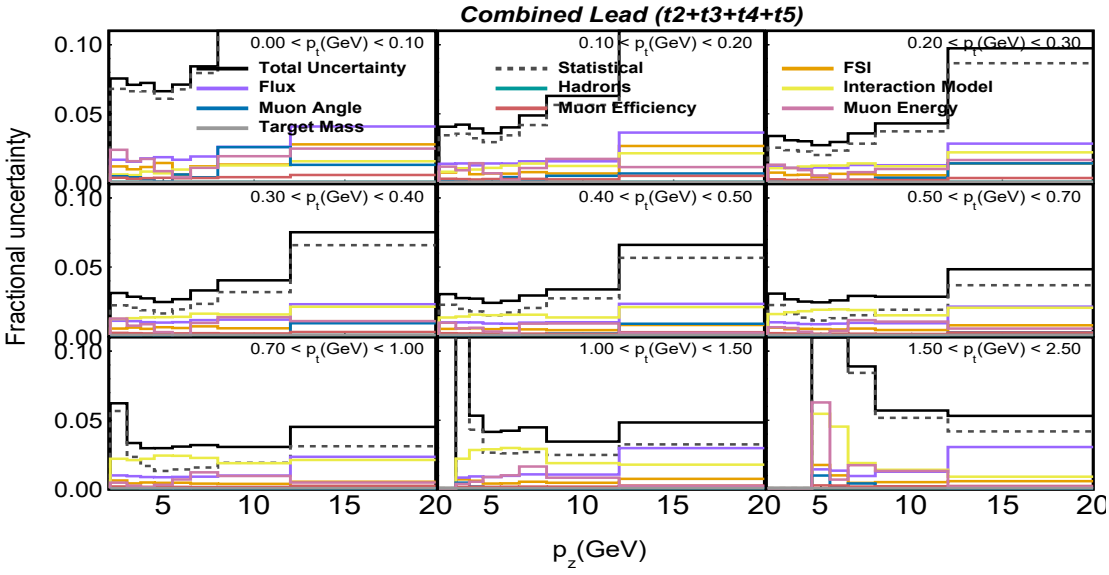

Figure 4.30: Systematic uncertainties as a fraction, in the background subtracted data, for lead in bins of antimuon momenta $p_z - p_t$. Detailed discussion on fractional uncertainties has been provided in Chapter 5.

At this step, we have dealt with the bracket in the numerator of the Eq. 4.4 i.e. $(N_{\text{data},\alpha\beta} - N^{\text{bkgd}}_{\text{data},\alpha\beta})$. Let us now move on to the next step of unfolding the true distribution of events.

4.5 Unfolding

Let us understand why we need to do the unfolding procedure with a simple analogy. Imagine we have a camera and the lens (the detector) was touched with oily hands making it blurry. We click a picture of a colourful object (true data). The photo that is captured (measured data) is blurry and doesn't capture the object in its full sharpness and detail. Unfolding is like applying a "deblurring" effect using software to the captured photo, to restore it closer to the actual object that was captured.

Particle detectors come with limitations and MINERvA is no exception. We have a finite resolution of the detector, for example, the position resolution at MINERvA is limited by the size of the scintillator strips that we have used and the the response of the detector to charged particles limits our energy resolution. As a result, reconstructed quantities are not exactly precise and may be reconstructed to values slightly higher or lower than the actual value. The reconstructed values may "migrate" from an original bin in the analysis to another bin. This results in smearing our distribution and has been demonstrated in Fig. 4.31, the distribution which was sharply peaked has been reconstructed with event migration to adjacent bins. The first step towards *unsmearing* the distribution is determining the amount of smearing in our reconstructed sample.

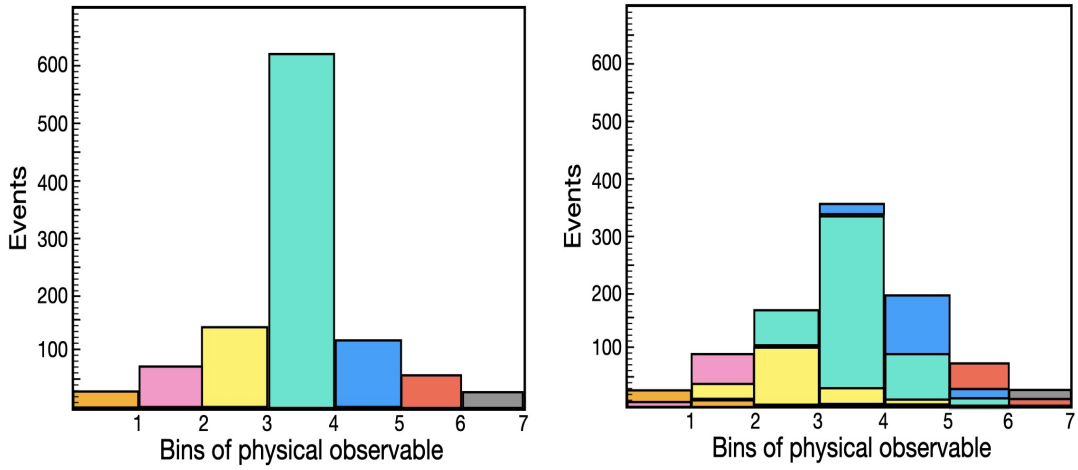

Figure 4.31: (Left) Expected true distribution peaked at the center compared to (right) smearing of distribution because of migration of events into other bins. Figure reproduced from Ref. [67] with permission.

4.5.1 Migration Matrices

Since the simulation sample contains information about both the true and the reconstructed values of simulation events, reconstructed events are mapped onto true events using two-dimensional matrices called **migration matrices**.

The migration matrix maps the event reconstructed in the bin (α, β) on the x-axis to the true generated bin (i, j) on the y-axis, represented as $U_{\alpha\beta ij}$. The entries on the diagonal represent the quantities that are reconstructed in the same bin in which they were generated. The more diagonal the migration matrix is, the less smeared our distribution. We optimize the binning of our chosen combination of variables in such a way that the migration matrix has more than 50% events on the diagonal for most (all) of the bins when we row normalise the event rate. We use the trial and error method, to obtain the optimised binning for our combination of variables using migration matrices. We choose a particular binning, and make the migration matrix for it, if we do not see at least 50 % events on the diagonal in the row normalised migration matrix that we plot with a chosen binning, we change

the binning until we have at least 50% diagonalization achieved in all of the bins. Fig. 4.32, 4.33 and 4.34 shows the migration matrices for combined iron, combined lead targets, carbon target, and tracker in bins of antimuon momenta $p_z - p_t$ and $x - Q^2$ respectively. It is important to note that regions beyond the chosen bin boundaries have also been looked at for these migration matrices, i.e. bin lower than the lowest chosen bin called *underflow* bin and higher than the highest chosen bin called *overflow* bin, as shown in Fig. 4.32-4.34. Similar migration matrices were made for $W - Q^2$ distributions in combined lead, iron, carbon, and tracker. Migration matrices for different target materials for individual targets were also obtained. These migration matrices can be found in Appendix C. The bin edges determined for the chosen combination of variables using the migration matrices are given in Table 4.6.

Variable	**Chosen bin edges**
bjorken x	$\{0.001, 0.05, 0.1, 0.2, 0.4, 1\}$
$W(GeV)$	$\{0, 2, 5, 8, 10\}$
Q^2 (GeV^2)	$\{0, 0.2, 0.5, 1, 2, 5, 20\}$
p_z (GeV)	$\{2, 3, 3.75, 4.5, 5.5, 6.5, 8, 12, 20\}$
p_t (GeV)	$\{0.0, 0.1, 0.2, 0.3, 0.4, 0.5, 0.7, 1.0, 1.5, 2.5\}$

Table 4.6: Bin edges for different variables presented in this analysis determined using two dimensional diagonalised migration matrices.

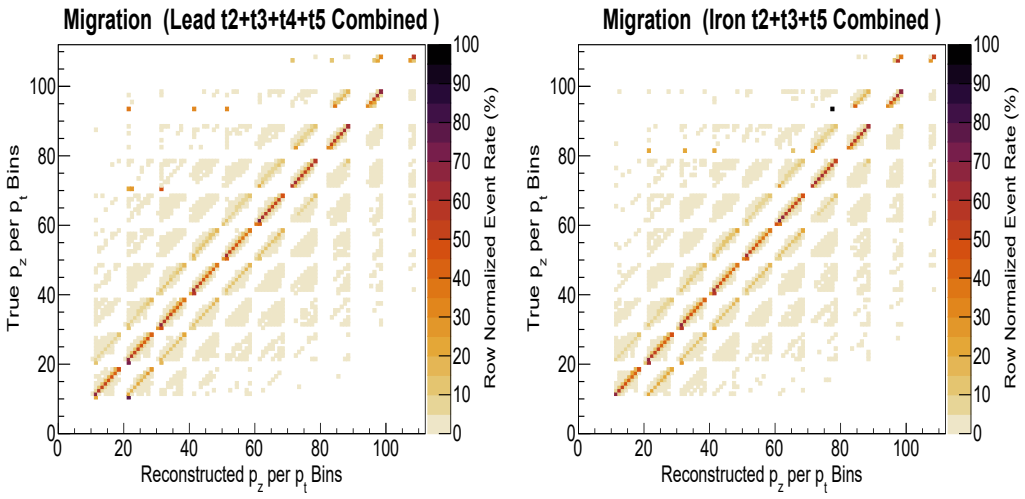

Figure 4.32: Migration matrices for combined lead, combined iron, mapping the reconstructed event distribution on the x-axis to the true event distribution on the y-axis. Each bigger block represents a p_t bin and the smaller blocks inside each of these represent p_z bins. The color coding of the z-axis shows the row normalised event rate percentage.

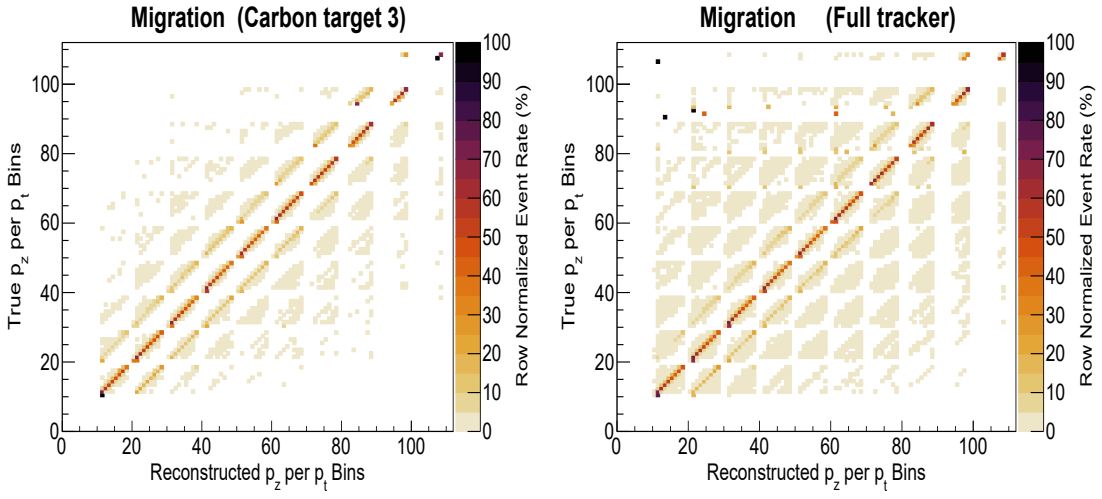

Figure 4.33: Migration matrices for carbon and tracker, mapping the reconstructed event distribution on the x-axis to the true event distribution on the y-axis. Each bigger block represents a p_t bin and the smaller blocks inside each of these represent p_z bins. The color coding of the z-axis shows the row normalised event rate percentage.

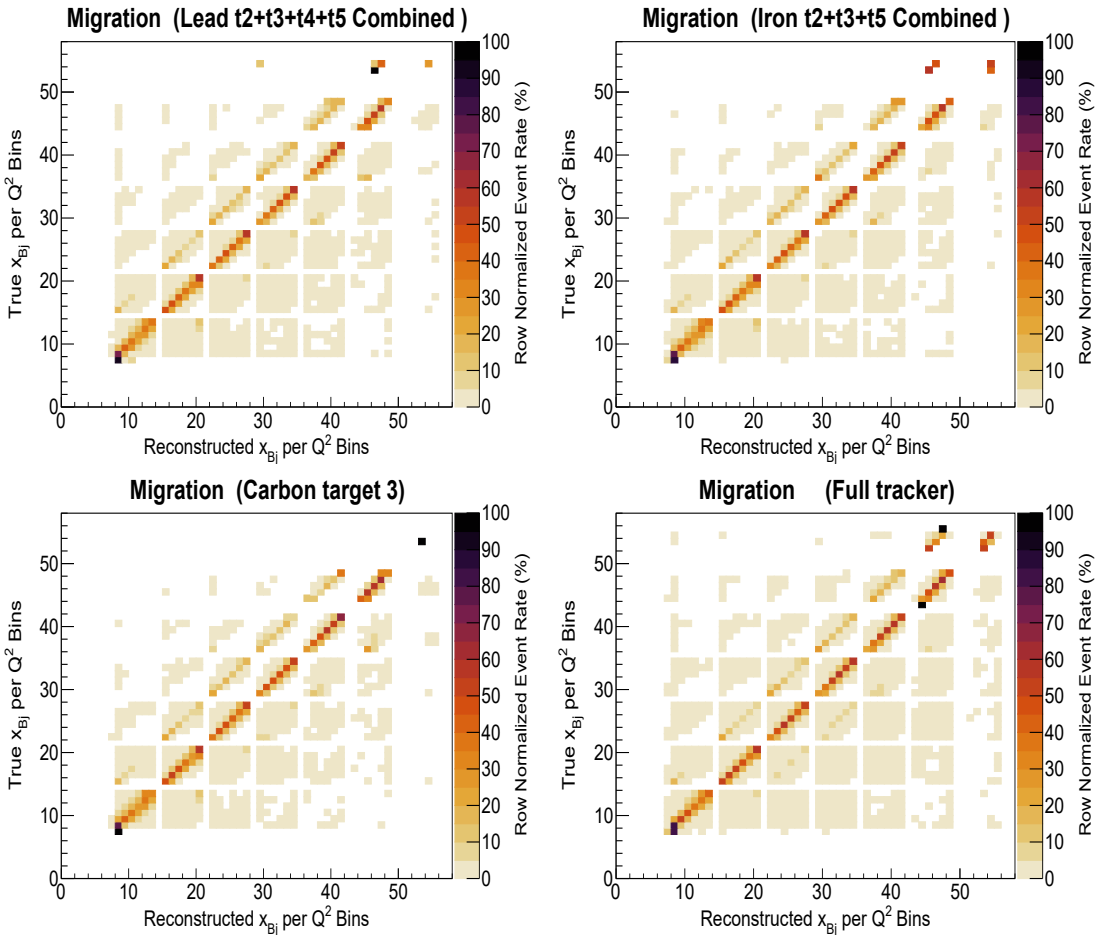

Figure 4.34: Migration matrices for combined lead, combined iron, carbon and tracker, mapping the reconstructed event distribution on the x-axis to the true event distribution on the y-axis. Each bigger block represents a Q^2 bin and the smaller blocks inside each of these represent bjorken x bins. The color coding of the z-axis shows the row normalised event rate percentage.

We now have to unfold the true distribution from the reconstructed distribution, to extract the double differential cross section. We are dealing with the term $\Sigma_{\alpha\beta}U_{\alpha\beta ij}$ in the numerator of the Eq. 4.4.

4.5.2 Unfolding Procedure

One way to unfold the distribution can be to simply invert the migration matrix. It is possible, but the matrix is not always invertible. When there is a migration of reconstructed events into too many non-diagonal bins, the matrix can become "ill-posed", such that changes in the input (reconstructed) distribution lead to wild fluctuations in the output (true) distribution. This has been discussed in detail in [114]. Also, matrix inversion can overcompensate for the smeared distribution leading to large errors in the resulting unfolded distribution. Small statistical errors in the reconstructed input distribution can be greatly amplified in the direct matrix inversion approach. Regularization techniques are implemented, by imposing additional constraints to stabilize the solution. At MINERvA, we use the D'Agostini iterative regularization technique [115, 116] for the unfolding procedure, implemented using the ROOT [117] package RooUnfold [118]. Using too many iterations to unfold the true distribution increases the systematic and statistical uncertainties on the resulting unfolded distribution, such that high variance is introduced. Using too few iterations leads to high bias in the unfolded distribution. The D'Agostini method looks to find the optimal number of iterations to unfold, by finding the sweet spot for bias and variance trade-off. This has been illustrated in Fig. 4.35. The D'Agostini iterative unfolding procedure is based on Bayes' theorem [115].

To understand it simply, this is how it works. We start with a guess of the true distribution, move forward to unfold our distribution, and calculate the χ^2 between the unfolded distribution using the starting guess and the original distribution. If the χ^2 is too high we update our guess, using Bayes' theorem which is a mathematical way of updation of beliefs based on new evidence [115]. This is now the second iteration, starting with a new guess. This process is repeated until we obtain a stable minimal χ^2 by comparison between unfolded and starting distribution, i.e. close to the number of degrees of freedom of the distribution.

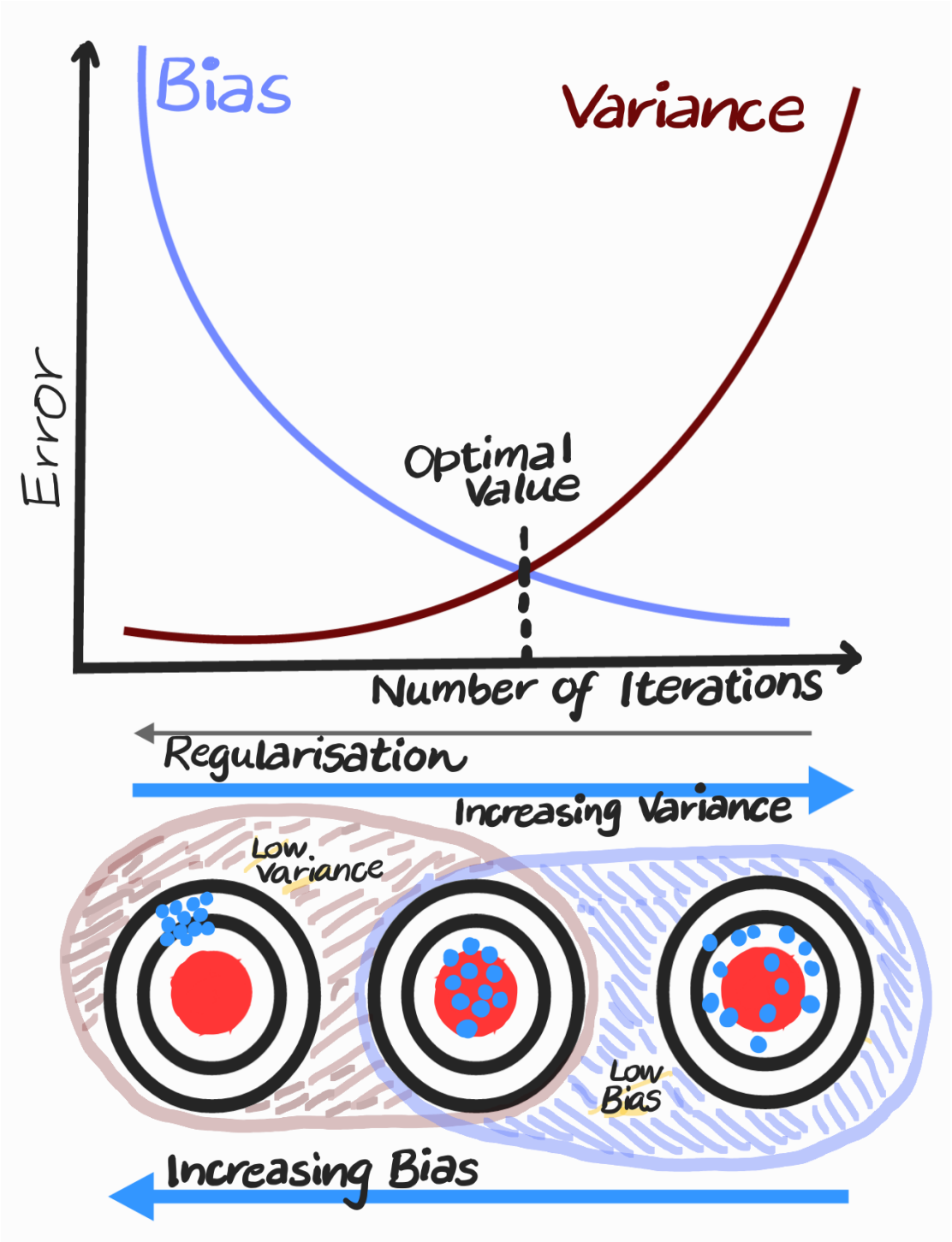

Figure 4.35: Cartoon illustrating how the optimal number of iterations can be extracted by finding the trade off between bias and variance.

The k^{th} iteration of the D'Agostini method for unfolding a two-dimensional distribution, as done in the analysis presented in this thesis, is determined by:

$$\lambda_{\alpha\beta}^{(k)} = \frac{\lambda_{\alpha\beta}^{(k-1)}}{\sum_{i,j} U_{ij\alpha\beta}} \sum_{i,j} \frac{U_{ij\alpha\beta}\ x_{ij}}{\sum_{\alpha,\beta} U_{ij\alpha\beta}\ \lambda_{\alpha\beta}^{(k-1)}} \tag{4.6}$$

4.5.3 Warping Studies

If we start with the underlying simulation predicted distribution to unfold and try to unfold it with the migration matrix that we obtained using the simulation, that would lead to unfolding in just one iteration, leading to maximal bias as illustrated in Fig. 4.35. Hence, we start with shifted versions of the simulation called fake data also called "warped MC". These distributions are slight deviations of the underlying simulation predicted distributions, where we change the weights used in the underlying model to obtain a warped MC. These warped MC are unfolded using the migration matrices obtained from the base model of the underlying simulation that we are using and then the number of iterations where we obtain a stable minimum χ^2 using Eq. 4.6 is the desired number of iterations for unfolding. We perform these warping studies using several versions of fake data and look for consistency in the number of iterations obtained using different warped models. Warping studies are performed using the central value (CV) only, such that systematic universes are not considered during unfolding and it is a statistical only study. 100 Poisson throws are used to generate statistical variations in the central value of the warped MC, creating 100 different universes corresponding to each generated Poisson distribution, with each Poisson distribution having a mean equal to the number of entries in the CV for that bin. Distributions are unfolded in each of these universes. The central value MC used in this analysis is MINERvA tuneV4, as discussed in Section 3.3. For this reweight, an additional weight was turned on called the *Deuterium Genie Pion tune reweight*, where the values of $M_{\text{A}}^{\text{RES}}$ and NormCCRes were changed from 1.12 GeV and 1.00 to 0.94 GeV and 1.15 respectively. Refer to Section 3.3 for a detailed explanation of the

shifts applied in the various MINERvA-specific re-weighting.

We used five different fake data for our unfolding studies:

1. Switching off "Deuterium Genie Pion tune reweight (DGPi)" - Switching from MINERvA tuneV4 to tuneV1: The value of resonant axial mass $M_{\mathrm{A}}^{\mathrm{RES}}$ and normalisation CCNormRes which were modified to obtain MINERvA tune V4 were changed back to their GENIE nominal values i.e. $M_{\mathrm{A}}^{\mathrm{RES}} =$ 1.12 GeV and CCNormRes =1.0.

2. One sigma shift taken for DGPi reweight: $M_{\mathrm{A}}^{\mathrm{RES}}$ changed from 0.94 GeV to 0.99 GeV and CCNormRes changed from 1.15 to 1.22.

3. Two sigma shift in non-resonant pion production reweight: The 43 % reweight used for the non-resonant pion production model (NRP) in the CV was changed by two sigma to 51% instead.

4. The RPA reweight applied to low Q^2 events for MINERvA tune V4 was changed by one sigma and a +25 % shift was taken.

5. The low recoil 2p2h reweight was shifted by 10 %.

It is important to note here that warping studies were performed for $x - Q^2$ and $W - Q^2$ variables to extract the number of iterations. For unfolding in $p_z - p_t$, which is a well-studied two-dimensional variable at MINERvA, we used 10 iterations for unfolding. Warping studies were performed for each target separately, as illustrated in Fig. 4.36, 4.37, 4.38, 4.39 and 4.40. The figures show the ratio of the warped MC to the original MC in different bins of $W - Q^2$ and $x - Q^2$ as a two-dimensional panel plot. We can see the effect of changing different weights for the different warped models used in these figures.

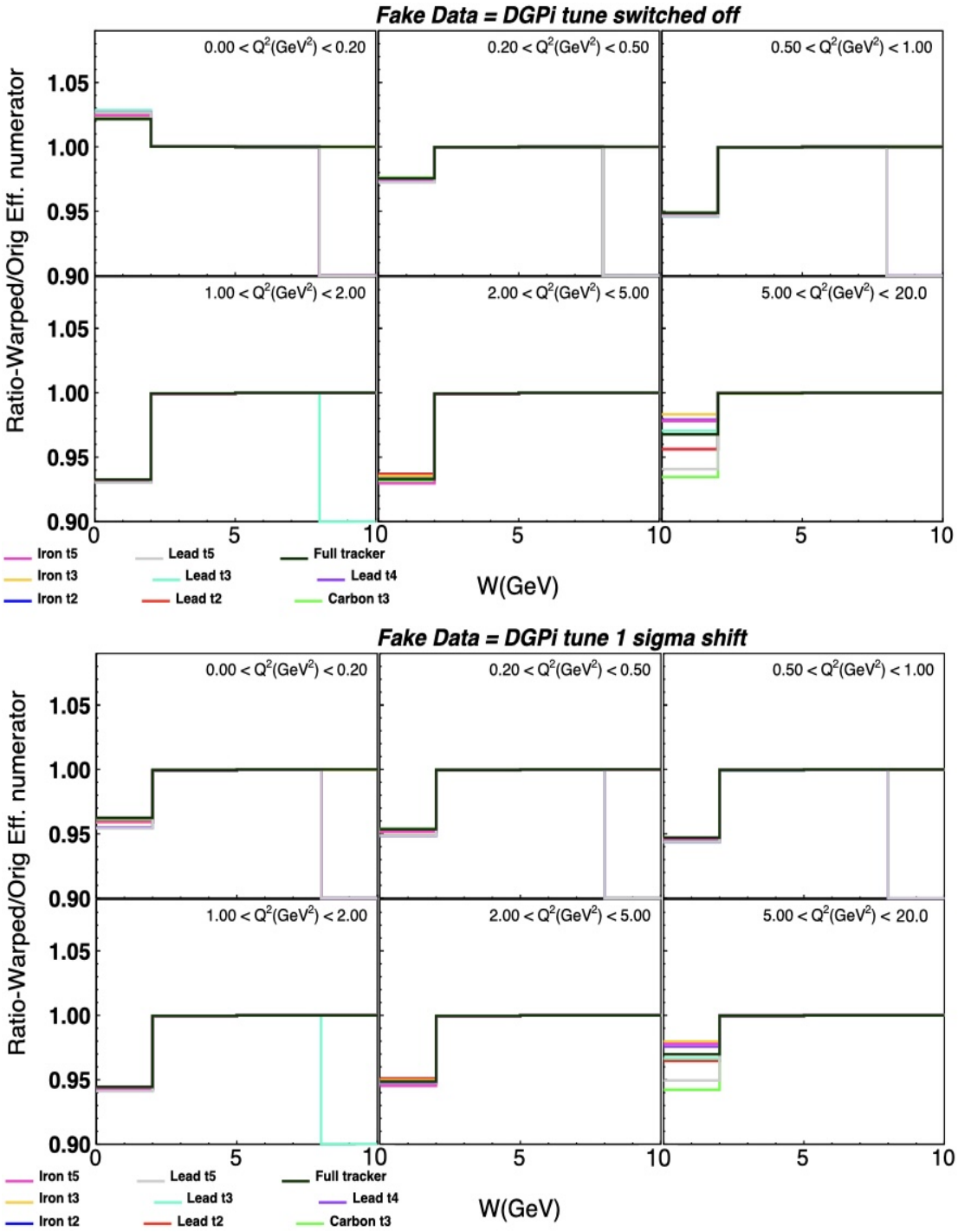

Figure 4.36: Ratio plot (Warped model to CV Minerva tuneV4) in bins of W and Q^2 depicting the effect of changing weights for different models in different bins on the y-axis. The colored lines represent the effect of changing the weight for different nuclear targets and the tracker region in the detector. The x-axis represents different bins of W and panels are different bins of Q^2. The title on the top of the plot shows the warping function used.

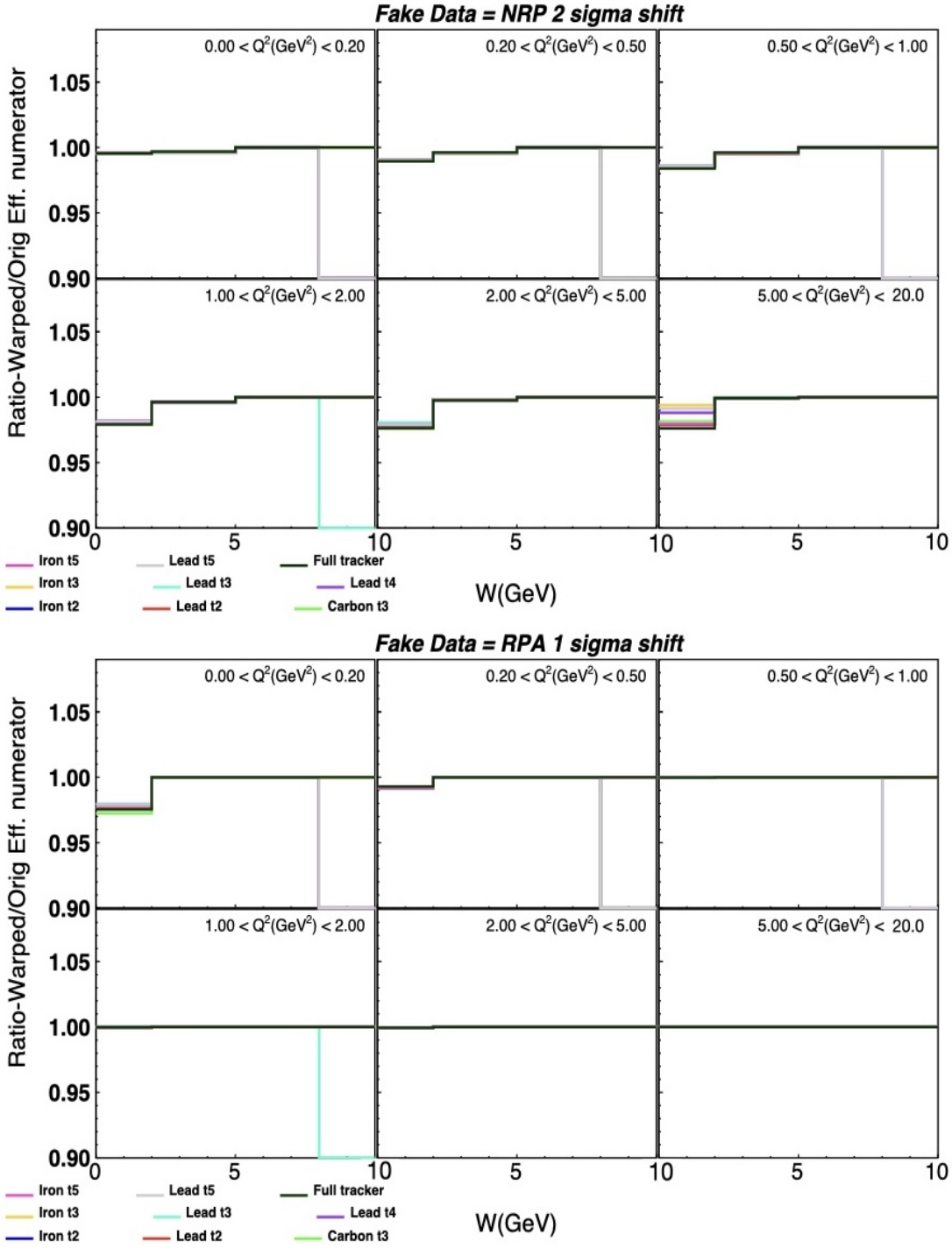

Figure 4.37: Ratio plot (Warped model to CV Minerva tuneV4) in bins of W and Q^2 depicting the effect of changing weights for different models in different bins on the y-axis. The colored lines represent the effect of changing the weight for different nuclear targets and the tracker region in the detector. The x-axis represents different bins of W and panels are different bins of Q^2. The title on the top of the plot shows the warping function used.

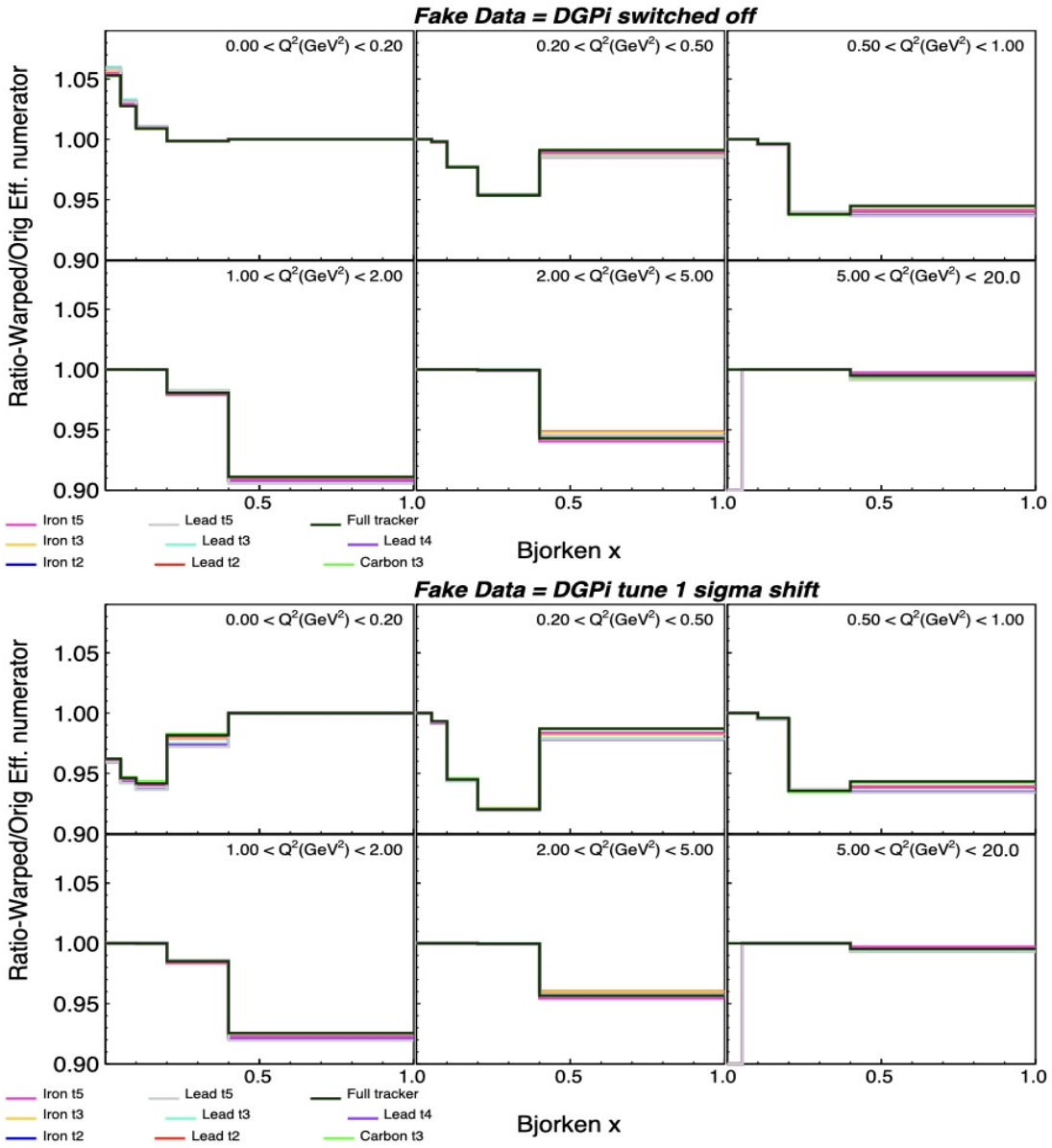

Figure 4.38: Ratio plot (Warped model to CV Minerva tuneV4) in bins of bjorken x and Q^2 depicting the effect of changing weights for different models in different bins on the y-axis. The colored lines represent the effect of changing the weight for different nuclear targets and the tracker region in the detector. The x-axis represents different bins of bjorken x and panels are different bins of Q^2. The title on the top of the plot shows the warping function used.

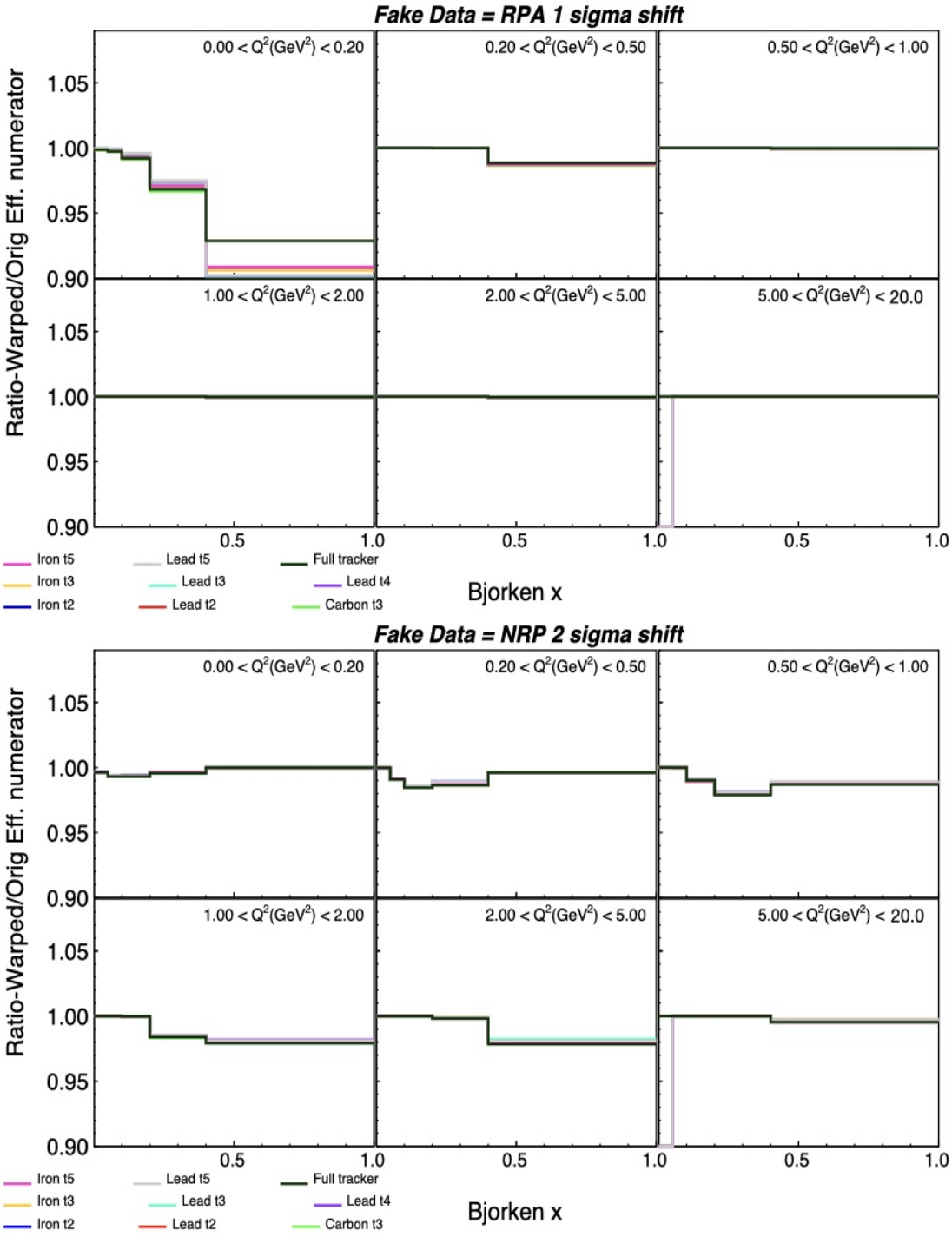

Figure 4.39: Ratio plot (Warped model to CV Minerva tuneV4) in bins of bjorken x and Q^2 depicting the effect of changing weights for different models in different bins. The colored lines represent the effect of changing the weight for different nuclear targets and the tracker region in the detector. The x-axis represents different bins of bjorken x and panels are different bins of Q^2. The title on the top of the plot shows the warping function used.

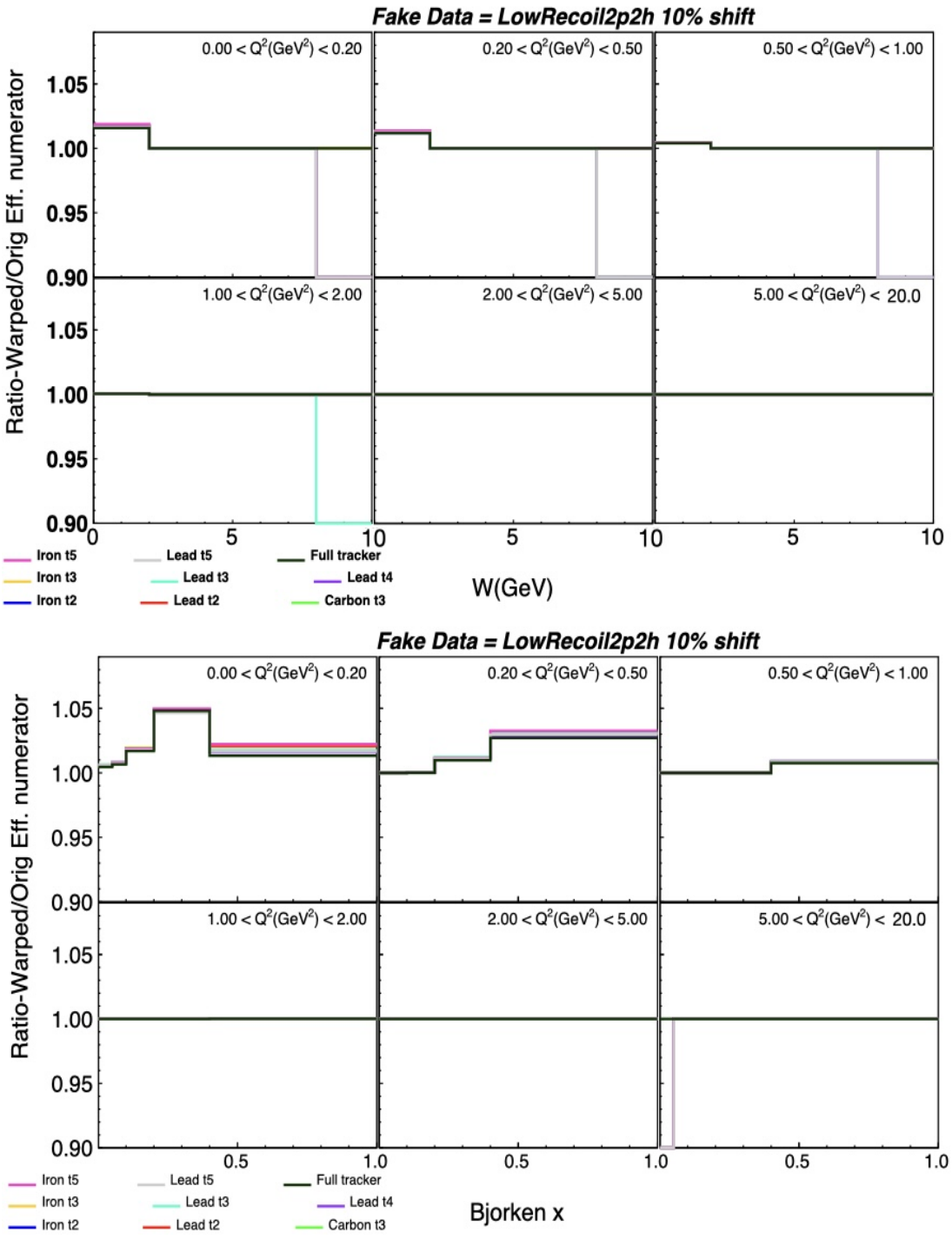

Figure 4.40: Ratio plot (Warped model to CV Minerva tuneV4) in bins of W (top) and bjorken x (bottom) and Q^2 depicting the effect of changing the low recoil 2p2h reweight by 10 % in different bins. The colored lines represent the effect of changing the weight for different nuclear targets and the tracker region in the detector. The x-axis represents different bins of W (top), bjorken x (bottom) and panels are different bins of Q^2.

Validation tests

A few internal tests were performed for the validation of the warping study procedure [119]. The first check that we do is to use the original CV simulation (MINERvA tuneV4) as fake data and unfold it with the migration matrix of the original simulation. For this test, the χ^2 should be stable at the number of degrees of freedom i.e. the number of bins for the two-dimensional distribution. When we performed this test, the χ^2 was found to be diverging instead. This is caused by the presence of low statistics bins that have small to negligible event populations. Fig. 4.41 illustrates this. To get around this problem, these low-population bins are excluded while the warping studies are being performed. Once we exclude the low statistics bins, we get a stable χ^2 at the number of degrees of freedom as shown in Fig. 4.42.

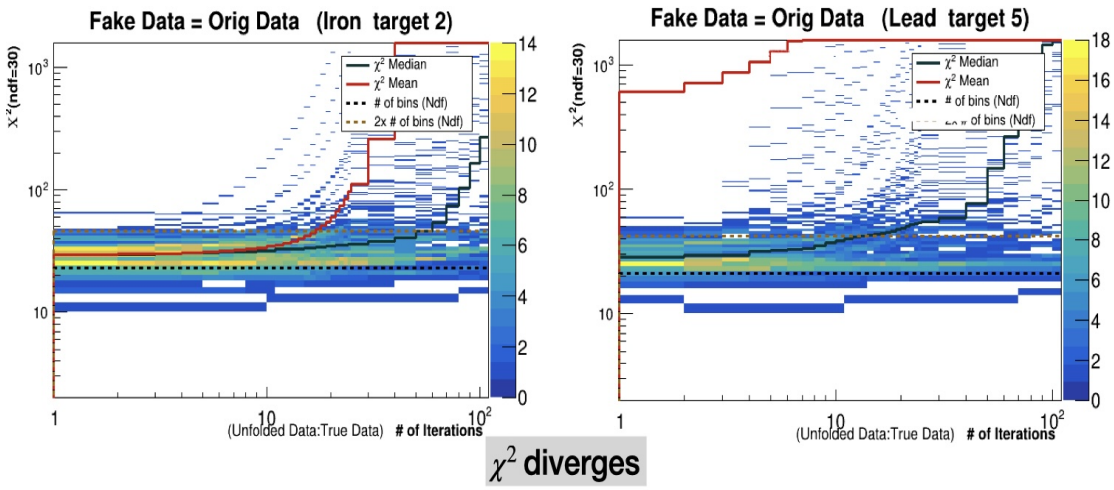

Figure 4.41: Example plots for target 2 iron and target 5 lead warping studies in $x - Q^2$, where fake data used is same as the original data. The solid red and black lines represent the χ^2 mean and median, respectively. The dashed line represents the number of degrees of freedom (ndf), equal to the number of bins for the $x - Q^2$ variable. The z-axis represents the calculated χ^2 between unfolded and true distributions for different universes (total of 100) generated using Poisson throws. The figure depicts the divergence of χ^2 in the validation test due to bins with low statistics being present in the two-dimensional distribution.

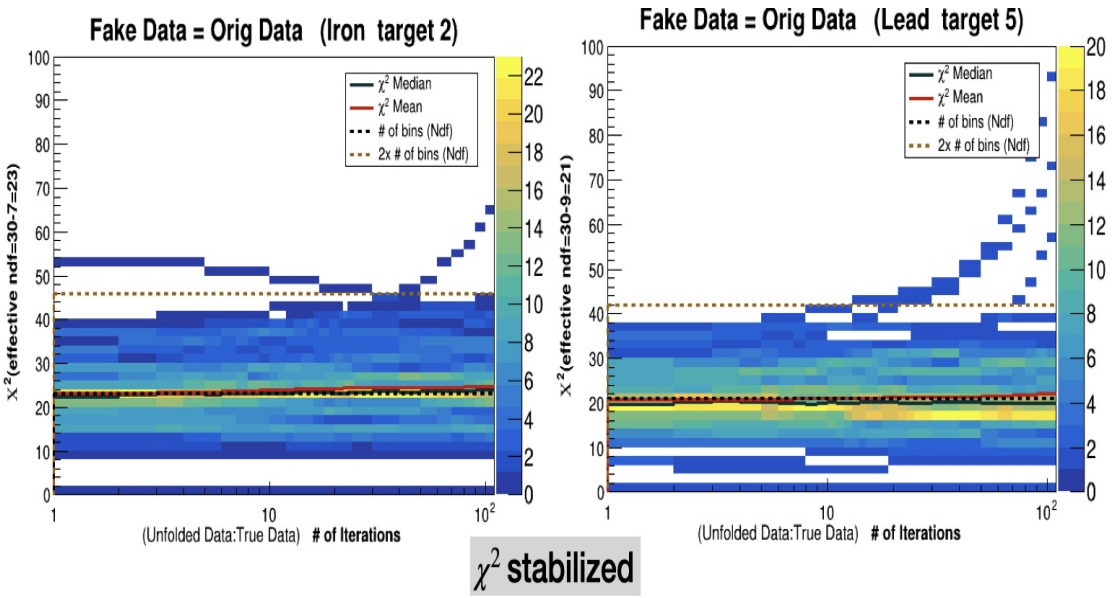

Figure 4.42: Example plots for target 2 iron and target 5 lead warping studies in $x - Q^2$ depicting χ^2 stabilized at the number of degrees of freedom after the exclusion of low event population bins.

Additional statistical uncertainty factor

The unfolding technique based on Bayes' theorem that we implement for this analysis using RooUnfold takes into account the errors in the input data sample, as a result, the statistical uncertainty on the unfolded sample is underestimated. A "correction factor" F is determined in the unfolding studies and the statistical covariance of the unfolded sample is multiplied by $\sqrt{1 + 1/F}$. To determine this factor F, various values of F were tried and tested to see if the χ^2 determined between the unfolded sample with the migration matrix corrected using this factor and the original distribution would converge to the number of degrees of freedom at the chosen number of iterations. This has been illustrated in Fig. 4.43. This study was performed for all of the targets and the tracker region and factors F were extracted. As an example, Table 4.44 shows the values of the correction factor calculated for different nuclear targets and tracker.

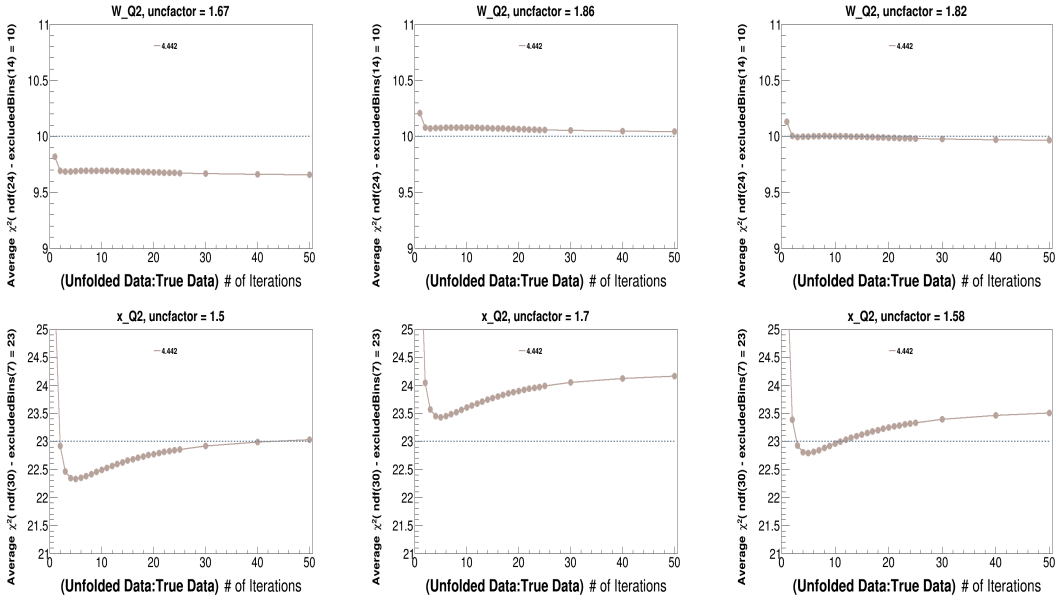

Figure 4.43: Uncertainty correction factor F applied to the statistical uncertainty of the unfolded sample, extracted for $W - Q^2$ in target 3 lead (top) and $x - Q^2$ in target 4 lead (bottom). The dashed line is the number of degrees of freedom and the solid line represents the χ^2. 4.442 is the fraction of data exposure (MCPOT/DataPOT). We chose the uncertainty factor F=1.82 for $W - Q^2$ and F=1.58 for $x - Q^2$, seen on the third (rightmost) plots, as the χ^2 converges to ndf for this factor at the chosen number of iterations.

Inclusive nubar CC	$x - Q^2$	$W - Q^2$
Iron target 2	1.37	2.24
Lead target 2	1.42	2.11
Carbon target 3	1.37	1.76
Iron target 3	1.49	1.67
Lead target 3	1.35	1.82
Lead target 4	1.58	2.4
Iron target 5	1.36	1.63
Lead target 5	1.31	1.66
Tracker	12	9.8

Table 4.44: Uncertainty correction factor F applied to the statistical uncertainty of the unfolded sample, extracted for $x - Q^2$ and $W - Q^2$ in different nuclear targets and the tracker region.

Warping studies: Results

The unfolded distributions were obtained, after applying the extracted statistical uncertainty factor discussed in the previous section, using different warped models.

Based on our study, the number of iterations chosen for $W - Q^2$ are given in Table 4.45 and for $x - Q^2$ are given in Table 4.47. Example plots for the warping studies performed for finding out the number of iterations for $x - Q^2$ and $W - Q^2$ have been shown for carbon and lead target 5 in Fig. 4.46. It must be noted that for unfolding in $x - Q^2$, some of the warping functions, for example, RPA 1 sigma and 2p2h 10 % shift, gave us more than 10 iterations for unfolding, as seen in Fig. 4.47. Although the χ^2 was fairly minimal at 10 iterations and close to ndf, we have used **10 iterations for unfolding in $x - Q^2$ overall**. This is because, using too many iterations for unfolding increases the variance in our unfolded distribution rapidly, as illustrated in Fig. 4.35. As a result, the systematic uncertainties in our unfolded distribution can blow up. Hence, we avoided taking more than 10 iterations for unfolding in $x - Q^2$, since χ^2 is fairly minimized and stabilized at 10 iterations. Combining the results from different warps, we used **5 iterations for unfolding in $W - Q^2$** for nuclear targets and **7 iterations** in the tracker region.

	← Number of Iterations →				
Warp used →	DGPi off	DGPi 1 sigma	RPA 1 sigma	2p2h (10% shift)	NRP 2 sigma
Iron target 2	5-7	5-7	4-6	2-4	2-4
Lead target 2	5-7	4-6	3-5	6-8	2-4
Carbon target 3	4-6	4-6	6-8	4-7	3-4
Iron target 3	5-7	4-6	6-8	2-4	4-6
Lead target 3	5-7	5-7	4-6	2-4	3-5
Lead target 4	5-7	4-6	4-6	3-4	3-5
Iron target 5	5-7	4-6	3-5	2-4	2-4
Lead target 5	5-7	3-5	3-5	2-4	4-6
Tracker	7-8	7-8	7-8	5-7	4-6

Table 4.45: Number of iterations extracted using different warped models for unfolding in $W - Q^2$.

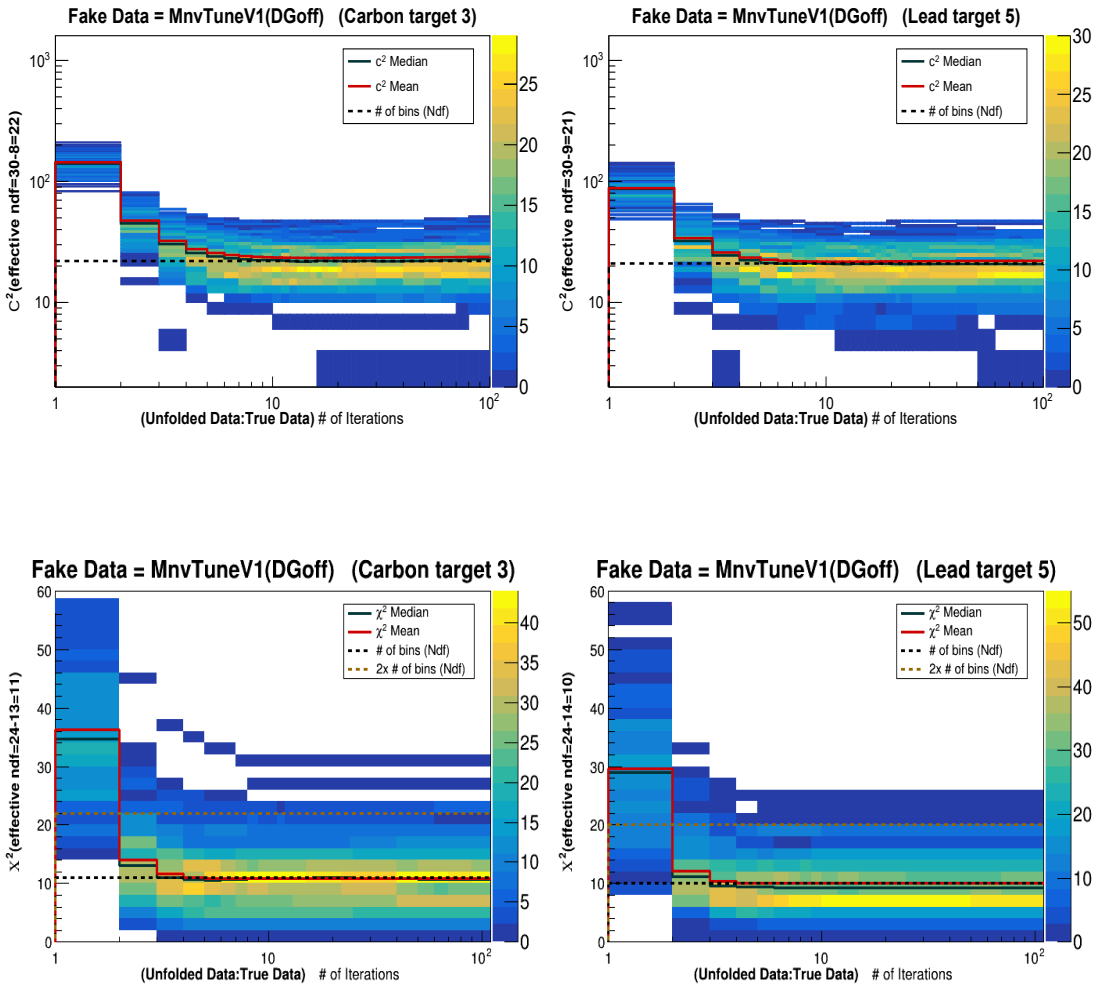

Figure 4.46: Example plots for carbon and target 5 lead warping studies in $x-Q^2$ (top) and $W-Q^2$ (bottom) bins, where MINERvA tune V1 is used as fake data by changing the values of $M_{\mathrm{RES}}^{\mathrm{A}}$ and CCNormRES to GENIE nominated values i.e. switching off the DGpi reweight. The solid red and black lines represent the χ^2 mean and median respectively. The dashed line represents the number of degrees of freedom (ndf) which is equal to the number of bins for the $x-Q^2$ variable. The z-axis represents the calculated χ^2 between unfolded and true distributions for different universes (total of 100) generated using Poisson throws. The χ^2 gets stable at the ndf at around 8-10 iterations for $x-Q^2$ and around 4 iterations for $W-Q^2$.

Similar plots for χ^2 against the number of iterations were made for other warp-

ing functions that were listed in subsection 4.5.3, for different nuclear targets and the tracker. These plots can be found in Appendix D.

	Number of Iterations				
Warp used ⟶	DGPi off	DGPi 1 sigma	RPA 1 sigma	2p2h (10% shift)	NRP 2 sigma
Iron target 2	10	~10	>10	>10	4-6
Lead target 2	10	~10	>10	>10	6-7
Carbon target 3	8-10	~10	>10	>10	3-5
Iron target 3	8-10	~10	>10	>10	3-5
Lead target 3	9-10	10	>10	>10	3-5
Lead target 4	10	10	~10	>10	4-6
Iron target 5	8-10	9-10	9-10	8-10	3-5
Lead target 5	6-10	9-10	9-10	7-10	3-5
Tracker	~10	>10	~10	>10	6-7

Table 4.47: Number of iterations extracted using different warped models for unfolding in $x - Q^2$.

4.5.4 Unfolded Distributions

Unfolded event distributions were obtained using the number of iterations extracted for different targets in the previous section. Fig. 4.48 and 4.49 illustrate the unfolded distributions in $x - Q^2$ for combined iron, combined lead, carbon, and tracker.

Plots for unfolded distributions in $W - Q^2$ and $p_z - p_t$ have been given in Appendix E. The fractional systematic uncertainties on data for unfolded distribution in combined iron targets have been shown in Fig. 4.50.

We also plotted the fractional uncertainties in data for the unfolded event distribution for the different combinations of chosen variables, which can be found in Appendix E. Unsurprisingly, interaction model uncertainty contributed dominantly as seen in the figure. The associated systematic uncertainties have been discussed in detail in Chapter 5.

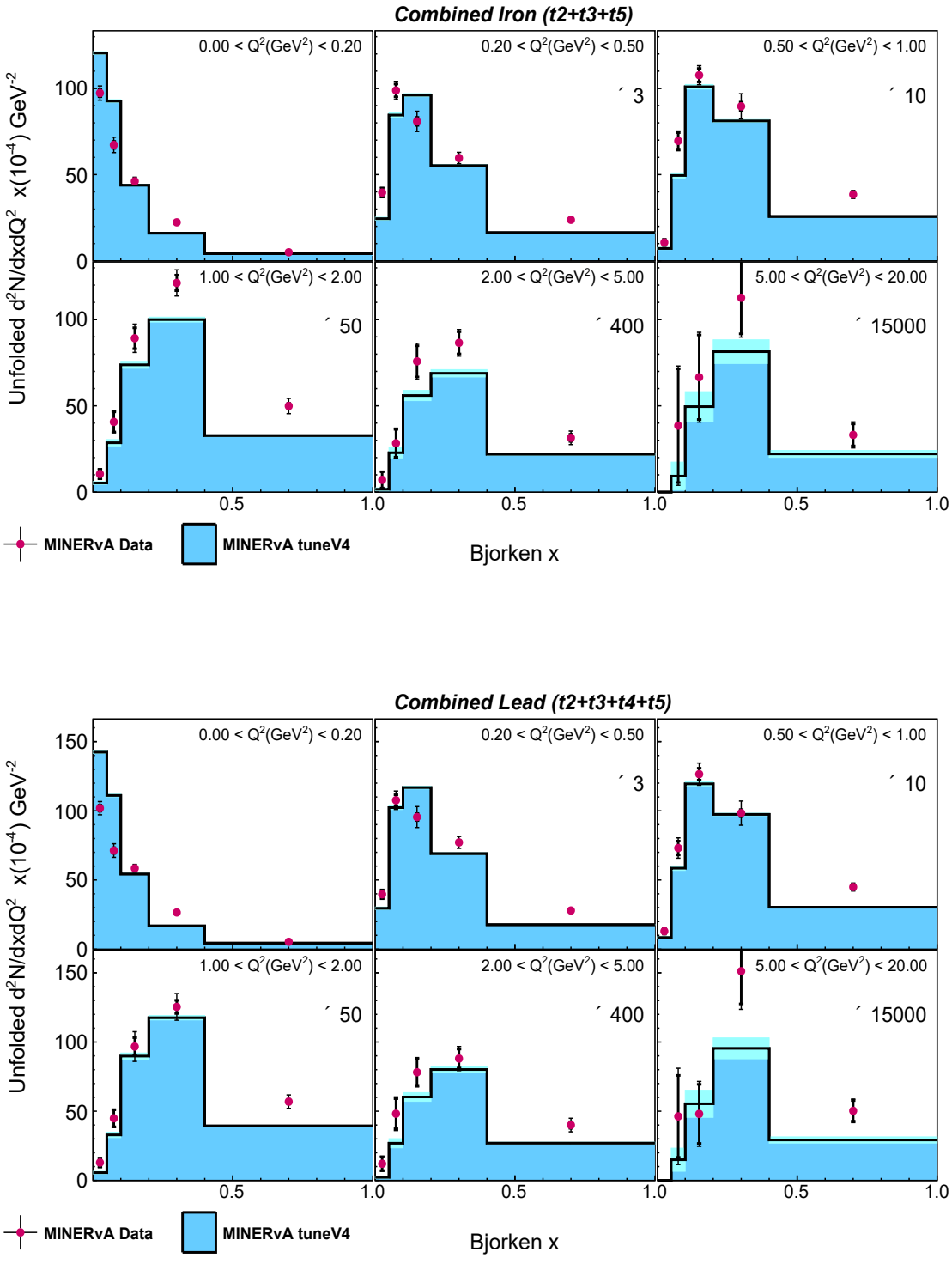

Figure 4.48: Unfolded distribution in bins of $x - Q^2$ for combined iron (top) and lead (bottom) targets. Each panel represents bins of Q^2 bins. Blue histograms indicate the unfolded MC, while pink dots represent the unfolded data. The cyan bands on the MC depict statistical errors, and the error bars on the data points reflect the combined statistical and systematic uncertainties.

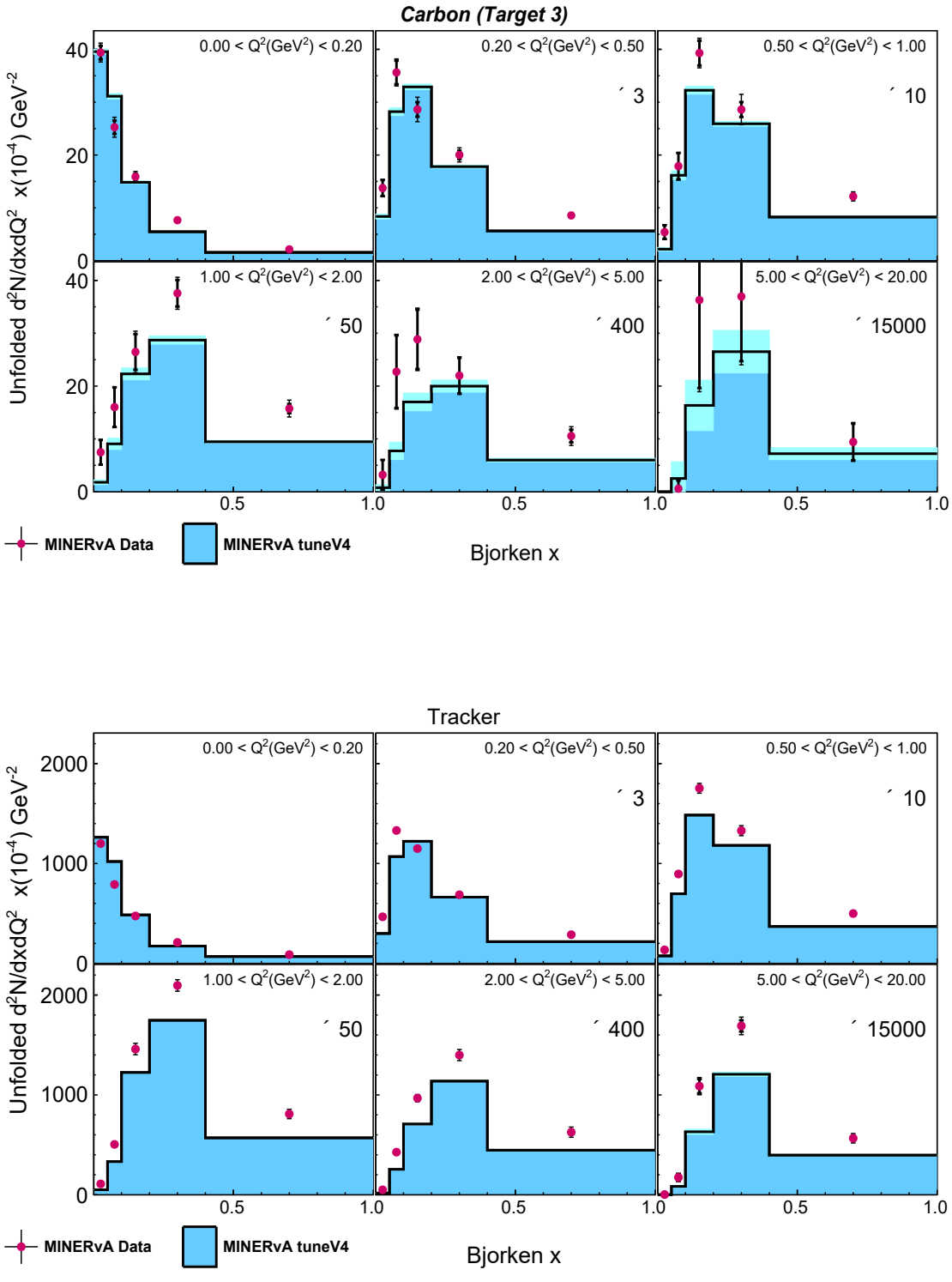

Figure 4.49: Unfolded distribution in bins of $x-Q^2$ for carbon and tracker. Blue histograms represent the unfolded MC, while pink dots are for unfolded data. The cyan color bands on MC represent the statistical errors on MC. Error bars on data points represent the statistical + systematic uncertainty on data.

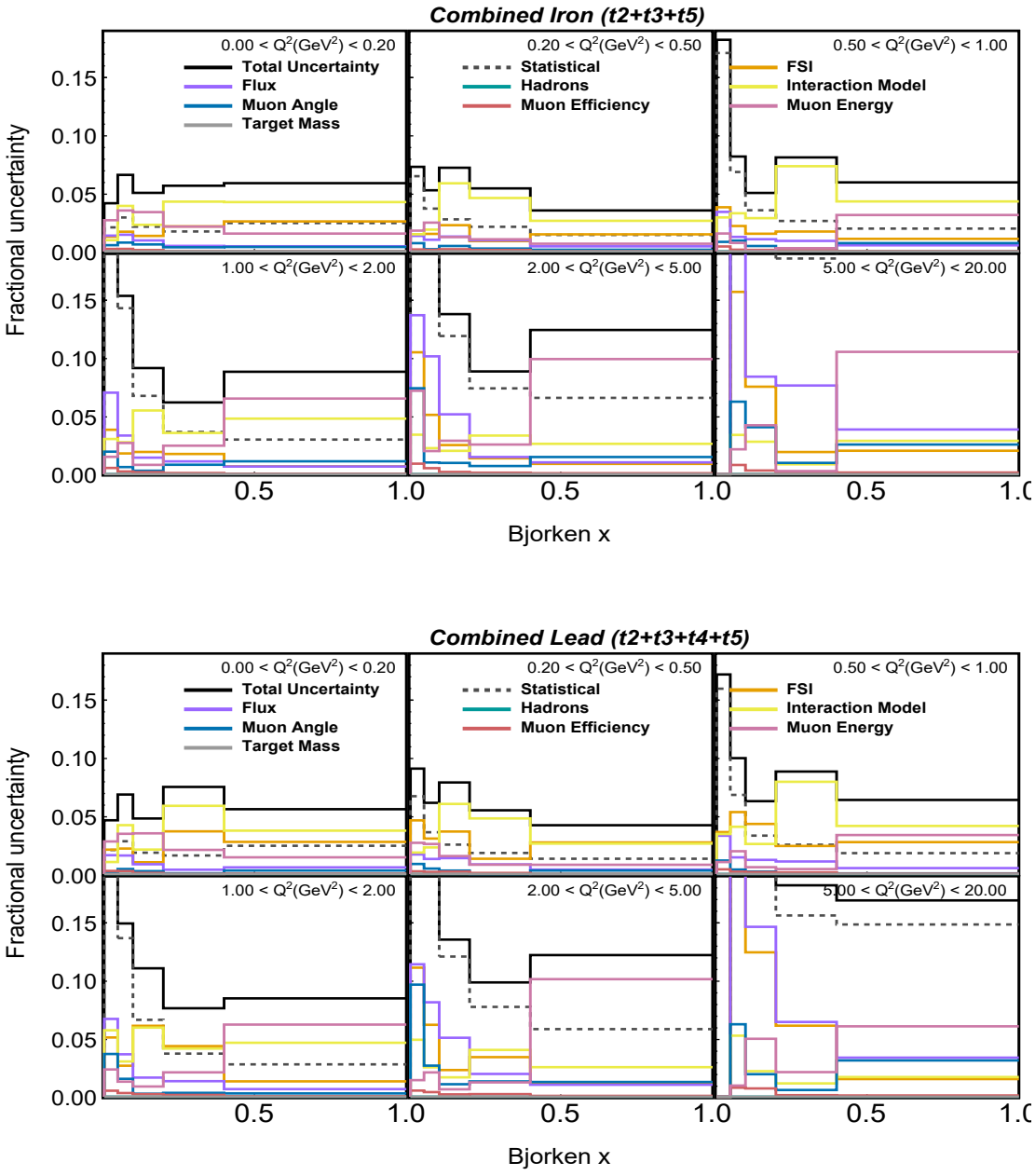

Figure 4.50: Systematic uncertainties on unfolded data distribution in bins of $x - Q^2$ for combined iron (top) and combined lead (bottom).

Once we obtain the unfolded distribution, we have dealt with the numerator on the right-hand side of the Eq. 4.4 i.e. $\Sigma_{\alpha\beta} U_{\alpha\beta ij}(N_{\text{data},\alpha\beta} - N^{\text{bkgd}}_{\text{data},\alpha\beta})$. For the next step to extract the cross section, we need to measure the denominator in Eq. 4.4. Hence, the next part is a correction for the detector acceptance and efficiency.

4.6 Efficiency Correction

We are not able to reconstruct 100% of our signal events in the MINERvA detector, due to the limitation of our detector's acceptance as well as the inefficiency of our reconstruction algorithms. The acceptance issue is because of the requirement of the antimuon to be matched in MINOS ND, with the cut on the energy and angle of antimuon, at MINERvA we are not able to reconstruct all of our signal events. The efficiency of the reconstruction algorithms is the fraction of signal events we can successfully reconstruct after applying our signal selection cuts. Hence, we calculate an efficiency correction factor ϵ_{ij} for each bin (i, j) defined as:

$$\epsilon_{ij} = \frac{N_{i,j}^{\text{generated and reconstructed}}}{N_{i,j}^{\text{generated}}} \tag{4.7}$$

Where, the term in the numerator is the total number of signal events in the bin (i, j) that passed through both the reconstruction and truth selection cuts. This means all the signal events that were generated and then reconstructed successfully. The denominator represents the signal events in bin (i, j) passing the truth cuts only which is all the signal events that the simulation generated, a superset of the numerator. In Table 4.51, we have listed these correction factors for carbon, combined iron, and combined lead targets.

It must be noted that the efficiency correction is calculated in each bin separately as reflected in Eq. 4.7. Figures 4.52, 4.53, 4.54 and 4.55 show the predicted signal events, the reconstructed signal events and their ratio to determine reconstruction efficiency, for carbon, combined iron, combined lead and tracker, respectively, as a function of $x - Q^2$. The numbers in Table 4.51 represent the overall integrated correction factor for different nuclear targets.

Material	Reconstruction Efficiency
Carbon	52.2%
Combined Iron	43.1%
Combined Lead	45.8%
Tracker	63.1%

Table 4.51: Integrated reconstruction efficiency for different materials in the nuclear targets and tracker.

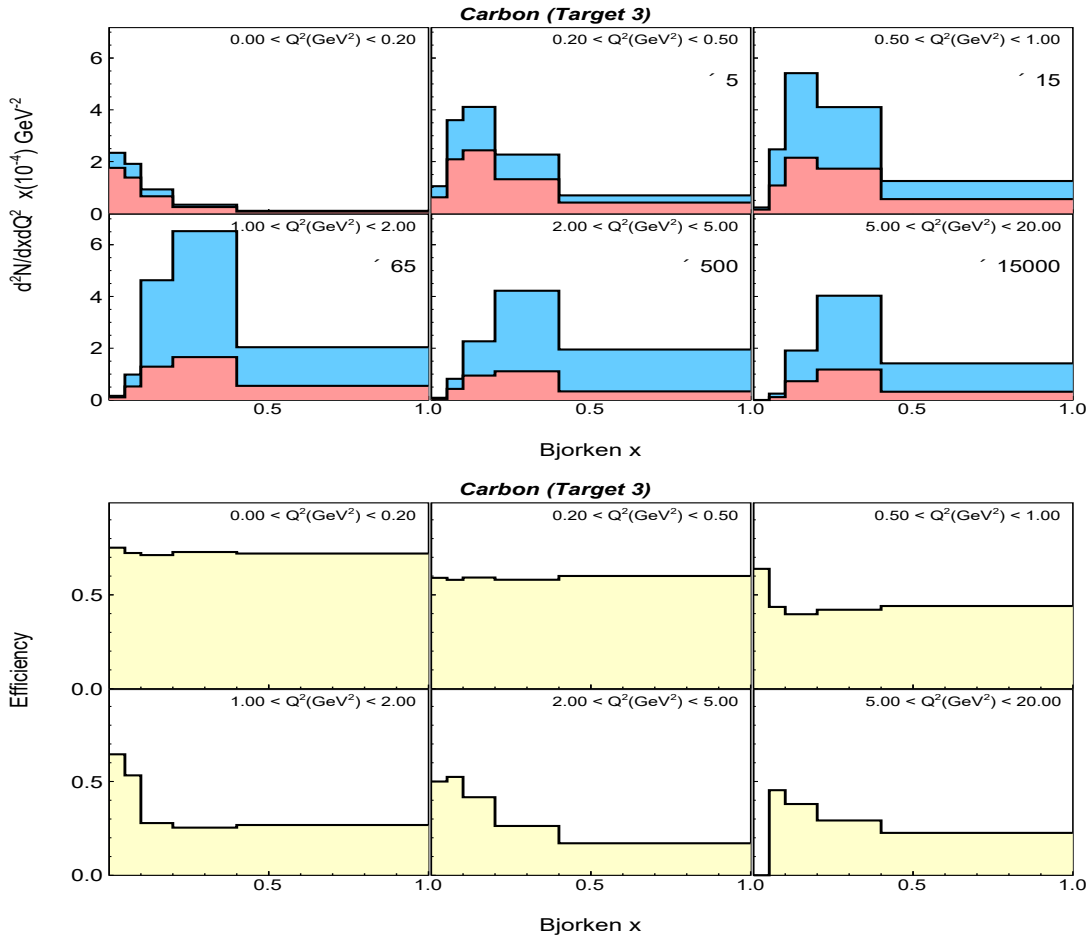

Figure 4.52: (Top) The Blue histogram represents the total number of generated signal events by the simulation and the red histogram is the number of events out of generated signal events that we could reconstruct. The ratio of the two (bottom) gives a measure of the reconstruction efficiency in different bins of $x - Q^2$ for carbon.

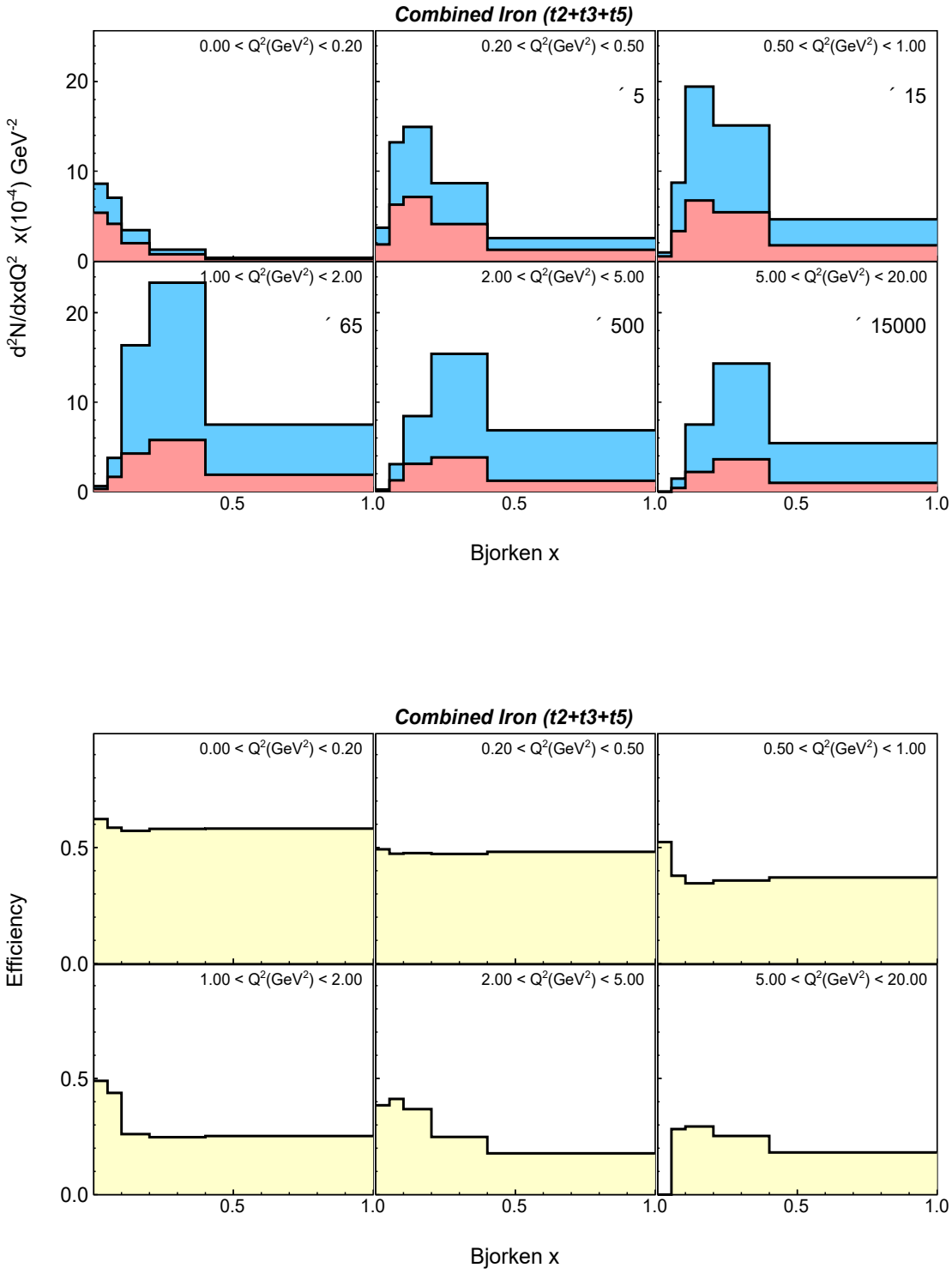

Figure 4.53: (Top) The Blue histogram represents the total number of generated signal events by the simulation and the red histogram is the number of events out of generated signal events that we could reconstruct. The ratio of the two (bottom) gives a measure of the reconstruction efficiency in different bins of $x - Q^2$ for combined iron of nuclear targets 2, 3 and 5.

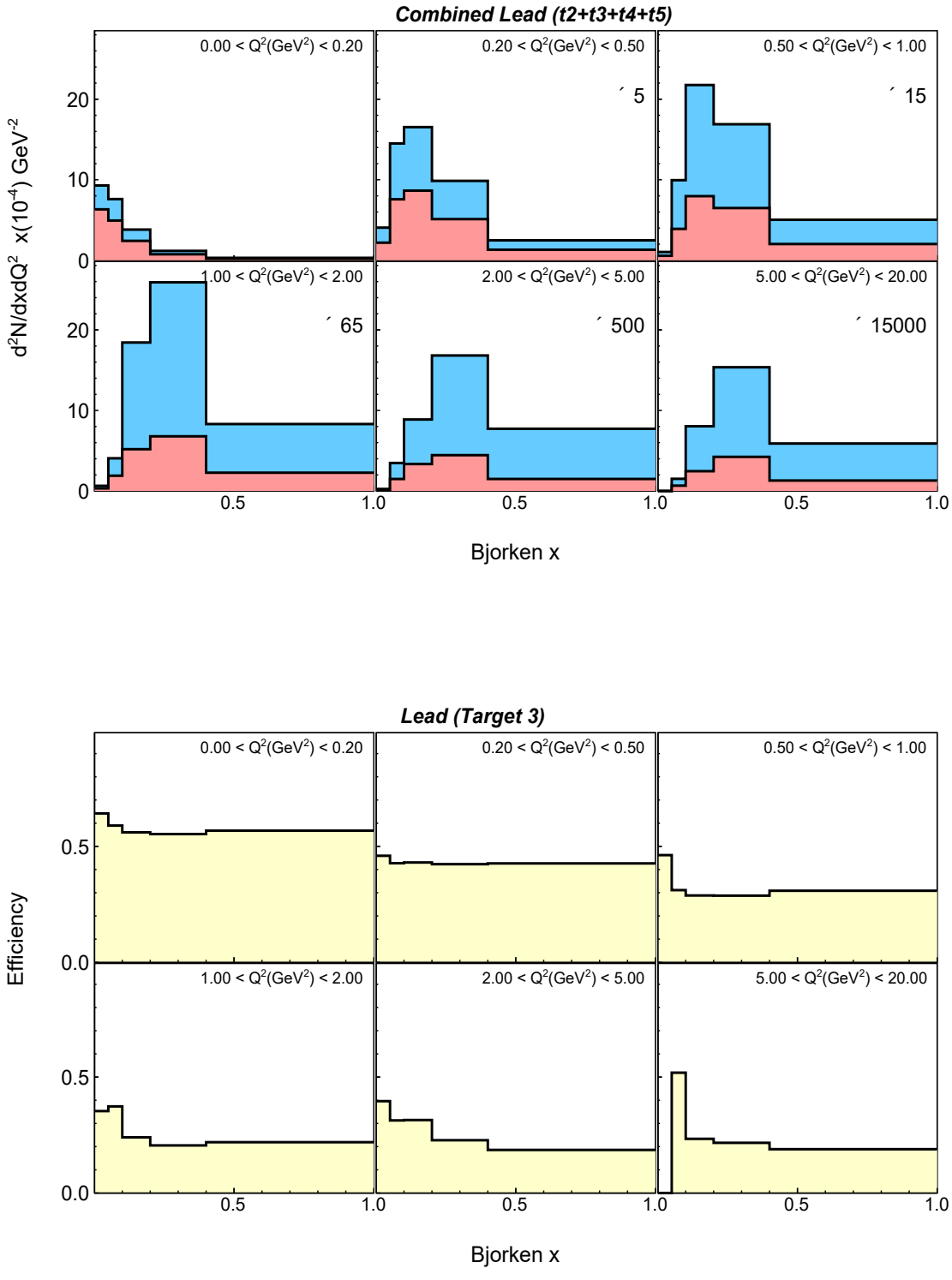

Figure 4.54: (Top) The Blue histogram represents the total number of generated signal events by the simulation and the red histogram is the number of events out of generated signal events that we could reconstruct. The ratio of the two (bottom) gives a measure of the reconstruction efficiency in different bins of $x - Q^2$ for combined lead of nuclear targets 2, 3, 4 and 5.

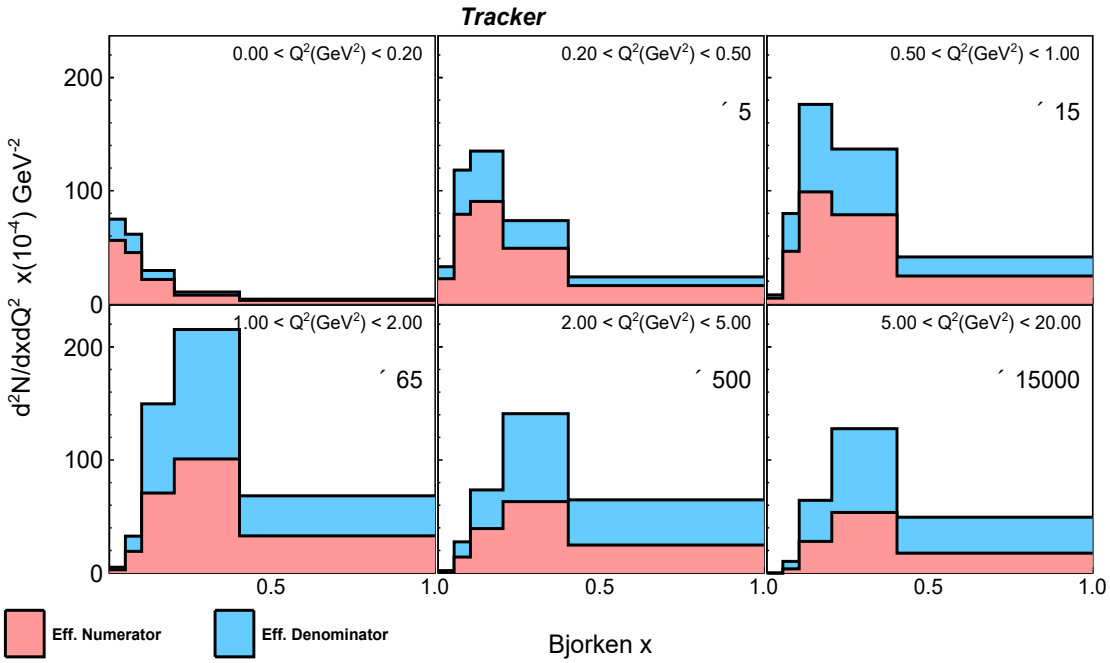

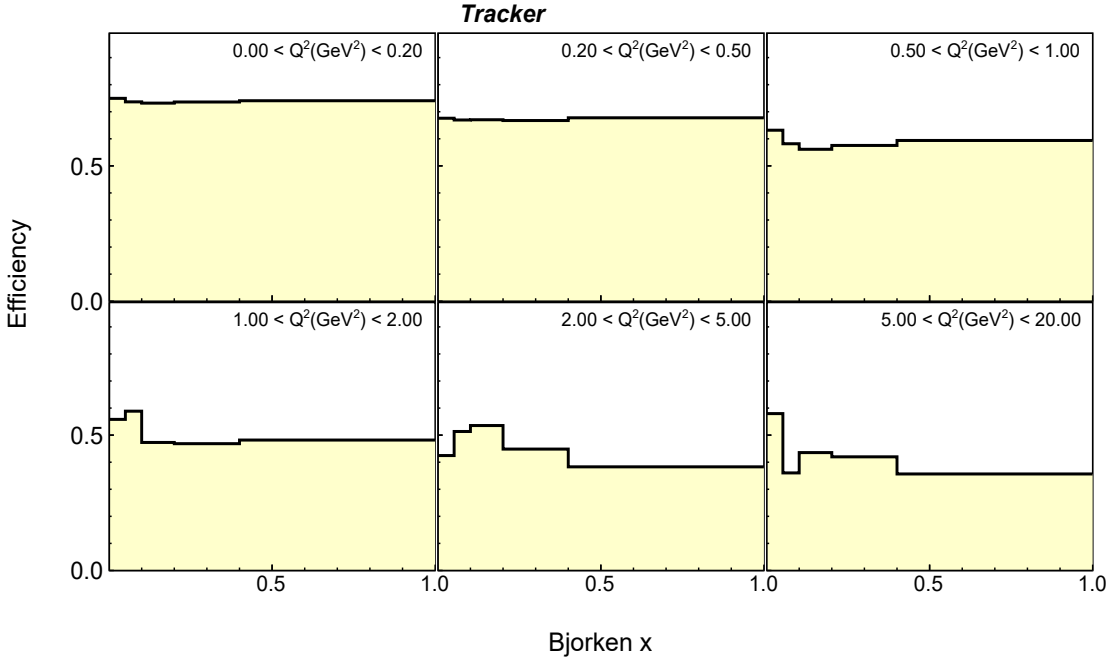

Figure 4.55: (Top) The Blue histogram represents the total number of generated signal events by the simulation and the red histogram is the number of events out of generated signal events that we could reconstruct. The ratio of the two (bottom) gives a measure of the reconstruction efficiency in different bins of $x - Q^2$ for tracker.

Plots for efficiencies in individual target materials are given in Appendix F. A point to note is that since the efficiency numerator is entirely a subset of the denominator, there is a correlation among them. When the ratio is taken to calculate efficiency, the correlation is taken care of by binomial error propagation for the statistical errors.

What we see from these plots is that the reconstruction efficiencies are overall higher for the tracker region as compared to nuclear targets. This is simply because of the geometric closer proximity of the tracker region to the MINOS ND, which allows more (anti)muons to be matched in MINOS, considering the (anti)muon angle reconstruction cut has been applied ($\theta_\mu < 17^o$). We can also see from the plots, that as the four-momentum transfer squared increases, the efficiency decreases. This is simply because, at higher Q^2, the muons get scattered at larger scattering angles. Also, the energy of the outgoing muons is expected to be lower at high Q^2, because much of the energy is carried by the recoiling nucleus. As a result, the efficiency is lowered because of the antimuon energy and angle requirements, for the antimuon matched in MINOS ND. What we see at low bjorken x in these distributions is that for intermediate to high Q^2, efficiencies are relatively higher at low values of bjorken x. This is justified because bjorken x is defined as $x = Q^2/2M\nu$ where ν is the energy difference between outgoing antimuon and incoming antineutrino. Low values of x, at intermediate to high values of Q^2 then mean that ν in the denominator is high, which means that outgoing antimuon goes out with higher energies. If the energy of the outgoing antimuon is high, it will be scattered at lower angles and will reach the MINOS ND more often, thus leading to higher efficiencies. Once we determine the efficiency correction, we apply it to the unfolded distribution by normalisation using the efficiency correction factor as seen in Eq. 4.4, to obtain unfolded efficiency corrected distributions.

Figures 4.56 and 4.57 illustrate the efficiency corrected event distributions across bins of $x - Q^2$. Similar plots in $p_z - p_t$ and $W - Q^2$ are given in Appendix G.

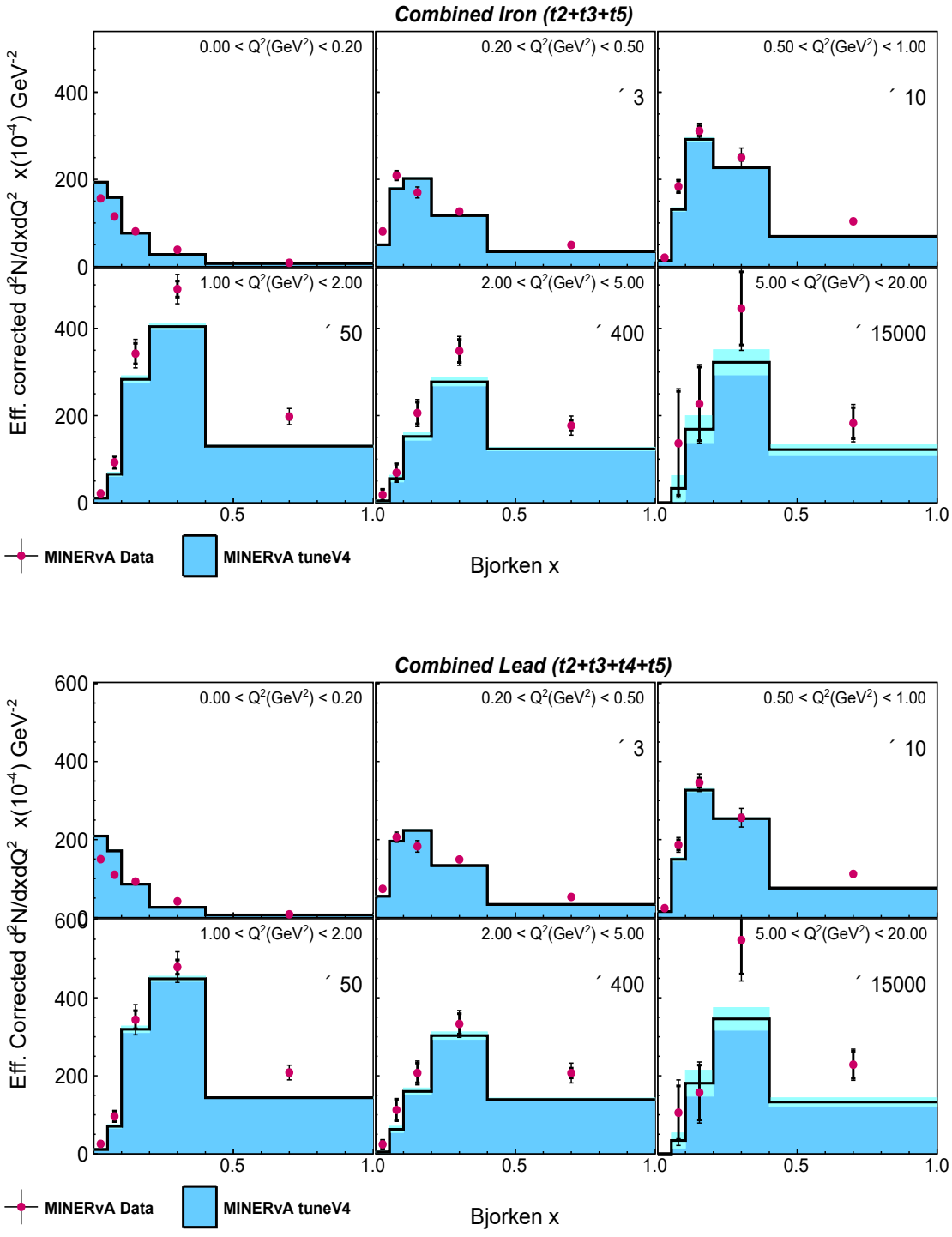

Figure 4.56: The plot shows unfolded, efficiency-corrected event rates for combined iron (top) and lead (bottom) across bjorken x bins, with panels for Q^2 bins. The blue histogram represents MC events, with cyan bands for statistical uncertainties. Red points depict the unfolded data, with bold black error bars for statistical uncertainties and thinner bars for total uncertainties (statistical plus systematic). The y-axis shows event rates normalized by bin width.

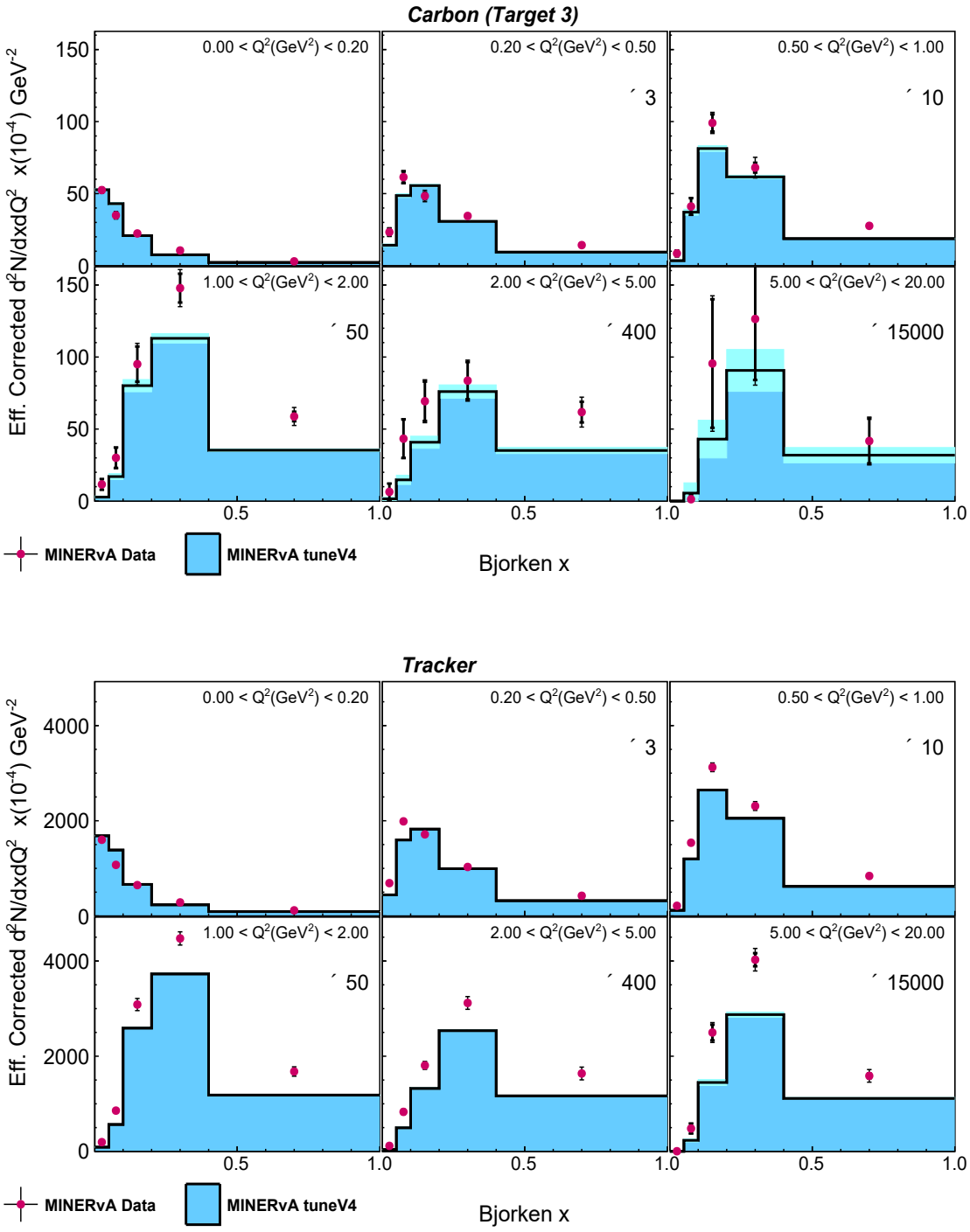

Figure 4.57: The plot displays event rates across bjorken x bins for carbon (top) and tracker scintillator (bottom), with panels for Q^2 bins. The blue histogram represents unfolded, efficiency-corrected MC events, with cyan bands indicating statistical uncertainties. Red points show the unfolded data, with bold black error bars for statistical uncertainties and thinner bars for total uncertainties (statistical plus systematic). The y-axis is normalized by bin width.

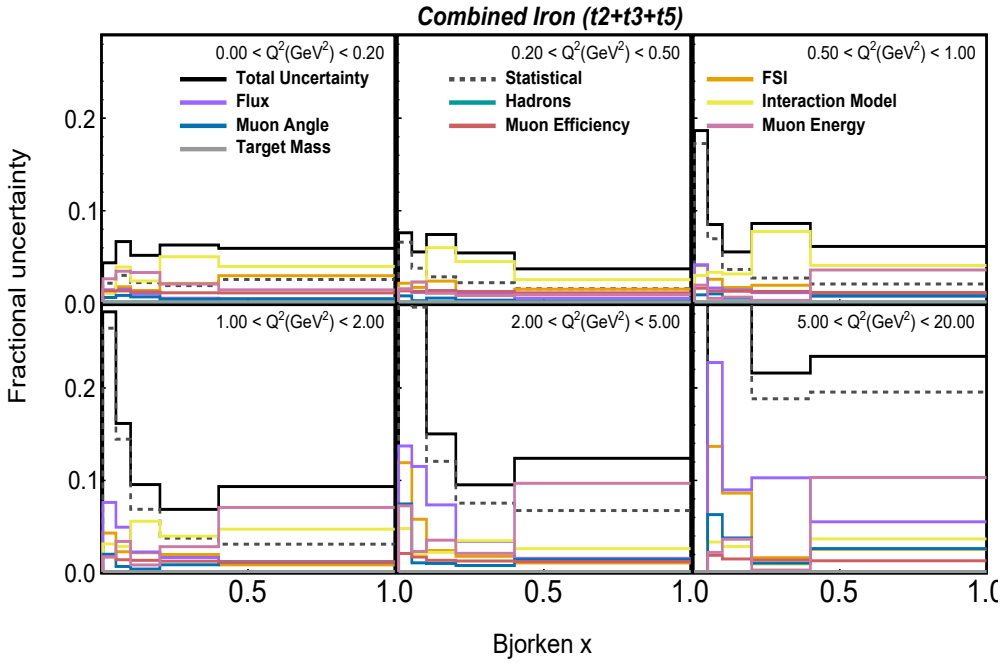

Figure 4.58: The plot shows the fractional uncertainties in the unfolded, efficiency-corrected distribution across $x - Q^2$ bins for the combined iron from all targets except target 1. The dashed line represents the statistical uncertainty, while the solid black line indicates the total uncertainty, including both statistical and systematic contributions. The colored lines correspond to different sources of systematic uncertainty.

Fig. 4.58 shows the fractional uncertainties associated with efficiency corrected distributions for data in combined iron from different targets, as a function of bjorken x and Q^2. We see that the interaction model and final state interaction uncertainties dominate in the low Q^2 region. This is expected because, in the low Q^2 region, the final state particles produced are of low energy and are more likely to undergo re-scattering, absorption, etc. in the nuclear medium. We notice that when Q^2 becomes high, the flux uncertainties are higher, which is because the flux of the antineutrino beam falls at the tail end of our antineutrino energy distribution, leading to larger uncertainties. So the background from the wrong sign events is higher. We also notice that the muon energy uncertainties dominate

above Q^2 of 1 GeV^2 and in the high x region. This is simply because, at these high values of momentum transfer, the outgoing muon is scattered at large angles, with low energies, leading to higher uncertainties because of our chosen muon energy scale ($2 < E_\mu < 20$ GeV). Similar plots for other nuclear targets and tracker in bins of $x - Q^2$, $p_z - p_t$ and $W - Q^2$ can be found in Appendix G.

4.7 Number of Target Nucleons and Flux

As seen from Eq. 4.4, the final step towards double differential cross section measurement, is normalising the efficiency corrected event rate by the total flux and the number of target nucleons, such that we are reporting cross section extracted per nucleon in units of "/cm^2/GeV^2/nucleon" for $p_z - p_t$ and $x - Q^2$ and "/cm^2/GeV^3/nucleon" for $W - Q^2$, because we are normalising by the bin widths of the kinematic variables in which we report the cross section. The number of target nucleons is extracted using the simple mole concept, where 1 mole of a given material has 6.023 $\times$ 10^{23} atoms. Table 4.7 lists the number of target nucleons for different target materials in the MINERvA detector, where we have excluded target 1. As seen from the table, we have the most number of nucleons for lead in the nuclear target region, followed by iron and carbon. The uncertainty referred to as "target mass" is associated with errors in measuring the masses of the targets, which consequently affects the determination of the number of target nucleons, as discussed in Chapter 5.

Material	Number of target nucleons
Carbon	9.610$\times$ 10^{28}
Iron	3.819 $\times$ 10^{29}
Lead	4.297 $\times$ 10^{29}
Tracker scintillator	3.235 $\times$ 10^{30}

Table 4.7: Number of target nucleons for different nuclear target materials and tracker scintillator.

After normalizing by the number of target nucleons, i.e. T in Eq. 4.4, the next and final step to extract the cross section is to normalise the unfolded and efficiency corrected distributions with the incoming antineutrino flux, depicted by ϕ in Eq. 4.4. Integrated flux is extracted from the flux simulation prediction, for true antineutrino energy from 0 to 20 GeV, as discussed in Chapter 3. Flux is extracted per POT, so we multiply by the total data exposure POT of 1.11707×10^{21}. Once we have performed this normalisation, all of the terms on the right-hand side of Eq. 4.4 have been accounted for, yielding us the measured double differential cross section in units mentioned in the above discussion.

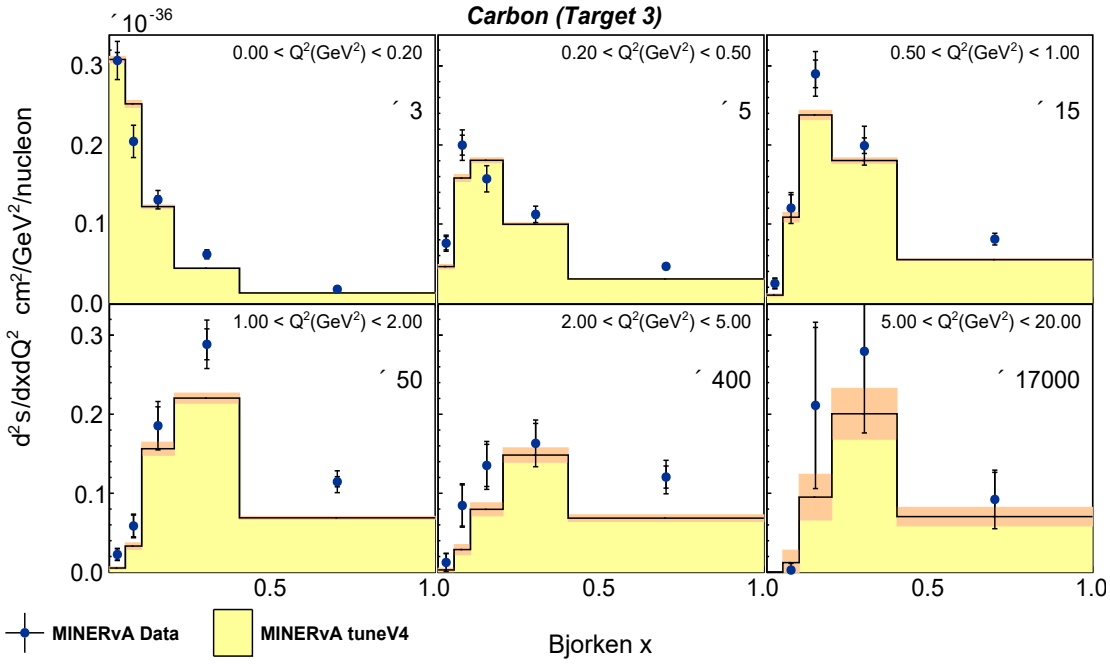

Figure 4.59: The plot illustrates the double differential cross section as a function of x and Q^2, for carbon. The yellow histograms depict the cross section extracted from Monte Carlo simulations, with the orange bands indicating the statistical uncertainties associated with the MC results. The blue dots represent the cross section measured from data, with smaller error bars reflecting statistical uncertainties alone, while the larger error bars encompass the total uncertainties, combining both statistical and systematic sources. This comprehensive visualization highlights the precision and reliability of the cross section measurements obtained from MINERvA data.

Fig. 4.59 shows the extracted double differential cross section in bins of $x - Q^2$ for target 3 carbon, as an example.

The results for cross section measurements for different nuclear target materials, as a function of the chosen combination of variables i.e. $x - Q^2$, $W - Q^2$ and $p_z - p_t$, along with their associated systematic uncertainties will be given, and discussed in Chapter 6. The breakdown of the different error bands associated with the cross section in data has been given in Chapter 5.

Chapter 5

Systematic Uncertainties

I can live with doubt and uncertainty. I think it's much more interesting to live not knowing than to have answers which might be wrong [120].

— **Richard P. Feynman**

(1965, Nobel Prize in Physics, development of quantum electrodynamics)

When the relentless human genius takes up a mega project, like the MINERvA experiment, so many things come together to build it up. These large-scale scientific endeavours involve intricate and complex experimental setups, often pushing the boundaries of current knowledge and technology. We are trying to detect the interaction of a particle that can not even be detected directly. As a result, encountering uncertainties in our measurement is inevitable. **Statistical uncertainties** arise from the inherent randomness in the detection of neutrino interactions. We try to mitigate this by increasing our sample size i.e. large data sets, but still, statistical fluctuations and variations are natural. This is due to the inherent randomness in each event, for example, while flipping a coin. The outcome of getting a head or a tail is equally probable, but in 10 flips, we might get 7 heads and 3 tails. This outcome will predict the probability of getting a head off by 40% from the actual value of 0.5. But if we increase the sample size, and flip the coin

1000 times, the variation becomes smaller relative to the total number of flips. We might see 510 heads and 490 tails. This is why, the concept of standard deviation (σ) exists, which is inversely proportional to the square root of the number of times we make measurements. The same goes for detecting (anti)neutrinos. The larger the sample size, the smaller is the fractional standard deviation from the mean expected value. In principle, there is no limit to how much can we increase our sample size, but we only took data for a limited period and hence some degree of statistical uncertainty always exists. At MINERvA, both the MC and data have their own statistical uncertainties, which are uncorrelated. To obtain total fractional statistical uncertainty, these two can be added in quadrature. We generated 4 times more events for MC as compared to data and hence the data statistics are twice as large in the total statistical uncertainty. While statistical uncertainties are limited by the finite number of measurements, **systematic uncertainties** arise from sources that affect the measurements in a correlated way. These uncertainties are associated with biases or errors in the measurement system, and experimental setup, for example, limitations of the resolution of the detector, errors in detector calibration, the knowledge of the incident (anti)neutrino beam, and the uncertainties coming from the underlying theoretical models used in the reconstruction process. Systematic uncertainties are more challenging to quantify as they require understanding the modeling of the potential sources of error.

5.0.1 Multi Universe Approach

As mentioned in Section 4.2 of the previous chapter, the data taken from the experiment and simulation generated MC are both stored as ROOT files, in ntuples. Measured quantities are stored in the form of histograms using the ROOT data analysis framework [121]. In order to evaluate systematic uncertainties, MINERvA uses the "multi-universe" approach. Each universe represents a different variation of parameters that are used as input in the models used in the design of the experiment and the related physics processes, such that the underlying pa-

rameter is "shifted" according to the uncertainty associated with that parameter. At MINERvA two different classes of shifts are used, *vertical and lateral shifts*. Vertical shifts alter the weight that a particular event is given in the analysis and cause the number of events in a particular bin to increase or decrease without directly affecting a kinematical variable. On the other hand, lateral shifts affect a kinematical variable directly and cause events to migrate in and out of a bin. The universe that uses our best estimate or the standard value for the simulation input parameters, without any shifts is called the CV universe (CV is the central value). The shifted universe contains an altered Monte Carlo, which is considered to be the result of the analysis in an alternate universe, where the physics simulation parameters have these alternate slightly shifted values. For this universe, the systematic uncertainty on measurement performed in each bin would be evaluated by measuring the difference between the event count in the shifted universe and the CV universe in that bin. Mostly, we use two variations, where we make the shift by both $+x\%$ and $-x\%$, determined by the known (or deduced) uncertainty in a measured parameter or by shifting by one standard deviation ($\pm 1\sigma$) of a Gaussian distribution. Hence, two ($\pm\sigma$) shifted universes are used, with respect to the central value. These shifted universes corresponding to the same systematic uncertainty are grouped together to form an error band. For the neutrino flux systematic uncertainties, using complex simulations, 100 universes are evaluated, varying many parameters within their uncertainties. When these shifted versions of simulation are used, changes are reflected in the acceptance correction, background estimation, the unfolding matrix, and hence the cross section. The extent to which the cross section gets modified by shifting these parameters quantifies the effect of the systematic uncertainty on our result.

MINERvA analysis toolkit (MAT) is used to facilitate this multi-universe method, by defining C++ classes named MnvH2D (for two-dimensional analysis presented in this thesis), based on the ROOT TH2D objects.

5.0.2 The Covariance Matrix

All the systematically shifted universes are used to predict the systematic uncertainty in each bin of the central value histogram. Systematic uncertainties are evaluated by forming a covariance matrix. The covariance matrix contains the systematic uncertainty value corresponding to a given bin and also the information regarding the correlation between different bins. This can be understood as follows: For example, a certain parameter was tuned to generate a new universe, which changed the event count in bin i. If this also causes the event count in say bin j to increase (decrease), we say that bin i and bin j are positively (negatively) correlated. For two-dimensional analysis, where we have two variables of interest, the covariance matrix is an N $\times$ N matrix, where N is the number of bins in the variable 1 times the number of bins in variable 2 (for example, variable 1 could be bjorken x and variable could be Q^2). The counting for the number of bins for both the variables includes the underflow and the overflow bins (the underflow bin contains all the events which fall in bins below the lowest value of the chosen bin for a given variable and the overflow bin contains all the events which lie outside the maximum chosen bin value for a given variable). For instance, if we chose 4 bins for Q^2 as 0.2,1,2,5,20, then including underflow (events with Q^2 lower than 0.2 GeV) and overflow (events with Q^2 higher than 20 GeV), 6 bins are counted for Q^2. For any two given combinations of bins of bjorken x and Q^2, i and j, the covariance matrix is defined as:

$$\mathrm{Cov}_{ij} = \mathrm{Cov}_{ji} = \frac{\Sigma_{k=1}^{n}(x_{i_k} - \bar{x}_i)(x_{j_k} - \bar{x}_j)\omega_k}{\Sigma_{k=1}^{n}\omega_k} \tag{5.1}$$

where, n is the total number of universes, Cov_{ij} is the element of the covariance matrix connecting the bin i and bin j (=Cov_{ji}, the matrix is symmetric). ω_k is the weight applied in the shifted universe k, with the default weight being 1. x_{i_k} is the number of events in the bin i of the universe k. $\bar{x}_i$ is the mean event count in bin i which is calculated as:

$$\bar{x}_i = \frac{\Sigma_{k=1}^{n} x_{i_k}\omega_k}{\Sigma_{k=1}^{n}\omega_k} \tag{5.2}$$

The systematic uncertainty shown in a plot for bin i is calculated by taking the square root of the diagonal element of the matrix Cov_{ii} as:

$$\sigma_i = \sqrt{\frac{\Sigma_{k=1}^{n}(x_{i_k} - \bar{x}_i)^2\omega_k}{\Sigma_{k=1}^{n}\omega_k}} \tag{5.3}$$

The off-diagonal elements are used to measure the goodness of fit between distributions (for example data and simulation), using chi-squared calculation. A χ^2 value of close to 1 per degree of freedom is considered a good fit.

Correlation matrix

The correlation of uncertainty between two different bins i and j is given by:

$$\mathrm{Corr}_{ij} = \frac{\mathrm{Cov}_{ij}}{\sigma_i\sigma_j} \tag{5.4}$$

The above equation returns values between -1 and +1, corresponding to completely anti-correlated (-1) and completely correlated (+1). If the above equation returns a value of 0, it means there is no correlation in the bins i and j, for a given systematic uncertainty source.

Now, it is time to discuss the various sources that contribute to the systematic uncertainties in the antineutrino interaction cross section measurement at MINERvA.

5.1 Model Uncertainties from GENIE

GENIE has an underlying interaction model and an final state interaction (FSI) model. Uncertainties coming from these models contribute a part to the systematic uncertainties in our cross section measurement at MINERvA. These models have various parameters, a total of 30, also called "knobs", which can be changed to vary the result from the models. Every knob corresponds to two universes, one each for

$+\sigma$ and $-\sigma$ shift to each knob. Changing one of the knobs in the interaction model, changes the probability of the initial neutrino interaction while changing the knobs corresponding to the FSI model changes the properties for the re-interaction that takes place within the nuclear medium, once the neutrino has interacted with the nucleon initially. The values of $\pm\sigma$ for different knobs are given in Table5.1 and 5.2. The values of these uncertainties ($\pm\sigma$) on different knobs for cross section modeling are based on the external studies of these uncertainties at MINOS [123] and T2K. The uncertainties associated with these knobs relating to the production of hadrons by neutrino interactions are based on Ref. [124].

The knobs corresponding to interaction model uncertainties come from individual models used by GENIE to simulate interactions in the different kinematical regions like quasielastic scattering, pion production, and deep inelastic scattering. Let us discuss them one by one.

5.1.1 QuasiElastic Model Uncertainties

The GENIE knob "**MaCCQE**" is related to the calculation of the axial mass M_A, which is used to define the axial vector form factor F_A. F_A was modified [125, 126] from a dipole shape (from neutrino-deuteron scattering) to a model-dependent representation. So previously, the dipole form of the axial vector form factor was given as:

$$F_A^{\text{dipole}}(q^2) = \frac{F_A(0)}{\left(1 - \frac{q^2}{m_A^2}\right)^2} \tag{5.5}$$

which has been changed to a z-expansion form:

$$F_A(q^2) = \sum_k a_k z(q^2)^k \tag{5.6}$$

where, a_k are dimensionless numbers, which encode nucleon structure information. This z-expansion approach gives a more accurate representation of our systematic uncertainties as compared to the dipole form. The universe name given to the

combination of the z expansion formalism and the dipole formalism, in the MINERvA framework, is "**GENIE_MaCCQE**". In the analysis presented in this thesis, 100 different systematic universes are used to account for the uncertainty in the measurement of F_A.

The knob "**NormCCQE**" corresponds to the overall normalisation uncertainty in the quasielastic event rate prediction, although the contribution is relatively small. "**VecFFCCQEshape**" deals with the vector form factor modeling. GENIE has implemented the BBBA05 model [91] for the vector form factor, which is related to the electric and magnetic form factors. This has been done because the initial dipole form of the electromagnetic potential was found to be a poor model as at high Q^2, the interaction happens at the quark substructure of the nucleon, and it can not be considered homogeneous. To measure the effect in the cross section shape from changing the form factor model from BBBA05 to a dipole, VecFFCCQEshape is used. This only introduces a change in the shape, as the overall normalisation is kept constant [127]. A $+1\sigma$ (-1σ) shift of 20% (15%) is used to vary the knob NormCCQE, to create two systematic error universes.

"**CCQEPauliSupViaKF**" knob accounts for Pauli blocking in charged current quasielastic events. According to Pauli's exclusion principle, no two nucleons can occupy the same energy state [128]. As a result, all the lower energy levels are occupied, up to an energy E_F. For events in the low Q^2 region, if the four-momentum transferred is small, the nucleon may not be able to get enough energy to overcome the binding energy (E_B) and have final energy greater than what is required to come out of the Fermi sea ($> E_F$). The minimum energy required for the interaction to occur is $E_{\text{nucleon}} > \kappa(E_F + E_B - Q^2)$, where κ is called the Pauli blocking parameter. From a CCQE measurement on Carbon, MiniBooNE found a better fit to their data using a value of $\kappa = 1.007$ [129]. Two systematic error universes are created by varying κ by $\pm 30\%$.

5.1.2 Pion Production Model Uncertainties

A charged current (anti)neutrino interaction event, where the struck nucleon gets excited to a higher energy intermediate state (called resonance e.g. Δ resonance) and then de-excites to produce a nucleon and a pion in the final state is resonant pion production. Among the GENIE knobs for non-resonant pion production, "**MaRES**" and "**MvRES**" correspond to resonant pion production, which is modeled by the Rein Sehgal model [132]. The vector and axial vector nucleon form factors associated with the Rein Sehgal model are analogous to the Llewellyn-Smith CCQE model. The nominal values are $M_A^{\text{Res}} = 1.12$ GeV and $M_V^{\text{Res}} = 0.84$ GeV. At MINERvA, two systematic universes with $\pm\sigma$ shifts of 20% and 10% are used to account for the uncertainty in the values of M_A^{Res} and M_V^{Res} respectively. "**NormNCRES**" corresponds to the normalisation in the pion production from resonances from the neutral current interactions, where instead of a $W^{\pm}$, a Z^0 is exchanged during the interaction. 1 σ shift in the normalisation NormNCRES corresponds to a 20% shift. "**NormCCRes**" corresponds to the normalisation in the pion production from resonances produced via charged current interactions. 1 σ shift in the normalisation NormCCRES corresponds to a 20% shift. Non-resonant pion production is controlled by 8 different knobs. "**Rνn1pi**" and "**Rνp1pi**" correspond to a single pion in the final state. "**Rνn2pi**" and "**Rνp2pi**" are related to the two pion non-resonant production, which is modeled using the Bodek-Yang model [136], where n and p represent the initial state to be a neutron or a proton. These have combined contributions from both the charged current (CC) and neutral current (NC) interactions. A $\pm\sigma$ shift corresponds to a change by 50% in the strength of the interaction type. The single pion production channels Rνn,p1pi has been constrained to an additional fit from pion production data from ANL and BNL [132], reducing the associated uncertainties to a mere $\pm$5%.

5.1.3 Deep Inelastic Scattering Model Uncertainties

"**NormDISCC**" knob corresponding to the overall normalisation in charged current deep inelastic scattering inclusive cross section, contribute to the systematic error band a $\pm\sigma$ effect of less than 0.5% over the whole phase space.

Four different DIS knobs for the Bodek-Yang model implemented by GENIE are **CV1uBY**, **CV2uBY**, **AhtBY** and **BhtBY**. Bodek-Yang model is an inelastic neutrino-nucleon scattering phenomenological model, which uses leading order (LO) parton distribution functions (PDFs) that were produced by fits to the experimental data from around the world (SLAC/NMC/BCDMS/H1)[133, 134, 135]. The model also takes into account the perturbative effects within Next-to-Leading Order (NLO)$\sim \frac{1}{Q^2}$ and Next-to-Next Leading Order (NNLO)$\sim \frac{1}{Q^4}$ QCD. These include additional twist corrections, which become significant in the low Q^2 region. This is simply because at low Q^2, the interaction time is longer and the probing particle (neutrino for this analysis) interacts with the nucleon in a way that allows it to feel the combined effects of multiple partons at once. This is similar to stirring a soup with a spoon slowly, where the spoon feels the pieces of vegetables that the soup contains and feels the resistance of the whole soup. In comparison, when the soup is stirred fast, the spoon only feels the resistance due to the liquid and it is hard to detect individual vegetables in the soup because the spoon is moving too fast. Twist corrections account for the correlation between partons, such as quark-quark, quark-gluon, and gluon-gluon interactions. Target mass corrections are used in the model to correct for the nuclei of different masses than those that were originally used to tune the model. The uncertainty knobs **CV1uBY** and **CV2uBY** are used to parameterize the PDFs, focusing on the distribution of valence up quarks. The "**AhtBY**" uncertainty is associated with higher twists and target mass corrections and "**BhtBY**" is associated with the uncertainty in the mass of the quark in the initial and final state and its transverse momentum in the initial state [136]. The values of the sigma shifts to these

parameters were determined by studying the effect of reducing χ^2 using model prediction comparison to experimental data.

Apart from these, GENIE also has **MaNCEL** and **EtaNCEL** knobs, for the elastic scattering channel. The axial mass for the elastic scattering channel M_A is shifted by ±25% for the MaNCEL knob. The elastic scattering form factor, from the Ahrens model [137] used by GENIE, has the following form:

$$G_A(Q^2) = \frac{1}{2}\frac{G_A(0)}{(1+\frac{Q^2}{M_A^2})^2}(1+\eta) \tag{5.7}$$

Where the parameter η corresponds to the strange axial form factor, with a value of 0.12. The EtaNCEL knob takes a ±30% shift in this parameter. All the uncertainties discussed so far, correspond to the interaction model uncertainties in GENIE. The summary of all the different GENIE knobs discussed in this section is provided in Table5.1.

GENIE knobs	$\pm\sigma$ shift	Fractional Uncertainty in Cross Section
MaNCEL	25%	< 2%
EtaNCEL	30%	< 2%
MaCCQE	15%	< 4%
VecFFCCQQEshape	100%	< 3%
CCQEPauliSupViaKF	30%	< 3%
MaRES	20%	< 5%
MvRES	10%	< 3%
NormNCRES	20%	< 3%
Rvn1pi	4%	< 2%
Rvp1pi	4%	< 2%
Rvn2pi	50%	< 4%
Rvp2pi	50%	< 2%
NORMDISCC	3%	< 2%
AhtBY	25%	< 2%
BhtBY	25%	< 3%
CV1uBY	30%	< 2%
CV2uBY	40%	< 2%

Table 5.1: Interaction GENIE model uncertainties showing shift values ($\pm\sigma$) and maximum fractional uncertainty at the extracted cross section in data. Taken from Ref. [63].

Fig. 5.1 shows the contribution to the fractional uncertainty, for cross section extracted using data, coming from interaction model error bands (knobs) in $x-Q^2$ for combined iron and lead targets. Similarly, Fig. 5.2, shows the contribution to the fractional uncertainty in $x-Q^2$ for carbon and tracker. Fig. 5.3 and 5.4 show the different interaction model fractional uncertainties in $W-Q^2$ bins, while Fig. 5.5 and 5.6 present these uncertainties in p_z-p_t bins.

The above-listed figures also show the contribution from the MINERvA-specific tunes applied, as discussed in Chapter 3, section 3.3, which include the "**RPA_Low Q2**", "**RPA_High Q2**" knobs and the "**Low_Recoil_**$2p2h$**_Tune**" knob.

These figures thus provide a comprehensive view of how different interaction model uncertainties, as well as specific tuning parameters, contribute to the overall cross section measurements. These adjustments and their impacts are critical for accurately interpreting the data and understanding the underlying physics processes.

Overall, the uncertainties are at a few percent level and when added in quadrature they are less than 5%.

Having discussed the systematic uncertainties associated with the underlying interaction model used in the analysis, let us now discuss the uncertainties associated with the final state interaction effects. When an (anti)neutrino interacts with a nucleon inside the nucleus, the hadrons produced in the interaction might re-interact while traversing the nuclear medium called final state interaction (FSI) effects, before exiting the nucleus. Simulation of these particles traversing the nucleus is done using mean free path steps.

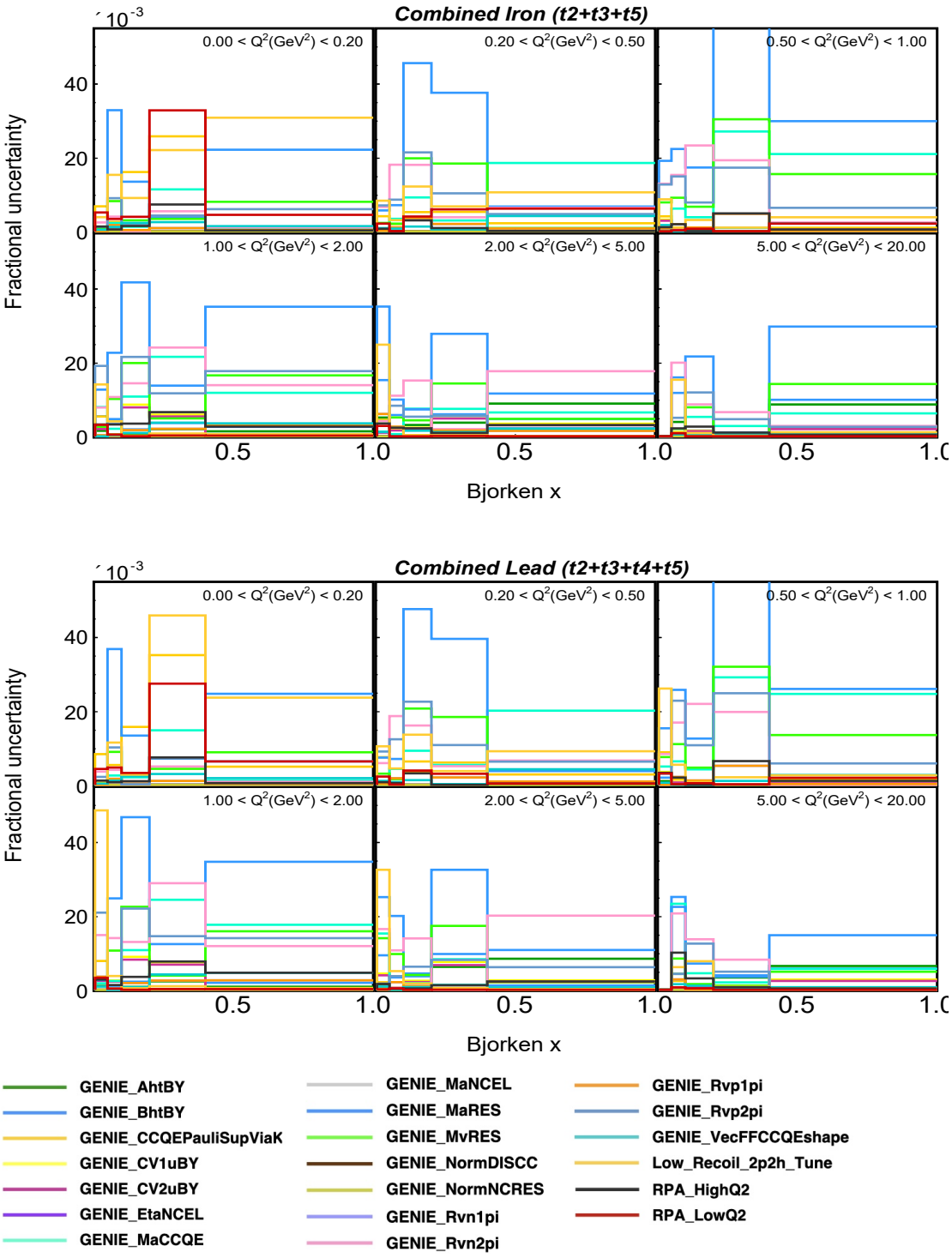

Figure 5.1: Breakdown of the contributions from the various interaction model error bands, as a function of x and Q^2 for combined iron and lead. Contribution from uncertainties associated with MINERvA-specific reweights have also been included in the plot.

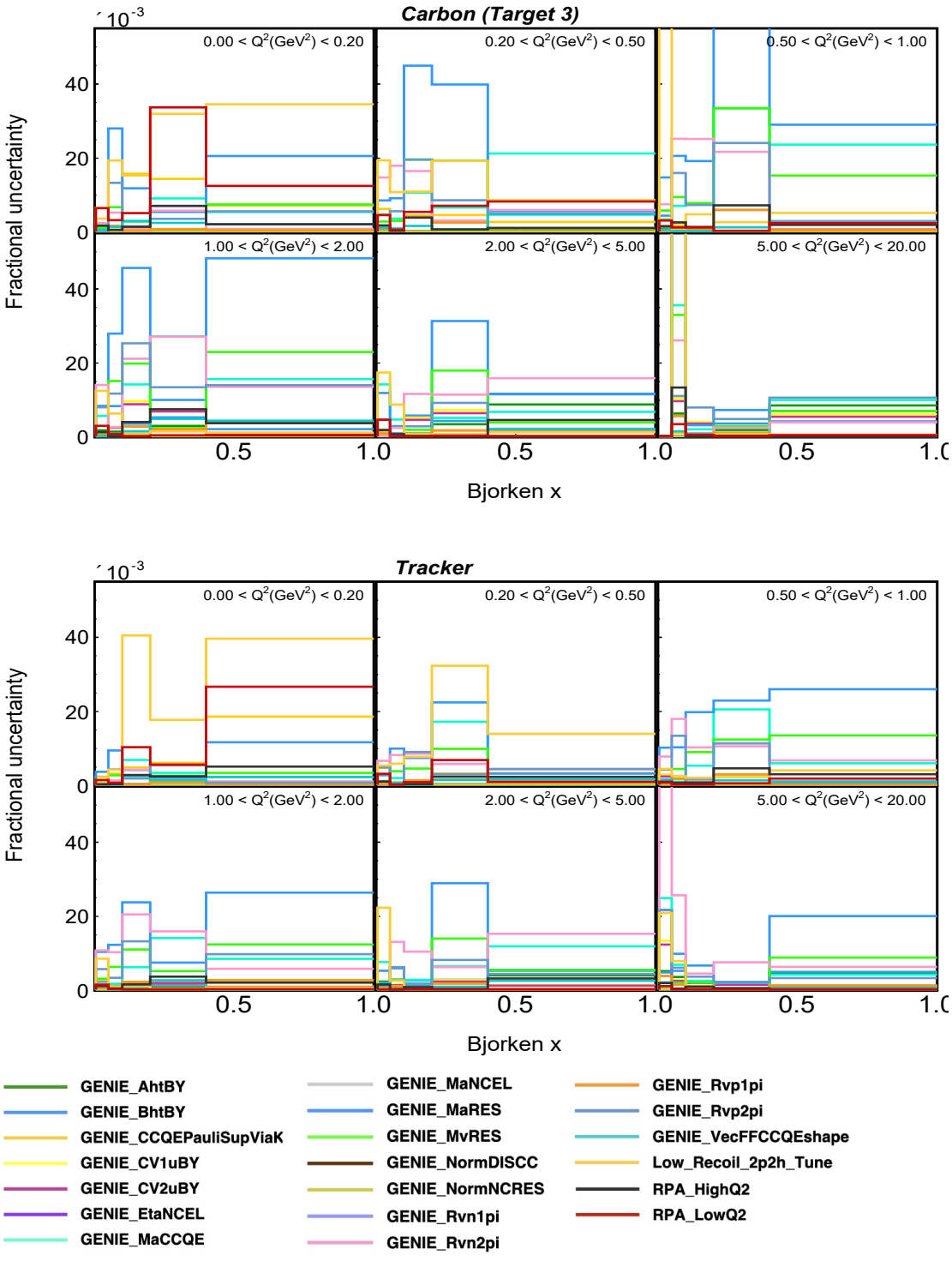

Figure 5.2: Breakdown of the contributions from the various interaction model error bands, as a function of x and Q^2 for carbon and tracker. Contribution from uncertainties associated with MINERvA-specific reweights have also been included in the plot.

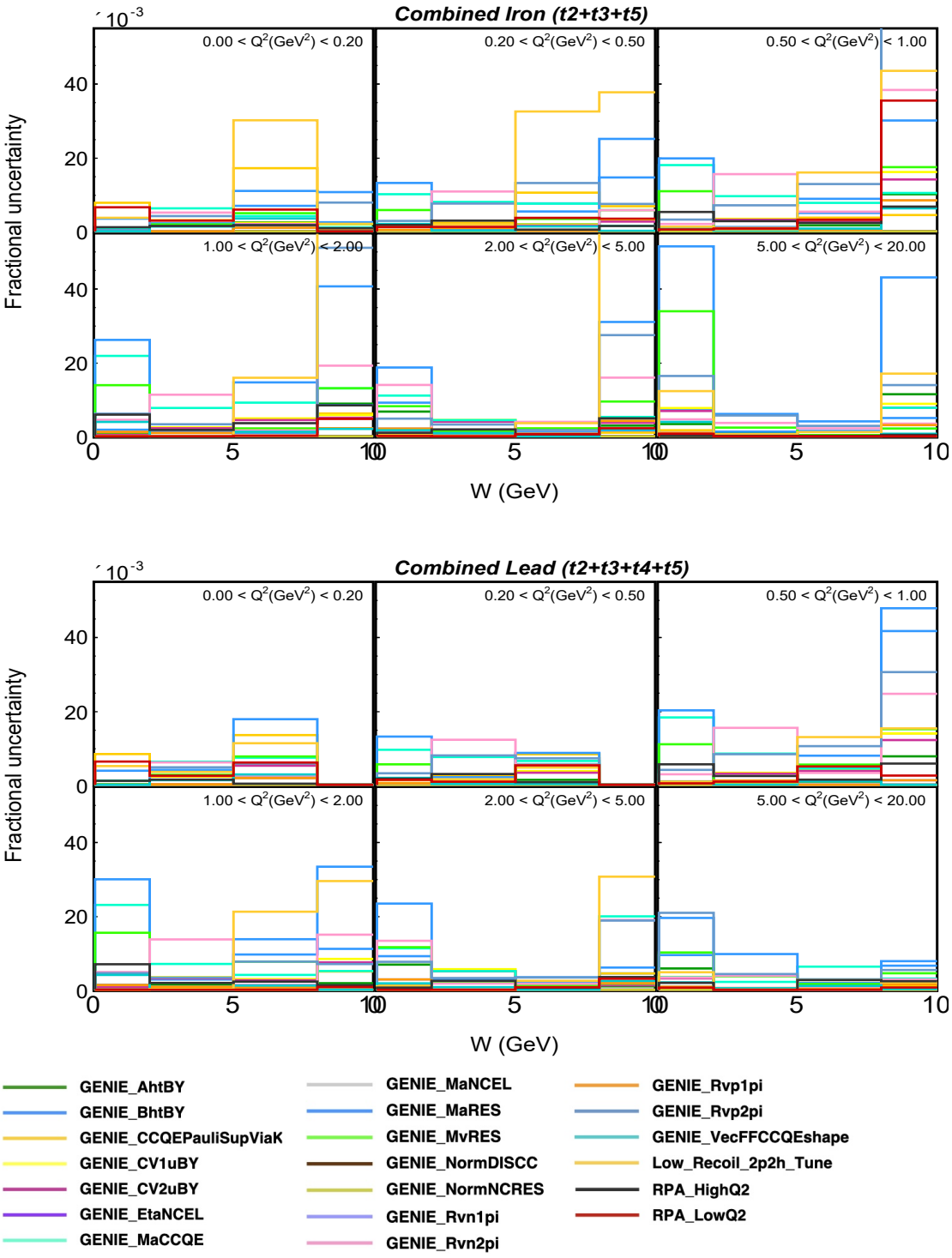

Figure 5.3: Breakdown of the contributions from the various interaction model error bands, as a function of W and Q^2 for combined iron and lead. Contribution from uncertainties associated with MINERvA-specific reweights have also been included in the plot.

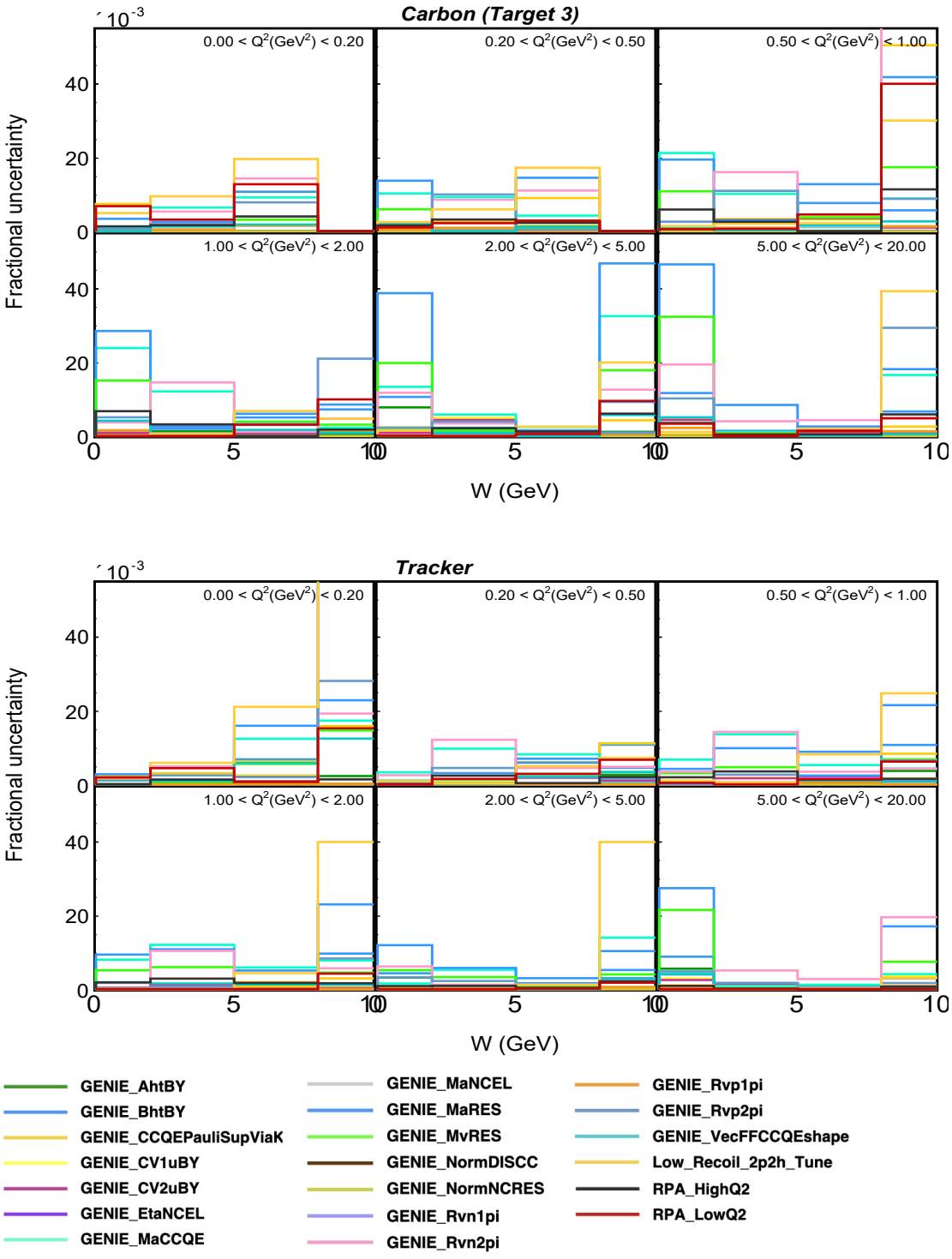

Figure 5.4: Breakdown of the contributions from the various interaction model error bands, as a function of W and Q^2 for carbon and tracker. Contribution from uncertainties associated with MINERvA-specific reweights have also been included in the plot.

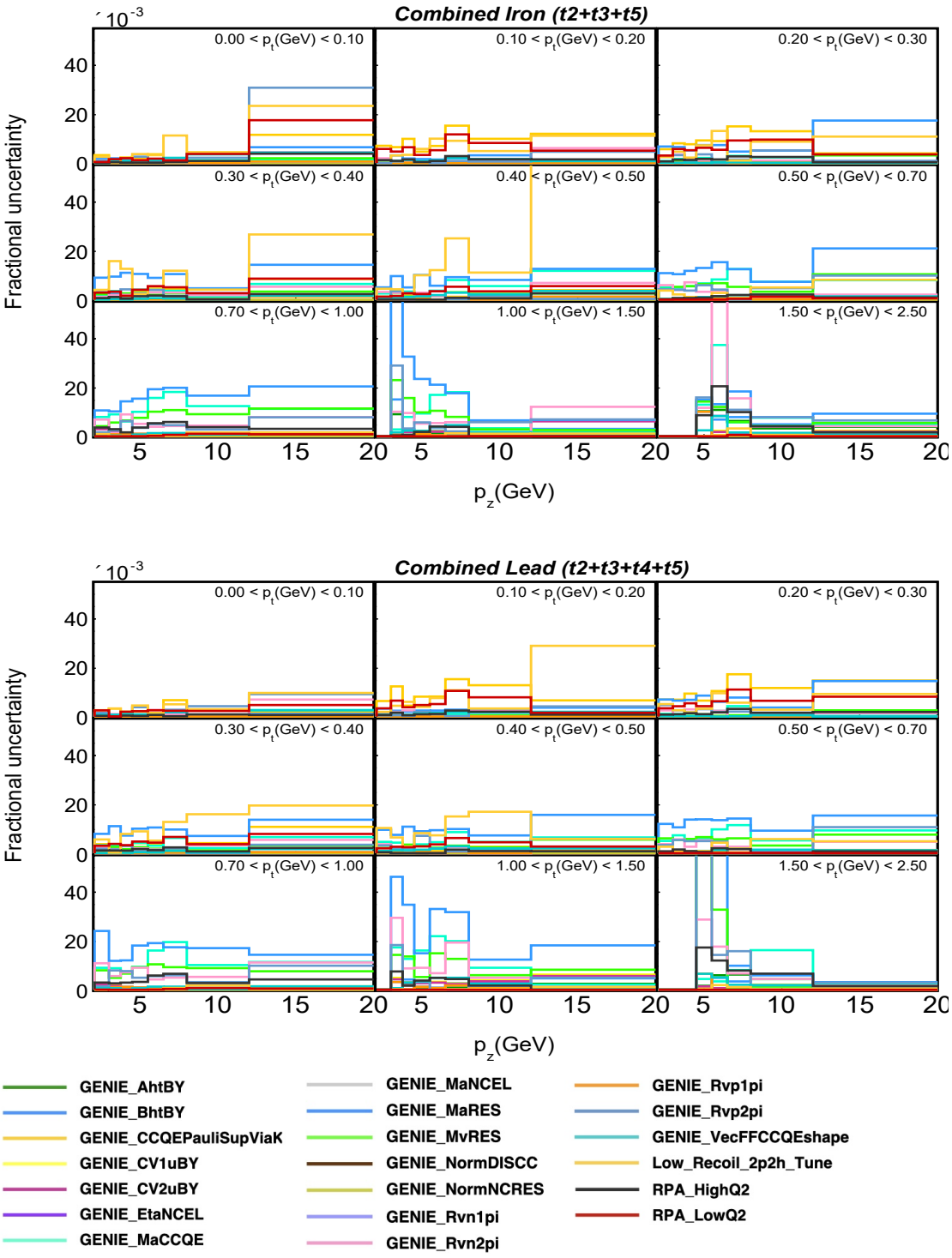

Figure 5.5: Breakdown of the contributions from the various interaction model error bands, as a function of p_z and p_t for combined iron and lead. Contribution from uncertainties associated with MINERvA-specific reweights have also been included in the plot.

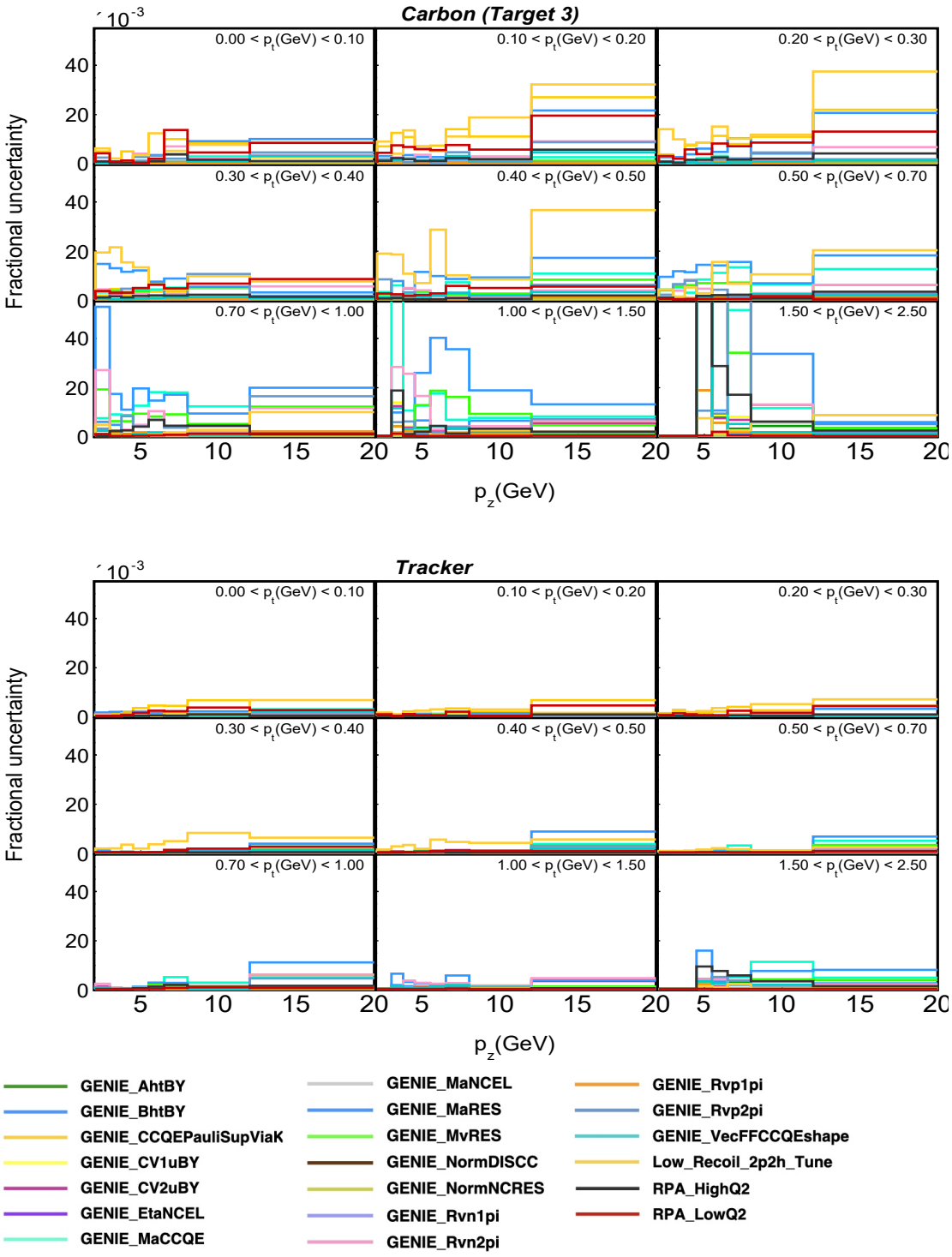

Figure 5.6: Breakdown of the contributions from the various interaction model error bands, as a function of p_z and p_t for carbon and tracker. Contribution from uncertainties associated with MINERvA-specific reweights have also been included in the plot.

5.1.4 Final State Interaction Uncertainties

Final state interaction uncertainties are associated with how the products of an (anti)neutrino interaction are affected when they are exiting the nuclear medium. The products of the initial neutrino interaction may undergo re-scattering or can be absorbed within the nucleus. The uncertainties associated affect the kinematic variables of hadronic energy, bjorken x, inelasticity y, W and Q^2 more than the momenta variables p_t and p_z. The version of GENIE used in this analysis uses GENIE's INTRANUKE/hA model. The hN FSI model was introduced later in GENIE version 3. The GENIE knobs corresponding to this model are listed in Table 5.2. GENIE knobs **MFP_pi** and **MFP_N** shift the mean free path of the particles produced by the interaction of (anti)neutrinos with the nucleons inside the nuclear medium, MFP_pi does this for pions and MFP_N for nucleons (protons and neutrons). The shorter the mean free path of the particle, the greater is the probability of the particle undergoing FSI before exiting the nucleus.

The knobs labeled **Fr ...{pi,N}** define the probabilities of the occurrence of different interactions before the pion or the nucleon exits the nucleus. The knobs labeled **abs** determined the probability of the particle getting absorbed within the nucleus and not exiting it. The knobs **Elas** and **InElas** define the probability of the particle to undergo re-scattering through the elastic and inelastic channels while traversing the nucleus. This re-scattering phenomenon changes the kinetic energy of the outgoing particle. **CEx** knob corresponds to the probability of the particle undergoing charge exchange process, such that the particle produced in the initial interaction changes sign when it exits the nucleus. The knob **FrPiProd** is associated with the probability of the pions being produced inside the nuclear medium to exit the nucleus. **AGKYxF1pi** knob determines the contribution to uncertainties associated with neutrino-induced hadronization and is calculated from the uncertainties of the parton distribution functions (PDFs) calculated from the bubble chamber data [138, 86]. The **Theta_Delta2Npi** knob corresponds

to the angular distribution of resonant pions produced inside the nuclear medium. GENIE uses an isotropic distribution of pions produced from resonance decays, but a more realistic angular distribution is taken using the Rein Sehgal model [132]. The **RDecBR1gamma** knob varies the branching ratio of radioactive resonance decays to photons.

GENIE knobs	$\pm\sigma$ shift	Fractional Uncertainty in Cross Section
FrAbs_N	20%	$< 3\%$
FrElas_N	30%	$< 3\%$
FrInElas_N	40%	$< 2\%$
FrCEx_N	50%	$< 8\%$
FrPiProd_N	20%	$< 3\%$
MFP_N	20%	$< 3\%$
FrAbs_pi	10%	$< 3\%$
FrElas_pi	15%	$< 5\%$
FrCEx_pi	10%	$< 3\%$
FrPiProd_pi	4%	$< 3\%$
MFP_pi	20%	$< 3\%$
AGKYxF1pi	20%	$< 3\%$
Theta_Delta2Npi	20%	$< 5.5\%$
RDecBR1gamma	4%	$< 10\%$

Table 5.2: Final state interaction (FSI) GENIE model uncertainties showing shift values ($\pm\sigma$) and maximum fractional uncertainty at the extracted cross section in data. Taken from Ref. [63].

Fig. 5.7 illustrates the contribution from final state interaction (FSI) effect error bands as a fractional uncertainty, to the cross section extracted from data, across $x-Q^2$ space, for combined iron and lead targets. Similarly, Fig. 5.8, displays the fractional uncertainty contributions for carbon and the tracker in $x-Q^2$ bins. Fig. 5.9 and 5.10 provide insights into the FSI fractional uncertainties within $W-Q^2$ bins, while Fig. 5.11 and 5.12 show these uncertainties in p_z-p_t bins.

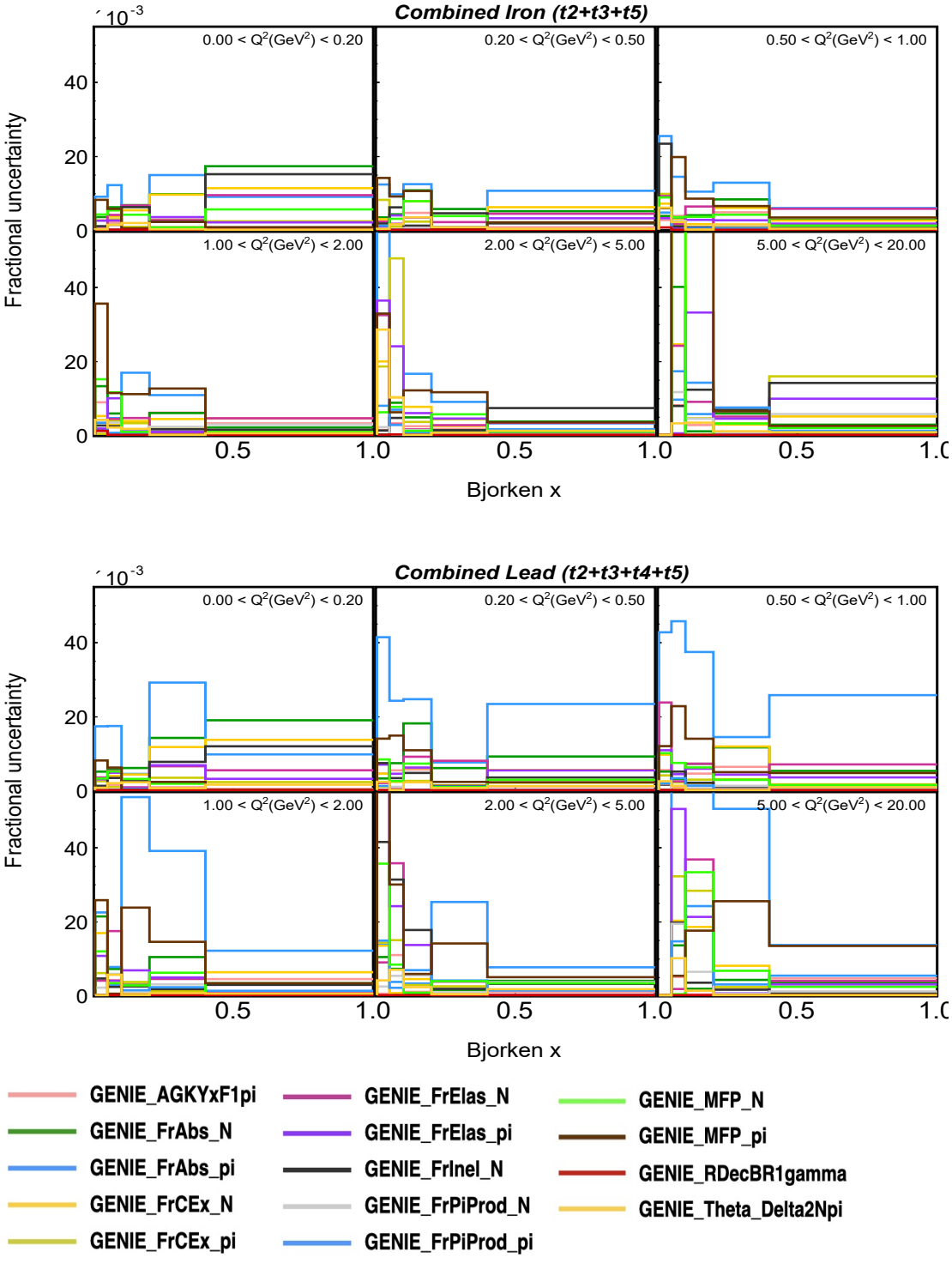

Figure 5.7: Breakdown of the contributions from the various FSI error bands to the extracted cross section in data, as a function of x and Q^2 for combined iron and lead.

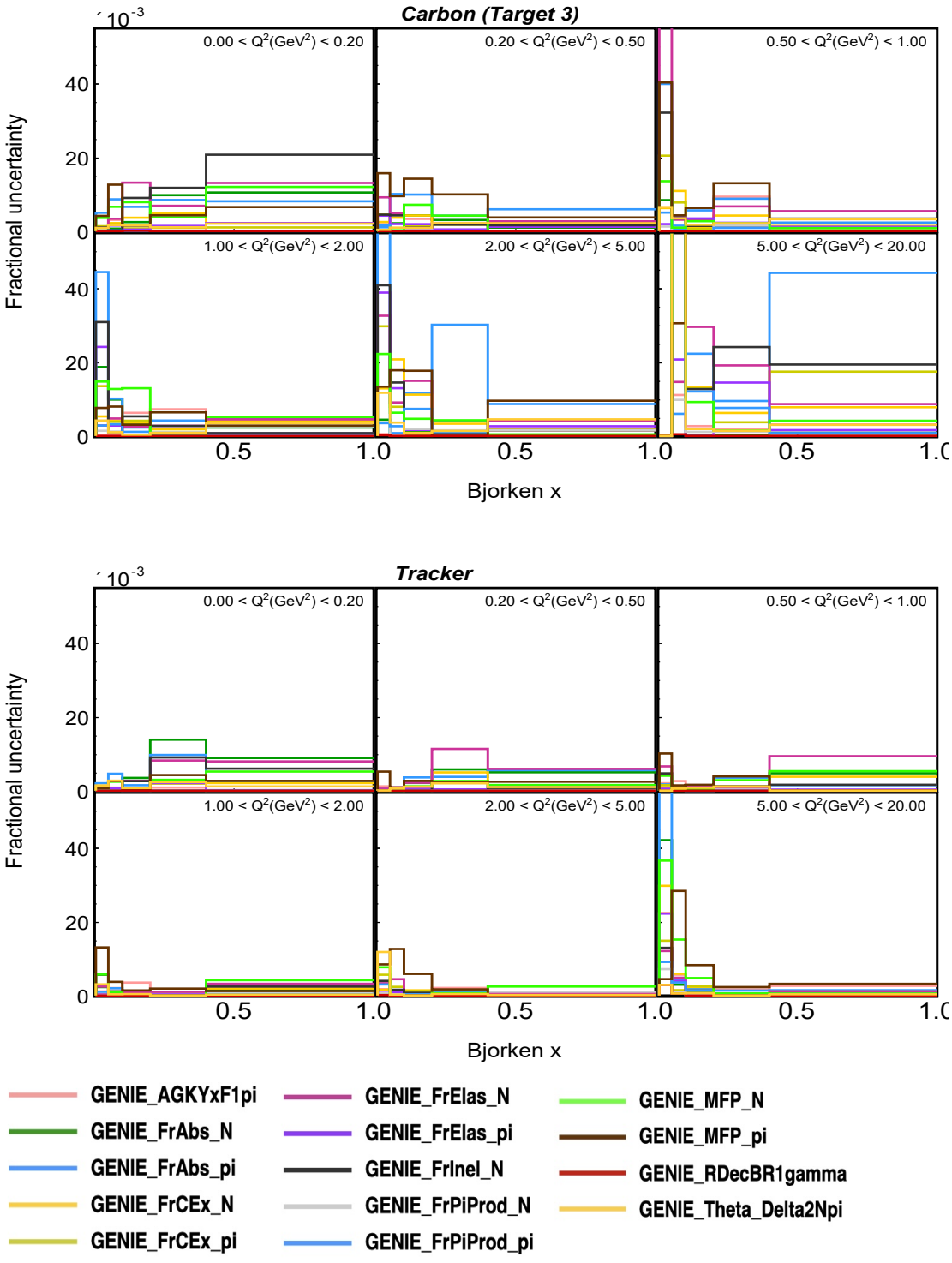

Figure 5.8: Breakdown of the contributions from the various FSI error bands to the extracted cross section in data, as a function of x and Q^2 for carbon and tracker.

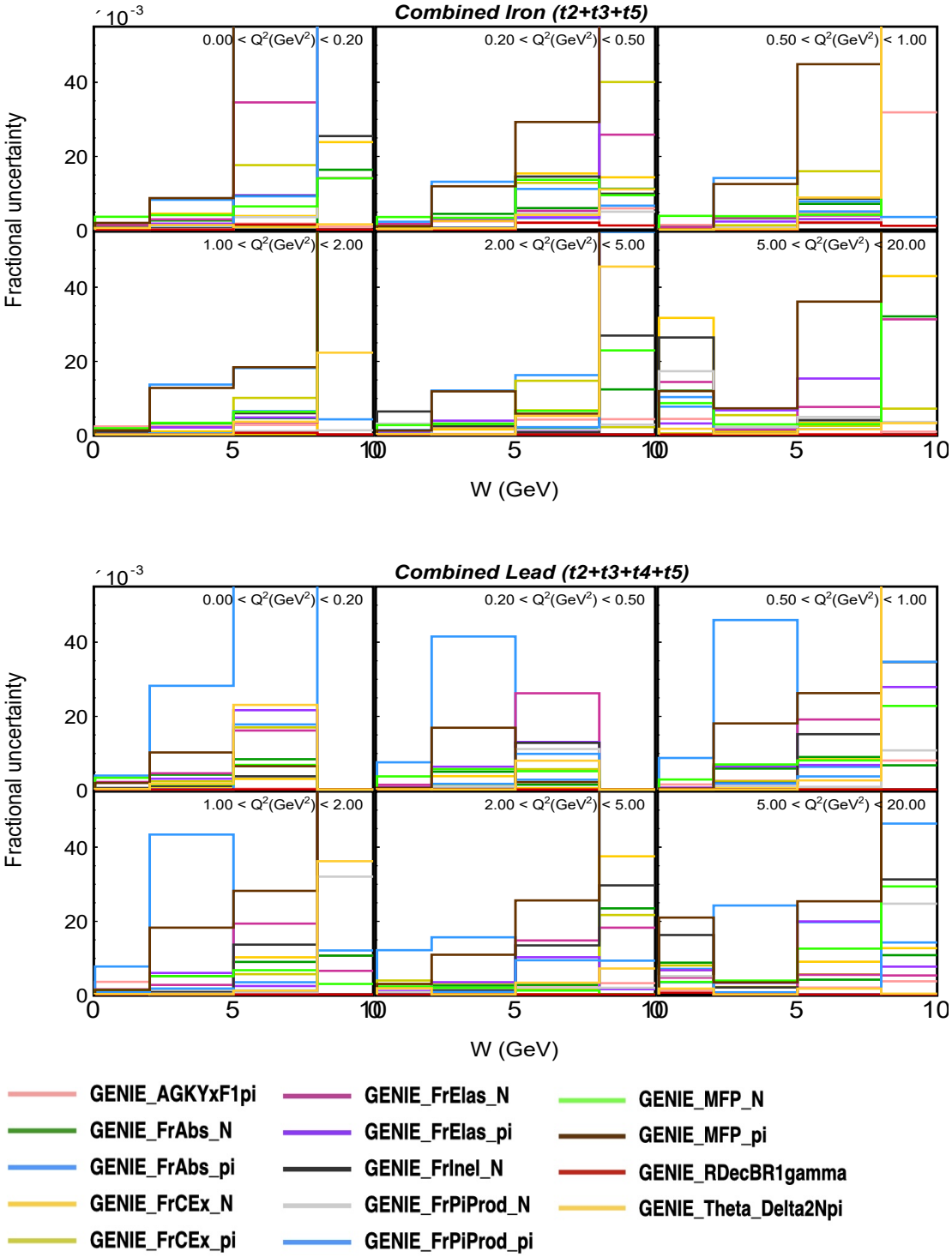

Figure 5.9: Breakdown of the contributions from the various FSI error bands to the extracted cross section in data, as a function of W and Q^2 for combined iron and lead.

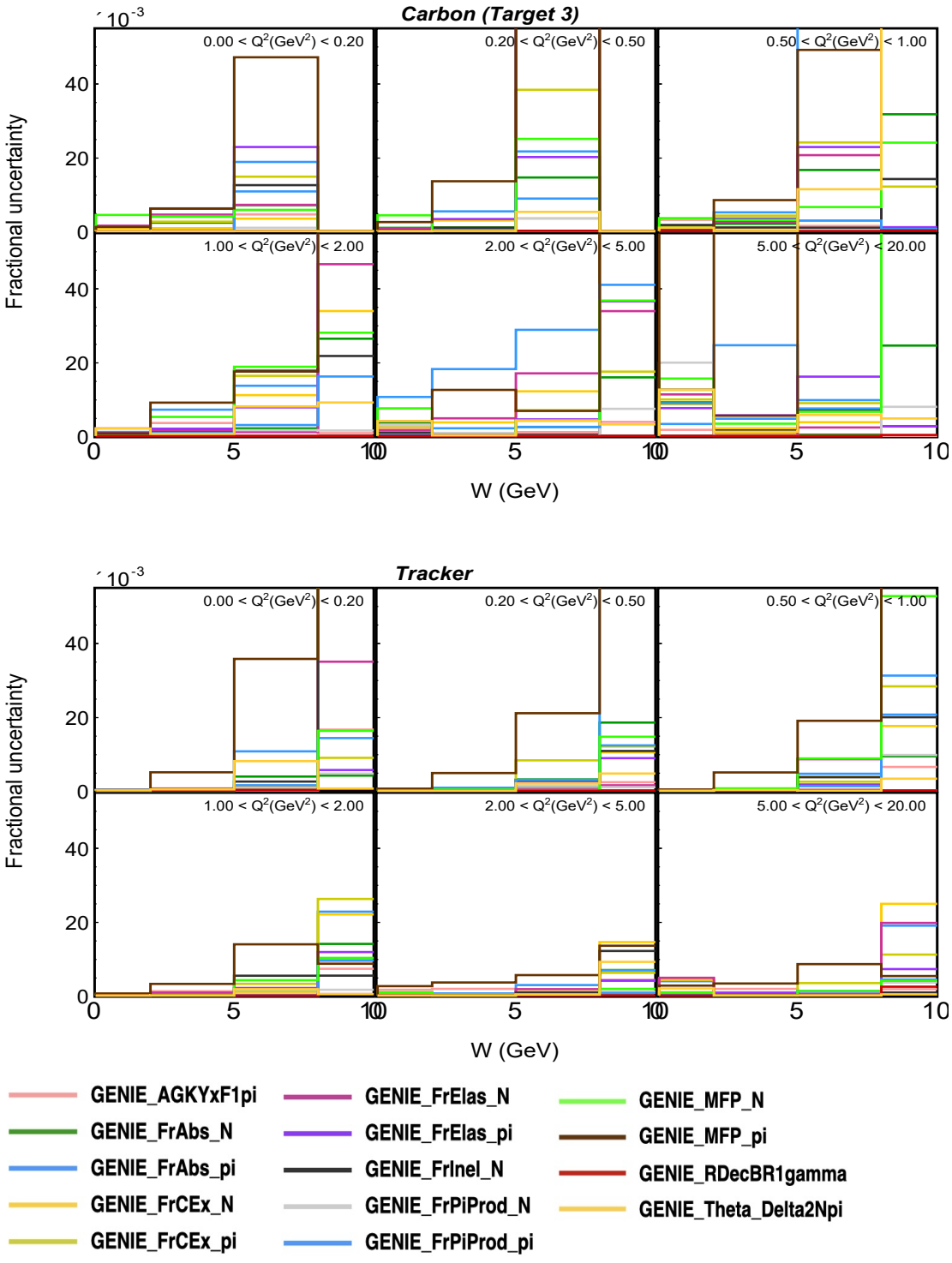

Figure 5.10: Breakdown of the contributions from the various FSI error bands to the extracted cross section in data, as a function of W and Q^2 for carbon and tracker.

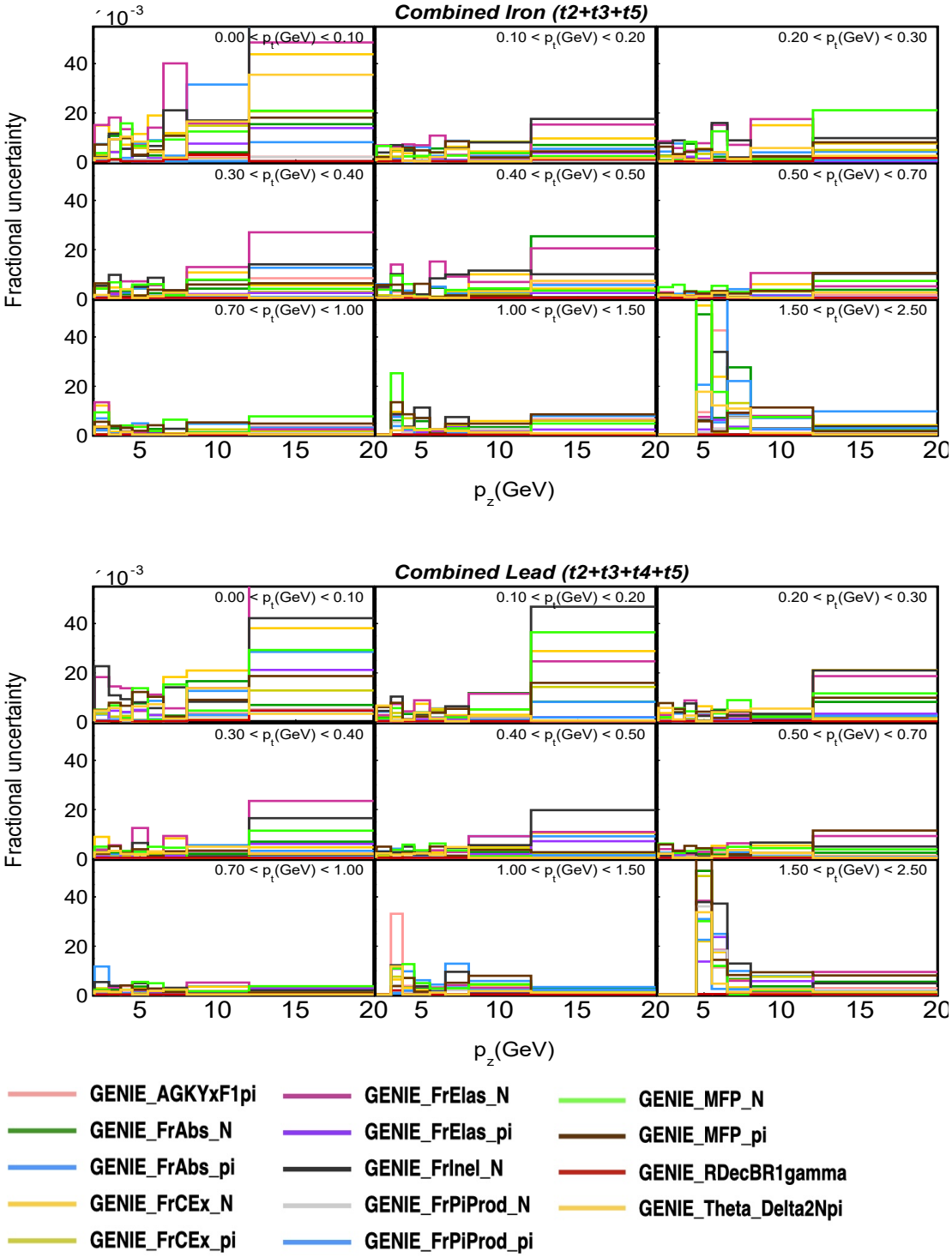

Figure 5.11: Breakdown of the contributions from the various FSI error bands to the extracted cross section in data, as a function of p_z and p_t for combined iron and lead.

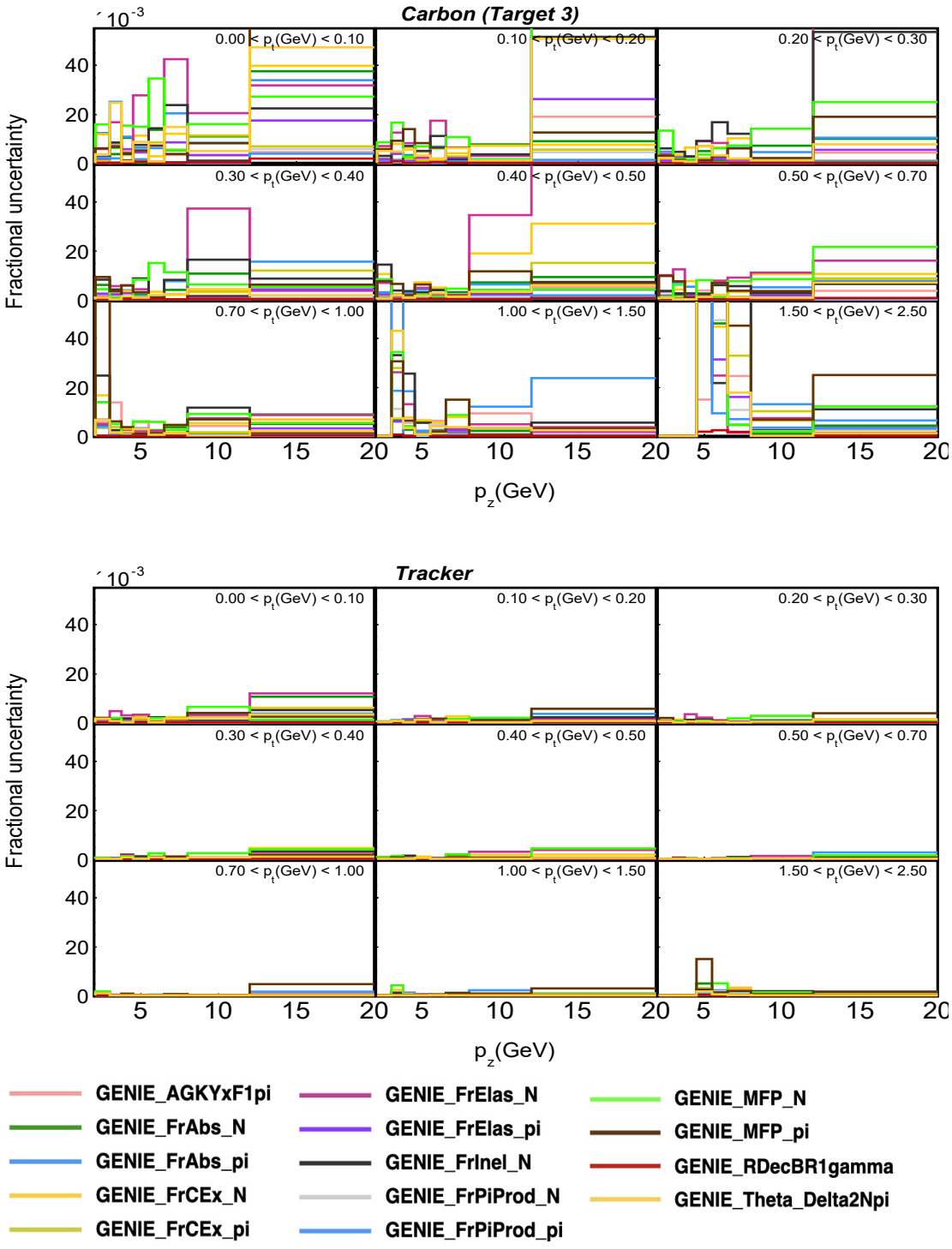

Figure 5.12: Breakdown of the contributions from the various FSI error bands to the extracted cross section in data, as a function of p_z and p_t for carbon and tracker.

5.2 Uncertainties in the (Anti)Neutrino Beam

In Chapter 3 Section 3.1, we discussed how the (anti)neutrino flux is simulated at the MINERvA experiment. To account for the correlation and variations in the various flux parameters, 100 different flux universes were used instead of just two universe method for other systematic uncertainties discussed so far. Various parameters are changed by using Gaussian throws, with a width of 1 σ of the parameter being altered. The event distribution is generated by varying 100 such parameters, creating 100 different universes, where the events have been reweighted with the altered value of the chosen parameter. There are two main sources for the uncertainties in the (anti)neutrino flux: beam focusing and hadron production uncertainties. These have been discussed in detail in the Section 3.1 of Chapter 3.

Apart from the uncertainties associated with flux, neutrino beam angle uncertainties must also be accounted for. The (anti)neutrino beam produced by the NuMI beamline is projected downwards by $\approx$ 50 mrad with respect to the detector coordinate system. This is simply because the NuMI beam serves various experiments at the Fermilab, including the oscillation experiments MINOS and NOvA, which also make use of a far detector to detect (anti)neutrino oscillations. For the (anti)neutrino beam to reach these far detectors, located in Minnesota, this downward direction is required. The uncertainty for the rotation of the beam coordinate system and the detector coordinate system needs to be accounted for and hence shifts of 0.1 mrad in the X coordinate and 0.09 mrad in the Y coordinate are taken, with names given as **BeamAngleX** and **BeamAngleY**. These values were determined using the NC neutrino electron scattering [84].

The error bands contributing to the total uncertainty, along with (anti)muon reconstruction uncertainties, are plotted for various nuclear targets and the tracker region in the $x - Q^2$, $W - Q^2$ and $p_z - p_t$ phase space.

5.3 Uncertainties in Reconstruction of Muon

Since the inclusive analysis depends only on the measurement of the properties of the (anti)muon matched in MINOS, we need to accurately determine the uncertainties associated with measuring the parameters associated with the (anti)muon in the final state. Two universe method is used to account for the uncertainties in the reconstruction of the (anti)muon at MINERvA. The most significant of these uncertainties is the **muon energy scale**. To account for this systematic error, the reconstructed (anti)muon energy is shifted by $\pm\sigma$ to create two universes, creating a lateral error band. An 11 MeV shift in (anti)muon momenta accounts for the uncertainty arising due to the assessment of the detection material composition at MINERvA, with another 30MeV arriving due to the uncertainty in the measurement of the energy deposition rate dE/dx for the tracker region. For the nuclear target region, these numbers are respectively, 17 MeV and 40 MeV. The total uncertainty is calculated by adding these two in quadrature: $\sigma_{\textbf{tracker}} \approx 32$ **MeV** and $\sigma_{\textbf{nuclear target}} \approx 43$ **MeV**. The associated error band is named "**Muon_Energy_MINERvA**" For MINOS, 2% shift accounts for the uncertainty in the measurement of the (anti)muon momentum using the range method, which is added in quadrature to the uncertainty in the curvature measurements: 0.6% for (anti)muons having kinetic energy greater than 1 GeV and 2.5% for (anti)muons with kinetic energy less than 1 GeV. This error band is named "**Muon_Energy_MINOS**". It is important to note that the range uncertainty for the (anti)muon is applied to all the (anti)muons matched in MINOS, while the curvature uncertainty is applied only when the (anti)muon can't be stopped within the MINOS near detector.

Uncertainty in the **muon energy resolution**, arises from the imperfect modeling of smearing between true and reconstructed MC, because of our reconstruction algorithms. This is modeled by applying up and down shifts in two universes, with $\sigma = 0.004(p_\mu^{\text{true}} - p_\mu^{\text{reco}})$. The error band is named "**Muon_Energy_Resolution**".

There is uncertainty in the tracking of (anti)muons in the MINOS ND. As discussed in Section 2.2.3 of Chapter 2, the MINERvA detector experiences a reset period called dead time. During this time, when the detector can not detect a (anti)neutrino event, it is possible that an (anti)neutrino interaction took place. Also, if two or more tracks in the MINOS ND overlap in time, (anti)muon tracks can be misidentified in MINOS. This is not simulated to infinite precision in the MC, but can be a real occurrence when recording data. This uncertainty was studied and found to be dependent on the proton beam batch intensity and measured (anti)muon momentum [139]. This error band has been labeled "**MINOS_Reconstruction_Efficiency**".

Let us now see the contribution of these error bands, associated with the reconstruction of the (anti)muon to the total fractional uncertainty in the double differential cross section extracted in data for the inclusive analysis presented in this thesis. We have also added the systematic uncertainties associated with the beam angle, alongside the (anti)muon reconstruction error bands.

Fig. 5.13 illustrates the contribution of final state interaction (FSI) effect error bands to the fractional uncertainty of the cross section extracted from data, across $x - Q^2$ space, for combined iron and lead targets.

Similarly, Fig. 5.14, displays the fractional uncertainty contributions for carbon and the tracker in $x - Q^2$ bins.

Fig. 5.15 and 5.16 provide insights into the FSI fractional uncertainties within $W - Q^2$ bins, while Fig. 5.17 and 5.18 show these uncertainties in $p_z - p_t$ bins.

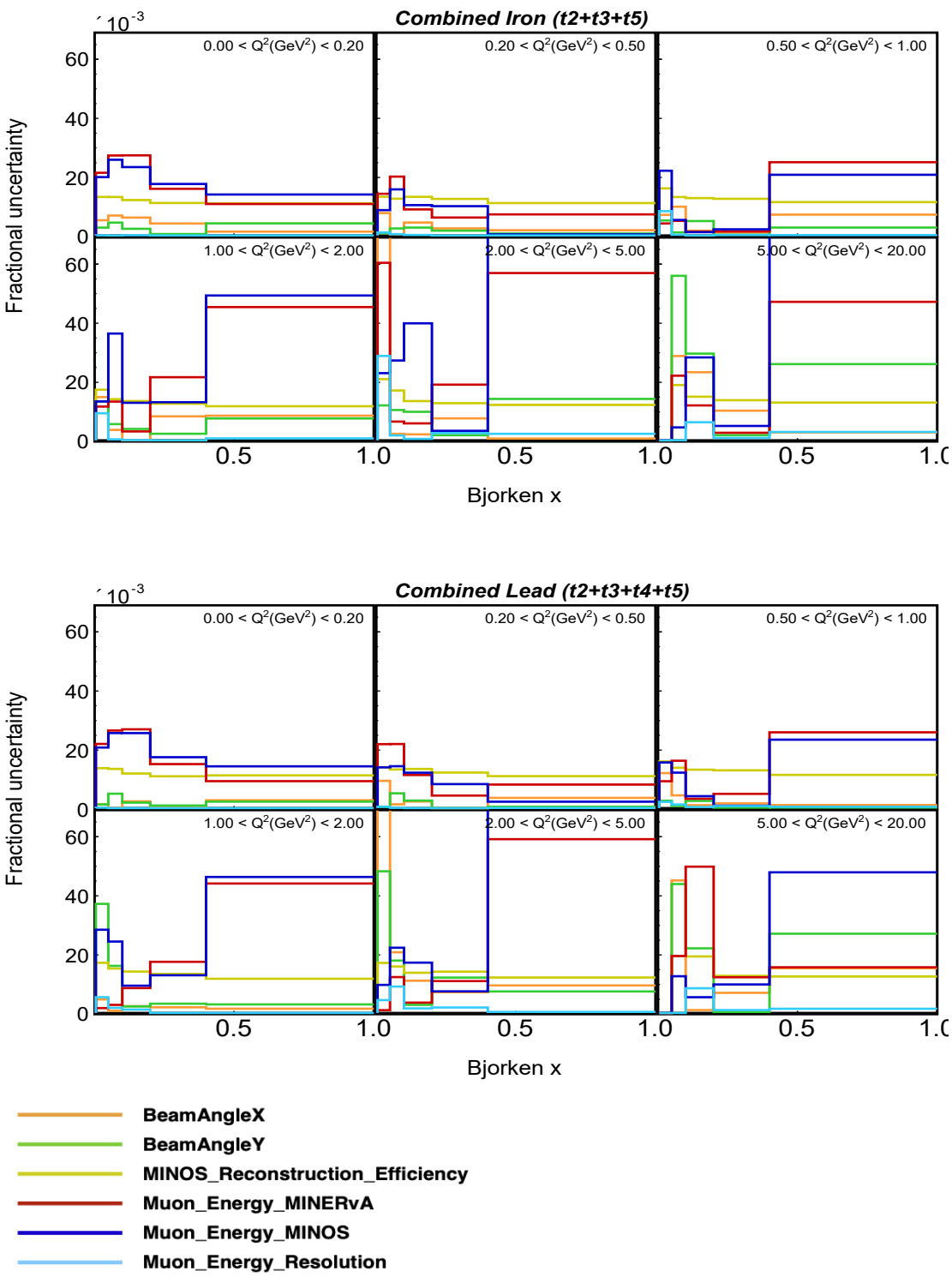

Figure 5.13: Breakdown of the contributions from the antineutrino beam and antimuon reconstruction error bands in the extracted cross section in data, as a function of x and Q^2 for combined iron and lead.

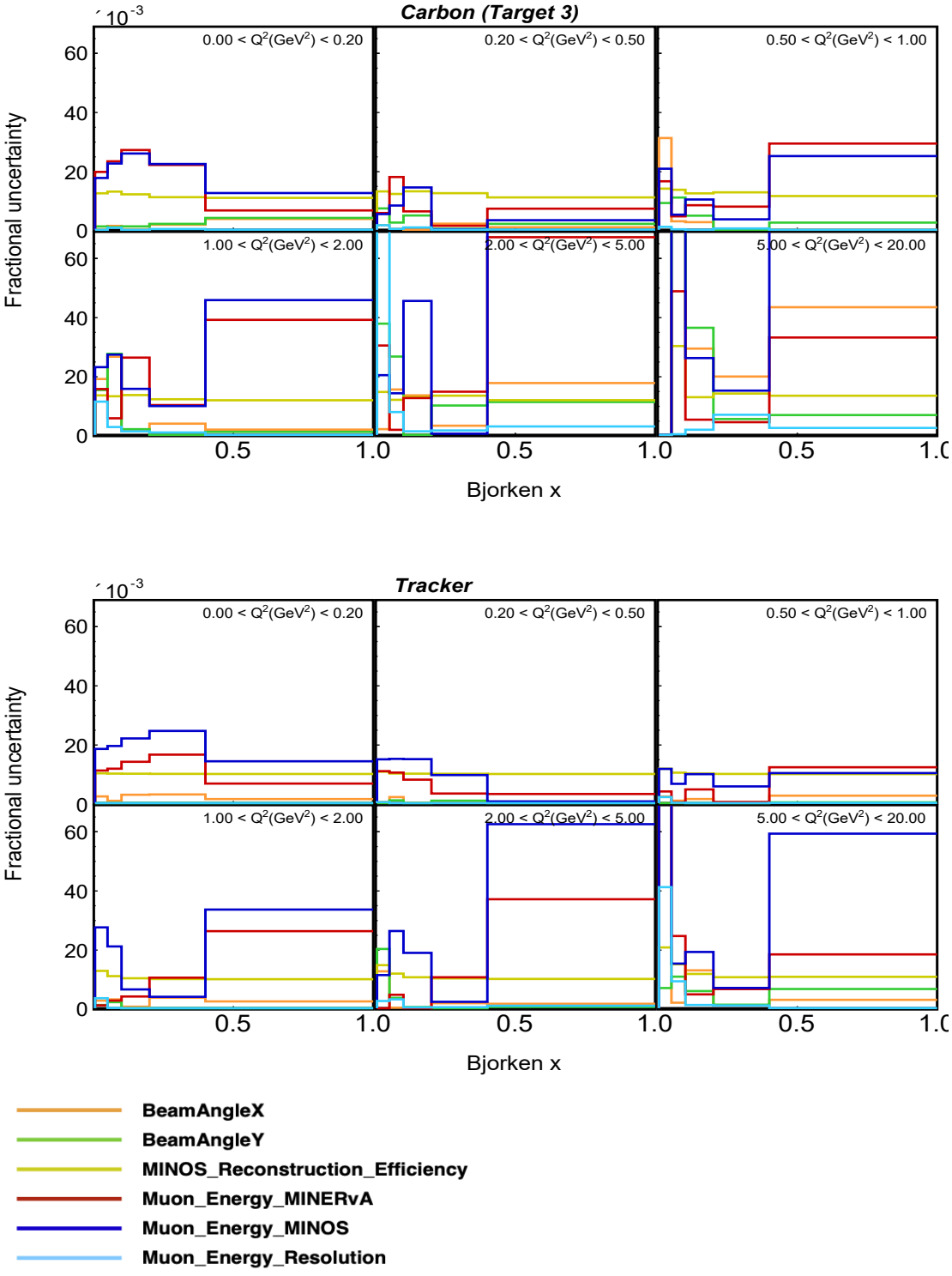

Figure 5.14: Breakdown of the contributions from the antineutrino beam and antimuon reconstruction error bands in the extracted cross section in data, as a function of x and Q^2 for carbon and tracker.

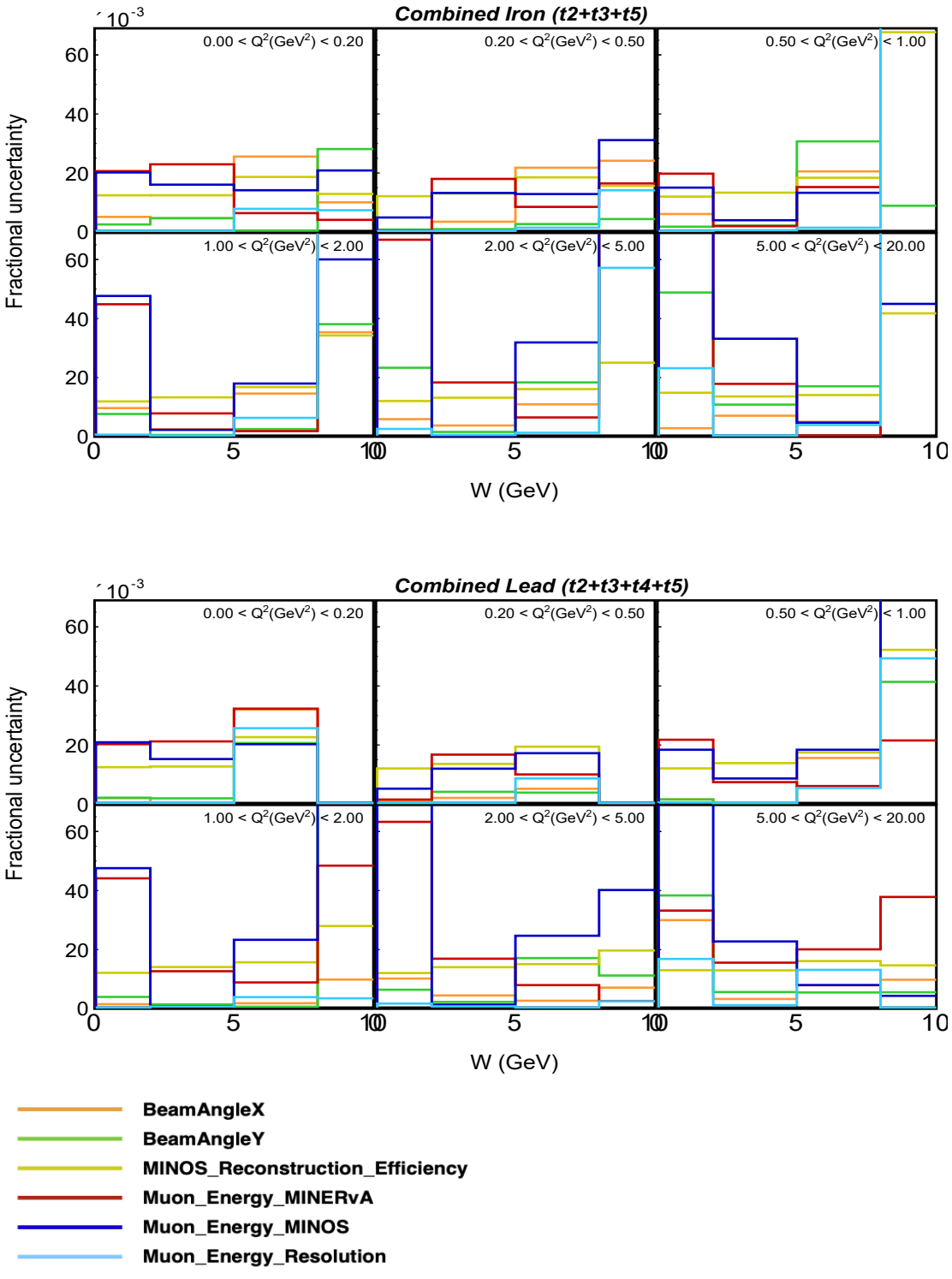

Figure 5.15: Breakdown of the contributions from the antineutrino beam and antimuon reconstruction error bands in extracted cross section in data, as a function of W and Q^2 for combined iron and lead.

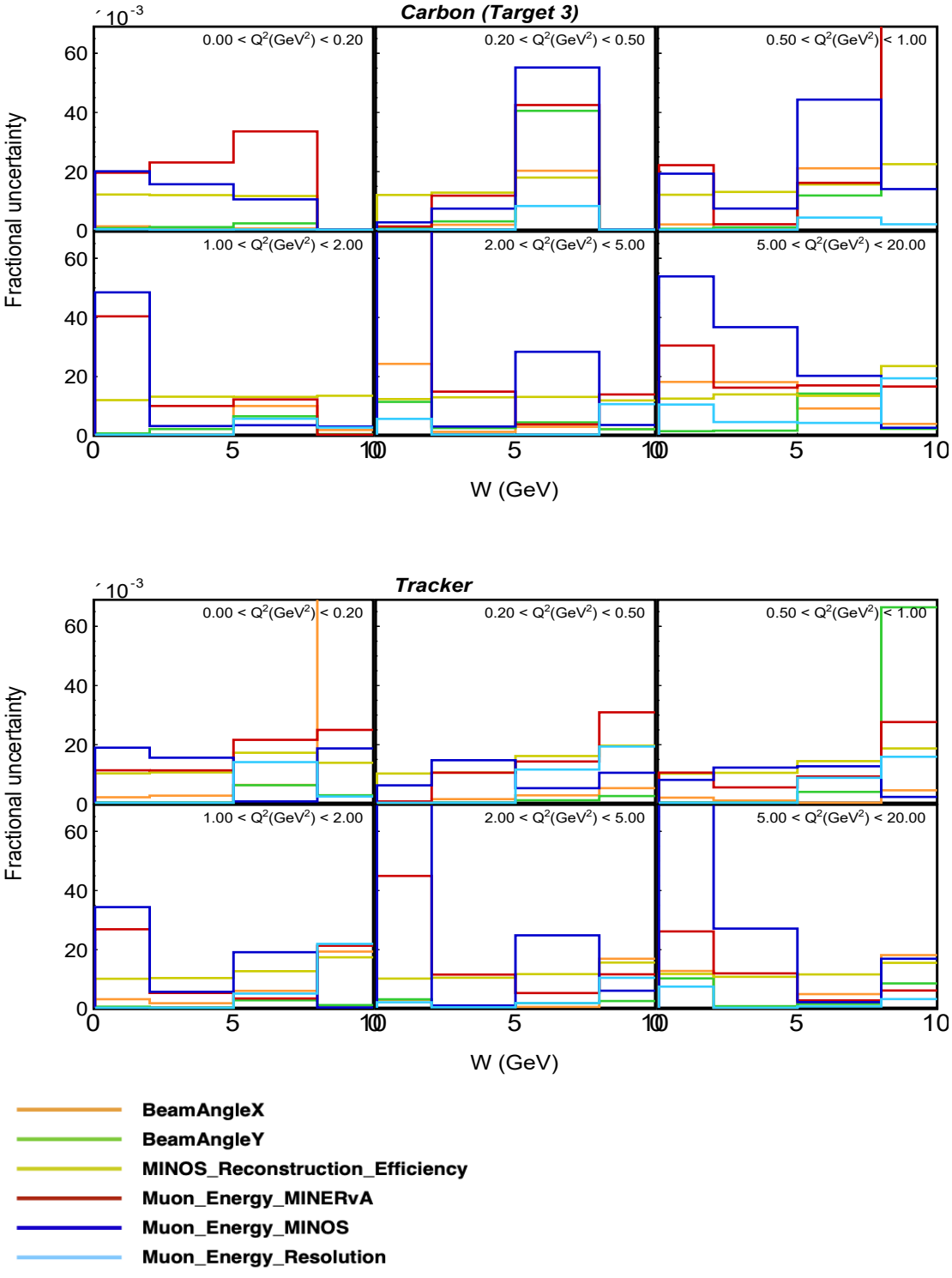

Figure 5.16: Breakdown of the contributions from the antineutrino beam and antimuon reconstruction error bands to extracted cross section in data, as a function of W and Q^2 for carbon and tracker.

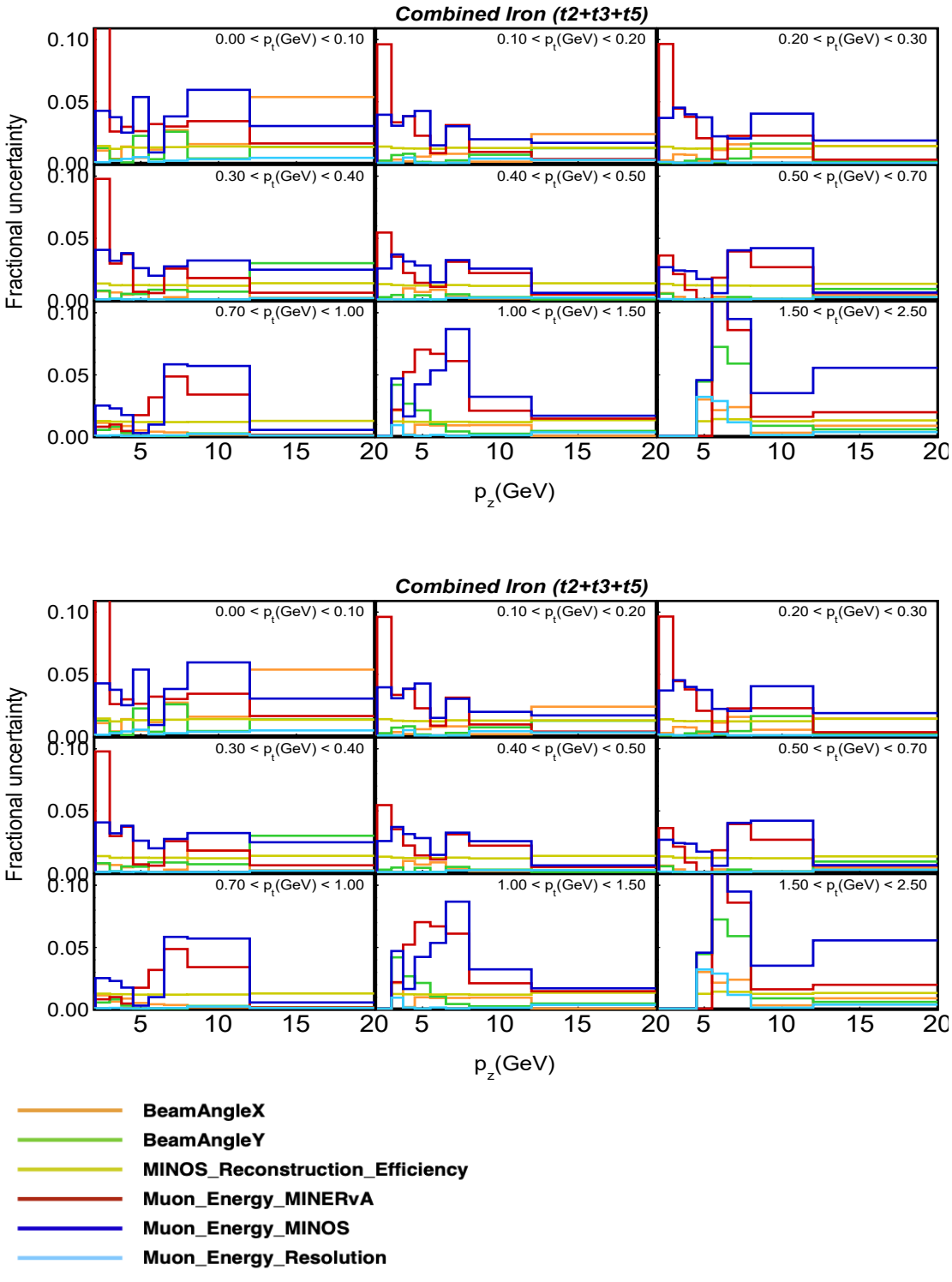

Figure 5.17: Breakdown of the contributions from the antineutrino beam and antimuon reconstruction error bands to extracted cross section in data, as a function of p_z and p_t for combined iron and lead.

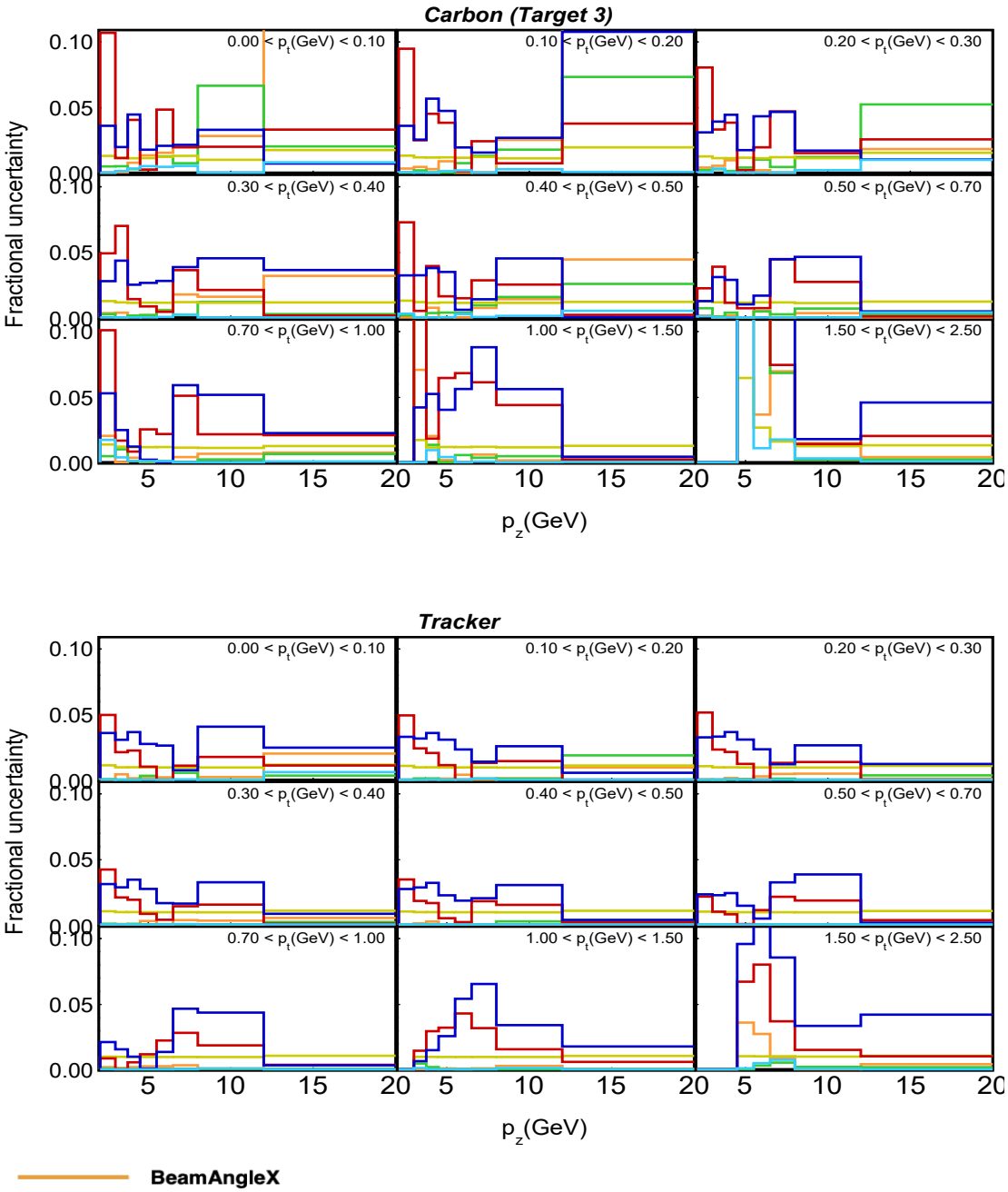

Figure 5.18: Breakdown of the contributions from the antineutrino beam and antimuon reconstruction error bands to extracted cross section in data, as a function of p_z and p_t for carbon and tracker.

5.4 Target Mass Uncertainties

The scintillator strips that make up the MINERvA detector, are glued together using epoxy glue. Also, the strips are coated with a reflective material. This has been discussed in Section 2.2.1. The mass of the glue and the reflective coating contributes to the total mass of the detector, known to a precision of ±1.4%. There is also uncertainty associated with the different nuclear target masses, listed in Table5.3. The details of mass uncertainties are documented in Ref. [140].

Target	Uncertainty in mass
CH	± 1.4 %
C	± 0.5 %
Fe	± 1 %
Pb	± 0.5 %

Table 5.3: Target mass uncertainties for different materials in the MINERvA detector

This sums up the systematic uncertainties used in the analysis presented in this dissertation. There is also an additional statistical uncertainty factor, which is implemented during the unfolding procedure of the analysis, to account for the finite MC statistics. This uncertainty has been discussed alongside the unfolding procedure in Chapter 4.

Chapter 6

Results and Conclusion

An experiment is a question which science poses to Nature and a measurement is the recording of Nature's answer [141].

— **Max Planck**
(Nobel Prize in Physics, 1918)

Chapter 4 detailed the various steps involved in the analysis presented in this thesis, to extract the inclusive double differential antineutrino charged current interaction cross section at the MINERvA experiment. The cross section results were obtained for different materials in the nuclear target region, specifically carbon, iron, and lead. As previously noted, for iron and lead, the materials from all nuclear targets were combined, except target 1 due to significant rock muon contamination in this target, particularly in the inclusive analysis presented in this thesis. Additionally, the cross section was extracted for the tracker scintillator region. Following the extraction of these cross sections, ratios of the cross sections in the nuclear target regions (carbon, iron, and lead) to those in the tracker region were calculated. Systematic uncertainties associated with all the measured cross sections were also evaluated.

In this chapter, we present and discuss these results.

6.1 Cross Section in bjorken x and Q^2

Fig. 6.1, 6.2, 6.3 and 6.4 show the results for the extracted double differential cross section for carbon, iron, lead and tracker, respectively, along with the cross section data to MC ratios. Looking at the distribution across bjorken x and Q^2 is particularly useful. Bjorken x is crucial for understanding how the structure of nucleons is altered when they are bound inside a nucleus, as compared to a free nucleon. The nuclear modification effects are associated with deep inelastic scattering, and we have significant contributions from DIS events in the presented inclusive analysis. It must be noted that for $x - Q^2$ cross section results, the upper left panels have the most number of events, which decrease consistently as we move into higher Q^2 bins. For example for iron, the first Q^2 bin has $\sim$ 40,000 events, followed by approximately 35000, 24000, 12000, 3400, and 500 events in the next Q^2 bins, respectively. The multiplier numbers on the plots reflect this. If we look at these cross section results, in the lowest Q^2 bin of 0.0-0.2 GeV^2 (leftmost upper panel), for the low values of bjorken x (< 0.1), we observe the cross section getting suppressed in comparison to MC, as we move to heavier targets, such that for lead the suppression is most pronounced, followed by iron and least for carbon. Fig. 6.5 and 6.6 show the double differential cross section ratios for carbon-, iron-, and lead- to the tracker scintillator. As seen from these figures for cross section ratios with tracker scintillator, the effect of the nuclear medium is evident. In the lowest x region ($x < 0.1$), the cross section is suppressed by the most amount in the heaviest target lead, followed by iron, as indicated by the red data points. This observation of a depleting cross section in the low x region can be attributed to the shadowing effect, a quantum mechanical phenomenon, that occurs due to destructive interference of the scattering amplitudes of partons (nucleons). The destructive interference leads to the suppression in the cross section, such that the overall scattering probability is less than the sum of the scattering probabilities from individual, non-interacting nucleons.

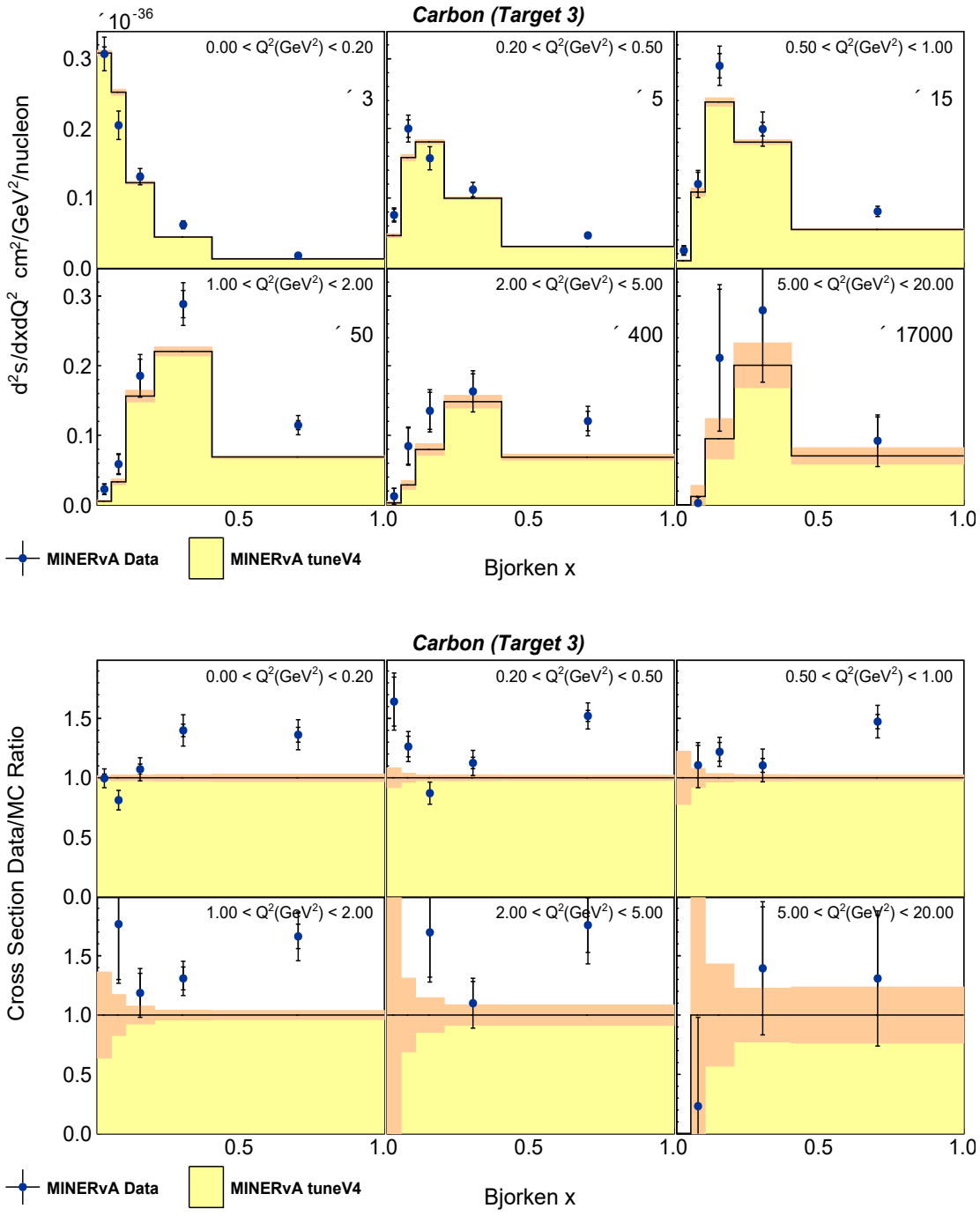

Figure 6.1: Top: The plot shows the cross section in bins of bjorken x for carbon, with panels for different Q^2 bins. The yellow histogram represents the cross section from MC simulations, with orange bands for statistical uncertainties. The blue points indicate the extracted cross section from data, with inner black error bars for statistical uncertainties and outer bars for total uncertainties (statistical plus systematic). The y-axis displays the double differential cross section. **Bottom:** Ratio of data to simulation cross section.

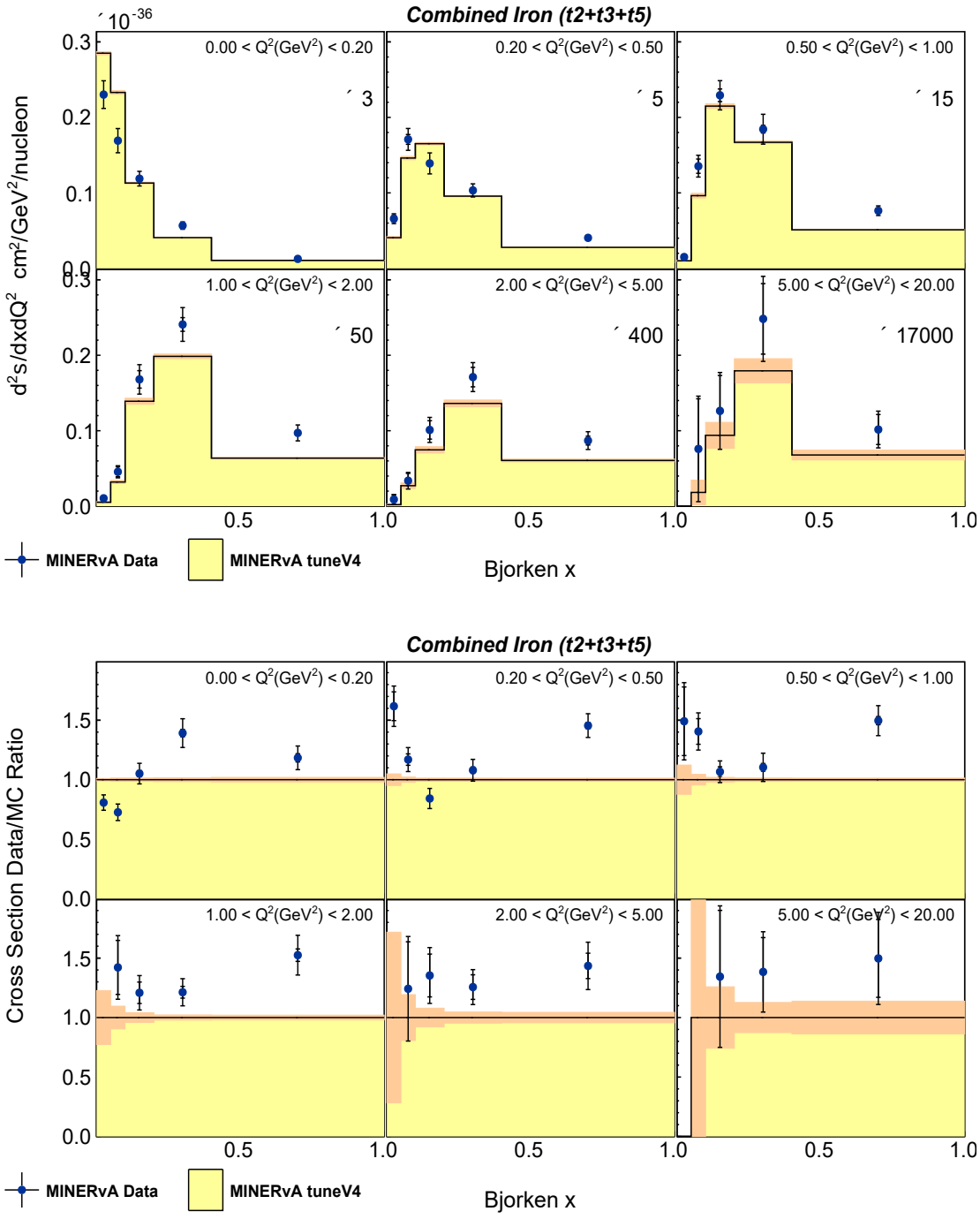

Figure 6.2: Top: The plot shows the cross section in bins of bjorken x for iron, with panels for different Q^2 bins. The yellow histogram represents the cross section from MC simulations, with orange bands for statistical uncertainties. The blue points indicate the extracted cross section from data, with inner black error bars for statistical uncertainties and outer bars for total uncertainties (statistical plus systematic). The y-axis displays the double differential cross section. **Bottom:** Ratio of data to simulation cross section.

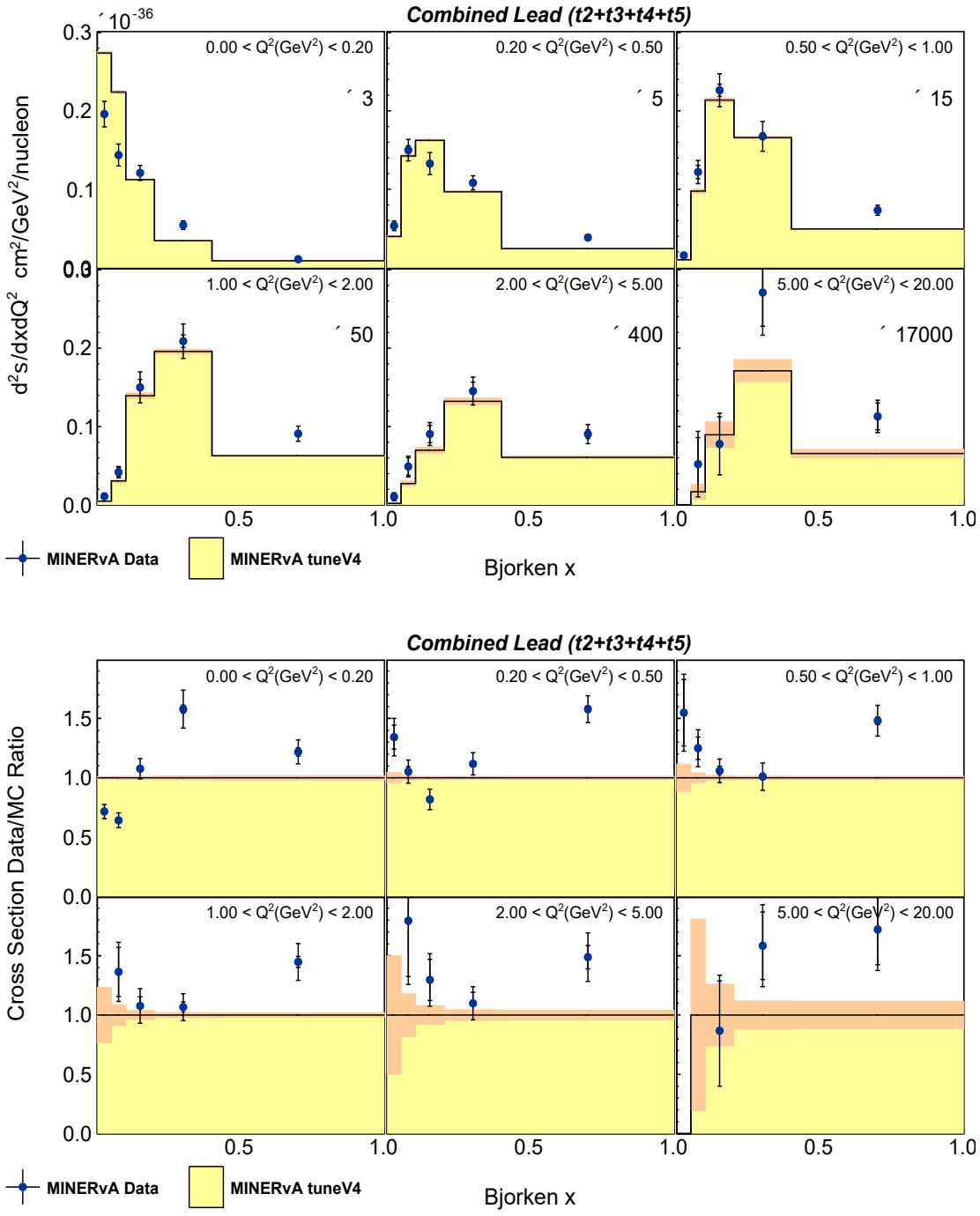

Figure 6.3: Top: The plot shows the cross section in bins of bjorken x for lead, with panels for different Q^2 bins. The yellow histogram represents the cross section from MC simulations, with orange bands indicating statistical uncertainties. The blue points depict the extracted cross section from data, with inner black error bars for statistical uncertainties and outer bars for total uncertainties (statistical plus systematic). The y-axis displays the double differential cross section. **Bottom:** Ratio of data to simulation cross section.

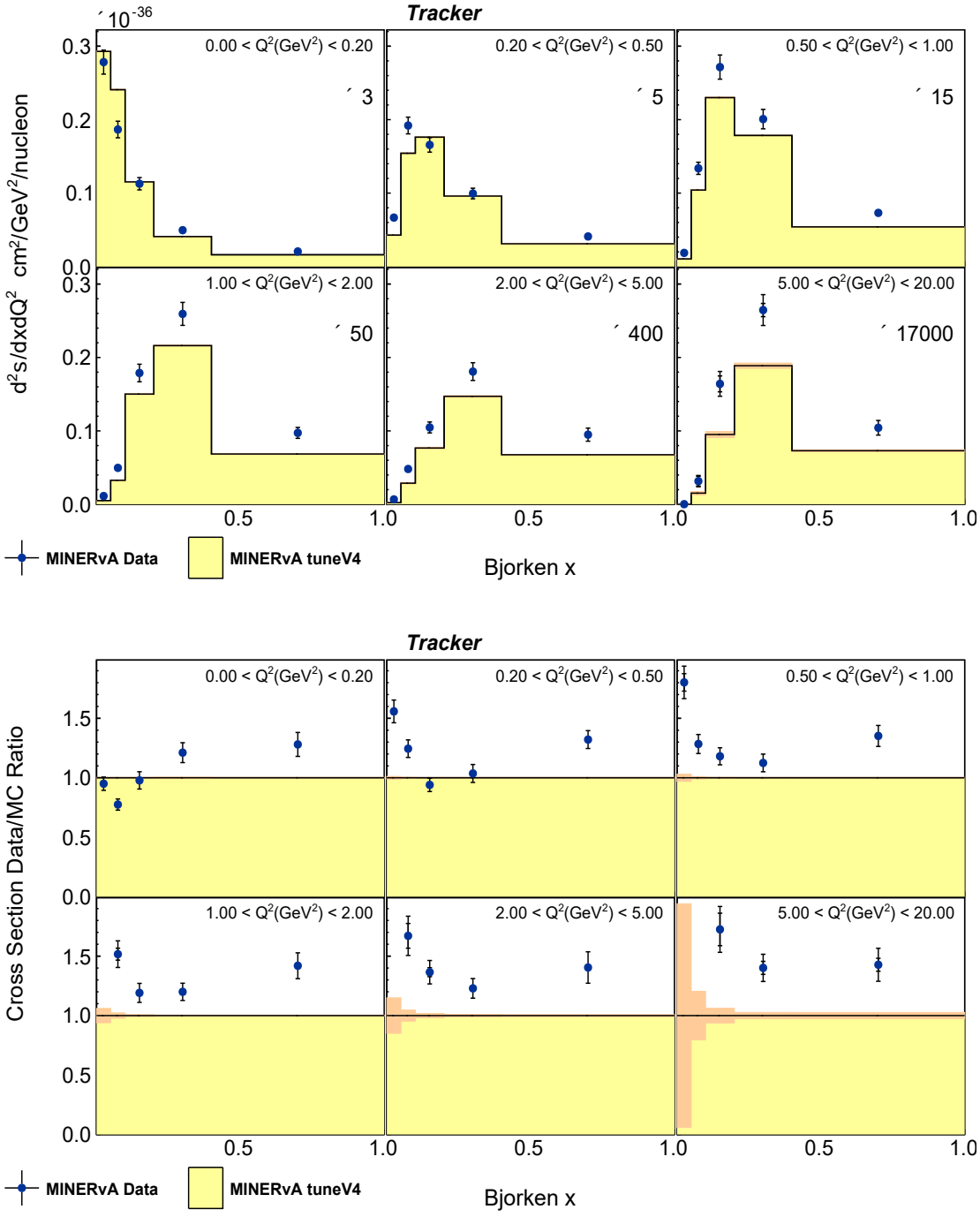

Figure 6.4: Top: The plot shows the cross section in bins of bjorken x for the tracker scintillator, with panels for different Q^2 bins. The yellow histogram represents the cross section from MC simulations, with orange bands indicating statistical uncertainties. The blue points depict the extracted cross section from data, with inner black error bars for statistical uncertainties and outer bars for total uncertainties (statistical plus systematic). The y-axis displays the double differential cross section. **Bottom:** Ratio of data to simulation cross section.

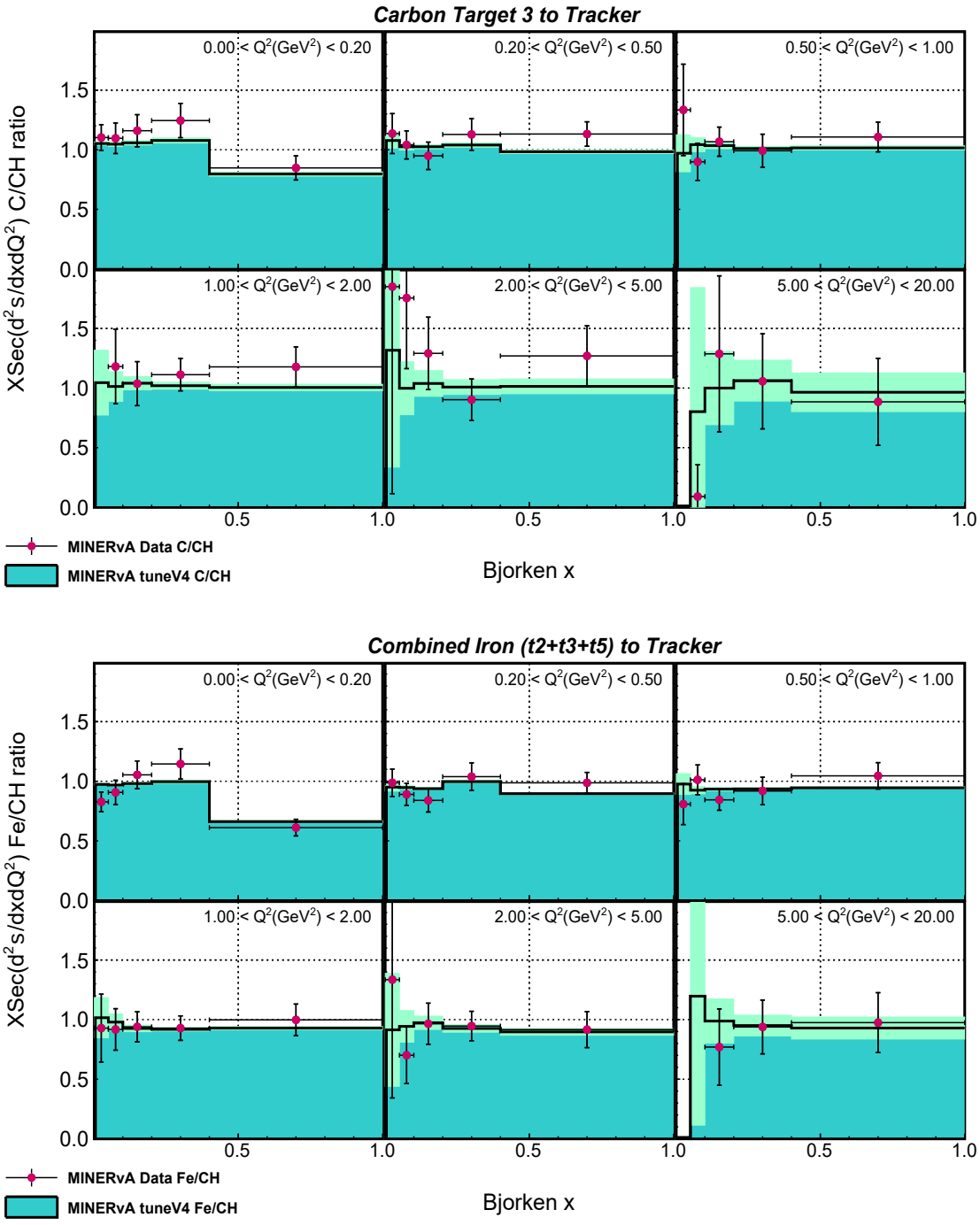

Figure 6.5: The plots display cross section ratios in bins of bjorken x for carbon to scintillator **(top)** and iron to scintillator **(bottom)**, with panels for different Q^2 bins. The green histogram represents the MC-extracted cross section ratio, with light green bands indicating statistical uncertainties. The red points show the extracted data ratio, with inner black error bars for statistical uncertainties and outer bars for total uncertainties (statistical plus systematic). The y-axis represents the double differential cross section ratio.

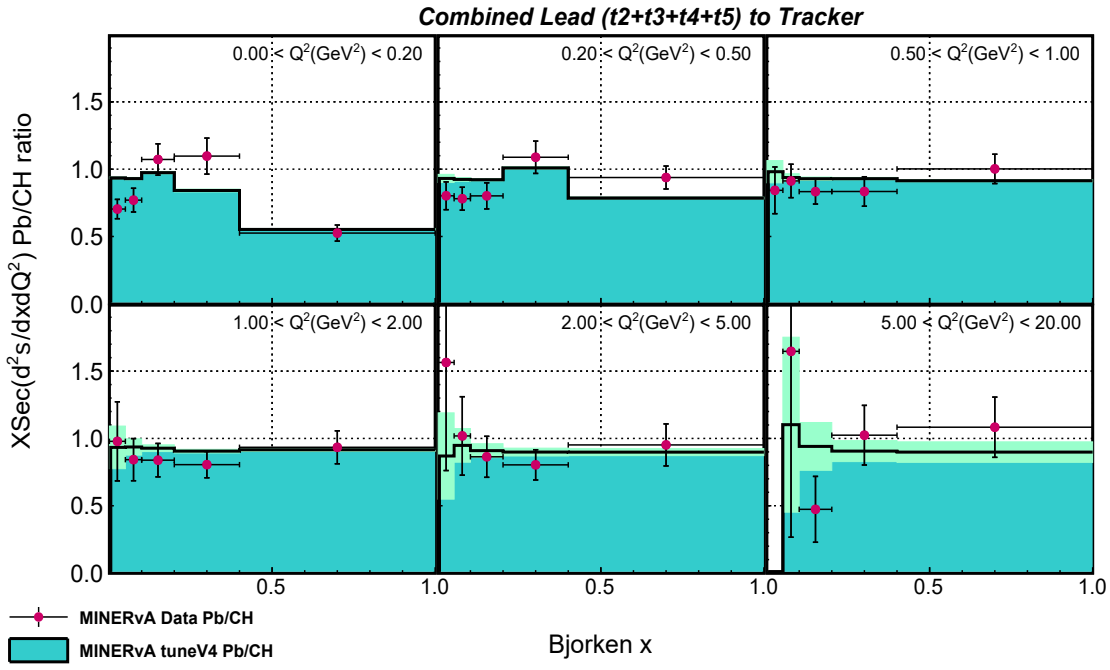

Figure 6.6: The plots show cross section ratios in bins of bjorken x for lead to scintillator, with panels for different Q^2 bins. The green histogram represents the MC-extracted cross section ratio, with light green bands indicating statistical uncertainties. The red points display the data ratio, with inner black error bars for statistical uncertainties and outer bars for total uncertainties (statistical plus systematic). The y-axis represents the double differential cross section ratio.

This effect was first observed by the EMC (European Muon Collaboration) [142]. However, for the inclusive analysis, this prediction is more complex as we also have to consider final state interaction effects along with the medium effects. As seen from the cross section ratios, for the high bjorken x region (x between 0.4 - 1.0), in the highest statistics bin of lowest Q^2 (between 0 and 0.2, and 0.2 - 0.5 GeV^2), the model predictions lower probability of interactions, most so, for lead, followed by iron and carbon. If we look at the bottom panels for Q^2 greater than 1 GeV^2, the MC prediction and data are very much in line for iron, compared to carbon and lead. This is because the shadowing correction in the underlying model is based on iron data and the same corrections have been applied for carbon and lead [136].

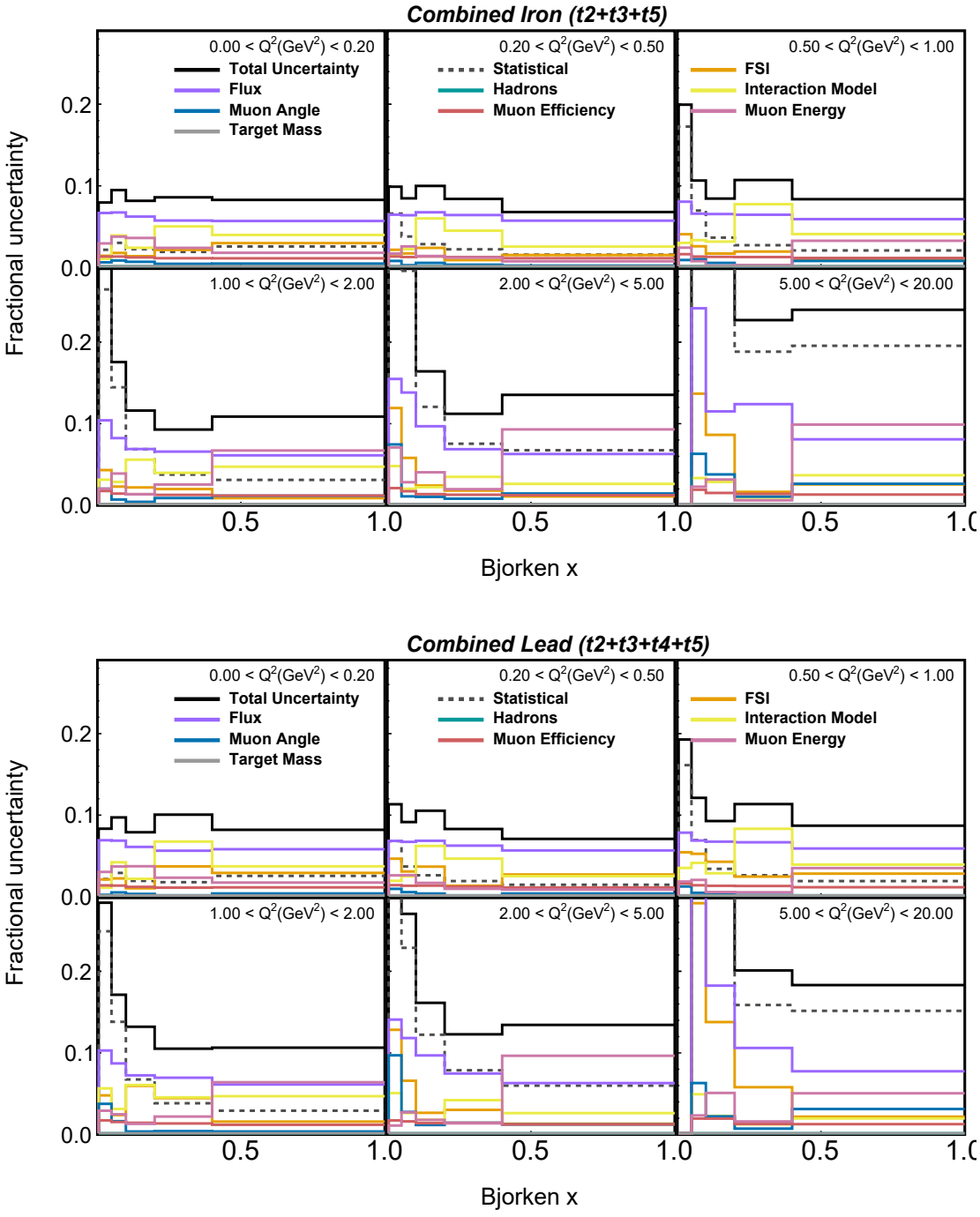

Figure 6.7: Fractional uncertainties for the data cross section in bins of bjorken x, segmented into different panels corresponding to bins of Q^2, for iron **(top)** and lead **(bottom)**.

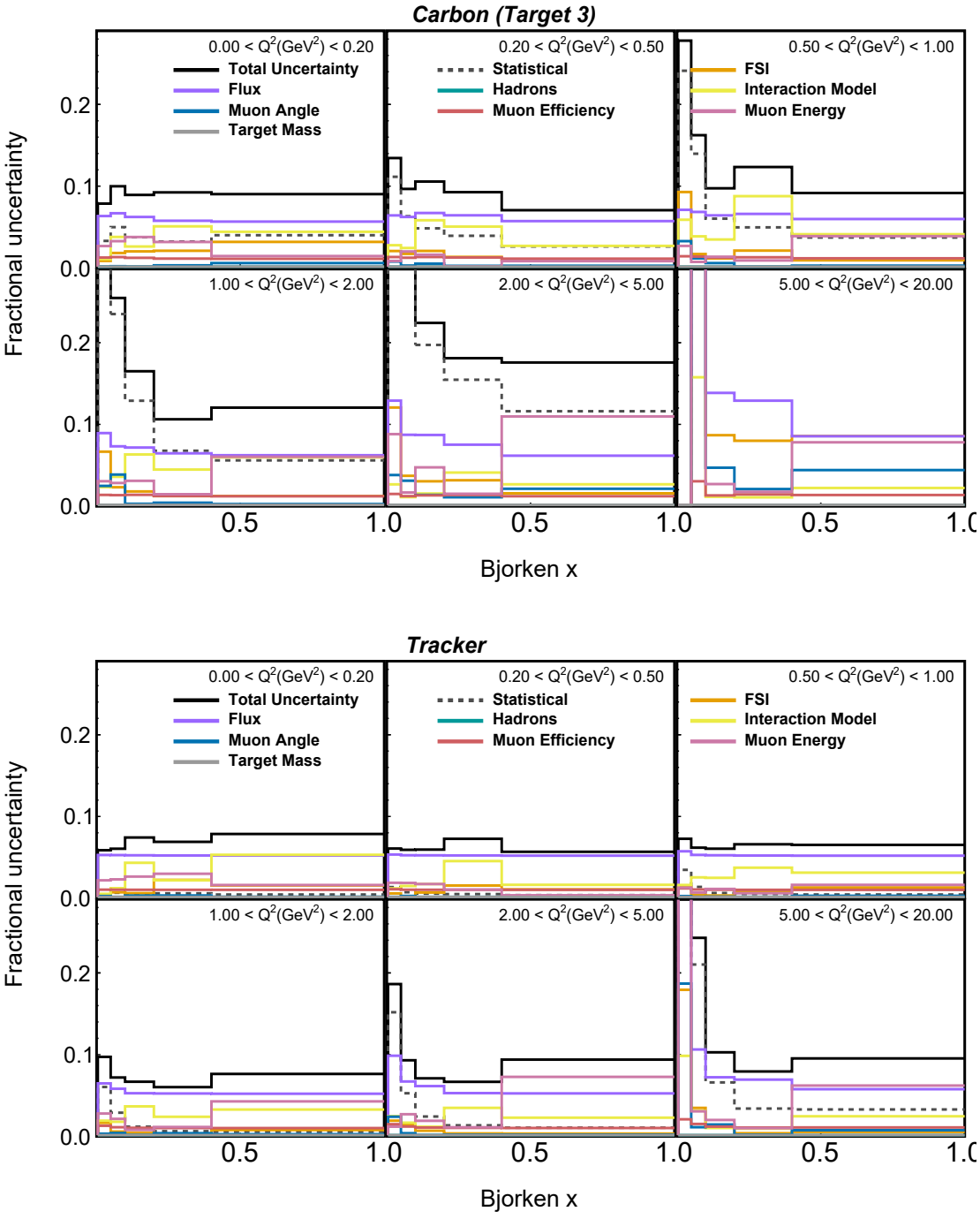

Figure 6.8: Fractional uncertainties for the data cross section in bins of bjorken x, segmented into different panels corresponding to bins of Q^2, for carbon **(top)** and tracker scintillator **(bottom)**.

Fig. 6.7 and 6.8 show the fractional uncertainties associated with iron, lead,

carbon, and tracker scintillator cross sections, respectively. We see that all the cross section results are dominated by the flux uncertainty. Uncertainties associated with the interaction model have a large contribution, particularly in the region of $Q^2 < 1$ GeV^2. Antimuon reconstruction uncertainties take over, once we go beyond the $Q^2 > 1$ GeV^2, at high values of x. Total uncertainties increase in the $Q^2 > 1$ GeV^2 region because of high statistical uncertainties in this region, particularly for low values of bjorken x.

Fig. 6.9 and 6.10 display the fractional uncertainties associated with the cross section ratios.

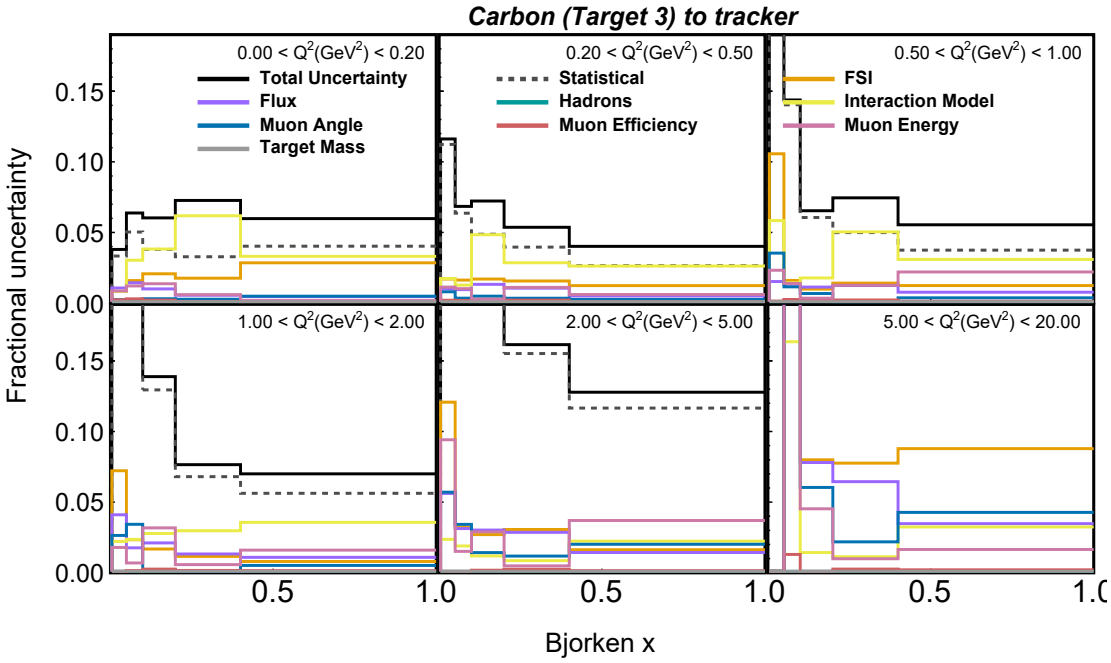

Figure 6.9: Fractional uncertainties for the cross section ratio in data in bins of bjorken x, segmented into different panels corresponding to bins of Q^2, for carbon to scintillator ratio.

We notice that the flux uncertainties cancel out in the ratios, with an overall increase in the statistical uncertainties (because the tracker has much higher statistics), particularly in the high Q^2 and low bjorken x region. Interaction model

uncertainties are the most dominant in the cross section ratios, with uncertainties associated with "MaRES" being the largest.

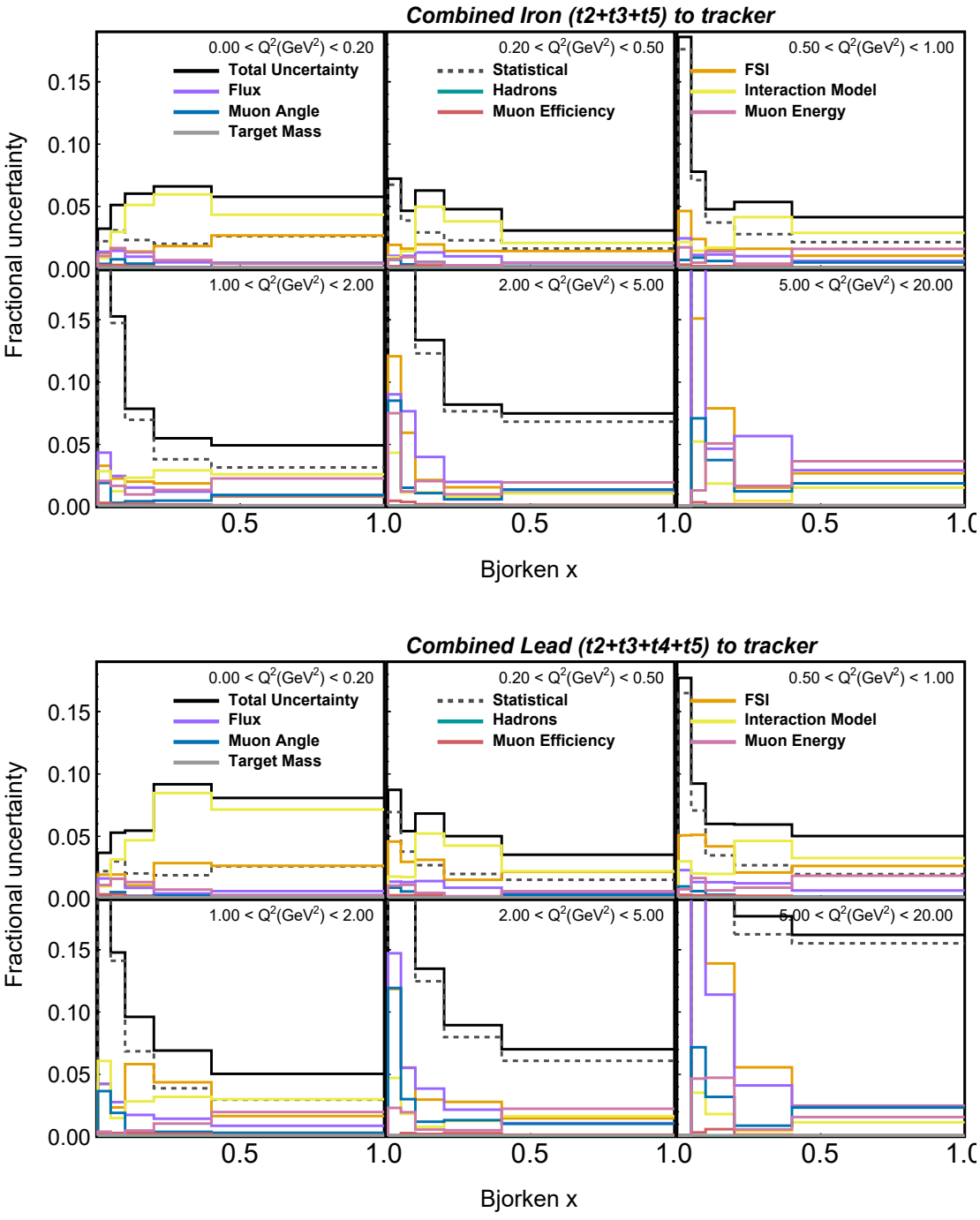

Figure 6.10: Fractional uncertainties for the cross section ratio in data in bins of bjorken x, segmented into different panels corresponding to bins of Q^2, for (**top**) iron to scintillator and (**bottom**) lead to scintillator ratio.

6.2 Cross Section in Antimuon $p_t - p_z$

Fig. 6.11, 6.13, 6.15 and 6.17 depict double differential cross section measurement in bins of antimuon momenta p_z and p_t, along with the ratio between the measured (data) and simulation predicted (MC) cross sections. For a different perspective, these antimuon momentum variables have been swapped for the results presented in Fig. 6.12, 6.14, 6.16 and 6.18. For results in Fig. 6.11, 6.13, 6.15 and 6.17, moving from the first p_t bin (top left panel) to the last bin in p_t (bottom right panel), the bin contents are reflected in the multiplier numbers. We observe the simulation overprediction of data for cross section throughout, in the lowest p_t bins, for all the targets. Then, there is good agreement in the simulation prediction and measured data in the low-intermediate p_t region of $0.2 < p_t < 0.5$ GeV. After this, the excess in data increases in the high p_t bins.

From Fig. 6.12, 6.14, 6.16 and 6.18, we observe a similar shape behaviour for all the nuclear targets (and scintillator), reflected in the more flat ratios. At low values of p_t, the model overpredicts the observed data, while an underprediction of data is consistently observed at higher values of p_t. The region in p_t from 0.2-0.5 GeV is where the data and mc have reasonable agreement.

The nuclear dependence in the measured inclusive cross section is reflected in the Fig. 6.12, 6.14, 6.16, at low values of p_t, the simulation underpredicts the data for the lighter nucleus, carbon, but shifts to a significant overprediction as the nuclei become heavier, such as for iron and lead, with lead being the heaviest. This is the first time such a result has been observed in an antineutrino dataset at medium energy, using multiple types of nuclei.

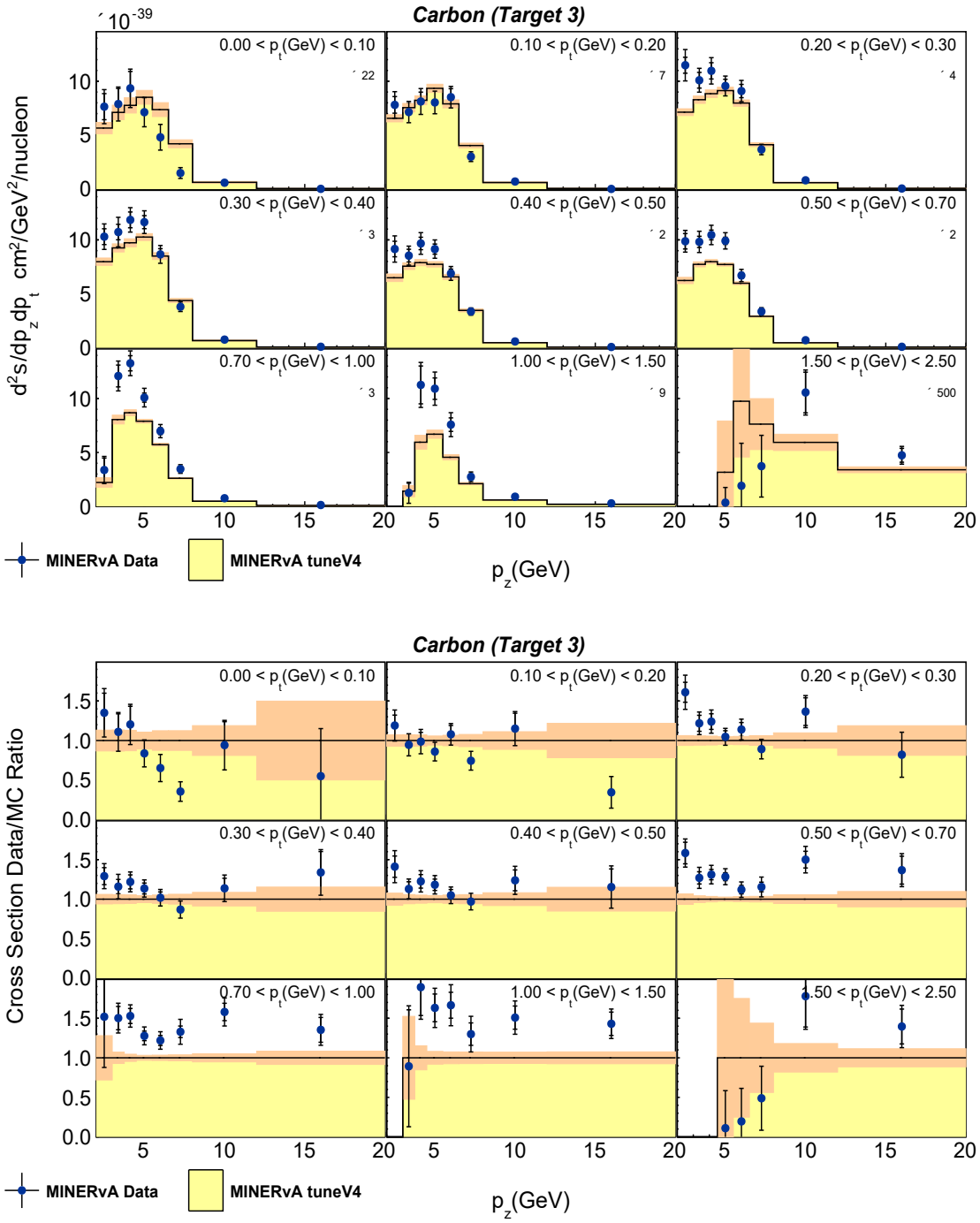

Figure 6.11: Top: The plot shows the cross section in bins of antimuon longitudinal momentum p_z, with panels for different transverse momentum p_t bins for carbon. The yellow histogram represents the MC cross section with orange bands for statistical uncertainties. Blue points indicate the data cross section, with inner black error bars for statistical uncertainties and outer bars for total uncertainties. The y-axis displays the double differential cross section. **Bottom:** Data-to-simulation cross section ratio.

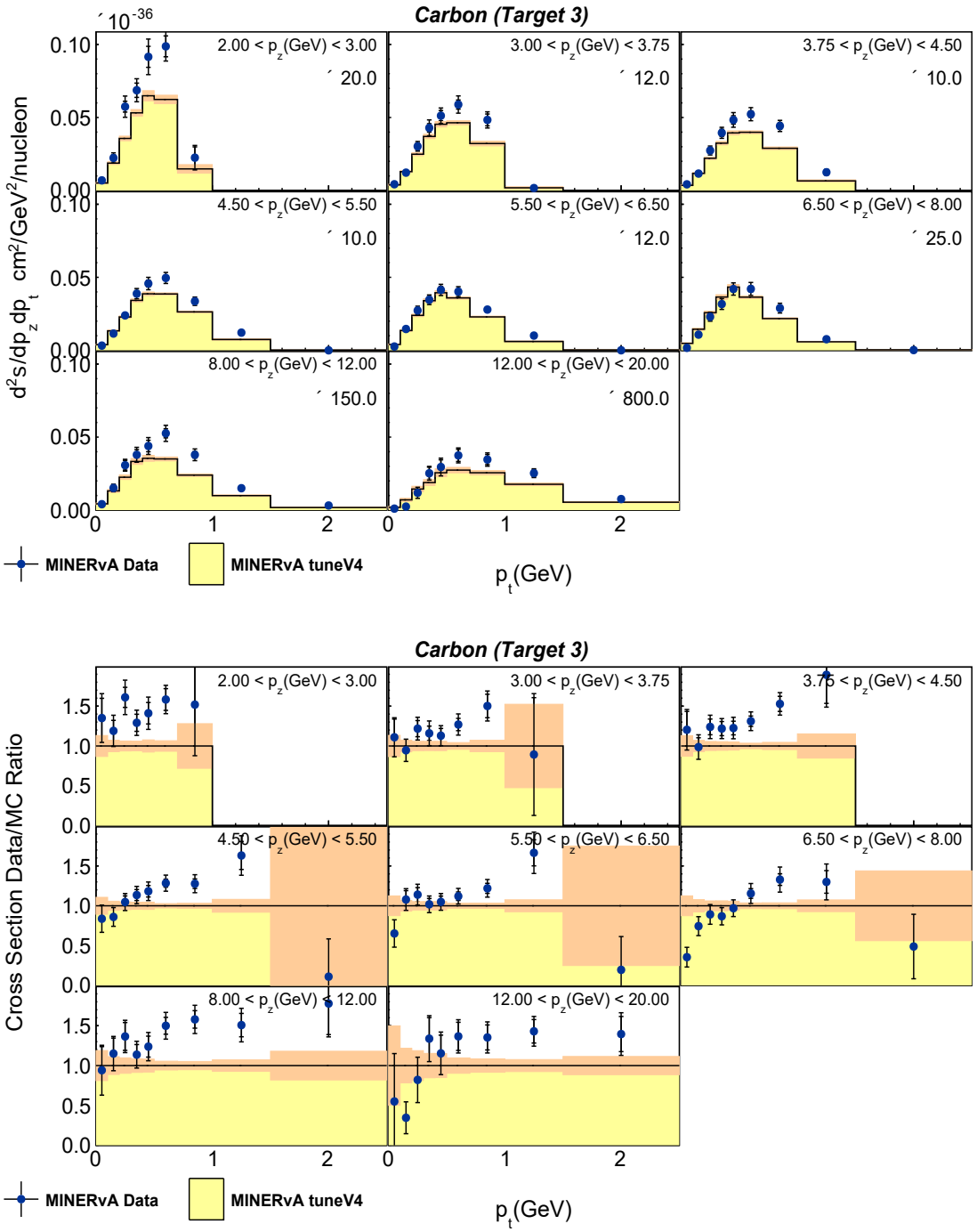

Figure 6.12: Top: The plot shows the cross section in bins of antimuon transverse momentum p_t, with panels for different longitudinal momentum p_z bins for carbon. The yellow histogram represents the MC cross section, with orange bands for statistical uncertainties. Blue points indicate the data cross section, featuring inner black error bars for statistical uncertainties and outer bars for total uncertainties. The y-axis displays the double differential cross section. **Bottom:** Data-to-simulation cross section ratio.

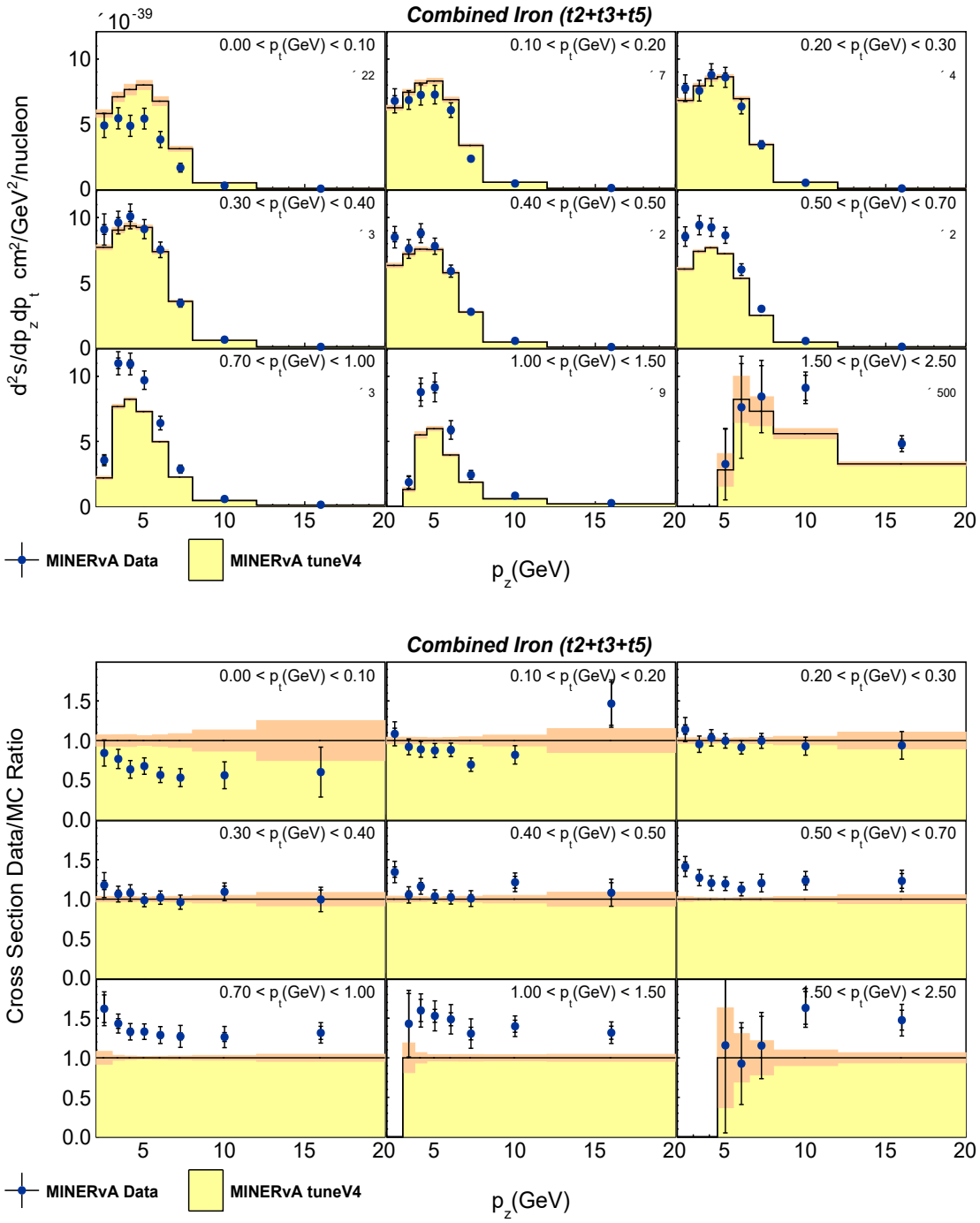

Figure 6.13: Top: The plot shows the cross section in bins of antimuon longitudinal momentum p_z, with panels for different transverse momentum p_t bins for iron. The yellow histogram represents the MC cross section, with orange bands indicating statistical uncertainties. Blue points depict the data cross section, with inner black error bars for statistical uncertainties and outer bars for total uncertainties. The y-axis displays the double differential cross section. **Bottom:** Data-to-simulation cross section ratio.

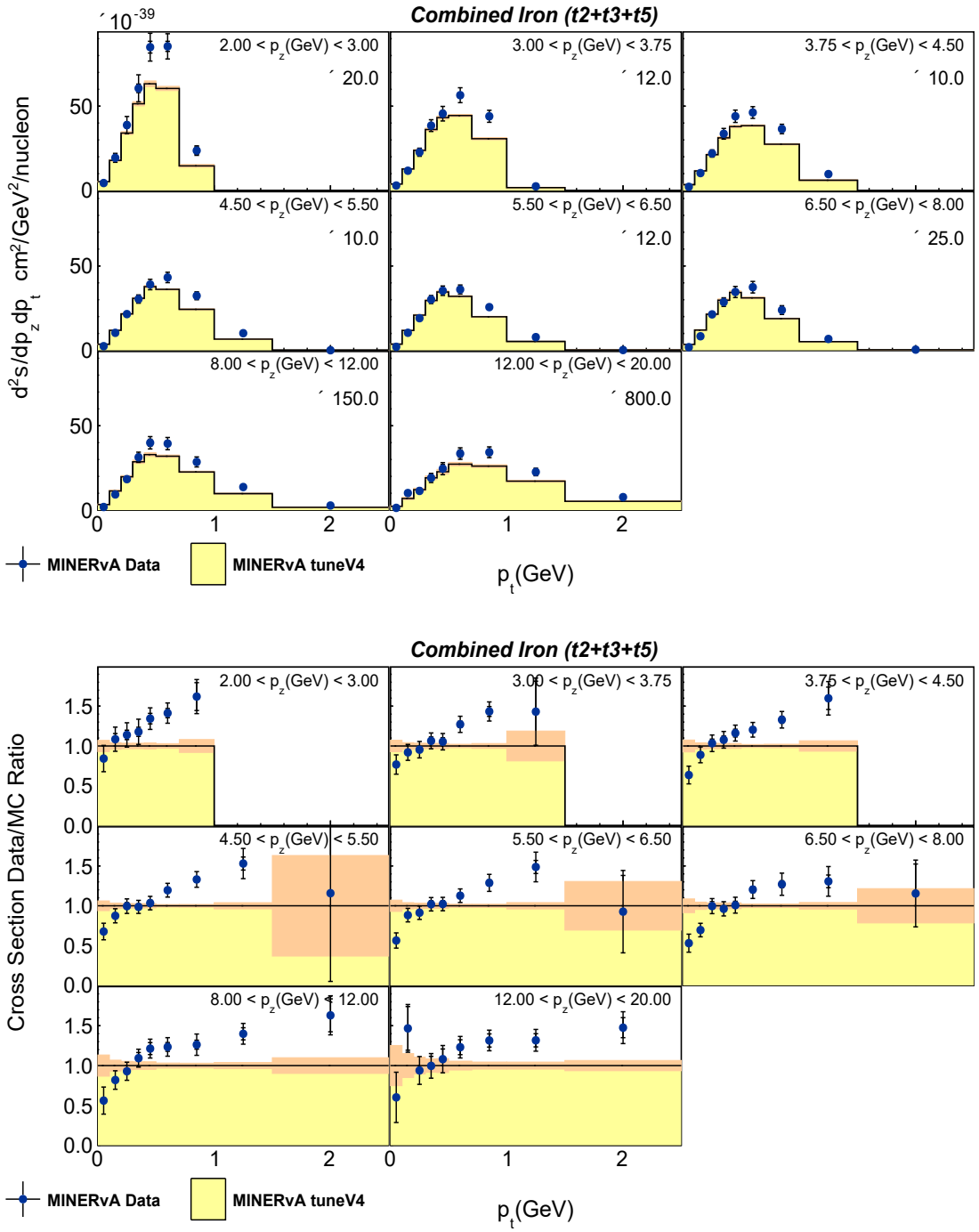

Figure 6.14: Top: The plot shows the cross section in bins of antimuon transverse momentum p_t, with panels for different longitudinal momentum p_z bins for iron. The yellow histogram represents the MC cross section, with orange bands indicating statistical uncertainties. Blue points depict the data cross section, with inner black error bars for statistical uncertainties and outer bars for total uncertainties. The y-axis displays the double differential cross section. **Bottom:** Data-to-simulation cross section ratio.

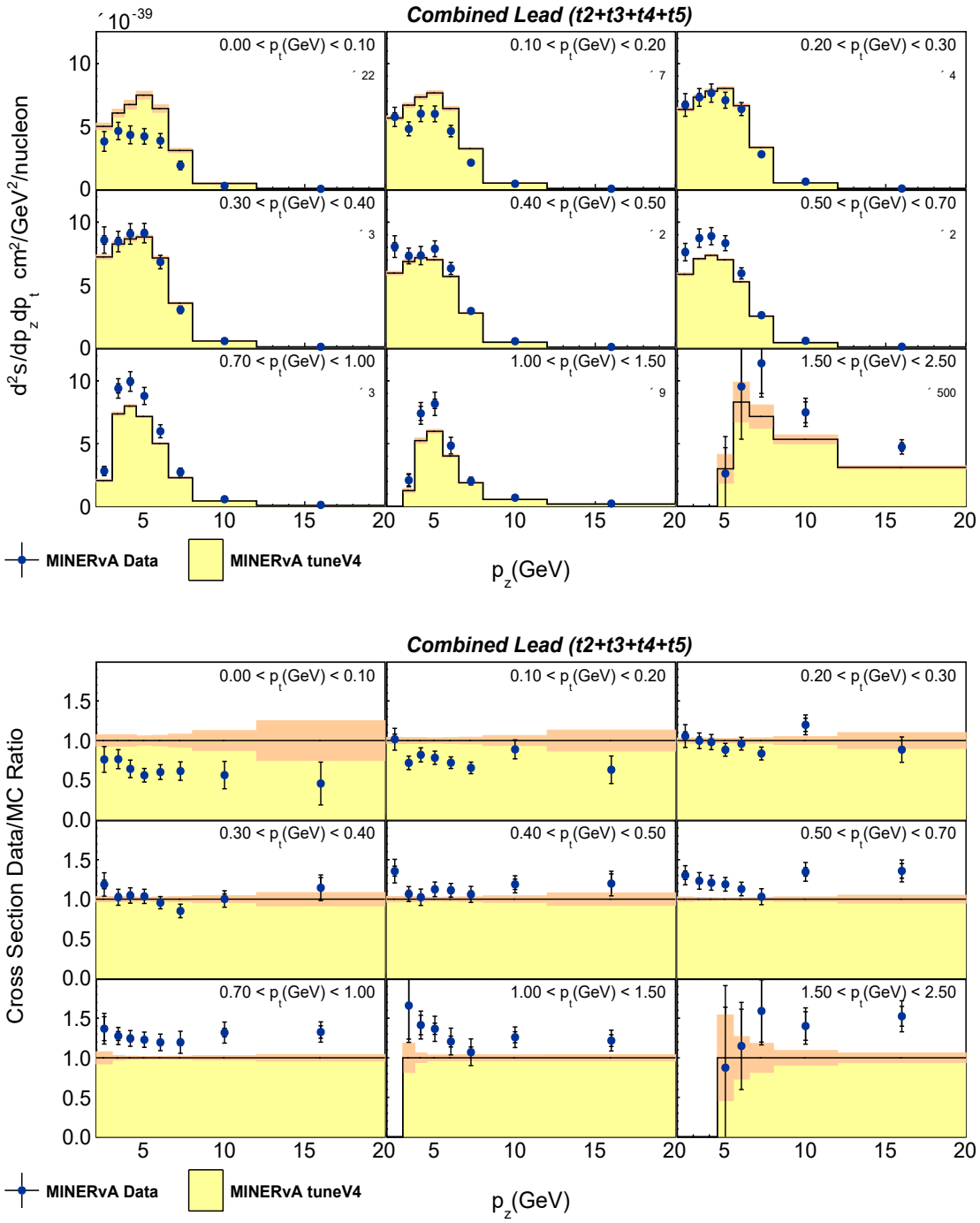

Figure 6.15: Top: The plot shows the cross section in bins of antimuon longitudinal momentum p_z, with panels for different transverse momentum p_t bins for lead. The yellow histogram represents the MC cross section, with orange bands indicating statistical uncertainties. Blue points depict the data cross section, with inner black error bars for statistical uncertainties and outer bars for total uncertainties. The y-axis displays the double differential cross section. **Bottom:** Data-to-simulation cross section ratio.

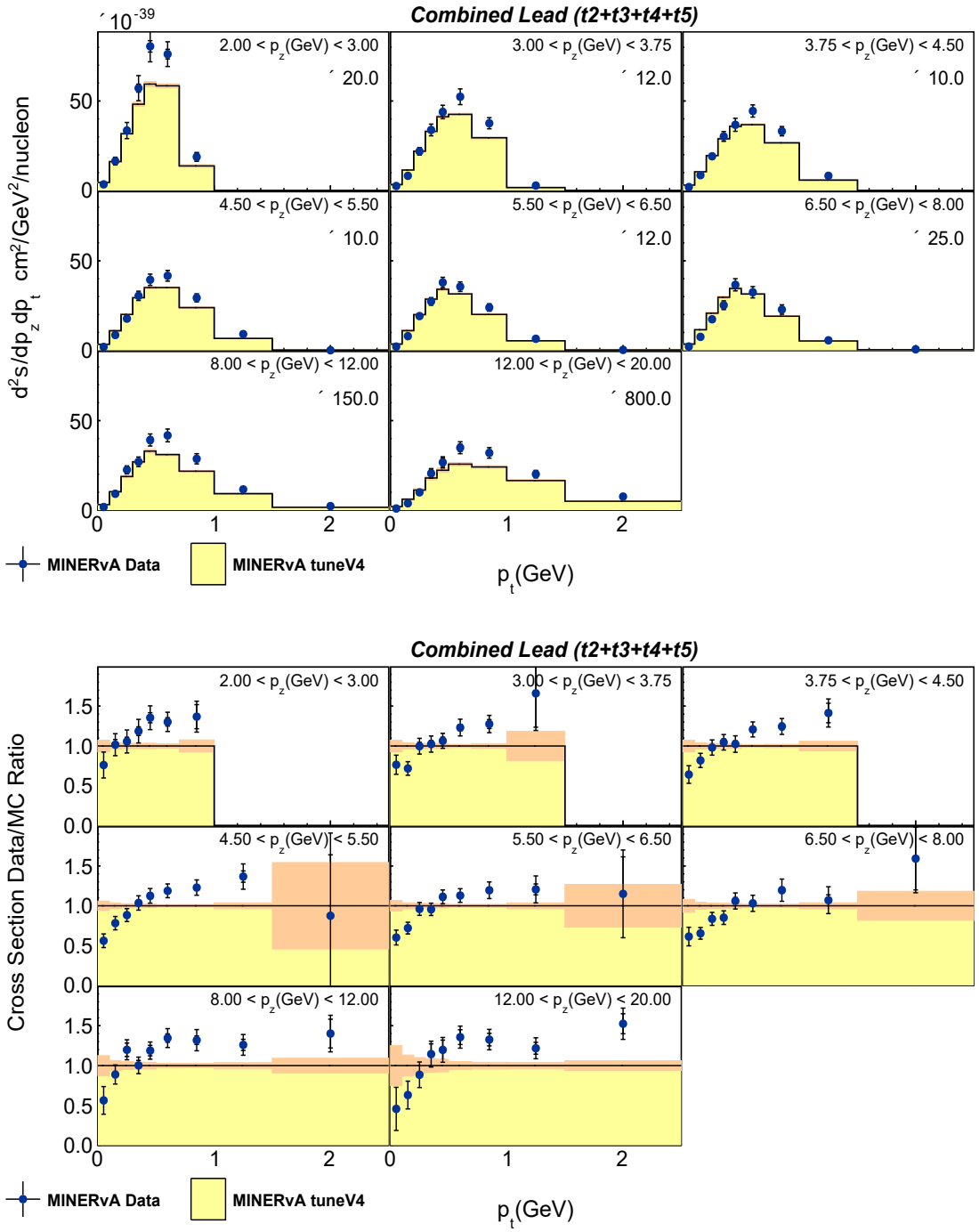

Figure 6.16: Top: The plot shows the cross section in bins of antimuon transverse momentum p_t, with panels for different longitudinal momentum p_z bins for lead. The yellow histogram represents the MC cross section, with orange bands indicating statistical uncertainties. Blue points depict the data cross section, with inner black error bars for statistical uncertainties and outer bars for total uncertainties. The y-axis displays the double differential cross section. **Bottom:** Data-to-simulation cross section ratio.

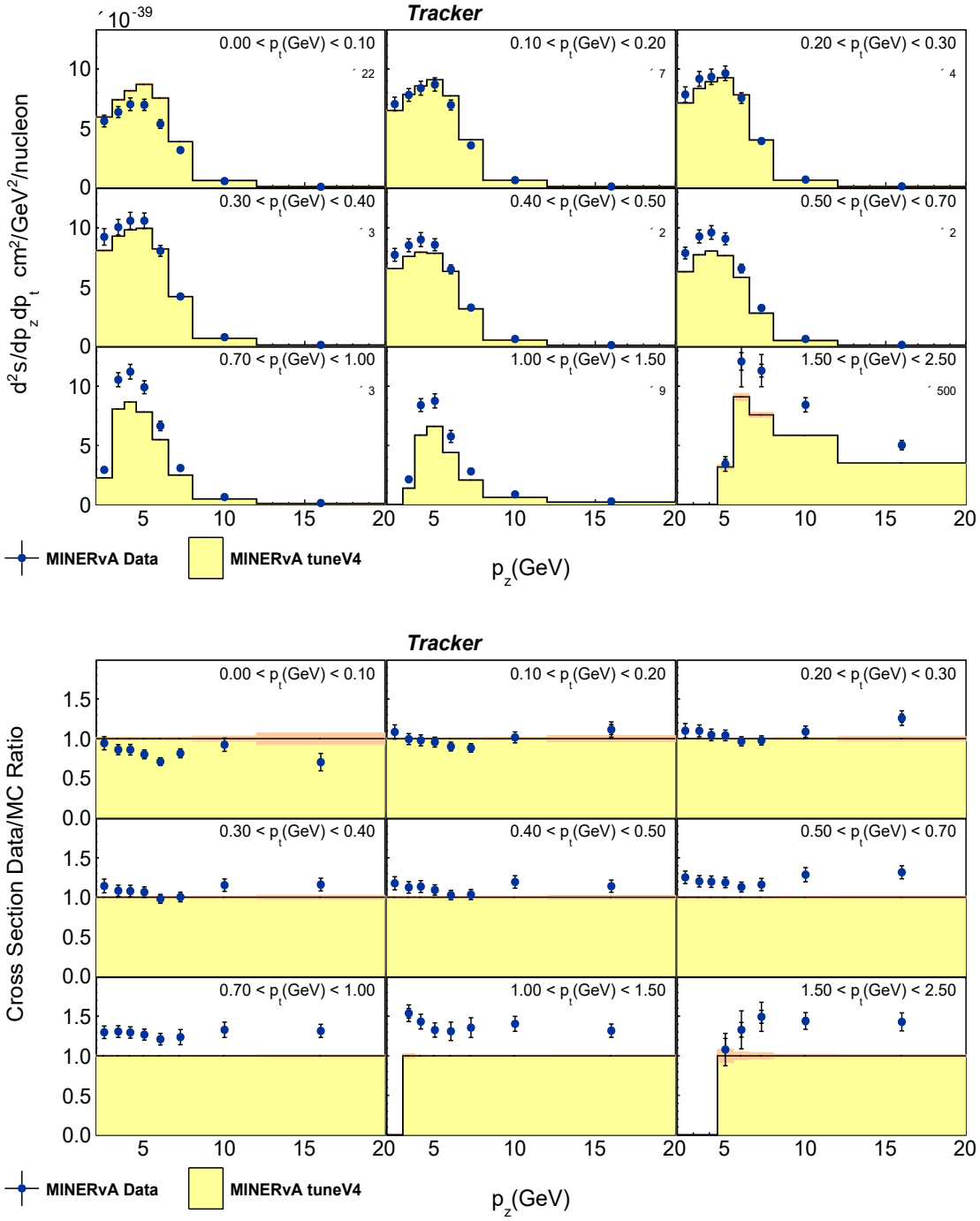

Figure 6.17: Top: The plot shows the cross section in bins of antimuon longitudinal momentum p_z, with panels for different transverse momentum p_t bins for tracker scintillator. The yellow histogram represents the MC cross section, with orange bands indicating statistical uncertainties. Blue points depict the data cross section, with inner black error bars for statistical uncertainties and outer bars for total uncertainties. The y-axis displays the double differential cross section. **Bottom:** Data-to-simulation cross section ratio.

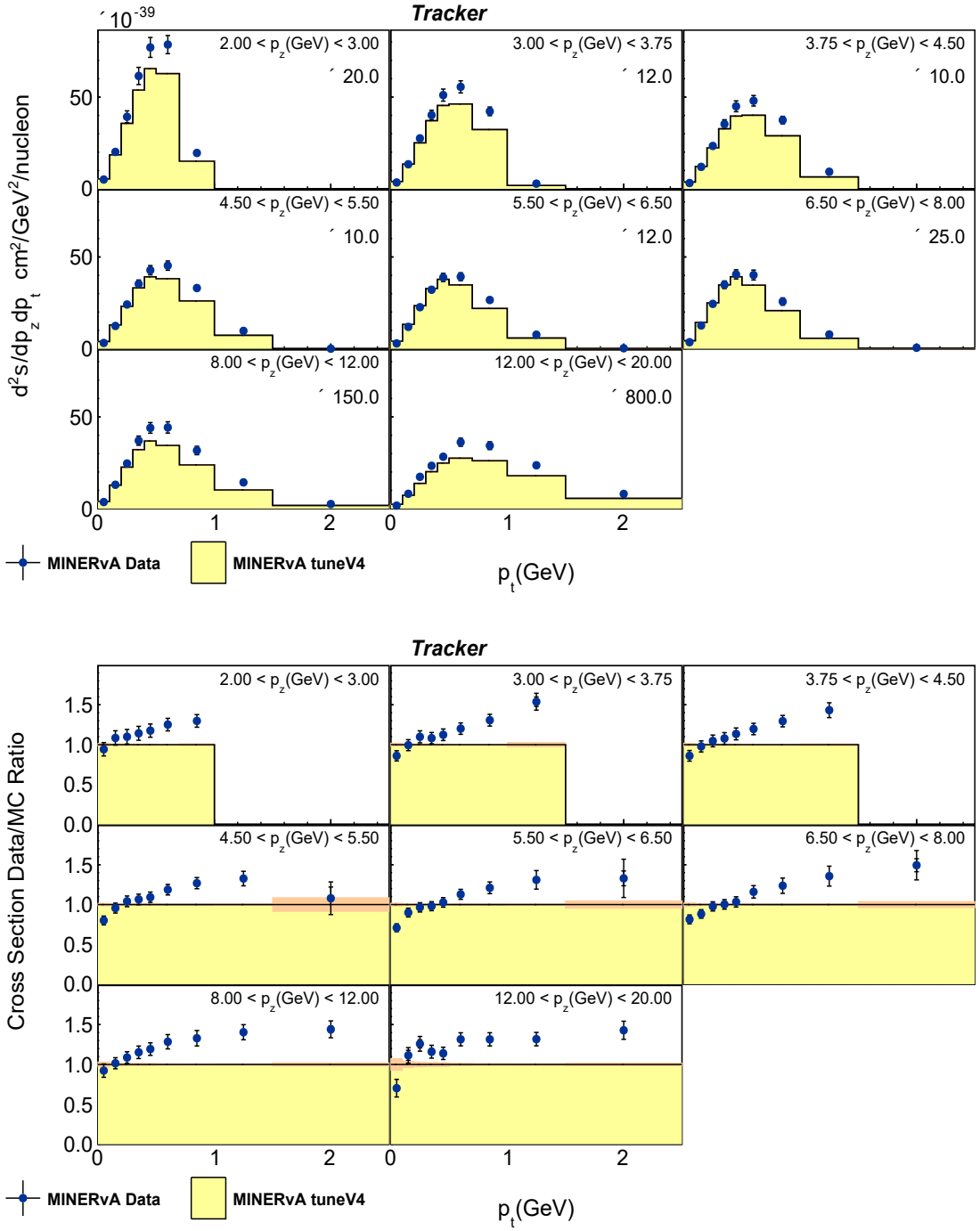

Figure 6.18: Top: The plot shows the cross section in bins of antimuon transverse momentum p_t, with panels for different longitudinal momentum p_z bins for tracker scintillator. The yellow histogram represents the MC cross section, with orange bands indicating statistical uncertainties. Blue points depict the data cross section, with inner black error bars for statistical uncertainties and outer bars for total uncertainties. The y-axis displays the double differential cross section. **Bottom:** Data-to-simulation cross section ratio.

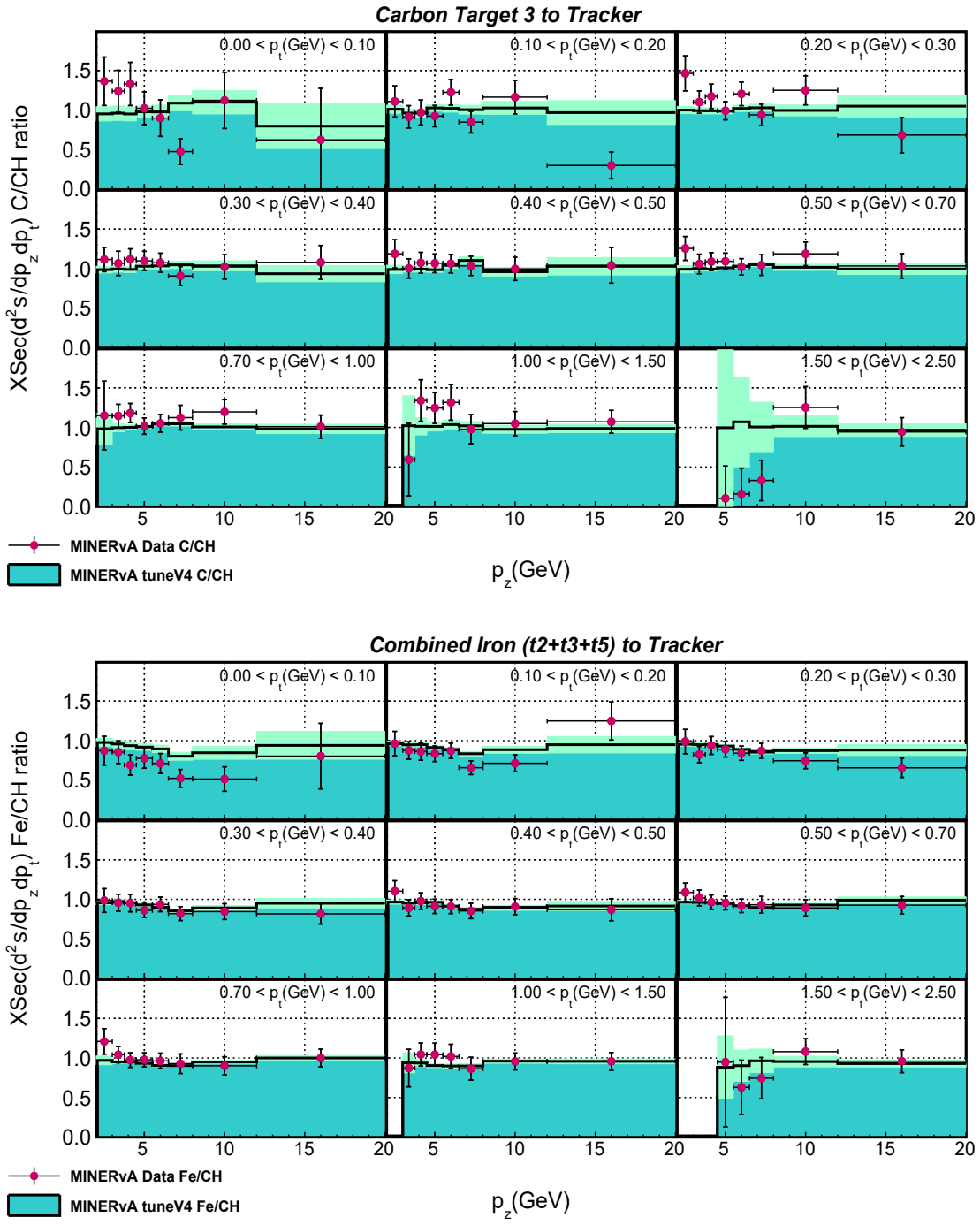

Figure 6.19: The plots display cross section ratios for antimuon longitudinal momentum p_z in panels of transverse momentum p_t for carbon to scintillator **(top)** and iron to scintillator **(bottom)**. The green histogram shows the MC-derived ratio with light green bands for statistical uncertainties. Red points represent the data cross section ratio, with shorter inner black error bars for statistical uncertainties and taller outer bars for total uncertainties. The y-axis shows the double differential cross section ratio.

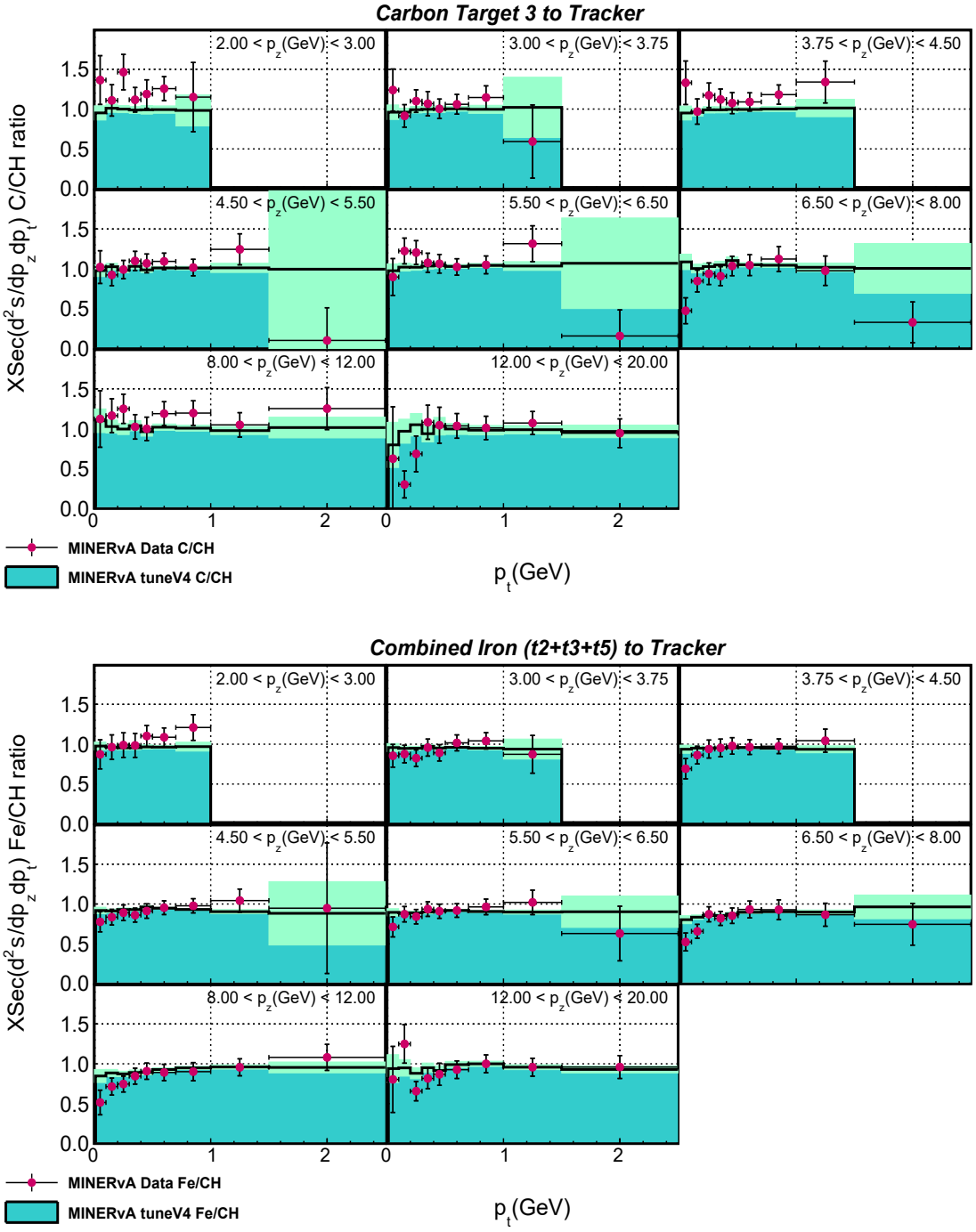

Figure 6.20: The plots display cross section ratios for antimuon transverse momentum p_t in panels of longitudinal momentum p_z for carbon to scintillator **(top)** and iron to scintillator **(bottom)**. The green histogram shows the MC-derived ratio with light green bands for statistical uncertainties. Red points represent the data cross section ratio, with shorter inner black error bars for statistical uncertainties and taller outer bars for total uncertainties. The y-axis shows the double differential cross section ratio.

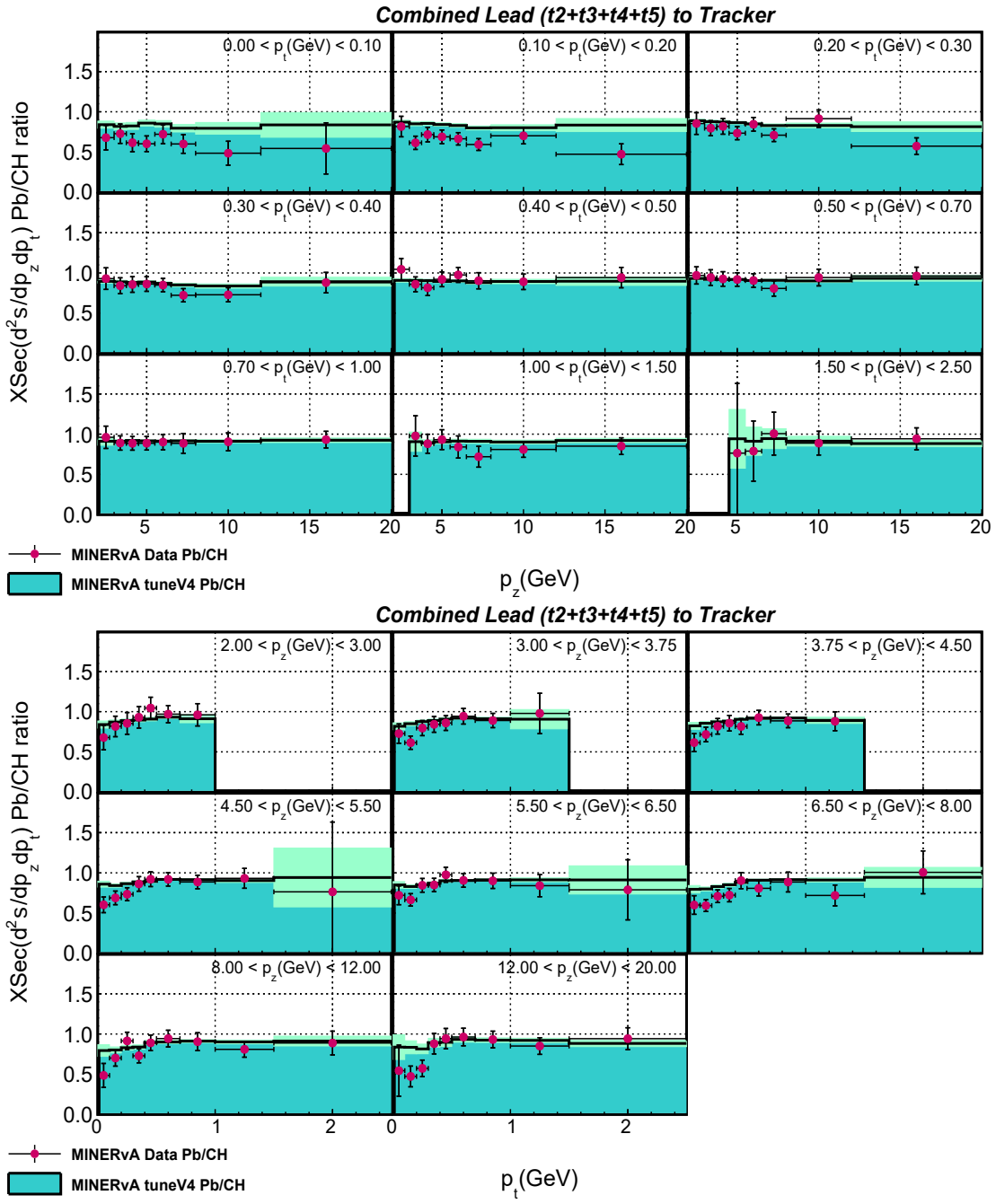

Figure 6.21: The plots show cross section ratios **(top)** in bins of antimuon longitudinal momentum p_z , with panels for antimuon transverse momentum p_t , and reversed variables **(bottom)** for lead to scintillator. The green histogram represents the MC-derived ratio, with light green bands for statistical uncertainties. Red points indicate the data cross section ratio, with shorter inner black error bars for statistical uncertainties and taller outer bars for total uncertainties. The y-axis displays the double differential cross section ratio.

Fig. 6.19 - 6.21 present the cross section carbon to-, iron to- and lead to-scintillator ratios, across $p_z - p_t$ and $p_t - p_z$ bins.

Nuclear effects can be observed in the ratios shown in Fig. 6.20 and 6.21. In the region of low p_t (top panels), significant A dependence is observed. The cross section ratio at low p_t gets suppressed as we go from lighter carbon to iron to much heavier lead. Since p_t mimics the behaviour of Q^2, low p_t is a reflection of low Q^2 events. The results suggest that the low Q^2 suppression applied has to be larger than what has been currently modelled. Also, it is interesting to note that the carbon to scintillator ratio, which is flat at unity for MC, doesn't agree with the data prediction. This is not what was expected. The ratio in data deviates from unity, particularly at the highest p_t values. This might be due to the uncertainties associated with the plastic sidebands, which have not been included in this analysis. This can also be attributed to the uncertainty coming from the hadron energy mis-modeling. Carbon was treated with plastic sideband studies and background was subtracted based on that, but for tracker, this was not the case.

Fig. 6.22 and 6.23 illustrate the fractional uncertainties associated with the measured double differential cross sections. As observed in the case of $x - Q^2$ results, flux is the dominant uncertainty, which is followed by the uncertainty associated with antimuon energy.

Uncertainties associated with cross section ratios (A = C, Fe, Pb to scintillator CH) are shown in Fig. 6.24 and 6.25. The flux uncertainties cancel out in the ratios, with a increase in overall statistical uncertainty.

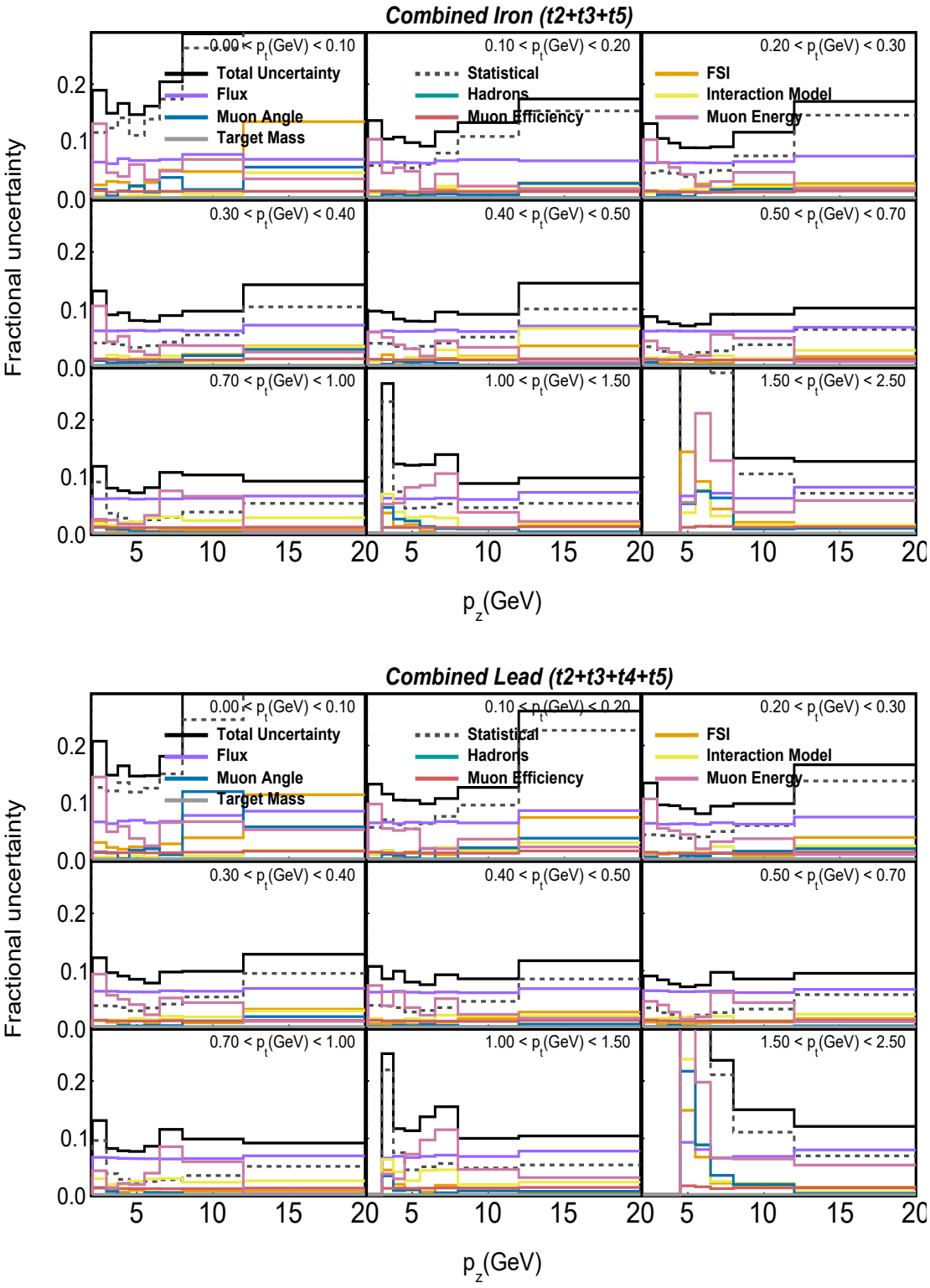

Figure 6.22: Fractional uncertainties for the data cross section in bins of antimuon longitudinal momentum p_z, segmented into different panels corresponding to bins of antimuon transverse momentum p_t for iron **(top)** and lead **(bottom)**.

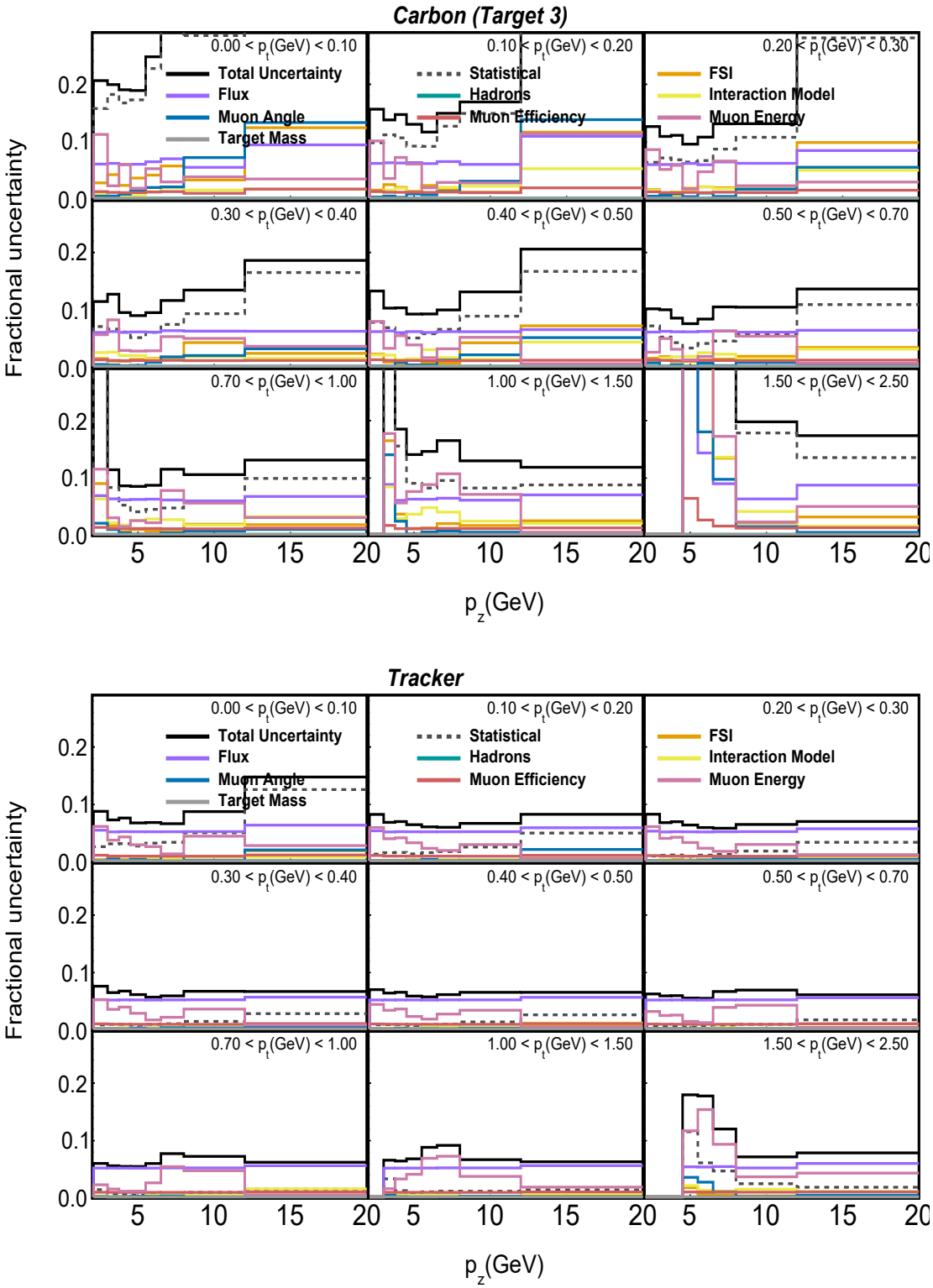

Figure 6.23: Fractional uncertainties for the data cross section in bins of antimuon longitudinal momentum p_z, segmented into different panels corresponding to bins of antimuon transverse momentum p_t, for carbon **(top)** and tracker scintillator **(bottom)**.

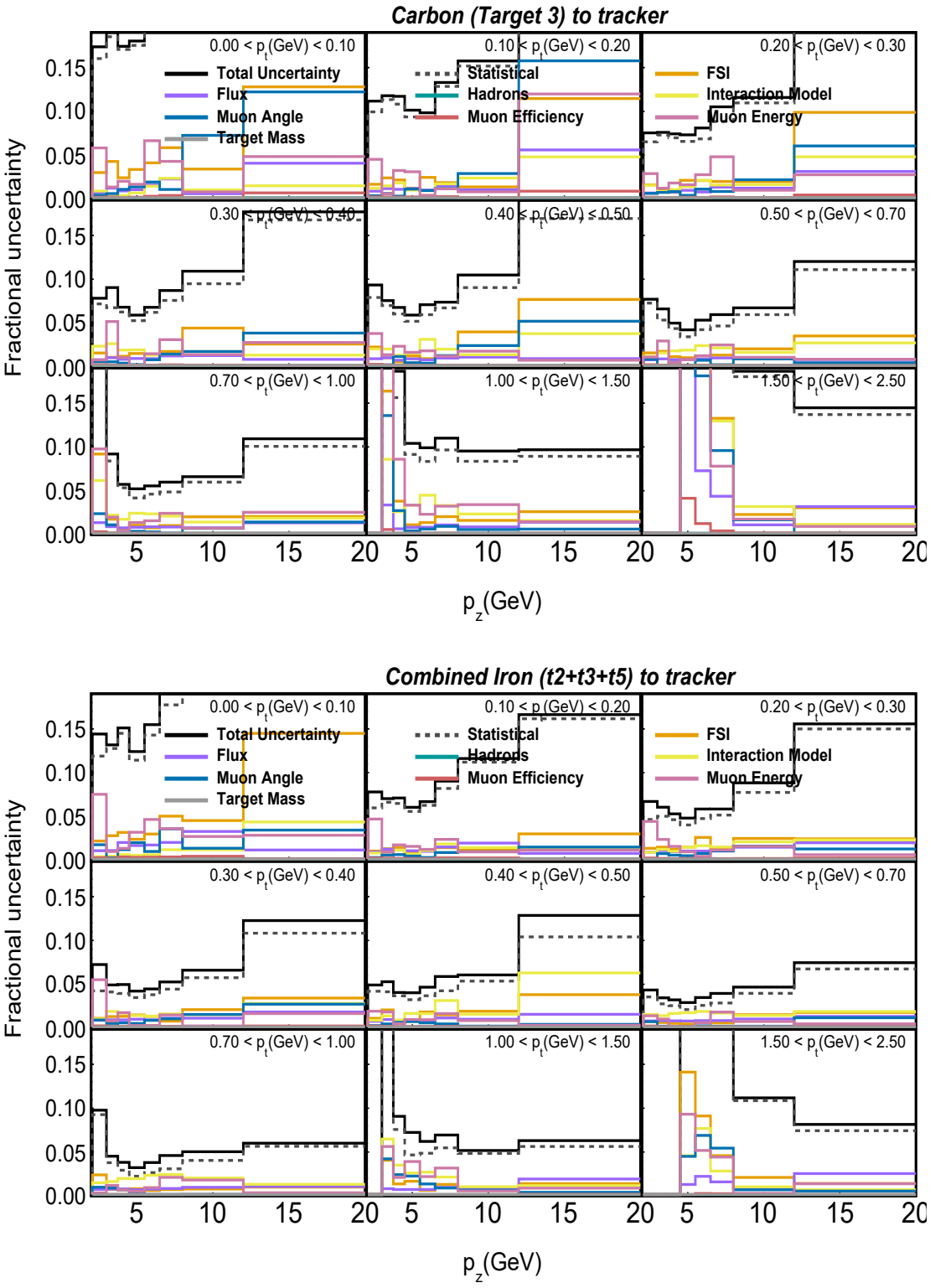

Figure 6.24: Fractional uncertainties for the cross section ratio in data in bins of antimuon longitudinal momentum p_z, segmented into different panels corresponding to bins of antimuon transverse momentum p_t, for carbon to scintillator **(top)** and iron to scintillator **(bottom)** ratio.

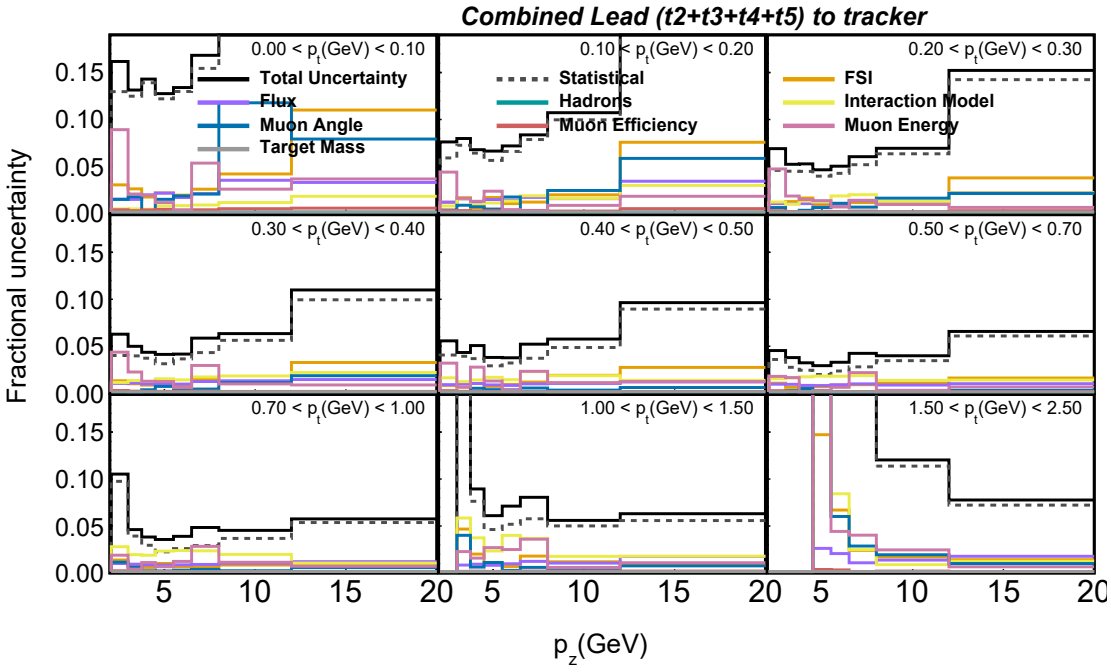

Figure 6.25: Fractional uncertainties for the cross section ratio in data in bins of antimuon longitudinal momentum p_z, segmented into different panels corresponding to bins of antimuon transverse momentum p_t, for lead to scintillator ratio.

6.3 Cross Section in W-Q^2

Finally, we have the inclusive double differential cross section measurements in invariant mass W and Q^2. Fig. 6.26, 6.27, 6.28 and 6.29 illustrate the measured and predicted cross section results. The number of events in each panel of Q^2 bin is reflected in the multiplier numbers, such that the highest population of events is in the lowest Q^2 bin (upper leftmost panel), which decreases as we move to higher Q^2. For the chosen binning for W, there are very few events in bins with $W > 4$ GeV, as seen. We observe that the simulation underpredicts the data, almost throught the kinematical space. If we concentrate on the $2 < W < 4$ GeV region (second data point on each panel), the probability of interaction gets suppressed as we move from lighter (carbon) to heavier nuclei (lead).

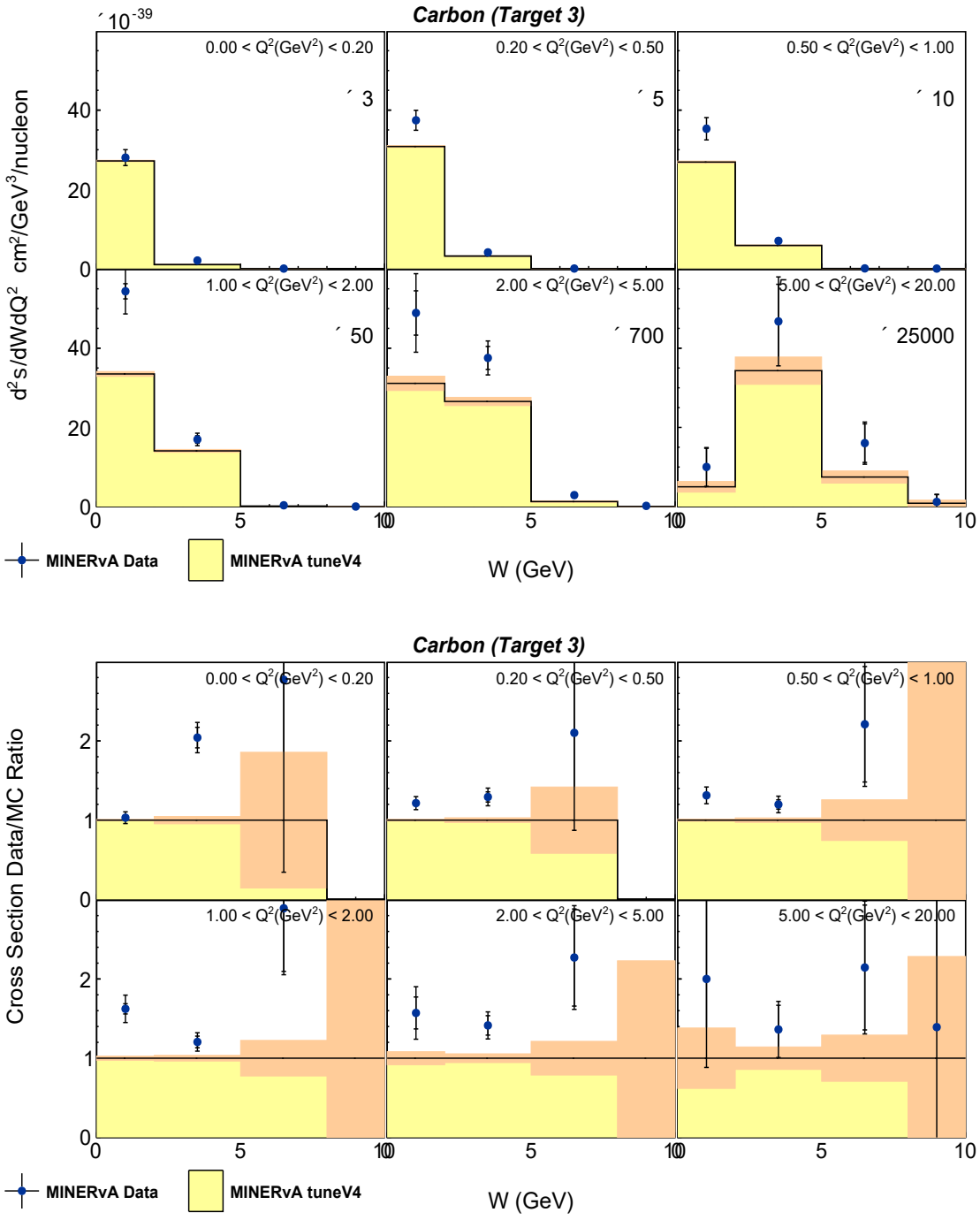

Figure 6.26: Top: The plot shows the cross section in invariant mass W bins, segmented into panels for Q^2 bins, for carbon. The yellow histogram represents the cross section from simulation (MC), with orange bands for statistical uncertainties. The blue points depict the extracted data cross section, with shorter inner black error bars for statistical uncertainties and taller outer bars for total uncertainties. The y-axis displays the double differential cross section. **Bottom:** The plot depicts the data-to-simulation cross section ratio.

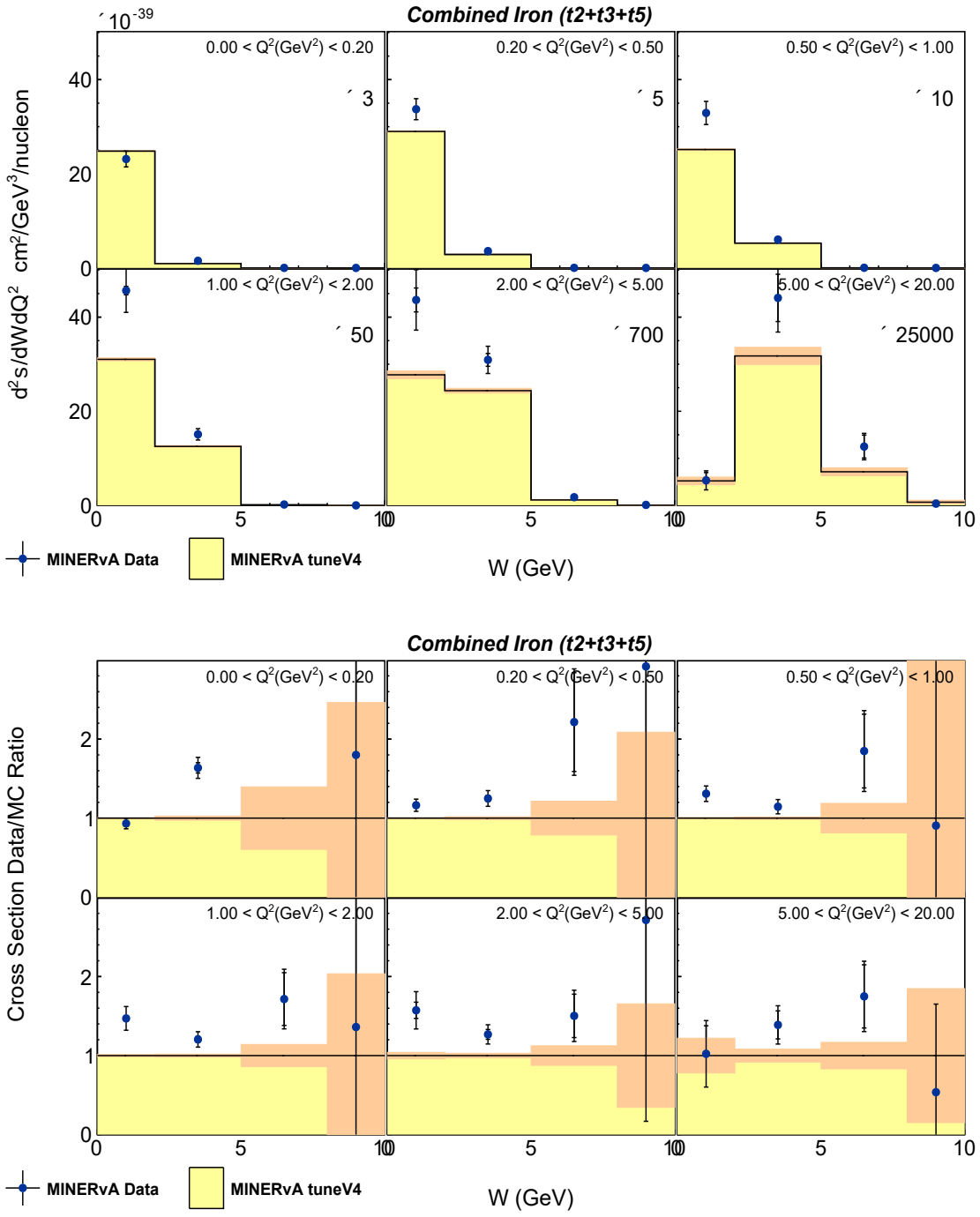

Figure 6.27: Top: The plot shows the cross section in invariant mass W bins, segmented into panels for Q^2 bins, for iron. The yellow histogram represents the cross section from simulation (MC), with orange bands indicating statistical uncertainties. The blue points depict the extracted data cross section, with shorter inner black error bars for statistical uncertainties and taller outer bars for total uncertainties. The y-axis displays the double differential cross section. **Bottom:** The plot depicts the data-to-simulation cross section ratio.

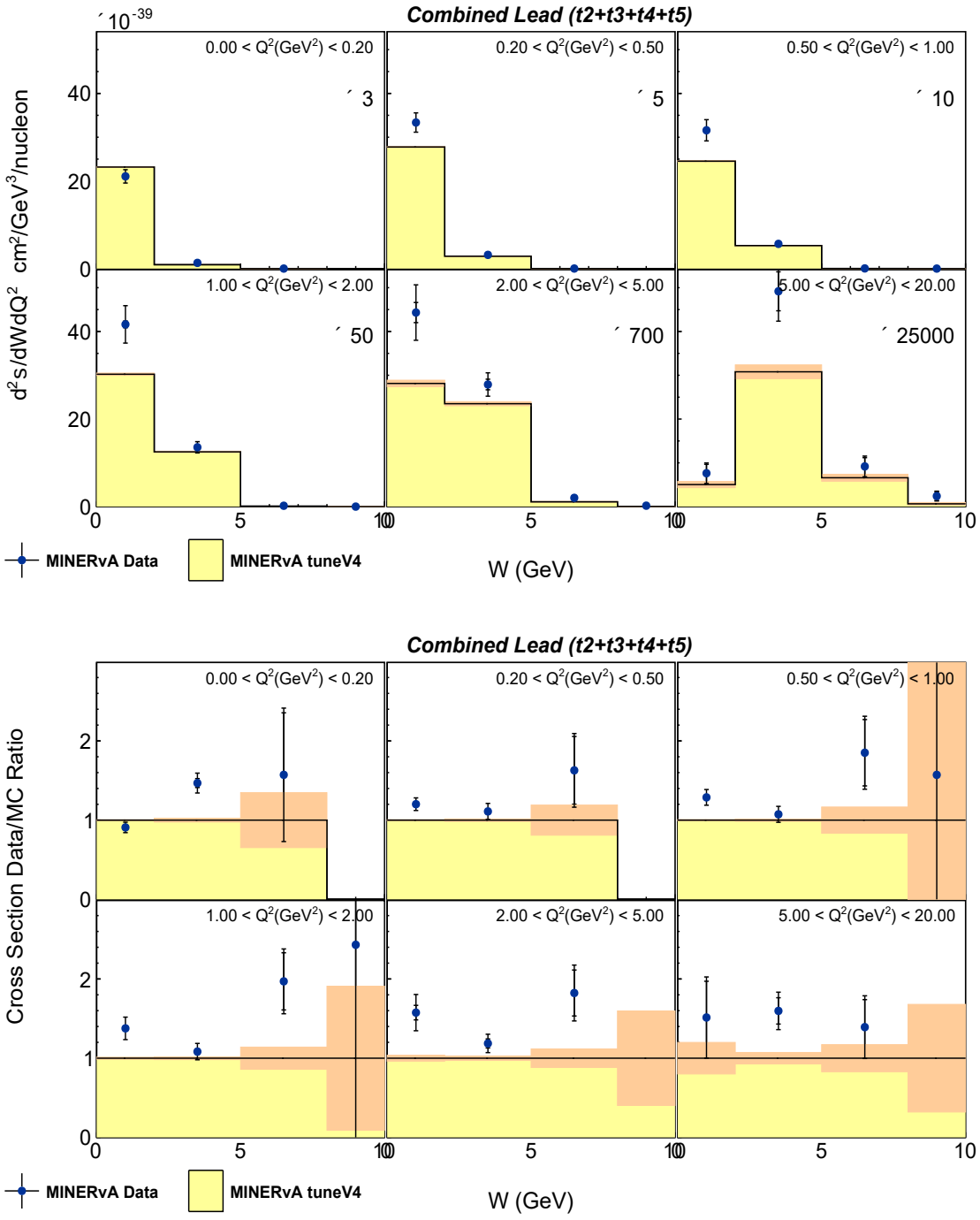

Figure 6.28: Top: The plot shows the cross section in invariant mass W bins, segmented into panels for Q^2 bins, for lead. The yellow histogram represents the cross section from simulation (MC), with orange bands indicating statistical uncertainties. The blue points depict the extracted data cross section, with shorter inner black error bars for statistical uncertainties and taller outer bars for total uncertainties. The y-axis displays the double differential cross section. **Bottom:** The plot depicts the data-to-simulation cross section ratio.

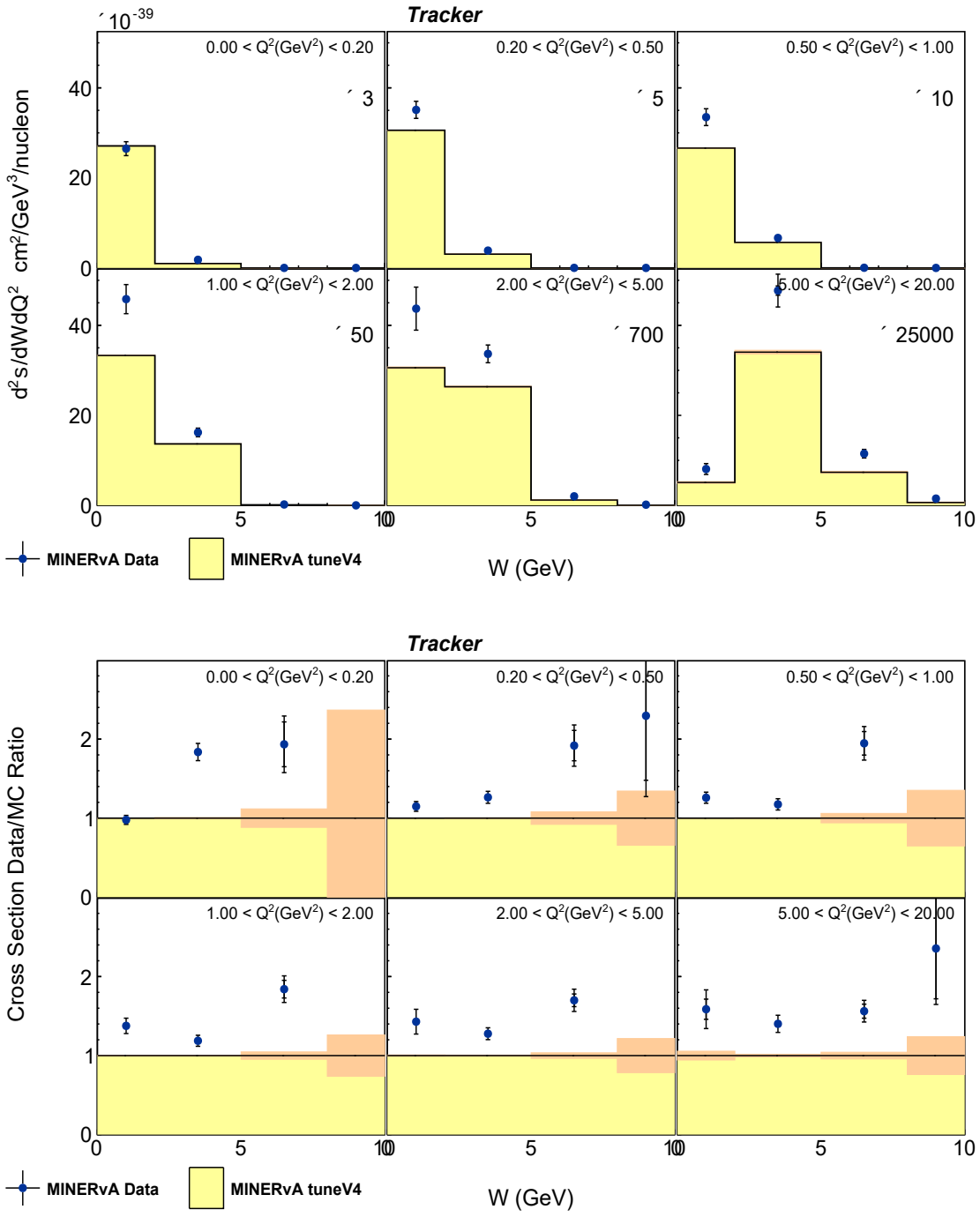

Figure 6.29: Top: The plot shows the cross section in invariant mass W bins, segmented into panels for Q^2 bins, for tracker scintillator. The yellow histogram represents the cross section from simulation (MC), with orange bands indicating statistical uncertainties. The blue points depict the extracted data cross section, with shorter inner black error bars for statistical uncertainties and taller outer bars for total uncertainties. The y-axis displays the double differential cross section. **Bottom:** The plot depicts the data-to-simulation cross section ratio.

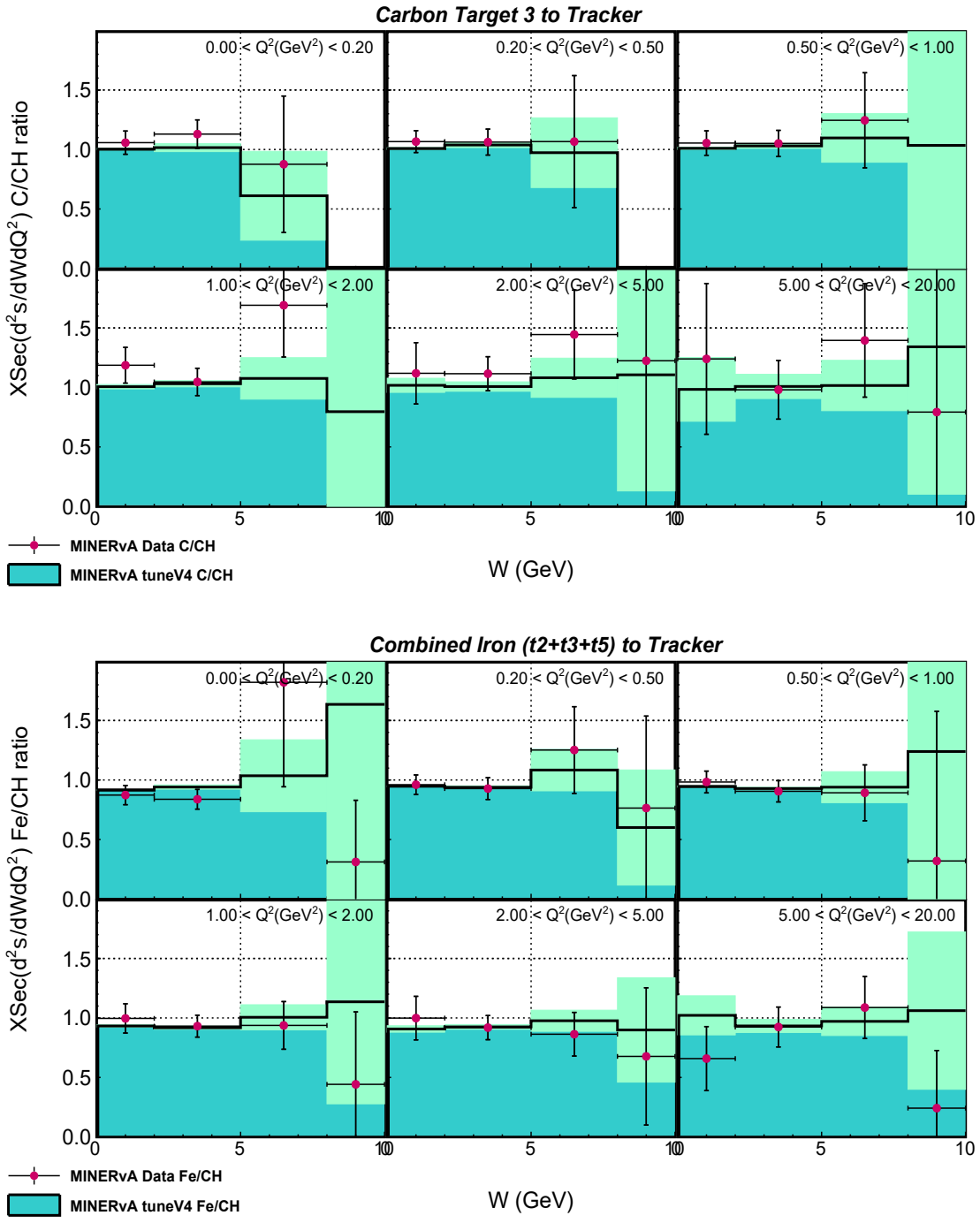

Figure 6.30: The plots show cross section ratios in invariant mass W bins (x-axis) for carbon to scintillator **(top)** and iron to scintillator **(bottom)**, with panels for Q^2 bins. The green histogram represents the MC-derived ratio, with light green bands for statistical uncertainties. Red points indicate the data ratio, with inner black error bars for statistical uncertainties and outer bars for total uncertainties. The y-axis displays the double differential cross section ratio.

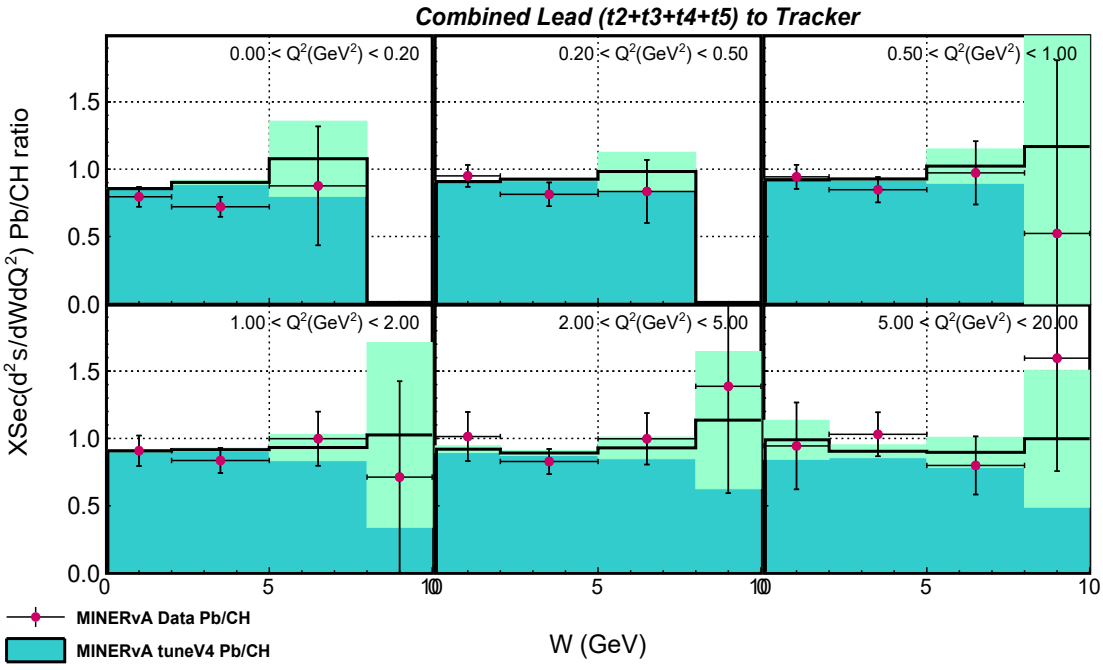

Figure 6.31: The plots show cross section ratios in invariant mass W bins (x-axis) for lead to scintillator, with panels for Q^2 bins. The green histogram represents the MC-derived ratio, with light green bands for statistical uncertainties. Red points indicate the data ratio, with inner black error bars for statistical uncertainties and outer bars for total uncertainties. The y-axis displays the double differential cross section ratio.

This is a reflection of the nuclear medium effects coming in to play, with the most amount of suppression in the data cross section in lead, followed by iron and then carbon. Fig. 6.30 and 6.31 depict the nuclear target to tracker scintillator ratios for carbon, iron, and lead. The above-mentioned suppression is highlighted in these ratios, for the entire $W < 4$ GeV region. In the region of higher W ($4 < W < 20$ GeV), we have very small statistics, as seen by the error bars in these bins. The associated fractional uncertainties for the cross section measurements in data are shown in Fig. 6.32 - 6.33. The high uncertainties in the high W bins of greater than 4 GeV are dominated by statistical uncertainties because we have a limited event sample in this region. The cross section results are dominated by flux uncertainty, like the results in $x - Q^2$ and $p_z - p_t$. FSI uncertainties are higher

for heavier nuclei, as expected.

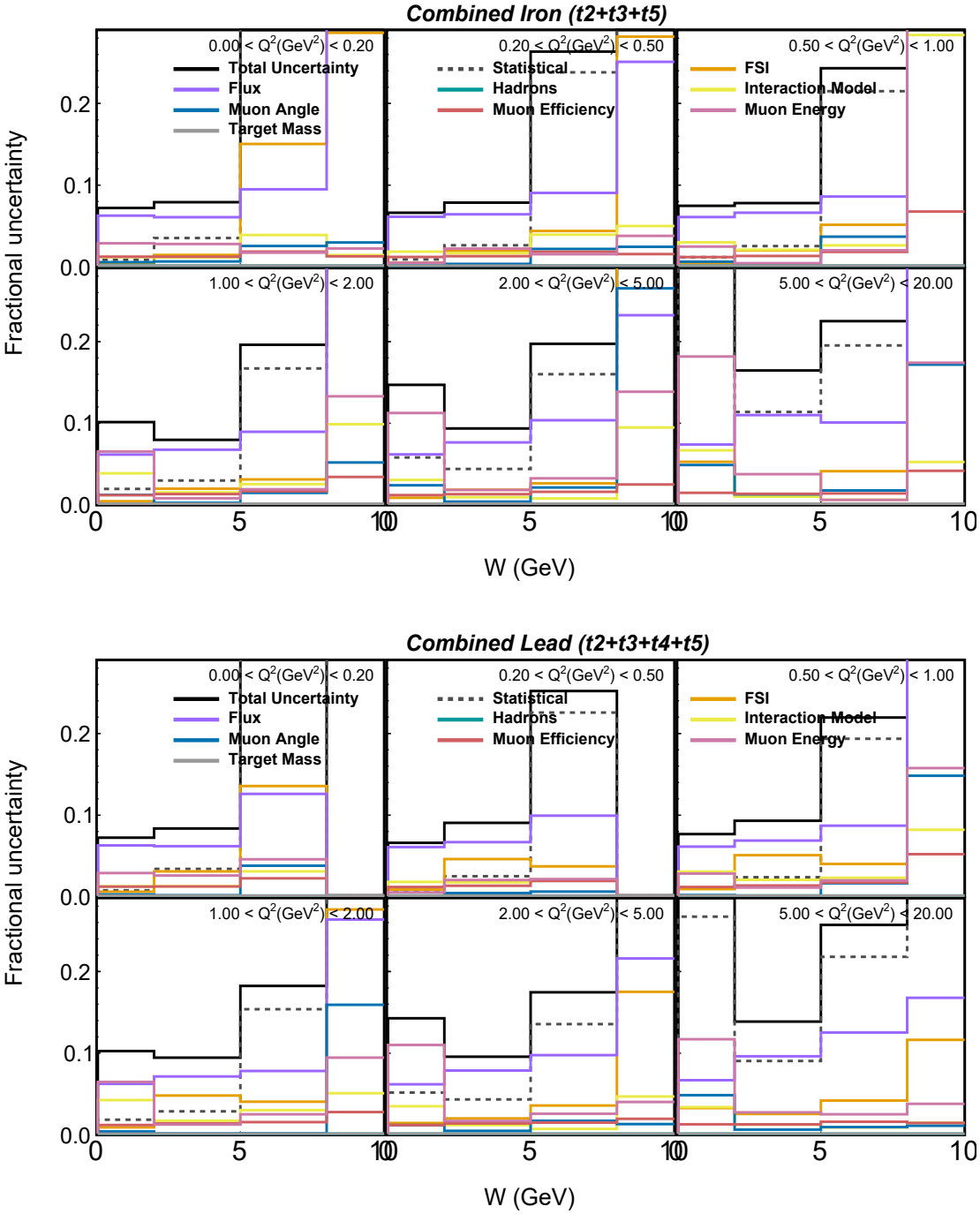

Figure 6.32: Fractional uncertainties for the data cross section in bins of invariant mass W, segmented into different panels corresponding to bins of Q^2, for iron **(top)** and lead **(bottom)**.

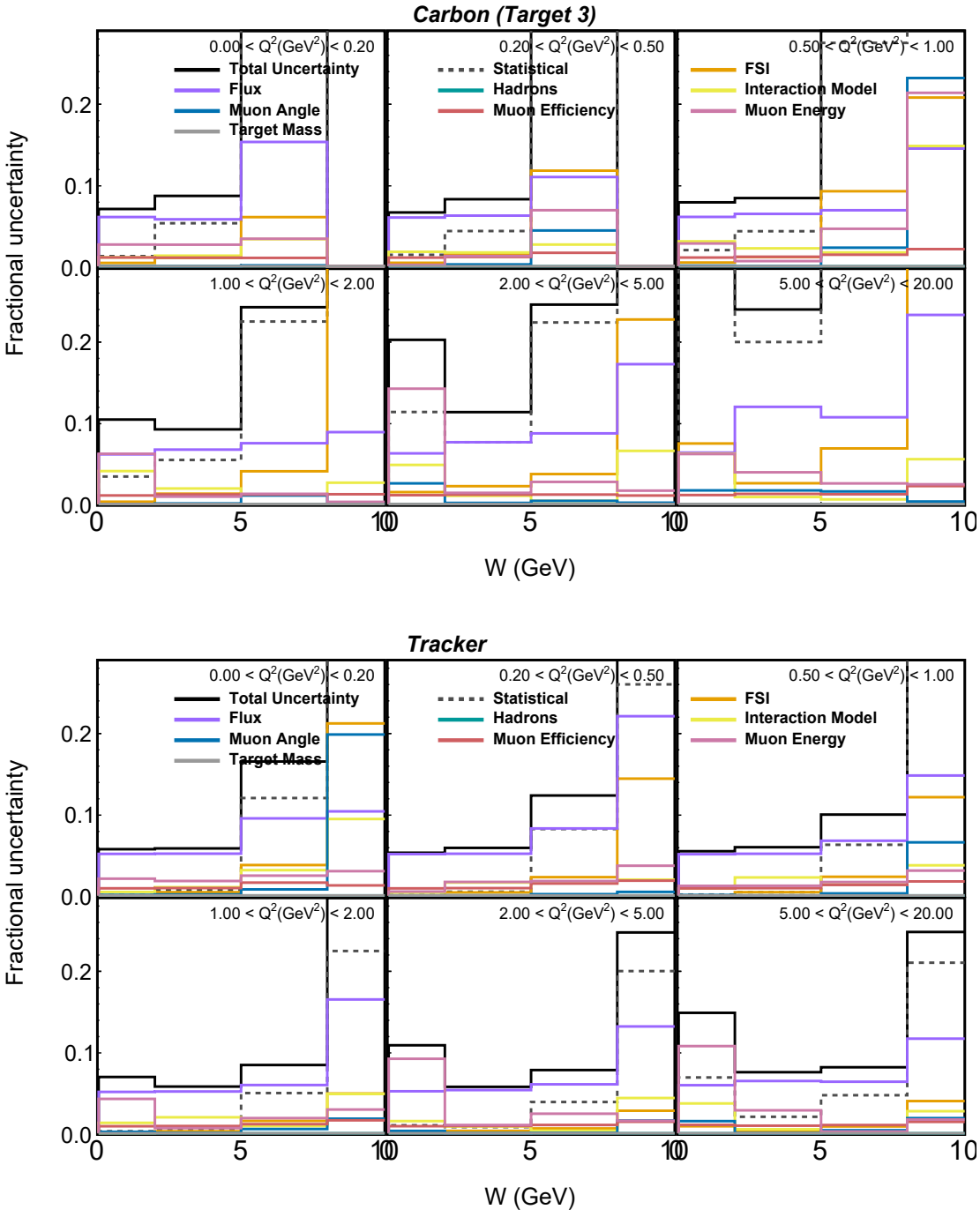

Figure 6.33: Fractional uncertainties for the data cross section in bins of invariant mass W, segmented into different panels corresponding to bins of Q^2, for carbon **(top)** and tracker scintillator **(bottom)**.

Fig. 6.34 and 6.35 display the fractional uncertainties associated with the cross

section ratios. Flux uncertainties mostly cancel out, with high flux uncertainties associated with high W bins, which is expected. FSI uncertainties are observed to dominate as we move from lighter to heavier nuclei.

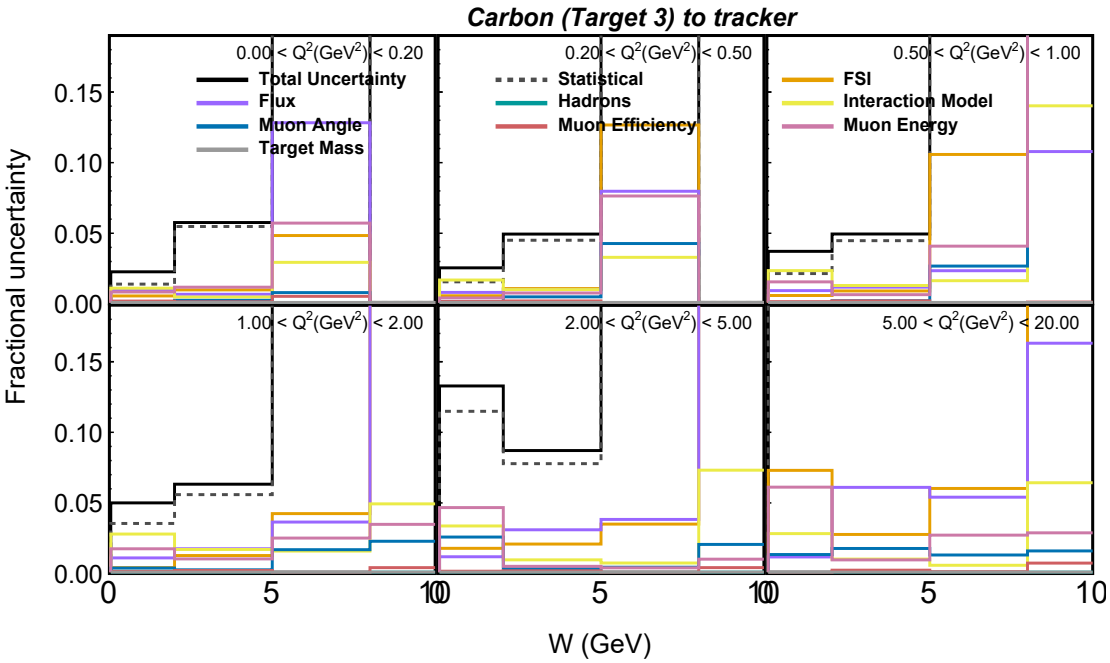

Figure 6.34: Fractional uncertainties for the cross section ratio in data in bins of invariant mass W, segmented into different panels corresponding to bins of Q^2, for carbon to scintillator ratio.

Higher uncertainties corresponding to the interaction model are observed in the cross section ratios, particularly dominant in the low W region ($W < 2$ GeV). Antimuon reconstruction uncertainties are notably larger in the high W region, as anticipated. Higher flux uncertainties in the high W region can be seen because this falls towards the tail end of our antineutrino beam, with larger associated flux uncertainties.

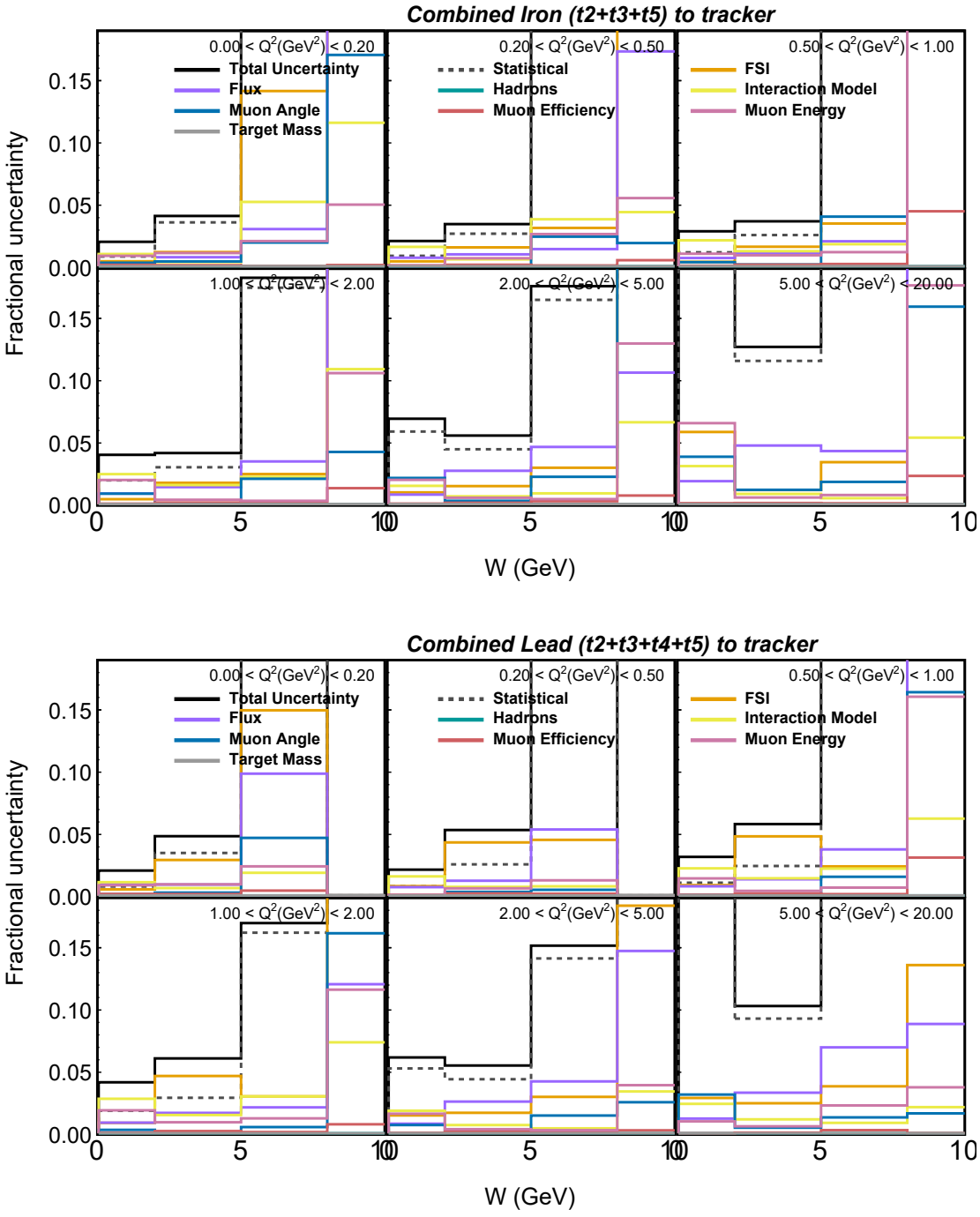

Figure 6.35: Fractional uncertainties for the cross section ratio in data in bins of invariant mass W, segmented into different panels corresponding to bins of Q^2, for (**top**) iron to scintillator and (**bottom**) lead to scintillator ratio.

6.4 Conclusion

In the presented work, we first briefly discussed the history of how (anti)neutrinos came into the picture followed by the various sources that produce (anti)neutrinos, focusing on the accelerator (anti)neutrinos, utilized in this analysis. We also discussed briefly the development of the theory of (anti)neutrino interactions. Then, how the (anti)neutrinos are produced at Fermilab, using the NuMI beamline was discussed in detail. Following this, we discussed in detail the construction and working of the MINERvA detector, highlighting all the different aspects of both the hardware and the computational (software) side of the experiment. Following this part, we discussed how the (anti)neutrino events in the MINERvA detector are reconstructed and we discussed the neutrino event generator GENIE, which is used for the simulation of neutrino interactions in the MINERvA detector. Following this was my analysis work performed at the MINERvA, where we discussed in detail all the analysis steps that we performed to arrive at the cross section measurement. Later, we discussed the sources of error in the measured cross section.

In this thesis, we presented the first simultaneous inclusive charged current double differential cross section measurement on multiple nuclear targets—carbon, iron, lead, and hydrocarbon, in the same antineutrino beam. The measurement is provided as a function of bjorken x and Q^2, W and Q^2 and antimuon longitudinal (p_z) and transverse momentum (p_t). The measurement was performed in the medium energy mode, at the MINERvA experiment, where the average energy of the antineutrinos in the beam around $\sim$ 6 GeV. For the inclusive analysis, because MINERvA uses MINOS near detector to detect and measure the final state (anti)muons, we limited our measurement to forward-going antimuons with scattering angle less than 17^0 and with energy not lower than 2 GeV, and not higher than 20 GeV. We saw that all the channels, including the quasielastic, pion production, and deep inelastic scattering had high statistics in the measurement.

We also measured the nuclear target to scintillator cross section ratios, for carbon-, iron- and lead- to scintillator in the tracker. This double differential cross section ratio showed the nuclear dependence in the antineutrino nucleus interactions. We observed suppression in the cross section, as we chose more dense atomic nuclei in the numerator of the cross section, in the low x region. We again noticed suppression for the results in the antimuon momenta, at low p_t values. Nuclear dependence, due to medium effects, was also observed in the W-Q^2 cross section ratios. In the W region of 2-4 GeV, the cross section got suppressed as we moved from lighter (carbon) towards heavier (lead) nuclei.

Finally, this two-dimensional cross section measurement was conducted using one of the largest antineutrino data set with a charged identified μ^+, in the energy range of approximately 6 GeV (peak energy), among all (anti)neutrino experiments. This measurement is crucial for benchmarking and refining models for future (anti)neutrino experiments in this energy range, enabling more accurate treatment of nuclear medium effects. Ultimately, this can lead to better tuning of the underlying interaction models, which will benefit future neutrino oscillation experiments facing significant challenges, particularly the DUNE experiment.

Bibliography

[1] Lawrence M. Krauss, *"Why I Love Neutrinos"*, Scientific American Magazine Vol. **302** No. 6 (June 2010) DOI:10.1038/scientificamerican062010-6OWp9o87WKQmYtT0IA5peJ.

[2] W. Pauli, Letter to L. Meitner and her colleagues dated 4 December 1930 (letter open to the participants of the conference in Tübingen) (1930), recorded in W. Pauli, Wissenschaftlicher Briefwechsel mit Bohr, Einstein, Heisenberg u.a ., Band 11(Springer, Berlin, 1985) p. 39. A reference to 'neutrino' is seen in a letter from Heisenberg to Pauli on 1 December 1930: "Zu Deinen Neutronen möchte ich noch bemerken: ..." .

[3] E. Fermi, *"Trends to a Theory of beta Radiation. (In Italian),"* Nuovo Cim. **11**, 1 (1934). DOI :10.1007/BF02959820.

[4] F. Perrin, in Structure et Proprietes des Noyaux Atomiques, Rapports et Discussions du Septiem e Conseil de Physique, idem p. 327; Compt. Rendus 197, 1625 (1933).

[5] P. A. M. Dirac, Proc. Roy. Soc. A **117**, no. 610, (1928), Proc. Roy. Soc. A **118**, no. 351, (1928), Proc. Roy. Soc. A **126**, no. 360, 692 (1930). DOI:10.1098/rspa.1928.0023.

[6] G. Gamow and E. Teller, *"Selection rules for the beta-disintegration,"* Phys. Rev. **49**, 895 (1936). DOI:10.1103/PhysRev.49.895.

[7] H. Bethe and R. Peierls, *"The 'neutrino',"* Nature **133**, 532 (1934) DOI:10.1038/133532a0.

[8] B. Pontecorvo, Chalk River Laboratory report, PD-205 (1946).

[9] L. W. Alvarez, *"A Proposed Experimental Test of the Neutrino Theory,"* DOI:10.2172/929771.

[10] E. Fermi, *"High-energy nuclear events,"* Prog. Theor. Phys. **5**, 570-583 (1950) DOI:10.1143/PTP.5.570.

[11] F. Reines and C. L. Cowan, *"Detection of the free neutrino,"* Phys. Rev. **92**, 830 (1953). DOI:10.1103/PhysRev.92.830.

[12] C. L. Cowan, F. Reines, F. B. Harrison, E. C. Anderson and F. N. Hayes, *"Large liquid scintillation detectors,"* Phys. Rev. **90**, 493 (1953). DOI:10.1103/PhysRev.90.493.

[13] F. Reines and C. L. Cowan, *"The neutrino,"* Nature **178**, 446 (1956). DOI:10.1038/178446a0.

[14] F. Reines and C. L. Cowan, *"Free anti-neutrino absorption cross-section. 1: Measurement of the free anti-neutrino absorption cross-section by protons,"* Phys. Rev. **113**, 273 (1959). DOI:10.1103/PhysRev.113.273.

[15] R. Davis, Jr., *"Attempt to detect the antineutrinos from a nuclear reactor by the Cl37(anti-nu,e-) A37 reaction,"* Phys. Rev. **97**, 766-769 (1955) DOI:10.1103/PhysRev.97.766.

[16] S. H. Neddermeyer and C. D. Anderson, *"Note on the Nature of Cosmic Ray Particles,"* Phys. Rev. **51**, 884-886 (1937) DOI:10.1103/PhysRev.51.884.

[17] B. Pontecorvo, *"Electron and Muon Neutrinos,"* Zh. Eksp. Teor. Fiz. **37**, 1751-1757 (1959)

[18] M. Schwartz, *"Feasibility of using high-energy neutrinos to study the weak interactions,"* Phys. Rev. Lett. **4**, 306-307 (1960) DOI:10.1103/PhysRevLett.4.306.

[19] T. D. Lee and C. N. Yang, *"THEORETICAL DISCUSSIONS ON POSSIBLE HIGH-ENERGY NEUTRINO EXPERIMENTS,"* Phys. Rev. Lett. **4**, 307-311 (1960) DOI:10.1103/PhysRevLett.4.307.

[20] M. L. Perl, G. S. Abrams, A. Boyarski, M. Breidenbach, D. Briggs, F. Bulos, W. Chinowsky, J. T. Dakin, G. J. Feldman and C. E. Friedberg, *et al. "Evidence for Anomalous Lepton Production in e+ - e- Annihilation,"* Phys. Rev. Lett. **35**, 1489-1492 (1975) DOI:10.1103/PhysRevLett.35.1489.

[21] K. Kodama *et al.* [DONUT Collaboration], *"Observation of tau neutrino interactions,"* Phys. Lett. B **504**, 218 (2001). DOI:10.1016/S0370-2693(01)00307-0.

[22] N. Agafonova *et al.* [OPERA Collaboration], *"Observation of a first ν_τ candidate in the OPERA experiment in the CNGS beam,"* Phys. Lett. B **691**, 138 (2010). [arXiv:1006.1623 [hep-ex]].

[23] Z. Li *et al.* [Super-Kamiokande], *"Measurement of the tau neutrino cross section in atmospheric neutrino oscillations with Super-Kamiokande,"* Phys. Rev. D **98**, no.5, 052006 (2018) [arXiv:1711.09436 [hep-ex]].

[24] R. Abbasi *et al.* [IceCube], *"Detection of astrophysical tau neutrino candidates in IceCube,"* Eur. Phys. J. C **82**, no.11, 1031 (2022) [arXiv:2011.03561 [hep-ex]].

[25] J. Orear, G. Harris, and S. Taylor. Phys. Rev. **102**, 1676 (1956).

[26] T. D. Lee and C. N. Yang, *"Question of Parity Conservation in Weak Interactions,"* Phys. Rev. **104**, 254 (1956). DOI:10.1103/PhysRev.104.254.

[27] T. D. Lee and C. N. Yang, *"Mass Degeneracy of the Heavy Mesons,"* Phys. Rev. **102**, no.1, 290-291 (1956). DOI:10.1103/PhysRev.102.290.

[28] C. S. Wu, E. Ambler, R. W. Hayward, D. D. Hoppes and R. P. Hudson, *"Experimental Test of Parity Conservation in β Decay,"* Phys. Rev. **105**, 1413 (1957). DOI:10.1103/PhysRev.105.1413.

[29] R. L. Garwin, L. M. Lederman and M. Weinrich, *"Observations of the Failure of Conservation of Parity and Charge Conjugation in Meson Decays: The Magnetic Moment of the Free Muon,"* Phys. Rev. **105**, 1415-1417 (1957) DOI:10.1103/PhysRev.105.1415.

[30] E. C. G. Sudarshan and R. E. Marshak, *"Chirality invariance and the universal Fermi interaction,"* Phys. Rev. **109**, 1860 (1958). DOI:10.1103/PhysRev.109.1860.2.

[31] R. P. Feynman and M. Gell-Mann, *"Theory of Fermi interaction,"* Phys. Rev. **109**, 193 (1958). DOI:10.1103/PhysRev.109.193.

[32] J. J. Sakurai, *"Mass reversal and weak interactions,"* Nuovo Cim. **7**, 649 (1958). DOI:10.1007/BF02781569.

[33] N. Cabibbo, *"Unitary Symmetry and Leptonic Decays,"* Phys. Rev. Lett. **10**, 531-533 (1963). DOI:10.1103/PhysRevLett.10.531.

[34] S. L. Glashow, J. Iliopoulos and L. Maiani, *"Weak Interactions with Lepton-Hadron Symmetry,"* Phys. Rev. D **2**, 1285-1292 (1970). DOI:10.1103/PhysRevD.2.1285.

[35] The Internal Constitution of the Stars, A. S. Eddington, The Scientific Monthly Vol. 11, No. 4 (Oct., 1920), pp. 297-303.

[36] P. Jenni and T. S. Virdee, *"The Discovery of the Higgs Boson at the LHC,"* DOI:10.1007/978-3-030-38207-0_6

[37] B. Messerly, *"Single Charged Pion Production by Muon Neutrinos in the MINERvA Detector Using the NuMI Beam"*, Ph.D. Thesis (2019) - DOI:10.2172/1599317.

[38] J. Steinberger, *"The history of neutrinos, 1930-1985. What have we learned about neutrinos? What have we learned using neutrinos?,"* Annals Phys. **327**, 3182-3205 (2012) DOI:10.1016/j.aop.2012.07.012

[39] M. Khabibullin [T2K], EPJ Web Conf. **191**, 03001 (2018) doi:10.1051/epjconf/201819103001

[40] B. Pontecorvo, *"Mesonium and anti-mesonium,"* Sov. Phys. JETP **6**, 429 (1957)

[41] Z. Maki, M. Nakagawa and S. Sakata, *"Remarks on the unified model of elementary particles,"* Prog. Theor. Phys. **28**, 870-880 (1962) DOI:10.1143/PTP.28.870.

[42] L. Wolfenstein, *"Neutrino Oscillations and Stellar Collapse,"* Phys. Rev. D **20**, 2634-2635 (1979) DOI:10.1103/PhysRevD.20.2634.

[43] S. P. Mikheyev and A. Y. Smirnov, *"Resonance Amplification of Oscillations in Matter and Spectroscopy of Solar Neutrinos,"* Sov. J. Nucl. Phys. **42**, 913-917 (1985)

[44] M. Sajjad Athar, A. Fatima and S. K. Singh, *"Neutrinos and their interactions with matter,"* Prog. Part. Nucl. Phys. **129**, 104019 (2023) DOI:10.1016/j.ppnp.2022.104019

[45] P. Lipari, M. Lusignoli and F. Sartogo, *"The Neutrino cross section and upward going muons,"* Phys. Rev. Lett. **74**, 4384 (1995). DOI:10.1103/PhysRevLett.74.4384.

[46] S. J. Barish, M. Derrick, T. Dombeck, *et al. "Study of Neutrino Interactions in Hydrogen and Deuterium: Inelastic Charged Current Reactions,"* Phys. Rev. D **19**, 2521 (1979) DOI:10.1103/PhysRevD.19.2521

[47] N. J. Baker, A. M. Cnops, P. L. Connolly, S. A. Kahn, H. G. Kirk, M. J. Murtagh, R. B. Palmer, N. P. Samios and M. Tanaka, *"Quasielastic*

Neutrino Scattering: A Measurement of the Weak Nucleon Axial Vector Form-Factor," Phys. Rev. D **23**, 2499-2505 (1981) DOI:10.1103/PhysRevD.23.2499

[48] R. A. Smith and E. J. Moniz, *"NEUTRINO REACTIONS ON NUCLEAR TARGETS,"* Nucl. Phys. B **43**, 605 (1972) [erratum: Nucl. Phys. B **101**, 547 (1975)] DOI:10.1016/0550-3213(75)90612-4

[49] Athar MS, Singh SK. *"The Physics of Neutrino Interactions,"* Cambridge University Press; 2020. DOI:10.1017/9781108489065

[50] M. Rafi Alam, M. Sajjad Athar, S. Chauhan and S. K. Singh, *"Weak charged and neutral current induced one pion production off the nucleon,"* Int. J. Mod. Phys. E **25**, 1650010 (2016). arXiv:1509.08622 [hep-ph].

[51] M. Rafi Alam, I. Ruiz Simo, M. Sajjad Athar and M. J. Vicente Vacas, *"$\bar{\nu}$ induced $\bar{K}$ production off the nucleon,"* Phys. Rev. D **8**5, 013014 (2012). [arXiv:1111.0863 [hep-ph]].

[52] A. Fatima, Z. Ahmad Dar, M. Sajjad Athar and S. K. Singh, *"Photon induced $K\Lambda$ production on the proton in the low energy region,"* Int. J. Mod. Phys. E **29**, 2050051 (2020). [arXiv:2001.10201 [hep-ph]].

[53] P. A. Zyla *et al.* [Particle Data Group], *"Review of Particle Physics,"* PTEP **2020**, no.8, 083C01 (2020) DOI:10.1093/ptep/ptaa104

[54] Robert D. Behn, *"Management and the Neutrino: The Search for Meaningful Metaphors"* DOI:https://doi.org/10.2307/976800

[55] M. Aker *et al.* [KATRIN], Phys. Rev. Lett. **123**, no.22, 221802 (2019) doi:10.1103/PhysRevLett.123.221802

[56] K. Anderson, B. Bernstein, *et al. "The NuMI Facility Technical Design Report,"* DOI:10.2172/1156372

[57] P. Adamson, K. Anderson, M. Andrews, *et al. "The NuMI Neutrino Beam,"* Nucl. Instrum. Meth. A **806**, 279-306 (2016) DOI:10.1016/j.nima.2015.08.063.

[58] I. Ambats *et al.* [MINOS], *"The MINOS Detectors Technical Design Report,"* DOI:10.2172/1861363.

[59] D. G. Michael *et al.* [MINOS], *"Observation of muon neutrino disappearance with the MINOS detectors and the NuMI neutrino beam,"* Phys. Rev. Lett. **97**, 191801 (2006) DOI : 10.1103/PhysRevLett.97.191801 [arXiv:hep-ex/0607088 [hep-ex]].

[60] D. S. Ayres *et al.* [NOvA], *"NOvA: Proposal to Build a 30 Kiloton Off-Axis Detector to Study $\nu_\mu \to \nu_e$ Oscillations in the NuMI Beamline,"* [arXiv:hep-ex/0503053 [hep-ex]].

[61] Fermilab, *"Fermilab accelerator complex"*.

[62] P. Adamson, K. Anderson, M. Andrews, R. Andrews, I. Anghel, D. Augustine, A. Aurisano, S. Avvakumov, D. S. Ayres and B. Baller, *et al. "The NuMI Neutrino Beam,"* Nucl. Instrum. Meth. A **806**, 279-306 (2016) [arXiv:1507.06690 [physics.acc-ph]].

[63] Christian Van Nguyen, *"Measurement of the muon neutrino and helium semi-inclusive single and double differential cross-section at MINERvA,"*, Ph.D. thesis, University of Florida, 2023.

[64] D. Ruterbories *et al.* [MINERvA], *"Measurement of inclusive charged-current ν_μ cross sections as a function of muon kinematics at $< E_\nu > \sim$ 6 GeV on hydrocarbon,"* Phys. Rev. D **104**, no.9, 092007 (2021) DOI:10.1103/PhysRevD.104.092007.

[65] L. Aliaga *et al.* [MINERvA], *"Design, Calibration, and Performance of the MINERvA Detector,"* Nucl. Instrum. Meth. A **743**, 130-159 (2014) [arXiv:1305.5199 [physics.ins-det]].

[66] MINERvA Doc-6514-v12.

[67] C. Patrick, *"Measurement of the Antineutrino Double-Differential Charged-Current Quasi-Elastic Scattering Cross Section at MINERvA,"* DOI:10.1007/978-3-319-69087-2.

[68] B. Hoeneisen J. Estrada, C. Garcia and P. Rubinov, *"MCM II and the Trip chip,"* FERMILAB-TM-2226, 2002.

[69] R. Brun and F. Rademakers, *"ROOT: An object oriented data analysis framework,"* Nucl. Instrum. Meth. A **389**, 81-86 (1997) DOI:10.1016/S0168-9002(97)00048-X.

[70] Patrick Fuhrmann, *"dCache, the Overview"*, Technical report, Deutsches Elektronen Synchrotron.

[71] A. Ramirez, *"First Direct Measurement of Nuclear Dependence of Coherent Pion Production"*, tech. rep. 30658. Fermilab Joint Theoretical and Experimental Physics Seminar (University of Pennsylvania, June 2022).

[72] D. G. Michael *et al.* [MINOS], *"The Magnetized steel and scintillator calorimeters of the MINOS experiment,"* Nucl. Instrum. Meth. A **596**, 190-228 (2008) DOI:10.1016/j.nima.2008.08.003.

[73] P. Adamson *et al.* [MINOS], *"Neutrino and Antineutrino Inclusive Charged-current Cross Section Measurements with the MINOS Near Detector,"* Phys. Rev. D **81**, 072002 (2010) [arXiv:0910.2201 [hep-ex]].

[74] R. P. Feynman, *"Simulating Physics with Computers"*, International Journal of Theoretical Physics, textbf21, 6-7 (1982).

[75] S. Agostinelli *et al.* [GEANT4], *"GEANT4–a simulation toolkit,"* Nucl. Instrum. Meth. A **506**, 250-303 (2003) DOI:10.1016/S0168-9002(03)01368-8.

[76] B. Andersson, G. Gustafson and B. Nilsson-Almqvist, *"A Model for Low p(t) Hadronic Reactions, with Generalizations to Hadron - Nucleus and Nucleus-Nucleus Collisions,"* Nucl. Phys. B **281**, 289-309 (1987) DOI:10.1016/0550-3213(87)90257-4.

[77] C. Alt *et al.* [NA49], *"Inclusive production of charged pions in p+C collisions at 158-GeV/c beam momentum,"* Eur. Phys. J. C **49**, 897-917 (2007) [arXiv:hep-ex/0606028 [hep-ex]].

[78] Andrey V. Lebedev, *"Ratio of pion kaon production in proton carbon interactions"*, PhD thesis, Harvard U., 2007.

[79] N. Abgrall *et al.* [NA61/SHINE], *"Measurements of Cross Sections and Charged Pion Spectra in Proton-Carbon Interactions at 31 GeV/c,"* Phys. Rev. C **84**, 034604 (2011) [arXiv:1102.0983 [hep-ex]].

[80] A. Ferrari, P. R. Sala, A. Fasso and J. Ranft, *"FLUKA: A multi-particle transport code (Program version 2005),"* DOI:10.2172/877507.

[81] T. T. Böhlen *et al. "The FLUKA Code: Developments and Challenges for High Energy and Medical Applications,"* Nucl. Data Sheets **120**, 211-214 (2014) DOI:10.1016/j.nds.2014.07.049.

[82] L. Aliaga, L. Fields, M. Kiveni, M. Kordosky, and A. Norrick, *"TN004: A brief documentation of the flux"*, 2015 Available at MINERvA DocDB.

[83] D. Ruterbories *et al.* [MINERvA], *"Constraining the NuMI neutrino flux using inverse muon decay reactions in MINERvA,"* Phys. Rev. D **104**, no.9, 092010 (2021) [arXiv:2107.01059 [hep-ex]].

[84] L. Zazueta *et al.*, *"Improved constraint on the MINERvA medium energy neutrino flux using $e^- \to e^-$ data"*, 2022 [arXiv:2209.05540 [hep-ex]] .

[85] Sheldon L. Glashow, *"TOWARDS A UNIFIED THEORY - THREADS IN A TAPESTRY"*, Nobel Lecture, December 8, 1979.

[86] C. Andreopoulos *et al. "The GENIE Neutrino Monte Carlo Generator,"* Nucl. Instrum. Meth. A **614**, 87-104 (2010) [arXiv:0905.2517 [hep-ph]].

[87] C. Andreopoulos, C. Barry, S. Dytman, H. Gallagher, T. Golan, R. Hatcher, G. Perdue and J. Yarba, *"The GENIE Neutrino Monte Carlo Generator: Physics and User Manual,"*, 2015 [arXiv:1510.05494 [hep-ph]].

[88] H. R. Gallagher [Soudan 2], *"Measurement of the atmospheric neutrino flavor ratio in Soudan 2,"* Nucl. Phys. B Proc. Suppl. **66**, 290-293 (1998) DOI:10.1016/S0920-5632(98)00054-1.

[89] A. Bodek and J. L. Ritchie, *"Fermi Motion Effects in Deep Inelastic Lepton Scattering from Nuclear Targets,"* Phys. Rev. D **23**, 1070 (1981) DOI:10.1103/PhysRevD.23.1070.

[90] C. H. Llewellyn Smith, *"Neutrino Reactions at Accelerator Energies,"* Phys. Rept. **3**, 261-379 (1972) DOI:10.1016/0370-1573(72)90010-5.

[91] R. Bradford, A. Bodek, H. S. Budd and J. Arrington, *"A New parameterization of the nucleon elastic form-factors,"* Nucl. Phys. B Proc. Suppl. **159**, 127-132 (2006) [arXiv:hep-ex/0602017 [hep-ex]].

[92] D. Rein and L. M. Sehgal, *"Neutrino Excitation of Baryon Resonances and Single Pion Production,"* Annals Phys. **133**, 79-153 (1981) DOI:10.1016/0003-4916(81)90242-6.

[93] A. Bodek, I. Park and U. k. Yang, *"Improved low Q**2 model for neutrino and electron nucleon cross sections in few GeV region,"* Nucl. Phys. B Proc. Suppl. **139**, 113-118 (2005) DOI:10.1016/j.nuclphysbps.2004.11.208.

[94] T. Yang, C. Andreopoulos, H. Gallagher and P. Kehayias, *"A hadronization model for the MINOS experiment,"* AIP Conf. Proc. **967**, no.1, 269-275 (2007) DOI:10.1063/1.2834490.

[95] R. Gran, J. Nieves, F. Sanchez and M. J. Vicente Vacas, *"Neutrino-nucleus quasi-elastic and 2p2h interactions up to 10 GeV,"* Phys. Rev. D **88**, no.11, 113007 (2013) DOI:10.1103/PhysRevD.88.113007.

[96] J. Nieves, I. Ruiz Simo and M. J. Vicente Vacas, *"Inclusive Charged–Current Neutrino–Nucleus Reactions,"* Phys. Rev. C **83**, 045501 (2011) DOI:10.1103/PhysRevC.83.045501.

[97] J. Schwehr, *et al.* *"GENIE implementation of IFIC Valencia model for QE-like 2p2h neutrino-nucleus cross section"*, Jan, 2016 [arXiv:1601.02038 [hep-ph]].

[98] S. Dytman, *"Neutrino event generators,"* AIP Conf. Proc. **896**, no.1, 178-184 (2007) DOI:10.1063/1.2720468.

[99] C. Wilkinson, P. Rodrigues, S. Cartwright, L. Thompson and K. McFarland, *"Reanalysis of bubble chamber measurements of muon-neutrino induced single pion production,"* Phys. Rev. D **90**, no.11, 112017 (2014) [arXiv:1411.4482 [hep-ex]].

[100] P. Rodrigues, C. Wilkinson and K. McFarland, *"Constraining the GENIE model of neutrino-induced single pion production using reanalyzed bubble chamber data,"* Eur. Phys. J. C **76**, no.8, 474 (2016) arXiv:1601.01888 [hep-ex].

[101] R. Gran, *"Model uncertainties for Valencia RPA effect for MINERvA,"* (May 2017) arXiv:1705.02932 [hep-ex].

[102] P. A. Rodrigues *et al.* [MINERvA], *"Identification of nuclear effects in neutrino-carbon interactions at low three-momentum transfer,"* Phys. Rev. Lett. **116**, 071802 (2016) DOI:10.1103/PhysRevLett.116.071802.

[103] R. Gran *et al.* [MINERvA], *"Antineutrino Charged-Current Reactions on Hydrocarbon with Low Momentum Transfer,"* Phys. Rev. Lett. **120**, no.22, 221805 (2018) arXiv:1803.09377 [hep-ex].

[104] J. Nieves, J. E. Amaro and M. Valverde, *"Inclusive quasi-elastic neutrino reactions,"* Phys. Rev. C **70**, 055503 (2004) [erratum: Phys. Rev. C **72**, 019902 (2005)] [arXiv:nucl-th/0408005 [nucl-th]].

[105] P. Stowell *et al.* [MINERvA], *"Tuning the GENIE Pion Production Model with MINERνA Data,"* Phys. Rev. D **100**, no.7, 072005 (2019) arXiv:1903.01558 [hep-ex].

[106] R. Fruhwirth, *"Application of Kalman filtering to track and vertex fitting,"* Nucl. Instrum. Meth. A **262**, 444-450 (1987) DOI:10.1016/0168-9002(87)90887-4.

[107] Iqbal H. Sarker, *"Machine Learning: Algorithms, Real-World Applications and Research Directions"* SN COMPUT. SCI. **2**, 160 (2021) DOI:10.1007/s42979-021-00592-x

[108] F. Akbar *et al.* [MINERvA], *"Vertex finding in neutrino-nucleus interaction: a model architecture comparison"* JINST **17**, T08013 (2022) DOI:10.1088/1748-0221/17/08/T08013

[109] G. N. Perdue *et al.* [MINERvA], *"Reducing model bias in a deep learning classifier using domain adversarial neural networks in the MINERvA experiment,"* JINST **13**, no.11, P11020 (2018) arXiv:1808.08332 [physics.data-an].

[110] M. O. Wospakrik, *"Measurement of Neutrino Absolute Deep Inelastic Scattering Cross Section in Iron, Lead, Carbon and Plastic Using MINERvA Detector at E_ν = 6 GeV,"* Ph.D. thesis, Florida U. (2018).

[111] G. Barrand et al. *"GAUDI - The software architecture and framework for building LHCb data processing applications."*, In Proceedings, 11th International Conference on Computing in High-Energy and Nuclear Physics (CHEP 2000), pages 92–95, 2000.

[112] J. Mousseau. *"Optimizing High Momentum MINOS Muon Selection. MINERvA Document, 10154-v2, 2014."* URL: https://minerva-docdb.fnal.gov/cgi-bin/ sso/ShowDocument?docid=10154.

[113] I. Ambats *et al. "The MINOS Detectors Technical Design Report."* 10 1998. DOI:10.2172/1861363.

[114] V. Blobel, *"An Unfolding method for high-energy physics experiments,"* arXiv:hep-ex/0208022 [hep-ex].

[115] G. D'Agostini, *"A Multidimensional unfolding method based on Bayes' theorem,"* Nucl. Instrum. Meth. A **362**, 487-498 (1995) DOI:10.1016/0168-9002(95)00274-X.

[116] G. D'Agostini, *"Improved iterative Bayesian unfolding"*, In Alliance Workshop on Unfolding and Data Correction, Hamburg, Germany, 27–28 May 2010. arXiv:1010. 0632[physics.data-an].

[117] R. Brun and F. Rademakers, *"ROOT: An object oriented data analysis framework,"* Nucl. Instrum. Meth. A **389**, 81-86 (1997) DOI:10.1016/S0168-9002(97)00048-X.

[118] T. Adye, *"Unfolding algorithms and tests using RooUnfold,"* DOI:10.5170/CERN-2011-006.313.

[119] Adrian L. *"Instructions for Warping Studies"*, MINERvA Document database, Doc.ID 31581-v1.

[120] Quoted in an interview by Feynman.

[121] Fons Rademakers, Rene Brun, *et al. "ROOT - An Object-Oriented Data Analysis Framework. root-project/root: v6.10/04,"* August 2017.

[122] B. Messerly *et al.* [MINERvA], *"An Error Analysis Toolkit for Binned Counting Experiments,"* EPJ Web Conf. **251**, 03046 (2021) DOI:10.1051/epjconf/202125103046.

[123] C. Andreoupoulos et al., *"Updated Cross Section Model Uncertainties for the Charged Current Analysis,"* minos-doc2989-v6, minerva-doc-7450-v1 (June 2007).

[124] S. Dytman, H. Gallagher and M. Kordosky, *"Hadronic Shower Energy Scale Uncertainty in the MINOS Experiment,"* arXiv:0806.2119 [hep-ex].

[125] B. Bhattacharya, R. J. Hill and G. Paz, *"Model independent determination of the axial mass parameter in quasielastic neutrino-nucleon scattering,"* Phys. Rev. D **84**, 073006 (2011) arXiv:1108.0423 [hep-ph].

[126] A. S. Meyer, M. Betancourt, R. Gran and R. J. Hill, *"Deuterium target data for precision neutrino-nucleus cross sections,"* Phys. Rev. D **93**, no.11, 113015 (2016) arXiv:1603.03048 [hep-ph].

[127] F. J. Ernst, R. G. Sachs and K. C. Wali, *"Electromagnetic form factors of the nucleon,"* Phys. Rev. **119**, 1105-1114 (1960) DOI:10.1103/PhysRev.119.1105.

[128] A. V. Butkevich and S. P. Mikheyev, *"Test of Fermi gas model and plane-wave impulse approximation against electron-nucleus scattering data,"* Phys. Rev. C **72**, 025501 (2005) DOI:10.1103/PhysRevC.72.025501.

[129] A. A. Aguilar-Arevalo *et al.* [MiniBooNE], *"First Measurement of the Muon Neutrino Charged Current Quasielastic Double Differential Cross Section,"* Phys. Rev. D **81**, 092005 (2010) DOI:10.1103/PhysRevD.81.092005.

[130] D. Rein and L. M. Sehgal, *"Neutrino Excitation of Baryon Resonances and Single Pion Production,"* Annals Phys. **133**, 79-153 (1981) DOI:10.1016/0003-4916(81)90242-6.

[131] A. Bodek, I. Park and U. k. Yang, *"Improved low Q**2 model for neutrino and electron nucleon cross sections in few GeV region,"* Nucl. Phys. B Proc. Suppl. **139**, 113-118 (2005) DOI:10.1016/j.nuclphysbps.2004.11.208.

[132] D. Rein and L. M. Sehgal, *"Neutrino Excitation of Baryon Resonances and Single Pion Production,"* Annals Phys. **133**, 79-153 (1981) DOI:10.1016/0003-4916(81)90242-6.

[133] L. W. Whitlow et al. (SLAC-MIT), Phys. Lett. B **282**, 433 (1995).

[134] A. C. Benvenuti et al. (BCDMS), Phys. Lett. B**237**, 592 (1990).

[135] M. Arneodo et al. (NMC), Nucl. Phys. B**483**, 3 (1997).

[136] A. Bodek, I. Park and U. k. Yang, *"Improved low Q**2 model for neutrino and electron nucleon cross sections in few GeV region,"* Nucl. Phys. B Proc. Suppl. **139**, 113-118 (2005) DOI:10.1016/j.nuclphysbps.2004.11.208.

[137] L. A. Ahrens, S. H. Aronson, P. L. Connolly, B. G. Gibbard, M. J. Murtagh, S. J. Murtagh, S. Terada, D. H. White, J. L. Callas and D. Cutts, *et al. "Measurement of Neutrino - Proton and anti-neutrino - Proton Elastic Scattering,"* Phys. Rev. D **35**, 785 (1987) DOI:10.1103/PhysRevD.35.785.

[138] A. Zee, *"Parametrizing the neutrino mixing matrix,"* Phys. Rev. D **68**, 093002 (2003) DOI:10.1103/PhysRevD.68.093002.

[139] Anushree Ghosh, *"Minos matched muons tracking efficiency at medium energy,"* MINERvA doc 20760, 2018.

[140] R. Ransome, *"MINERvA Physical Description,"* MINERvA doc 6016.

[141] Max Planck, *"Scientific Autobiography: And Other Papers"*, Citadel Press, 1949 DOI:10.2307/2103486.

[142] J. J. Aubert *et al.* [European Muon], *"The ratio of the nucleon structure functions $F2_n$ for iron and deuterium,"* Phys. Lett. B **123**, 275-278 (1983) DOI:10.1016/0370-2693(83)90437-9.

Appendices

Appendix A

Selected Event Distribution

This appendix contains the figures for selected event distribution in individual target materials in the chosen combination of variables, $x - Q^2$, $W - Q^2$ and $p_z - p_t$. The selected events have been categorized by interaction channel and by the contribution of different backgrounds in the event sample. The y axis in all the figures has been scaled by a factor of 10^{-4}. The multiplier numbers in different panels represent the amount of times the events in that particular panel were scaled, to see the distribution of events in the panel better. The shaded bands represent the total (statistical + systematic uncertainties) on MC, while black bars on data points represent statistical uncertainties.

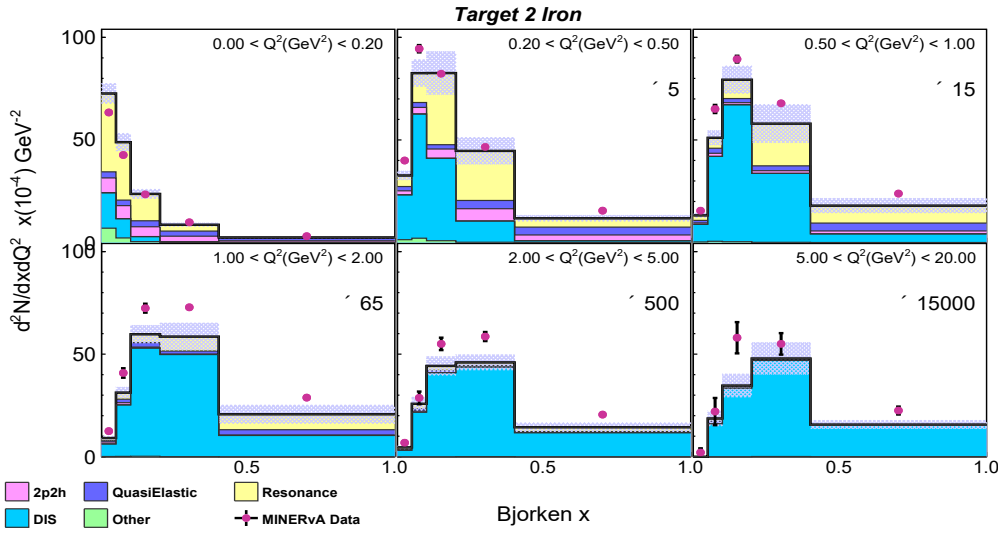

Figure A.1: Distribution of selected events for target 2 iron, in bins of $x - Q^2$.

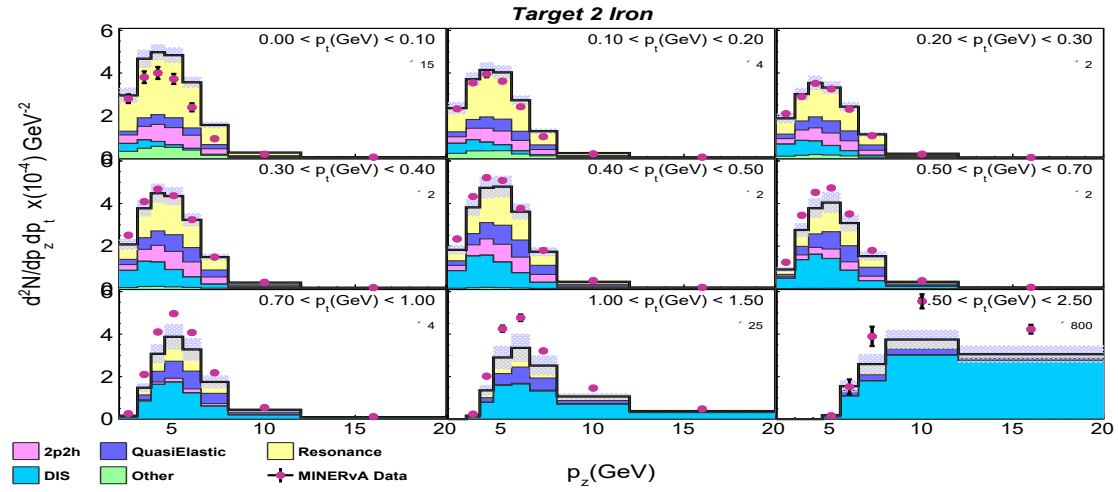

(a)

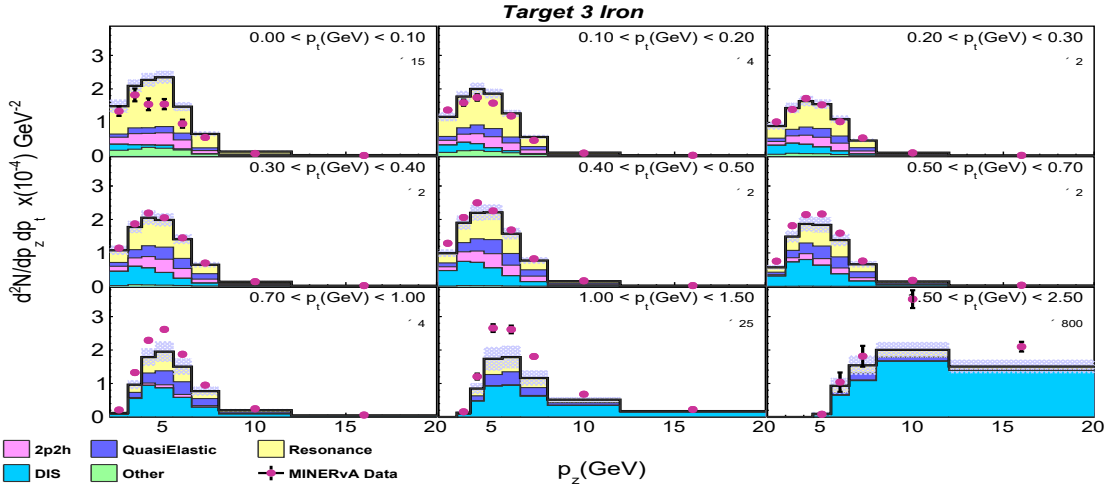

(b)

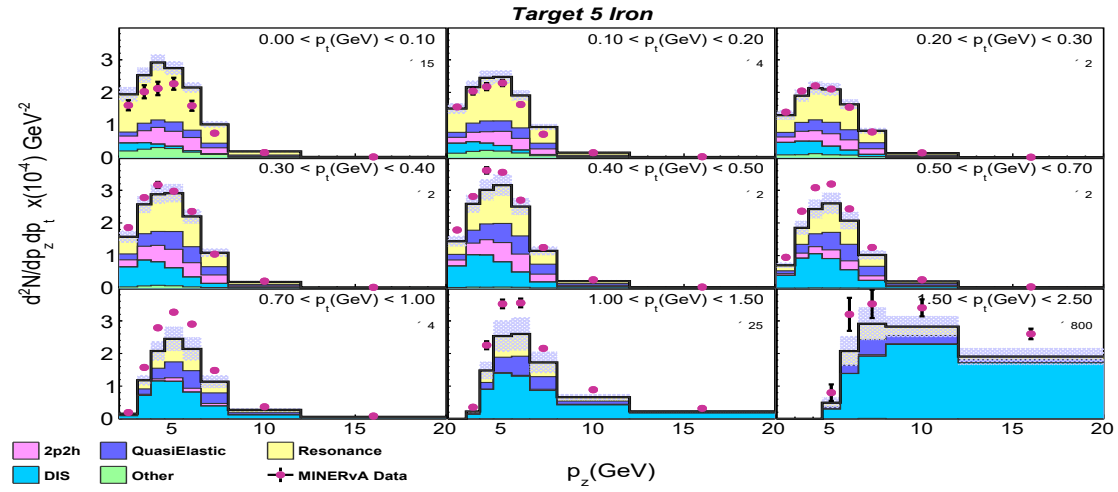

(c)

Figure A.2: Selected event distribution for iron in p_z-p_t bins for (a) target 2, (b) target 3, and (c) target 5.

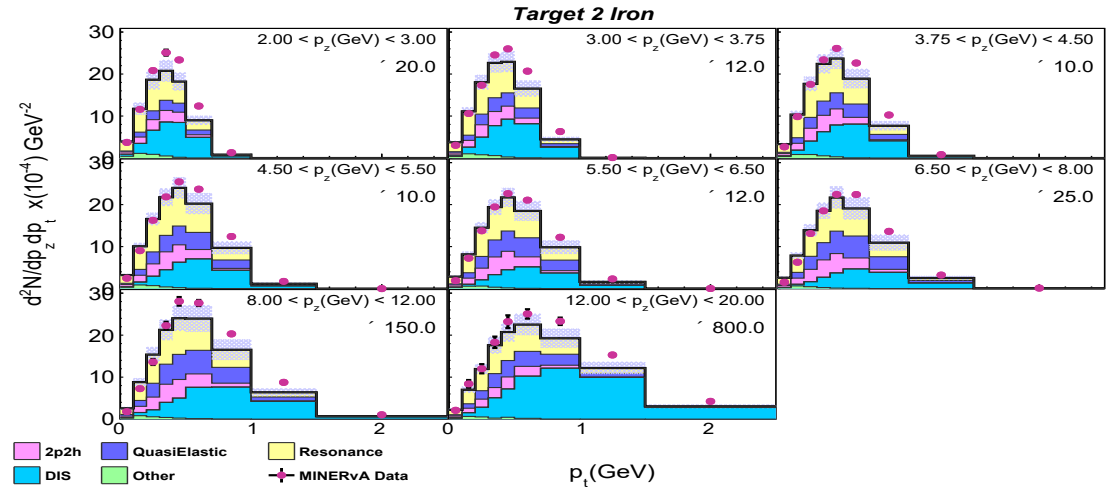

(a)

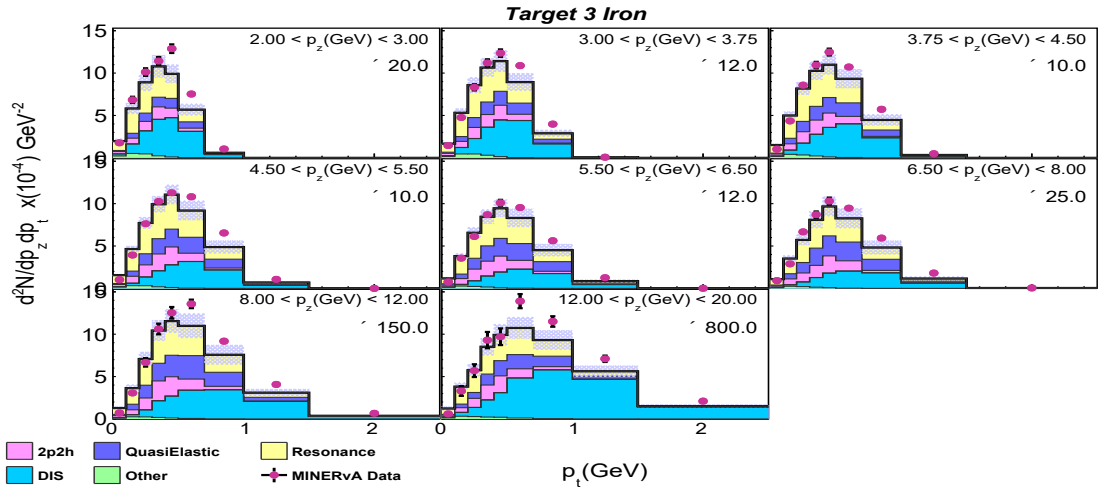

(b)

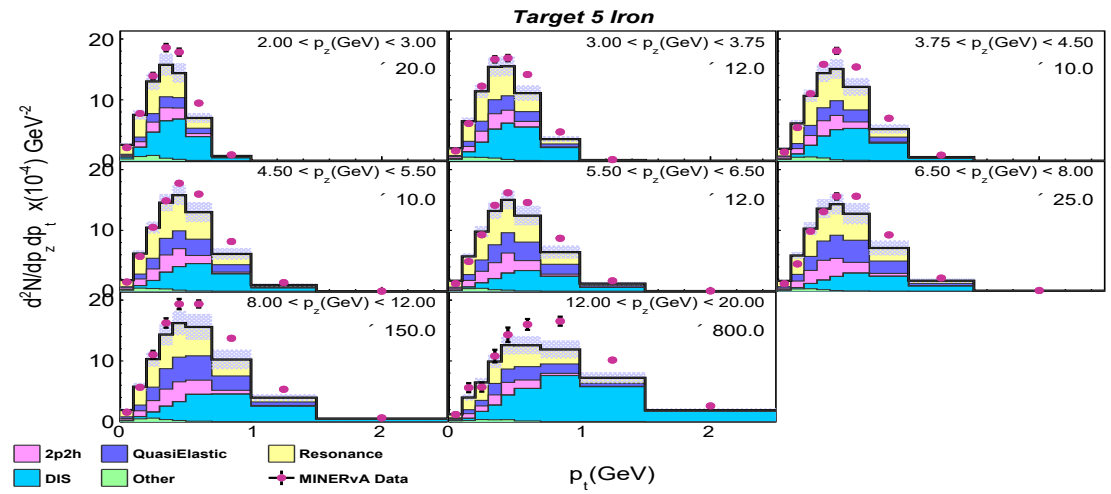

(c)

Figure A.3: Selected event distribution for iron in (a) target 2, (b) target 3, and (c) target 5, in p_t-p_z bins.

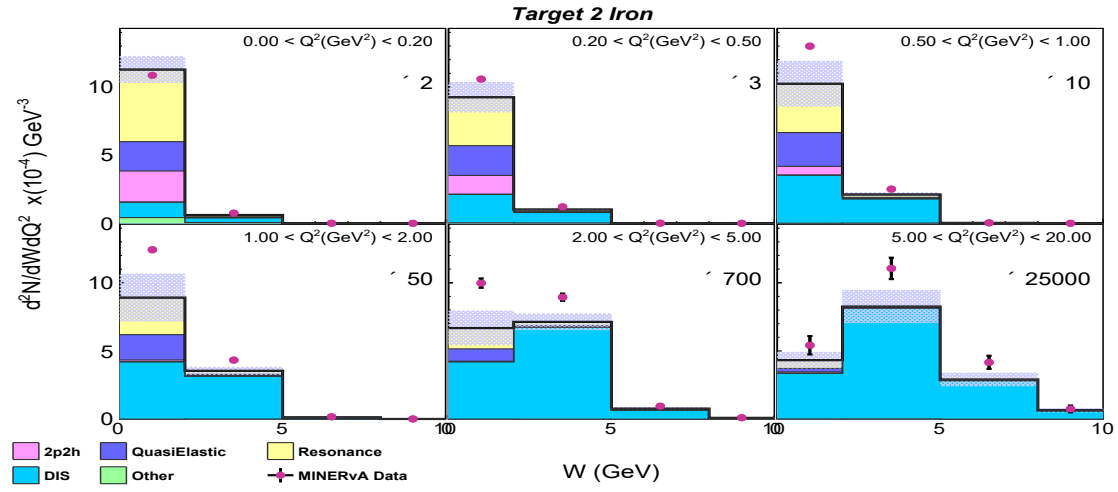

(a)

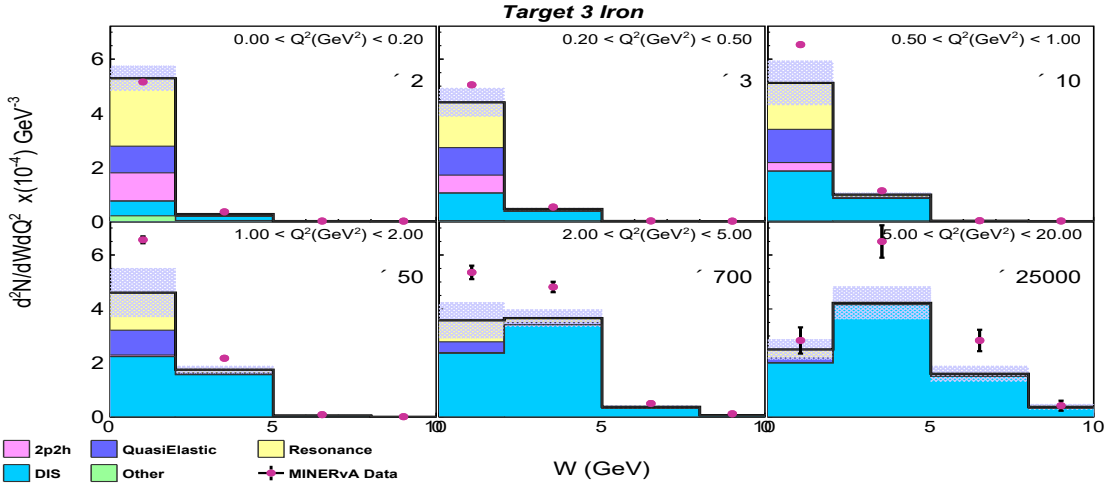

(b)

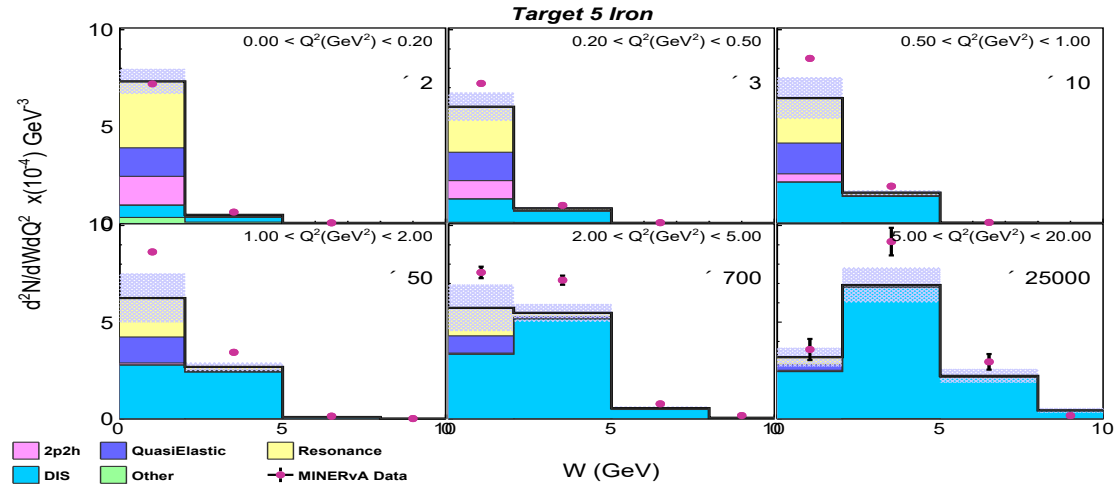

(c)

Figure A.4: Selected event distribution for iron in (a) target 2, (b) target 3, and (c) target 5, in $W - Q^2$ bins.

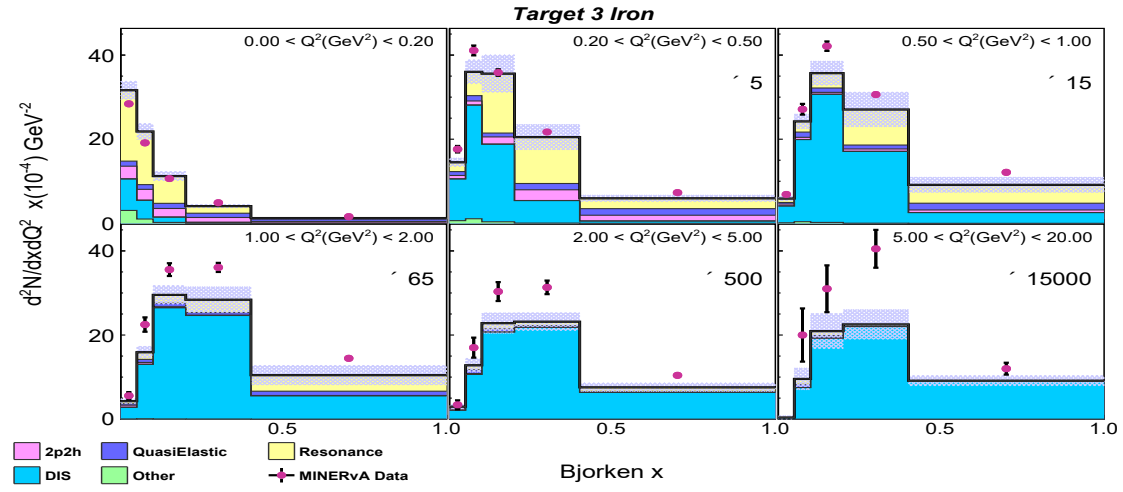

(a)

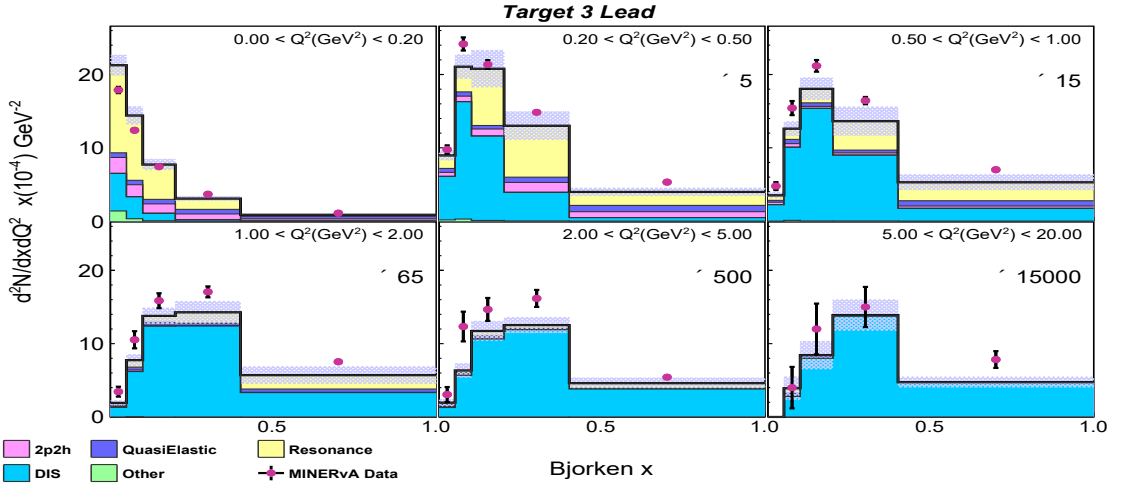

(b)

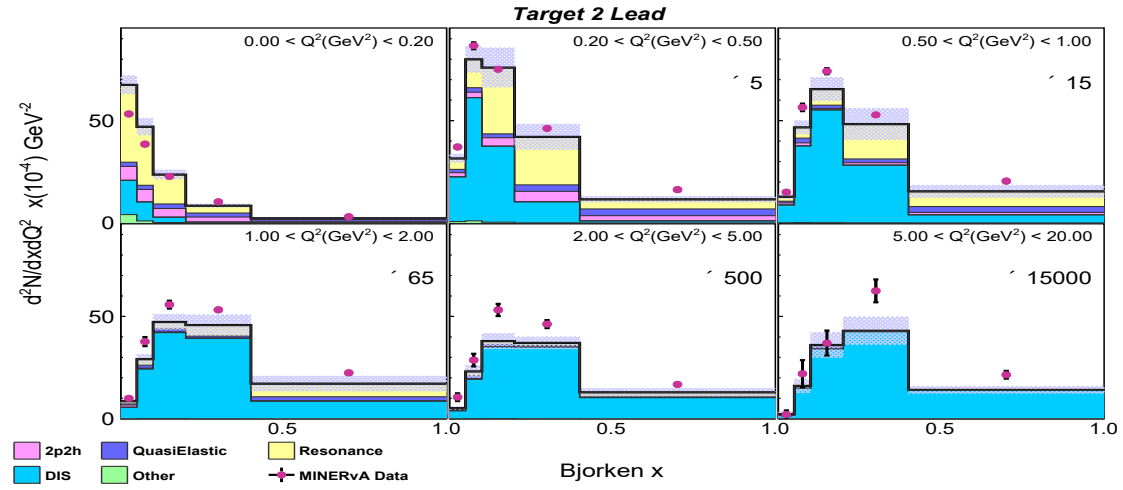

(c)

Figure A.5: Selected event distribution in (a) iron target 3, (b) lead target 3, and (c) lead target 2, in $x - Q^2$ bins.

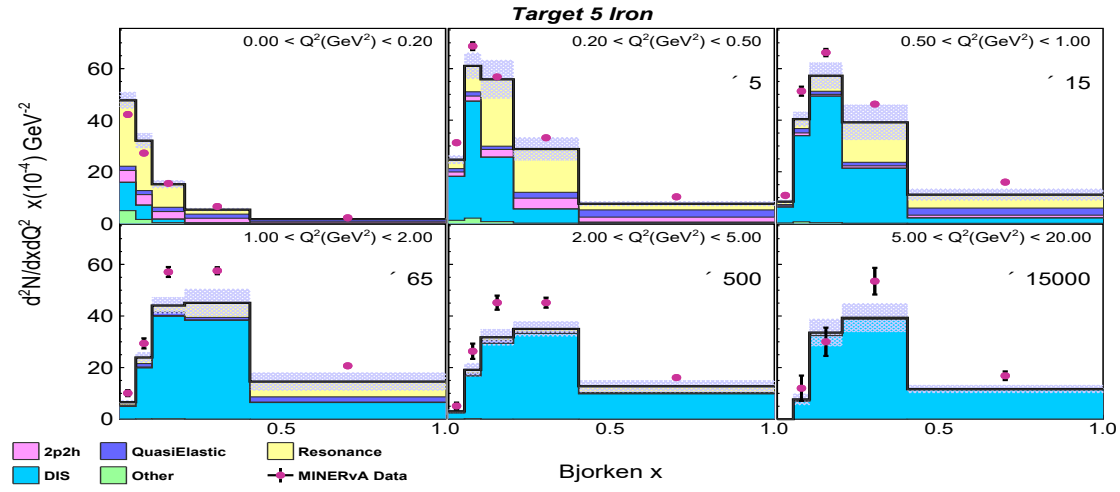

(a)

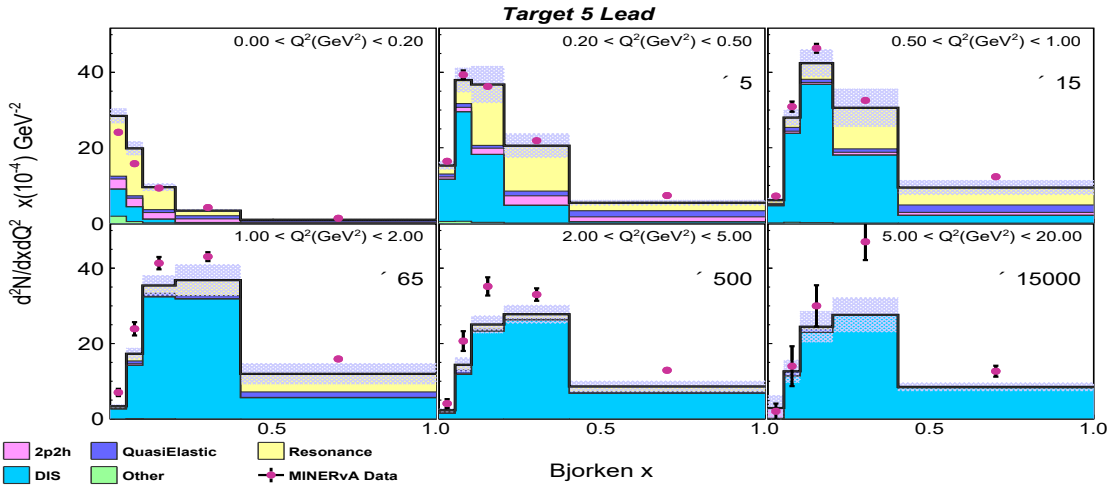

(b)

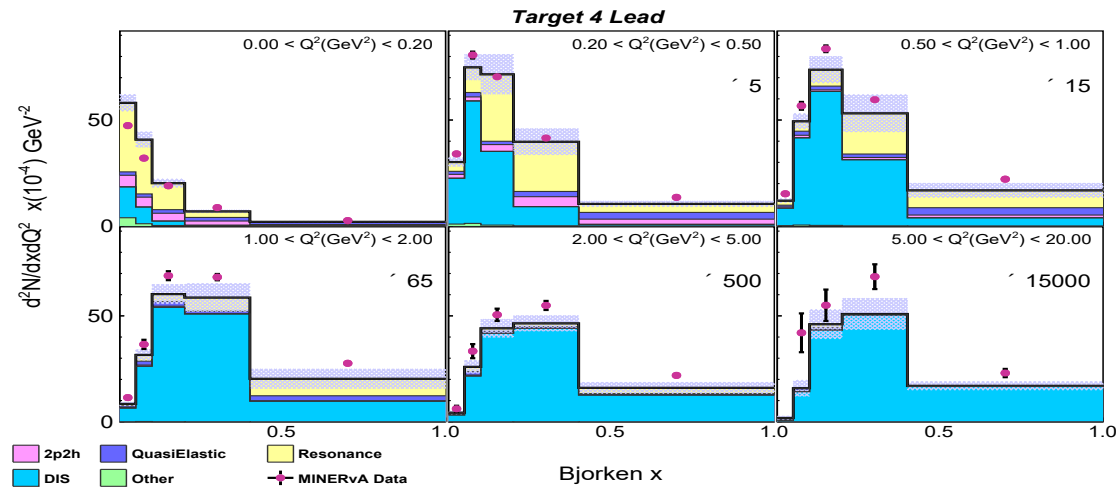

(c)

Figure A.6: Selected event distribution in (a) iron target 5, (b) lead target 5, and (c) lead target 4, in $x - Q^2$ bins.

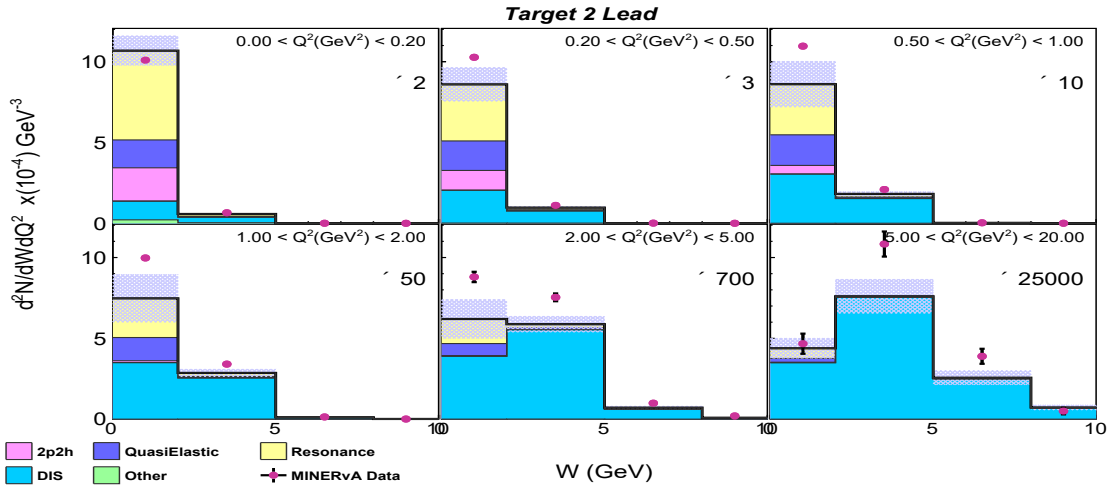

(a)

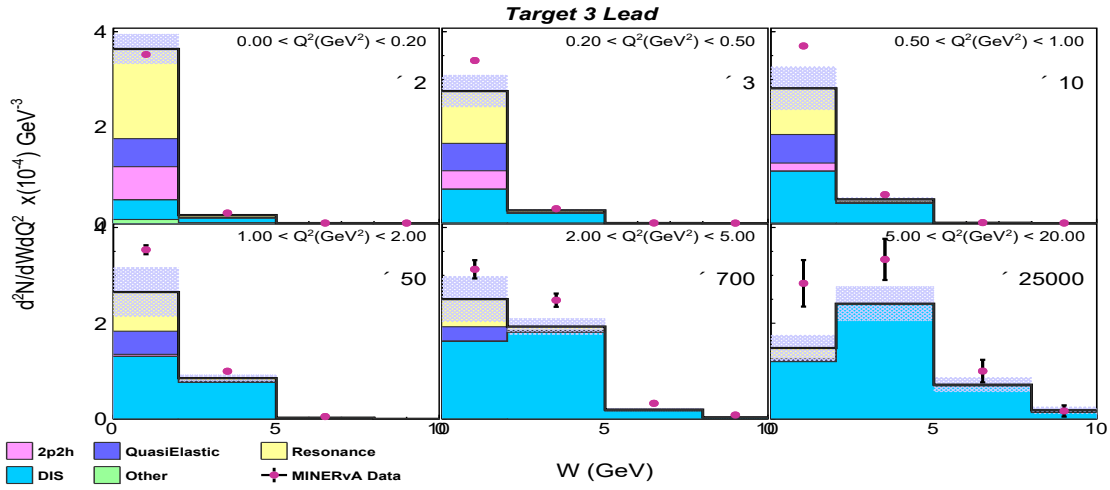

(b)

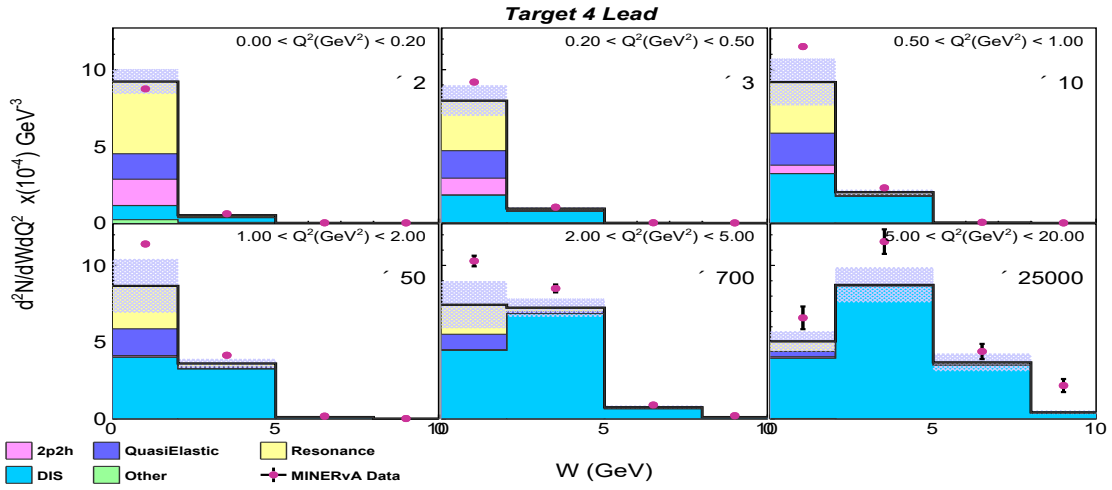

(c)

Figure A.7: Selected event distribution for lead in (a) target 2, (b) target 3 and (c) target 4, in $W - Q^2$ bins.

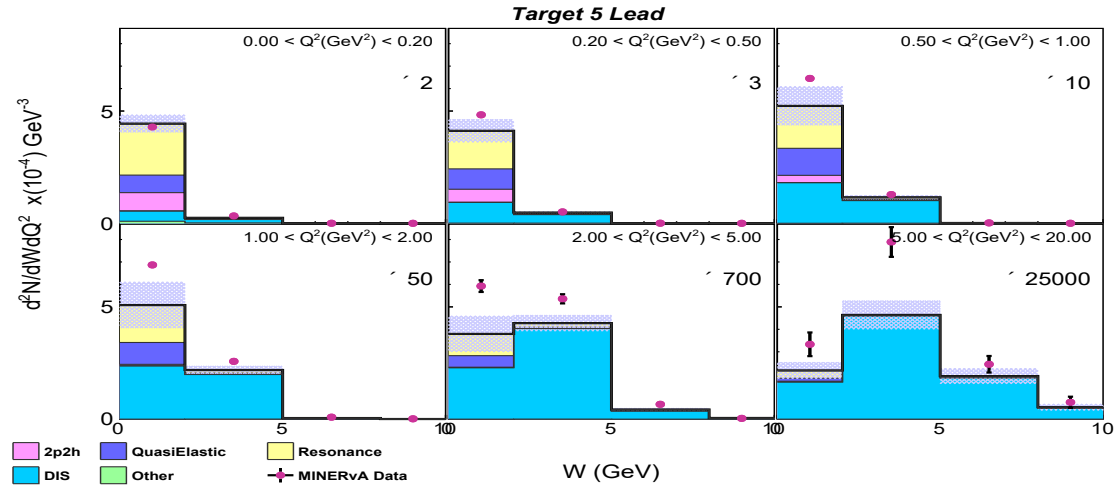

(a)

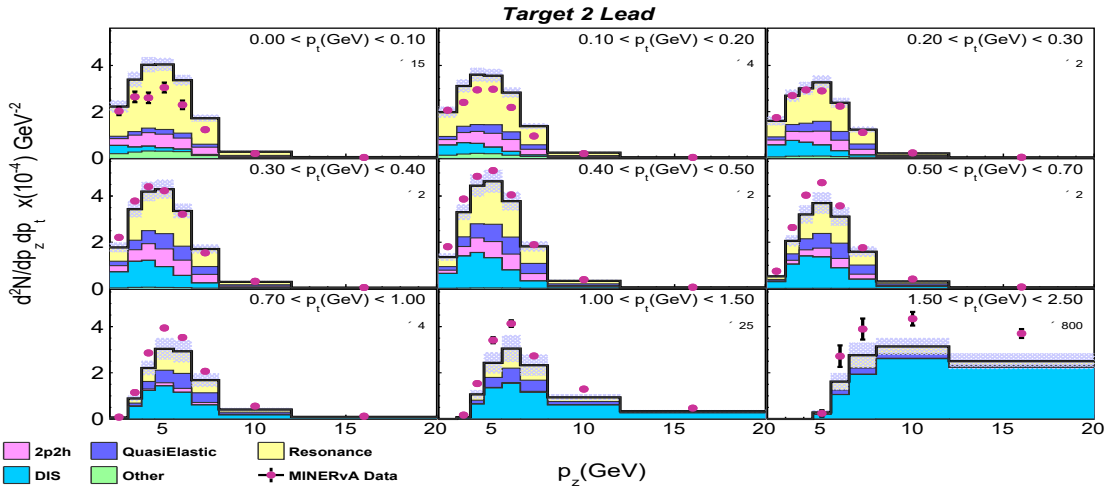

(b)

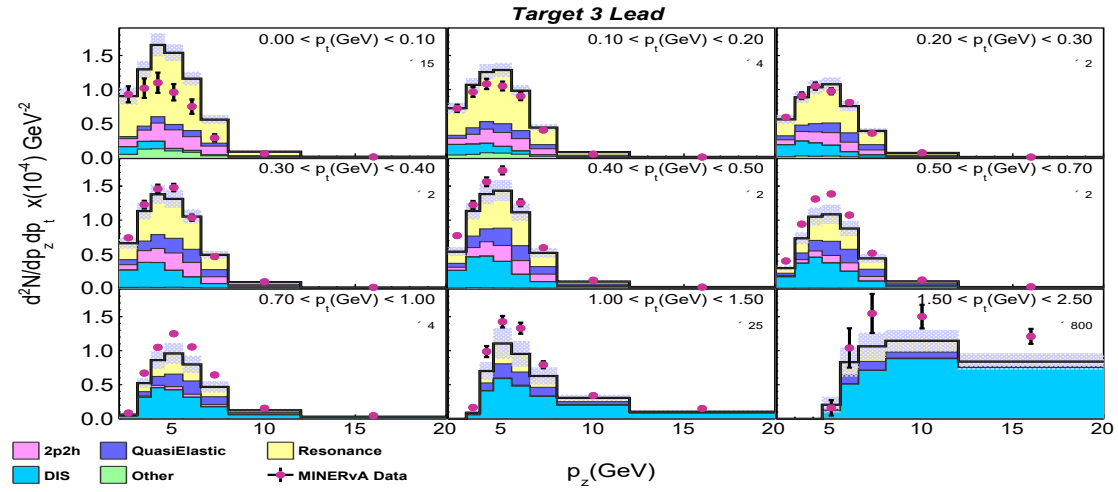

(c)

Figure A.8: Selected event distribution for lead: (a) target 5 in W-Q^2 bins, and (b) target 2 and (c) target 3 in p_z-p_t bins.

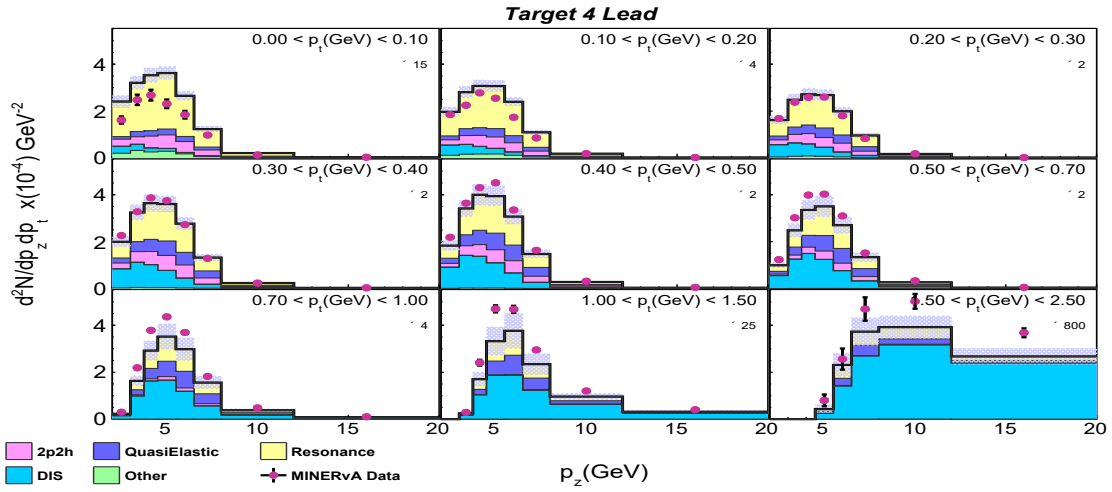

(a)

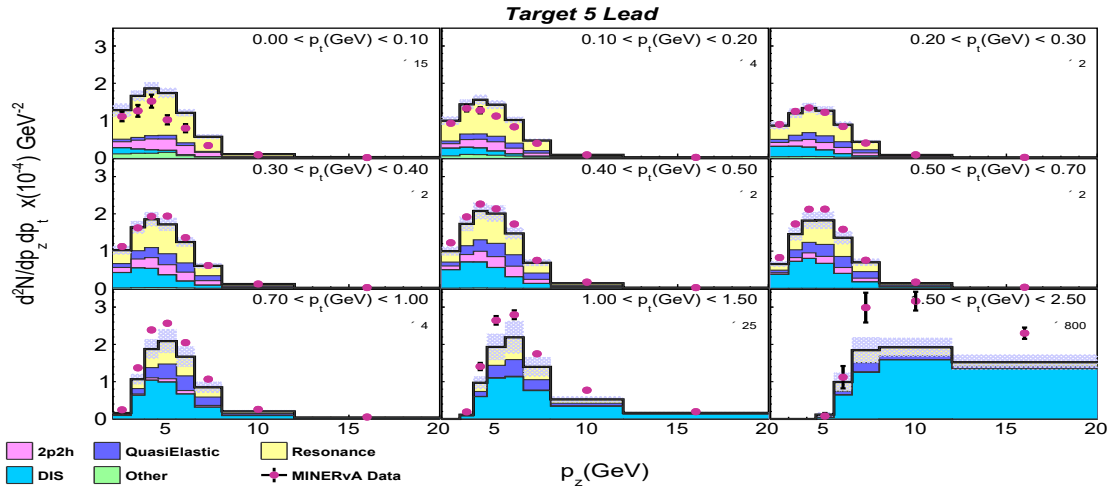

(b)

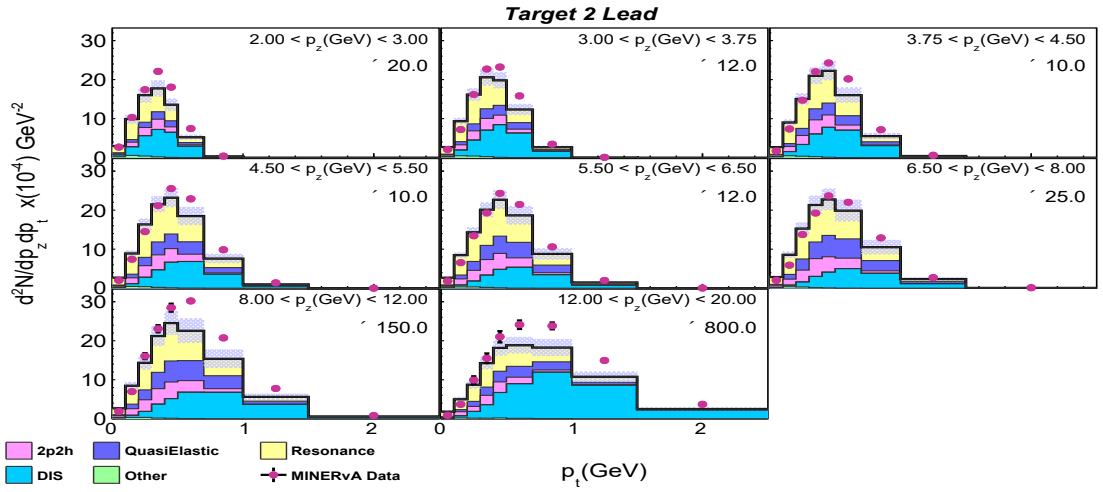

(c)

Figure A.9: Selected event distribution for lead: (a) target 4 and (b) target 5 in $p_z - p_t$ bins and (c) target 2 in p_t-p_z bins.

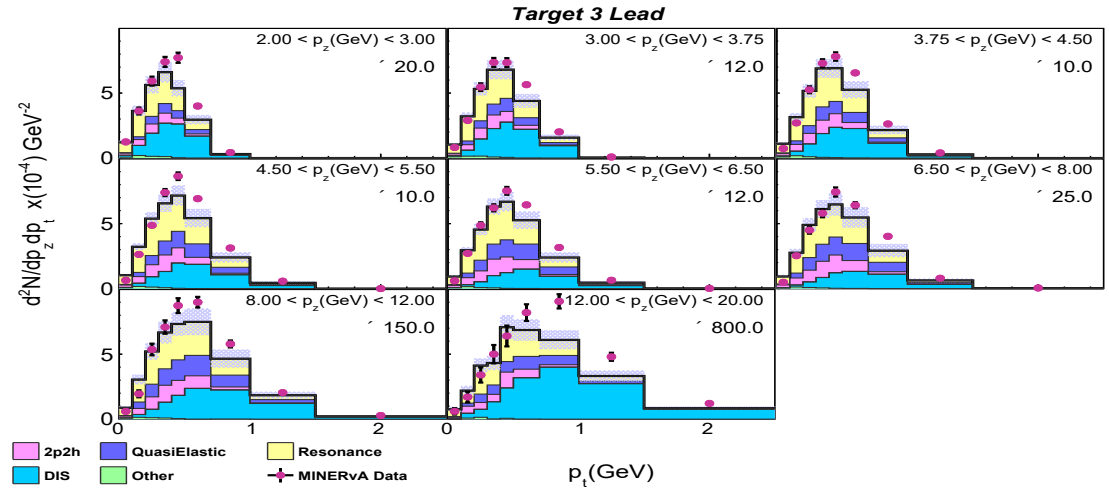

(a)

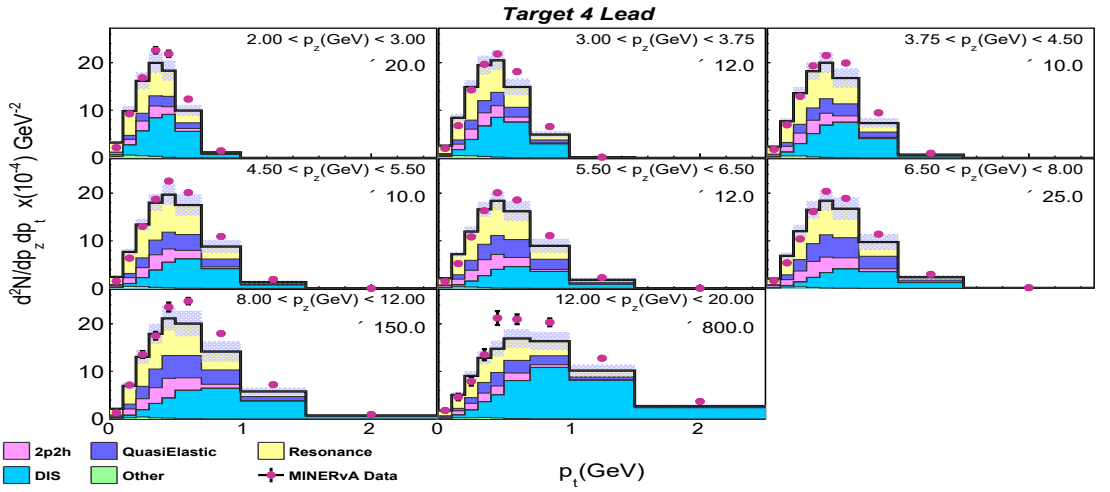

(b)

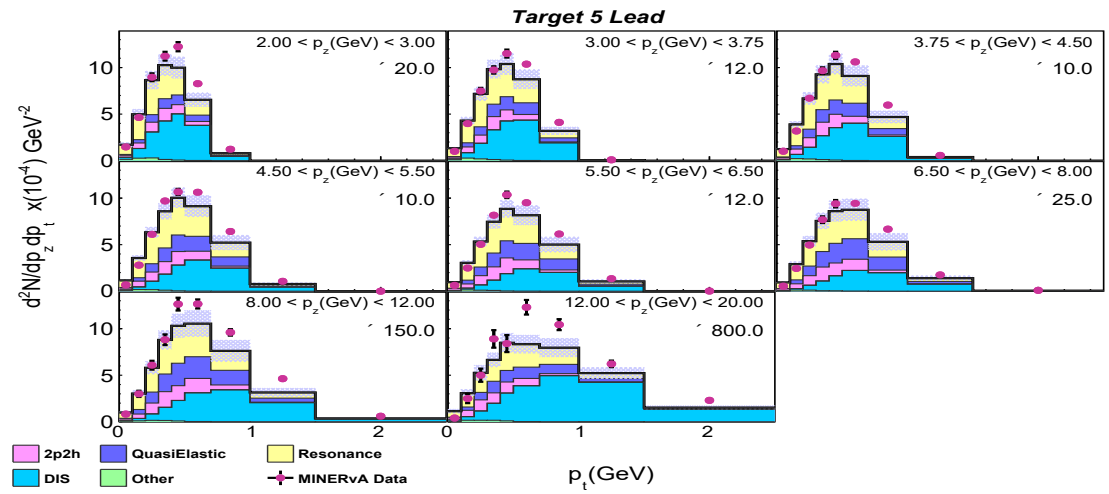

(c)

Figure A.10: Selected event distribution for lead: (a) target 3, (b) target 4 and (c) target 5 in p_t-p_z bins.

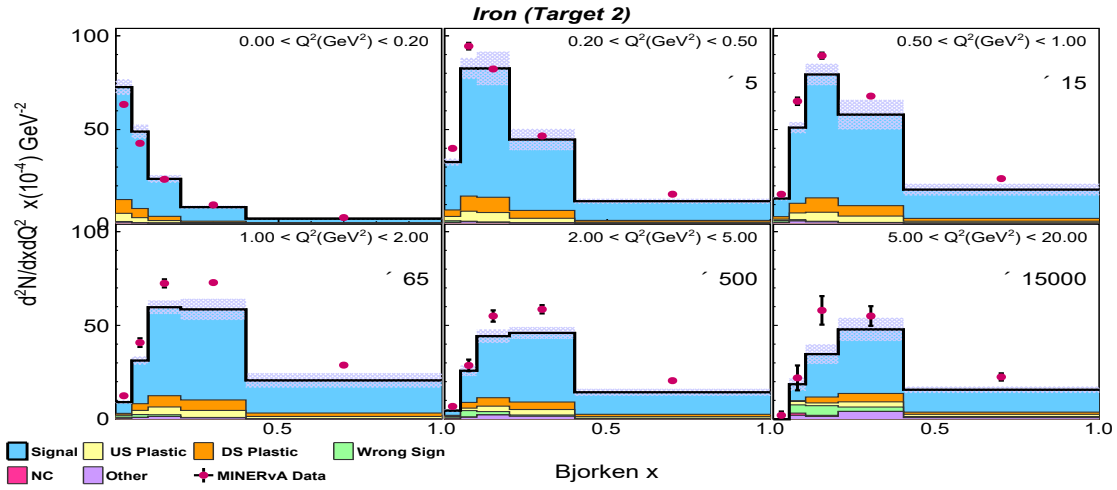

(a)

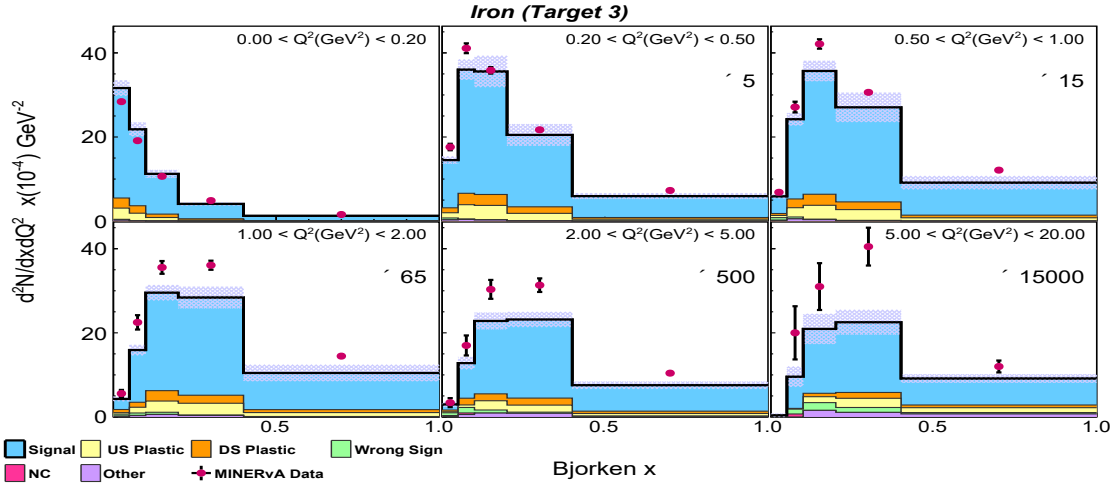

(b)

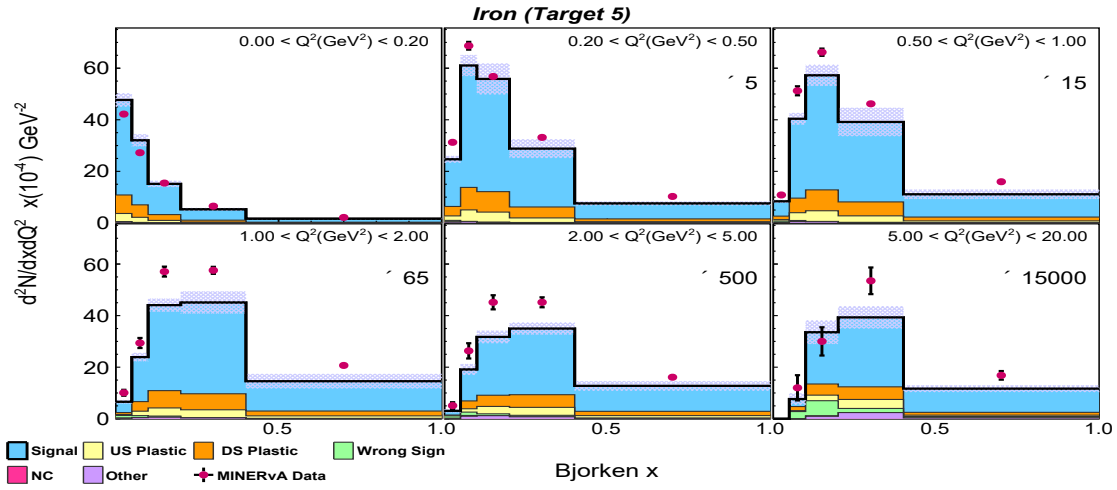

(c)

Figure A.11: Selected event distribution for iron: (a) target 2, (b) target 3 and (c) target 5 in $x - Q^2$ bins.

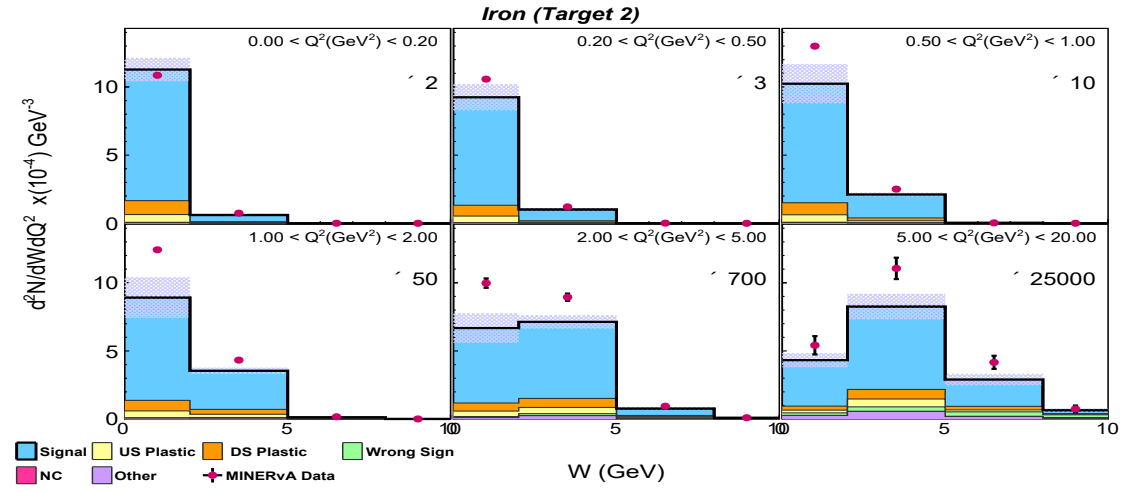

(a)

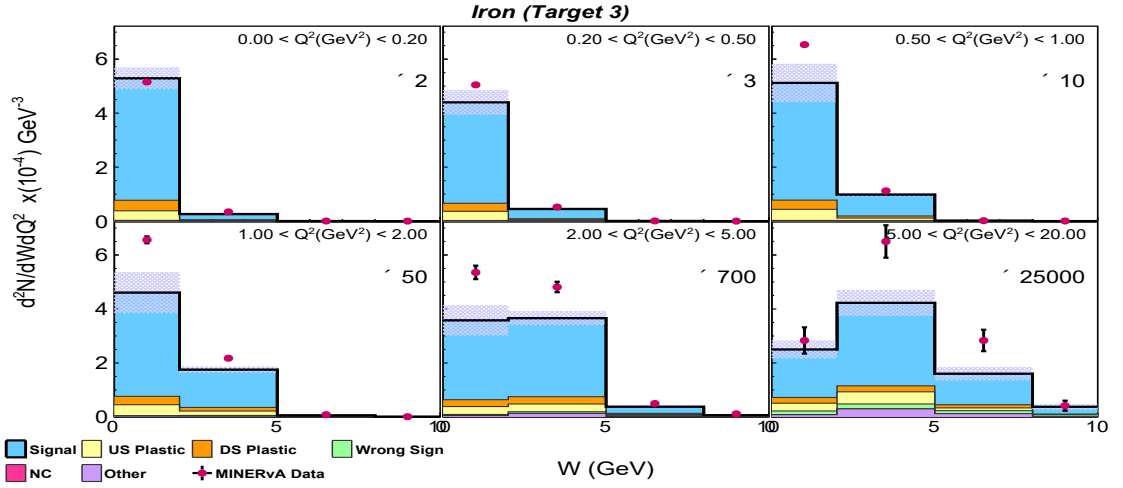

(b)

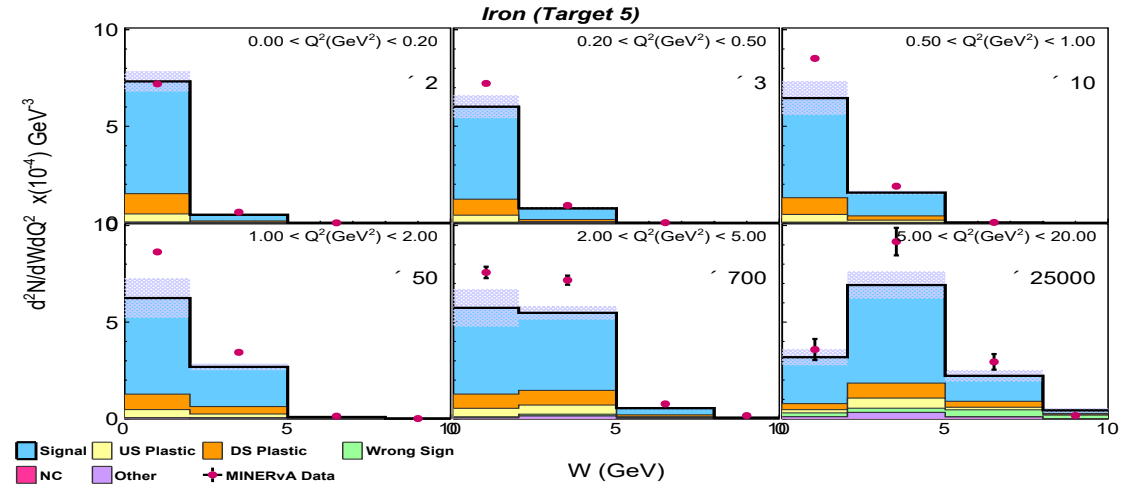

(c)

Figure A.12: Selected event distribution for iron: (a) target 2, (b) target 3 and (c) target 5 in $W - Q^2$ bins.

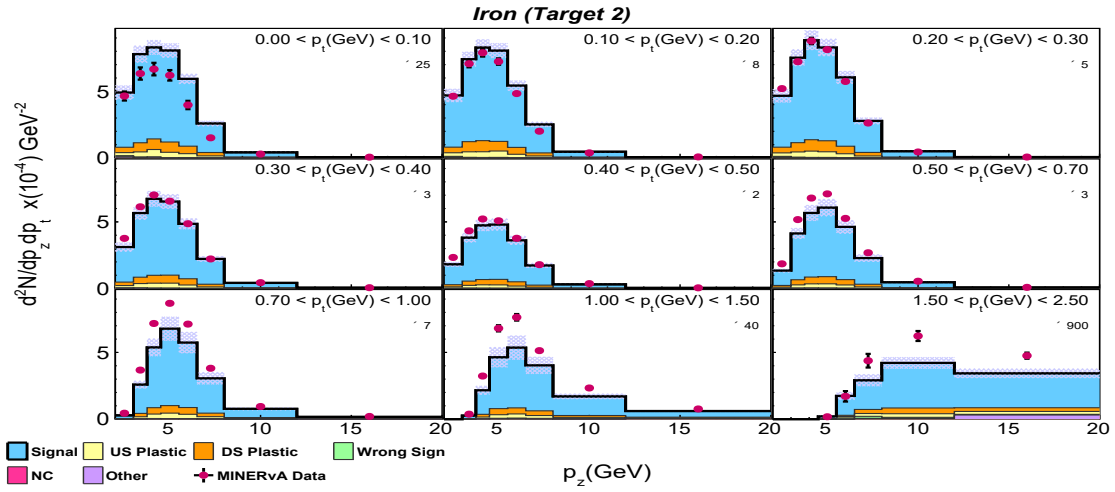

(a)

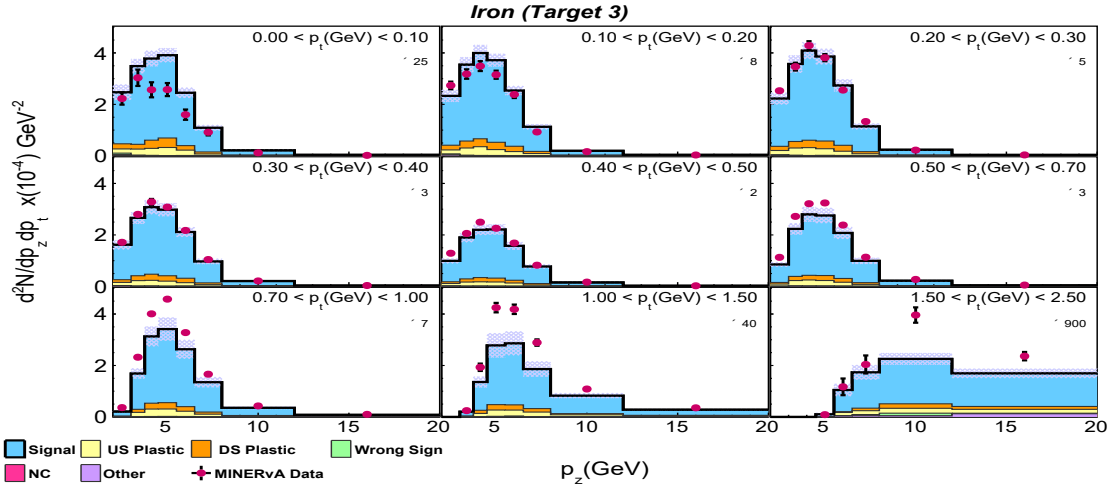

(c)

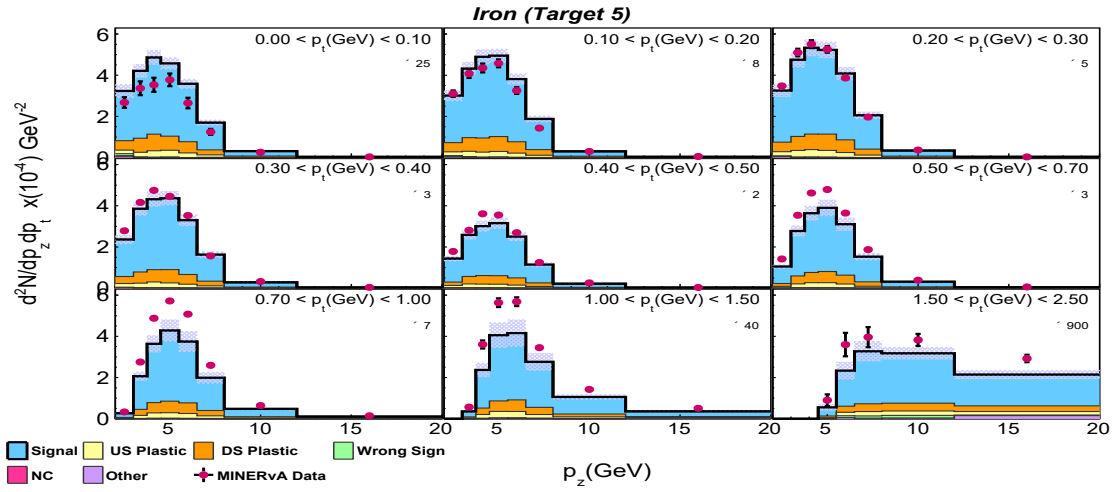

(c)

Figure A.13: Selected event distribution for iron: (a) target 2, (b) target 3 and (c) target 5 in $p_z - p_t$ bins.

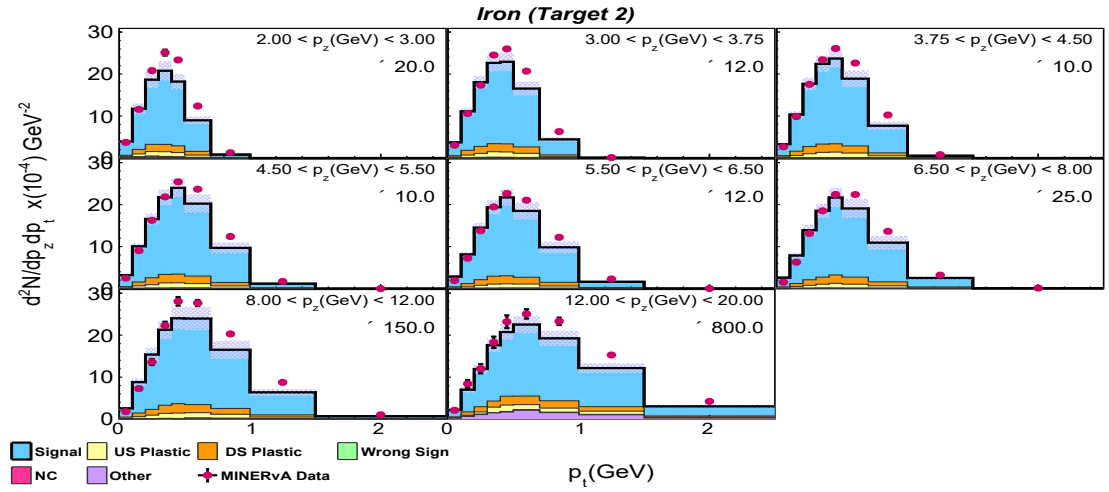

(a)

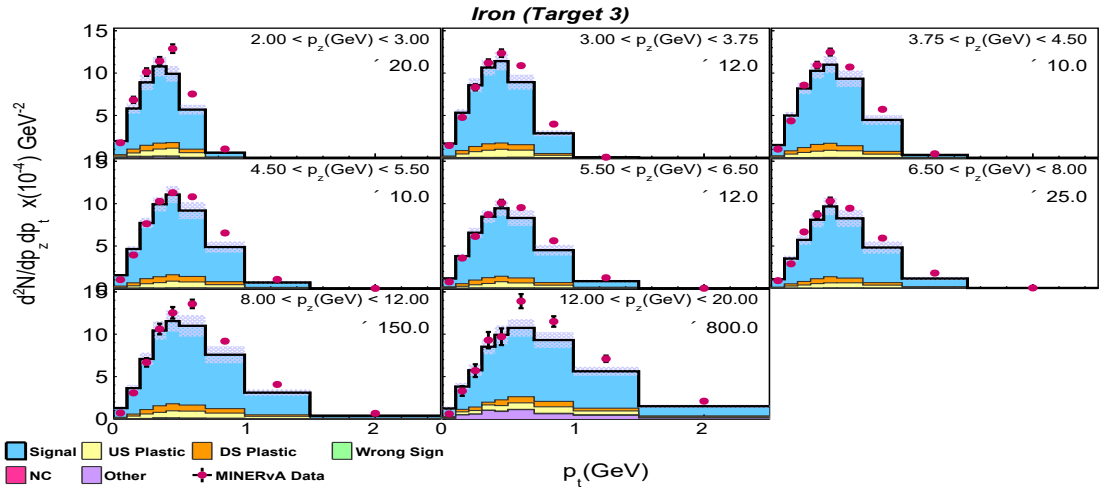

(b)

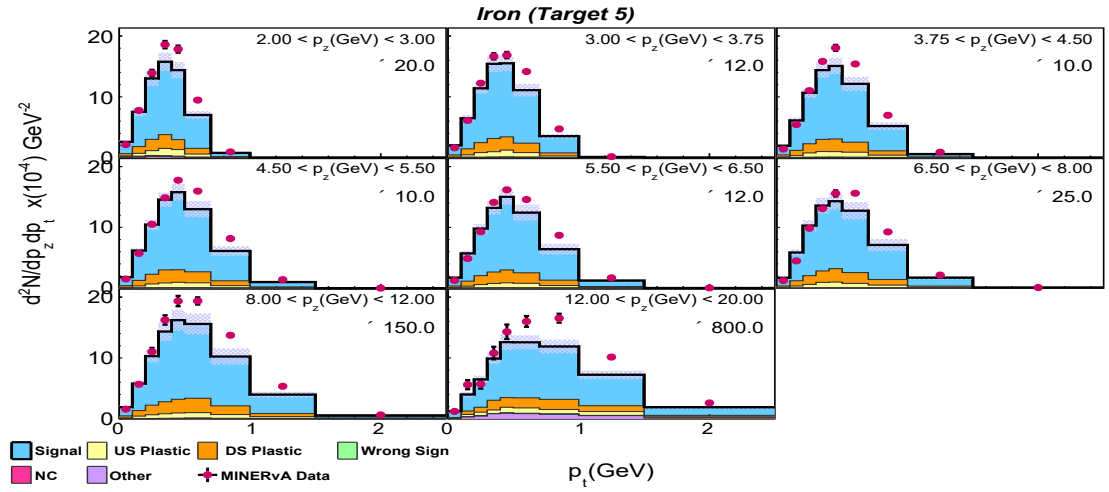

(c)

Figure A.14: Selected event distribution for iron: (a) target 2, (b) target 3 and (c) target 5 in $p_t - p_z$ bins.

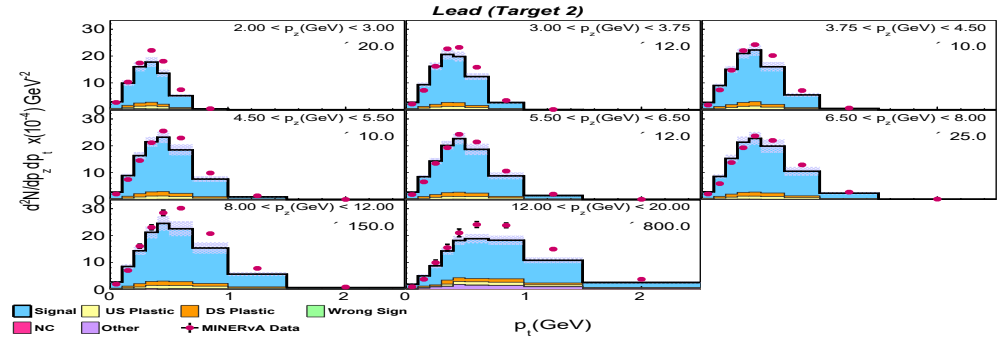

(a)

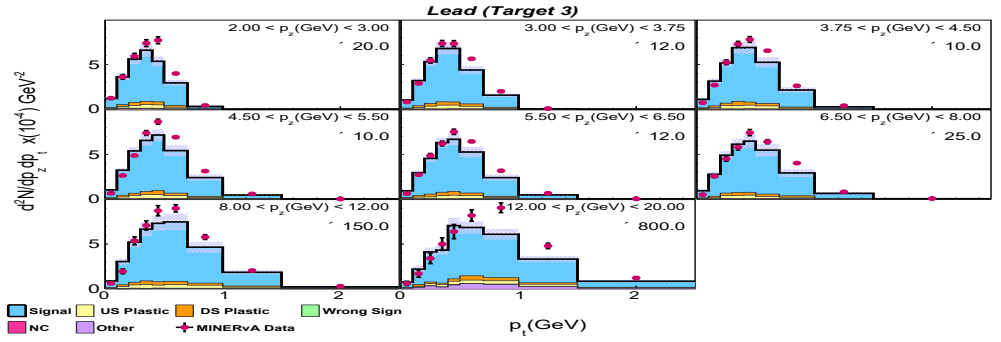

(b)

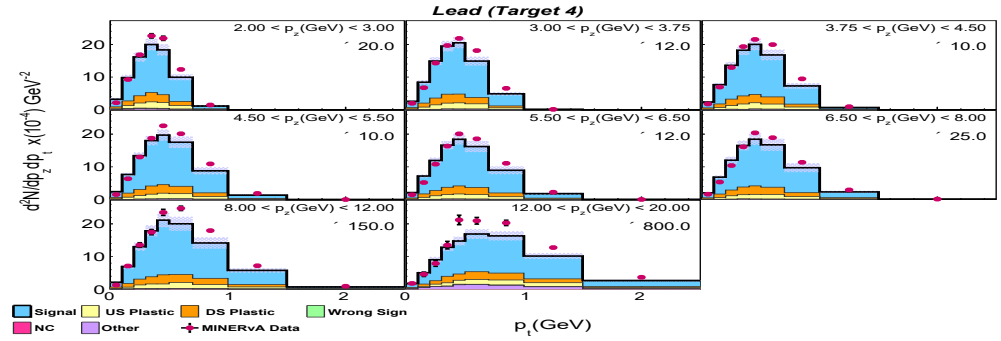

(c)

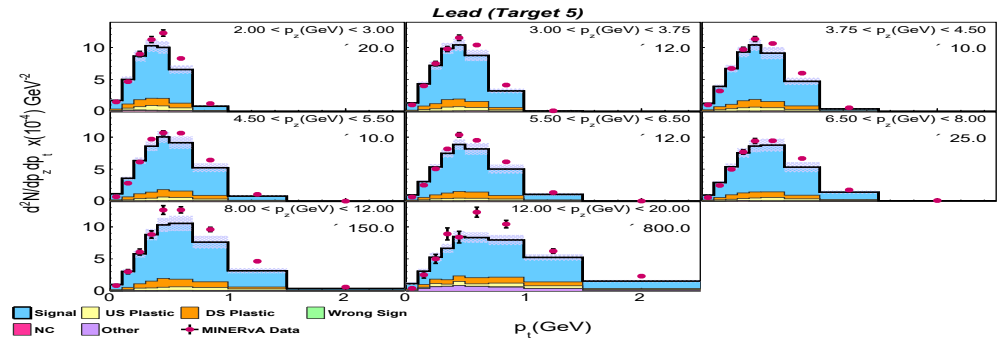

(d)

Figure A.15: Selected event distribution for lead: (a) target 2, (b) target 3, (c) target 4 and (d) target 5 in $p_t - p_z$ bins.

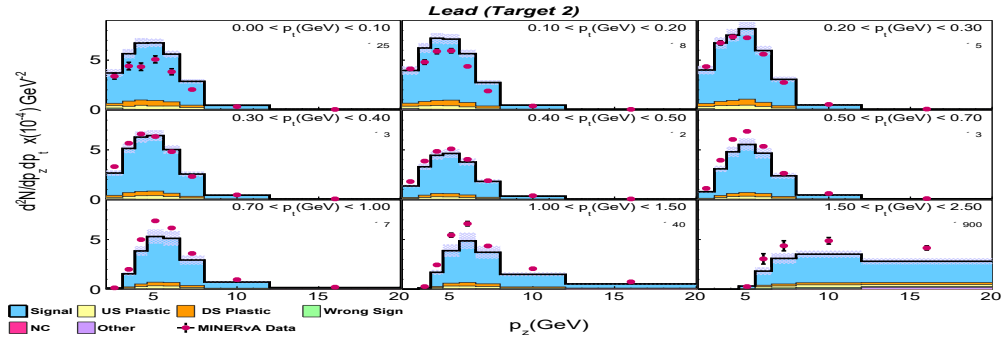

(a)

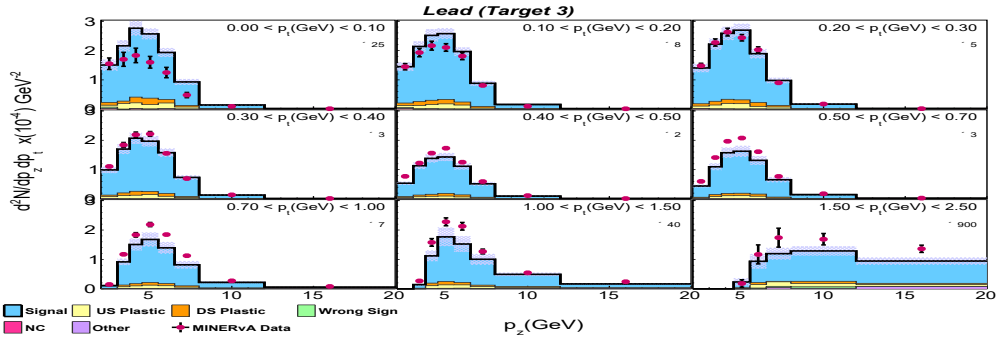

(b)

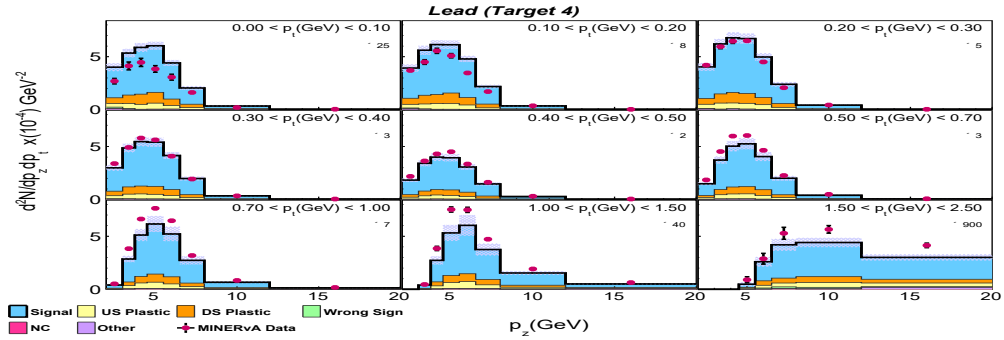

(c)

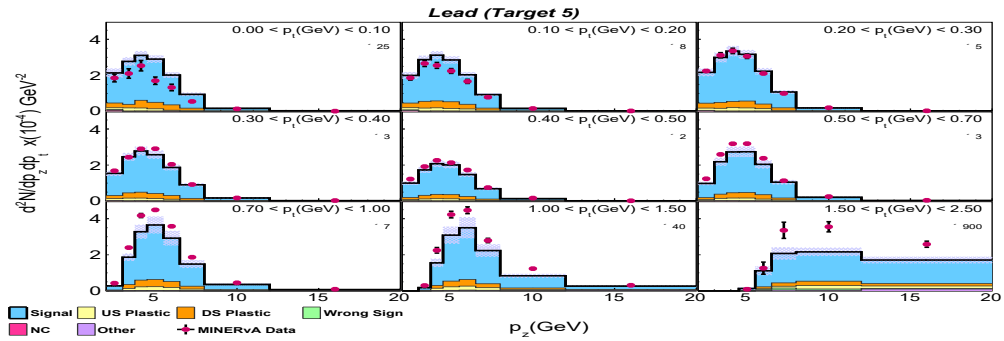

(d)

Figure A.16: Selected event distribution for lead: (a) target 2, (b) target 3, (c) target 4 and (d) target 5 in $p_z - p_t$ bins.

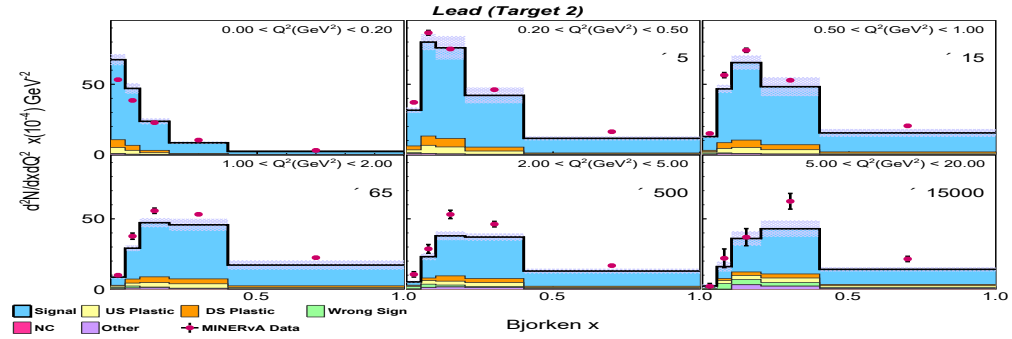

(a)

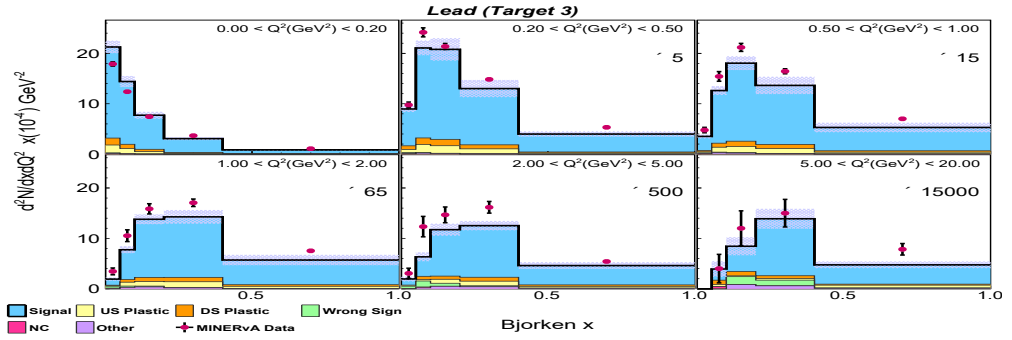

(b)

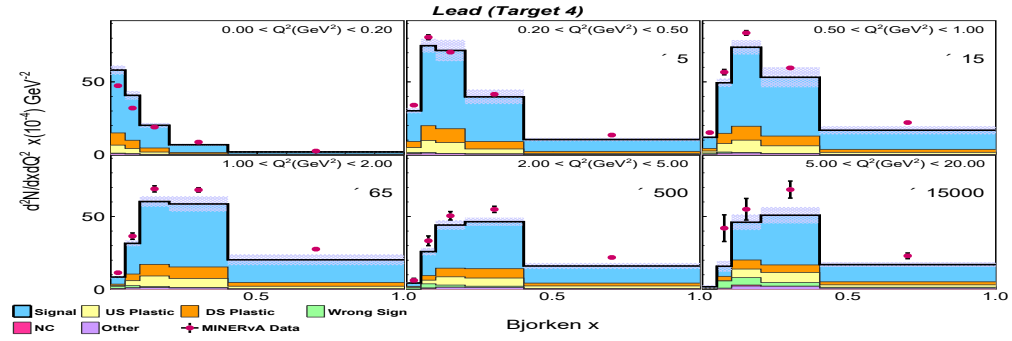

(c)

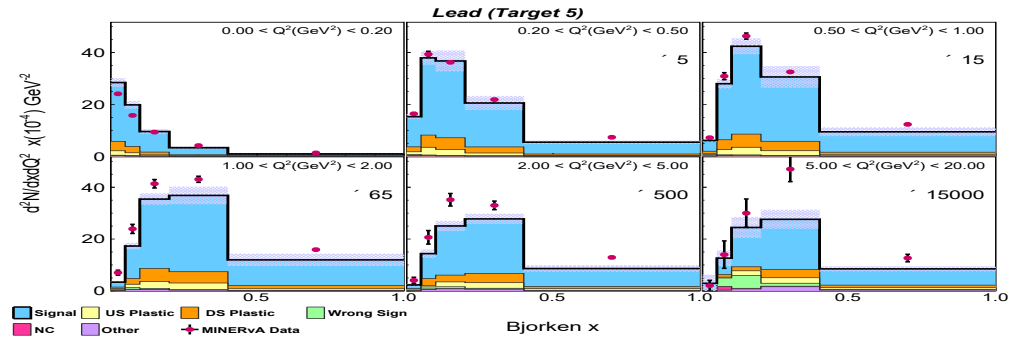

(d)

Figure A.17: Selected event distribution for lead: (a) target 2, (b) target 3, (c) target 4 and (d) target 5 in $x - Q^2$ bins.

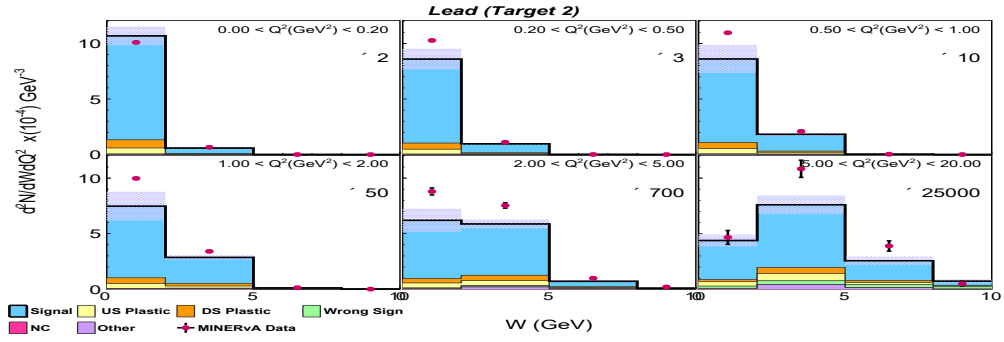

(a)

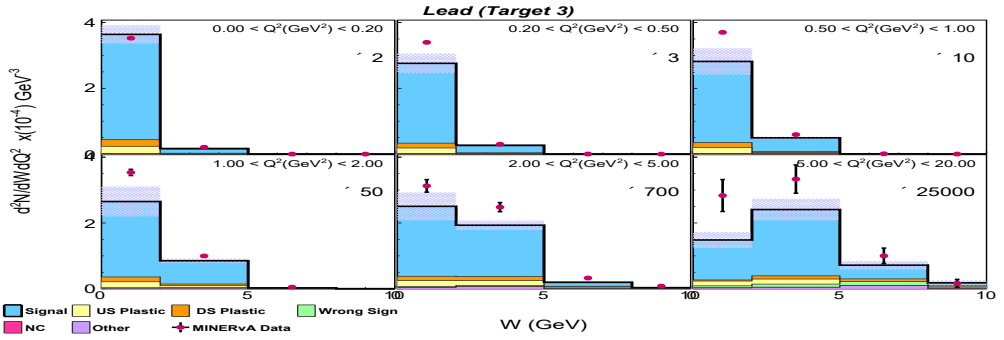

(b)

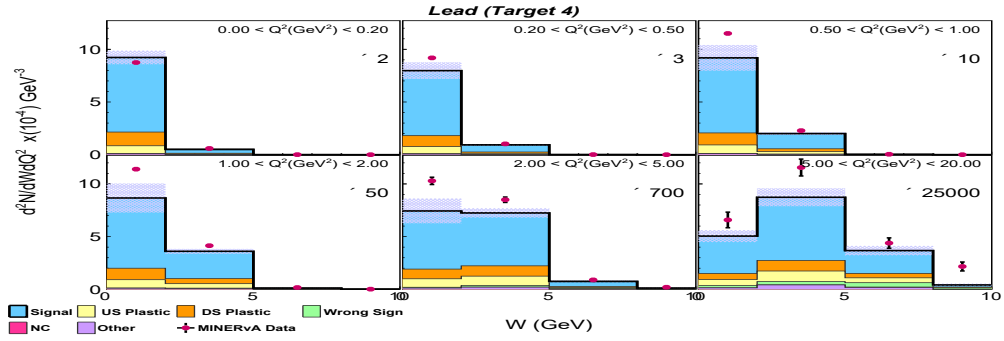

(c)

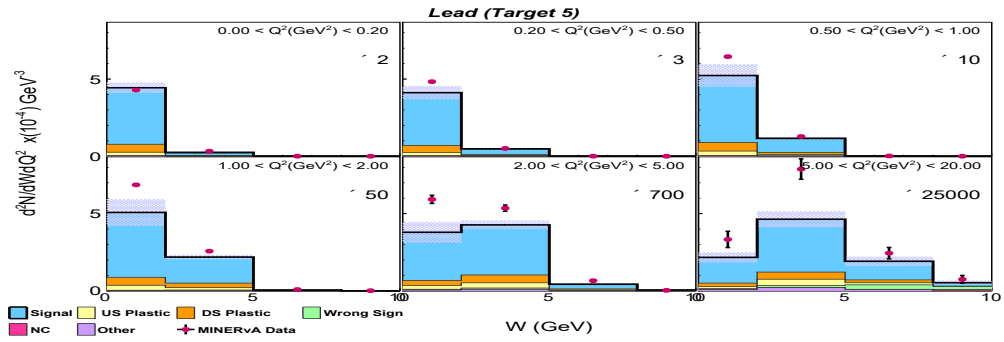

(d)

Figure A.18: Selected event distribution for lead: (a) target 2, (b) target 3, (c) target 4 and (d) target 5 in $W - Q^2$ bins.

Appendix B

Background Subtraction

B.1 Plastic Sidebands

Figures in this section show the sideband distribution plots before the tuning (labelled "untuned") and after the scaling factors were applied to tune the distributions in MC to data (labelled "tuned"). Plots have been shown for both the upstream and downstream sidebands. Example for combined iron in bins of $p_t - p_z$ was shown in the main text for the downstream sideband. Legend is read as follows: for the upstream (downstream) sideband, light blue represents the upstream (downstream) events in upstream, red represents the downstream (upstream) events in upstream (downstream), signal represents events from target material in upstream (downstream) sideband and other represents other non sideband events in upstream (downstream) sideband. The purple bands on all the plots represent the total (statistical and systematic) uncertainty in MC.

$x - Q^2$ and $W - Q^2$ distributions

Scaling factors were extracted per bin of Q^2 to tune the distributions in the two dimensional $x - Q^2$ and $W - Q^2$ variables.

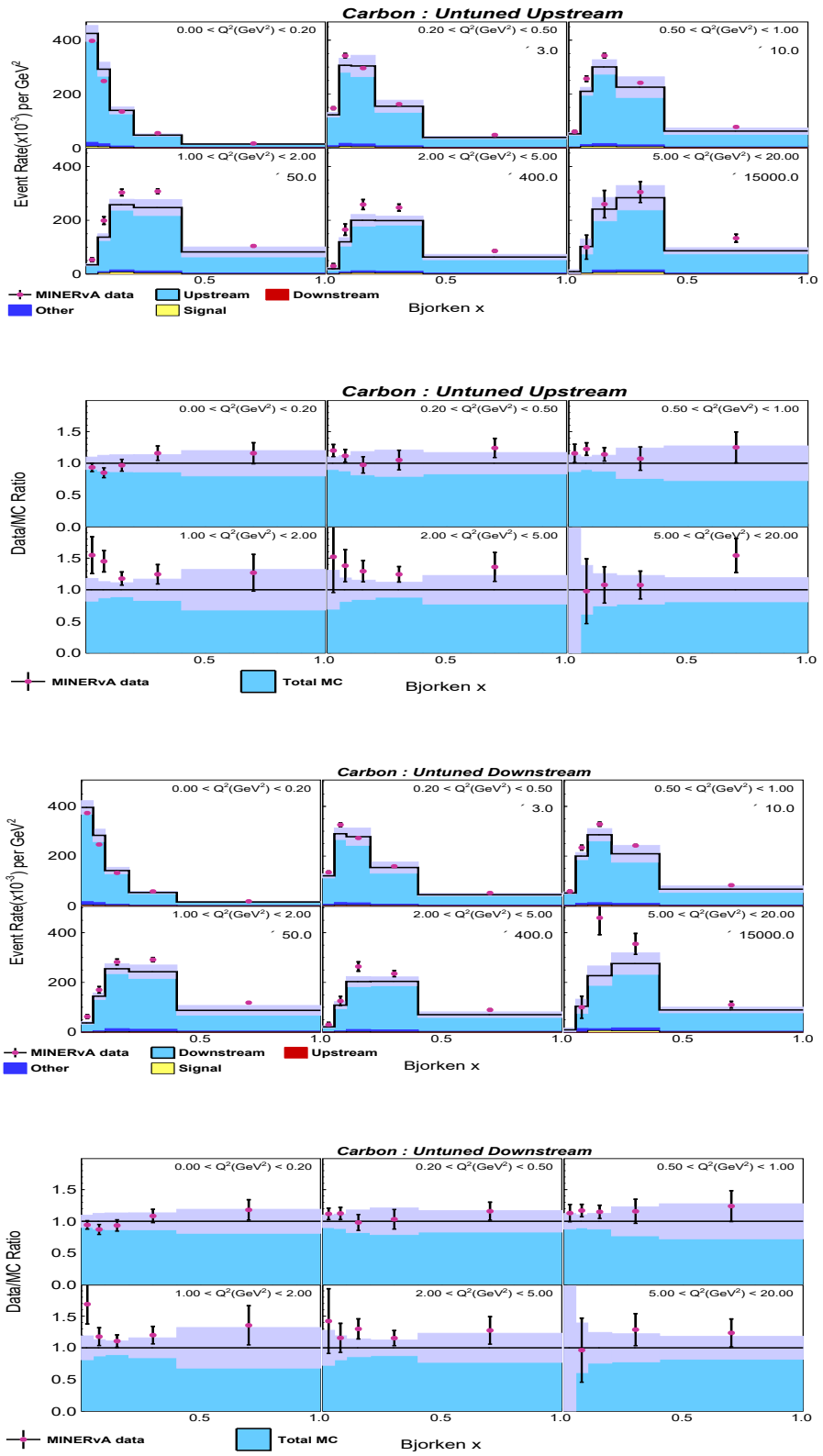

Figure B.1: Untuned sideband distribution for carbon along with the data MC ratios for upstream and downstream sidebands.

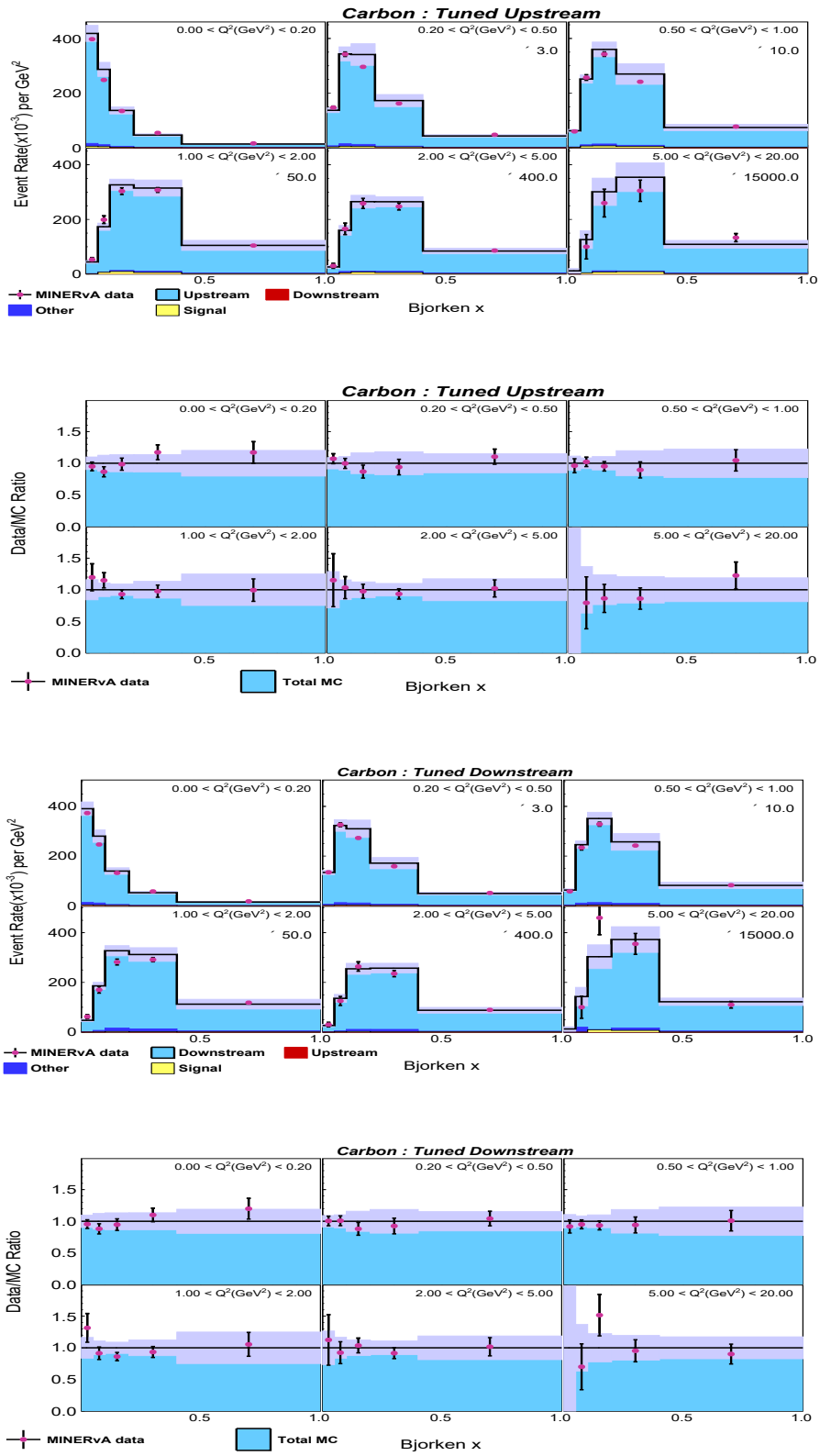

Figure B.2: Tuned sideband distribution for carbon along with the data MC ratios for upstream and downstream sidebands.

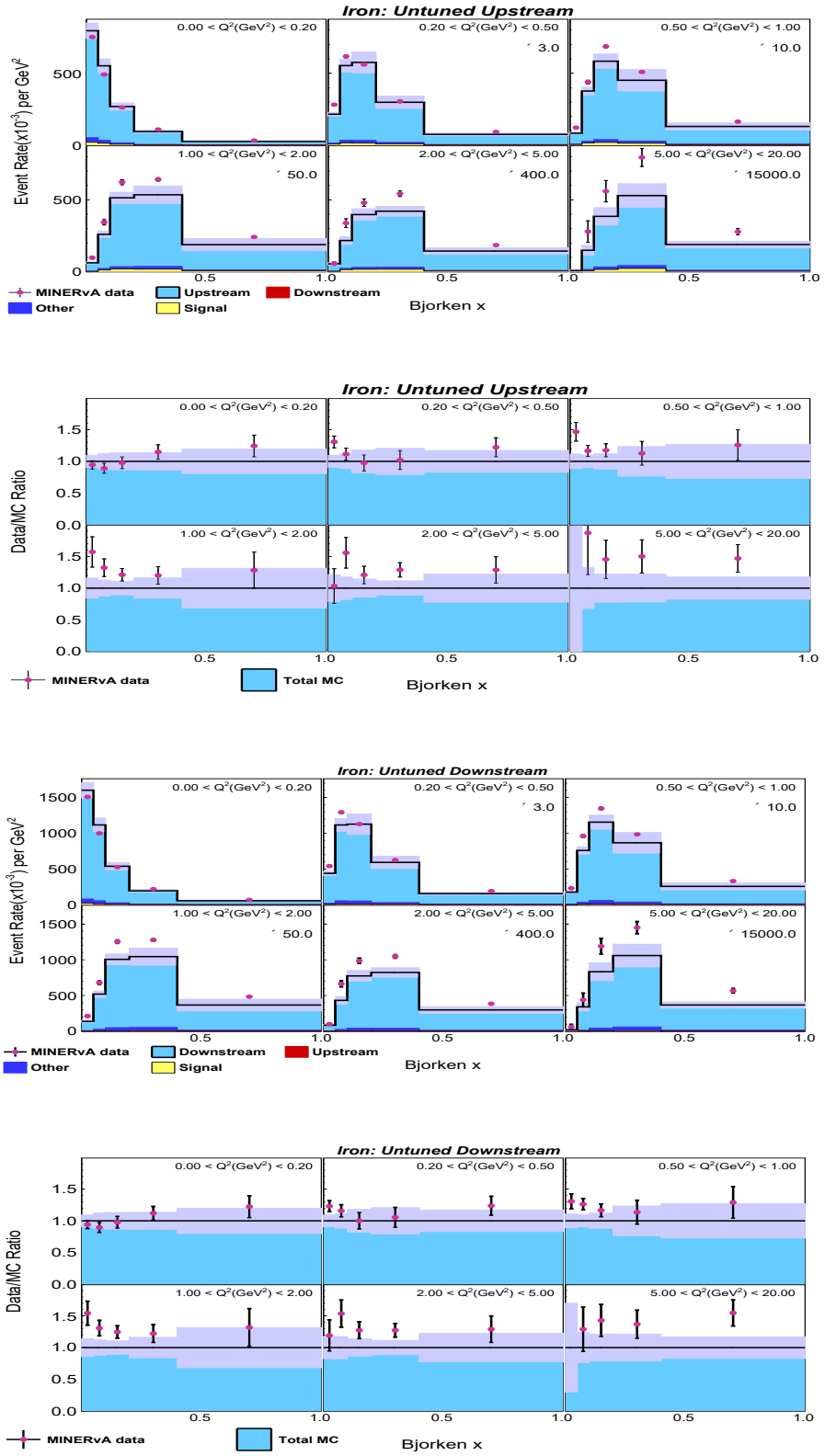

Figure B.3: Untuned sideband distribution for iron along with the data MC ratios for upstream and downstream sidebands.

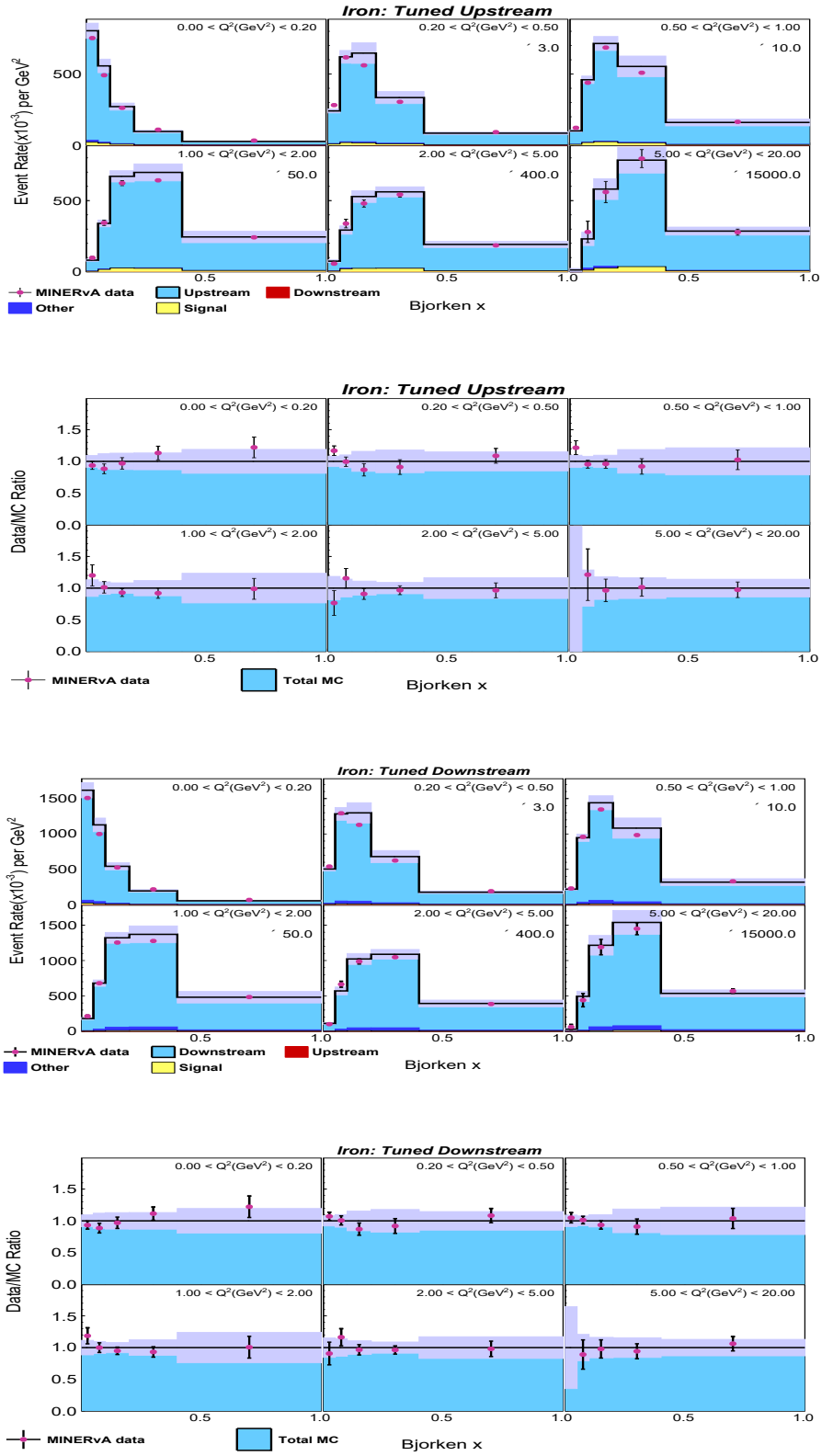

Figure B.4: Tuned sideband distribution for iron along with the data MC ratios for upstream and downstream sidebands.

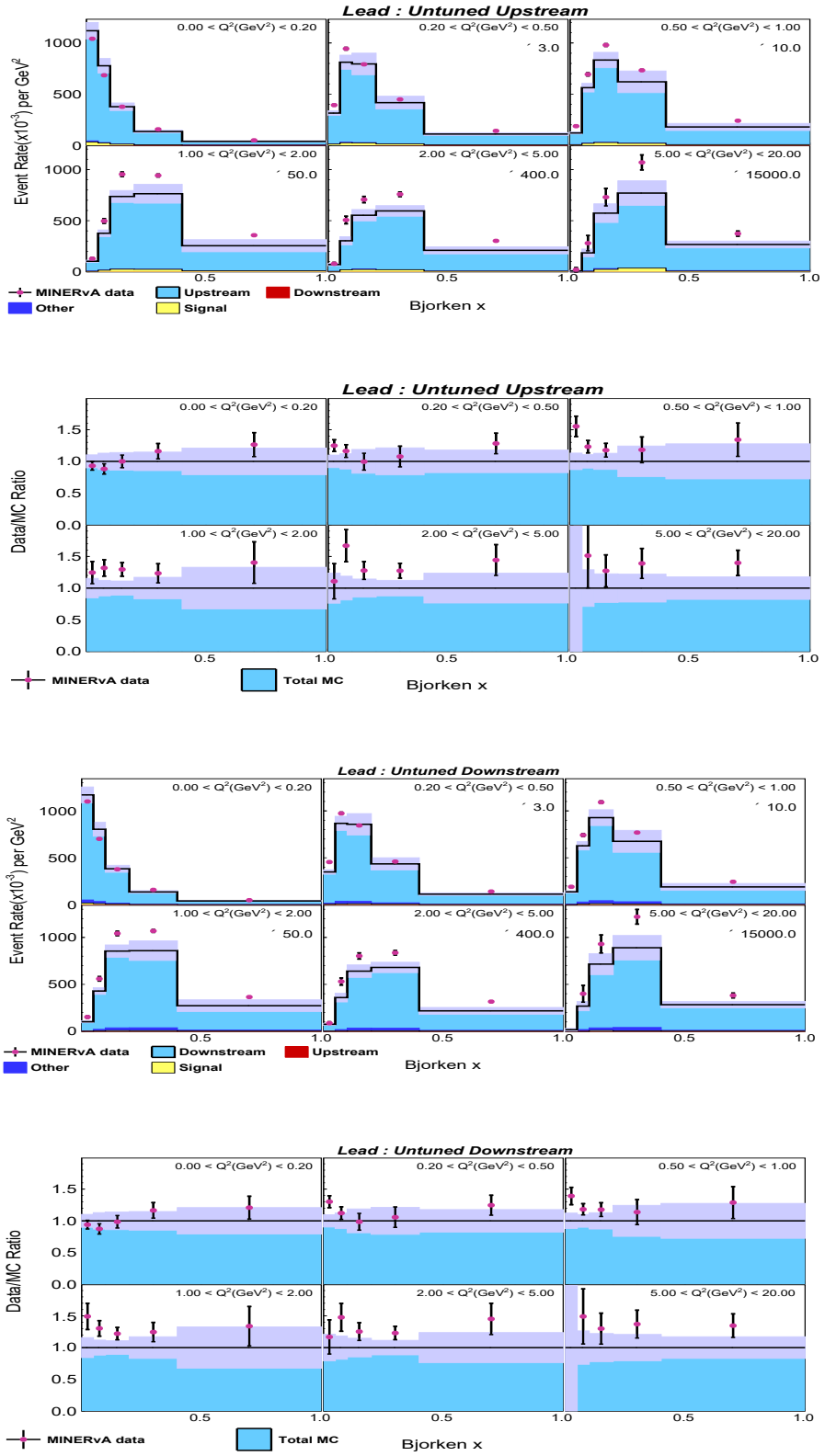

Figure B.5: Untuned sideband distribution for lead along with the data MC ratios for upstream and downstream sidebands.

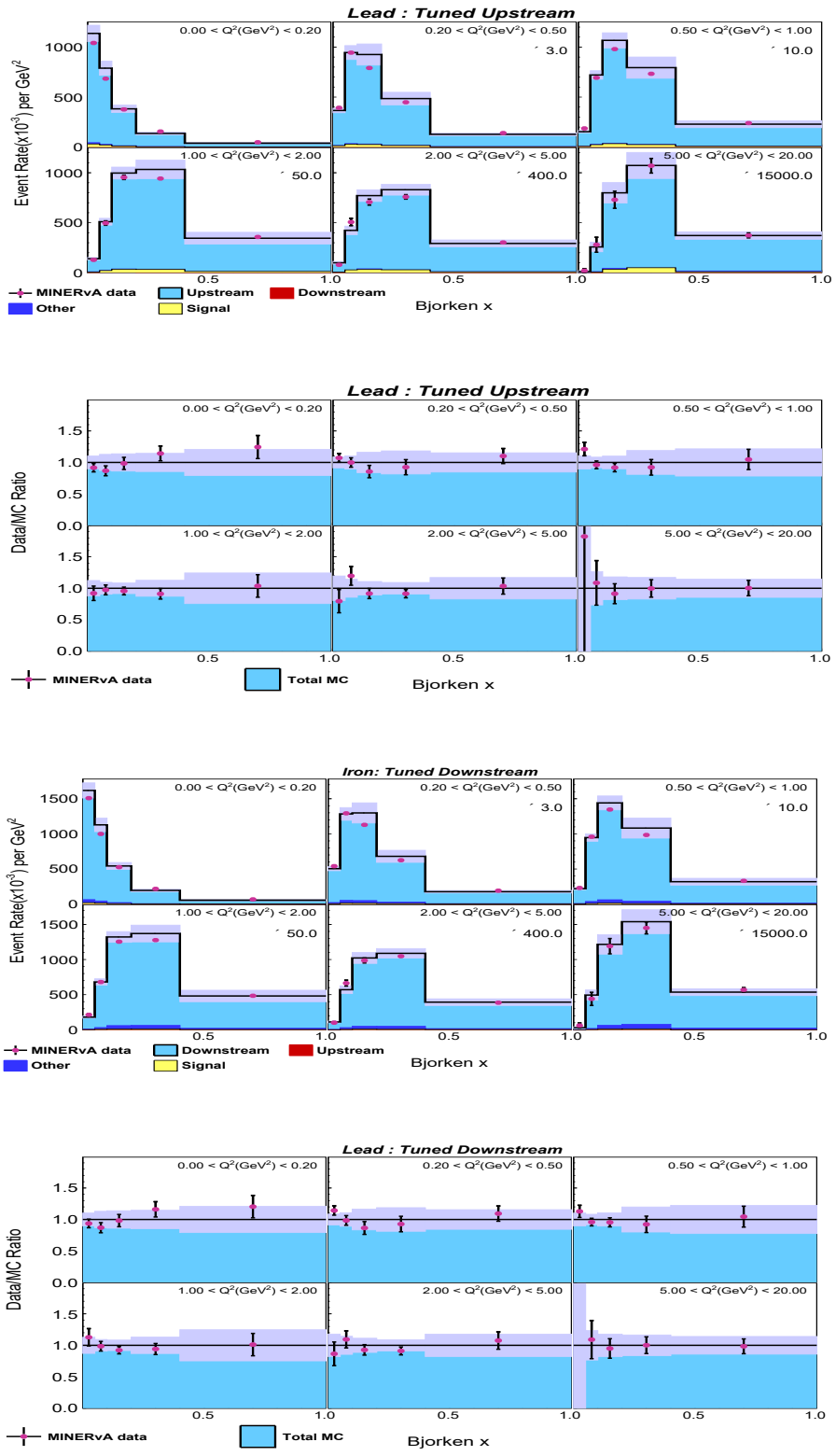

Figure B.6: Tuned sideband distribution for lead along with the data MC ratios for upstream and downstream sidebands.

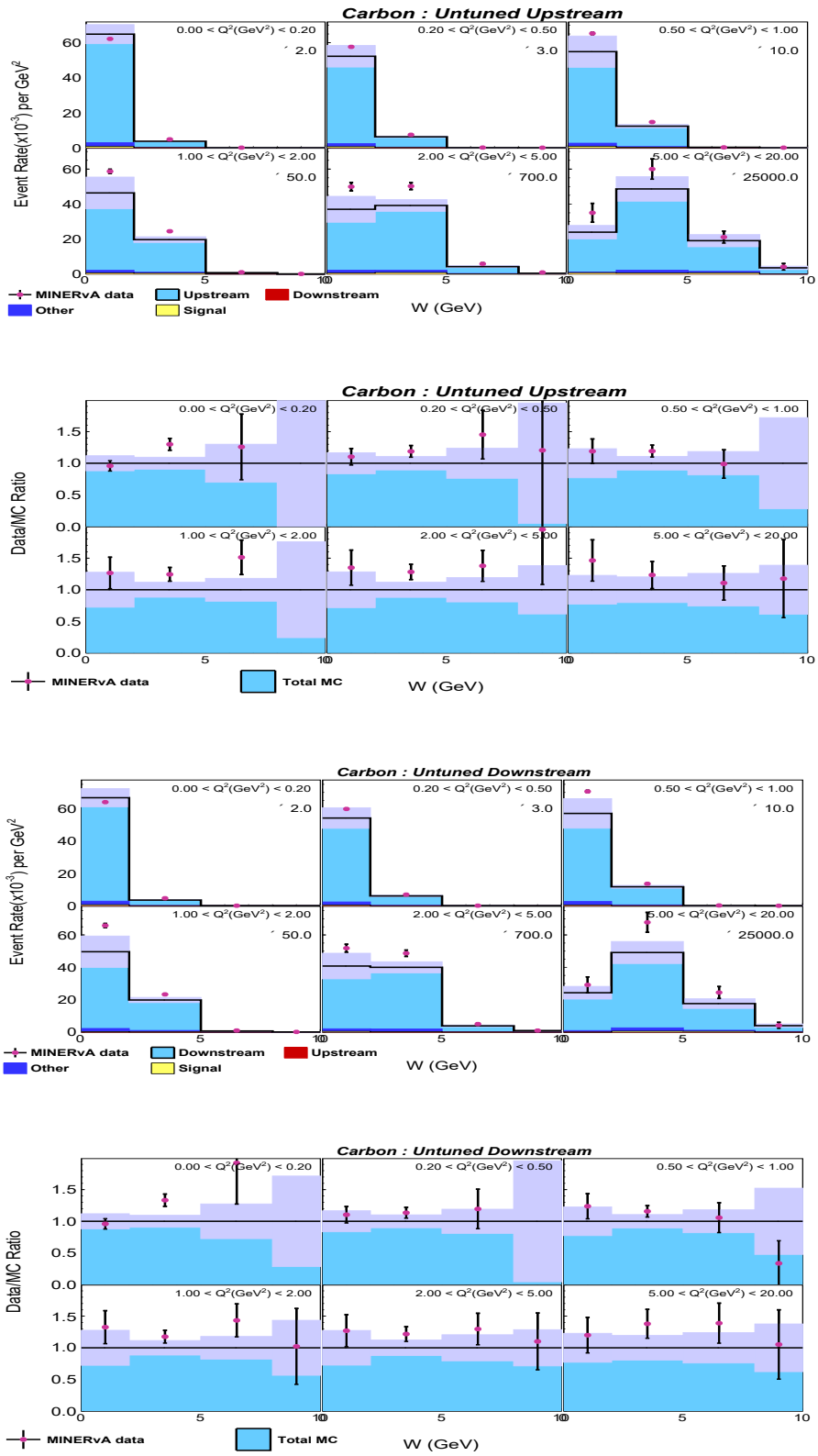

Figure B.7: Untuned sideband distribution for carbon along with the data MC ratios for upstream and downstream sidebands.

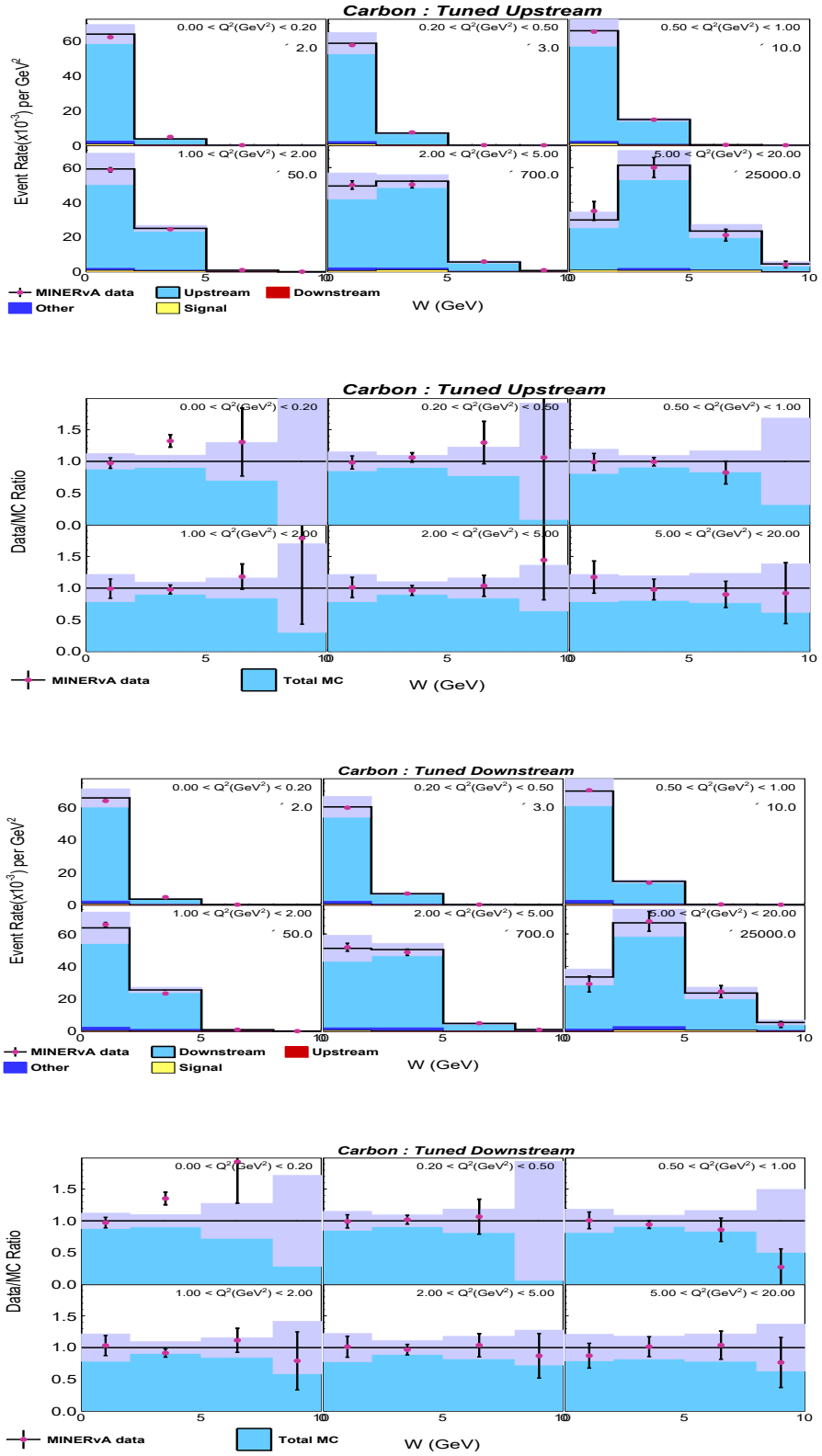

Figure B.8: Tuned sideband distribution for carbon along with the data MC ratios for upstream and downstream sidebands.

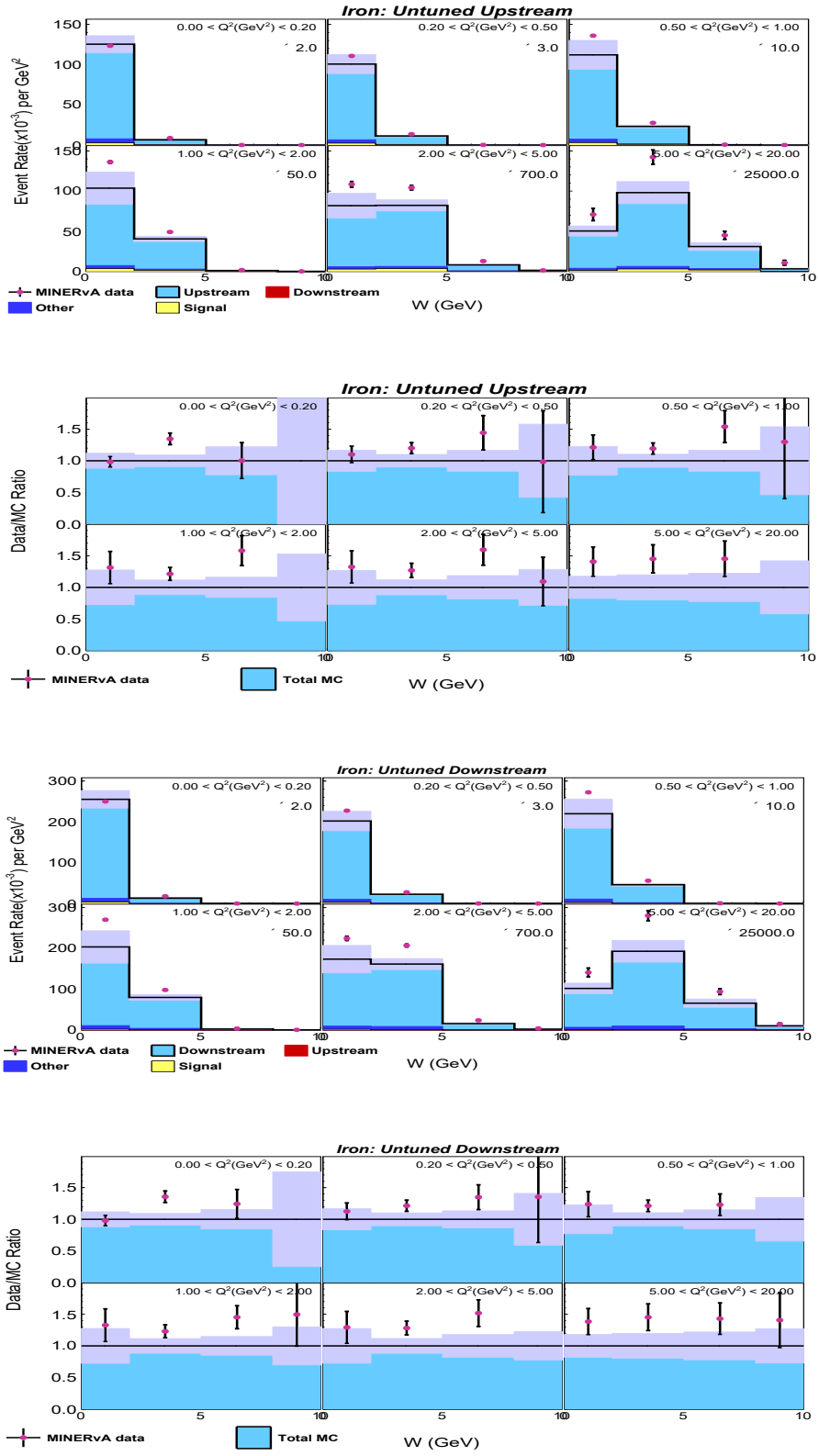

Figure B.9: Untuned sideband distribution for iron along with the data MC ratios for upstream and downstream sidebands.

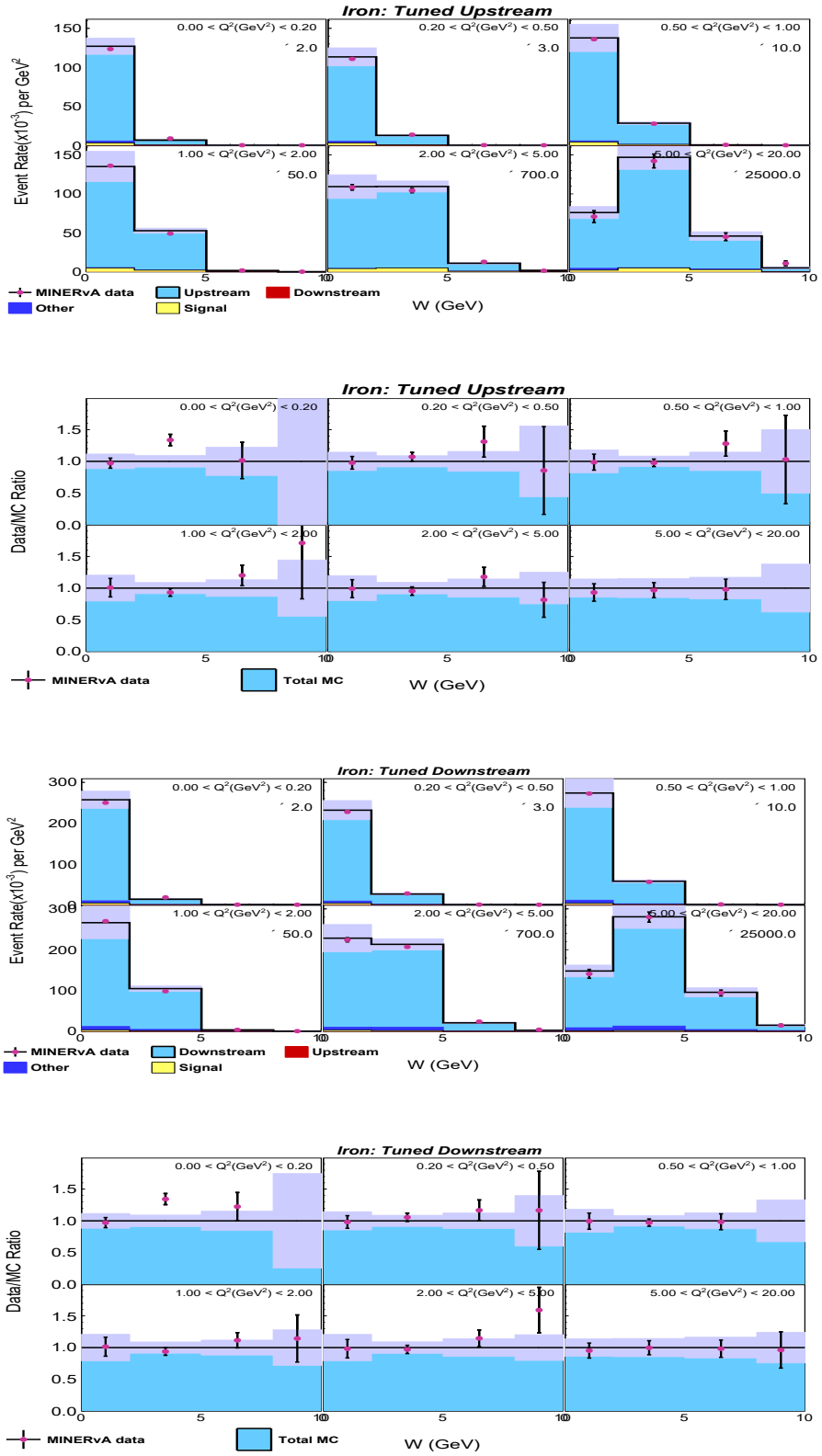

Figure B.10: Tuned sideband distribution for iron along with the data MC ratios for upstream and downstream sidebands.

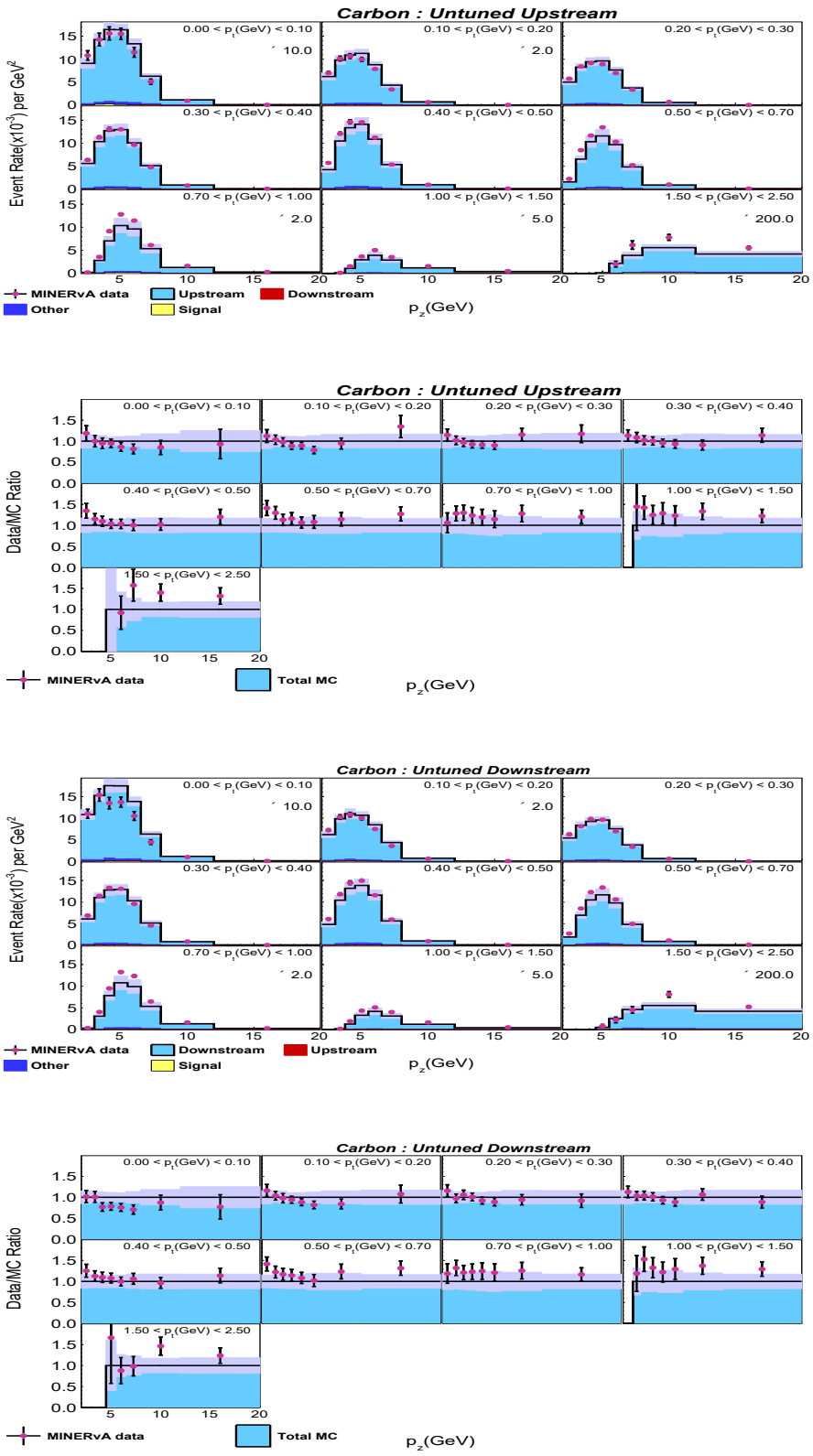

Figure B.11: Untuned sideband distribution for carbon along with the data MC ratios for upstream and downstream sidebands.

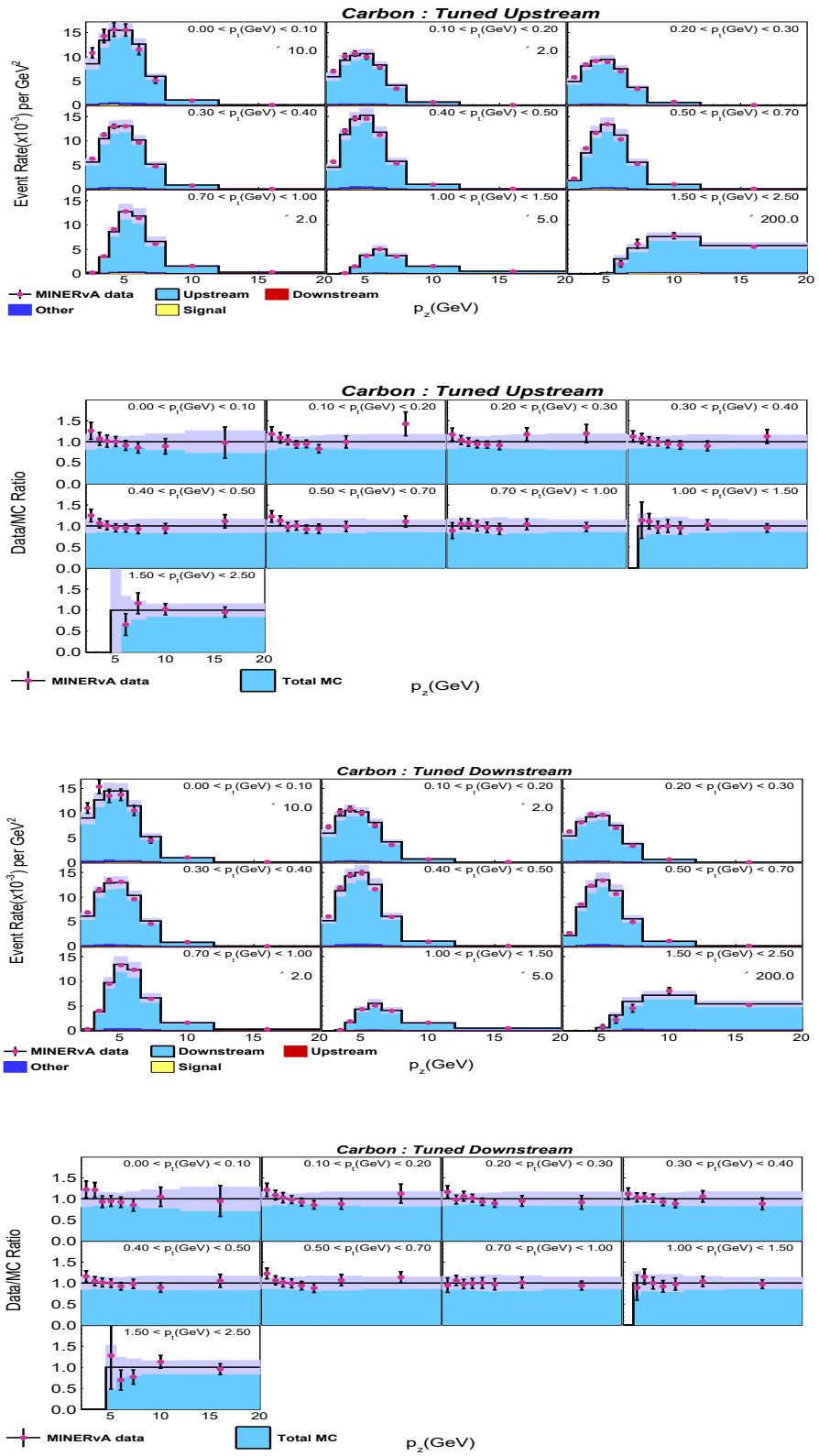

Figure B.12: Tuned sideband distribution for carbon along with the data MC ratios for upstream and downstream sidebands.

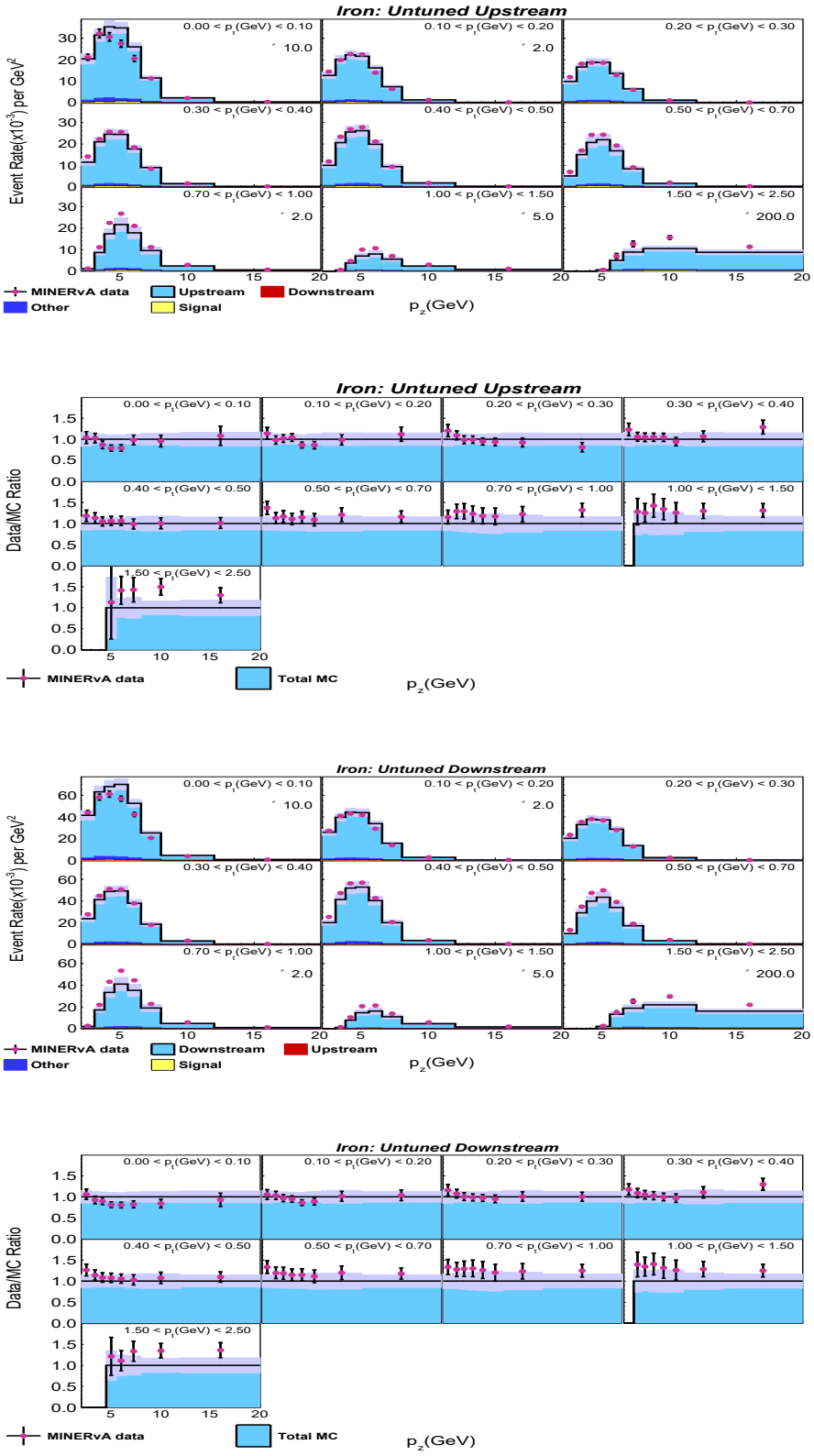

Figure B.13: Untuned sideband distribution for iron along with the data MC ratios for upstream and downstream sidebands.

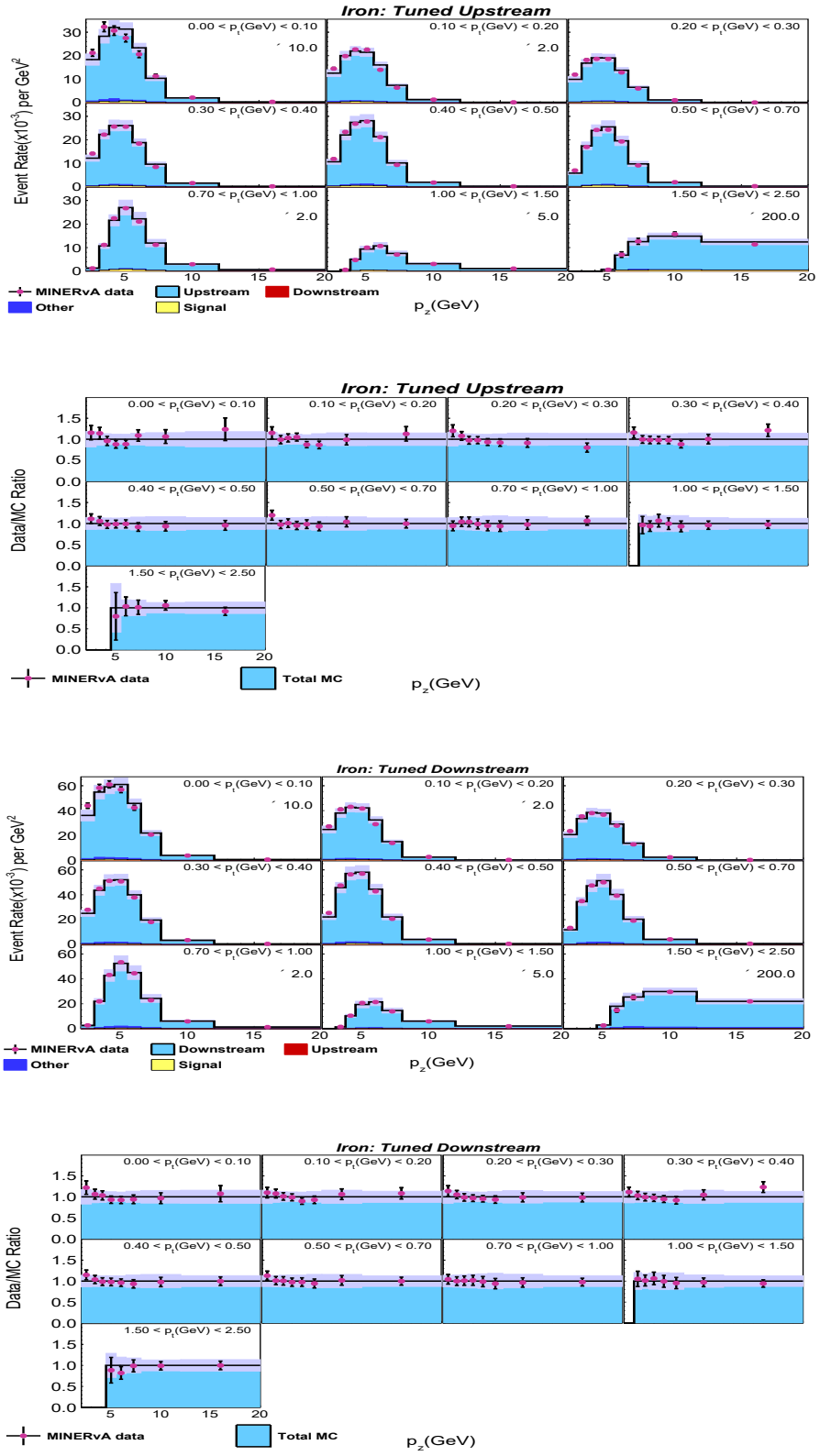

Figure B.14: Tuned sideband distribution for iron along with the data MC ratios for upstream and downstream sidebands.

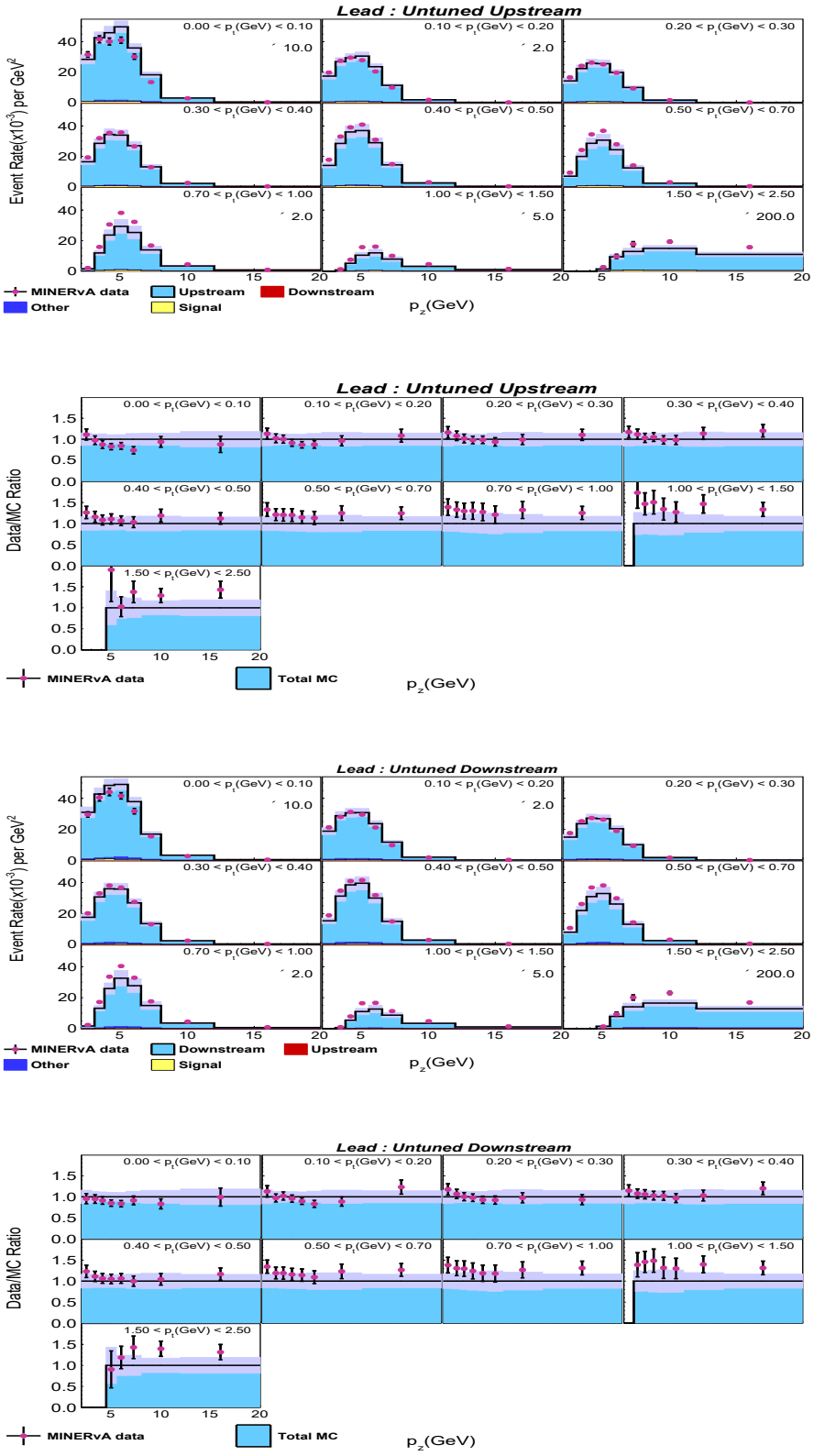

Figure B.15: Untuned sideband distribution for lead along with the data MC ratios for upstream and downstream sidebands.

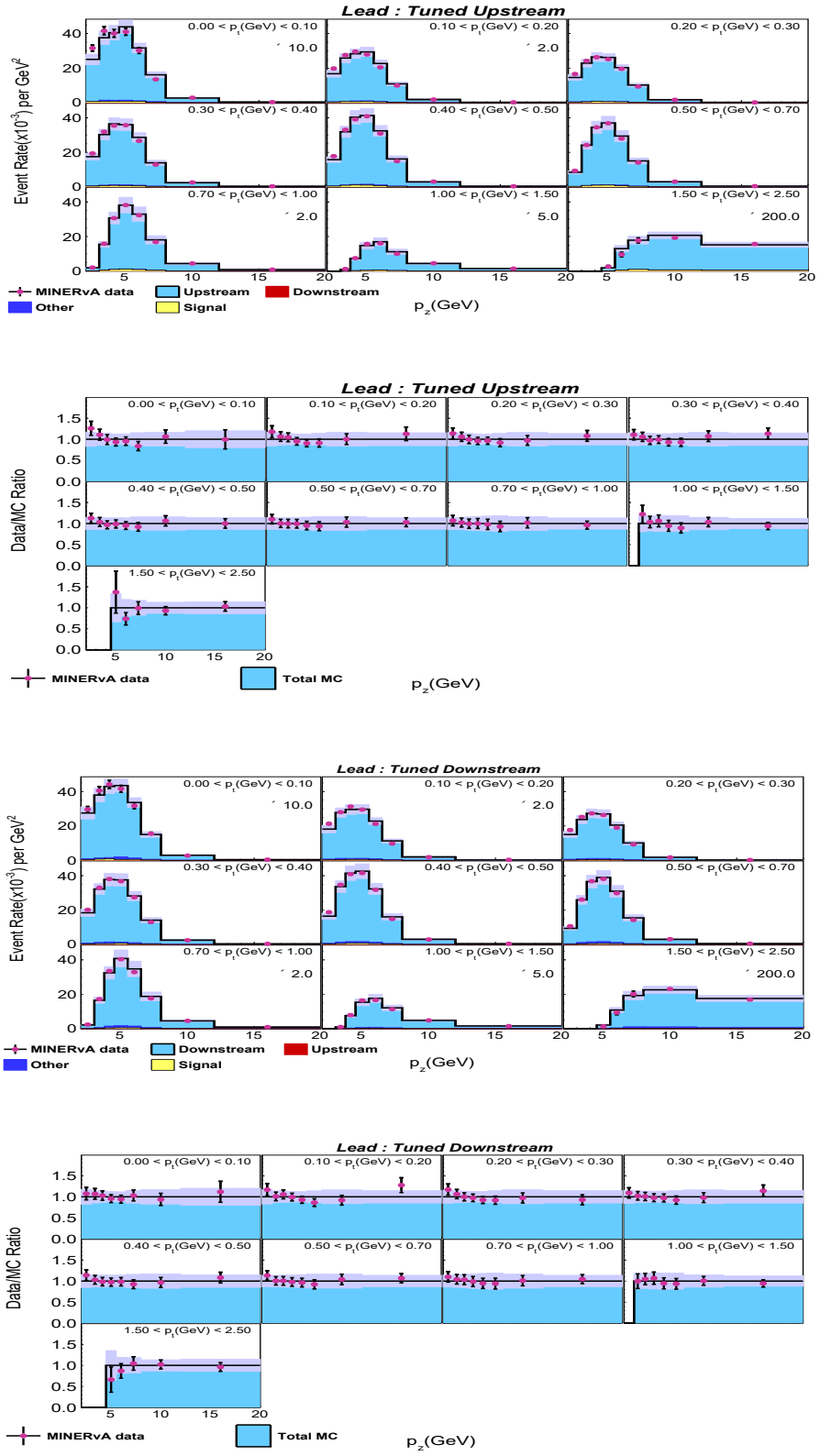

Figure B.16: Tuned sideband distribution for lead along with the data MC ratios for upstream and downstream sidebands.

B.2 Data constrained background prediction

This section contains plots for the data constrained background prediction obtained after extracting the scaling factors using the sideband studies. Plots for carbon in $p_z - p_t$ and $x - Q^2$ were provided in the main text.

$x - Q^2$ distributions

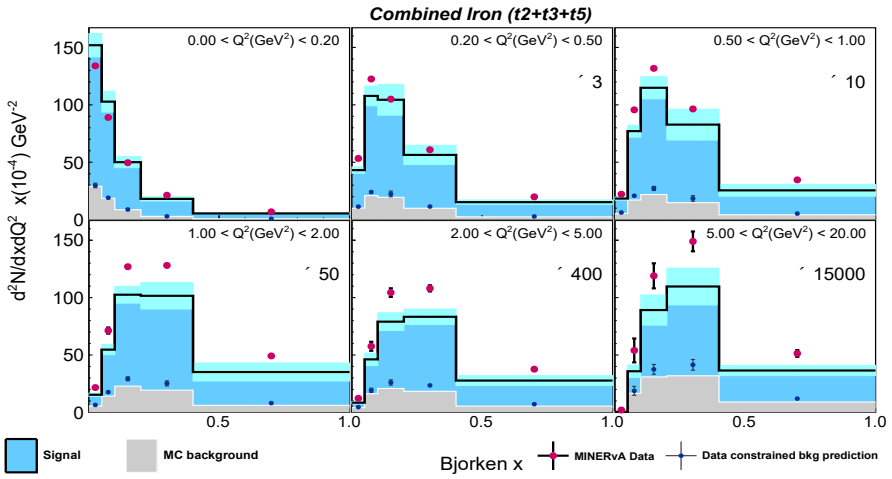

(a)

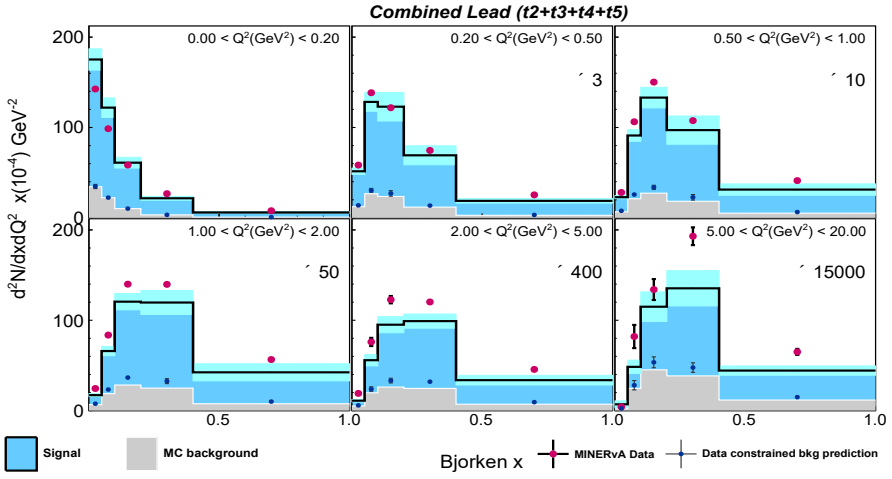

(b)

Figure B.17: The figure shows the signal in MC (blue histogram) and data (red dots) for (a) iron and (b) lead, alongside the MC-predicted background (gray) and data-constrained background (blue dots) from sideband studies.

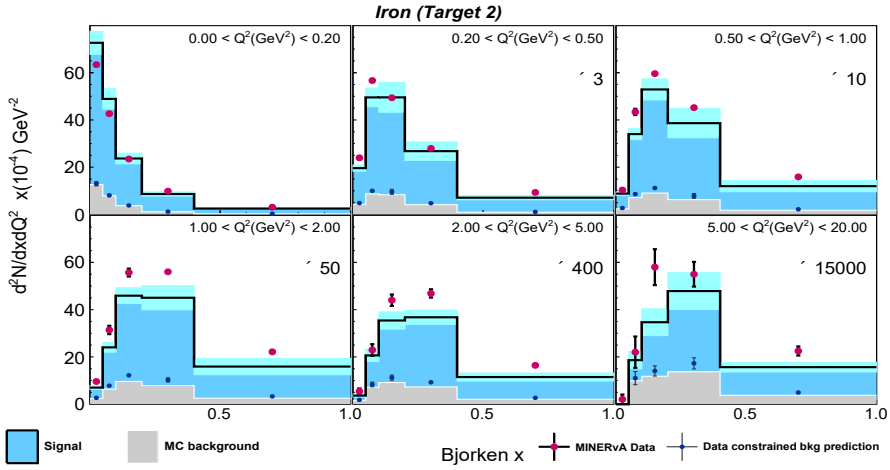

(a)

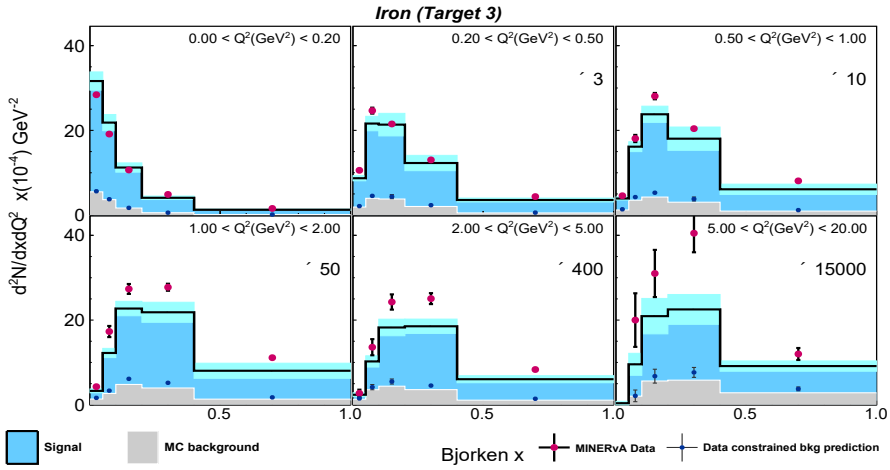

(b)

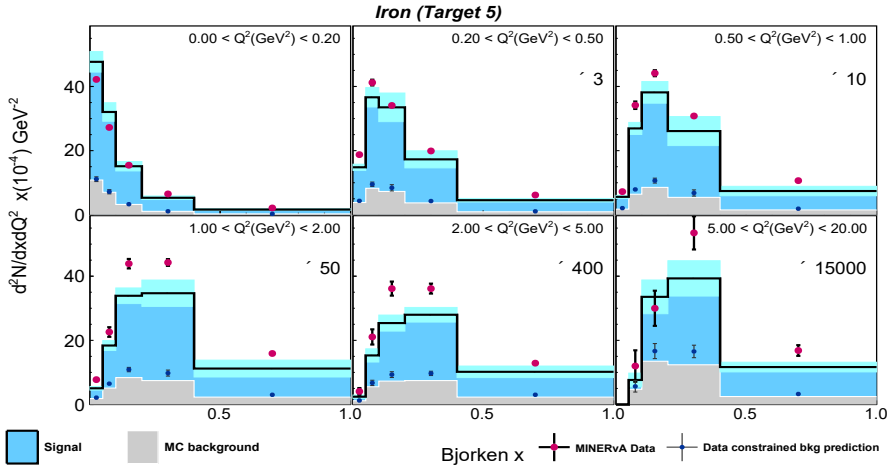

(c)

Figure B.18: Figure depicts the signal in MC (blue histogram) and data (red dots) for iron (a) target 2, (b) target 3 and (c) target 5, along with background predicted by MC (gray) and data constrained background (blue dots).

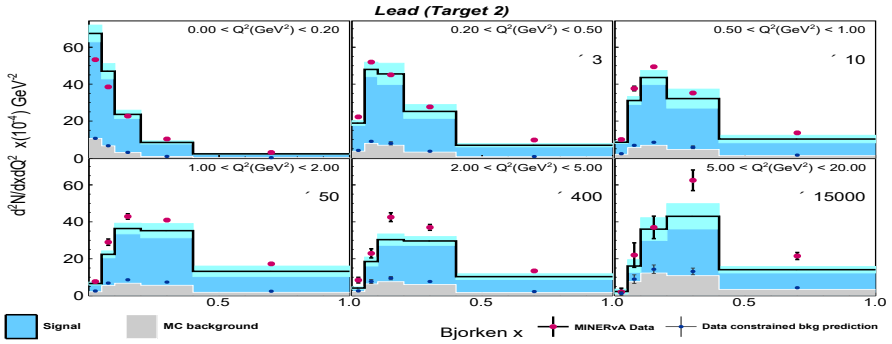

(a)

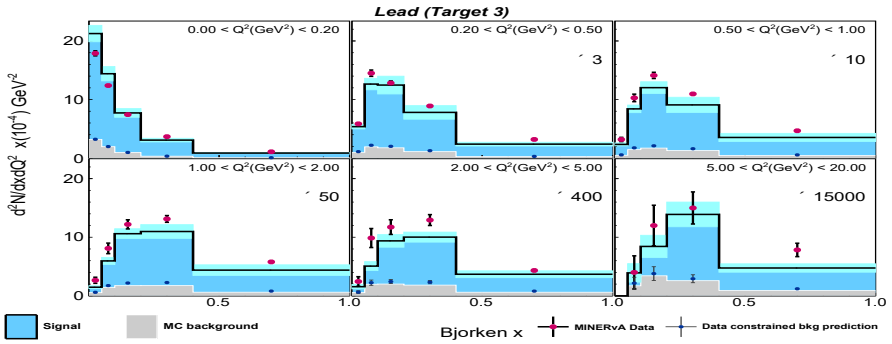

(b)

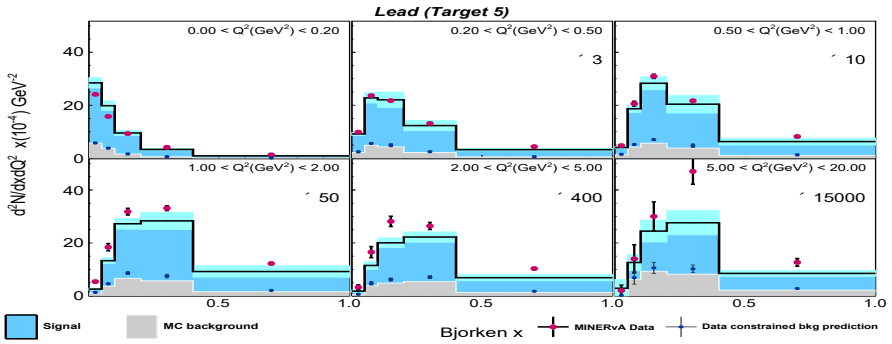

(c)

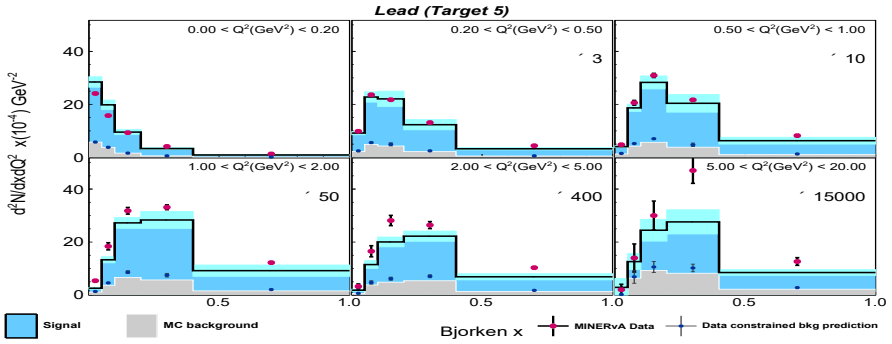

(d)

Figure B.19: Signal and background distribution in data and MC for lead (a) target 2, (b) target 3, (c) target 4 and (d) target 5.

$W - Q^2$ distributions

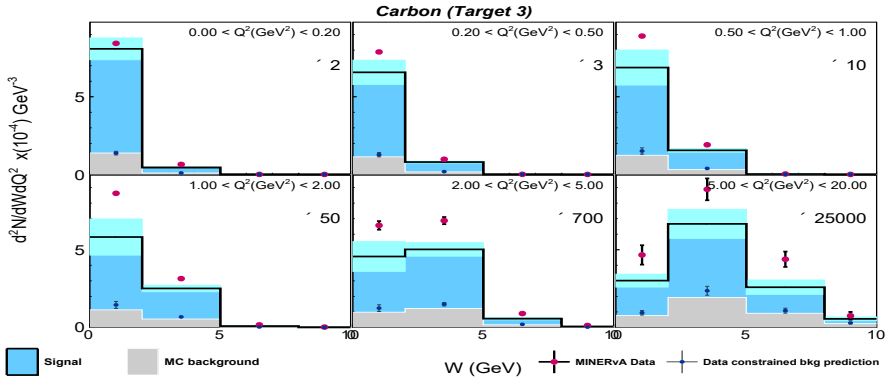

(a)

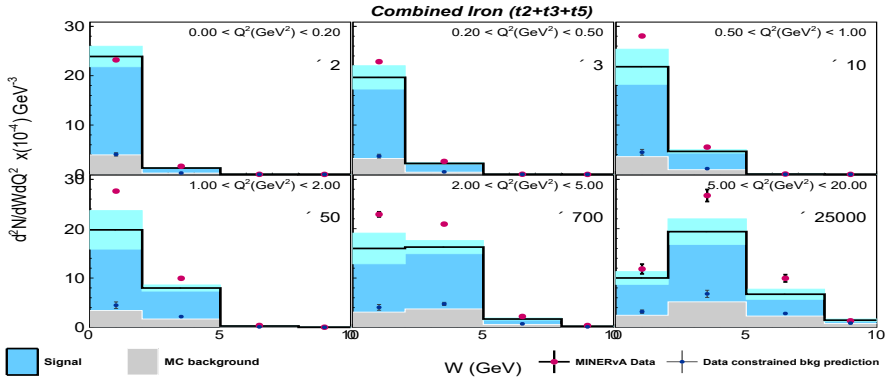

(b)

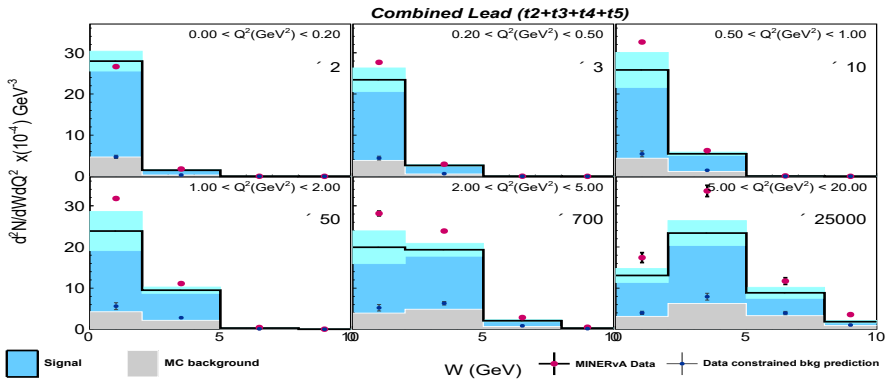

(c)

Figure B.20: Figure depicts the signal in MC(blue histogram) and data (red dots) for combined (a) iron and (b) lead and (c) carbon, along with background predicted by MC (gray) and data constrained background (blue dots).

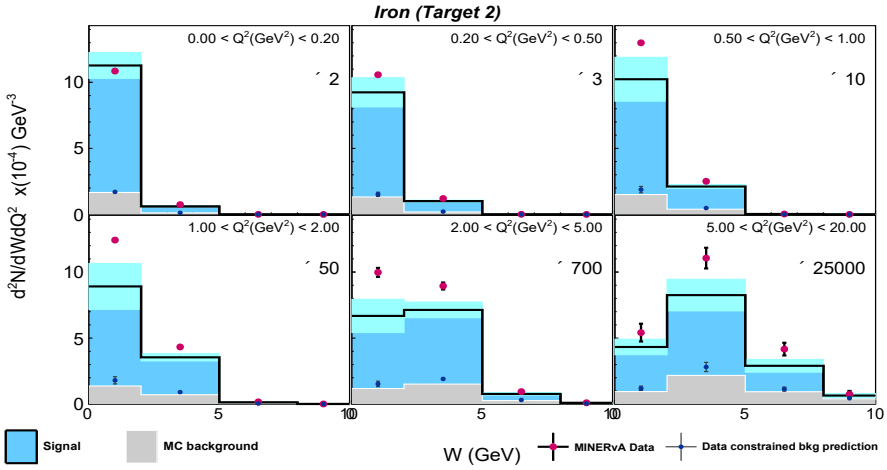

(a)

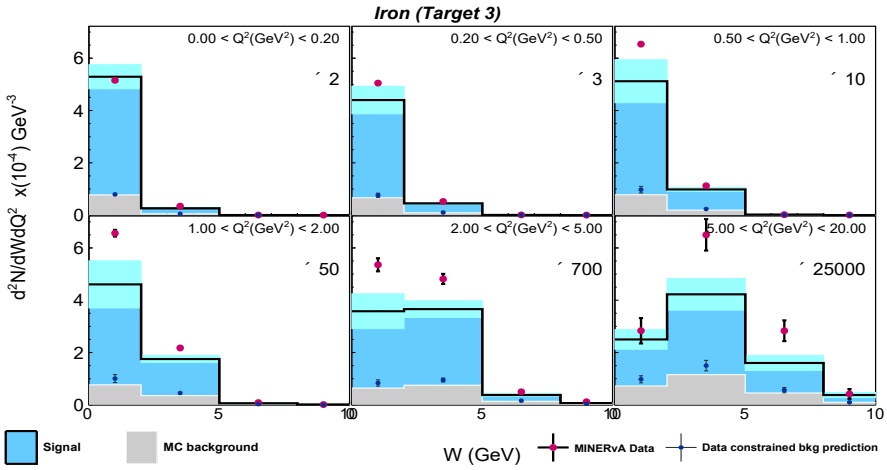

(b)

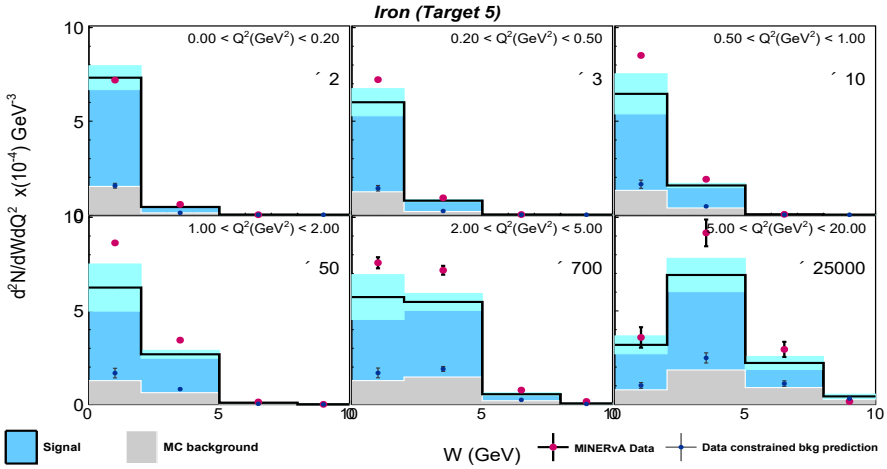

(c)

Figure B.21: Figure depicts the signal in MC (blue histogram) and data (red dots) for iron (a) target 2, (b) target 3 and (c) target 5, along with background predicted by MC (gray) and data constrained background (blue dots).

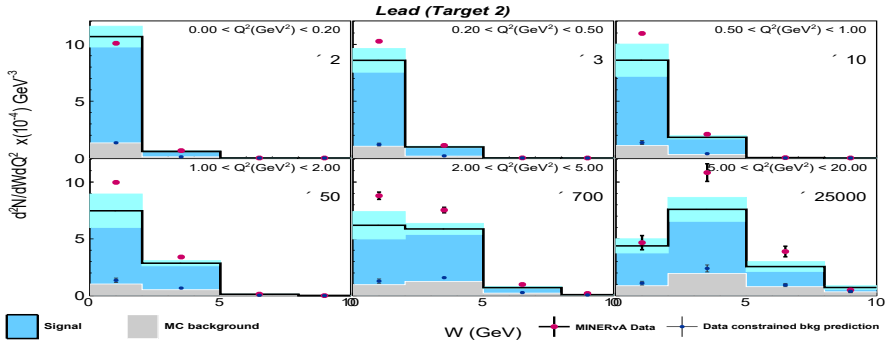

(a)

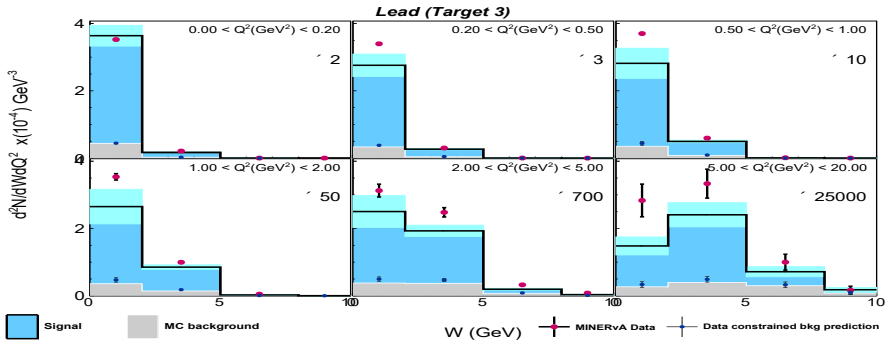

(b)

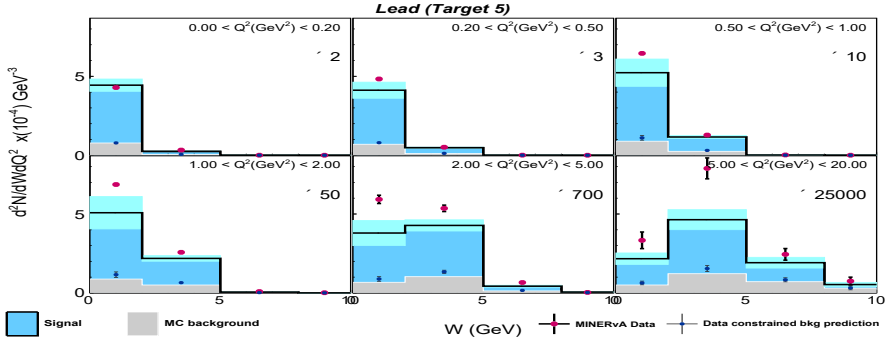

(c)

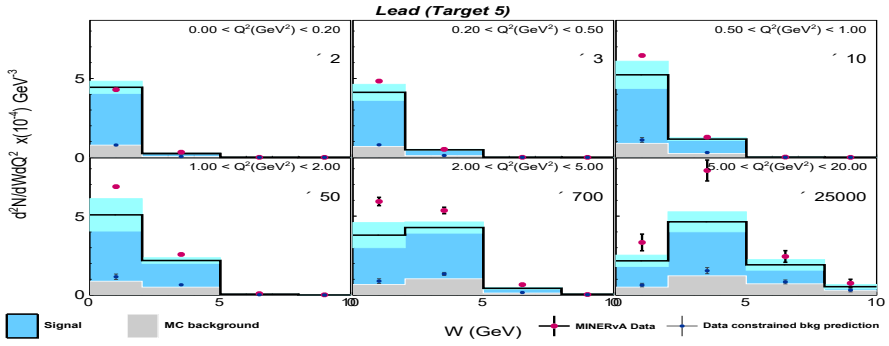

(d)

Figure B.22: Figure depicts the signal and background predictions in MC and data for lead (a) target 2, (b) target 3, (c) target 4 and (d) target 5.

$p_z - p_t$ **distributions**

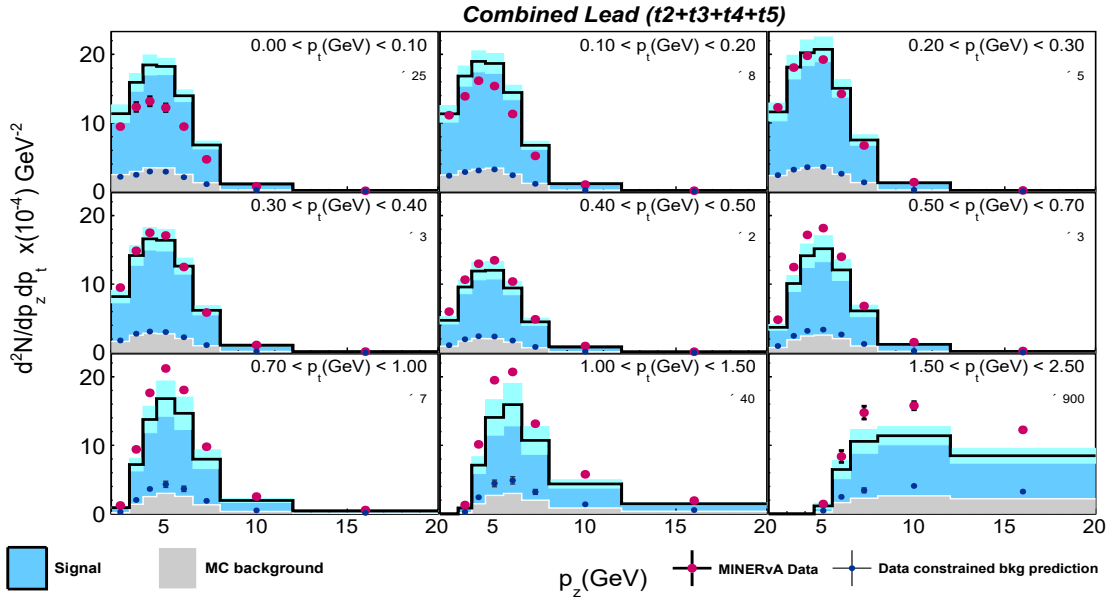

(a)

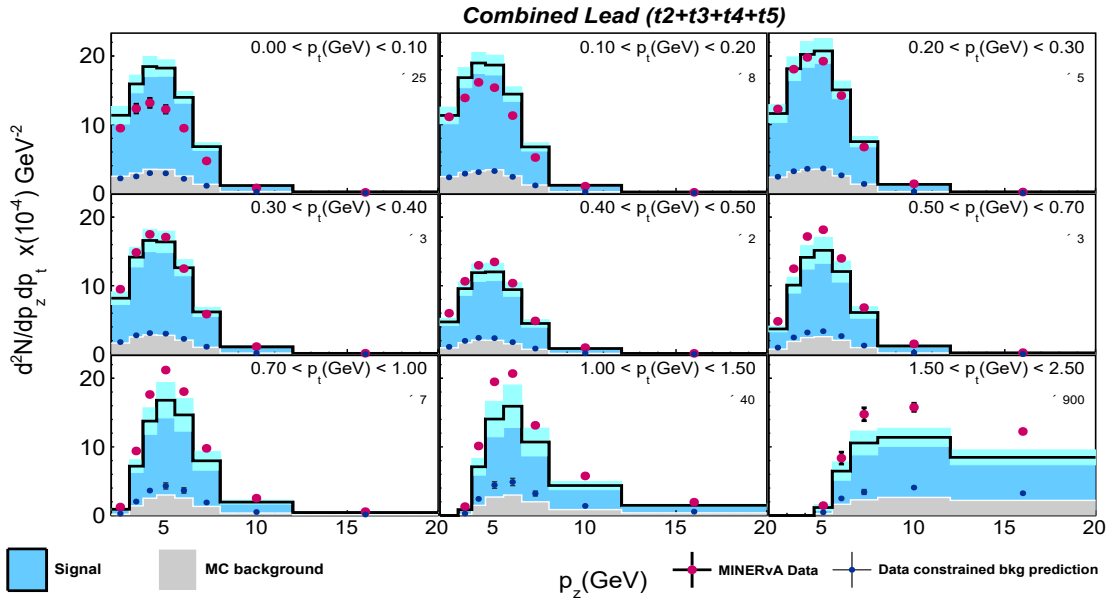

(b)

Figure B.23: Figure depicts the signal in MC (blue histogram) and data (red dots) for combined (a) iron and (b) lead, along with background predicted by MC (gray) and data constrained background (blue dots).

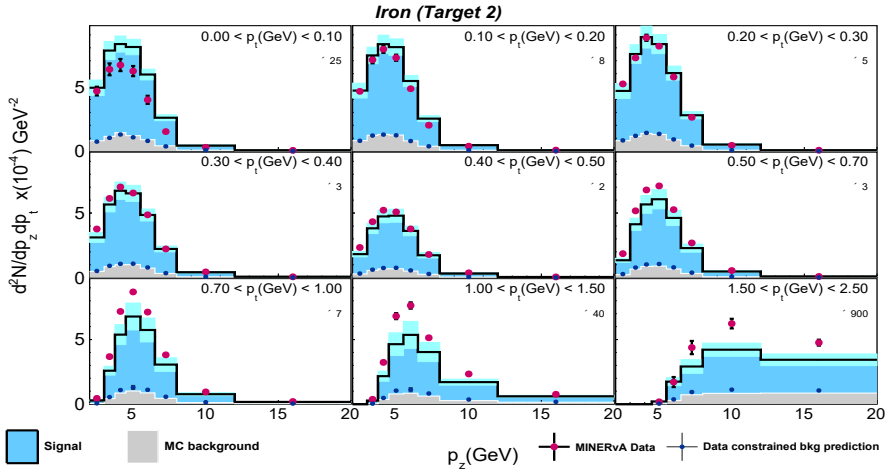

(a)

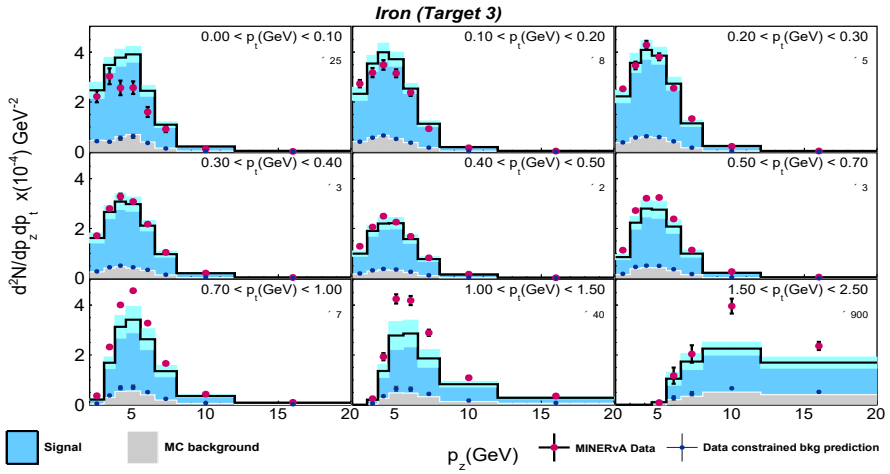

(b)

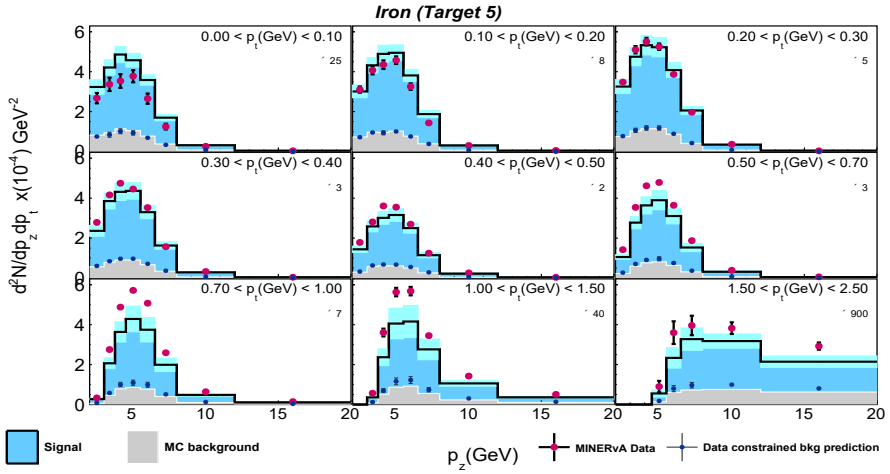

(c)

Figure B.24: Figure depicts the signal in MC (blue histogram) and data (red dots) for iron (a) target 2, (b) target 3 and (c) target 5, along with background predicted by MC (gray) and data constrained background (blue dots).

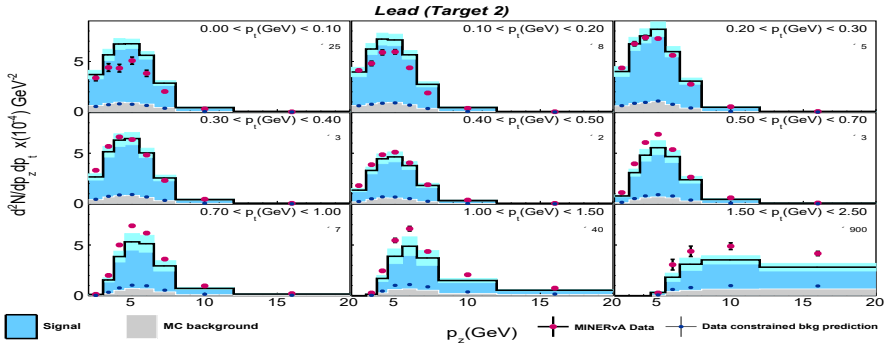

(a)

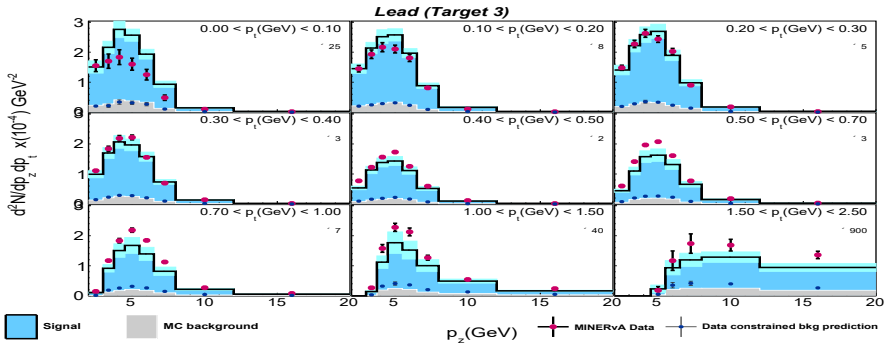

(b)

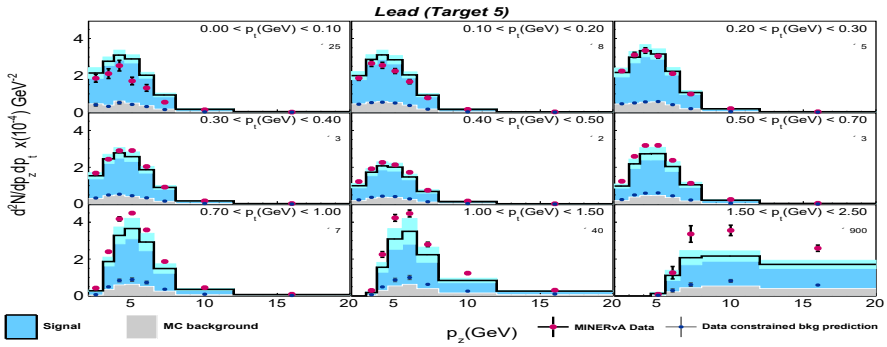

(c)

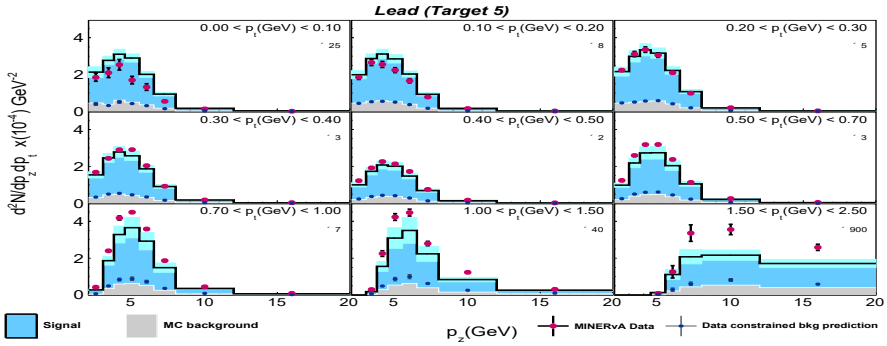

(d)

Figure B.25: Figure depicts the signal and background predictions for data and MC for lead (a) target 2, (b) target 3, (c) target 4 and (d) target 5.

B.3 Background subtracted distributions

This section contains the distribution for background subtracted data and MC. Plots for combined iron, lead and carbon in $x - Q^2$ and $p_z - p_t$ were provided in the main text. Provided here are the distributions in $W - Q^2$ and target materials from individual targets.

$W - Q^2$ distribution

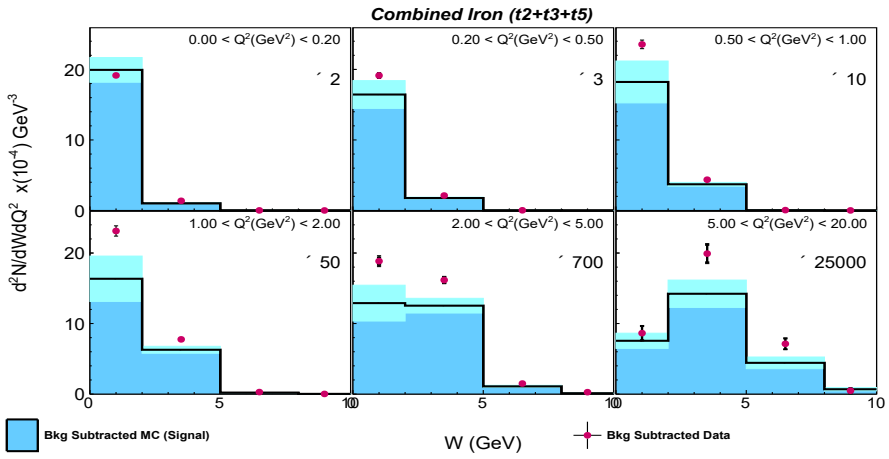

(a)

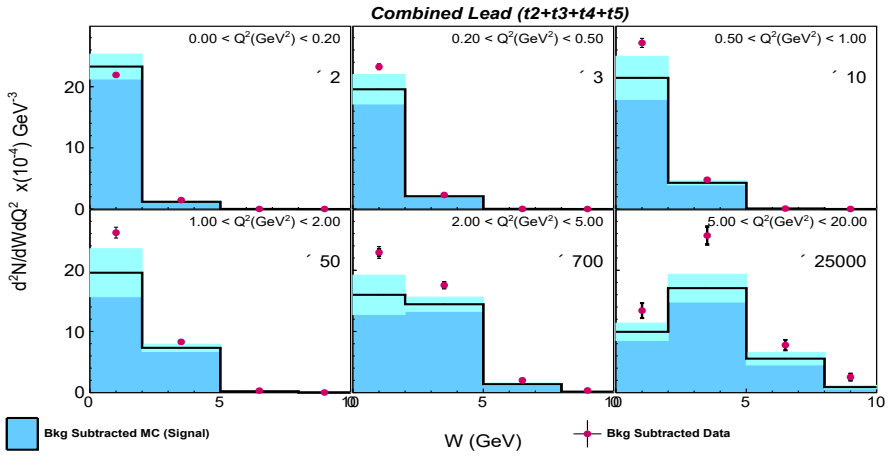

(b)

Figure B.26: Figure depicts background subtracted distributions in $W - Q^2$ bins for combined (a) iron and (b) lead.

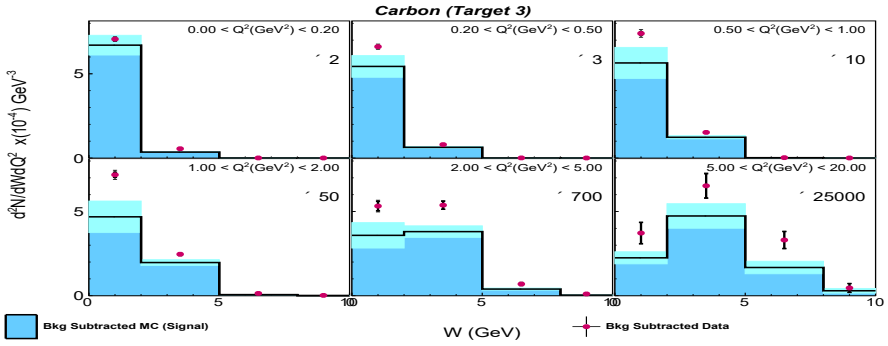

(a)

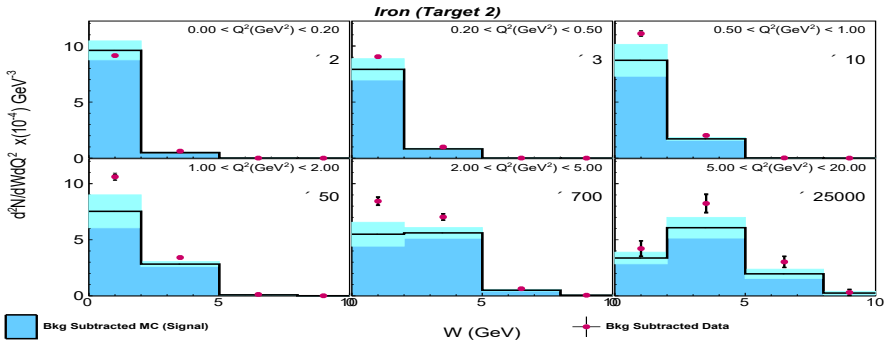

(b)

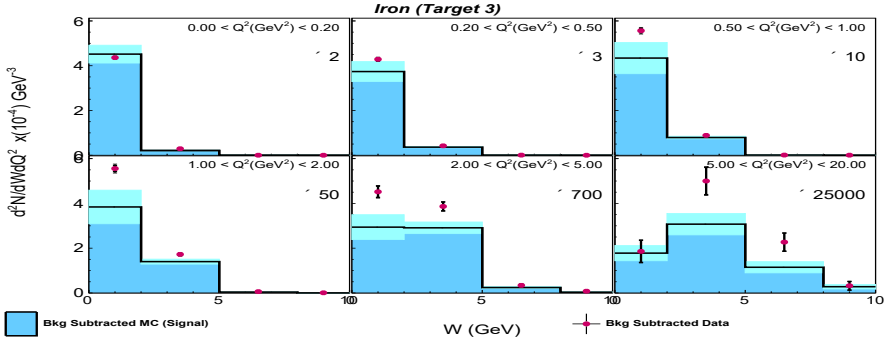

(c)

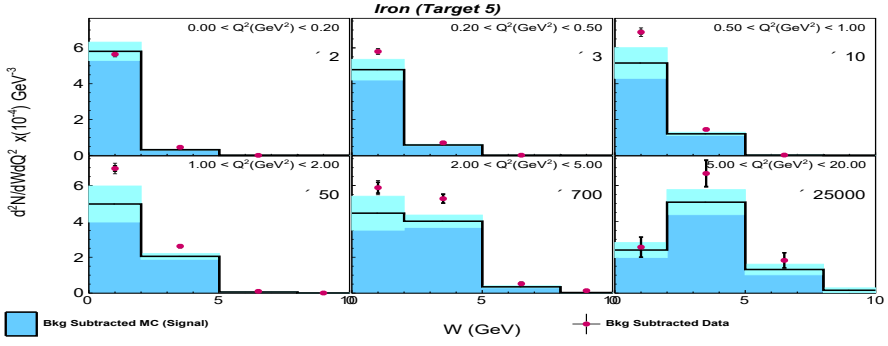

(d)

Figure B.27: Figure depicts background subtracted distributions in $W-Q^2$ bins for (a) carbon and iron in (b) target 2, (c) target 3 and (d) target 5.

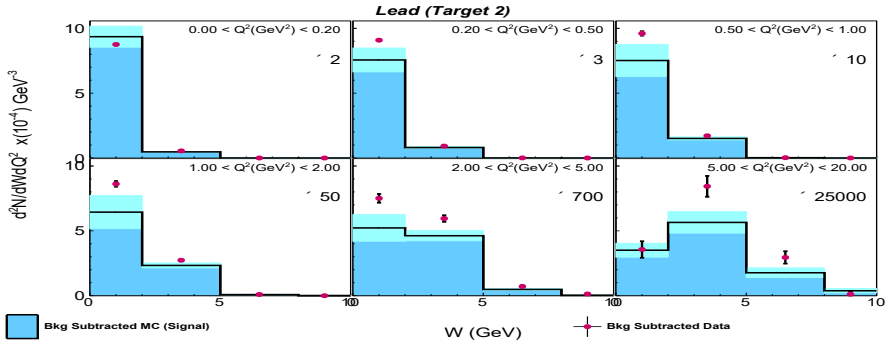

(a)

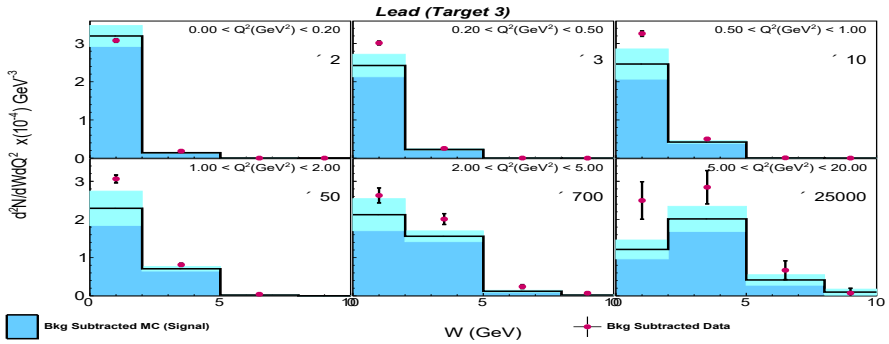

(b)

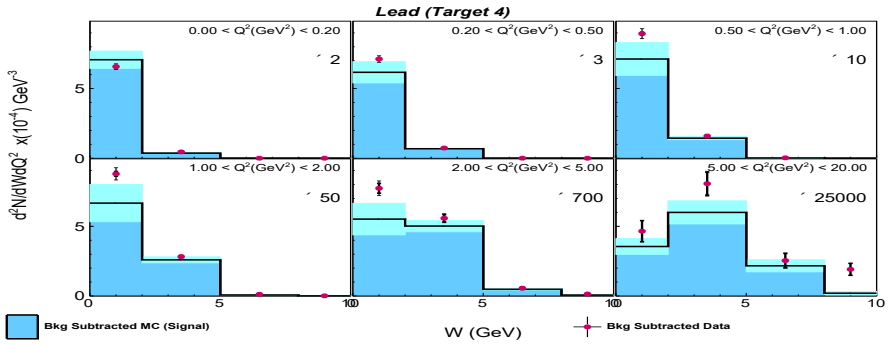

(c)

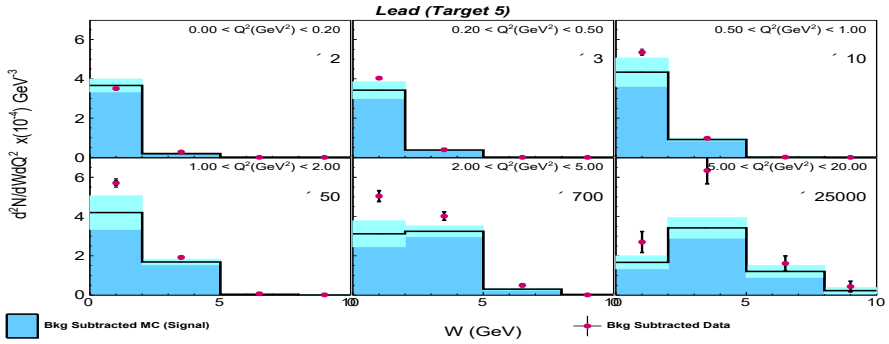

(d)

Figure B.28: Figure depicts background subtracted distributions in $W-Q^2$ bins for lead (a) target 2, (b) target 3, (c) target 4 and (d) target 5.

$x - Q^2$ distribution

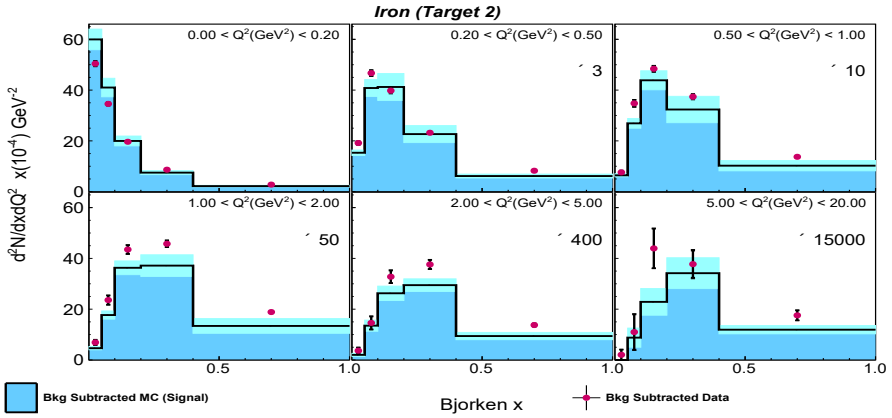

(a)

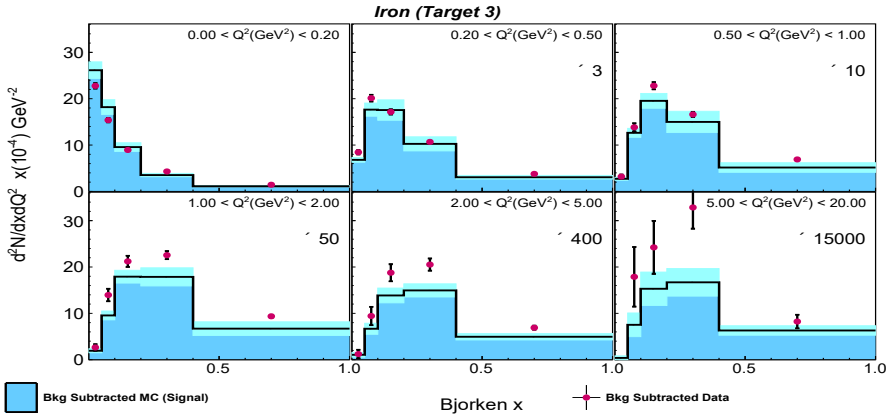

(b)

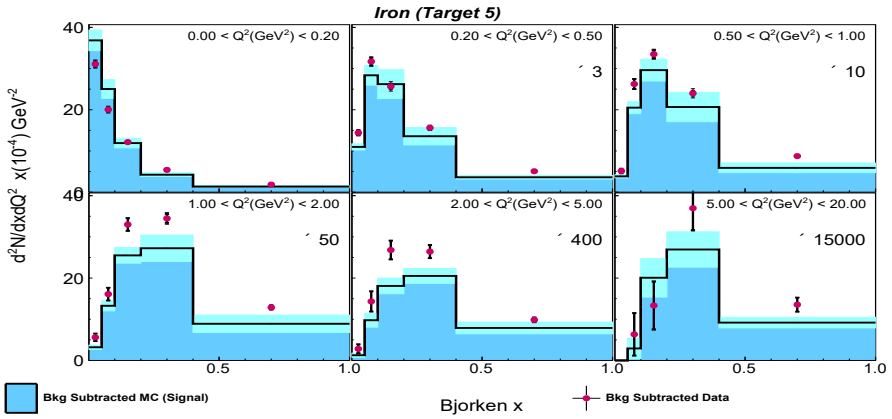

(c)

Figure B.29: Figure depicts background subtracted distributions in $x - Q^2$ bins for iron in (a) target 2, (b) target 3 and (c) target 5.

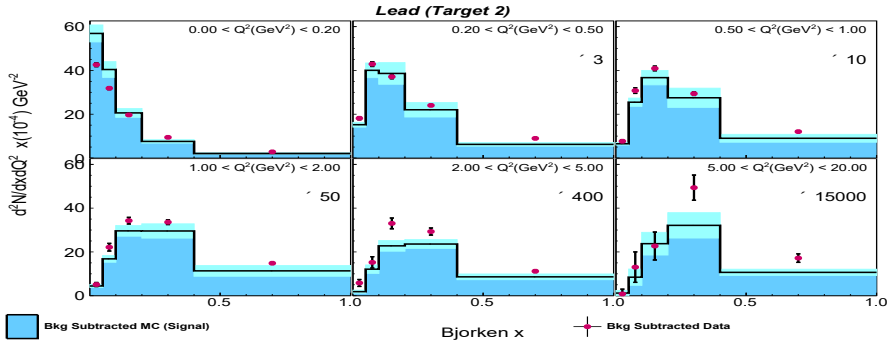

(a)

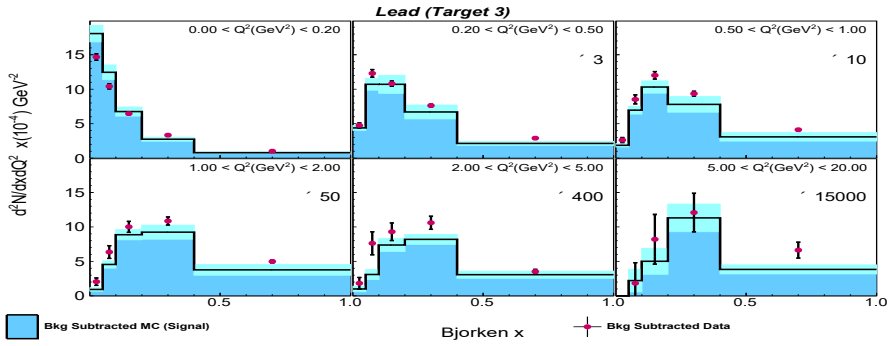

(b)

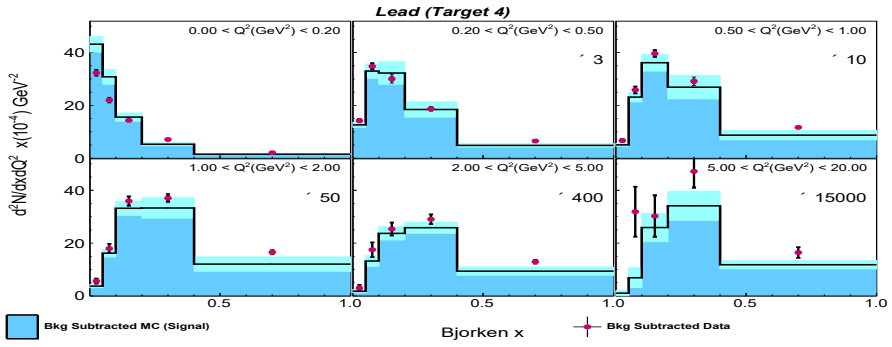

(c)

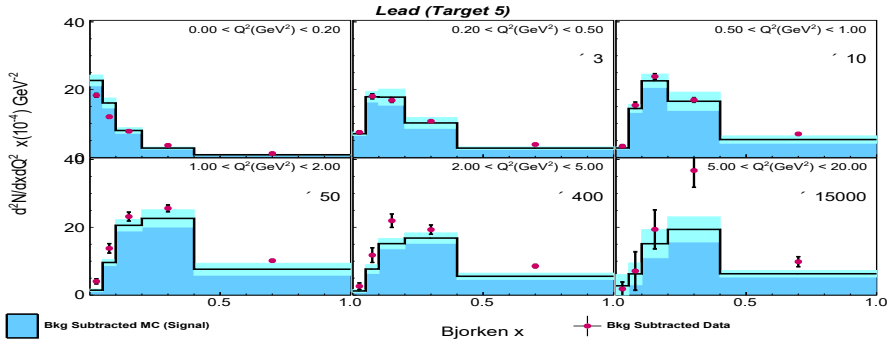

(d)

Figure B.30: Figure depicts background subtracted distributions in $x - Q^2$ bins for lead (a) target 2, (b) target 3, (c) target 4 and (d) target 5.

$p_z - p_t$ distribution

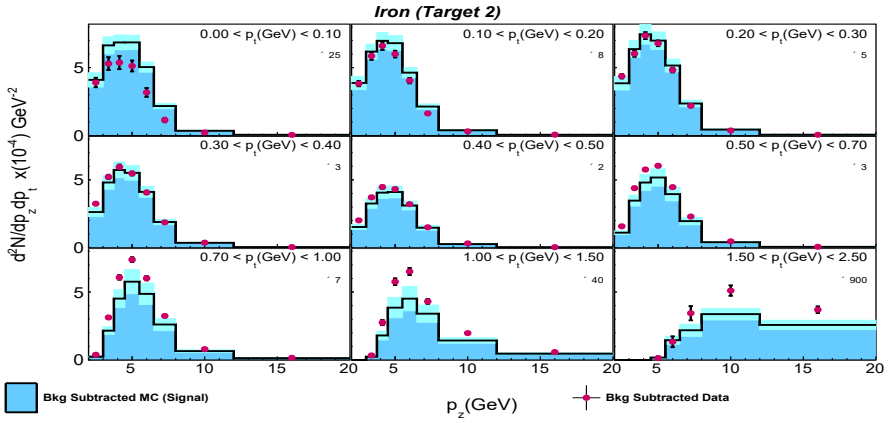

(a)

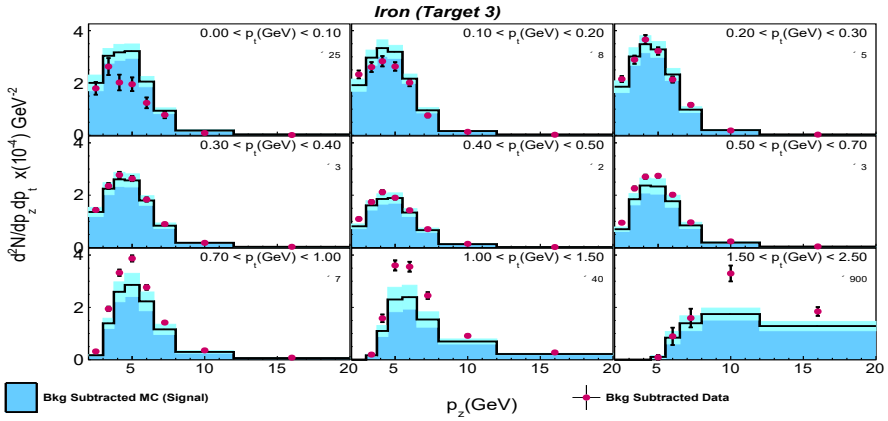

(b)

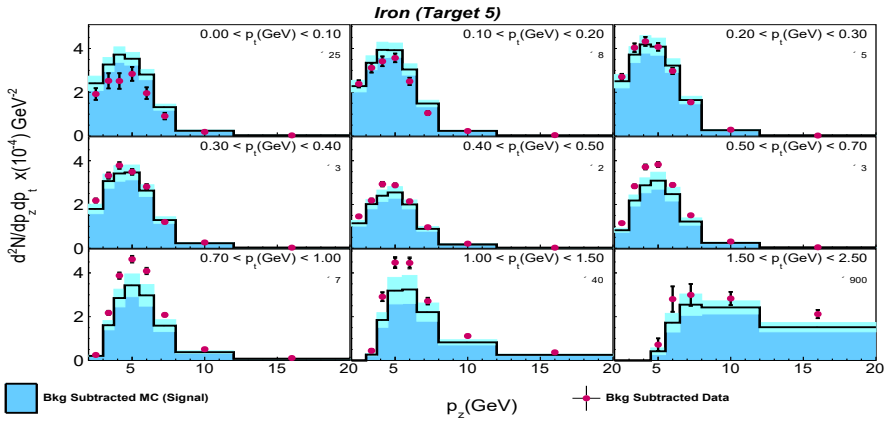

(c)

Figure B.31: Figure depicts background subtracted distributions in $p_z - p_t$ bins for iron in (a) target 2, (b) target 3 and (c) target 5.

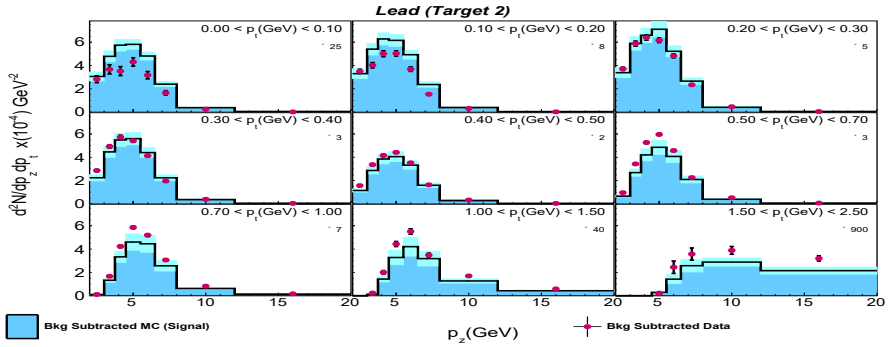

(a)

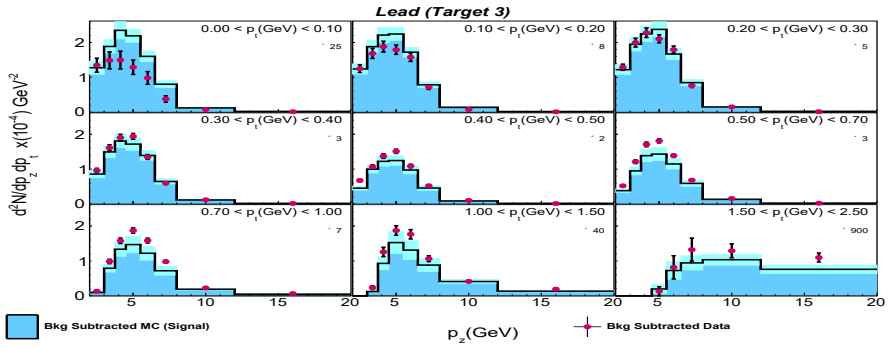

(b)

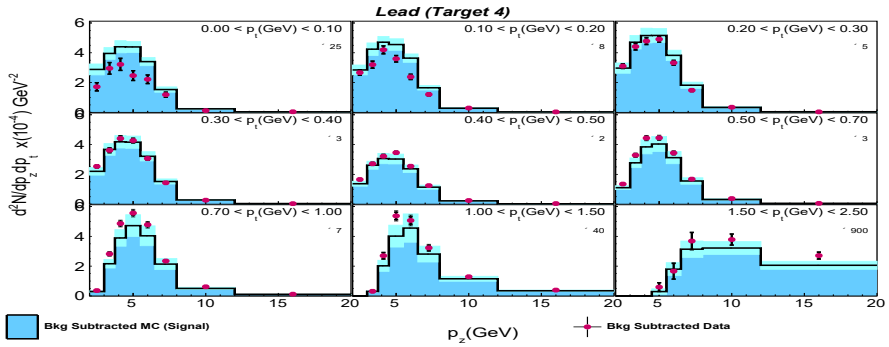

(c)

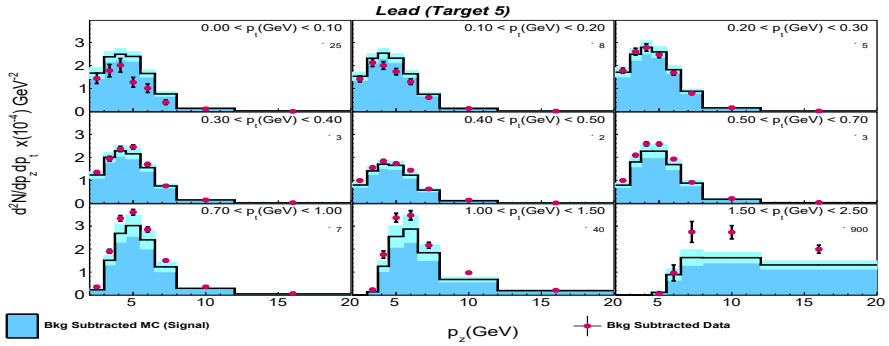

(d)

Figure B.32: Figure depicts background subtracted distributions in $p_z - p_t$ bins for lead (a) target 2, (b) target 3, (c) target 4 and (d) target 5.

$p_t - p_z$ **distributions**

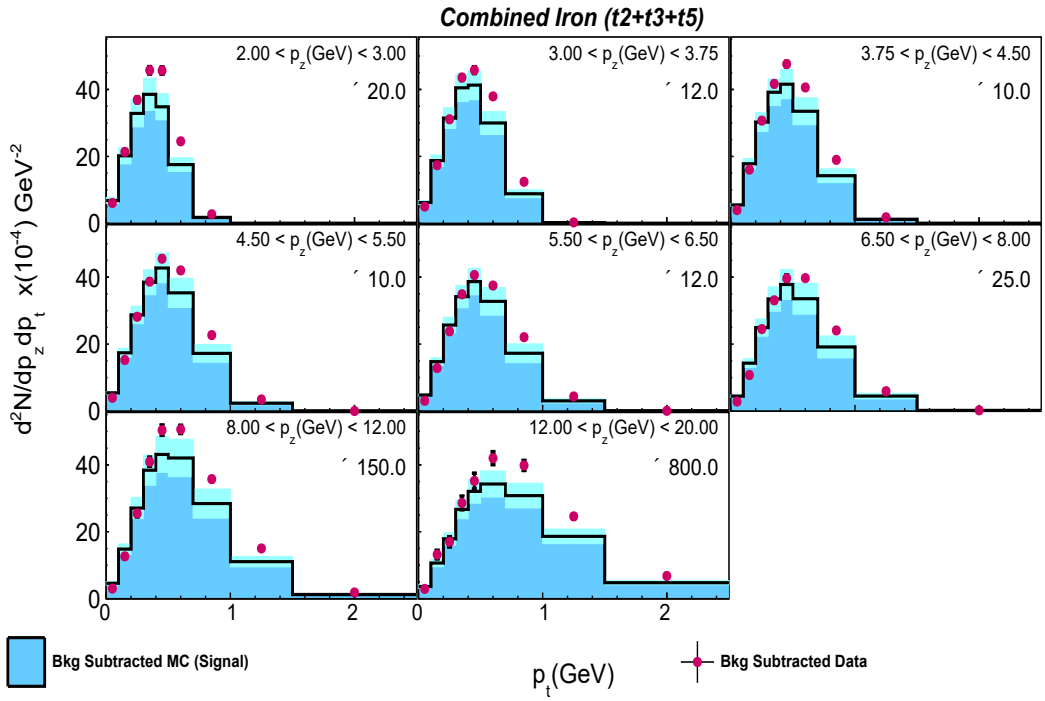

(a)

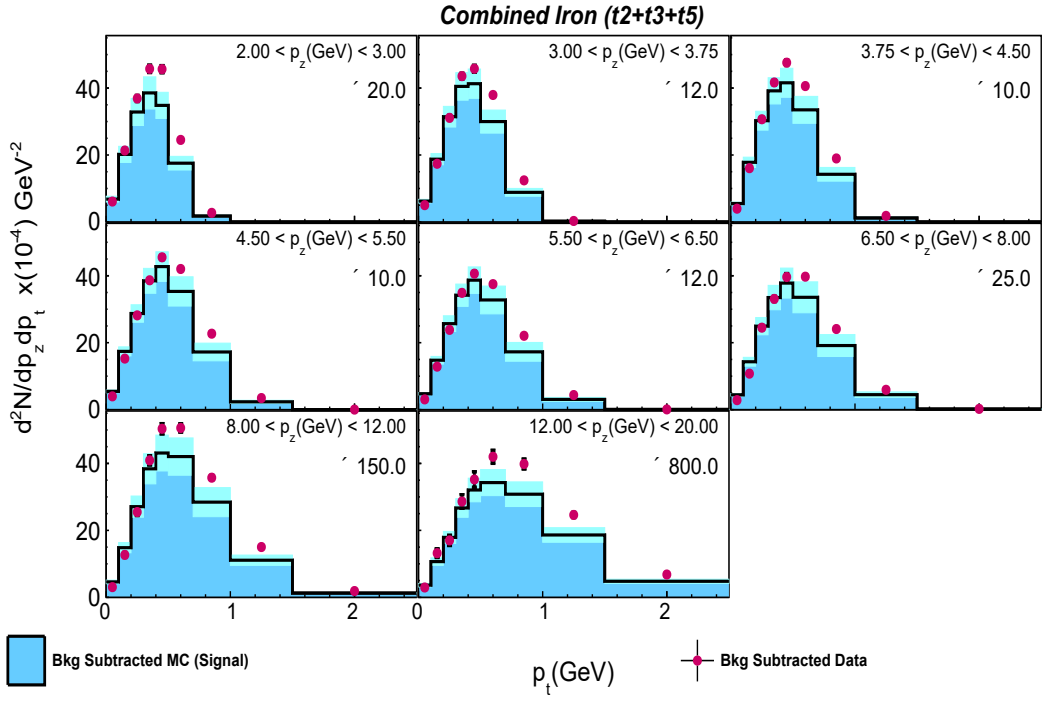

(b)

Figure B.33: Figure depicts background subtracted distributions in $p_t - p_z$ bins for combined (a) iron and (b) lead.

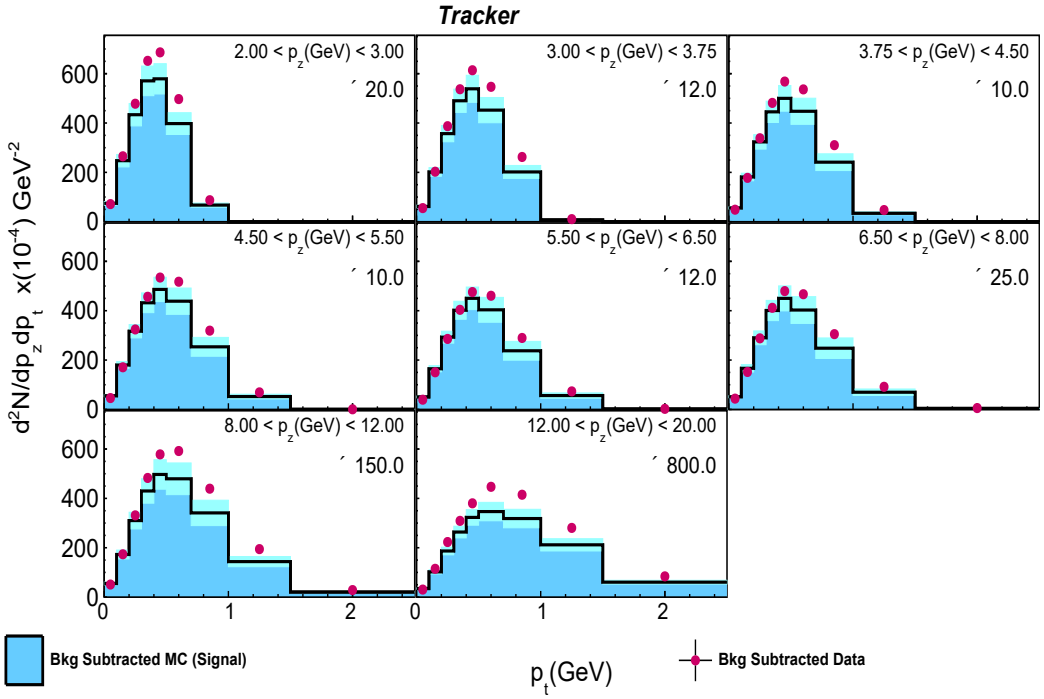

(a)

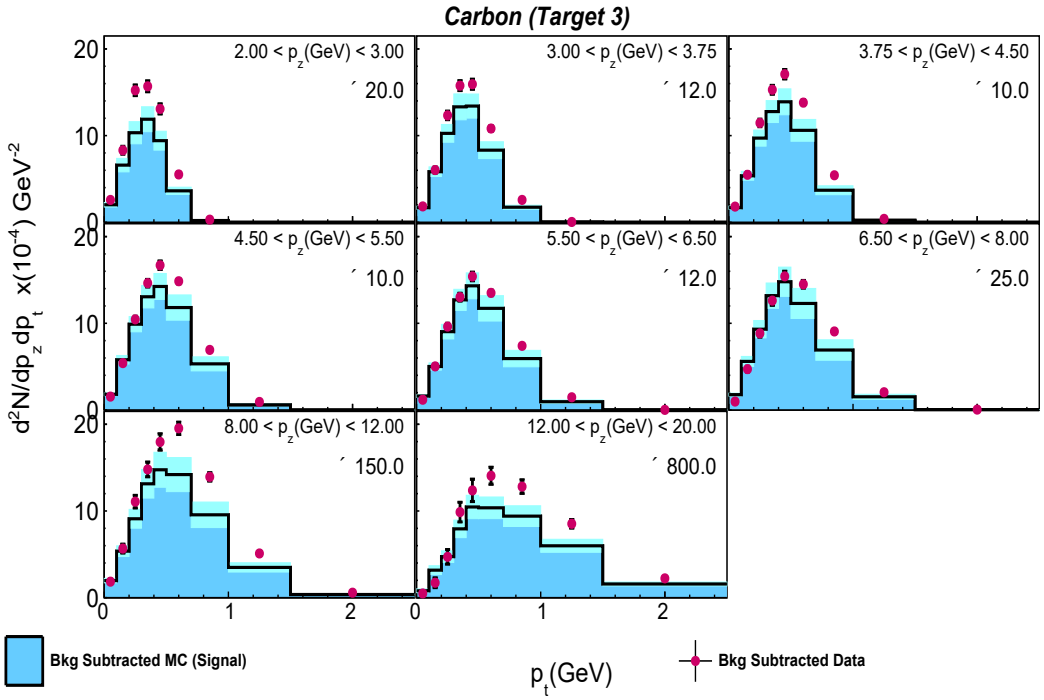

(b)

Figure B.34: Figure depicts background subtracted distributions in $p_t - p_z$ bins for (a) tracker and (b) carbon.

B.4 Fractional uncertainties

This section presents the fractional systematic uncertainties in data associated with background subtracted distributions.

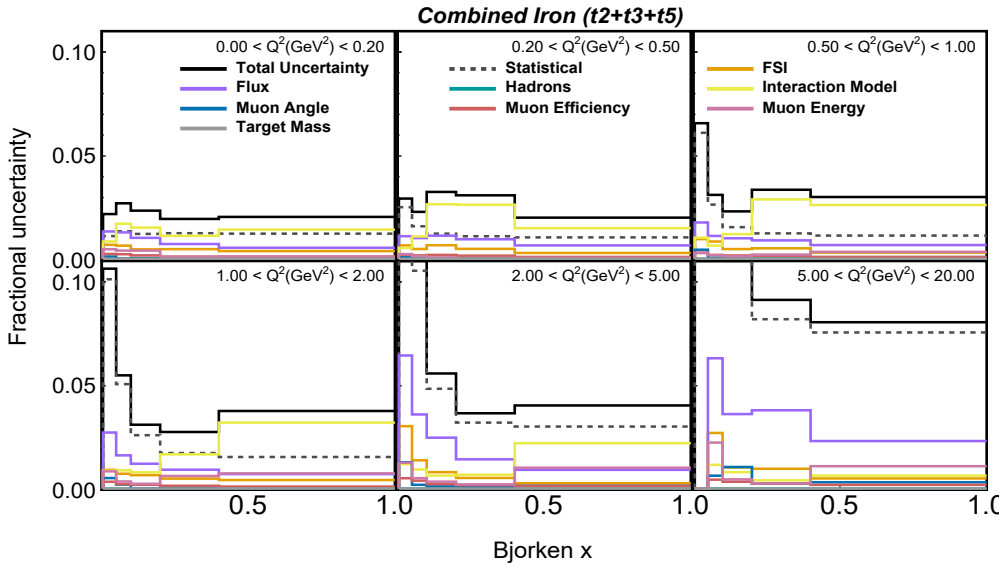

(a)

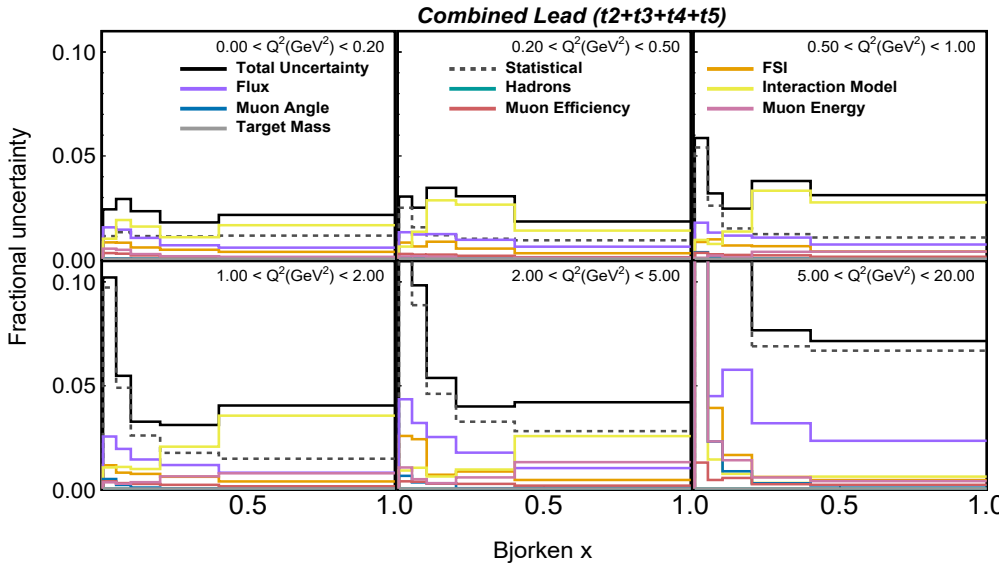

(b)

Figure B.35: Fractional uncertainties in background subtracted data for (a) combined iron and (b) combined lead in bins of $x - Q^2$.

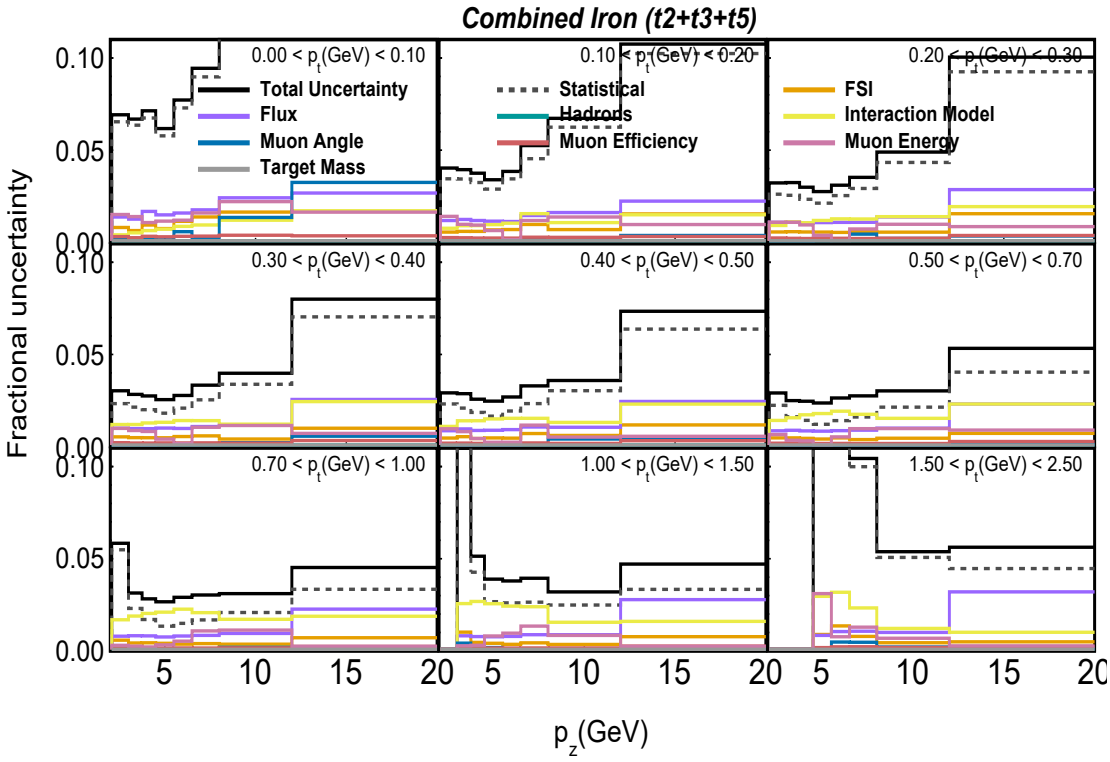

(a)

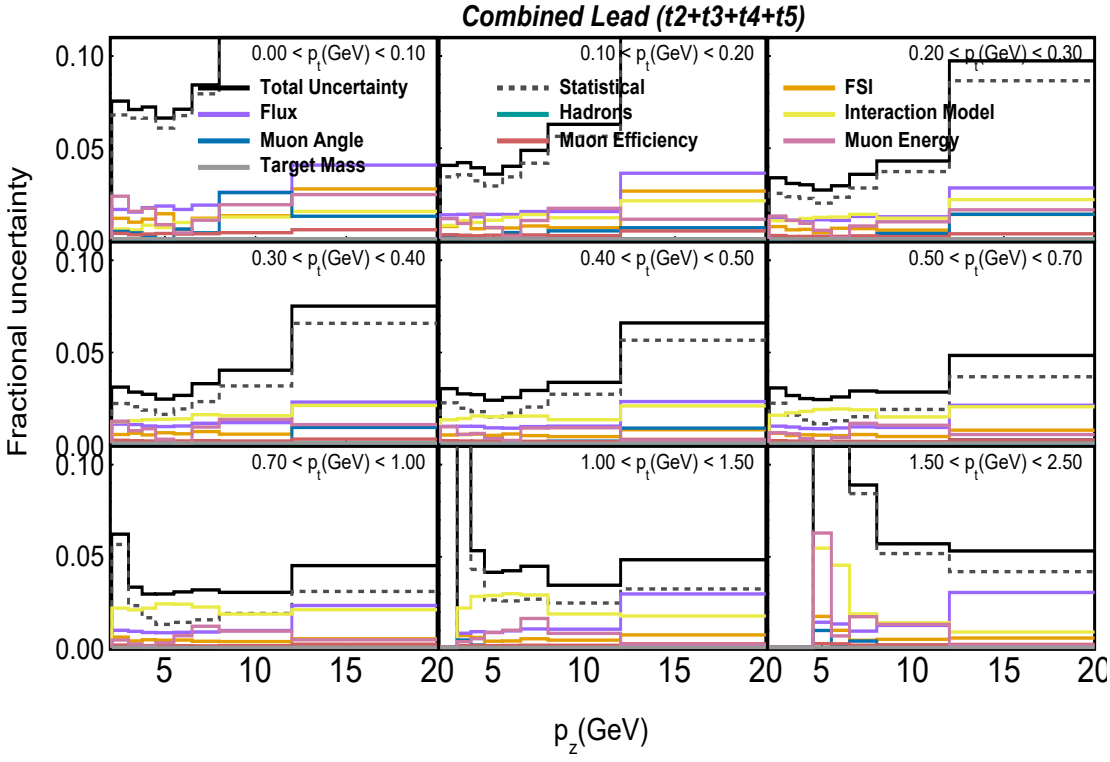

(b)

Figure B.36: Fractional uncertainties in background subtracted data for (a) combined iron and (b) combined lead in bins of $p_z - p_t$.

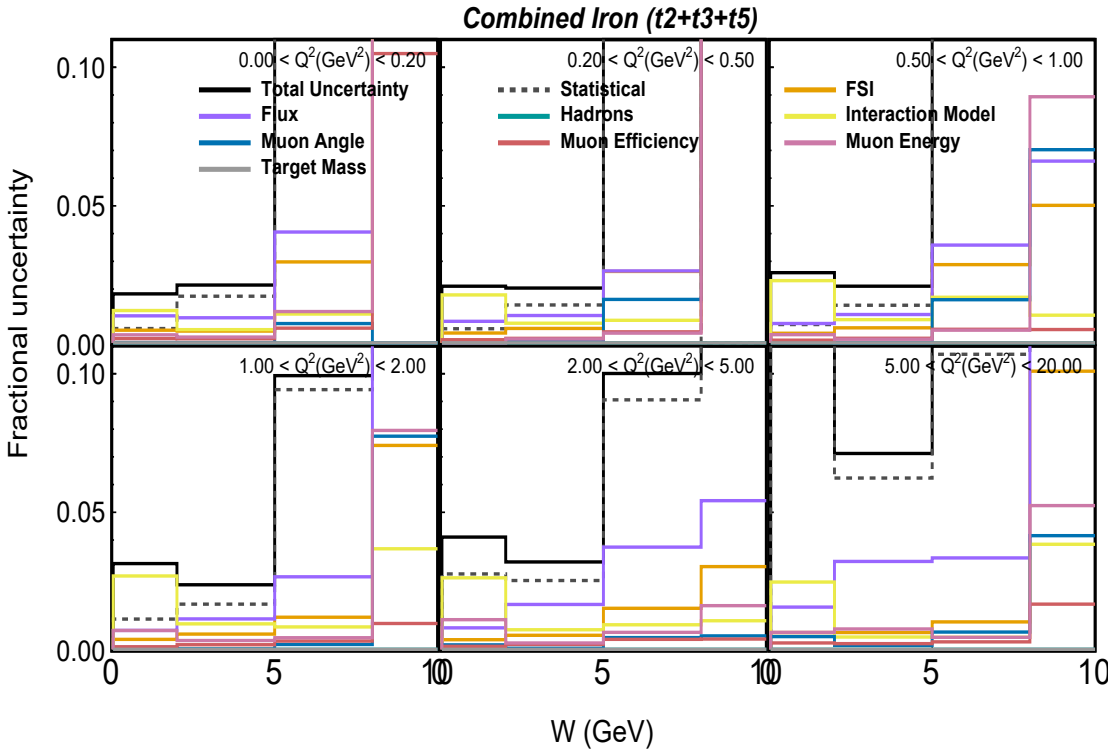

(a)

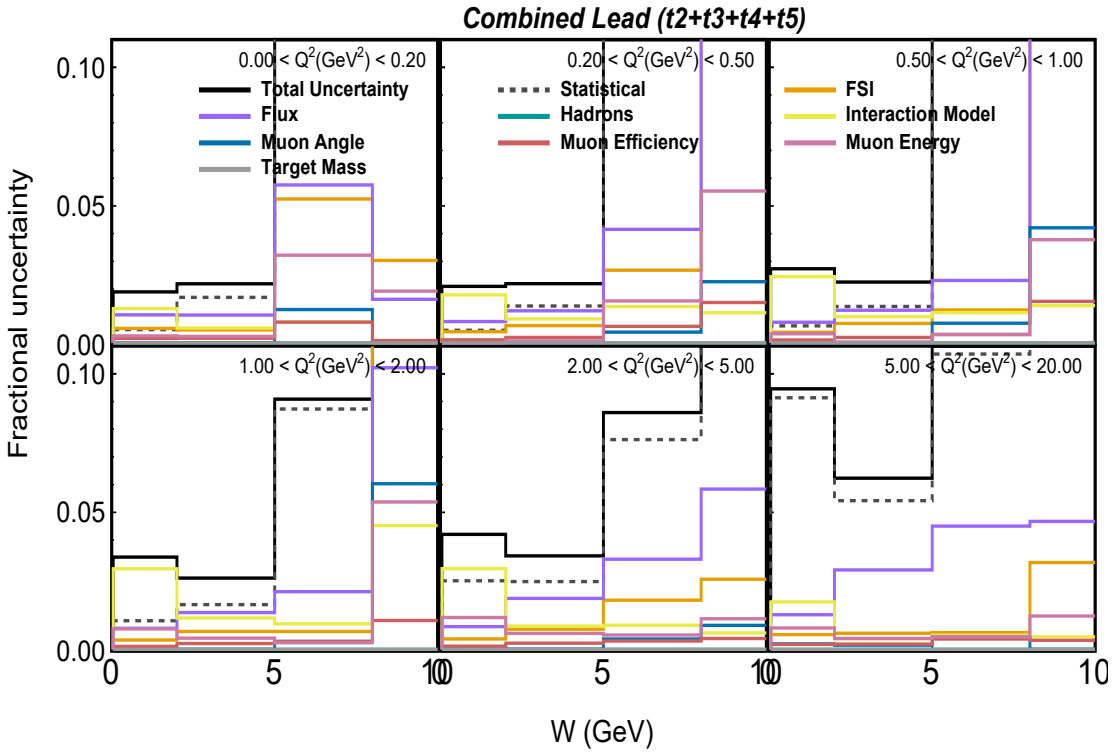

(b)

Figure B.37: Fractional uncertainties in background subtracted data for (a) combined iron and (b) combined lead in bins of $W - Q^2$.

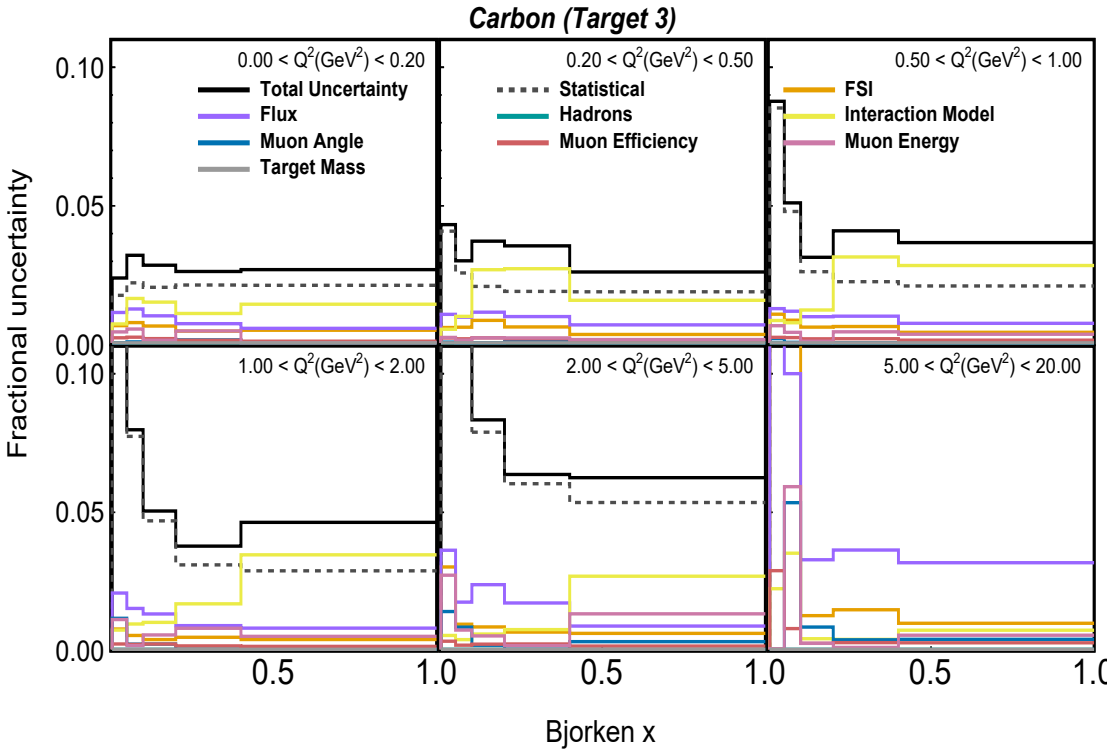

(a)

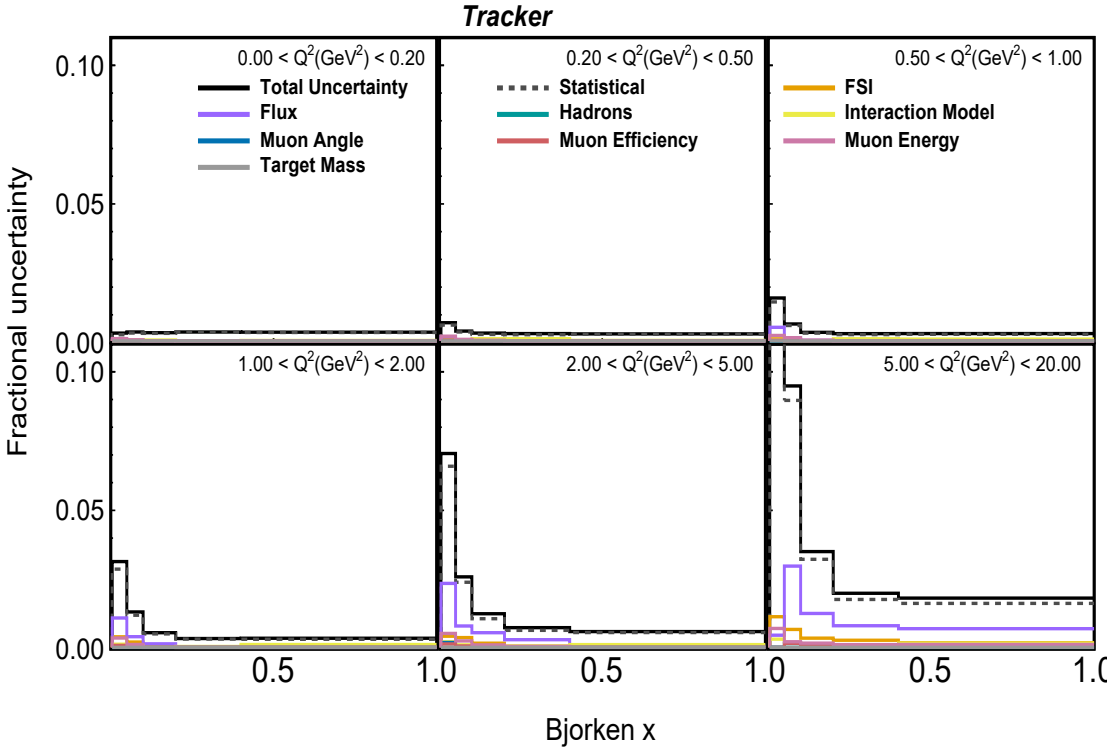

(b)

Figure B.38: Fractional uncertainties in background subtracted data for (a) carbon and (b) tracker in bins of $x - Q^2$.

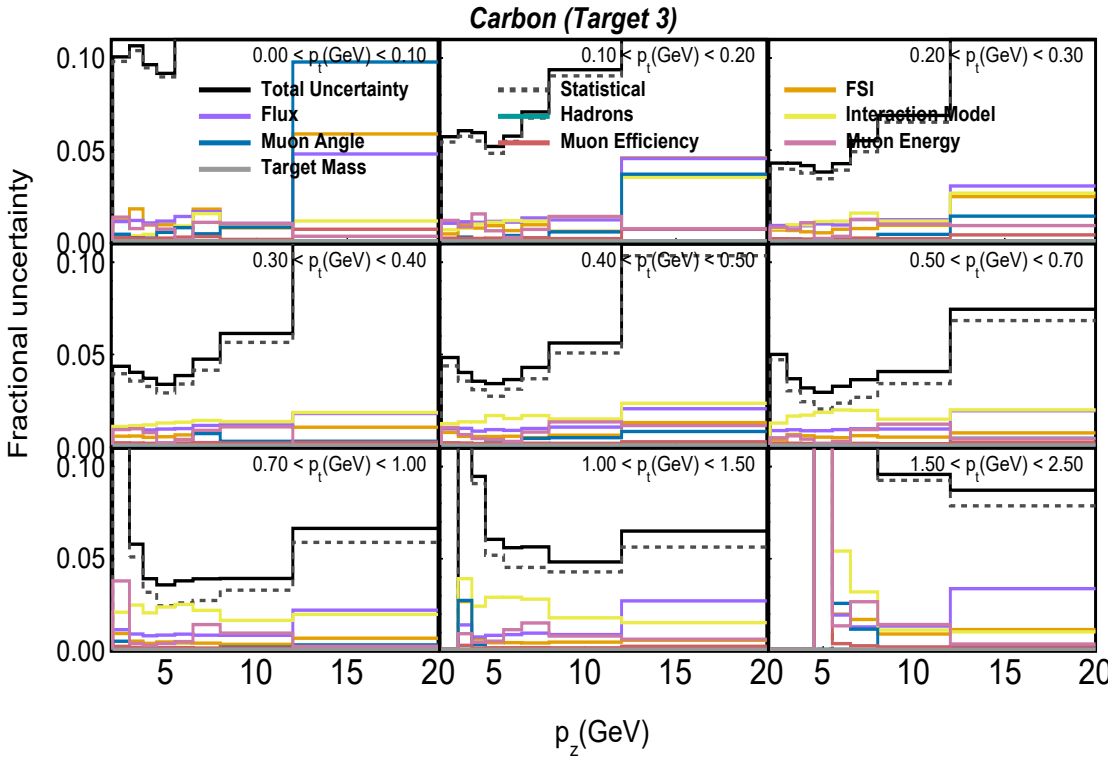

(a)

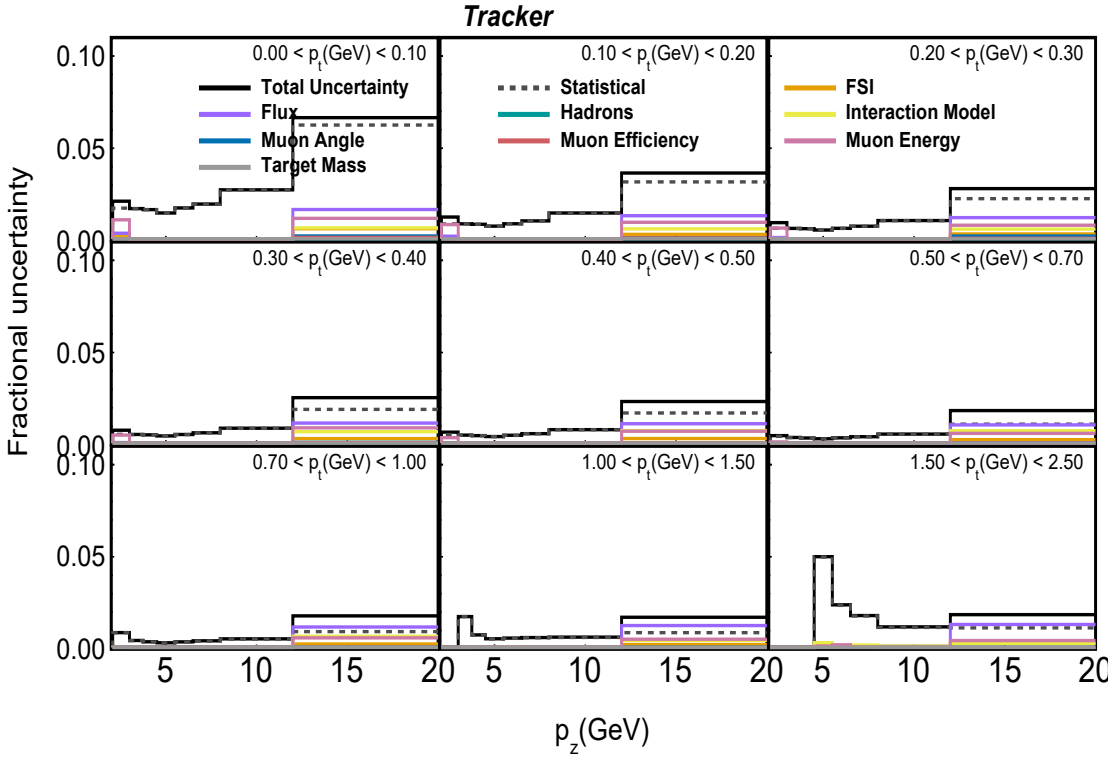

(b)

Figure B.39: Fractional uncertainties in background subtracted data for (a) carbon and (b) tracker in bins of $p_z - p_t$.

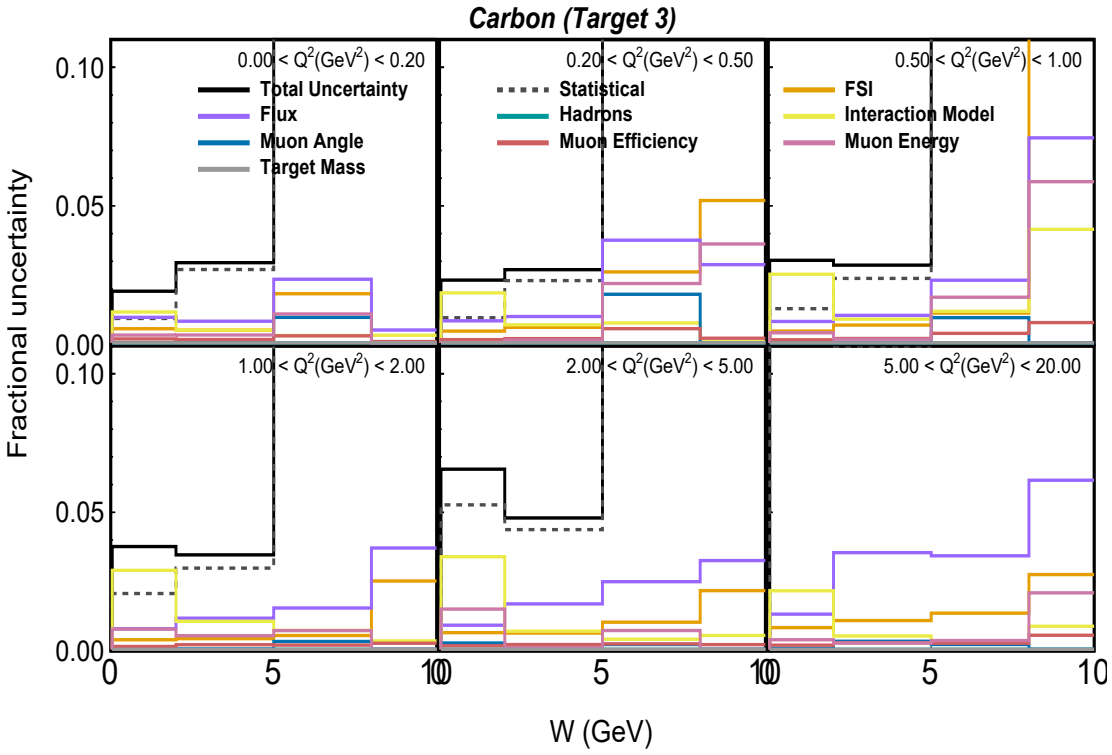

(a)

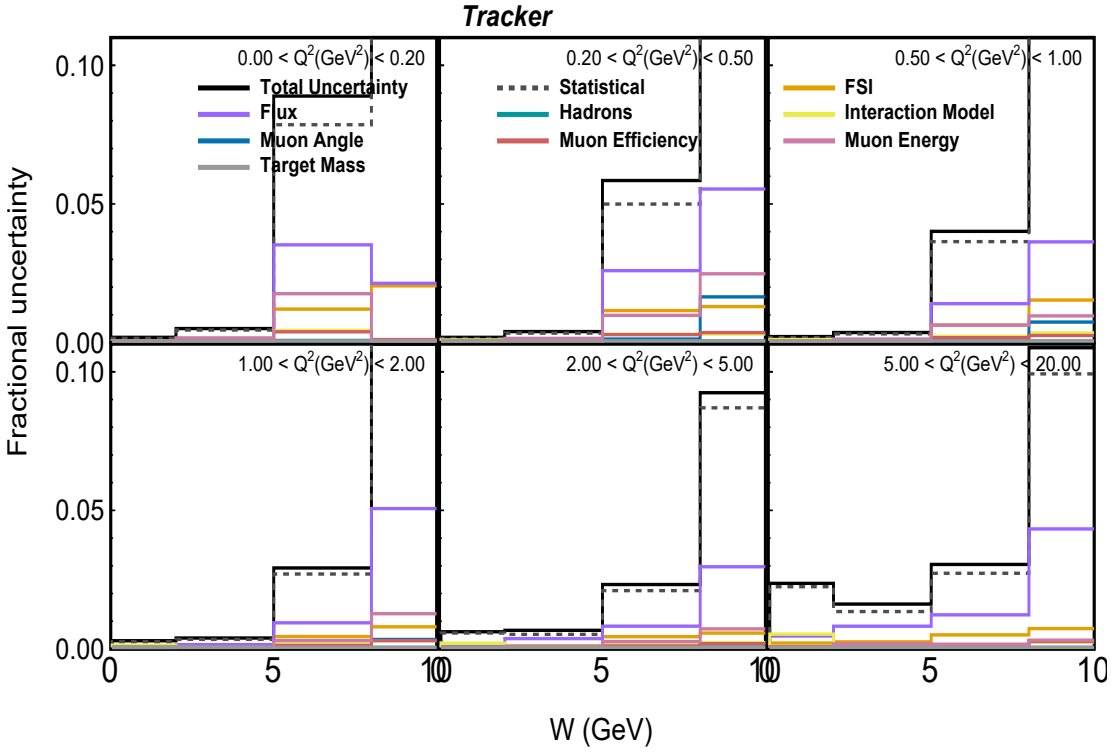

(b)

Figure B.40: Fractional uncertainties in background subtracted data for (a) carbon and (b) tracker in bins of $W - Q^2$.

Appendix C

Migration matrices

The presented migration matrices have been row normalised. Migration matrices for combined iron, combined lead, carbon and tracker were presented in the main text for $p_z - p_t$ and $x - Q^2$.

$W - Q^2$ migration matrices

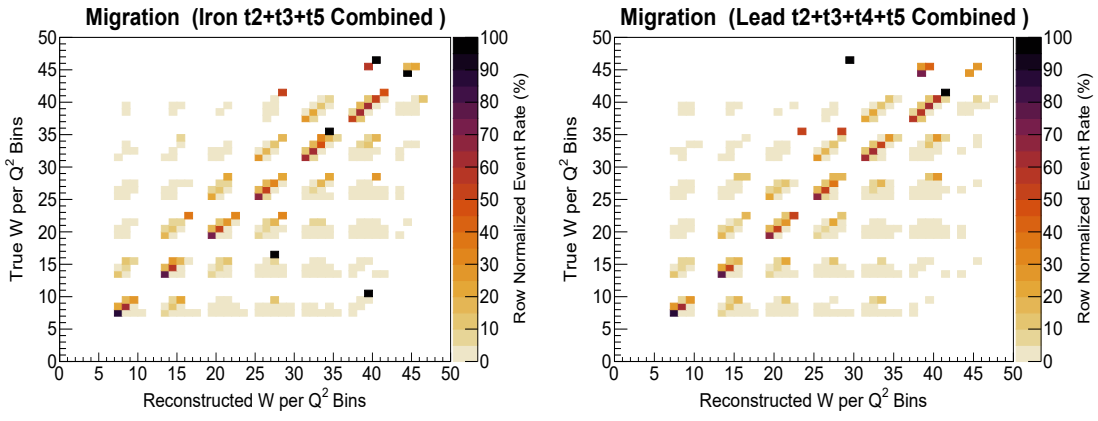

(a) **(b)**

Figure C.1: Row normalised migration matrices in $W - Q^2$ for (a) combined iron, (b) combined lead.

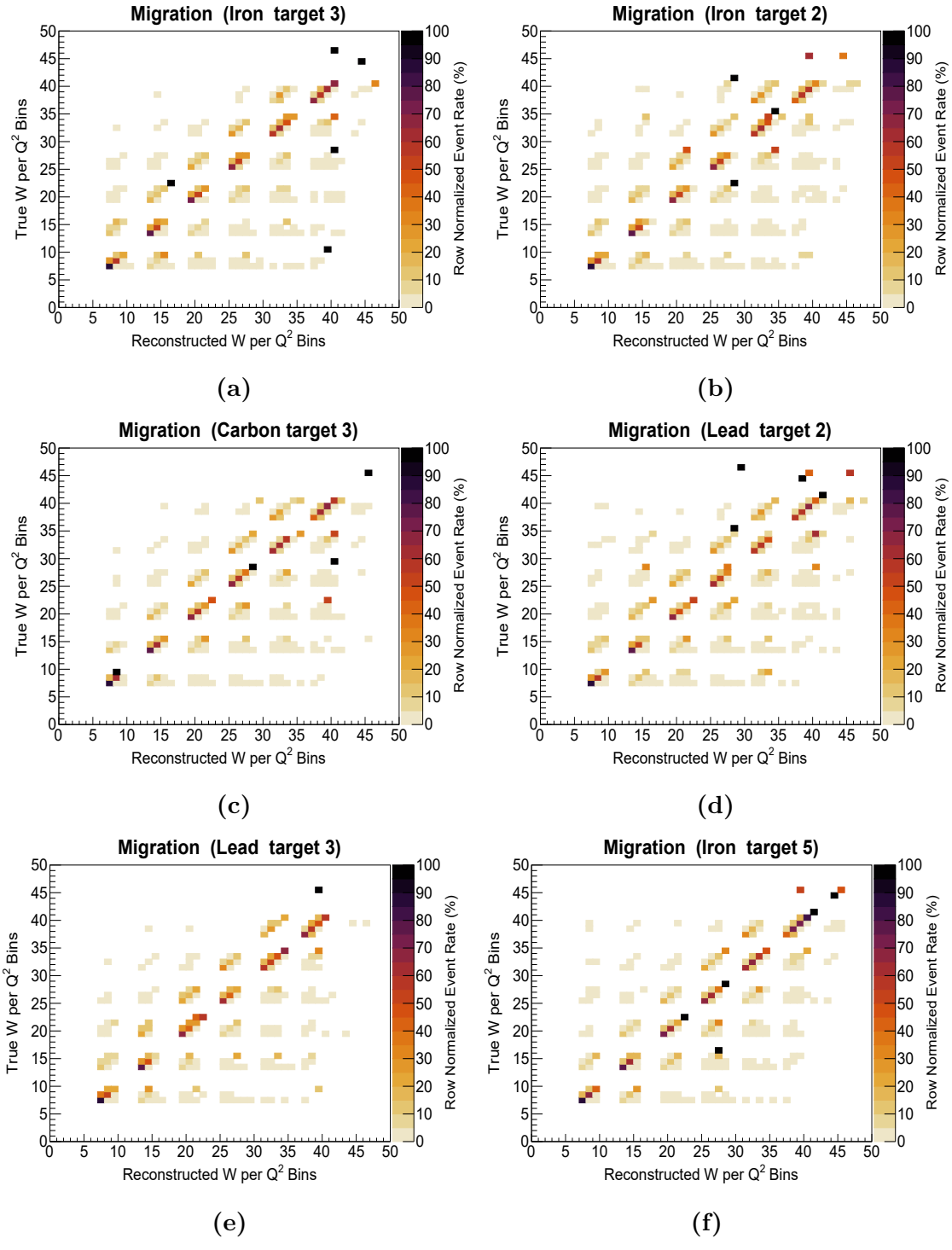

Figure C.2: Row normalised migration matrices in $W - Q^2$ for (a) target 3 iron (b) target 2 iron, (c) carbon, (d) lead target 2, (e) target 3 lead and (f) tracker.

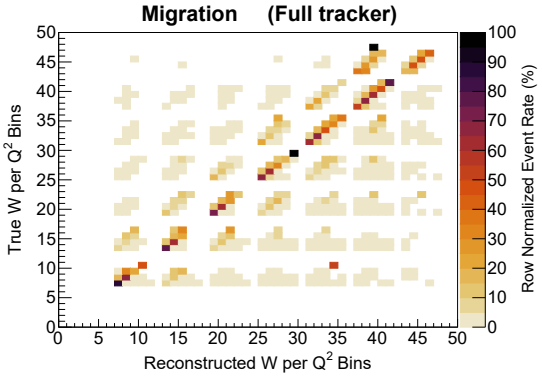

Figure C.3: Row normalised migration matrix in $W - Q^2$ for tracker.

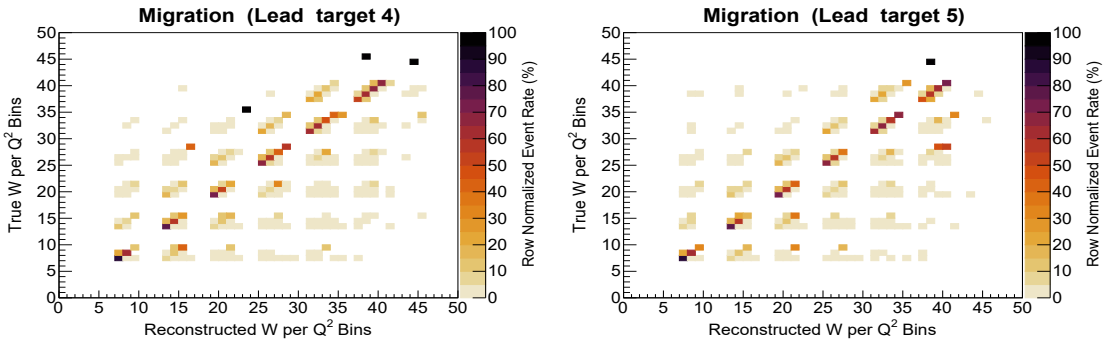

(a) **(b)**

Figure C.4: Row normalised migration matrices in $W - Q^2$ for (a) target 4 lead and (b) target 5 lead.

$x - Q^2$ migration matrices

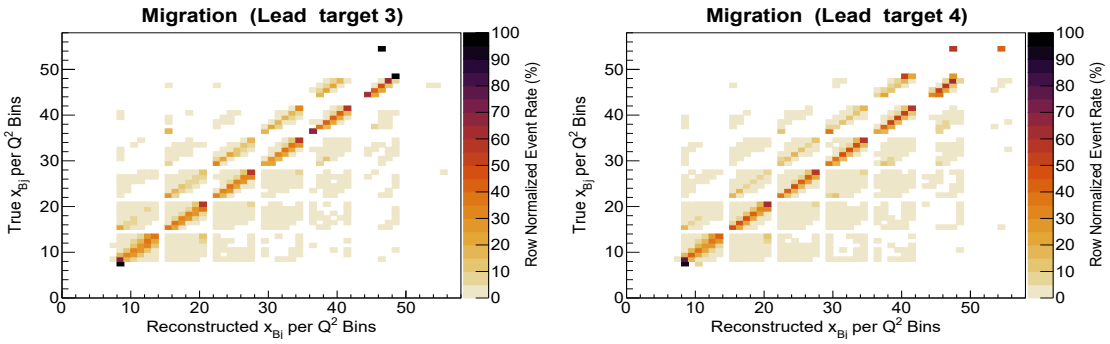

(a) **(b)**

Figure C.5: Row normalised migration matrices in $x - Q^2$ for (a) target 3 lead and (b) target 4 lead.

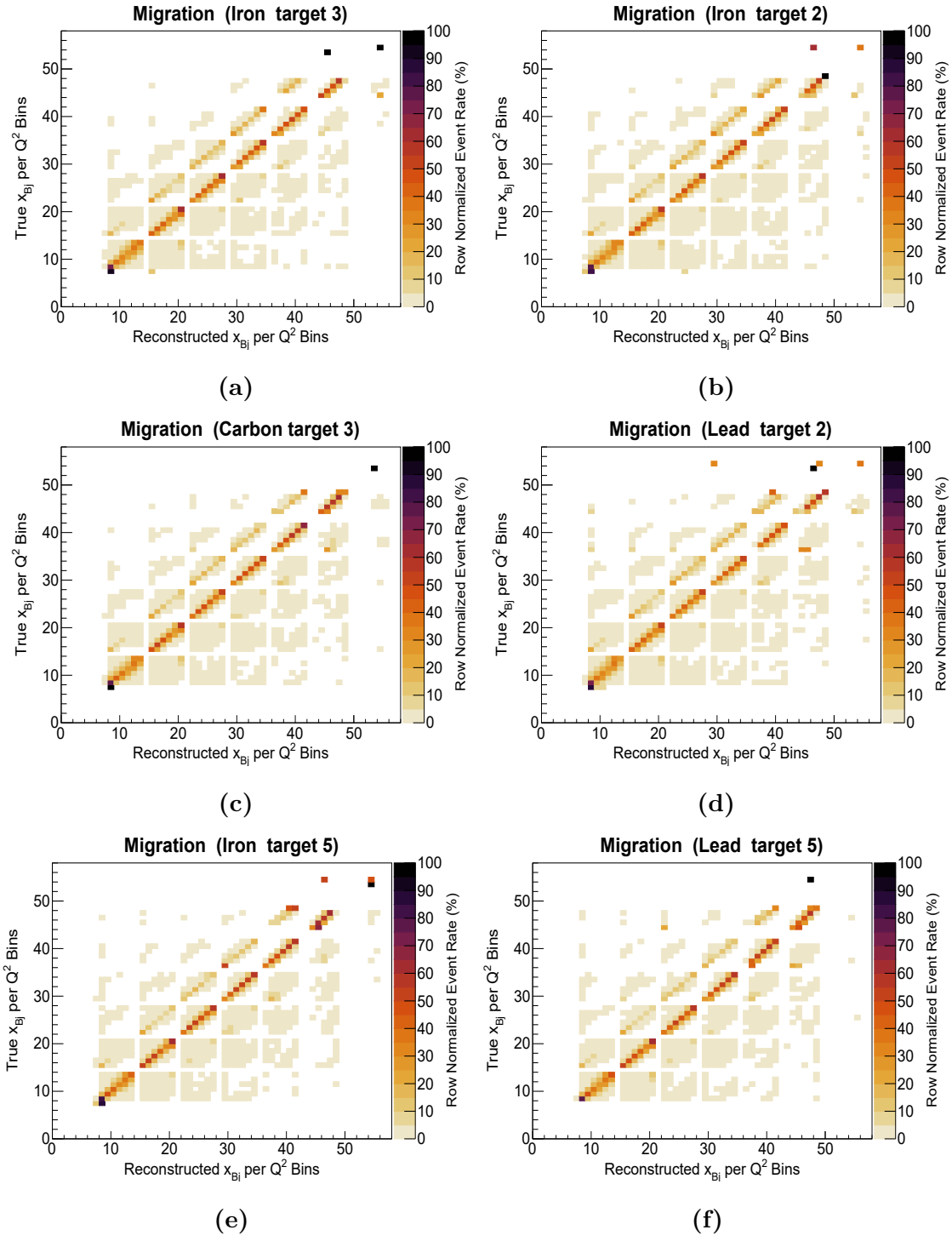

Figure C.6: Row normalised migration matrices in $W - Q^2$ for (a) target 3 iron (b) target 2 iron, (c) carbon, (d) lead target 2, (e) target 5 iron and (f) target 5 lead.

$p_z - p_t$ migration matrices

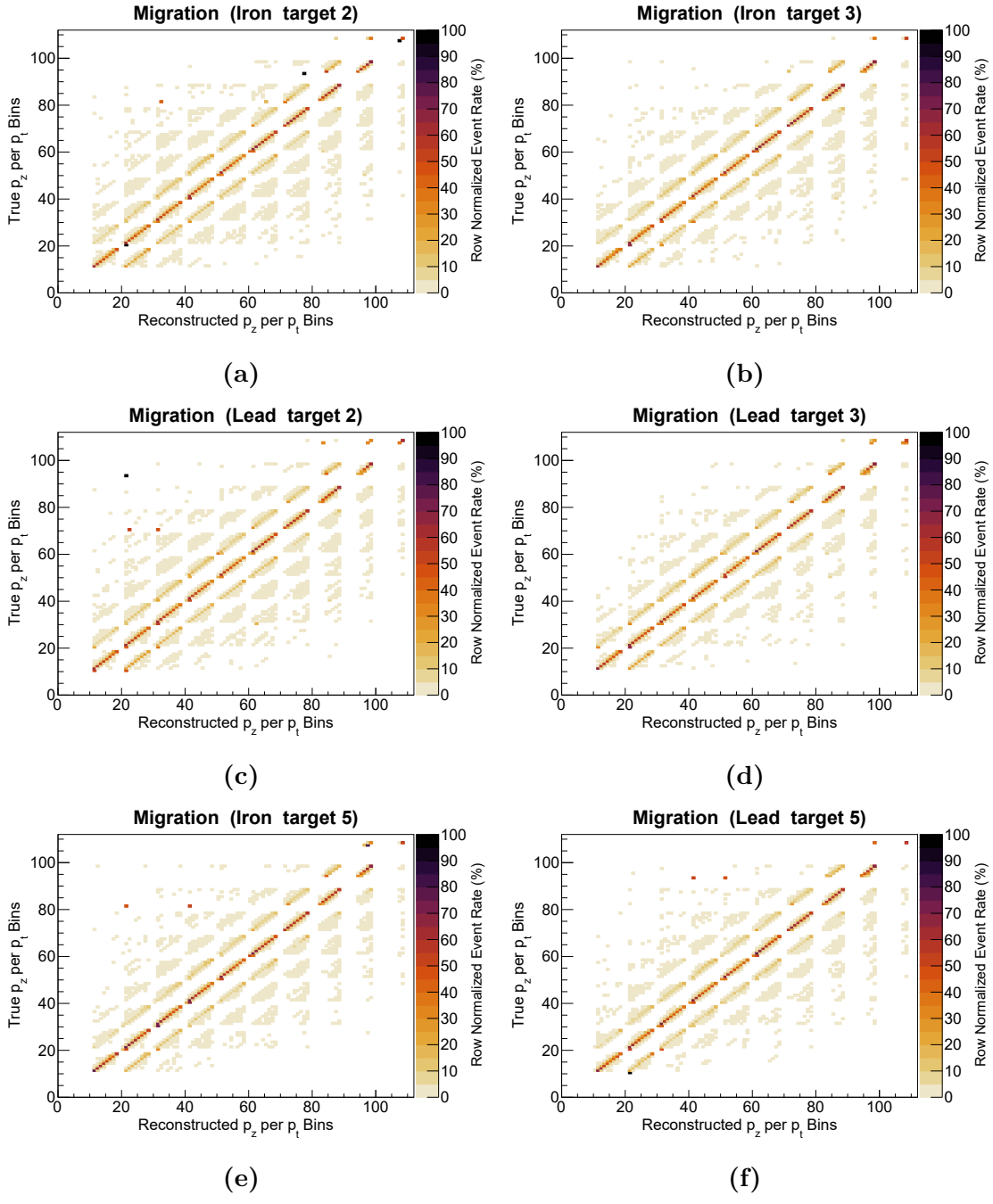

Figure C.7: Row normalised migration matrices in $p_z - p_t$ for (a) target 2 iron (b) target 3 iron, (c) target 2 lead, (d) lead target 3, (e) iron target 5 and (f) lead target 5.

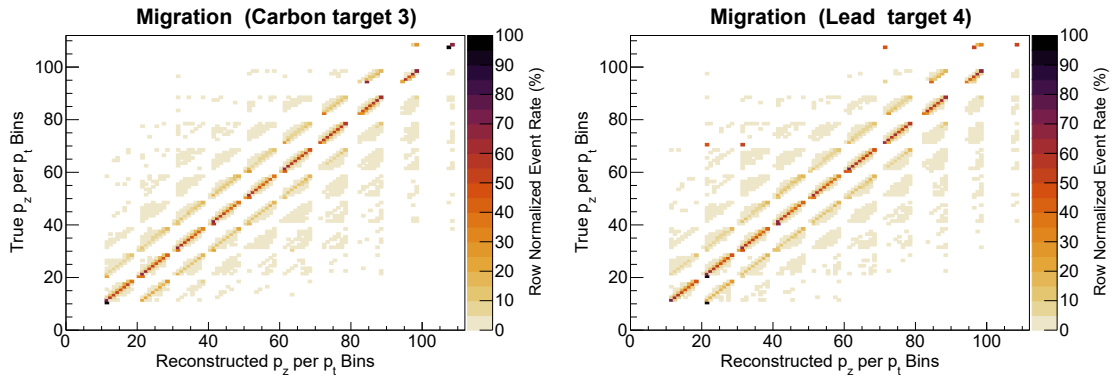

(a) **(b)**

Figure C.8: Row normalised migration matrices in $p_z - p_t$ for (a) carbon (b) target 4 lead

Appendix D

Warping Studies

This appendix contains figures for warping studies performed, for unfolding in $x - Q^2$ and $W - Q^2$ bins, using different warping functions. The figures have been plotted for χ^2 against the number of iterations used for unfolding. The mean and median χ^2 have been plotted in red and black solid lines respectively and the dashed line represents number of degrees of freedom which is total number of bins in the two dimensional chosen variables.

x-Q^2 warping studies

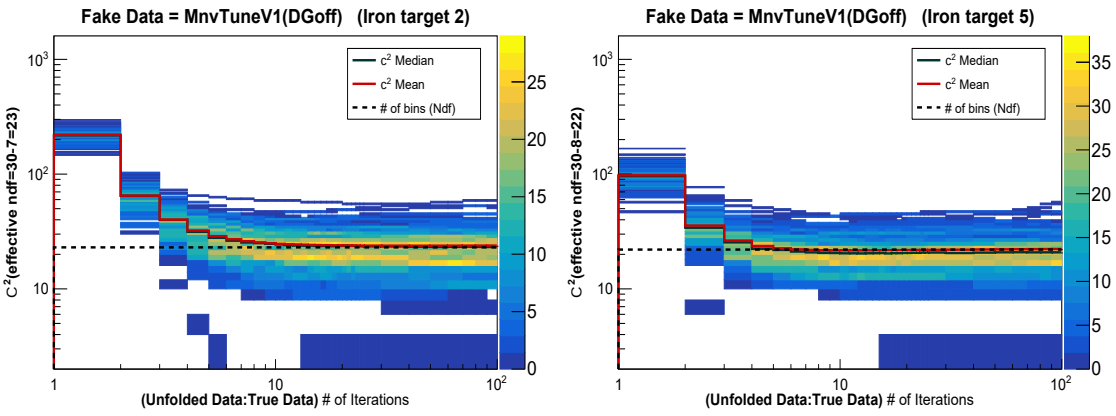

(a) **(b)**

Figure D.1: Warp 1: Fake data as switching off the DeuteriumGeniePion tune reweight in the CV MC. Plot shows χ^2 against number of iterations for for $x - Q^2$ in (a) target 2 iron and (b) target 5 iron.

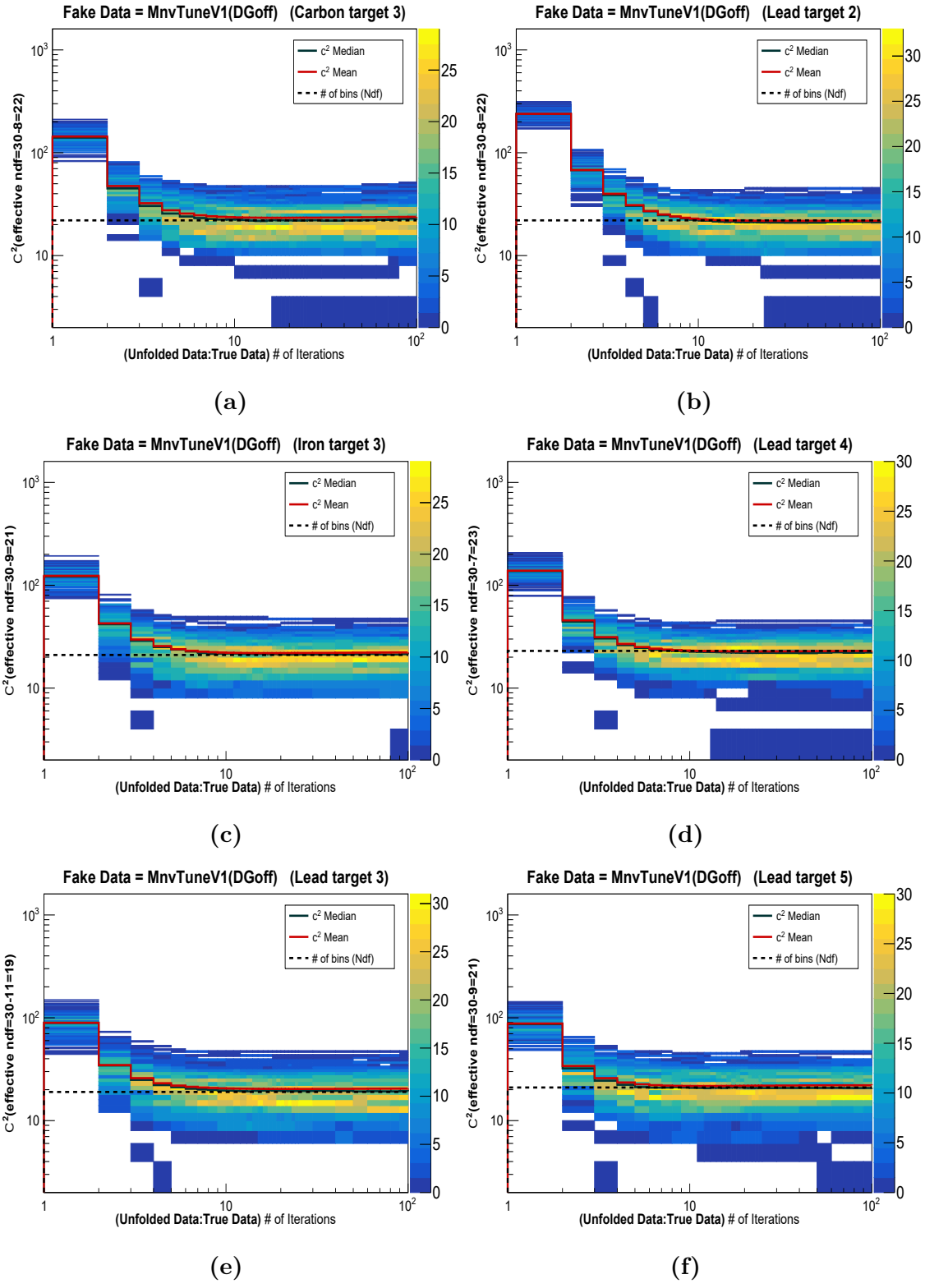

Figure D.2: Warp 1: Fake data as switching off the DeuteriumGeniePion tune reweight in the CV MC. Plot shows χ^2 against number of iterations for for $x - Q^2$ in (a) carbon, (b) target 2 lead, (c) target 3 iron, (d) target 4 lead, (e) target 3 lead and (f) target 5 lead.

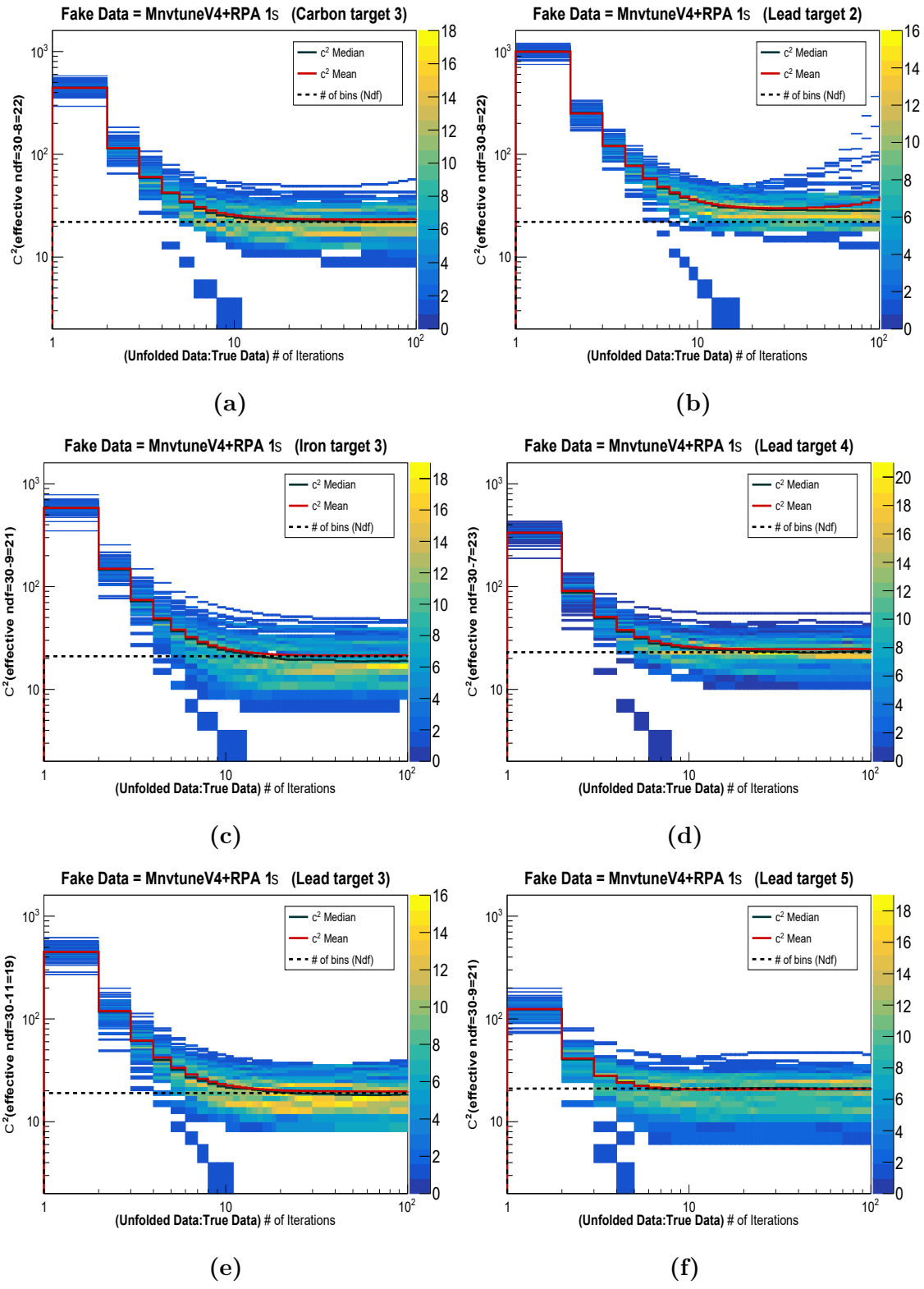

Figure D.3: Warp 2: Fake data as 1 σ shift in RPA reweight in the CV MC. Plot shows χ^2 against number of iterations for for $x - Q^2$ in (a) carbon, (b) target 2 lead, (c) target 3 iron, (d) target 4 lead, (e) target 3 lead and (f) target 5 lead.

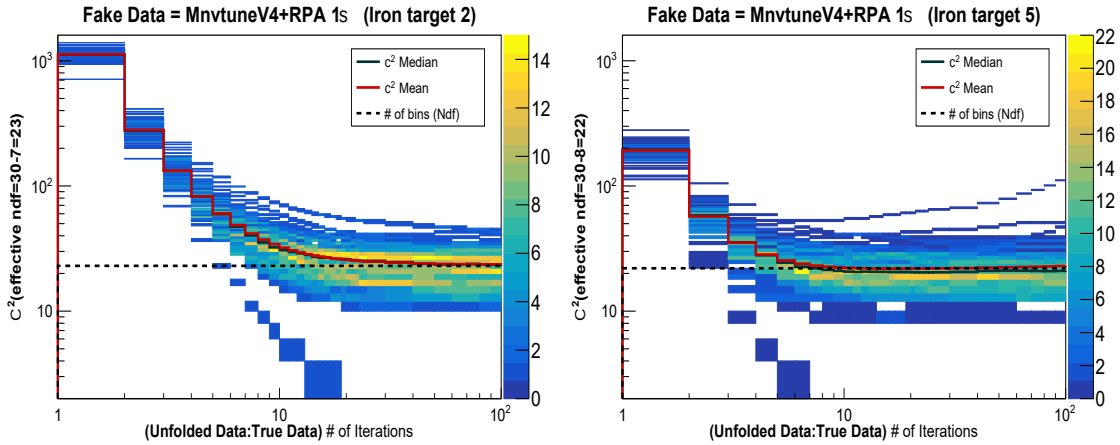

(a) **(b)**

Figure D.4: Warp 2: Fake data as 1 σ shift in RPA reweight in the CV MC. Plot shows χ^2 against number of iterations for for $x - Q^2$ in (a) target 2 iron, (b) target 5 iron.

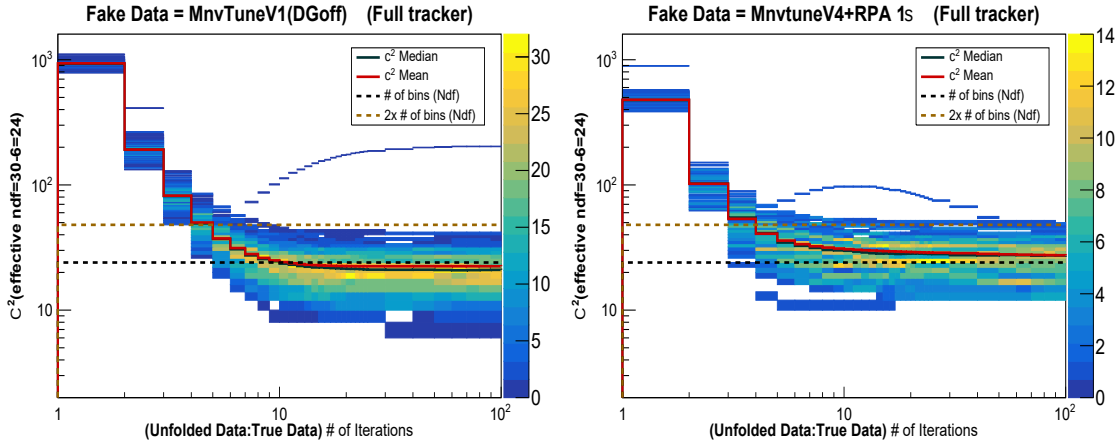

(a) **(b)**

Figure D.5: (a)Fake data as switching off DeuteriumGenie pion tune reweight, (b) Fake data as 1 σ shift in RPA reweight in the CV MC. Plot shows χ^2 against number of iterations for for $x - Q^2$ in tracker.

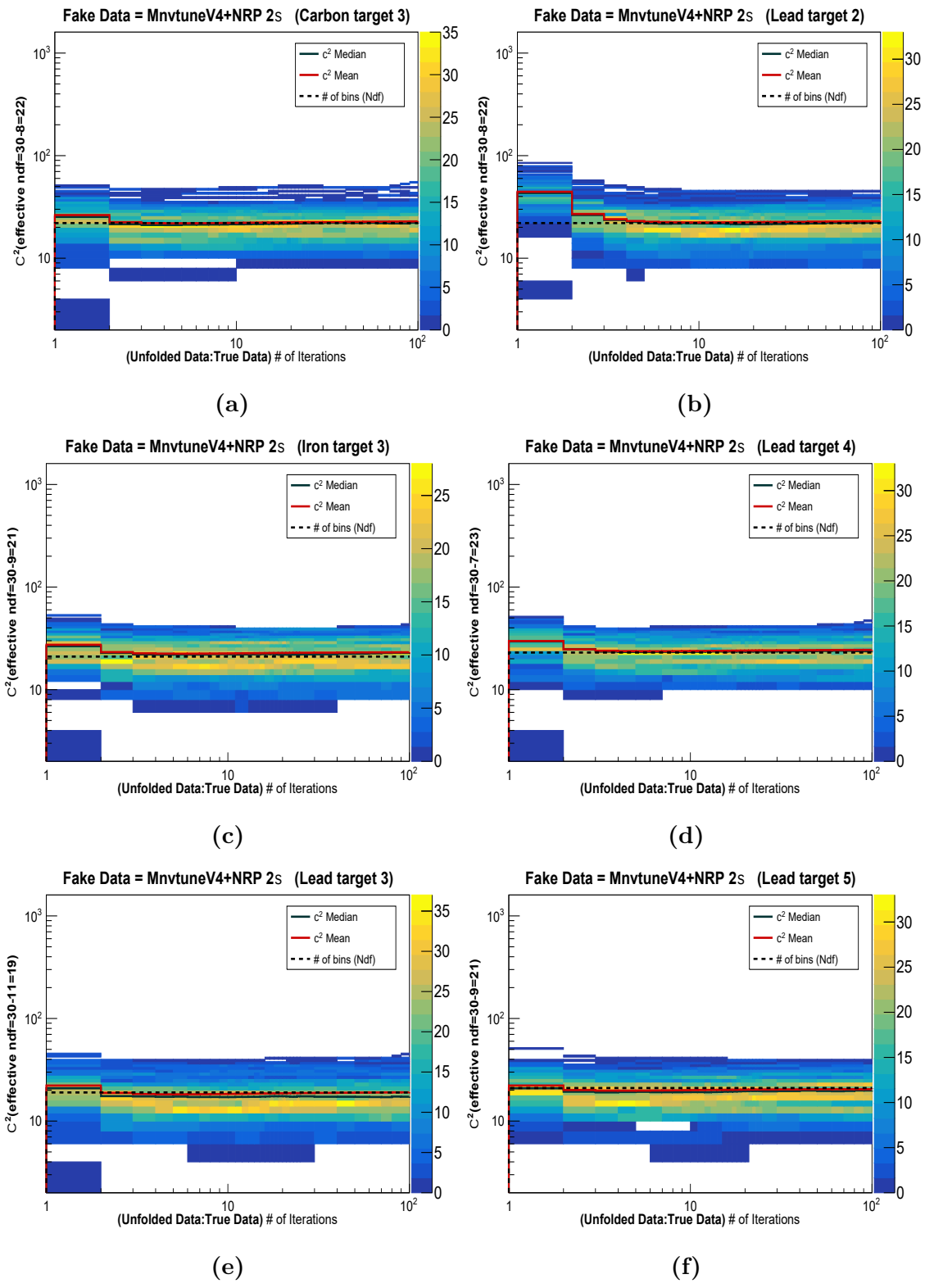

Figure D.6: Warp 3: Fake data as 2 σ shift in NRP reweight in the CV MC. Plot shows χ^2 against number of iterations for $x - Q^2$ in (a) carbon, (b) target 2 lead, (c) target 3 iron, (d) target 4 lead, (e) target 3 lead and (f) target 5 lead.

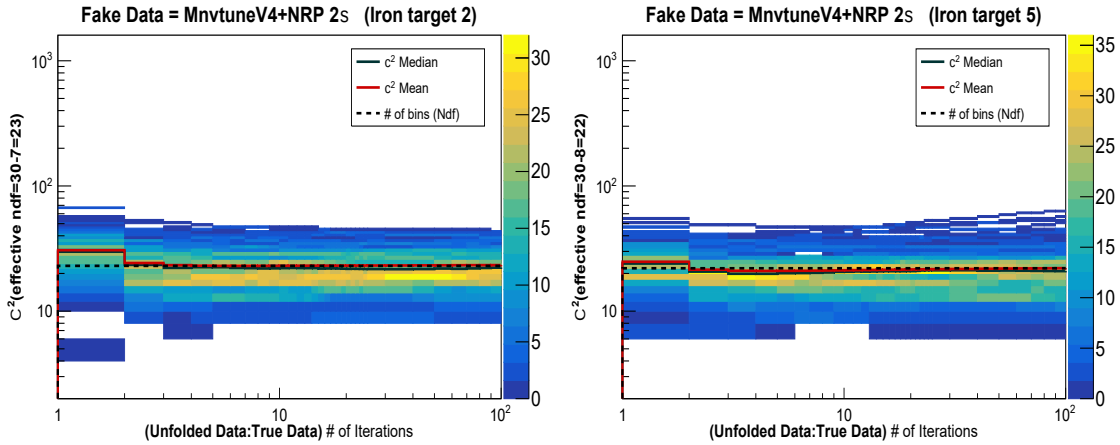

(a) **(b)**

Figure D.7: Warp 3: Fake data as 2 σ shift in NRP reweight in the CV MC. Plot shows χ^2 against number of iterations for for $x - Q^2$ in (a) target 2 iron, (b) target 5 iron.

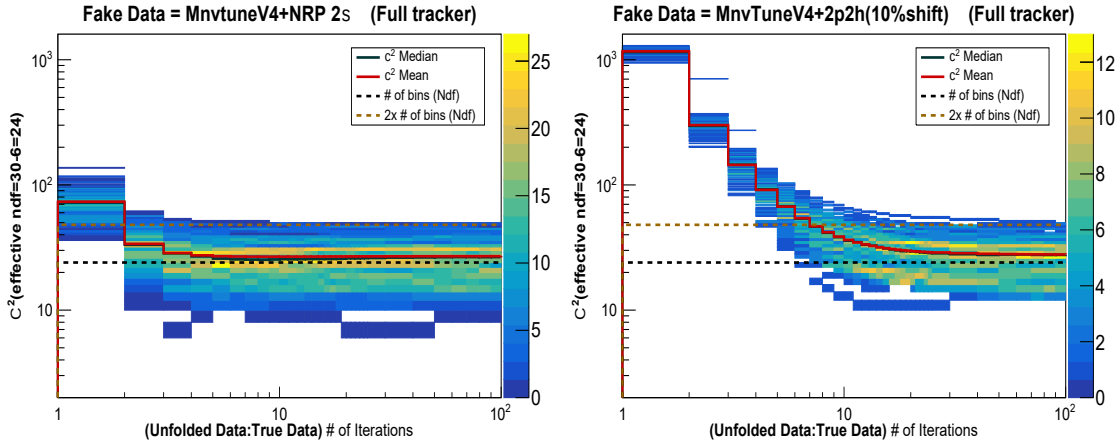

(a) **(b)**

Figure D.8: (a) Fake data as 2 σ shift in NRP reweight, (b) Fake data as 10% shift in 2p2h reweight in the CV MC. Plot shows χ^2 against number of iterations for for $x - Q^2$ in tracker.

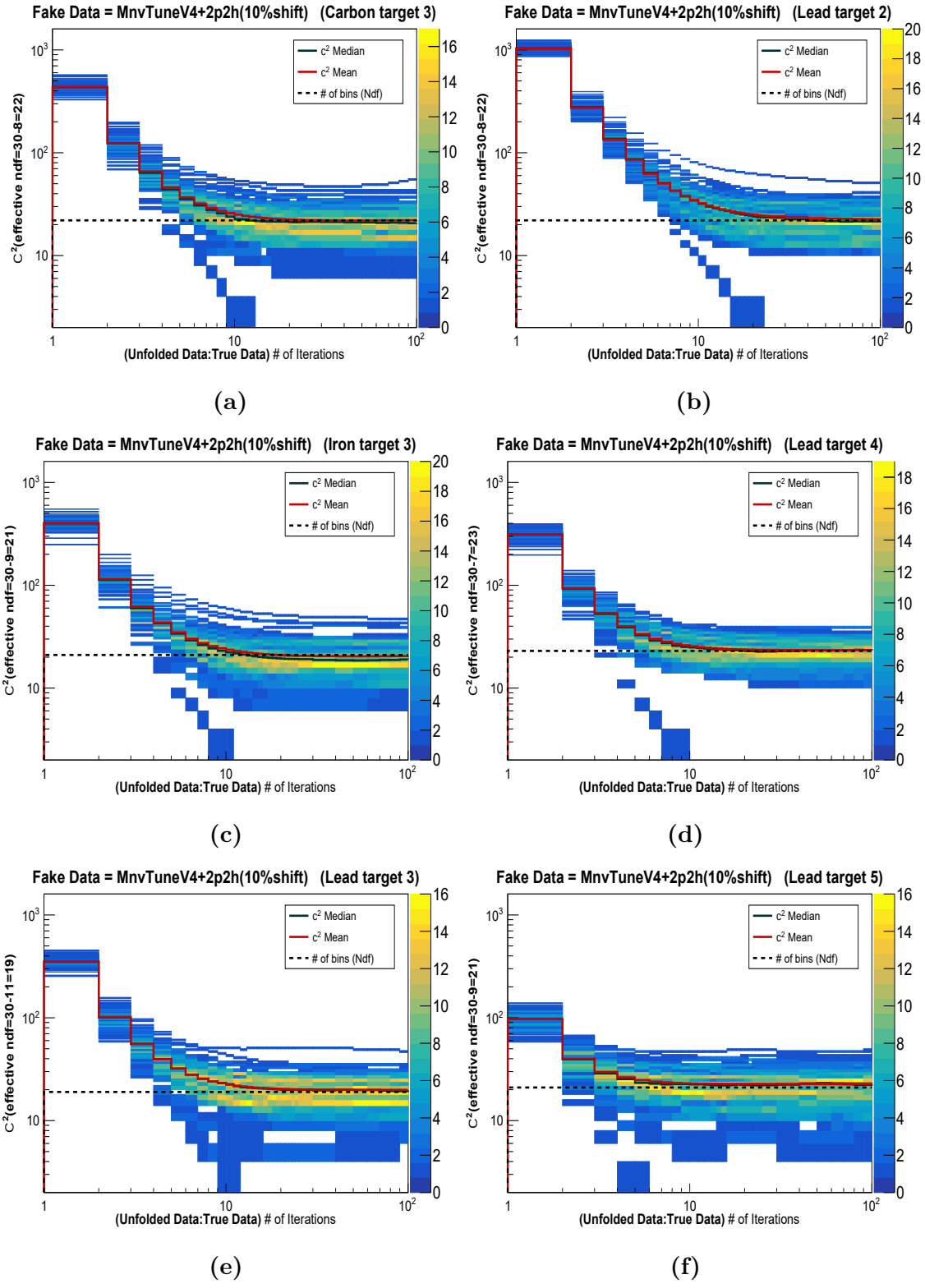

Figure D.9: Warp 4: Fake data as 10 % shift in 2p2h reweight in the CV MC. Plot shows χ^2 against number of iterations for $x - Q^2$ in (a) carbon, (b) target 2 lead, (c) target 3 iron, (d) target 4 lead, (e) target 3 lead and (f) target 5 lead.

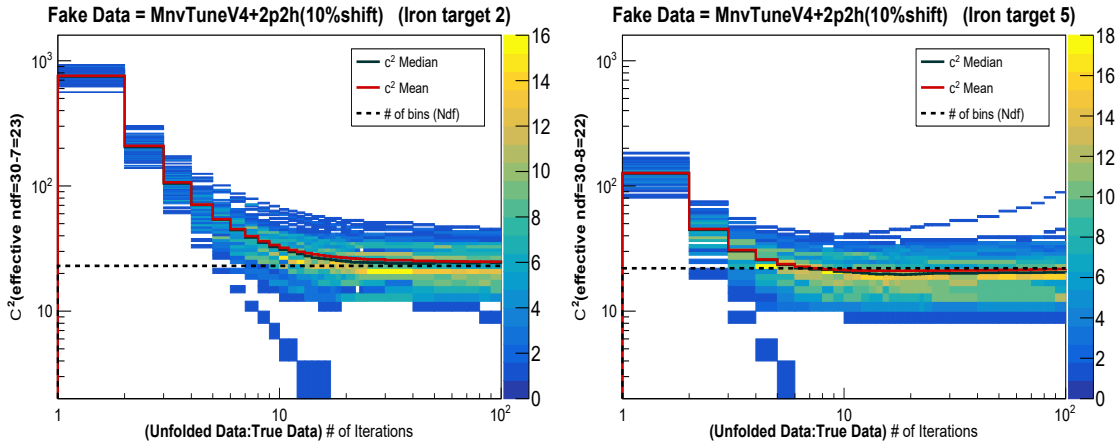

(a) **(b)**

Figure D.10: Warp 4: Fake data as 10 % shift in 2p2h reweight in the CV MC. Plot shows χ^2 against number of iterations for for $x - Q^2$ in (a) target 2 iron, (b) target 5 iron.

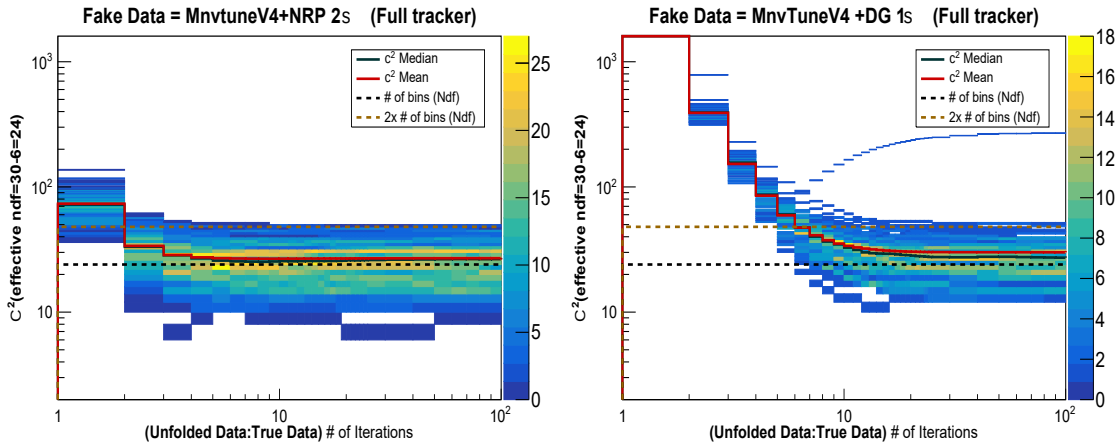

(a) **(b)**

Figure D.11: (a) Fake data as 10% shift in 2p2h reweight, (b) Fake data as 1 σ shift in DeuteriumGenie pion tune reweight in the CV MC. Plot shows χ^2 against number of iterations for for $x - Q^2$ in tracker.

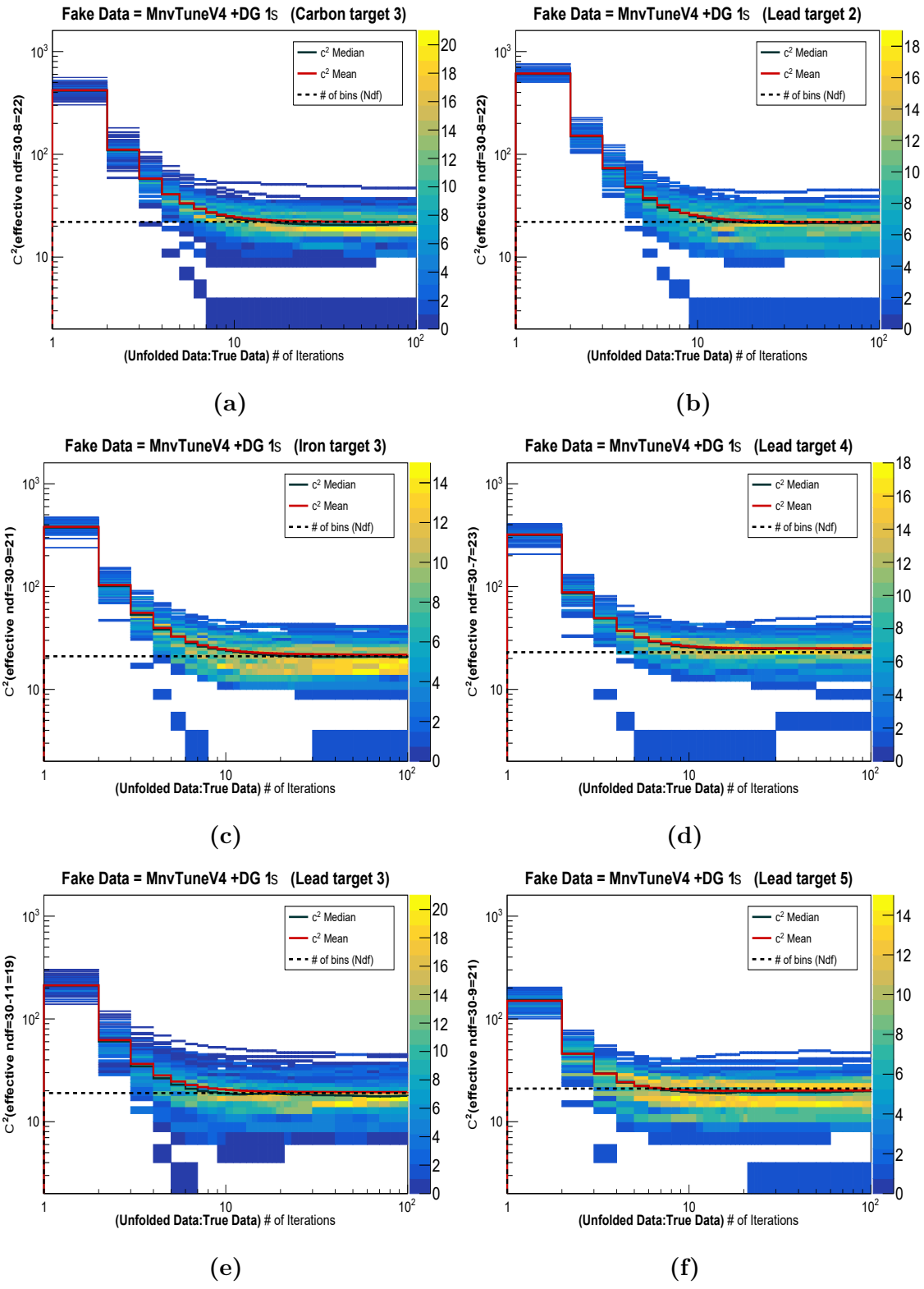

Figure D.12: Warp 5: Fake data as 1 σ shift in DeuteriumGenie pion tune reweight in the CV MC. Plot shows χ^2 against number of iterations for $x - Q^2$ in (a) carbon, (b) target 2 lead, (c) target 3 iron, (d) target 4 lead, (e) target 3 lead and (f) target 5 lead.

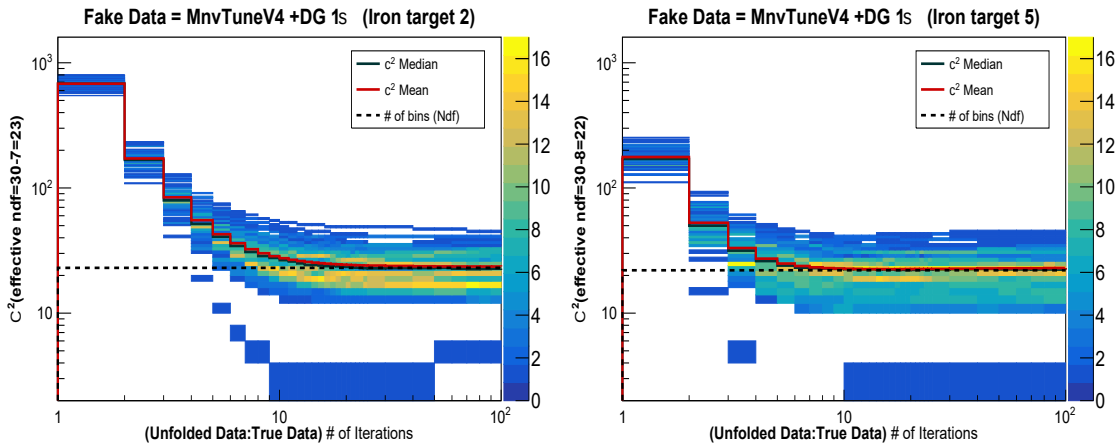

(a) **(b)**

Figure D.13: Warp 5: Fake data as 1 σ shift in DeuteriumGenie pion tune reweight in the CV MC. Plot shows χ^2 against number of iterations for for $x - Q^2$ in (a) target 2 iron, (b) target 5 iron.

W-Q^2 warping studies

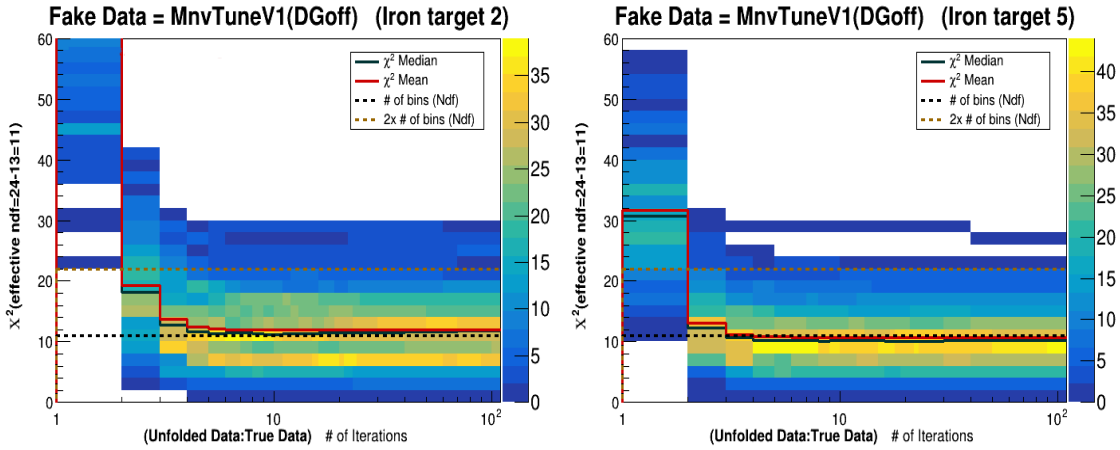

(a) **(b)**

Figure D.14: Warp 1: Fake data as switching off the DeuteriumGeniePion tune reweight in the CV MC. Plot shows χ^2 against number of iterations for for $W - Q^2$ in (a) target 2 iron and (b) target 5 iron.

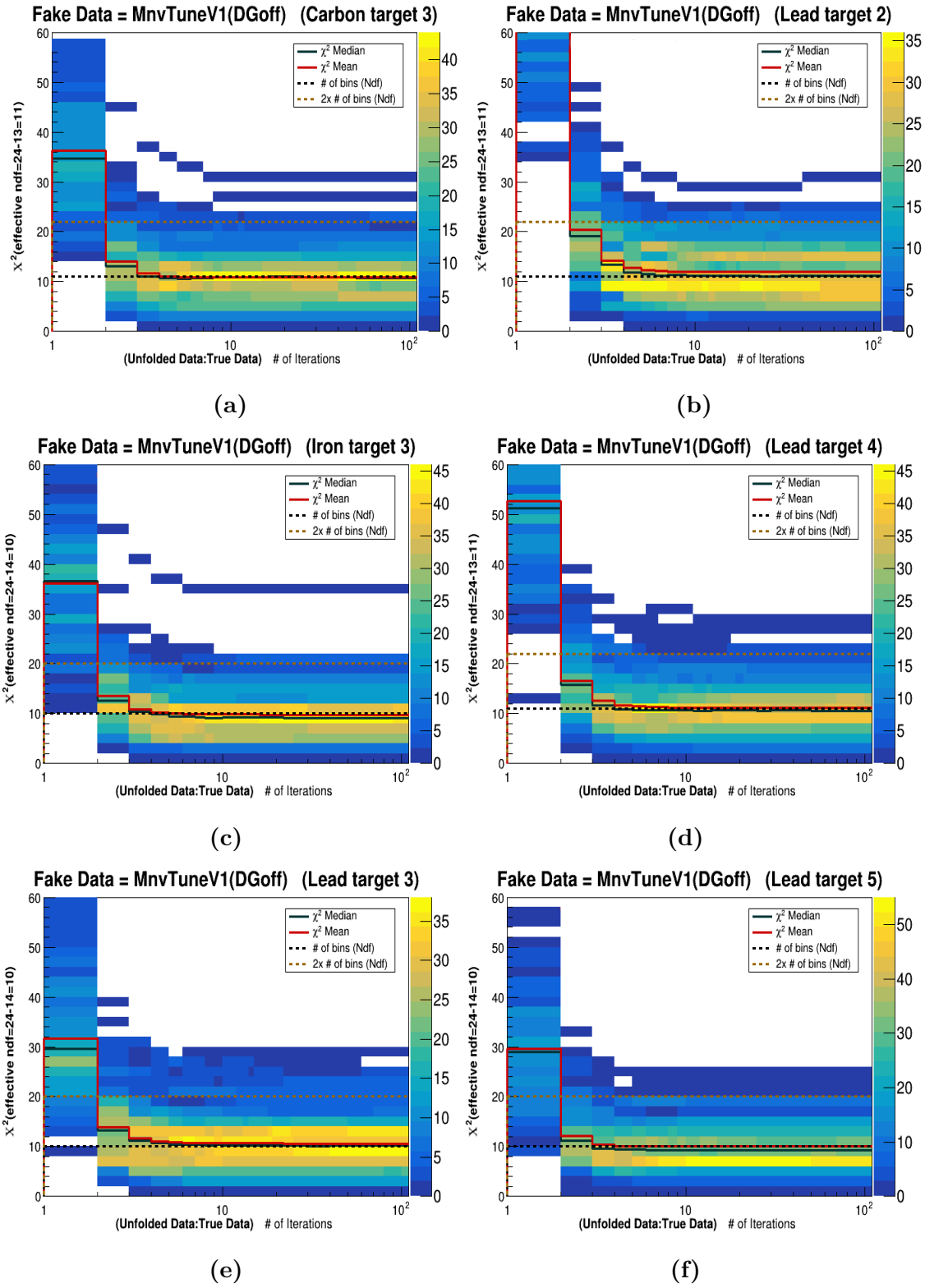

Figure D.15: Warp 1: Fake data as switching off the DeuteriumGeniePion tune reweight in the CV MC. Plot shows χ^2 against number of iterations for for $W-Q^2$ in (a) carbon, (b) target 2 lead, (c) target 3 iron, (d) target 4 lead, (e) target 3 lead and (f) target 5 lead.

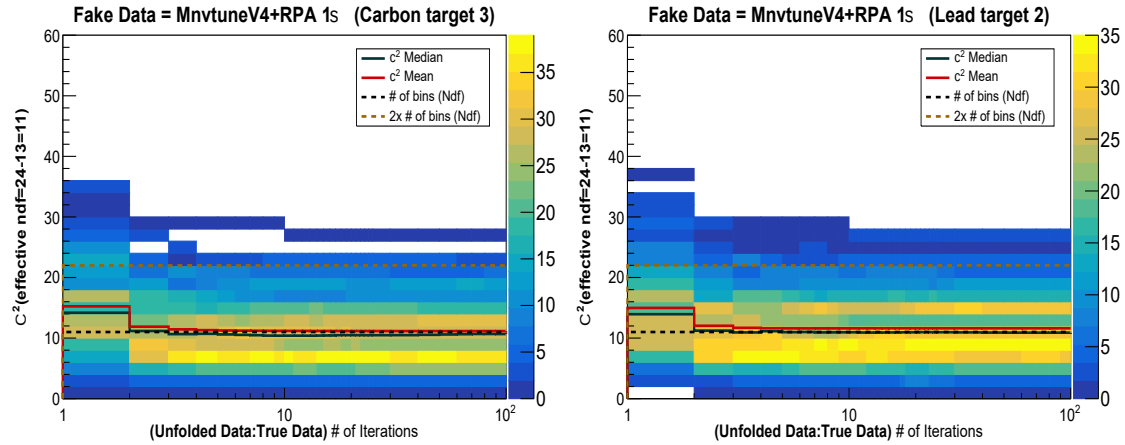

(a)

(b)

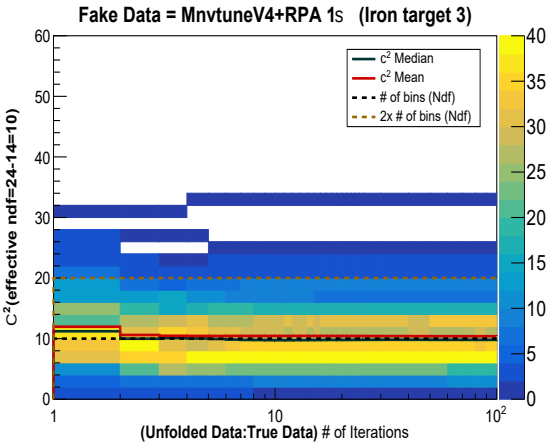

(c)

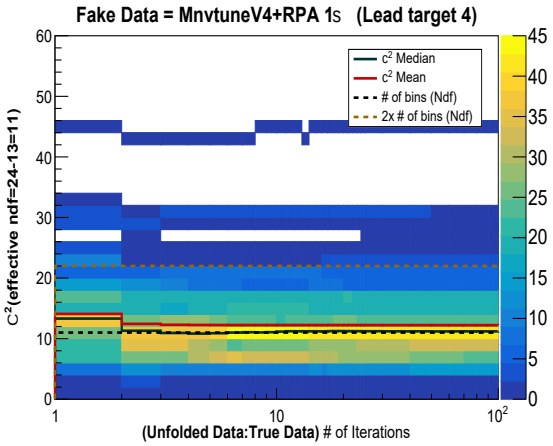

(d)

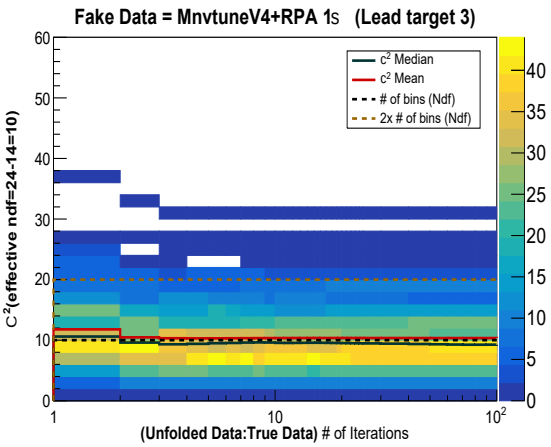

(e)

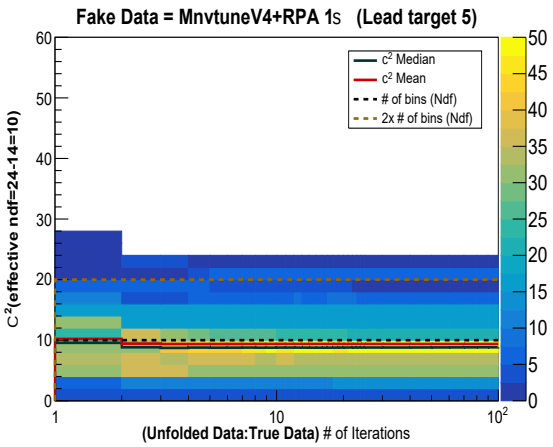

(f)

Figure D.16: Warp 2: Fake data as 1 σ shift in RPA reweight in the CV MC. Plot shows χ^2 against number of iterations for for $W - Q^2$ in (a) carbon, (b) target 2 lead, (c) target 3 iron, (d) target 4 lead, (e) target 3 lead and (f) target 5 lead.

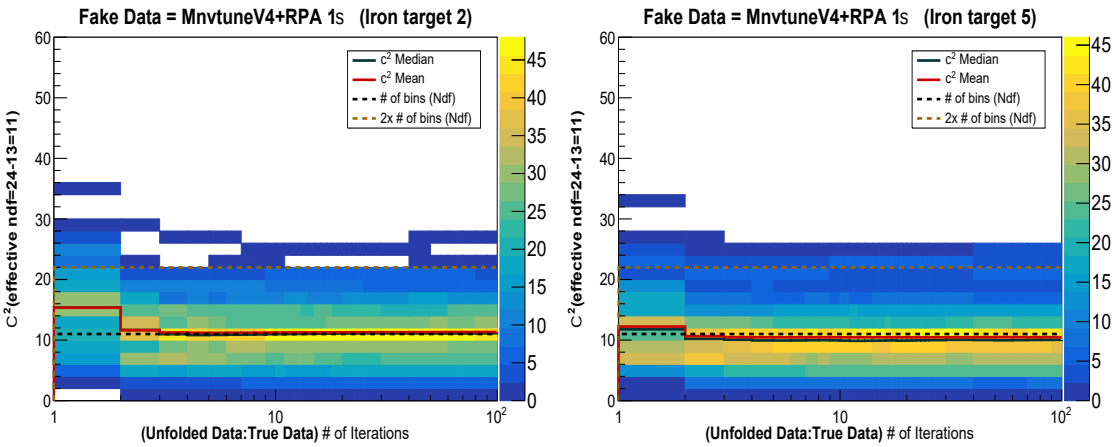

(a) **(b)**

Figure D.17: Warp 2: Fake data as 1 σ shift in RPA reweight in the CV MC. Plot shows χ^2 against number of iterations for for $W - Q^2$ in (a) target 2 iron, (b) target 5 iron.

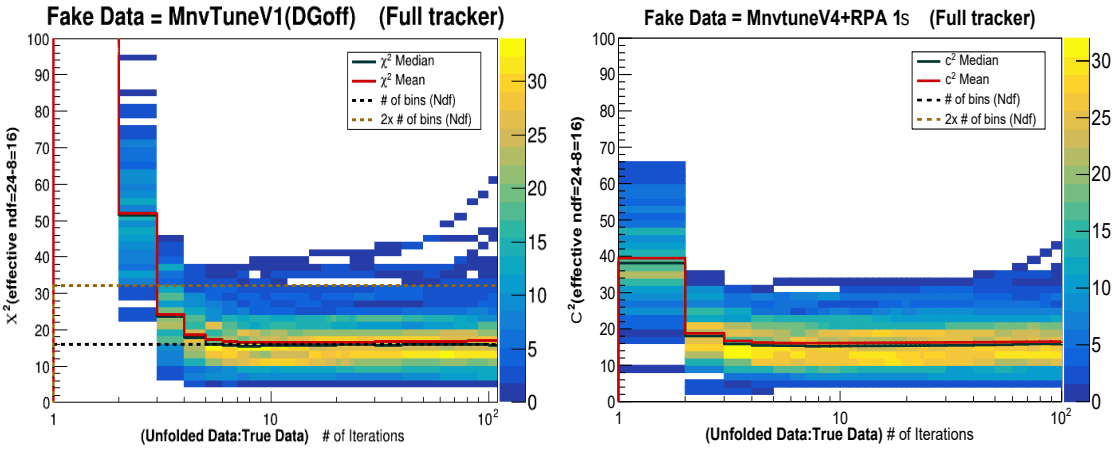

(a) **(b)**

Figure D.18: (a)Fake data as switching off DeuteriumGenie pion tune reweight, (b) Fake data as 1 σ shift in RPA reweight in the CV MC. Plot shows χ^2 against number of iterations for for $W - Q^2$ in tracker.

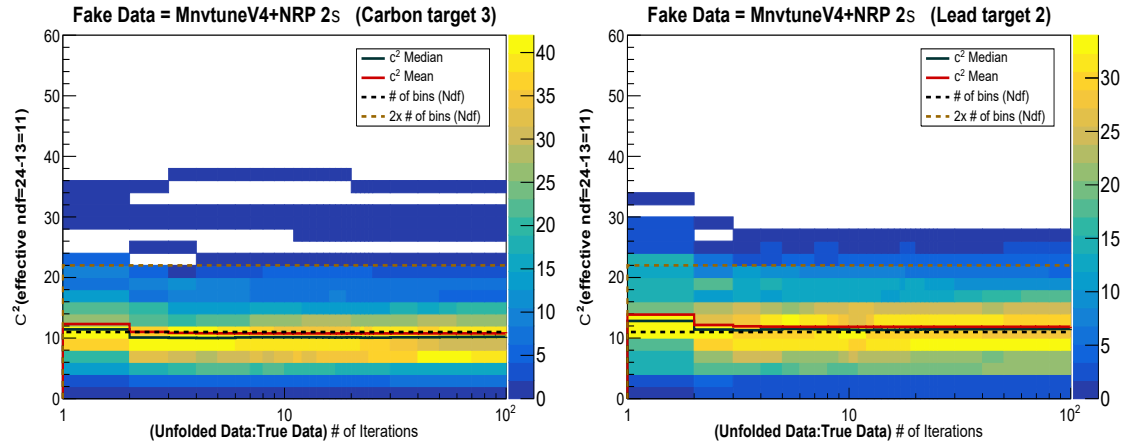

(a)

(b)

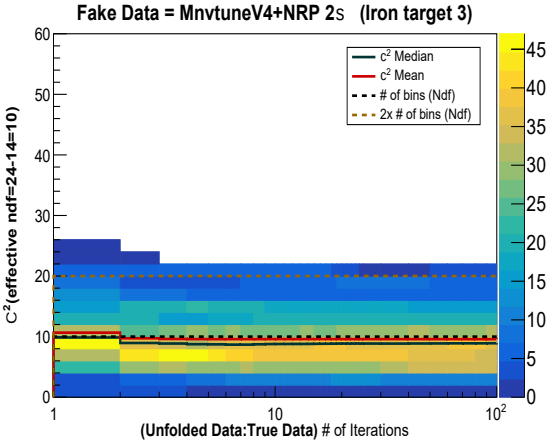

(c)

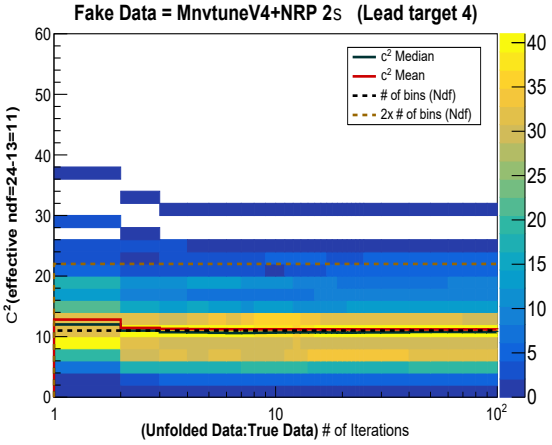

(d)

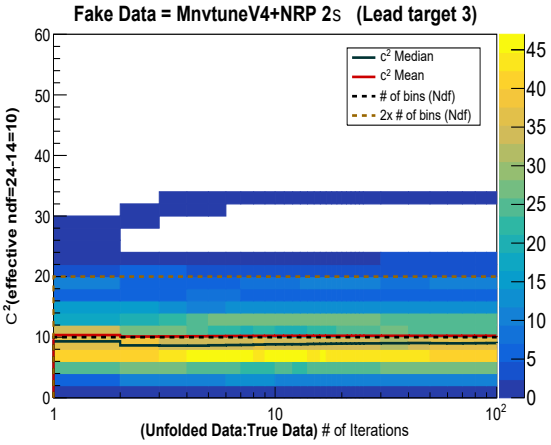

(e)

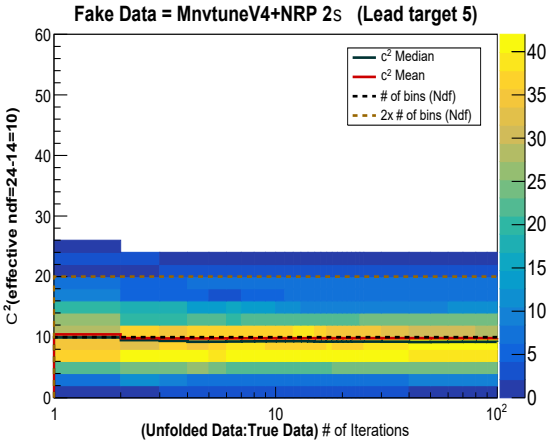

(f)

Figure D.19: Warp 3: Fake data as 2 σ shift in NRP reweight in the CV MC. Plot shows χ^2 against number of iterations for $W - Q^2$ in (a) carbon, (b) target 2 lead, (c) target 3 iron, (d) target 4 lead, (e) target 3 lead and (f) target 5 lead.

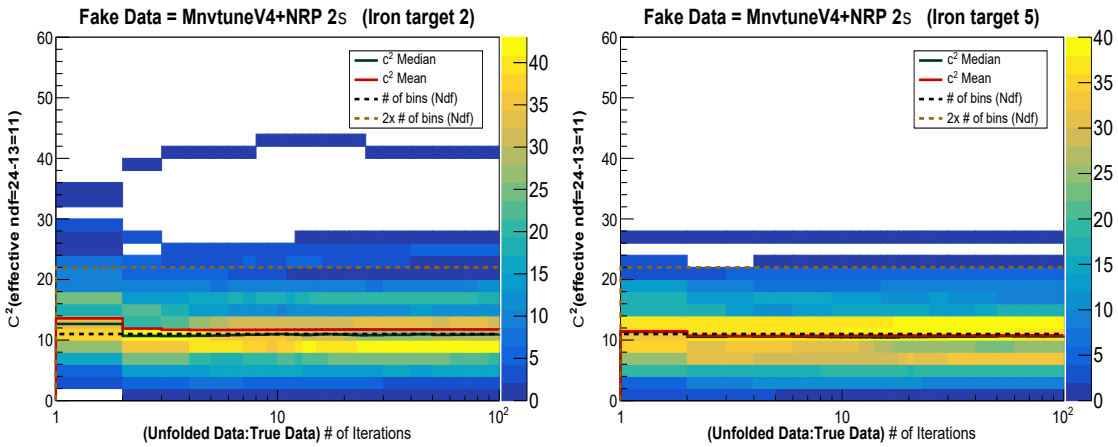

(a) **(b)**

Figure D.20: Warp 3: Fake data as 2 σ shift in NRP reweight in the CV MC. Plot shows χ^2 against number of iterations for for $W - Q^2$ in (a) target 2 iron, (b) target 5 iron.

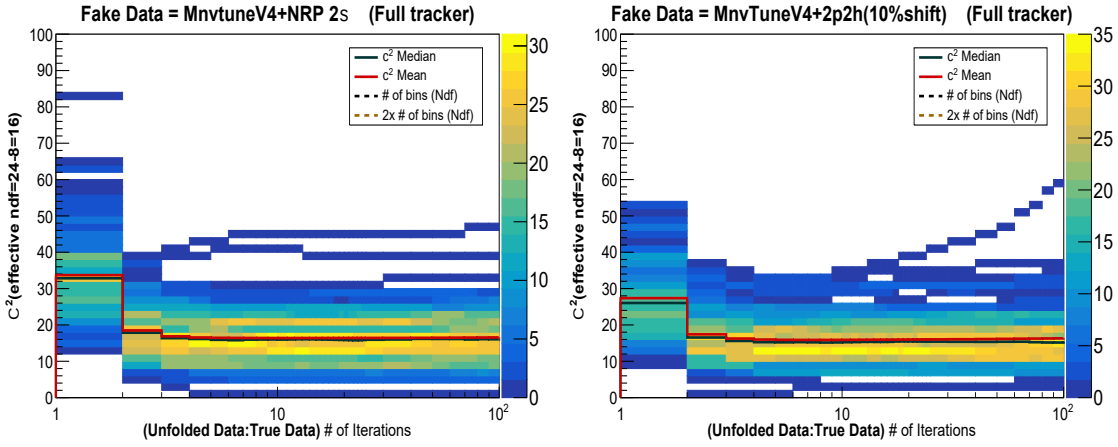

(a) **(b)**

Figure D.21: (a) Fake data as 2 σ shift in NRP reweight, (b) Fake data as 10% shift in 2p2h reweight in the CV MC. Plot shows χ^2 against number of iterations for for $W - Q^2$ in tracker.

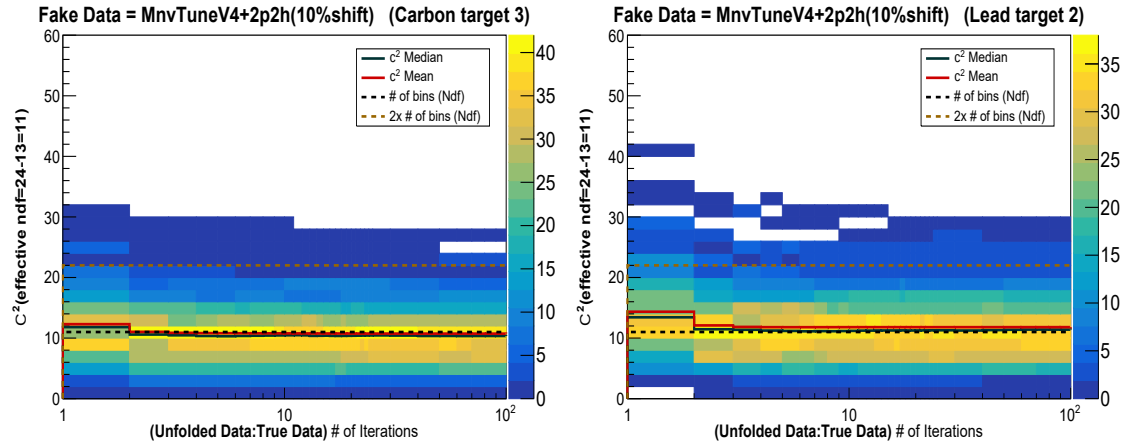

(a)

(b)

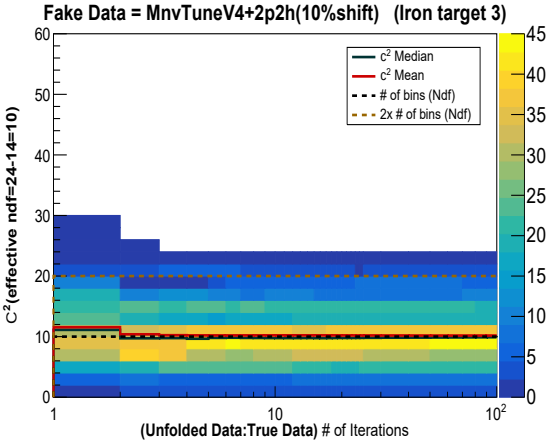

(c)

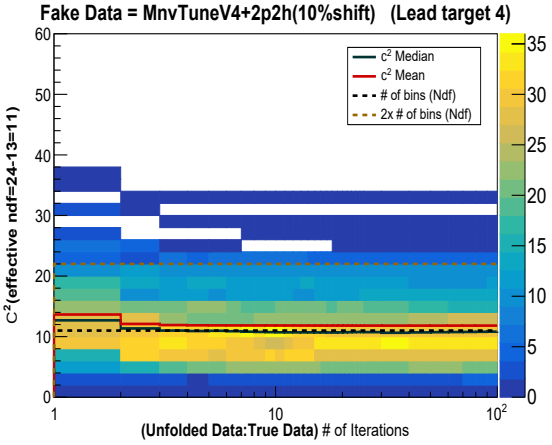

(d)

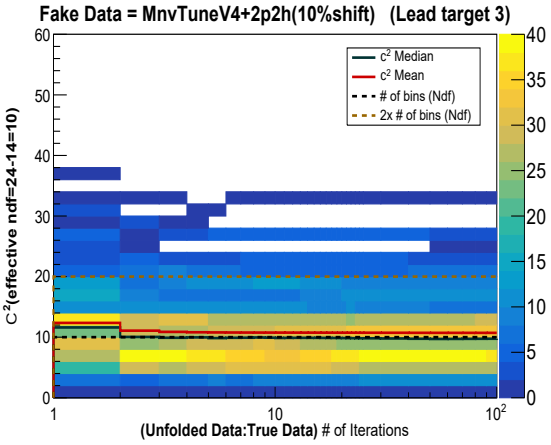

(e)

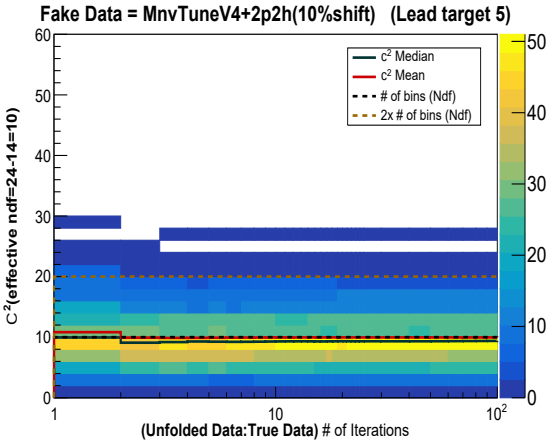

(f)

Figure D.22: Warp 4: Fake data as 10 % shift in 2p2h reweight in the CV MC. Plot shows χ^2 against number of iterations for $W - Q^2$ in (a) carbon, (b) target 2 lead, (c) target 3 iron, (d) target 4 lead, (e) target 3 lead and (f) target 5 lead.

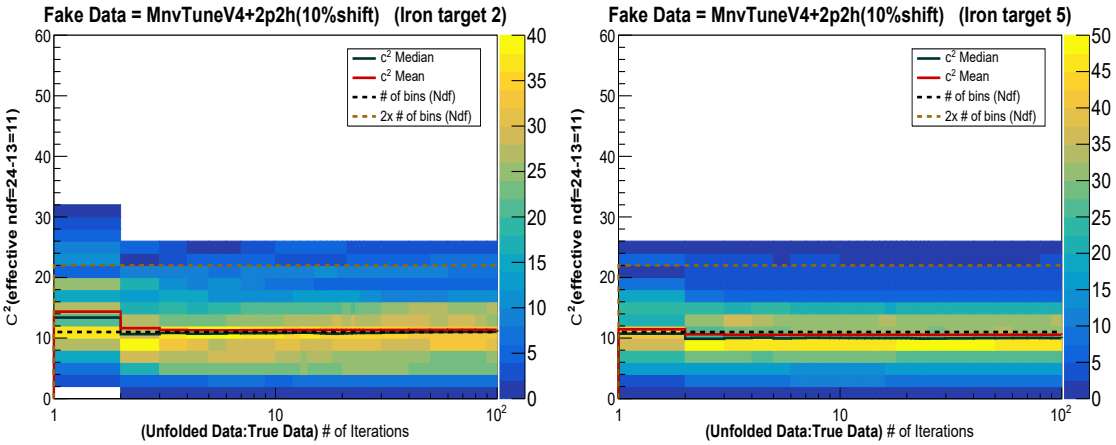

(a) **(b)**

Figure D.23: Warp 4: Fake data as 10 % shift in 2p2h reweight in the CV MC. Plot shows χ^2 against number of iterations for for $W - Q^2$ in (a) target 2 iron, (b) target 5 iron.

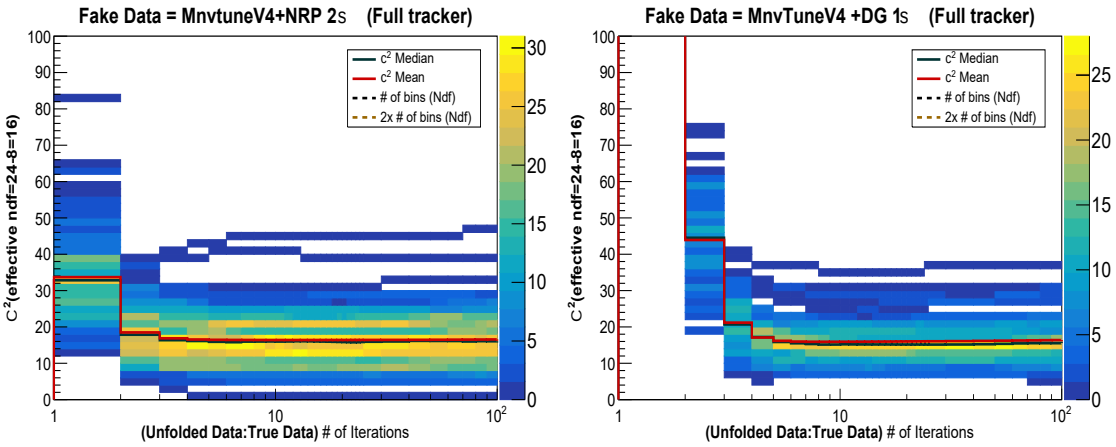

(a) **(b)**

Figure D.24: (a) Fake data as 10% shift in 2p2h reweight, (b) Fake data as 1 σ shift in DeuteriumGenie pion tune reweight in the CV MC. Plot shows χ^2 against number of iterations for for $W - Q^2$ in tracker.

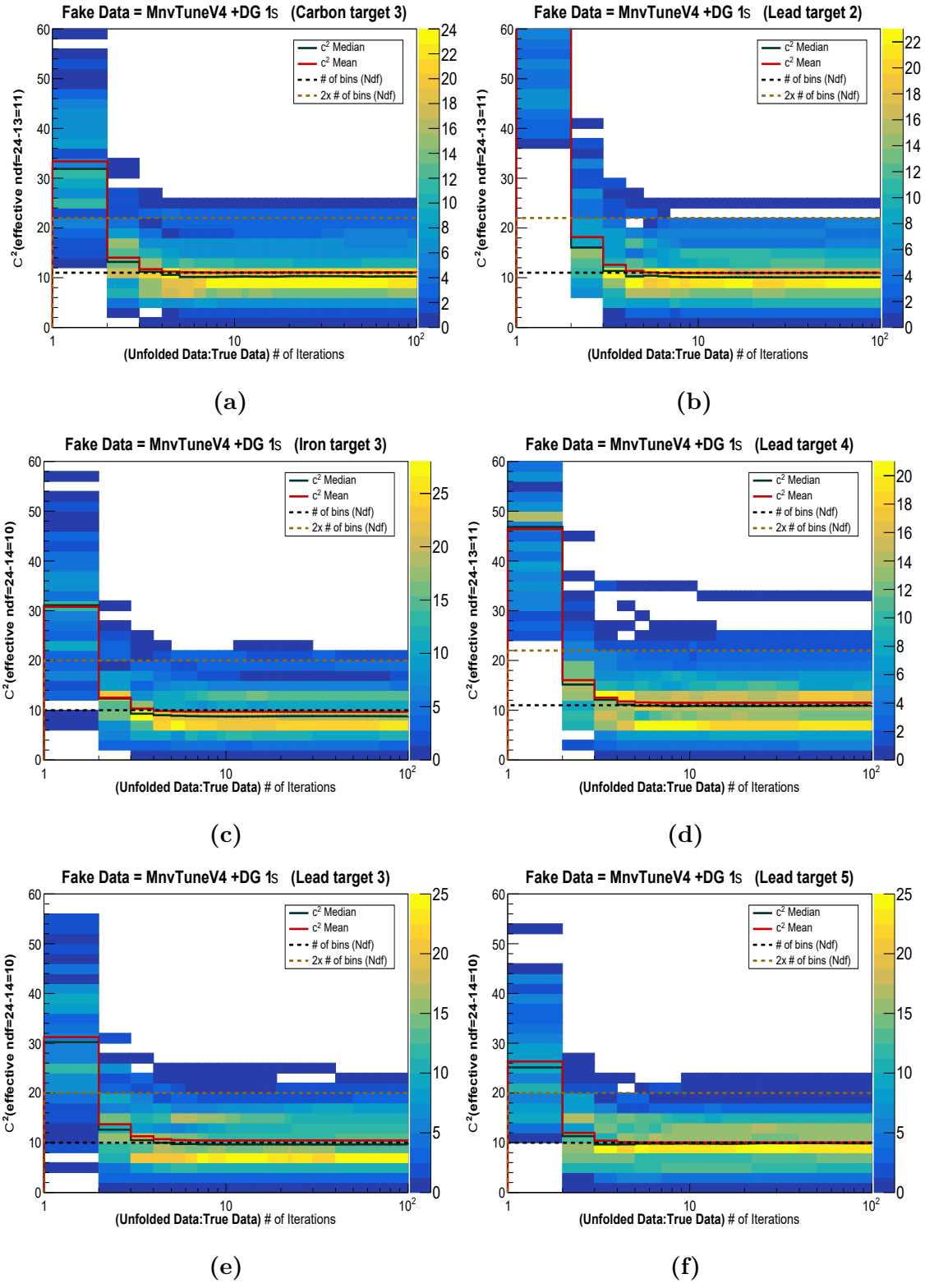

Figure D.25: Warp 5: Fake data as 1 σ shift in DeuteriumGenie pion tune reweight in the CV MC. Plot shows χ^2 against number of iterations for $W - Q^2$ in (a) carbon, (b) target 2 lead, (c) target 3 iron, (d) target 4 lead, (e) target 3 lead and (f) target 5 lead.

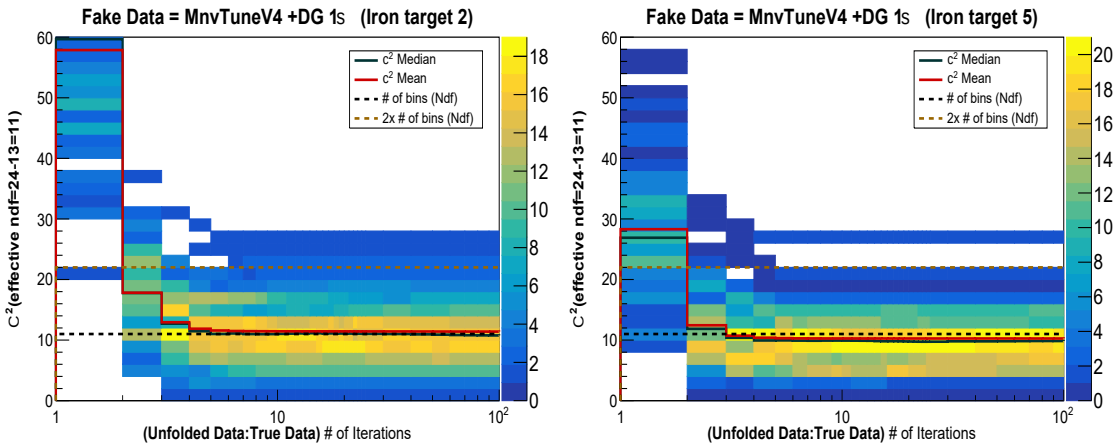

(a) **(b)**

Figure D.26: Warp 5: Fake data as 1 σ shift in DeuteriumGenie pion tune reweight in the CV MC. Plot shows χ^2 against number of iterations for for $W - Q^2$ in (a) target 2 iron, (b) target 5 iron.

Appendix E

Unfolded Distributions

This appendix contains the background subtracted unfolded distribution plots, along with the associated systematic uncertainties. Unfolded distribution in $x-Q^2$ for combined iron, lead and carbon and tracker were given in the main text in 4. For brevity, systematic uncertainties for target materials in individual targets have not been included here.

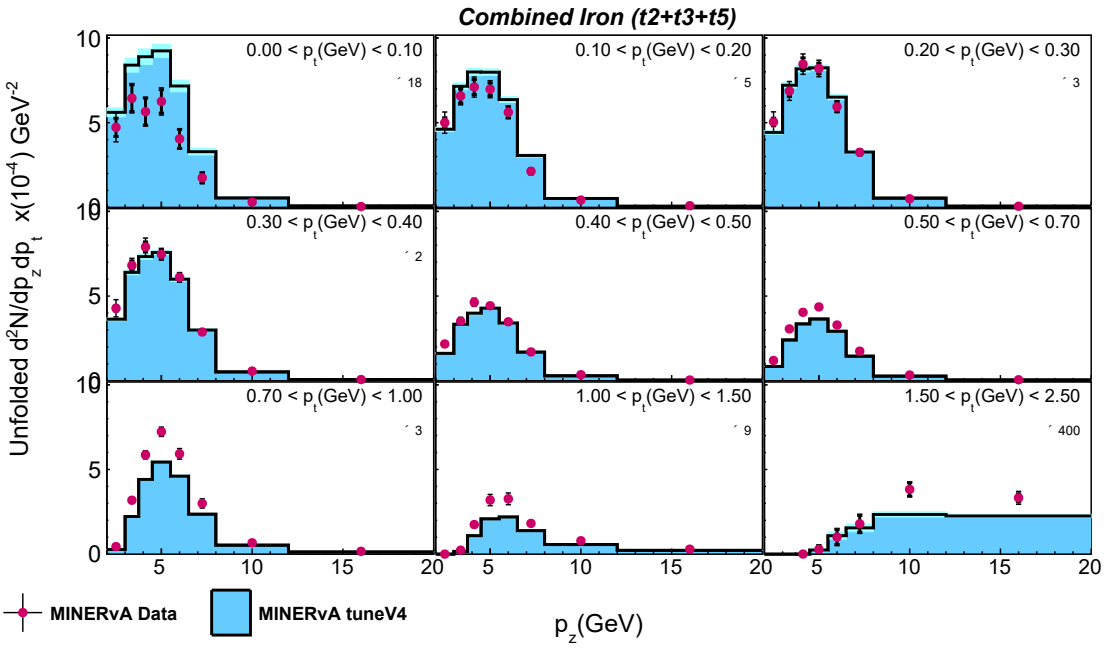

Figure E.1: Unfolded distributions for combined iron in bins of $p_z - p_t$.

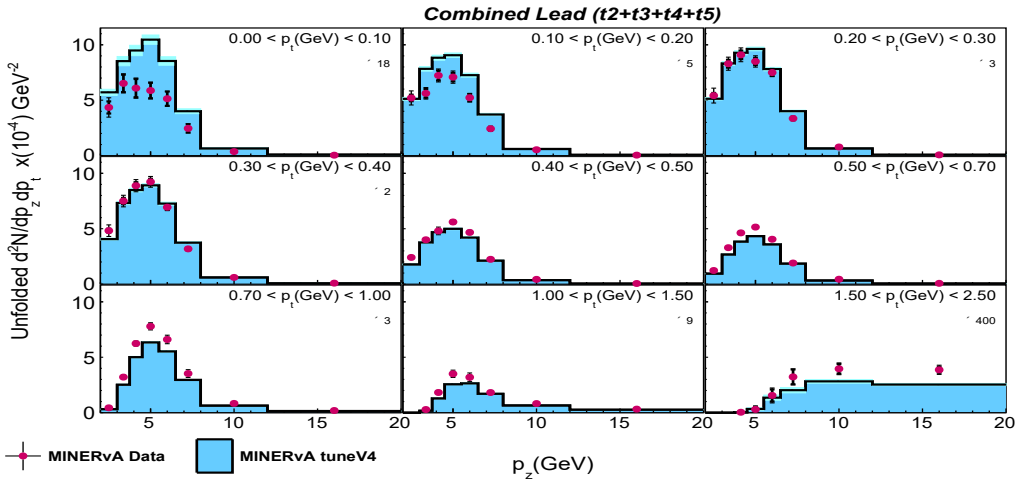

(a)

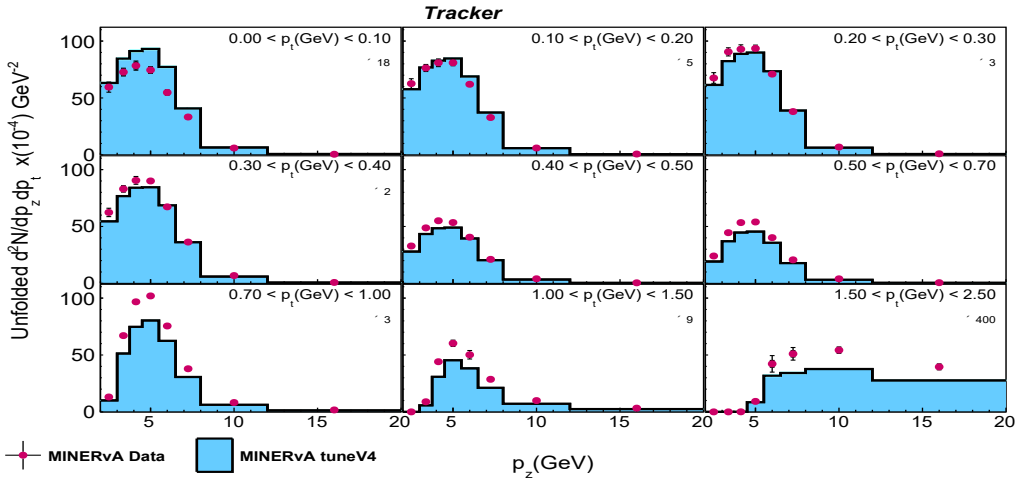

(b)

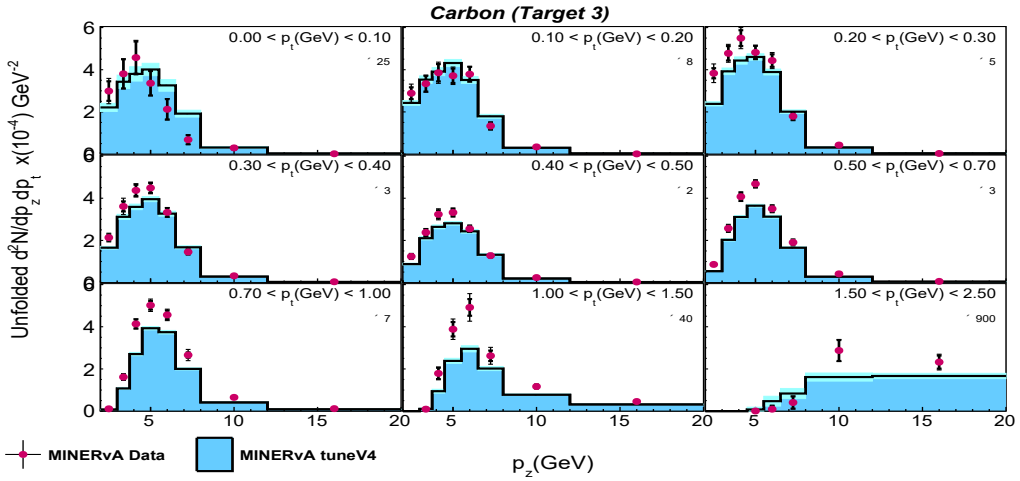

(c)

Figure E.2: Unfolded distributions for (a) combined lead, (b) scintillator tracker and (c) carbon in bins of $p_z - p_t$.

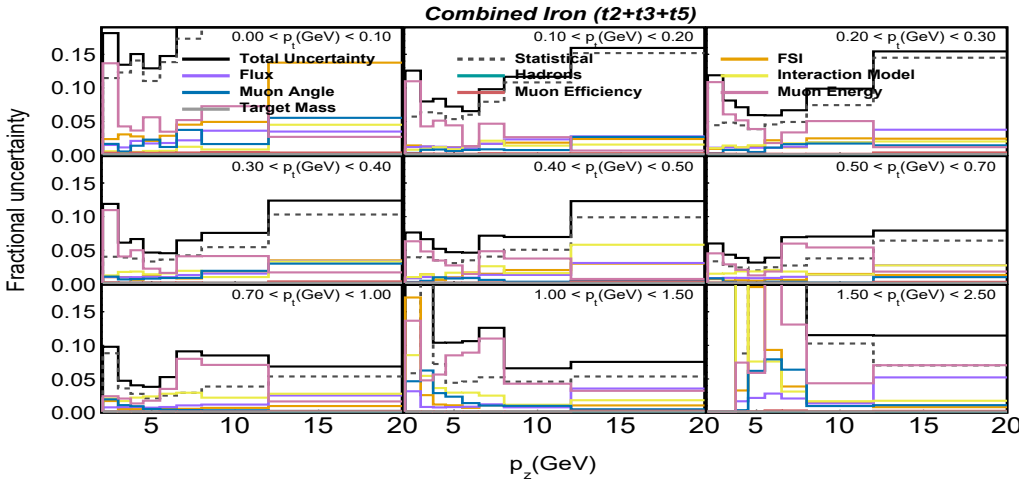

(a)

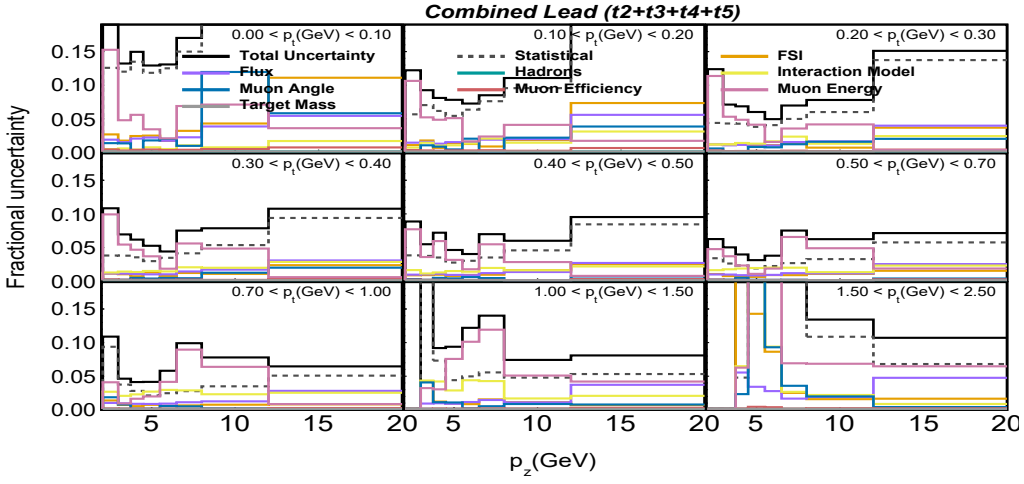

(b)

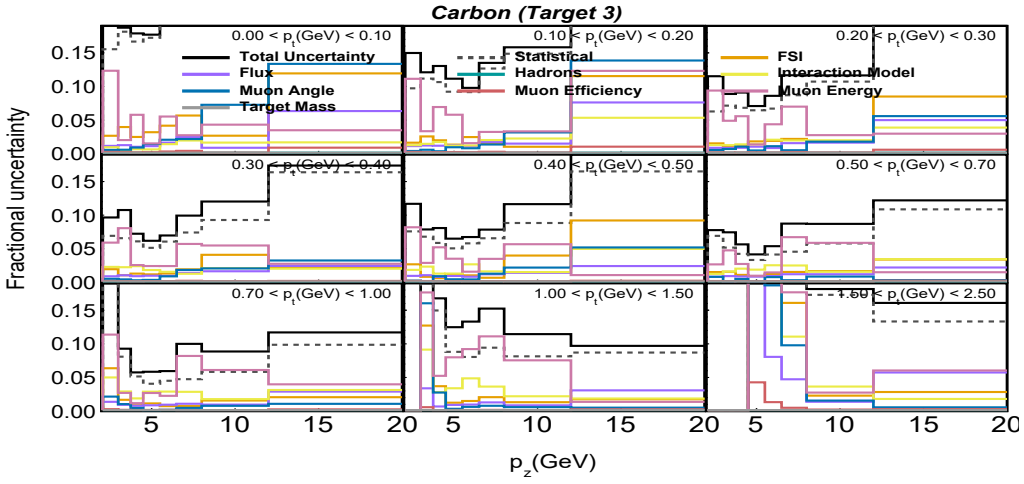

(c)

Figure E.3: Fractional systematic uncertainties in unfolded distributions for (a) combined iron, (b) combined lead and (c) carbon in bins of $p_z - p_t$.

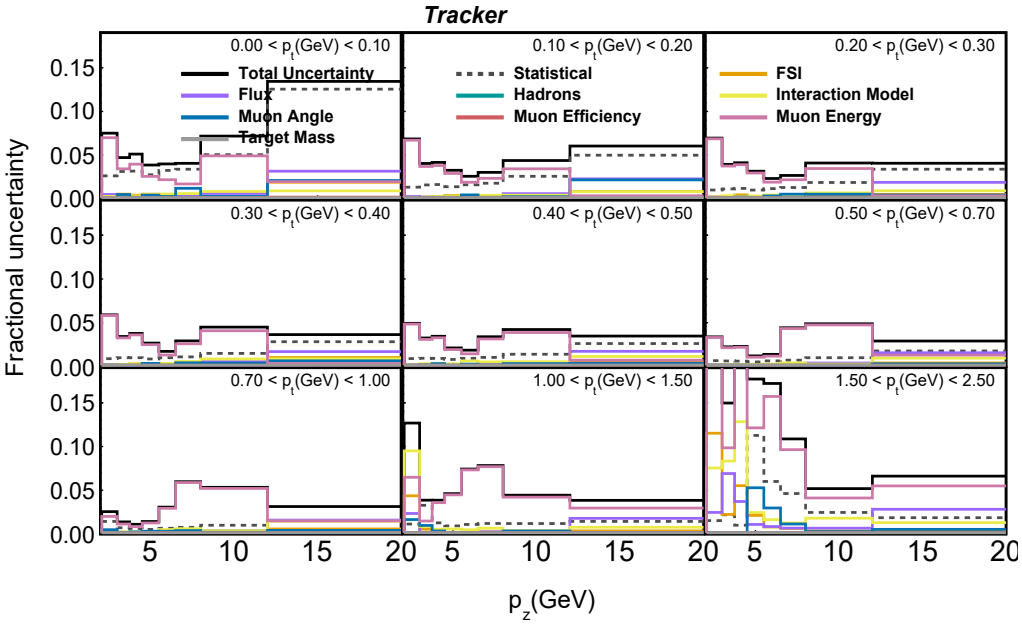

Figure E.4: Fractional systematic uncertainties in unfolded distributions for scintillator tracker in bins of $p_z - p_t$.

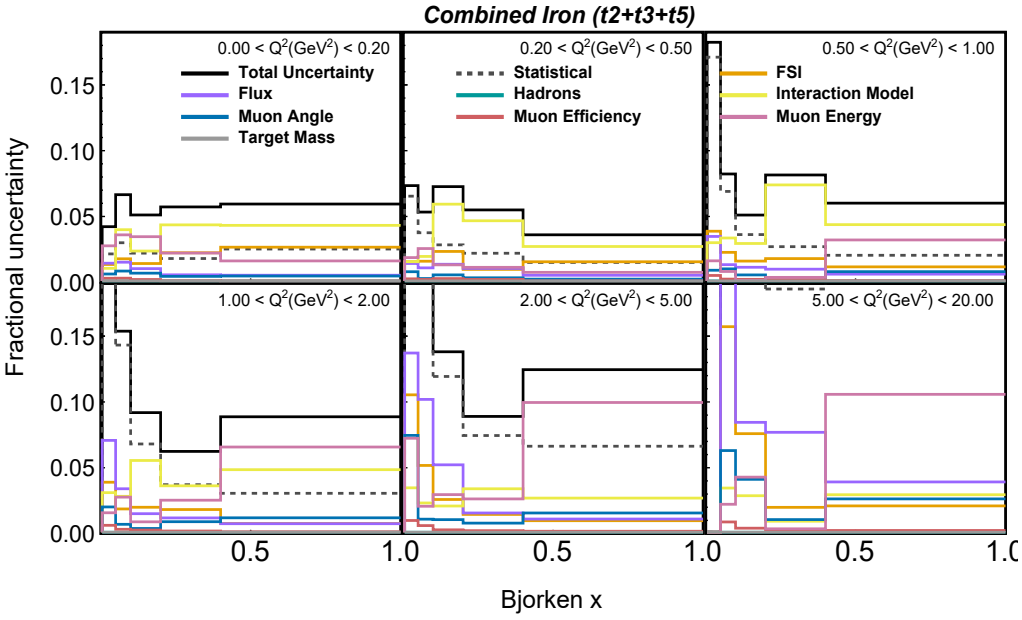

Figure E.5: Fractional systematic uncertainties in unfolded distributions for combined iron in bins of $x - Q^2$.

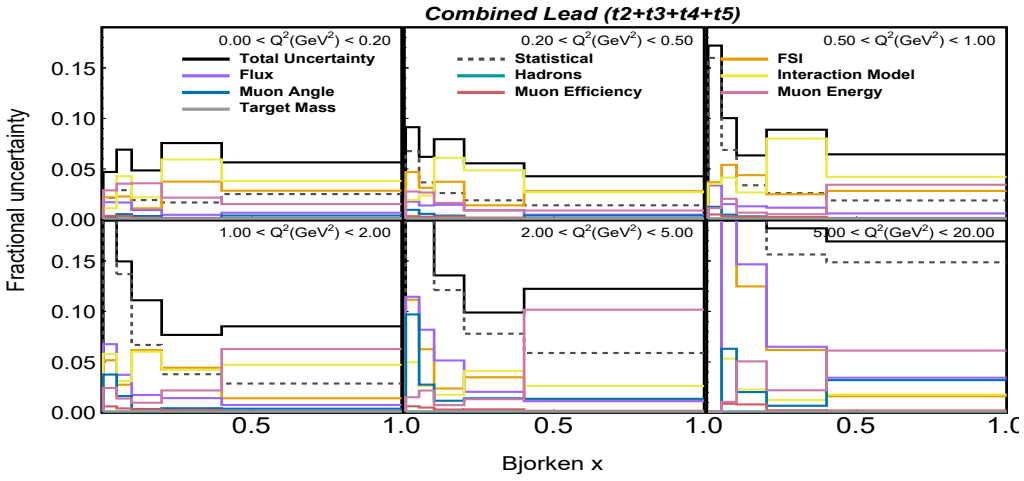

(a)

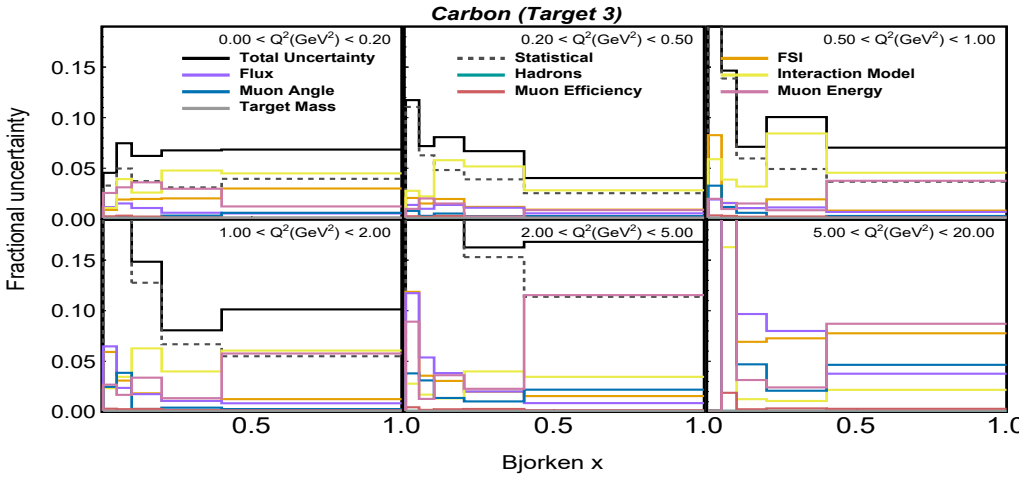

(b)

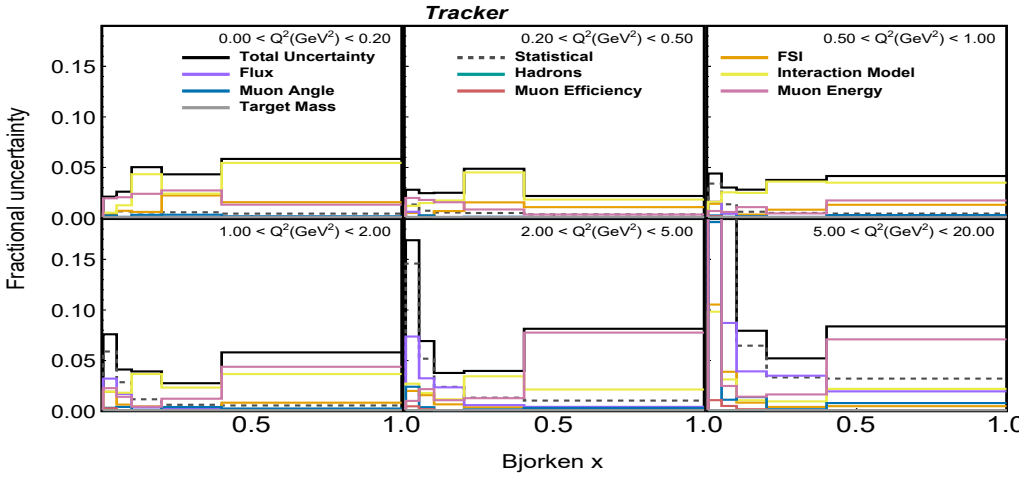

(c)

Figure E.6: Fractional systematic uncertainties in unfolded distributions for (a) combined lead, (b) carbon and (c) tracker in bins of $x - Q^2$.

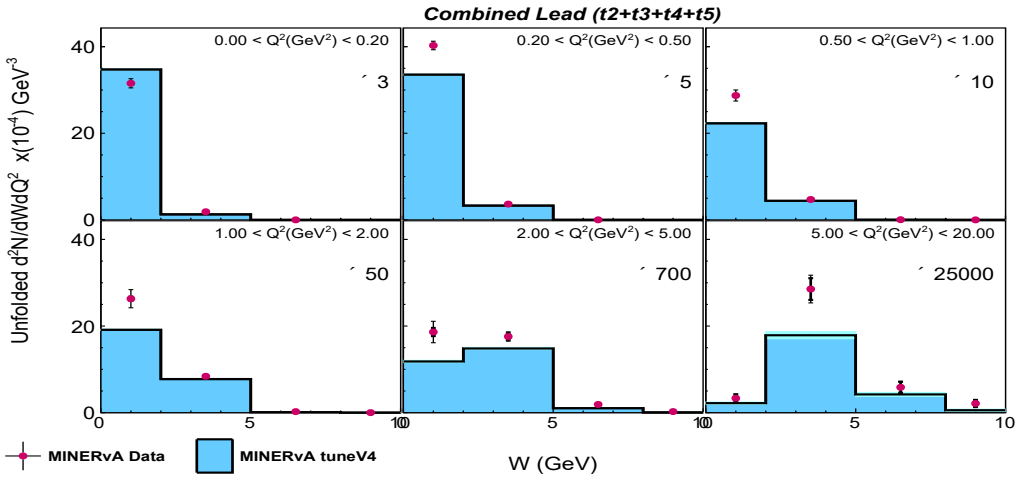

(a)

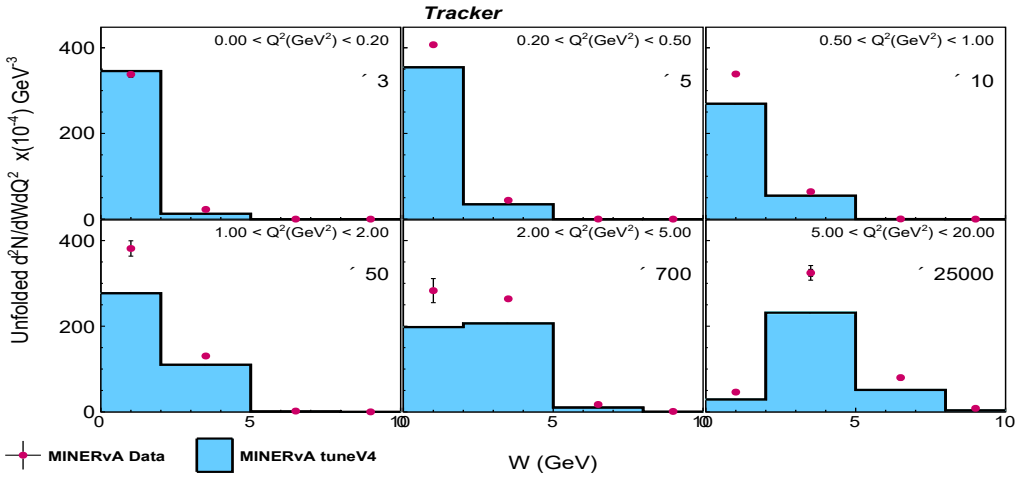

(b)

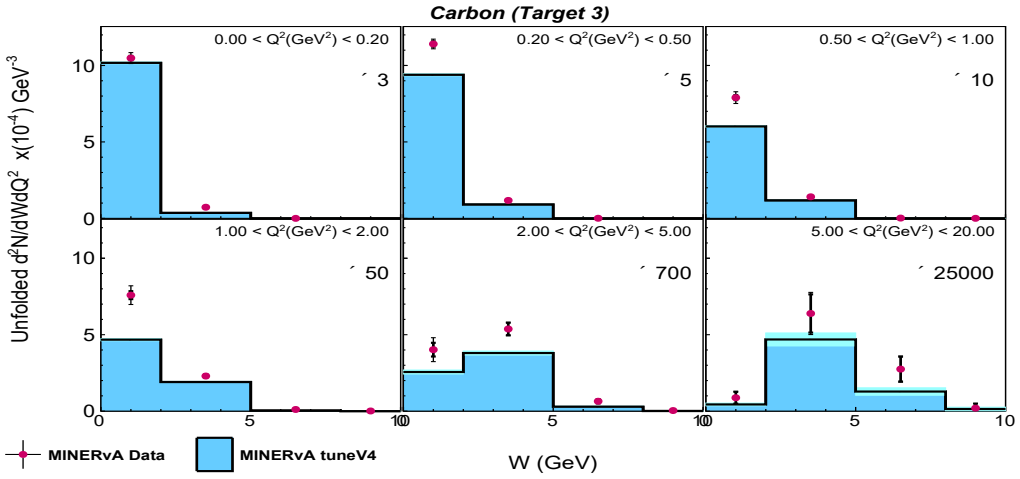

(c)

Figure E.7: Unfolded distributions for (a) combined lead, (b) scintillator tracker and (c) carbon in bins of $W - Q^2$.

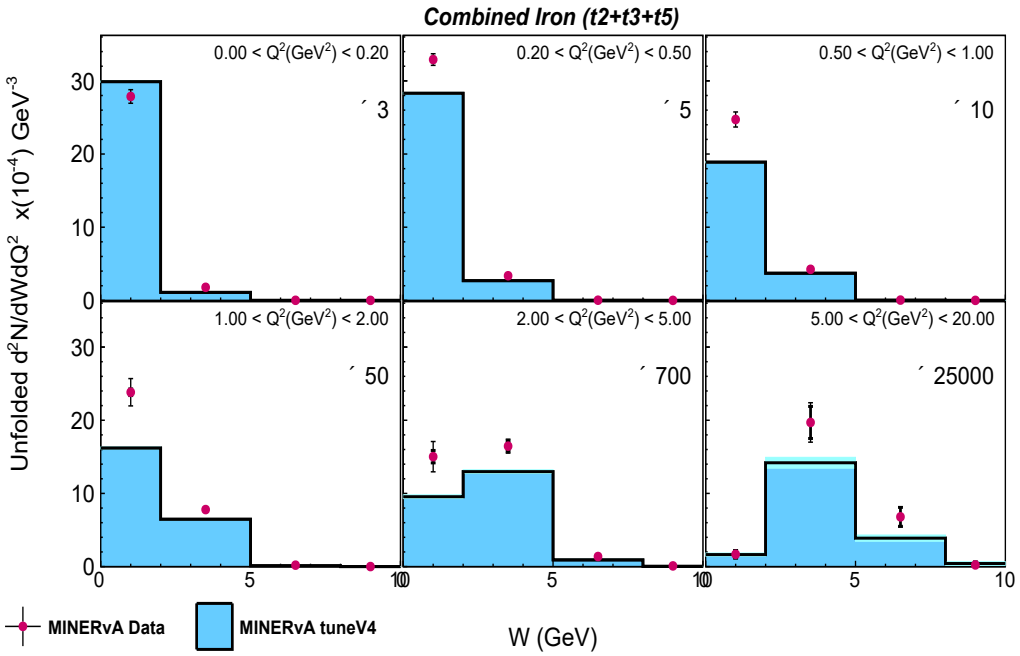

Figure E.8: Unfolded distributions for combined iron in bins of $W - Q^2$.

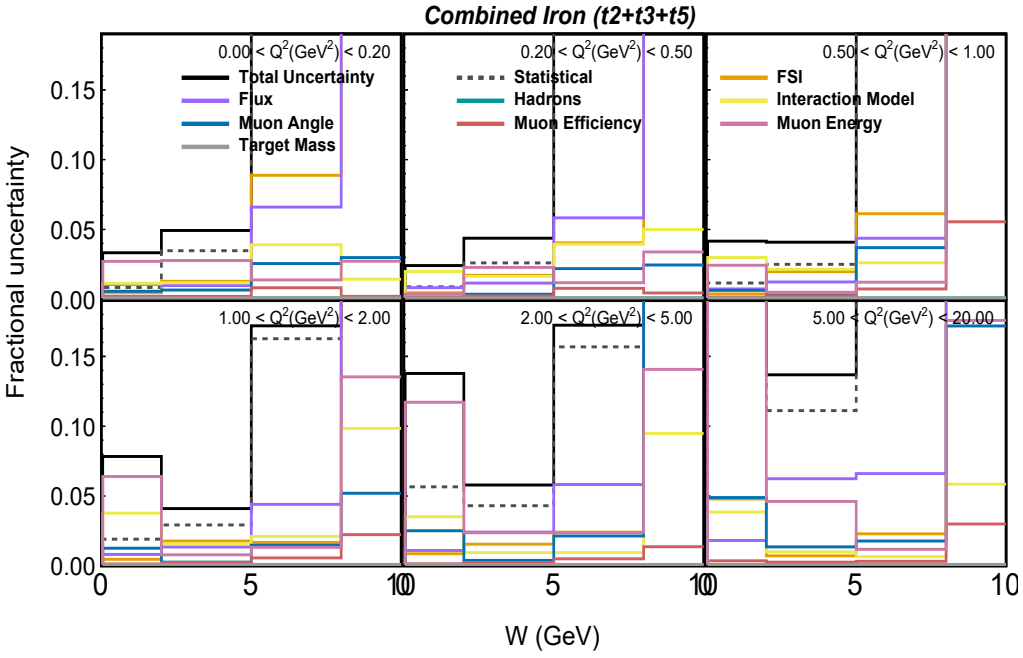

Figure E.9: Fractional systematic uncertainties in unfolded distributions for combined iron in bins of $W - Q^2$.

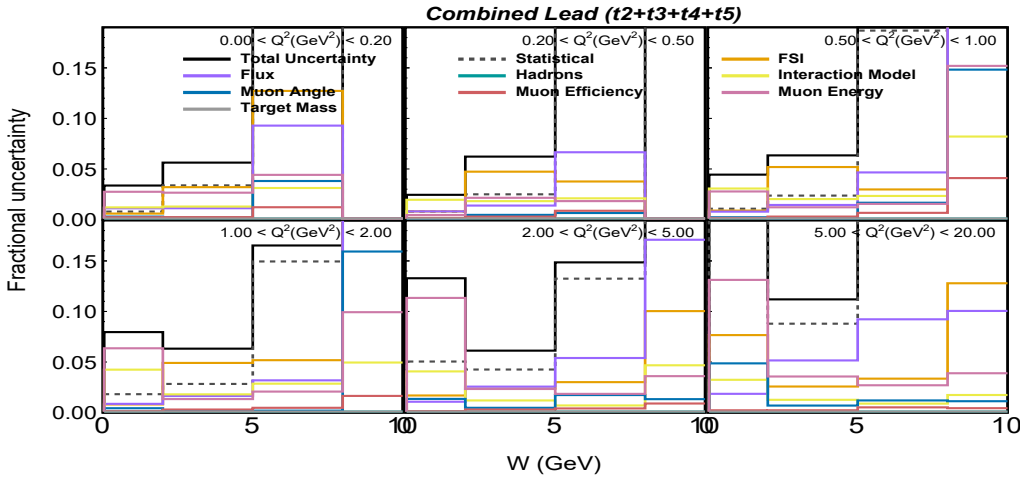

(a)

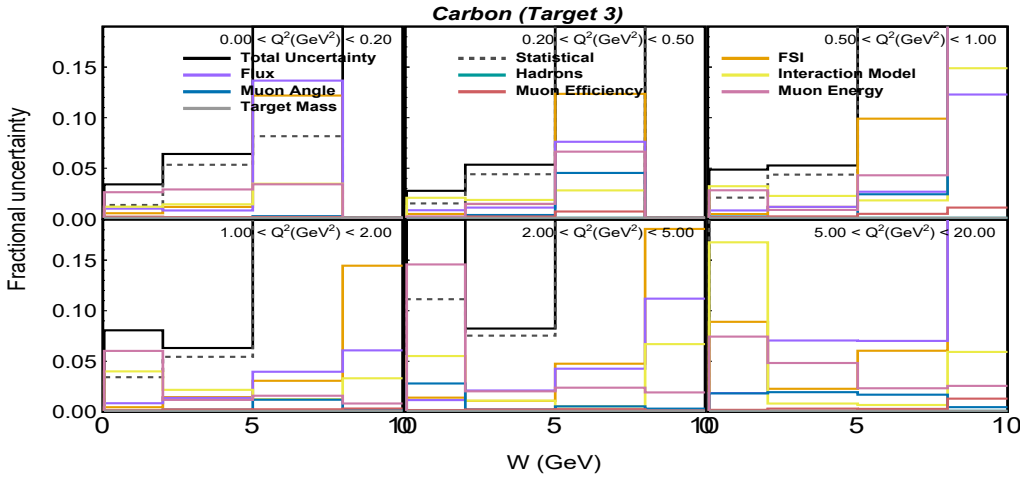

(b)

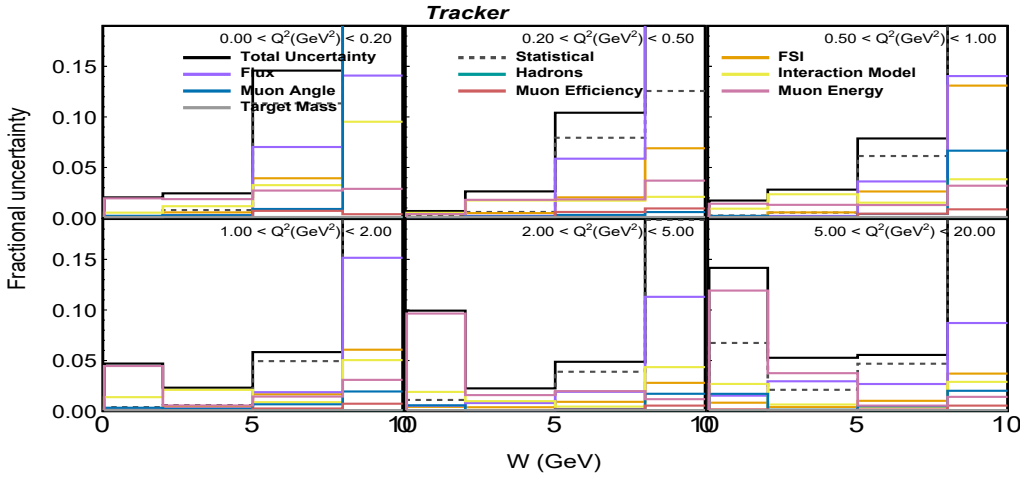

(c)

Figure E.10: Fractional systematic uncertainties in unfolded distributions for (a) combined lead, (b) carbon and (c) tracker in bins of $W - Q^2$.

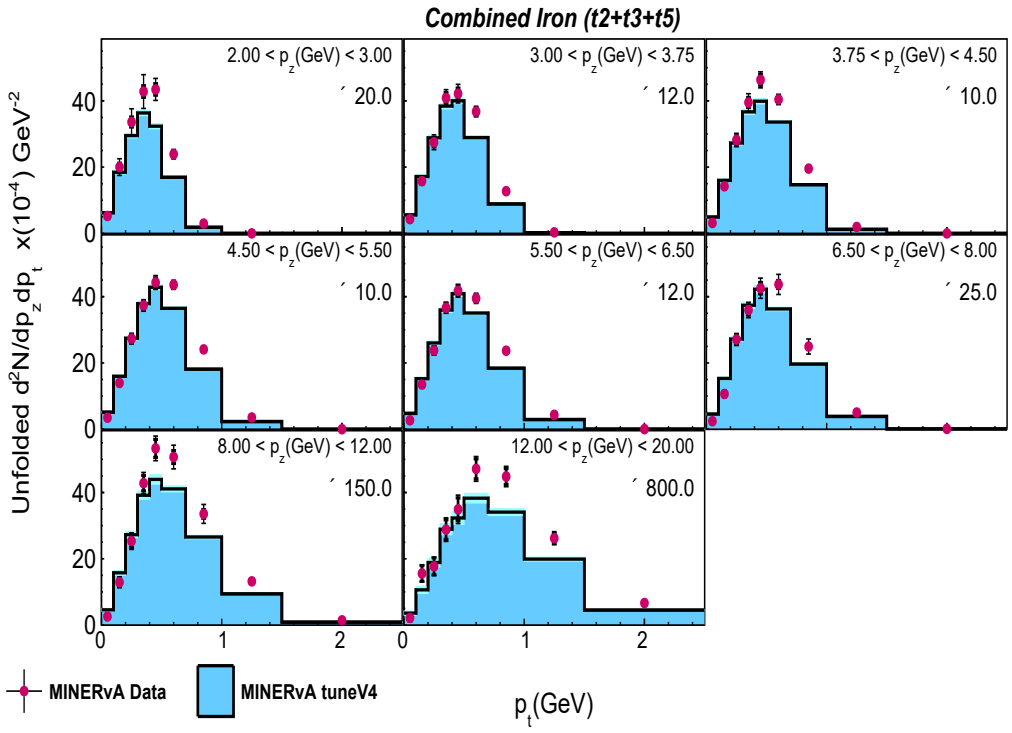

(a)

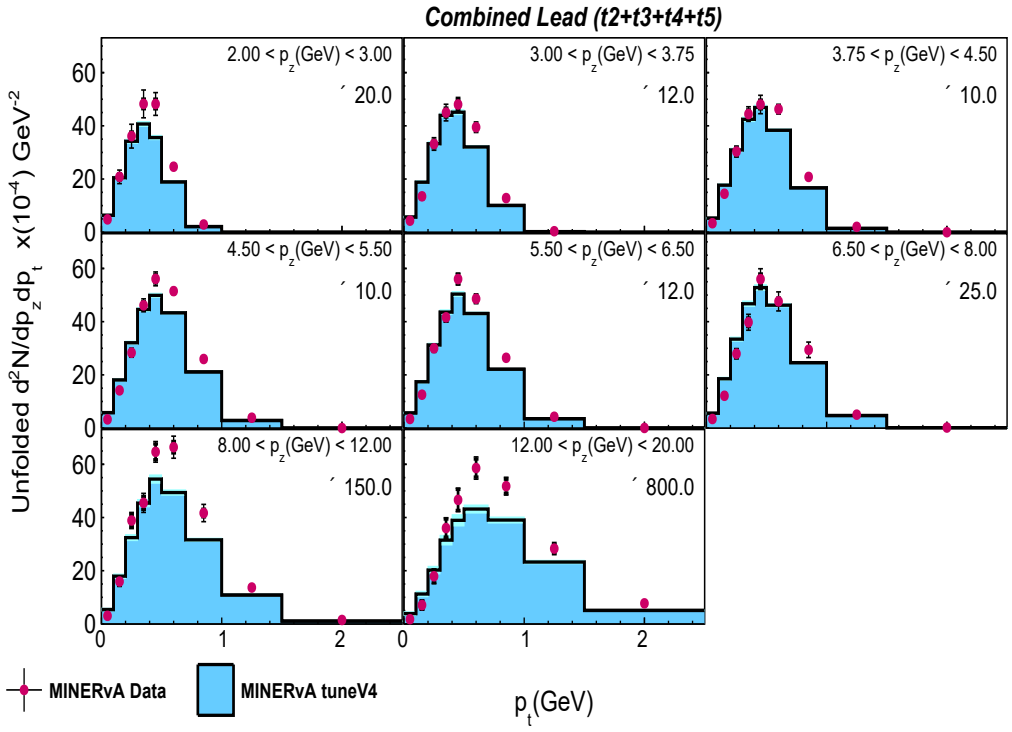

(b)

Figure E.11: Unfolded distributions for combined (a) iron and (b) lead in bins of $p_t - p_z$.

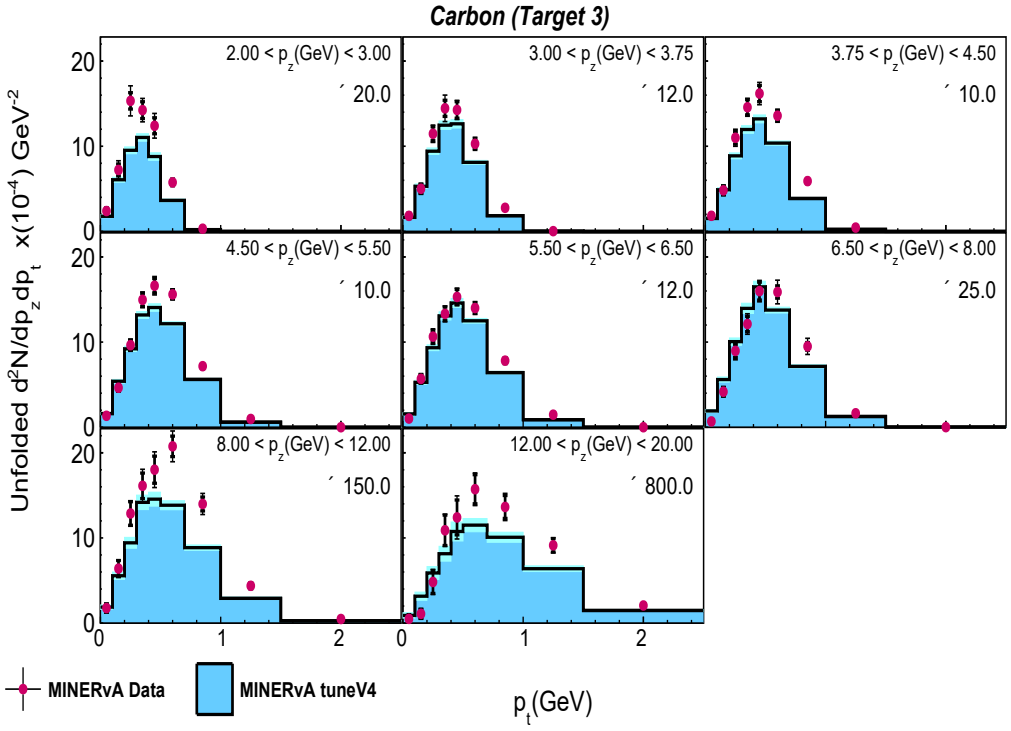

(a)

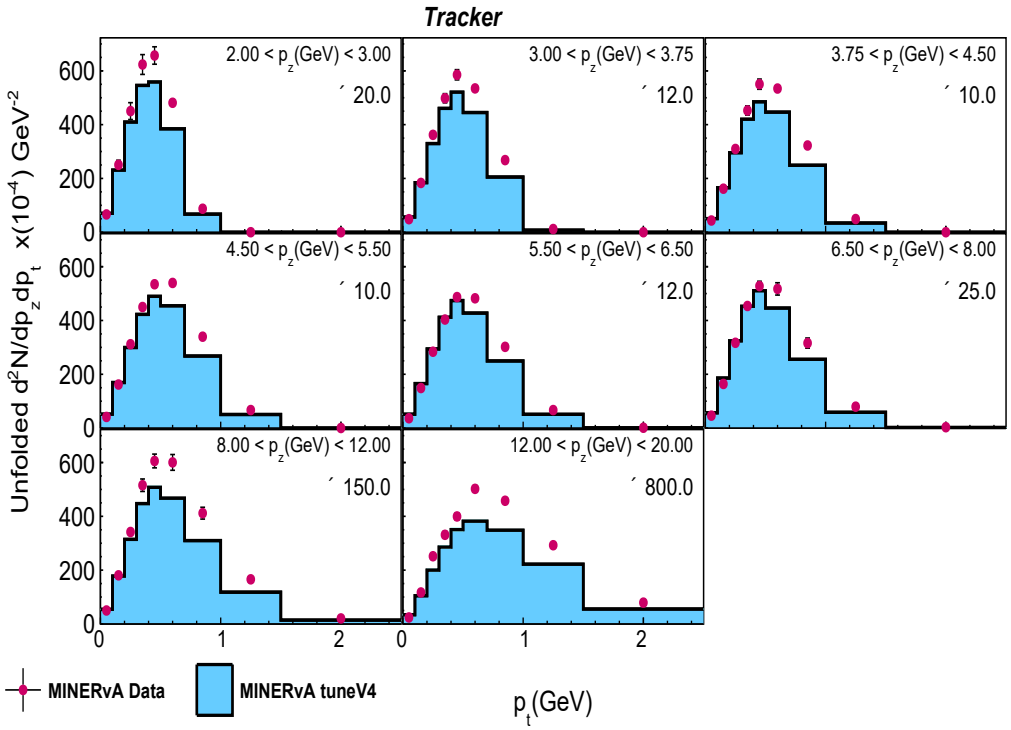

(b)

Figure E.12: Unfolded distributions for (a) carbon and (b)tracker in bins of $p_t - p_z$.

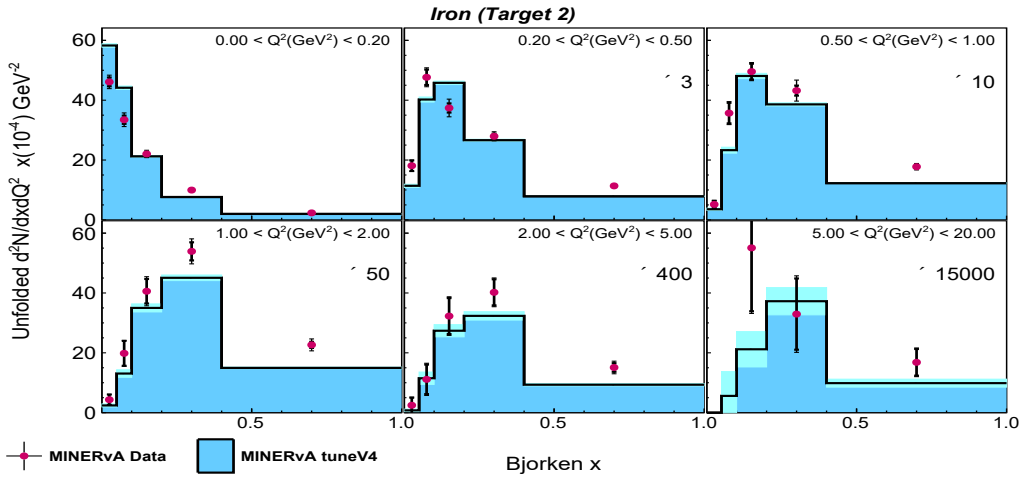

(a)

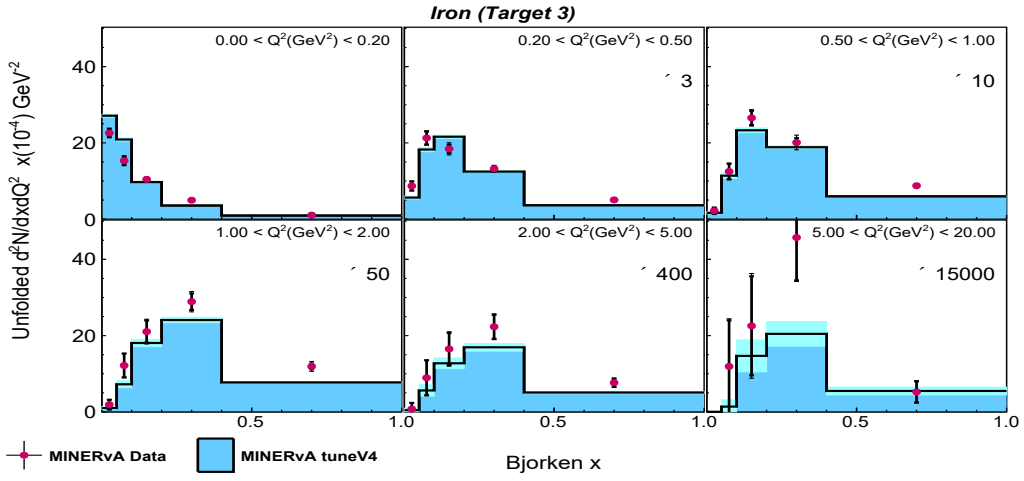

(b)

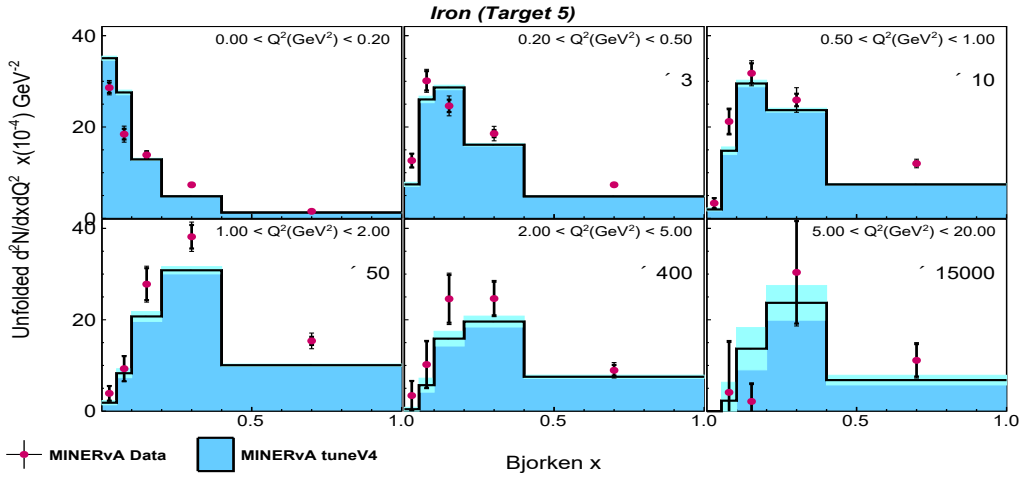

(c)

Figure E.13: Unfolded distributions for iron in (a) target 2, (b) target 3 and (c) target 5 in bins of $x - Q^2$.

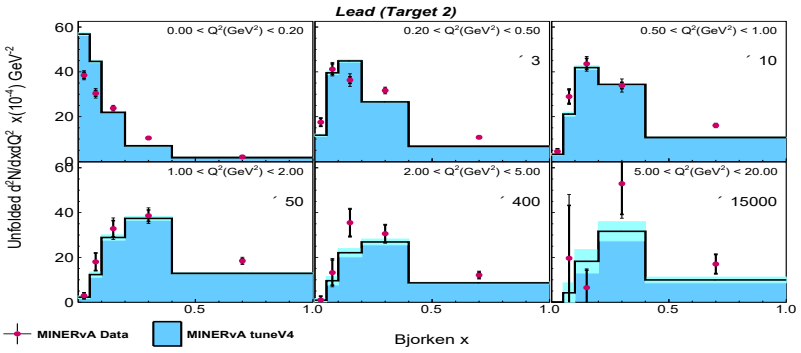

(a)

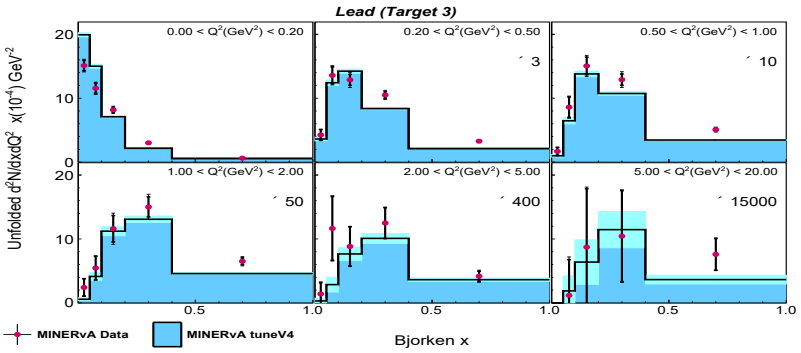

(b)

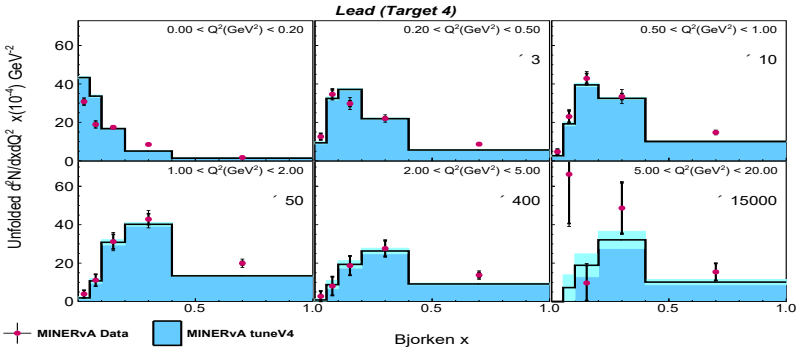

(c)

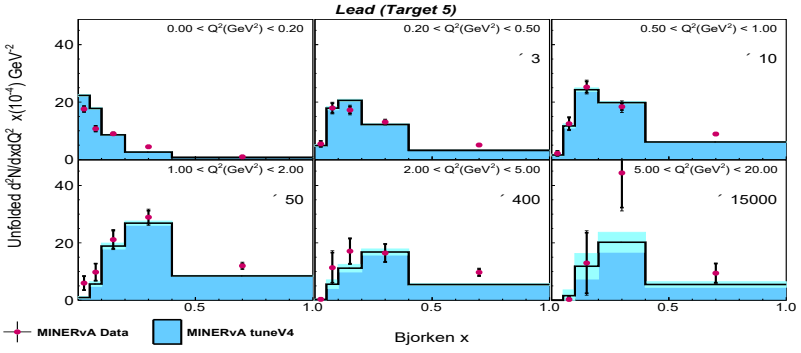

(d)

Figure E.14: Unfolded distributions for lead in (a) target 2, (b) target 3, (c) target 4 and (d) target 5 in bins of $x - Q^2$.

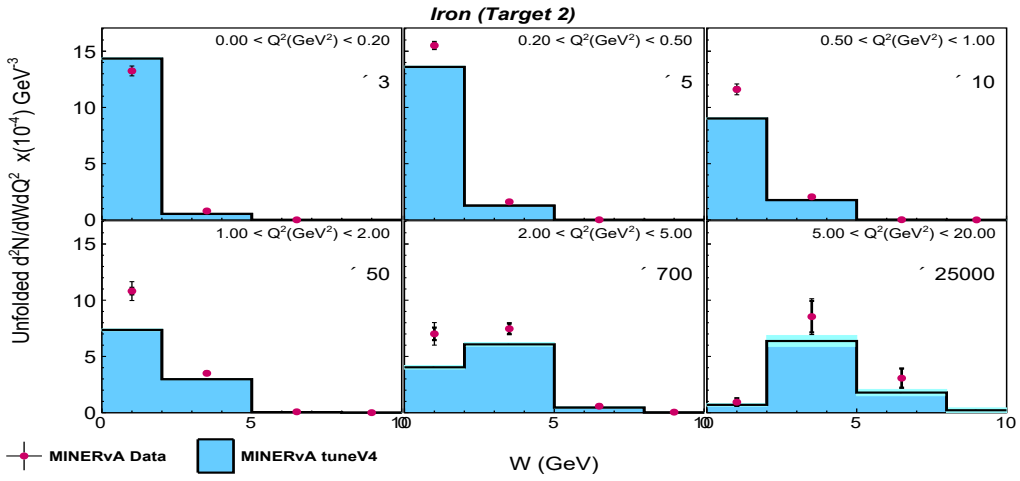

(a)

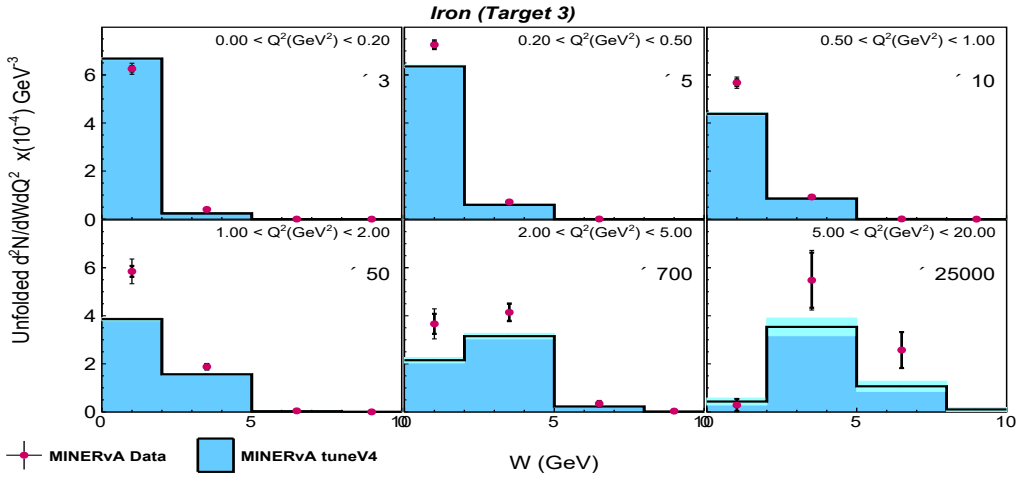

(b)

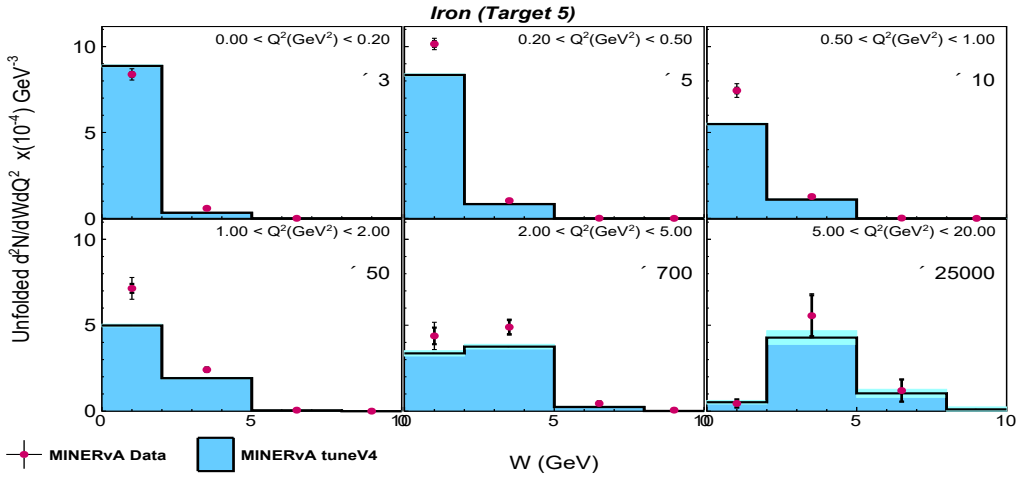

(c)

Figure E.15: Unfolded distributions for iron in (a) target 2, (b) target 3 and (c) target 5 in bins of $W - Q^2$.

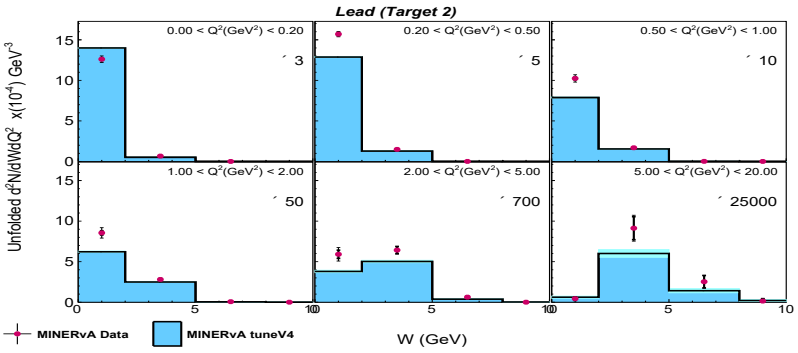

(a)

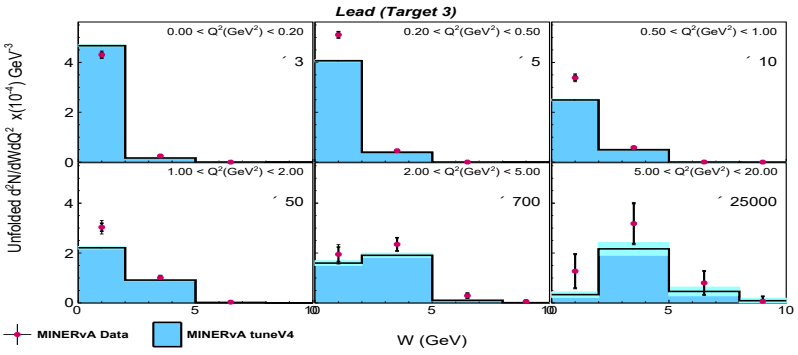

(b)

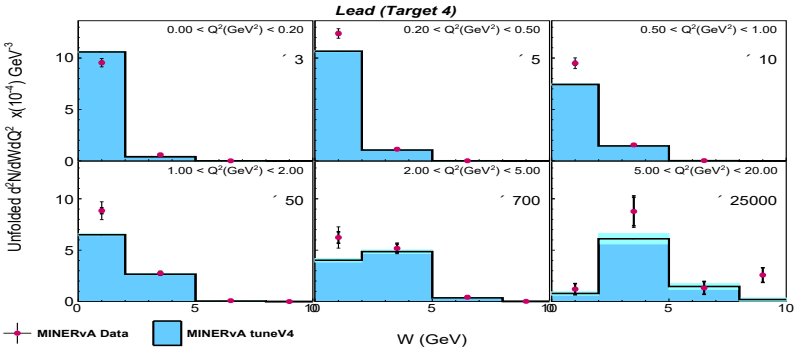

(c)

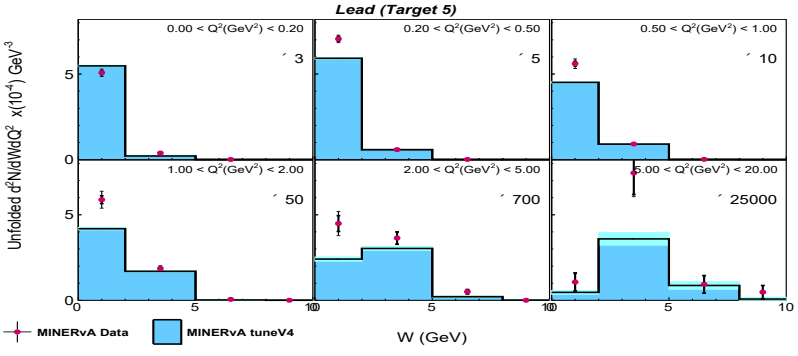

(d)

Figure E.16: Unfolded distributions for lead in (a) target 2, (b) target 3, (c) target 4 and (d) target 5 in bins of $W - Q^2$.

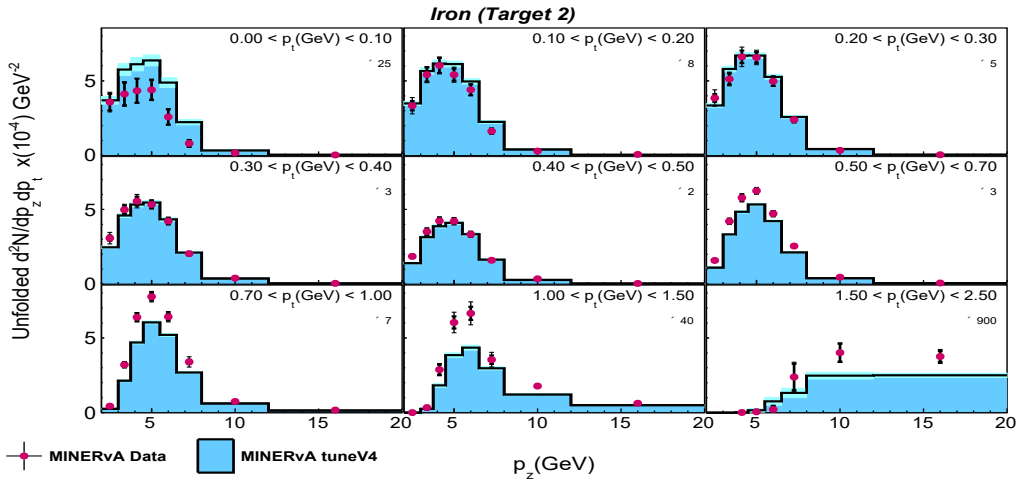

(a)

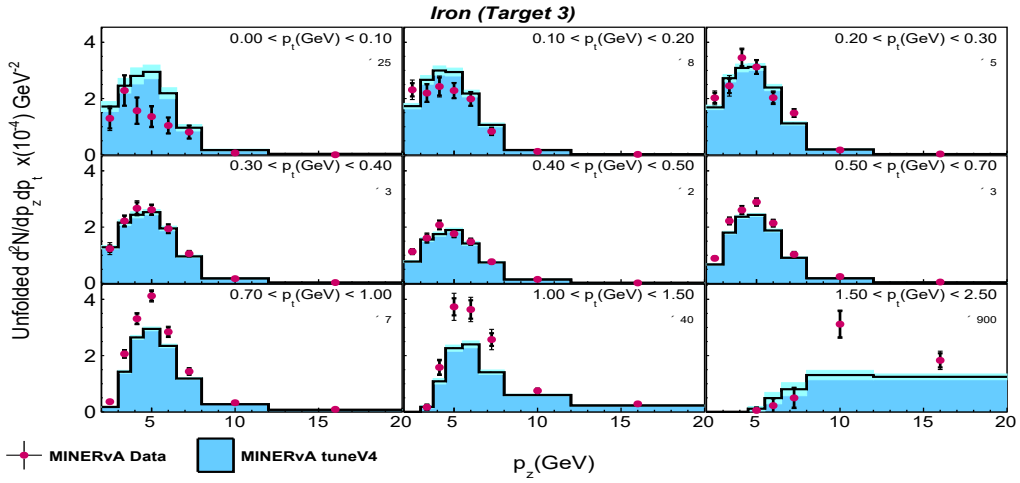

(b)

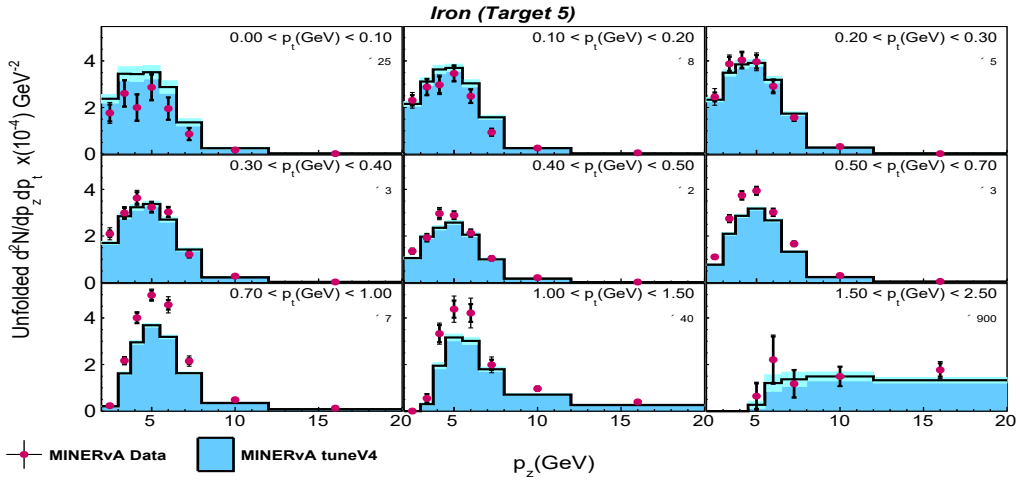

(c)

Figure E.17: Unfolded distributions for iron in (a) target 2, (b) target 3 and (c) target 5 in bins of $p_z - p_t$.

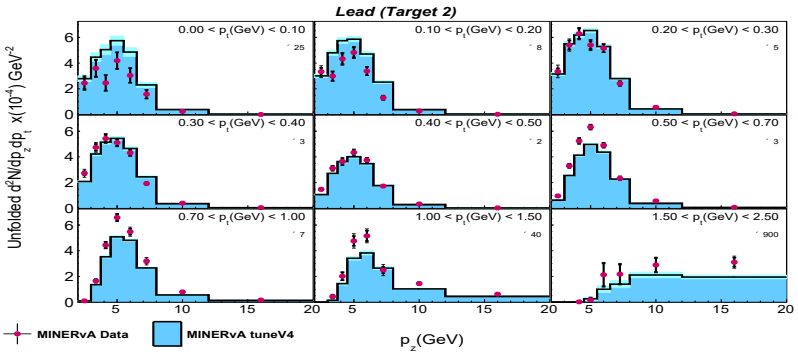

(a)

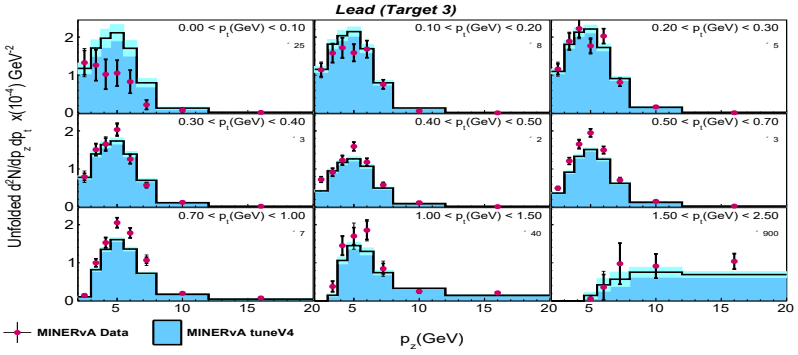

(b)

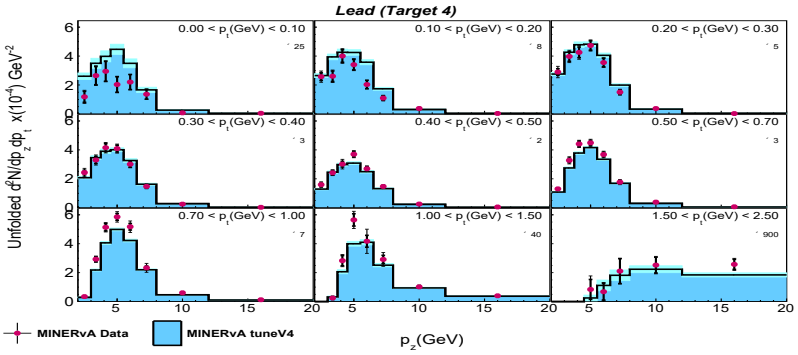

(c)

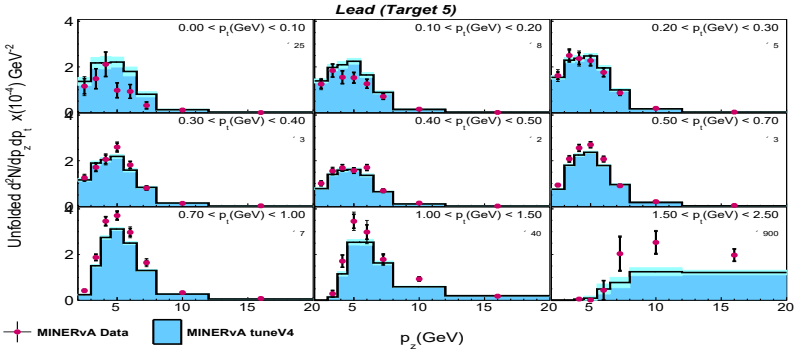

(d)

Figure E.18: Unfolded distributions for lead in (a) target 2, (b) target 3, (c) target 4 and (d) target 5 in bins of $p_z - p_t$.

Appendix F

Efficiency

Here, I have included the plots for efficiency distributions for combined iron, lead, carbon and tracker scintillator targets in $W - Q^2$ and $p_z - p_t$ bins. Efficiency distributions for materials from individual targets are also shown here.

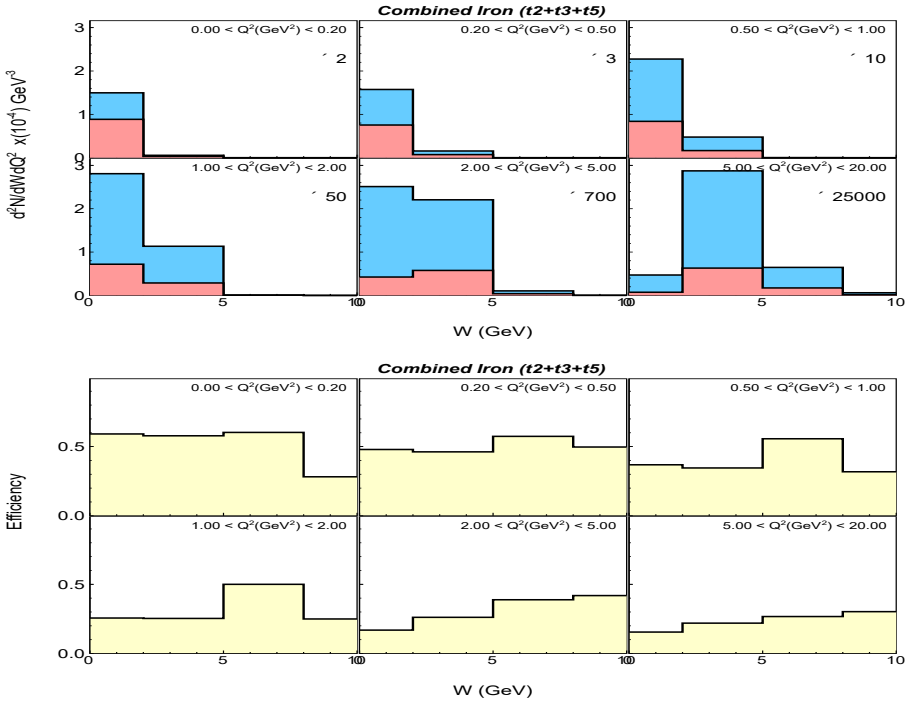

Figure F.1: (Top) The blue histogram shows total generated signal events, and the red histogram shows the reconstructed events. (Bottom) The ratio gives the reconstruction efficiency across $W - Q^2$ bins for combined iron targets 2, 3 and 5. Histograms are not stacked.

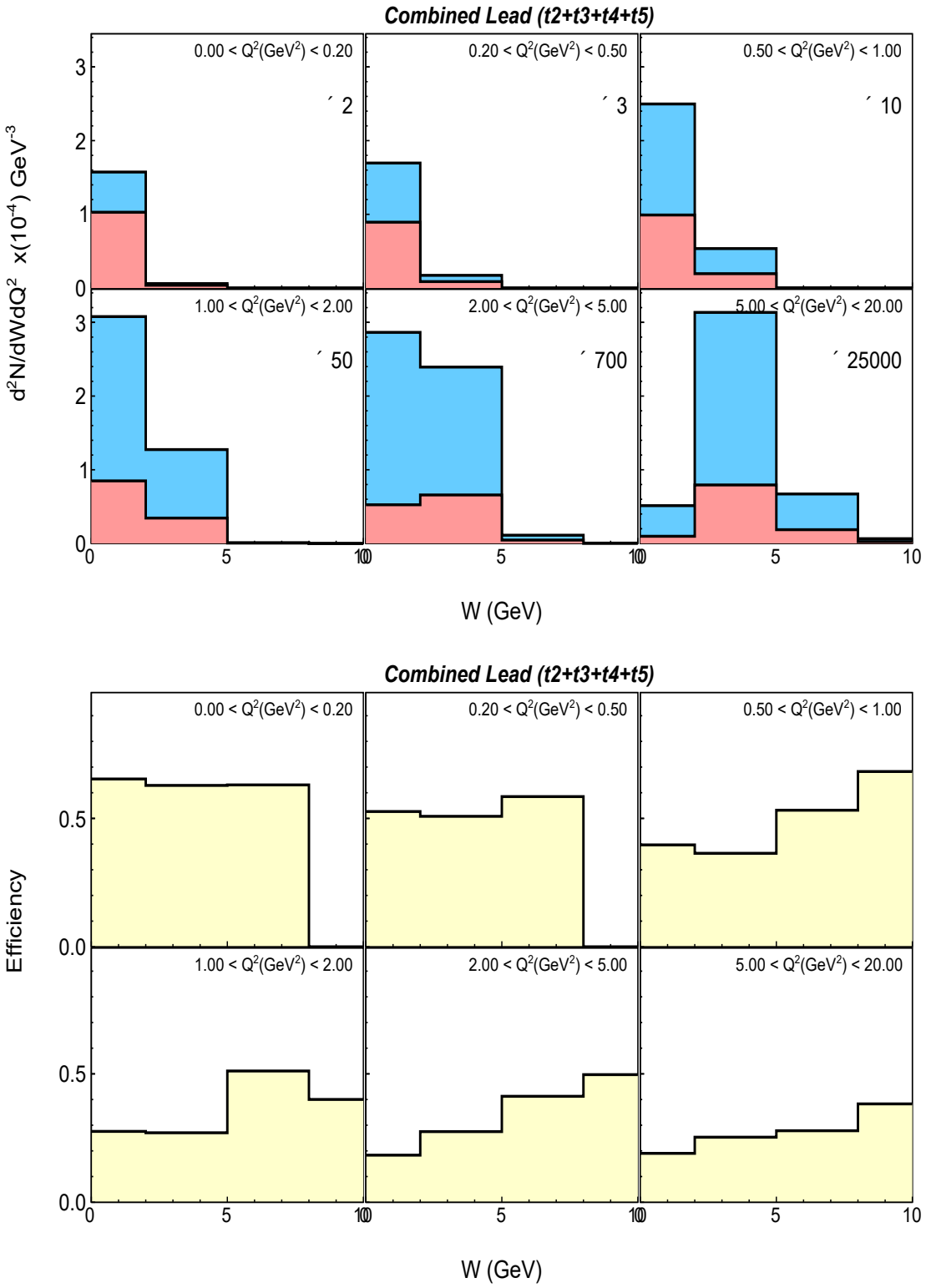

Figure F.2: (Top) The blue histogram shows total generated signal events, and the red histogram shows the reconstructed events. (Bottom) The ratio gives the reconstruction efficiency across $W - Q^2$ bins for combined lead from targets 2, 3, 4 and 5. Histograms are not stacked.

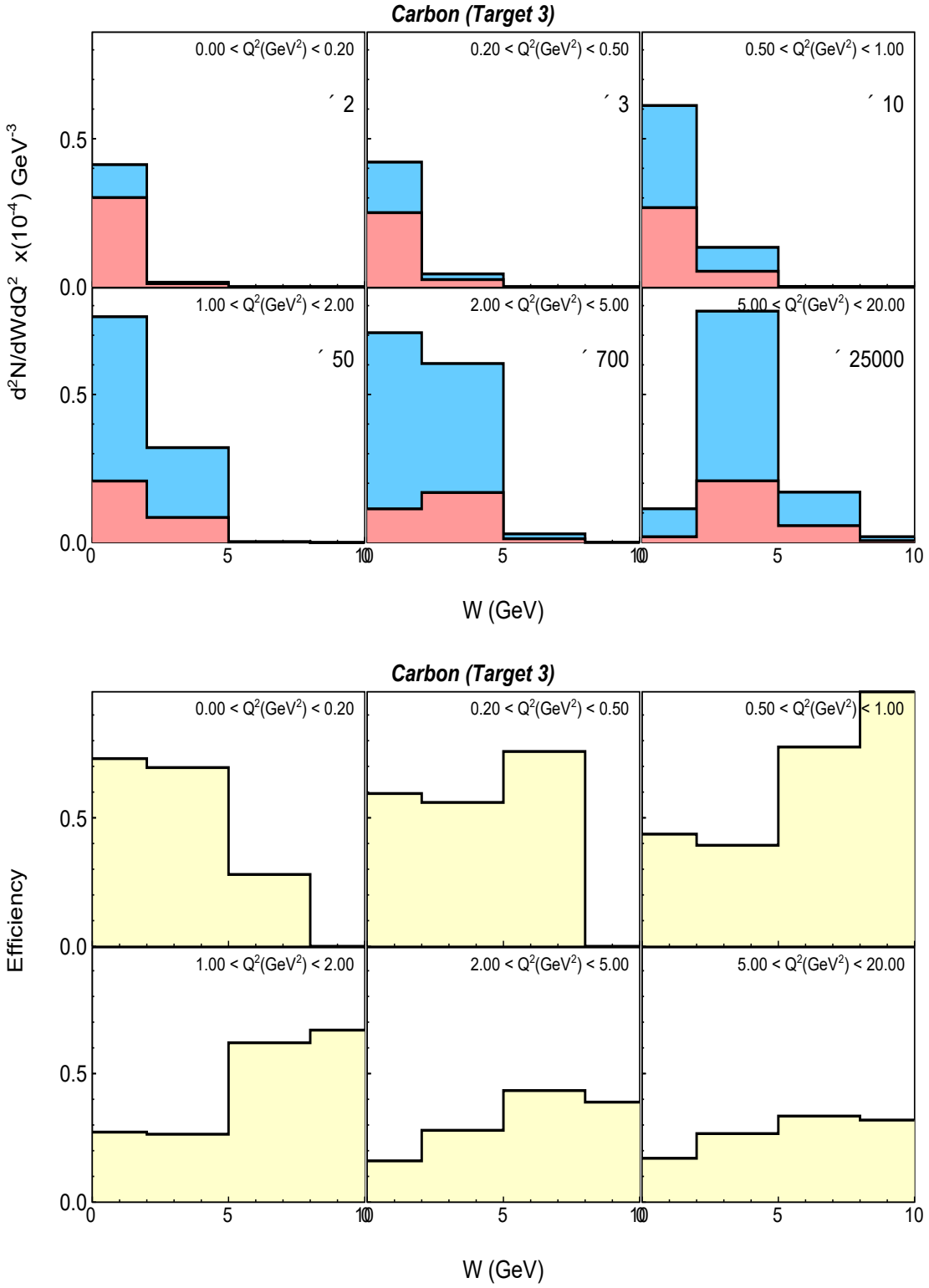

Figure F.3: (Top) The blue histogram shows total generated signal events, and the red histogram shows the reconstructed events. (Bottom) The ratio gives the reconstruction efficiency across $W - Q^2$ bins for carbon target. Histograms are not stacked.

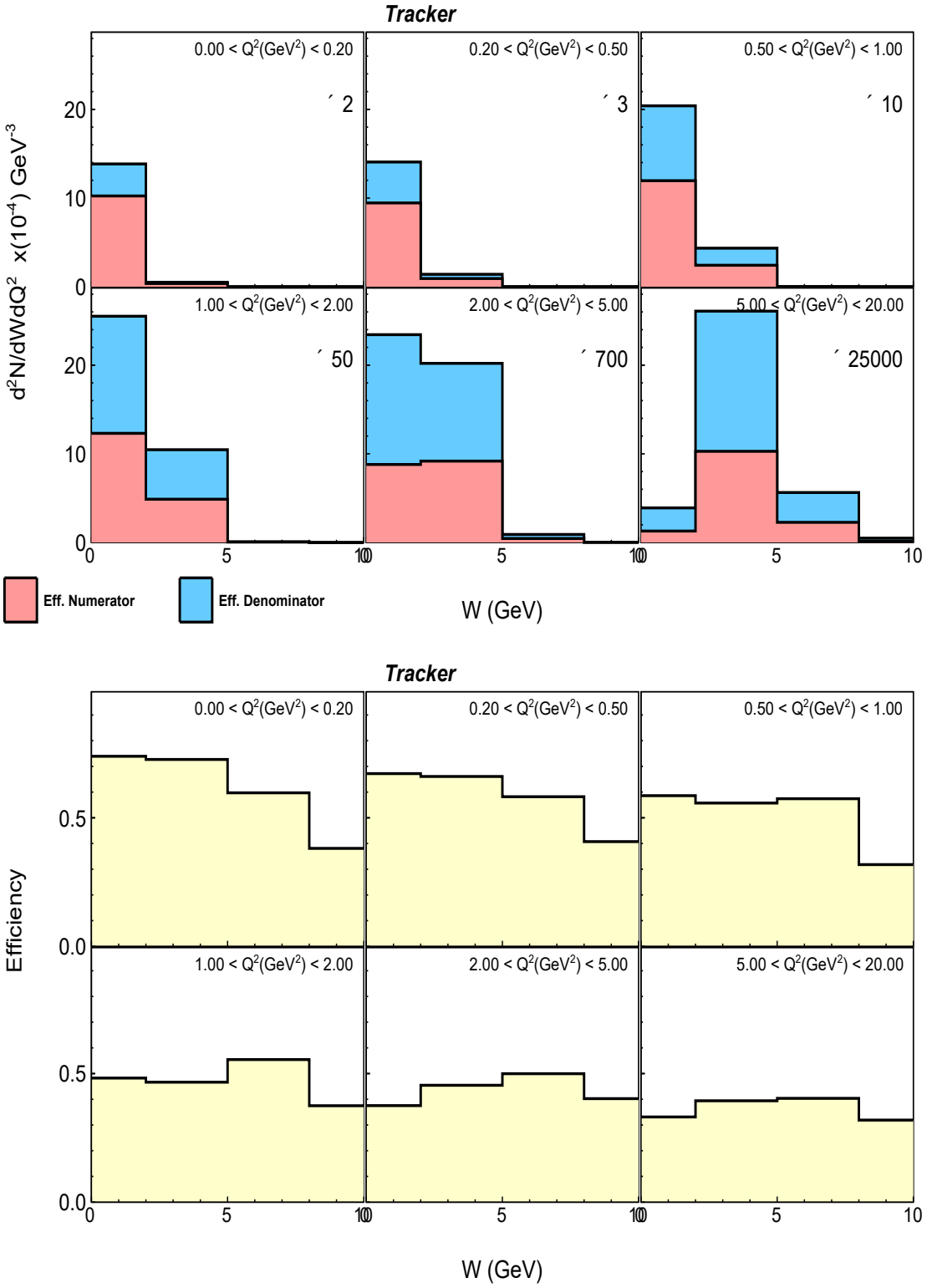

Figure F.4: (Top) The blue histogram shows total generated signal events, and the red histogram shows the reconstructed events. (Bottom) The ratio gives the reconstruction efficiency across $W - Q^2$ bins for tracker scintillator. Histograms are not stacked.

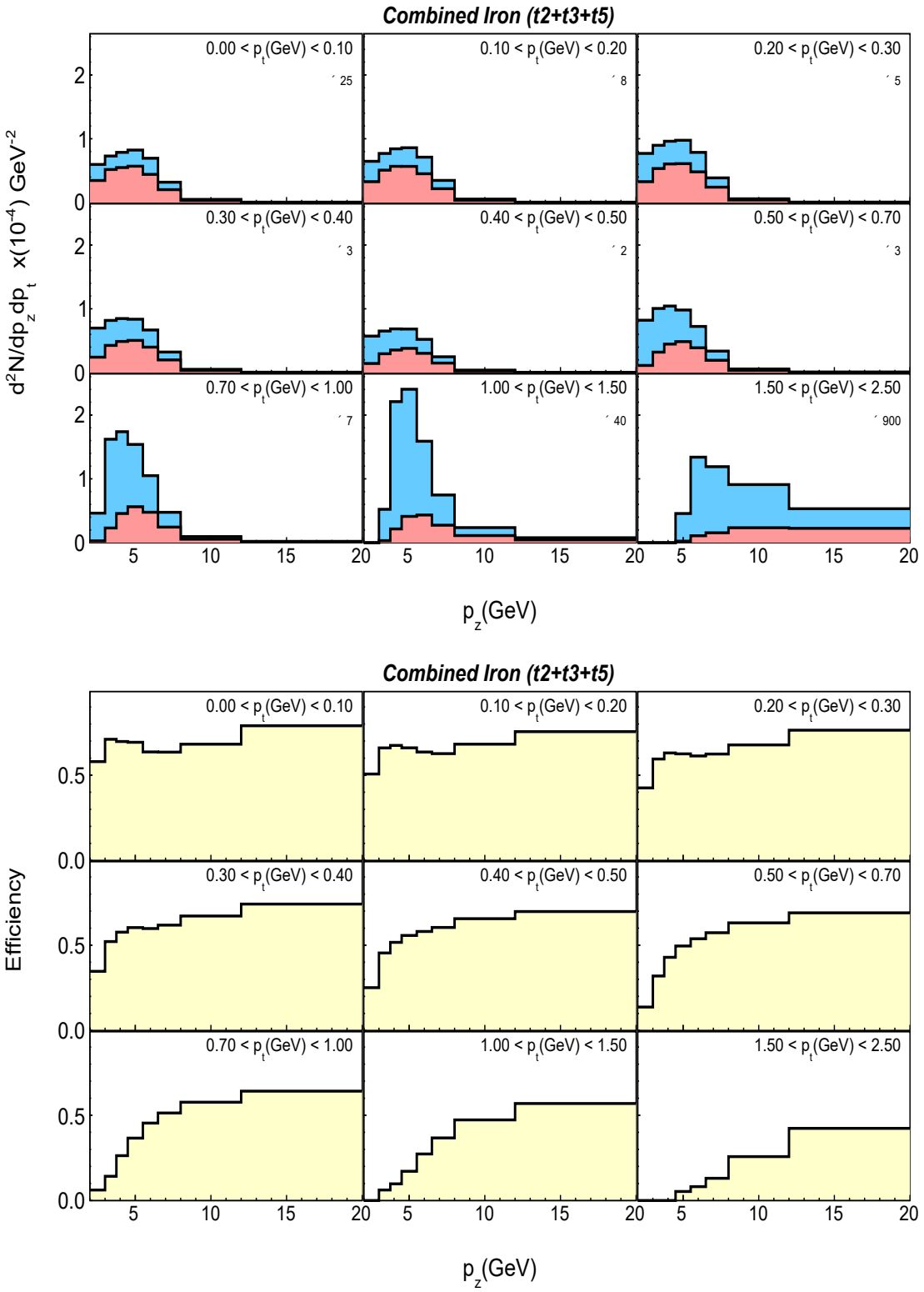

Figure F.5: (Top) The blue histogram shows total generated signal events, and the red histogram shows the reconstructed events. (Bottom) The ratio gives the reconstruction efficiency across $p_z - p_t$ bins for combined iron targets 2, 3 and 5. Histograms are not stacked.

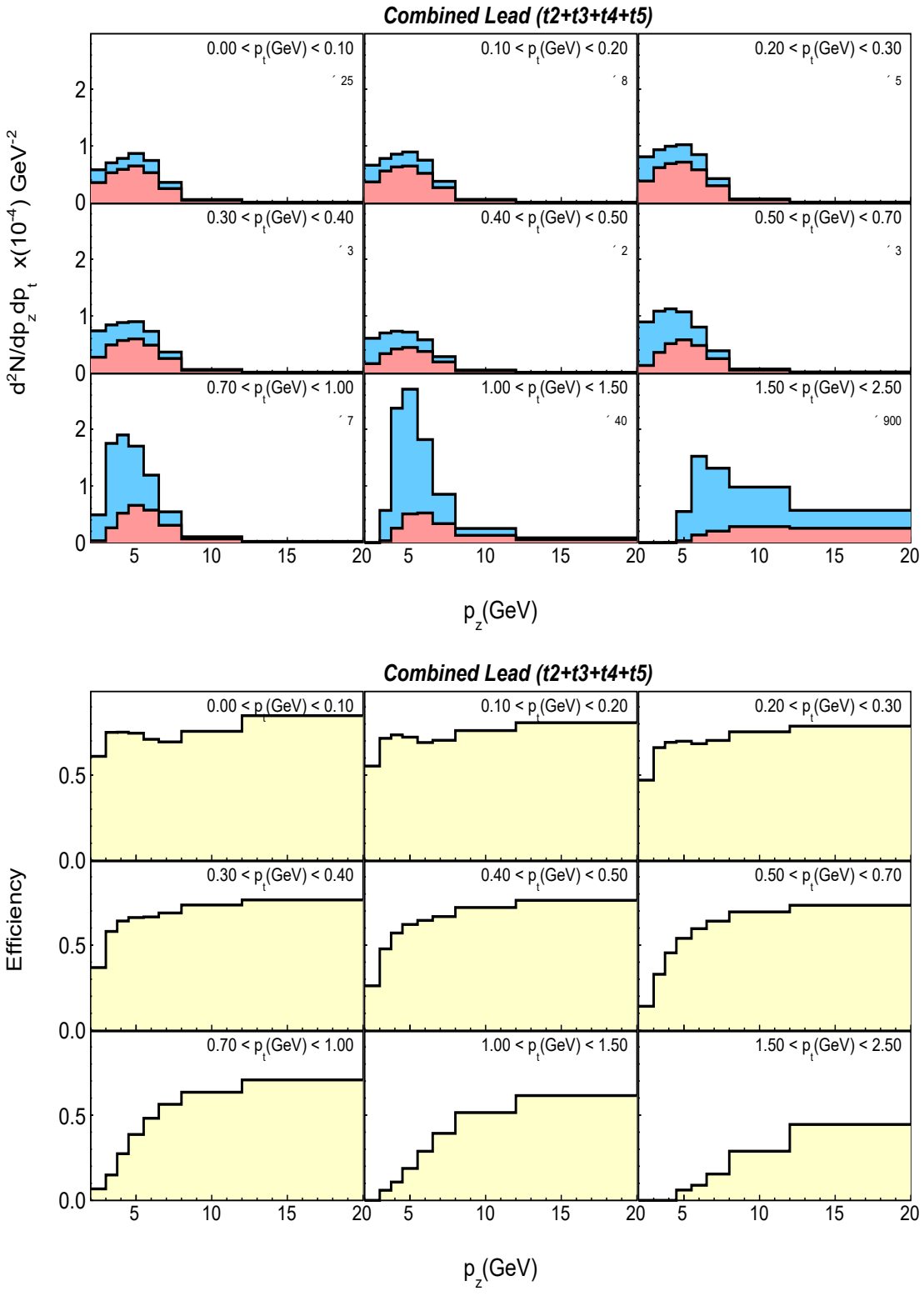

Figure F.6: (Top) The blue histogram shows total generated signal events, and the red histogram shows the reconstructed events. (Bottom) The ratio gives the reconstruction efficiency across $p_z - p_t$ bins for combined lead from targets 2, 3, 4 and 5. Histograms are not stacked.

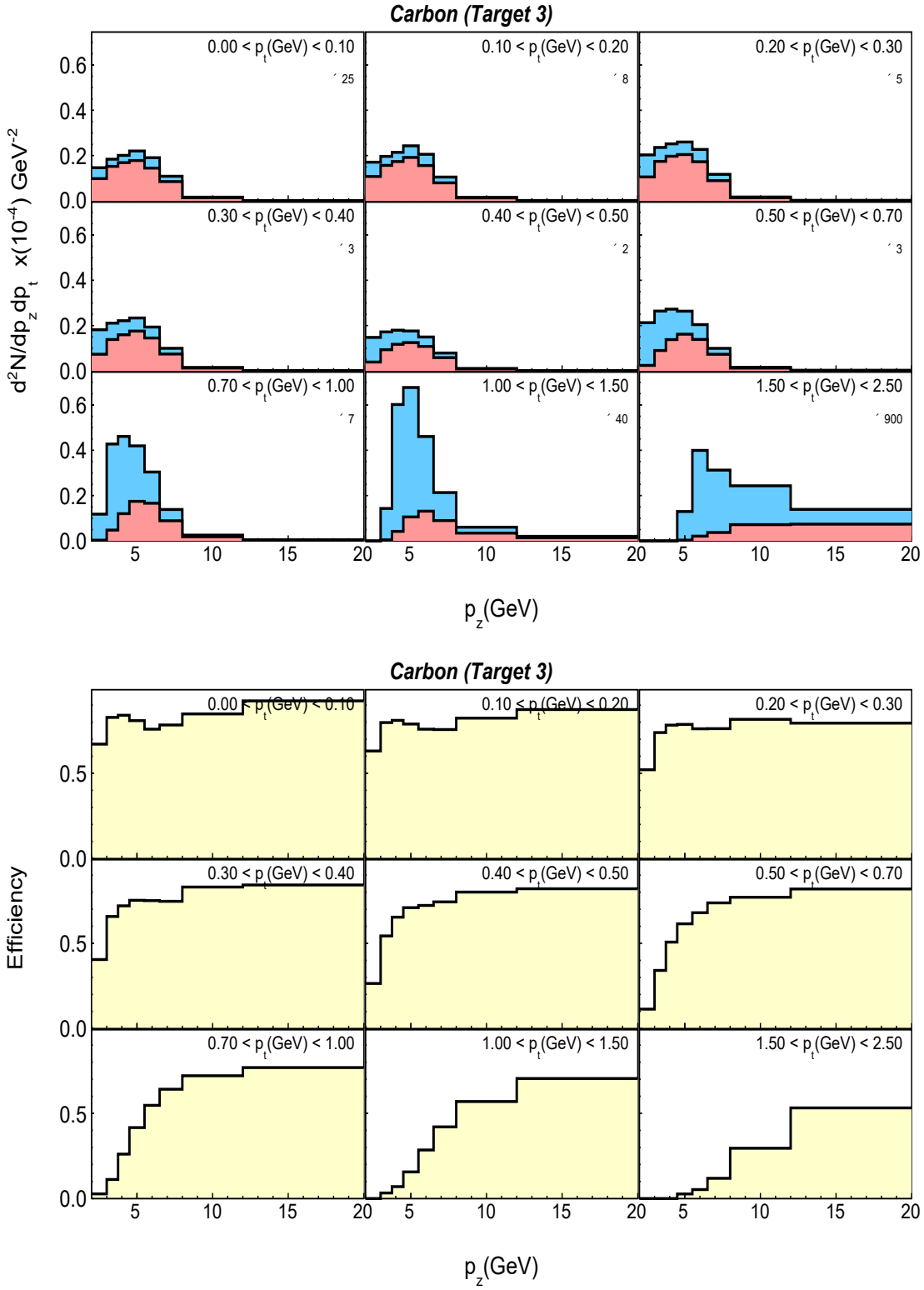

Figure F.7: (Top) The blue histogram shows total generated signal events, and the red histogram shows the reconstructed events. (Bottom) The ratio gives the reconstruction efficiency across $p_z - p_t$ bins for carbon target. Histograms are not stacked.

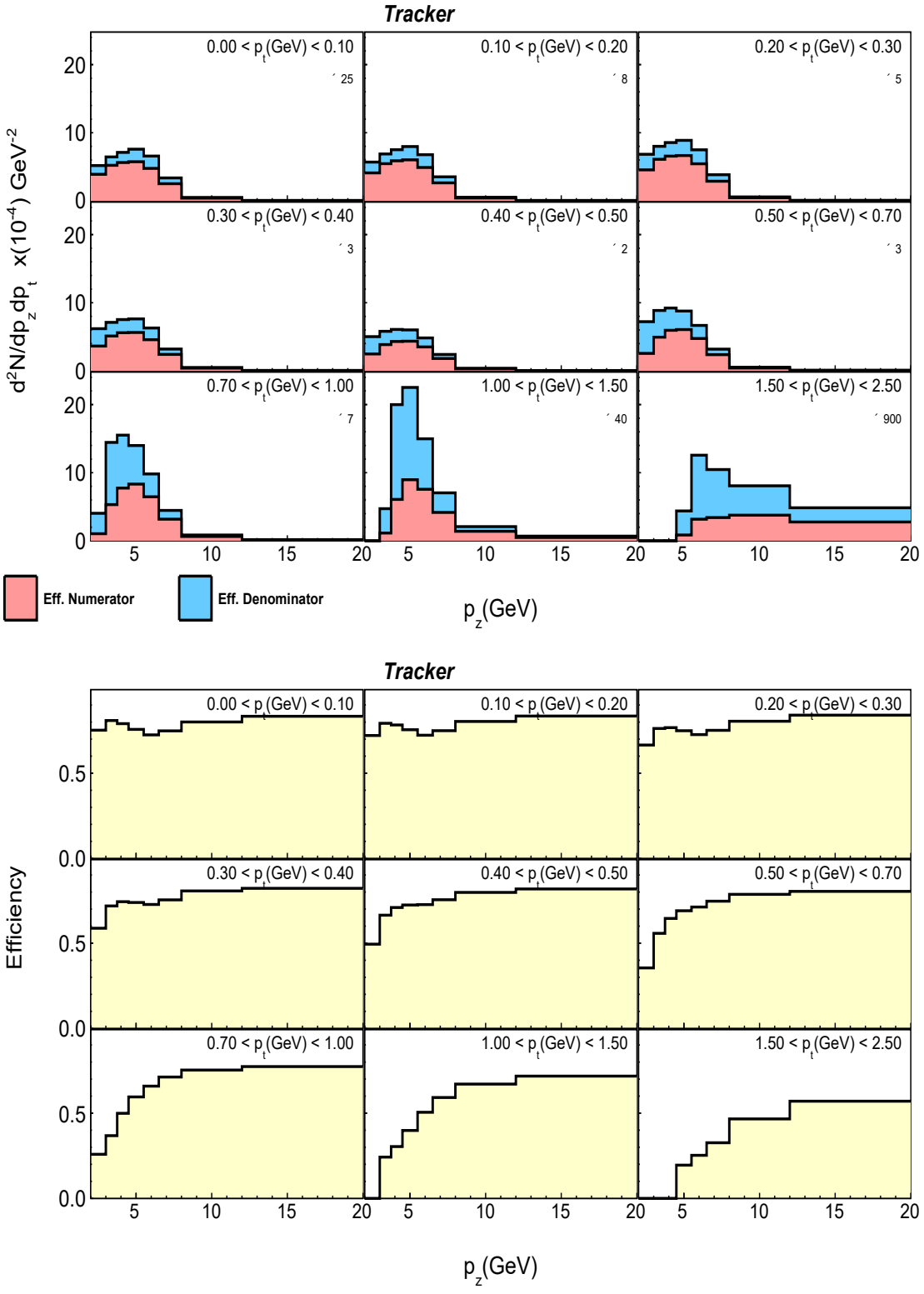

Figure F.8: (Top) The blue histogram shows total generated signal events, and the red histogram shows the reconstructed events. (Bottom) The ratio gives the reconstruction efficiency across $p_z - p_t$ bins for tracker scintillator. Histograms are not stacked.

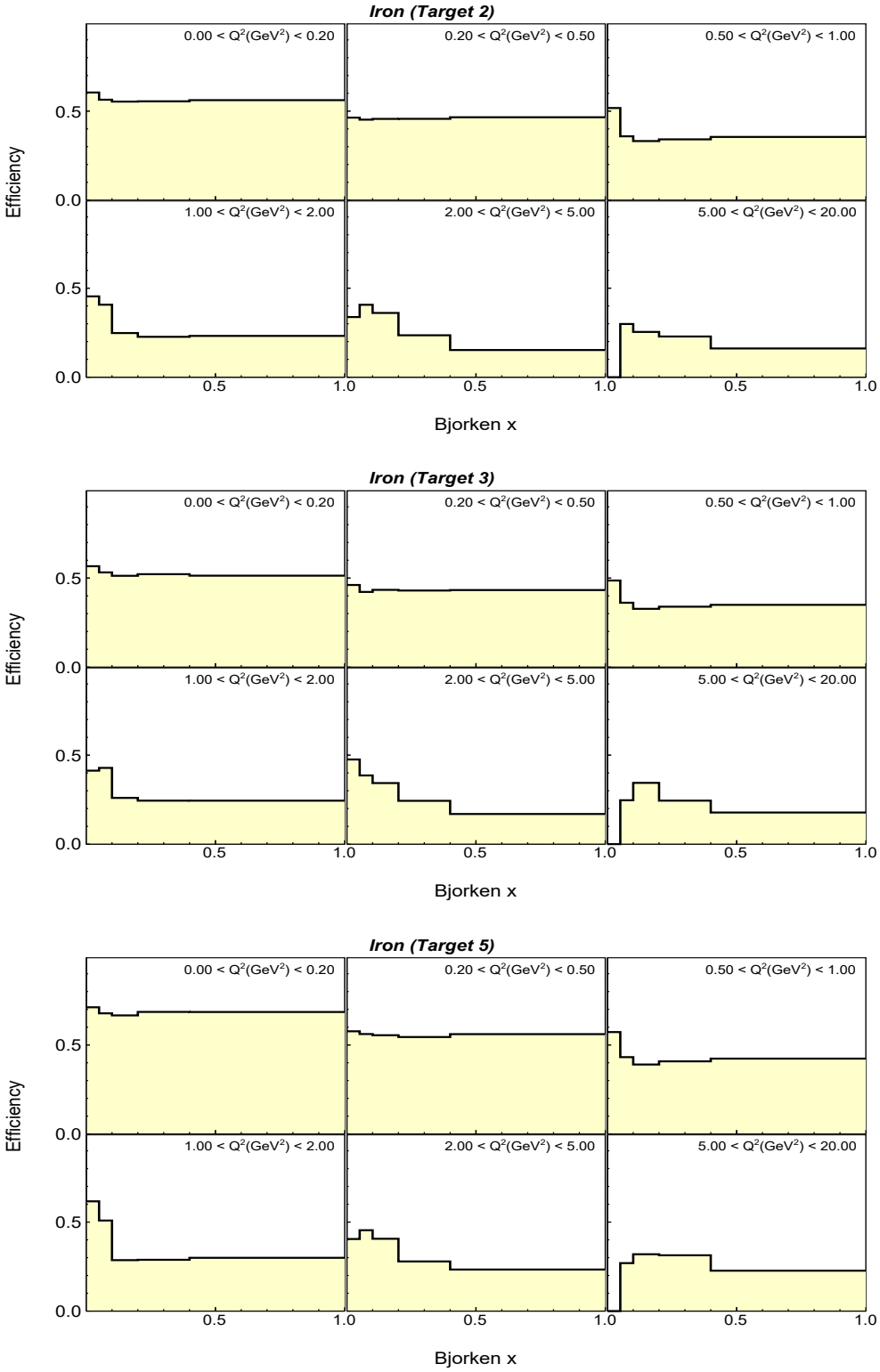

Figure F.9: Efficiency distributions across $x - Q^2$ bins for different iron targets.

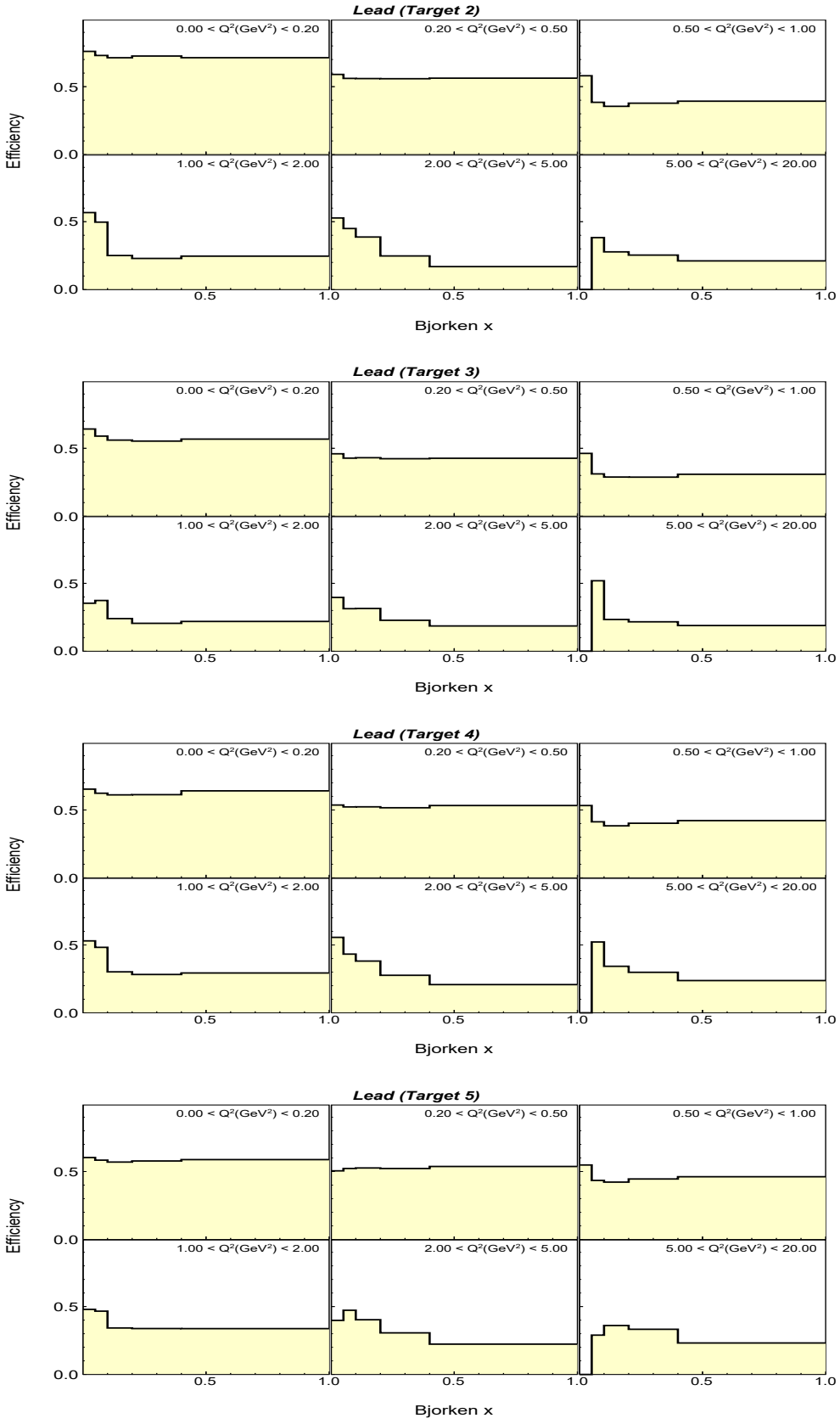

Figure F.10: Efficiency distributions across $x - Q^2$ bins for different lead targets.

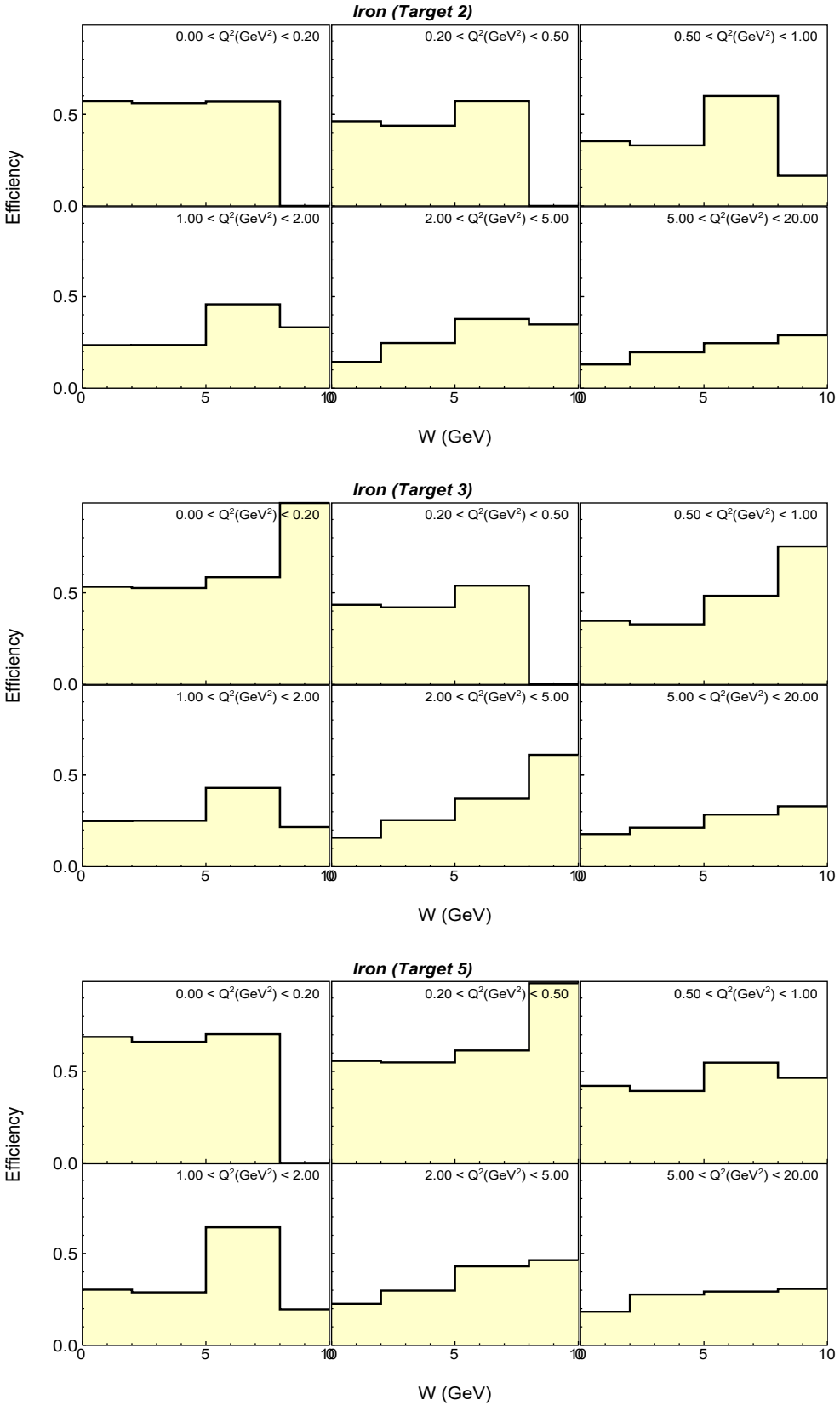

Figure F.11: Efficiency distributions across $W - Q^2$ bins for iron targets.

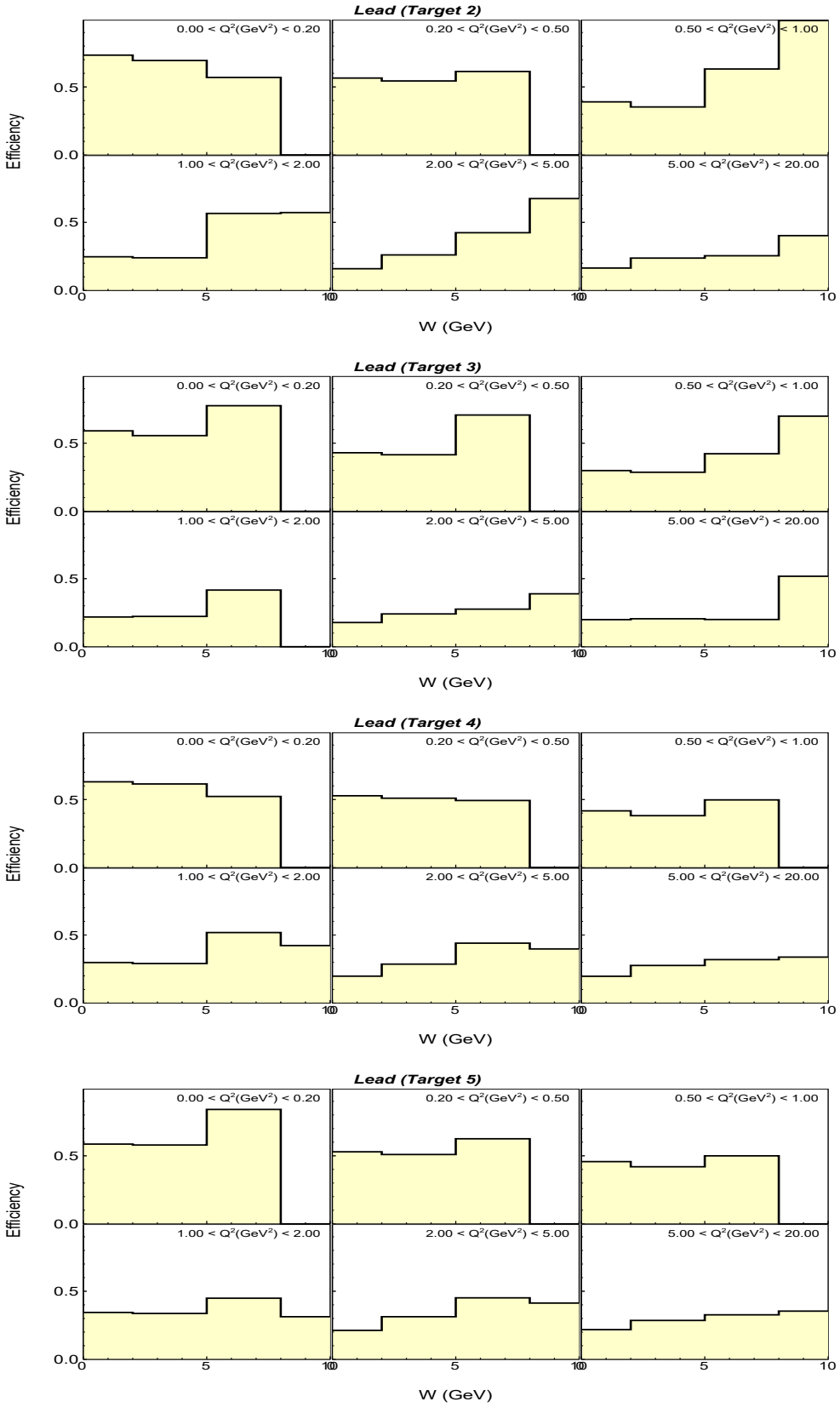

Figure F.12: Efficiency distributions across $W - Q^2$ bins for lead targets.

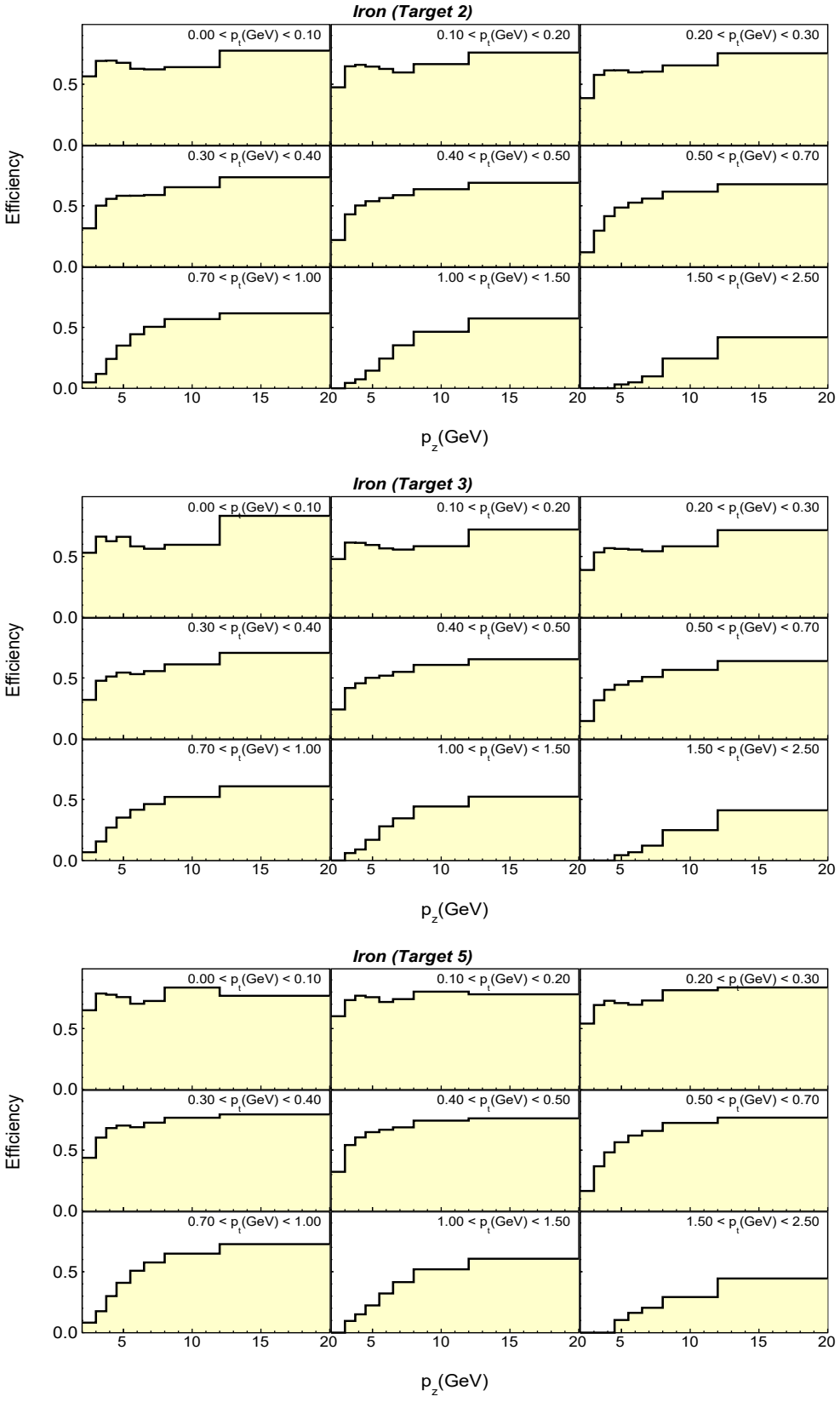

Figure F.13: Efficiency distributions across $p_z - p_t$ bins for iron targets.

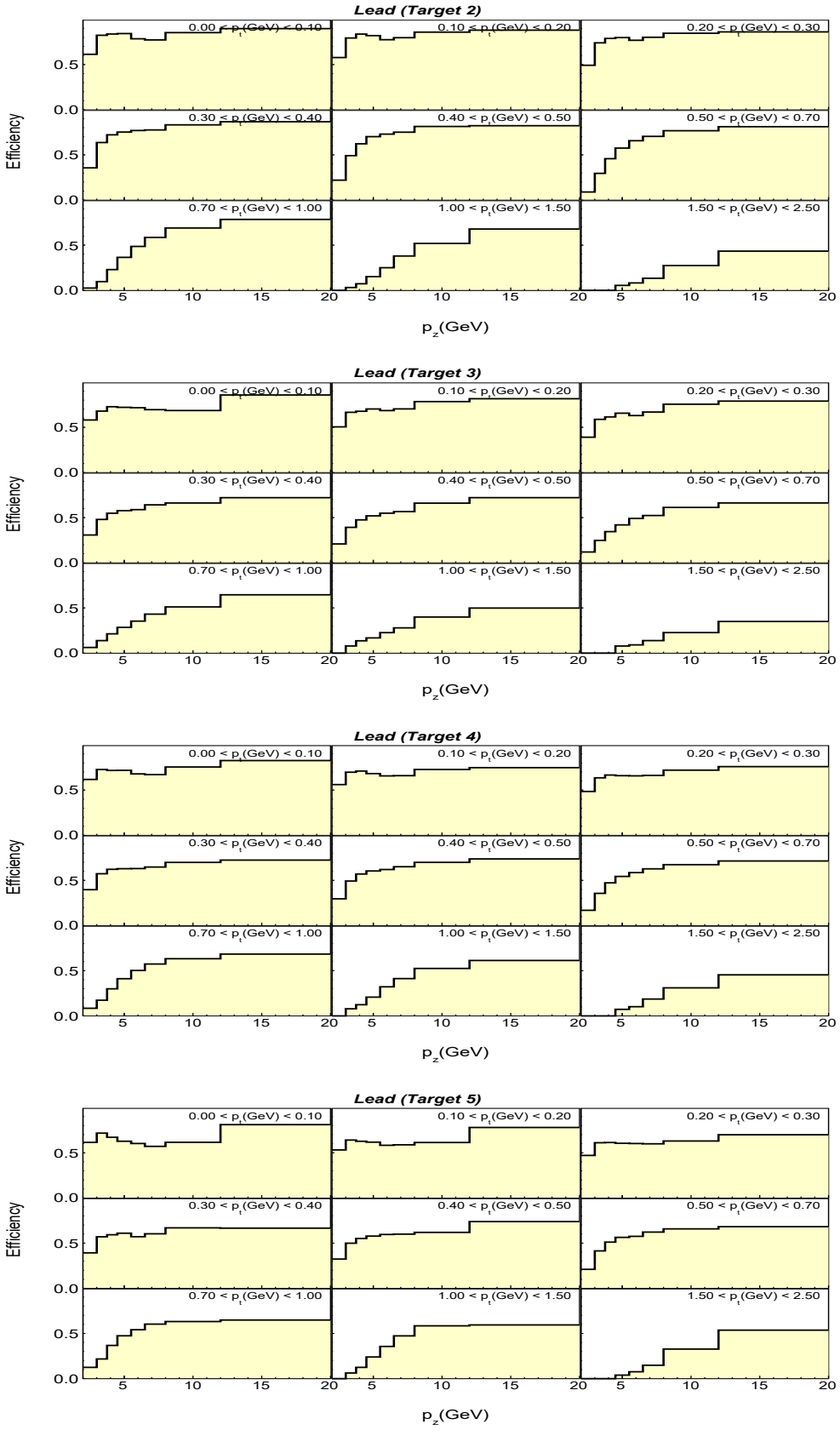

Figure F.14: Efficiency distributions across $p_z - p_t$ bins for lead targets.

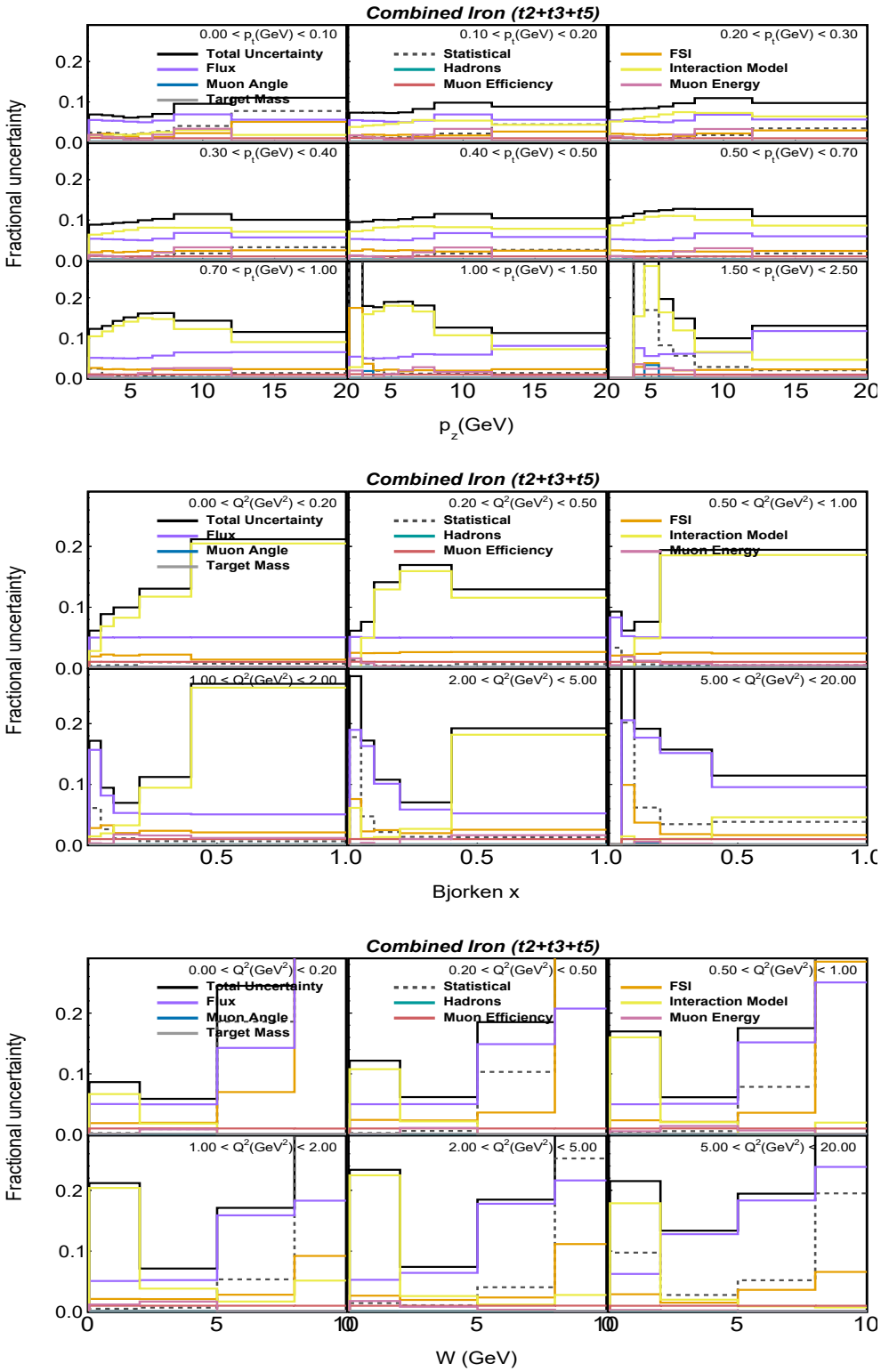

Figure F.15: Fractional uncertainties in generated, reconstructed MC for combined iron across $p_z - p_t$ (top), $x - Q^2$ (middle) and $W - Q^2$ (bottom).

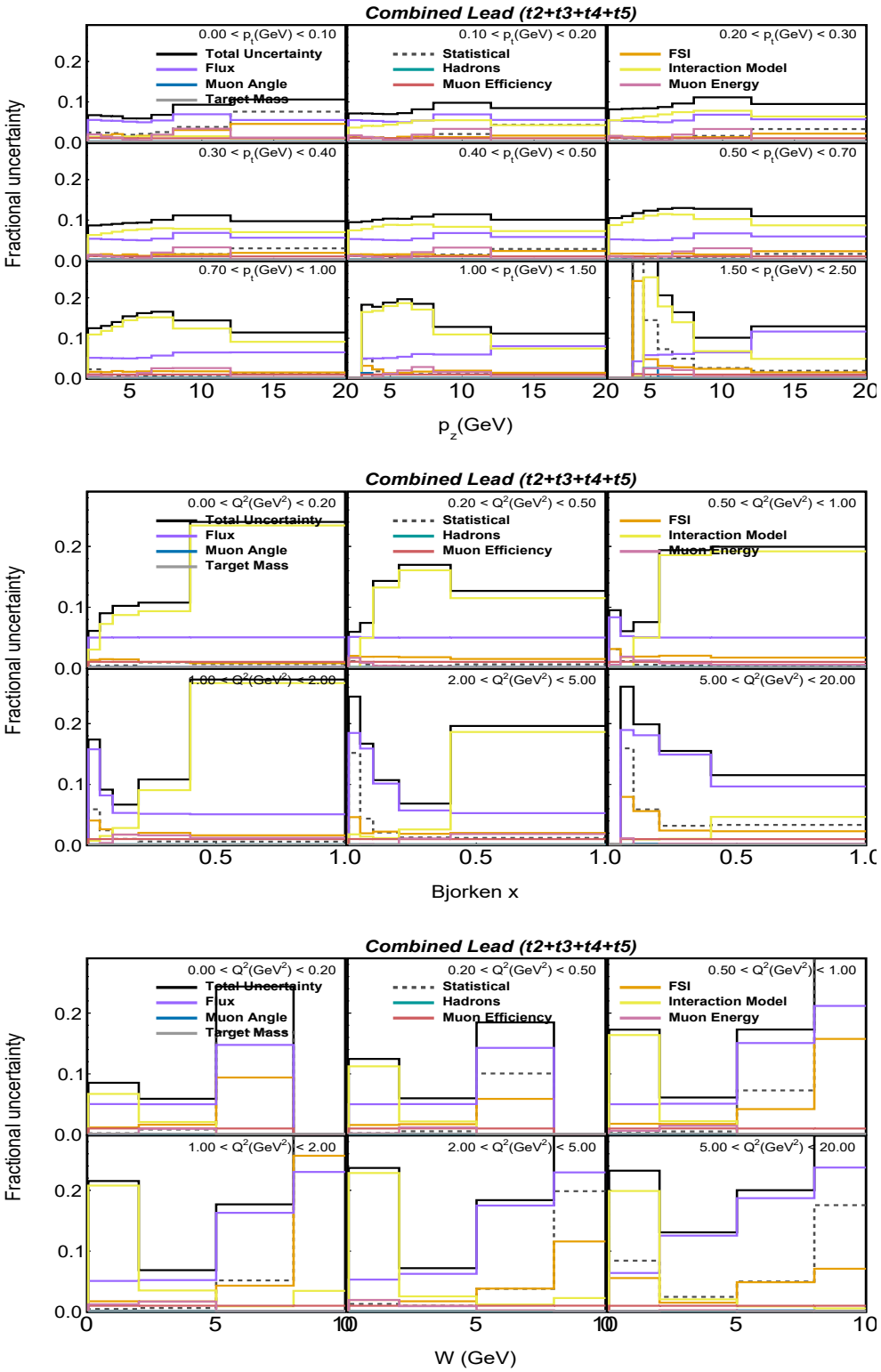

Figure F.16: Fractional uncertainties in generated, reconstructed MC for combined lead across $p_z - p_t$ (top), $x - Q^2$ (middle) and $W - Q^2$ (bottom).

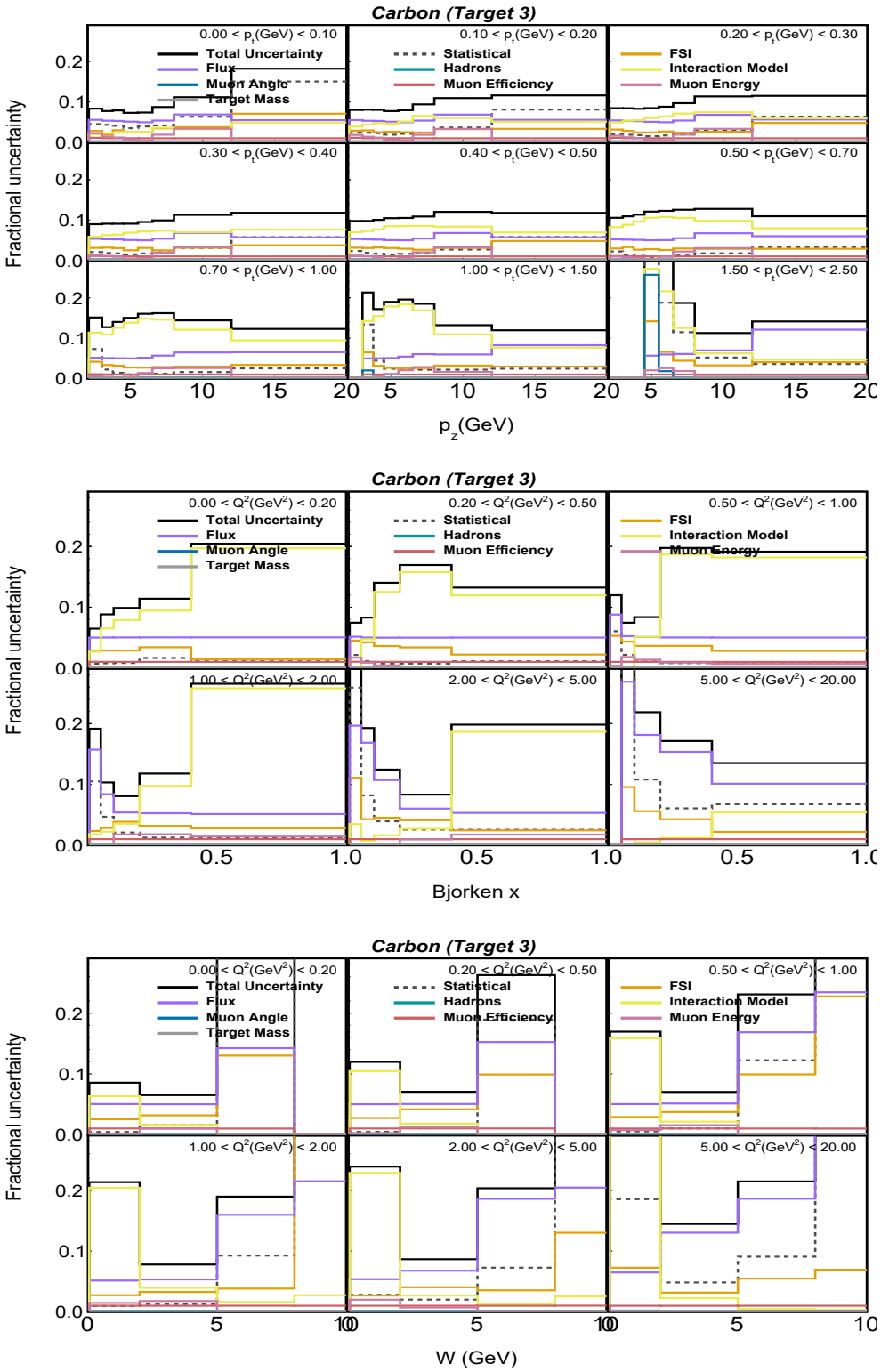

Figure F.17: Fractional uncertainties in generated, reconstructed MC for carbon across $p_z - p_t$ (top), $x - Q^2$ (middle) and $W - Q^2$ (bottom).

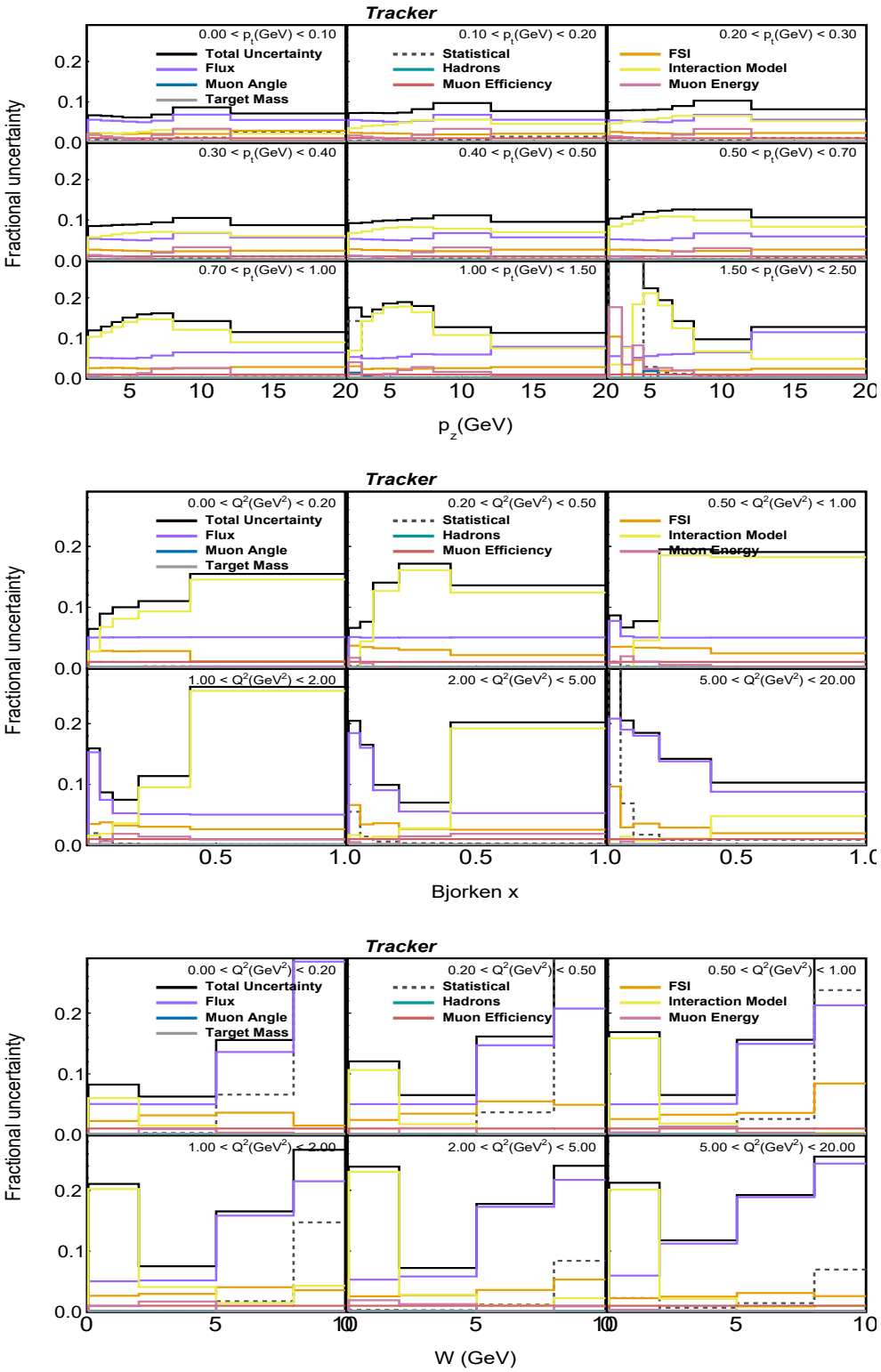

Figure F.18: Fractional uncertainties in generated, reconstructed MC for scintillator tracker across $p_z - p_t$ (top), $x - Q^2$ (middle) and $W - Q^2$ (bottom).

Appendix G

Efficiency corrected distributions

Background subtracted, unfolded and efficiency corrected distributions for combined iron, lead, carbon and tracker in $W-Q^2$ and p_t-p_z are presented here, along with the associated systematic uncertainties. Efficiency corrected distributions for iron and lead in individual targets are also shown.

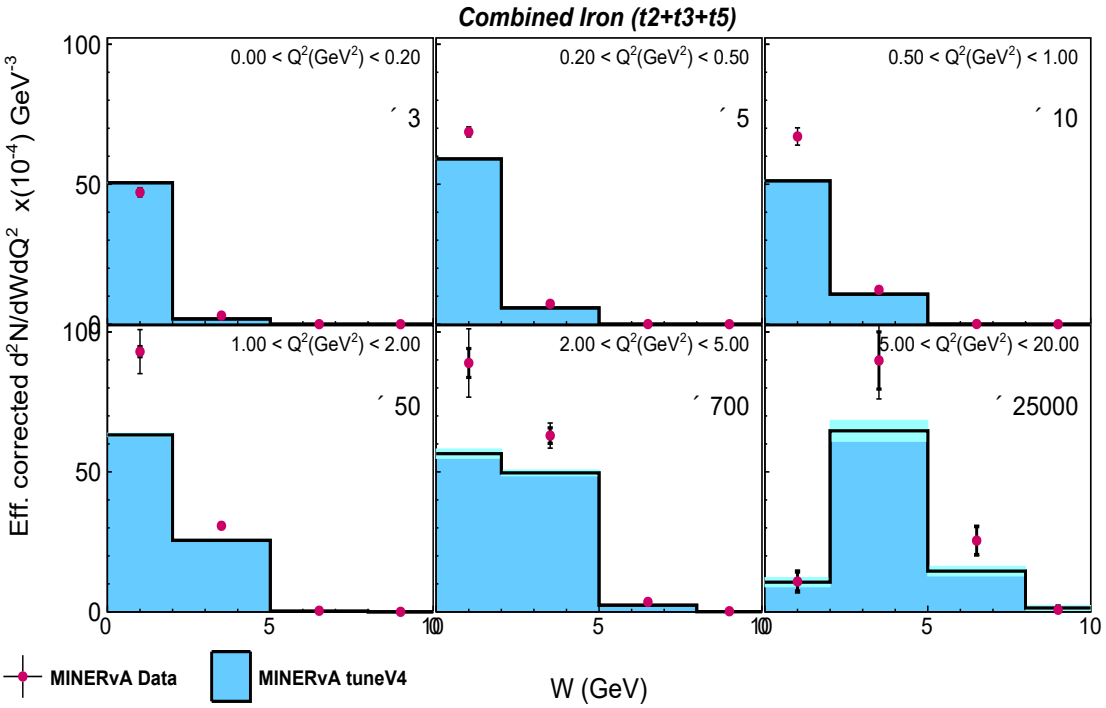

Figure G.1: Background subtracted, unfolded and efficiency corrected distributions across $W-Q^2$ bins for combined iron targets 2, 3 and 5.

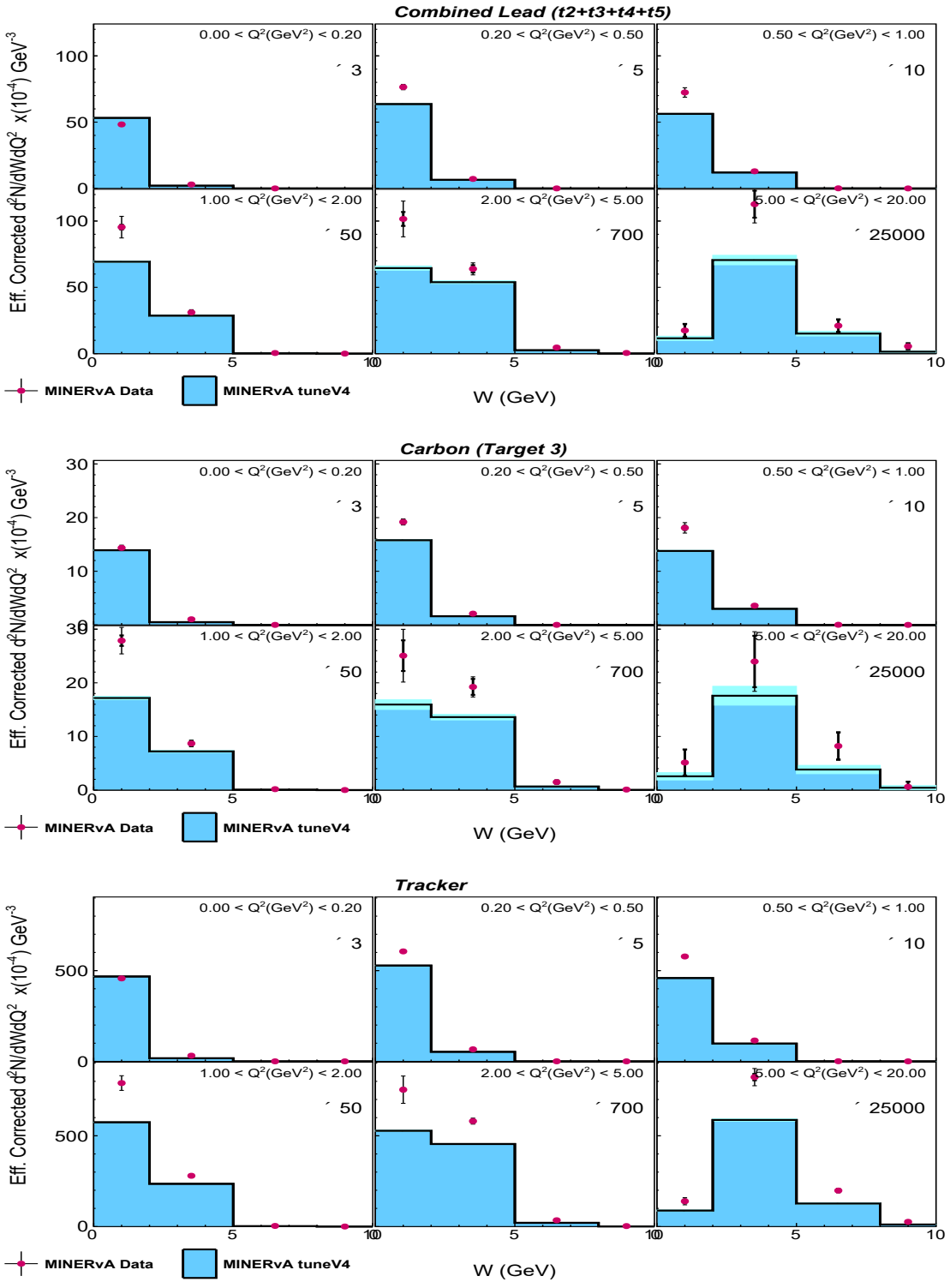

Figure G.2: Background subtracted, unfolded and efficiency corrected distributions across $W - Q^2$ bins for combined lead targets 2, 3, 4 and 5 (top), carbon (middle) and scintillator tracker (bottom).

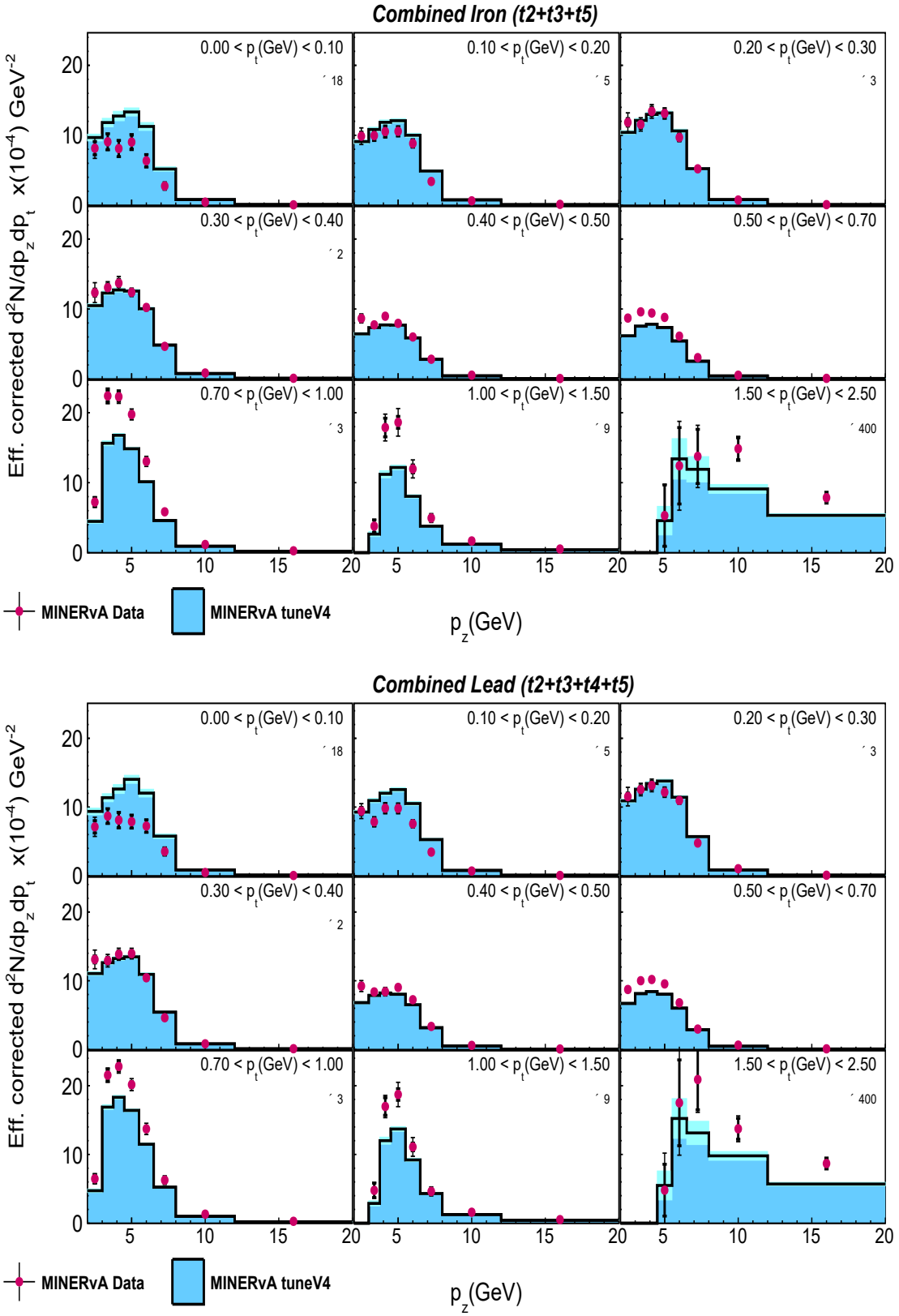

Figure G.3: Background subtracted, unfolded and efficiency corrected distributions across $p_z - p_t$ bins for combined iron targets 2, 3 and 5 (top) and combined lead targets 2, 3, 4 and 5 (bottom).

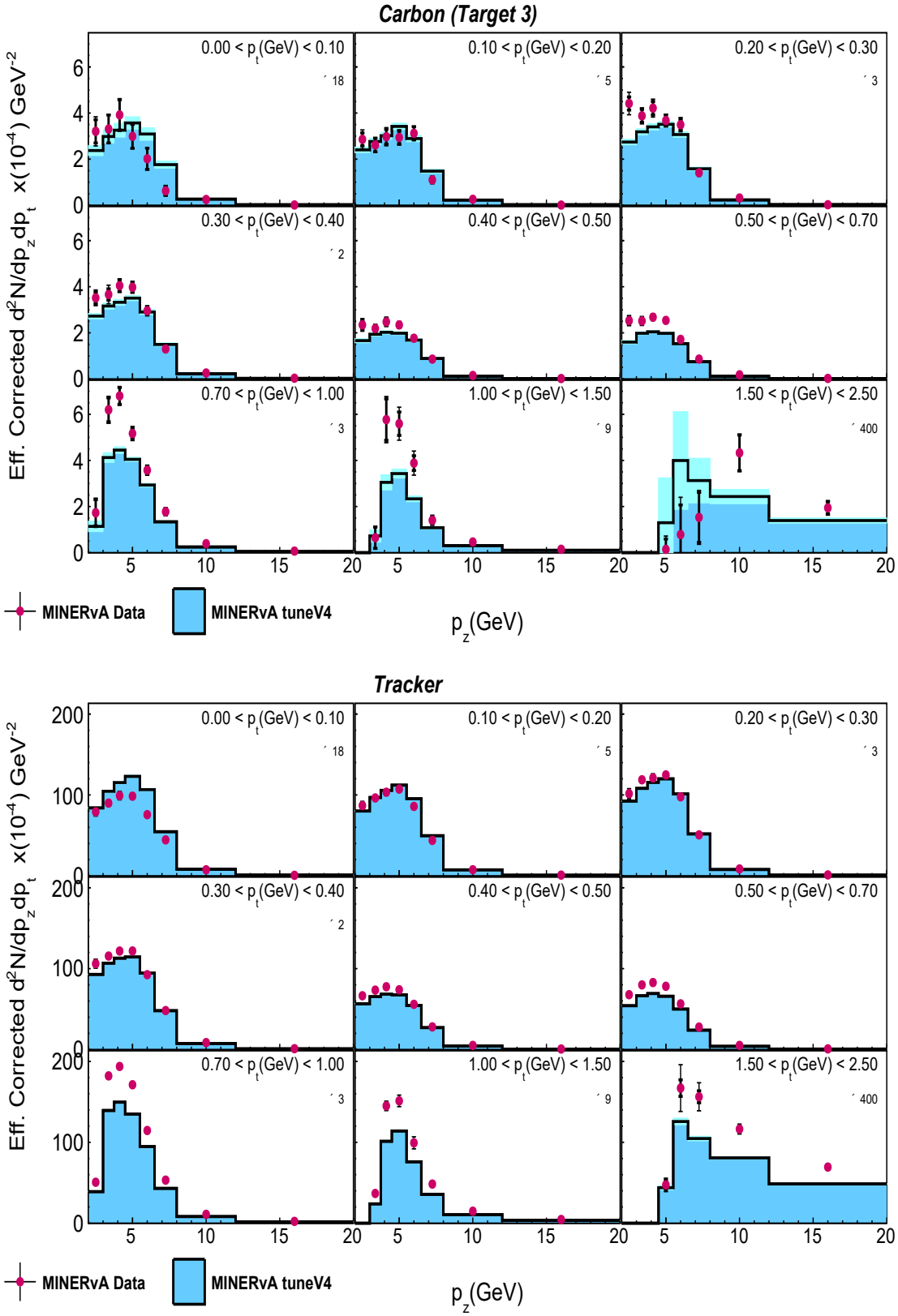

Figure G.4: Background subtracted, unfolded and efficiency corrected distributions across $p_z - p_t$ bins for carbon (top) and scintillator tracker (bottom).

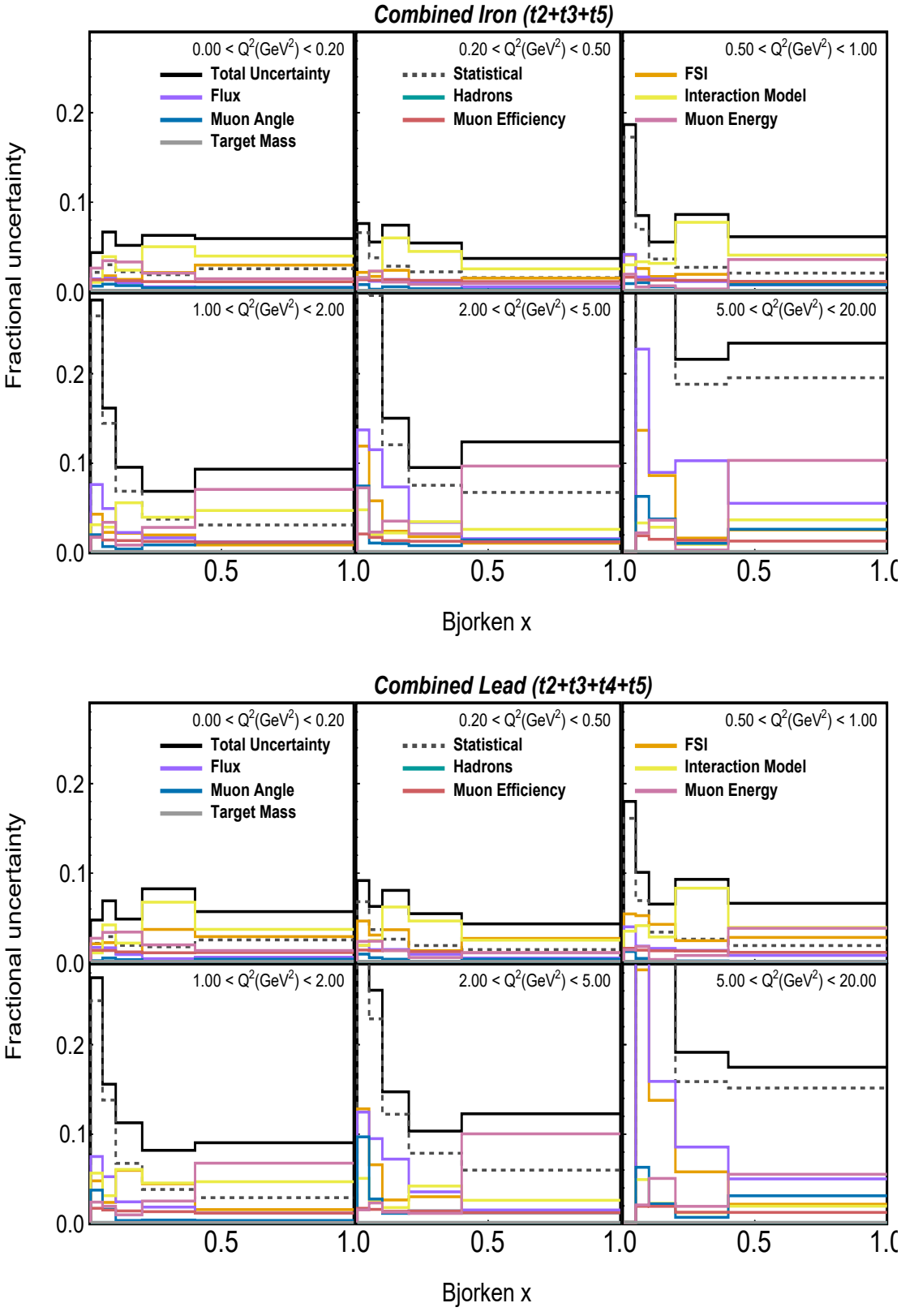

Figure G.5: Systematic uncertainties as a fraction in background subtracted, unfolded and efficiency corrected distributions across $x - Q^2$ bins for combined iron (top) and combined lead (bottom).

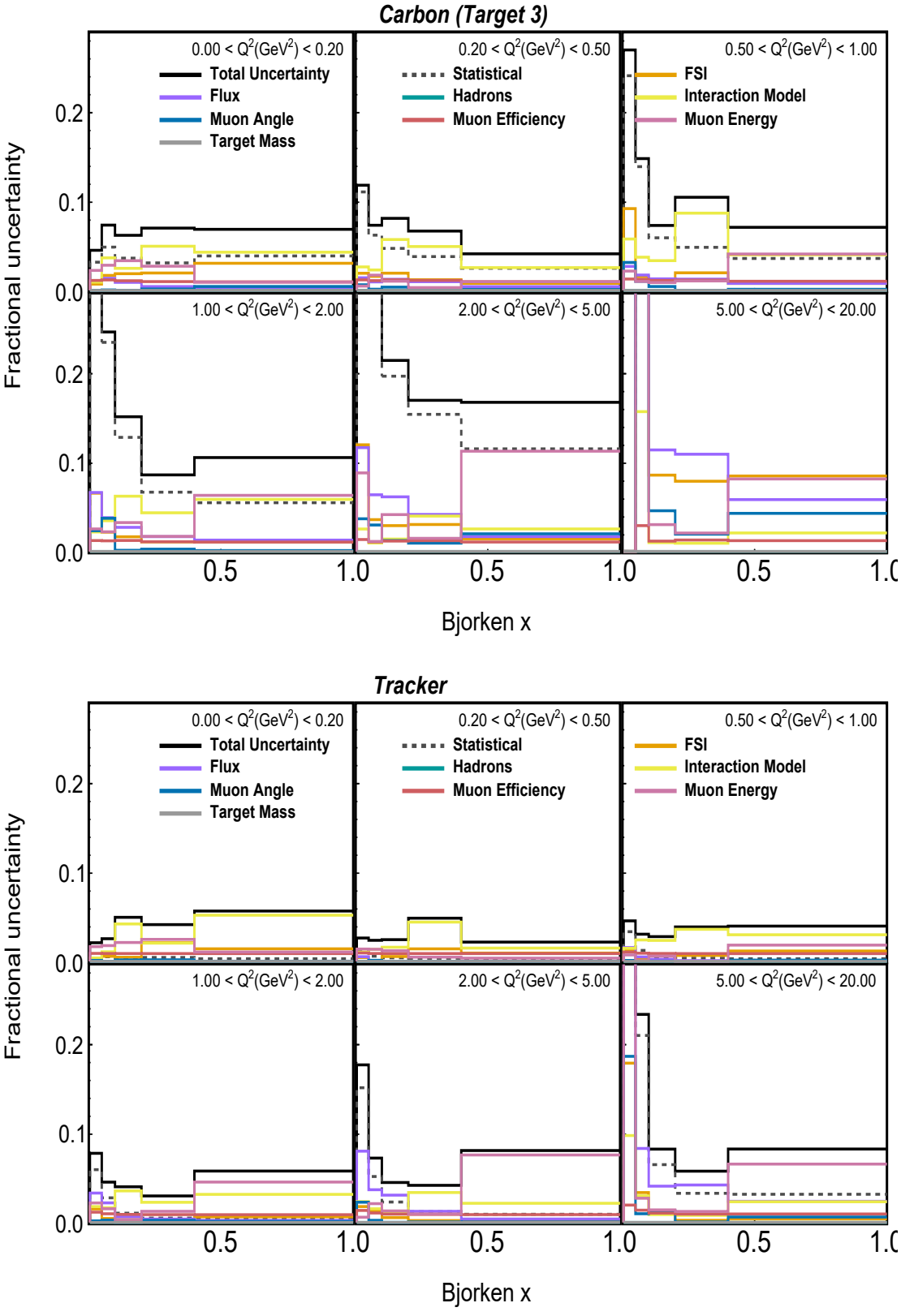

Figure G.6: Systematic uncertainties as a fraction in background subtracted, unfolded and efficiency corrected distributions across $x - Q^2$ bins for carbon (top) and scintillator tracker (bottom).

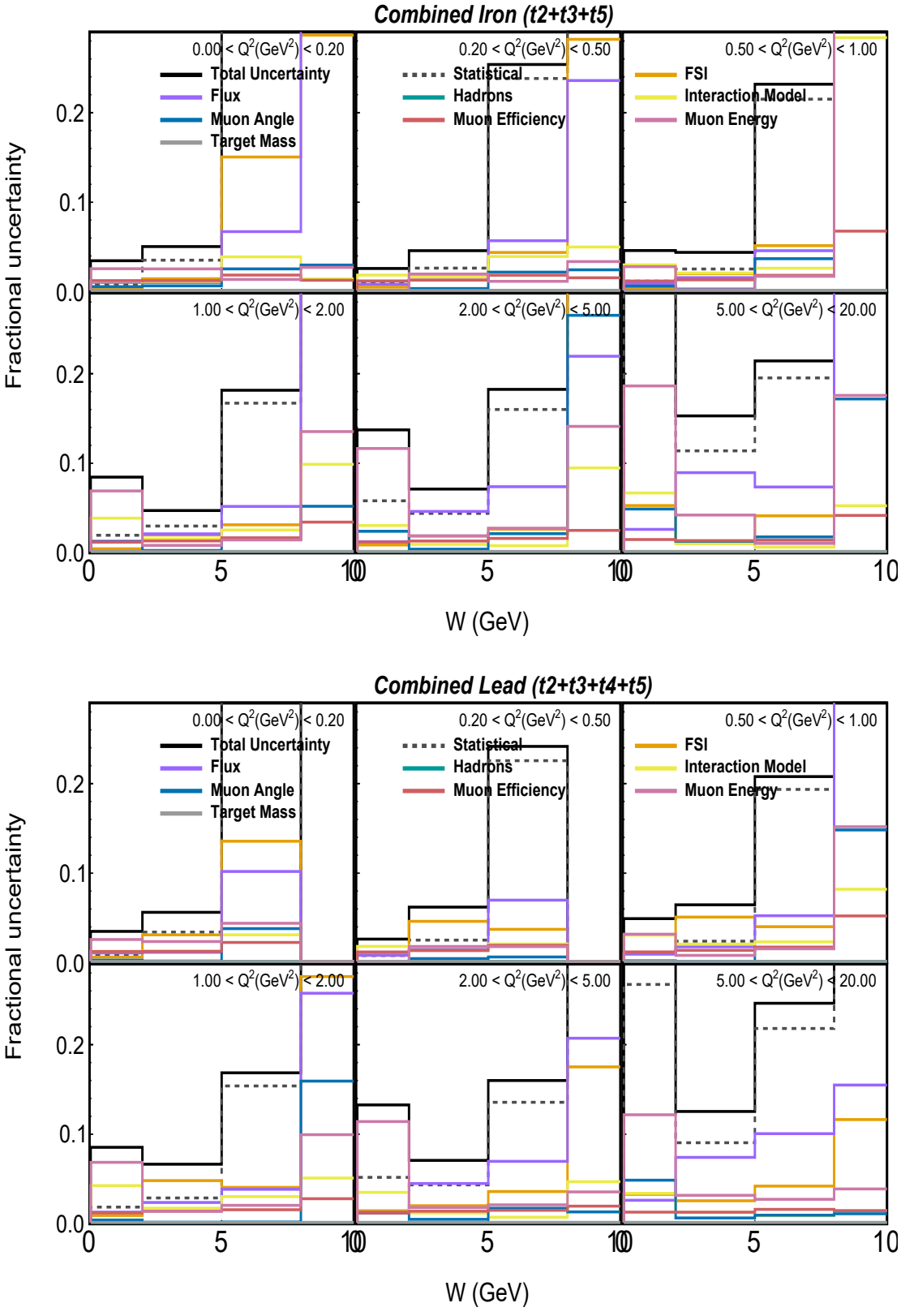

Figure G.7: Systematic uncertainties as a fraction in background subtracted, unfolded and efficiency corrected distributions across $W - Q^2$ bins for combined iron (top) and combined lead (bottom).

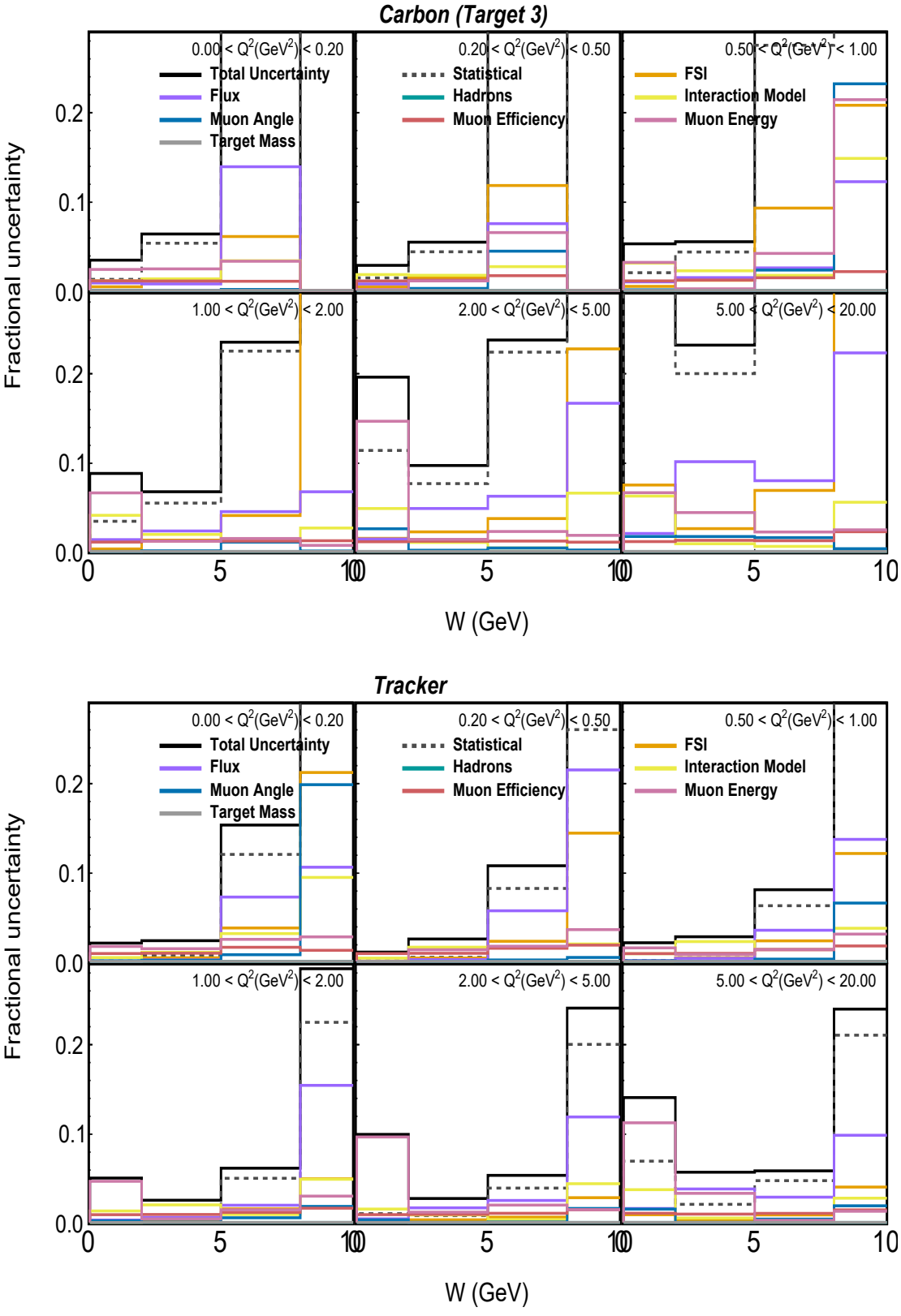

Figure G.8: Systematic uncertainties as a fraction in background subtracted, unfolded and efficiency corrected distributions across $W - Q^2$ bins for carbon (top) and scintillator tracker (bottom).

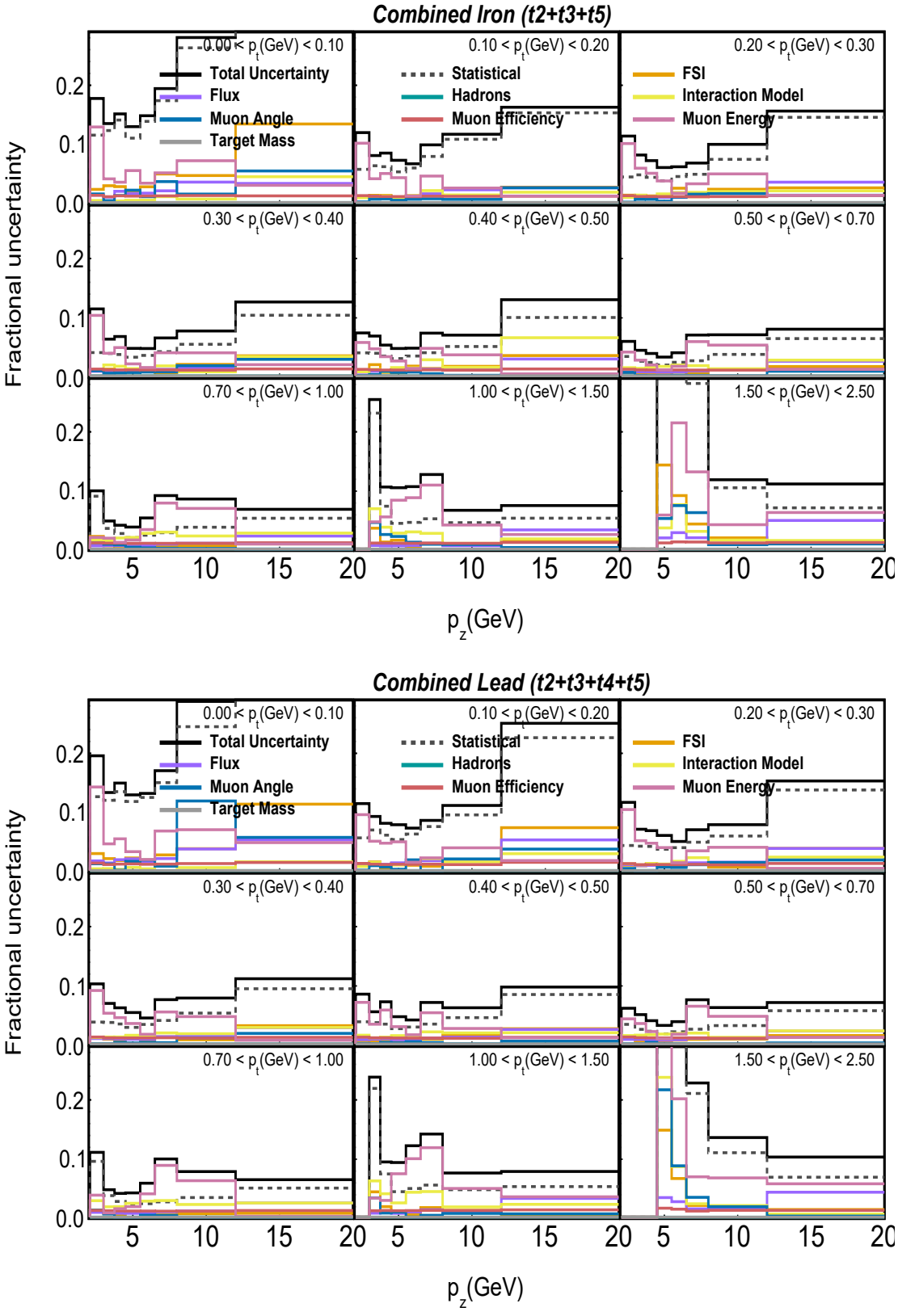

Figure G.9: Systematic uncertainties as a fraction in background subtracted, unfolded and efficiency corrected distributions across $p_z - p_t$ bins for combined iron (top) and combined lead (bottom).

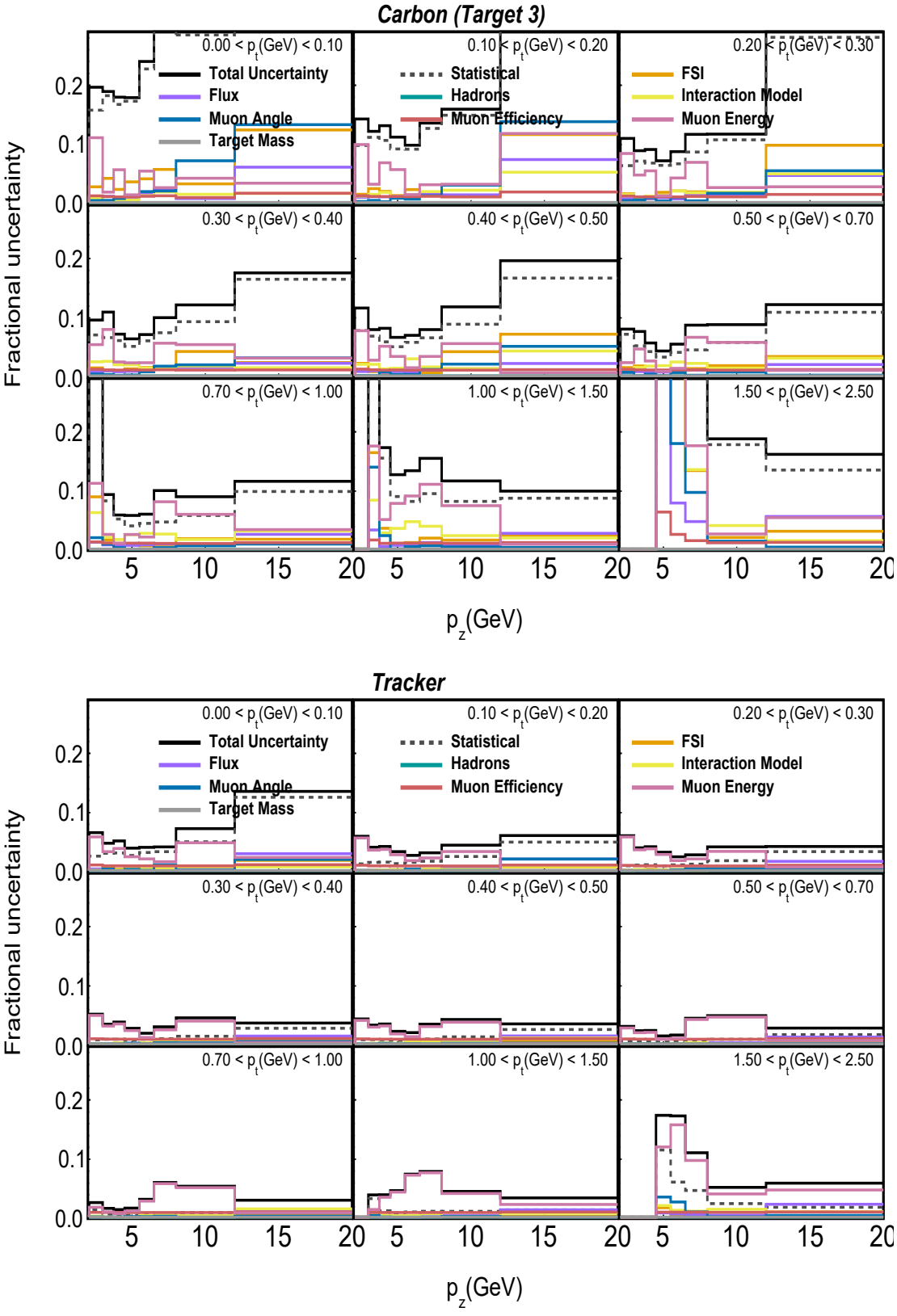

Figure G.10: Systematic uncertainties as a fraction in background subtracted, unfolded and efficiency corrected distributions across $p_z - p_t$ bins for carbon (top) and scintillator tracker (bottom).

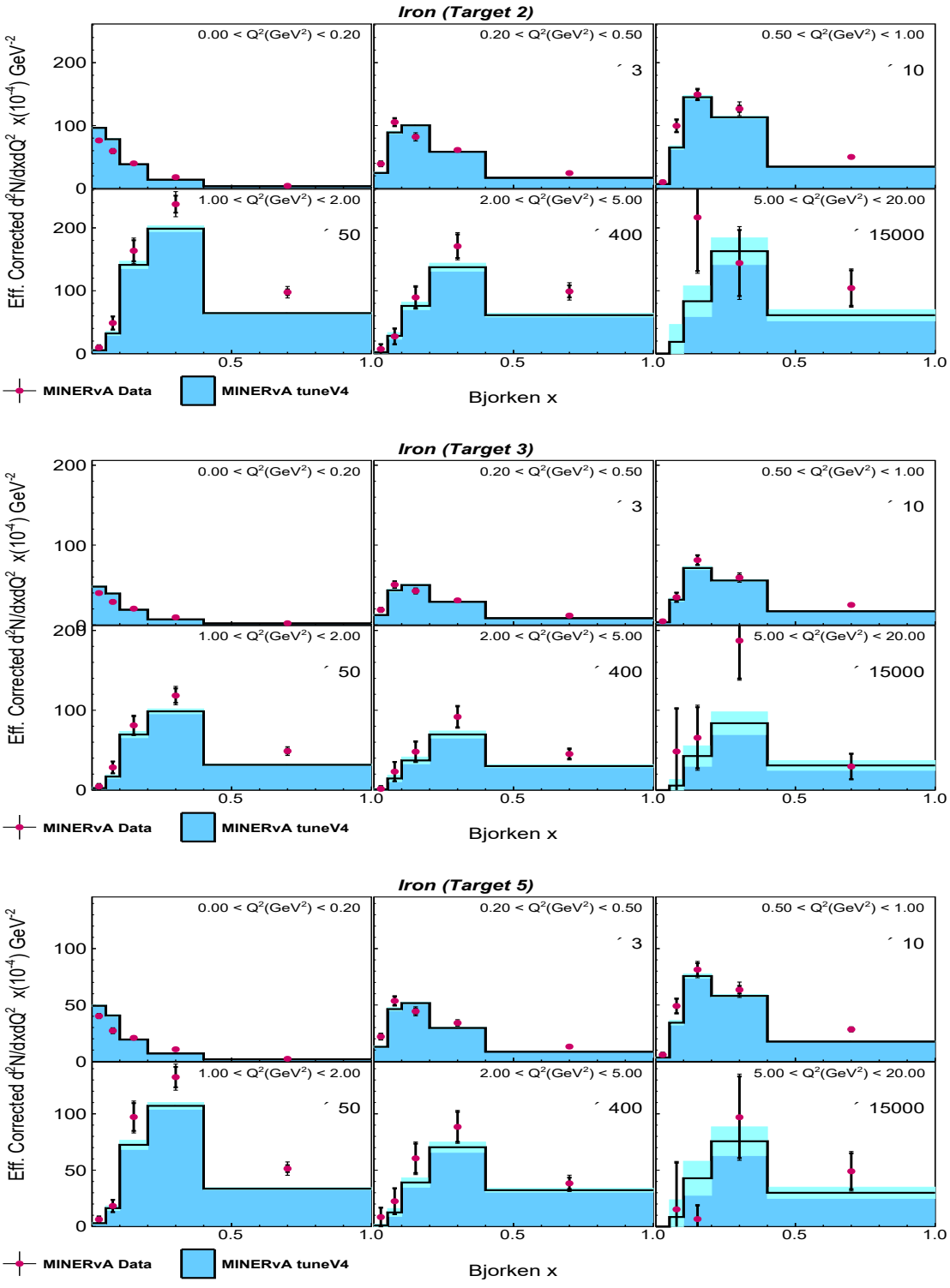

Figure G.11: Background subtracted, unfolded and efficiency corrected distributions across $x - Q^2$ bins for different iron targets.

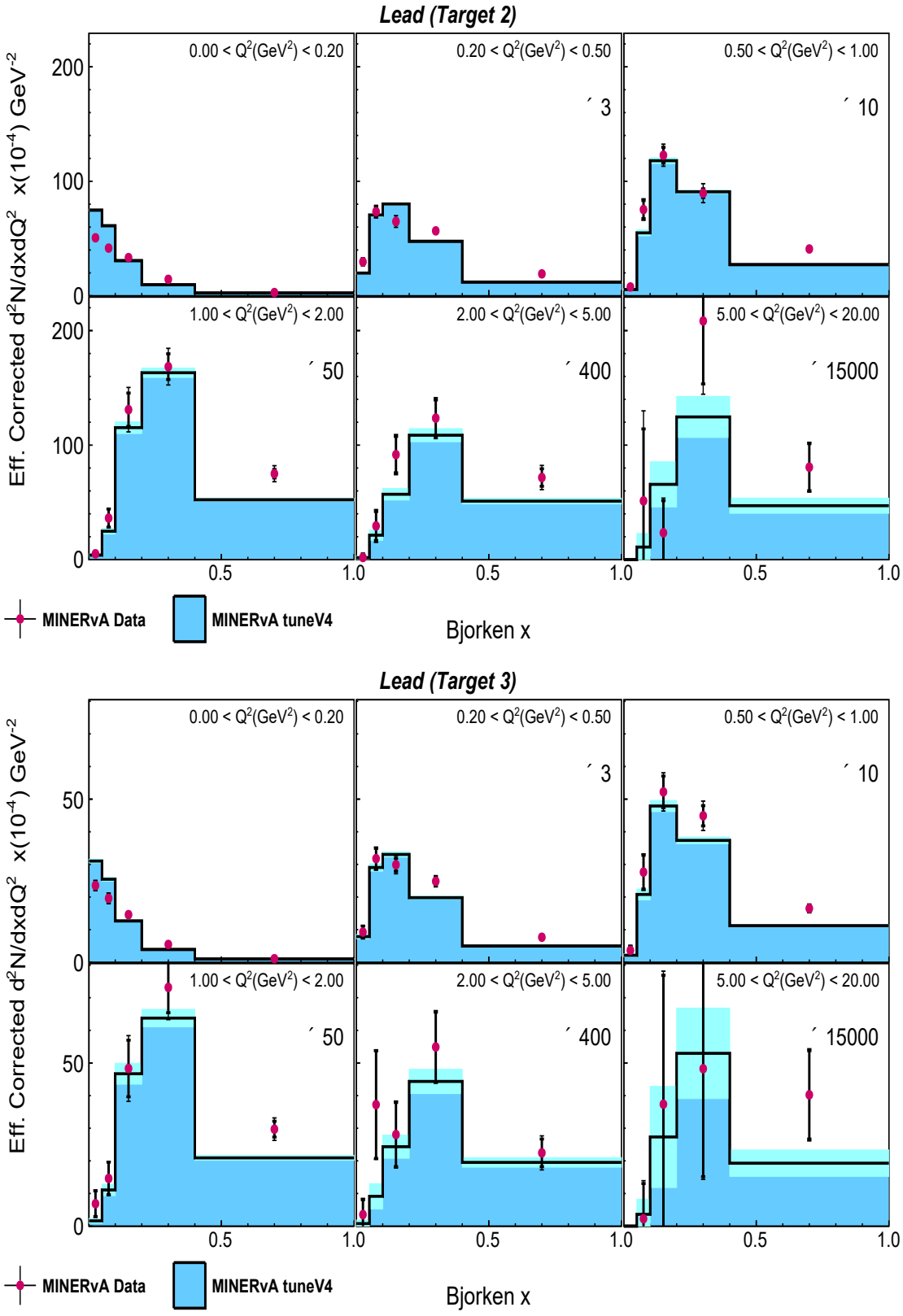

Figure G.12: Background subtracted, unfolded and efficiency corrected distributions across $x - Q^2$ bins for lead from targets 2 and 3.

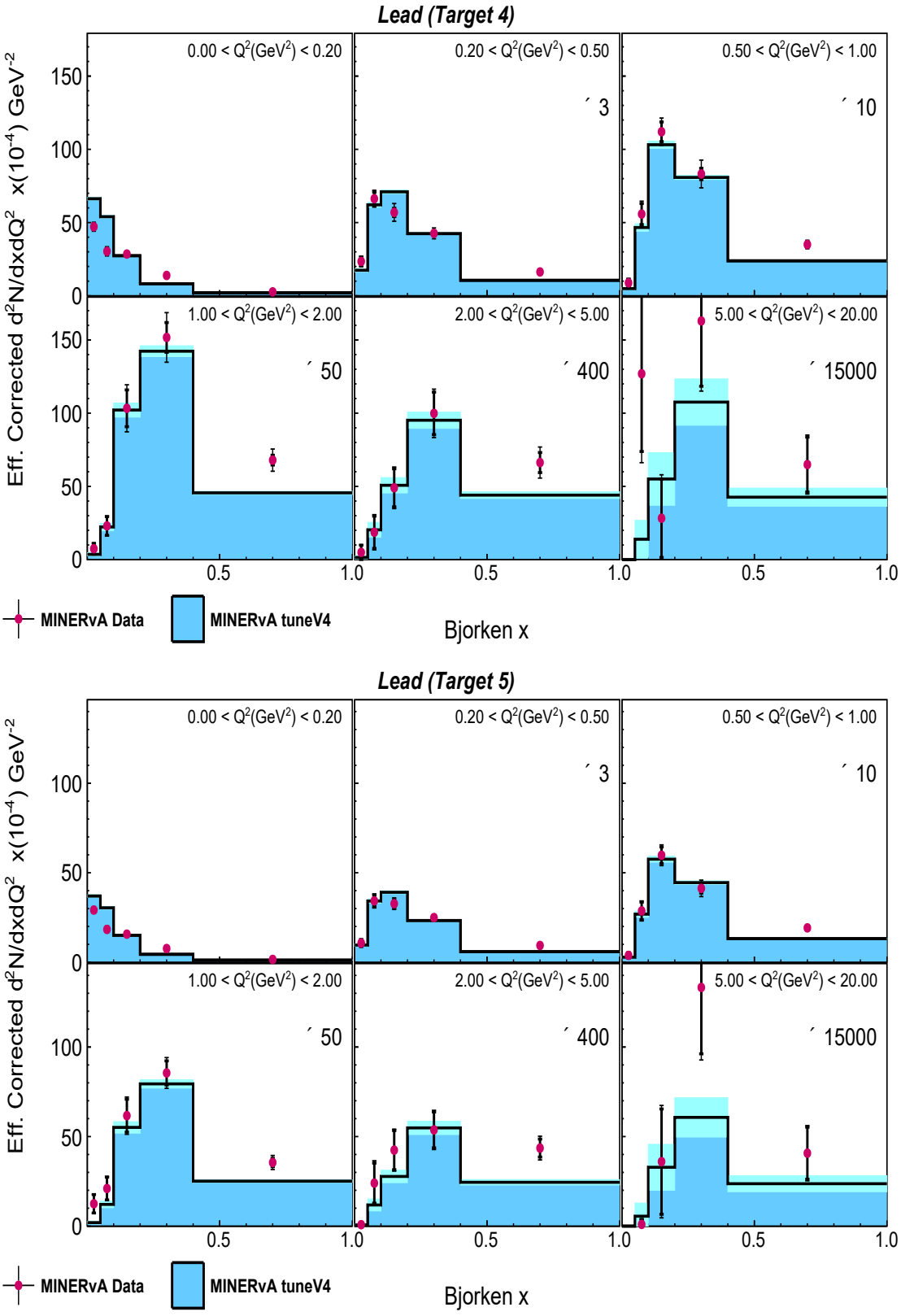

Figure G.13: Background subtracted, unfolded and efficiency corrected distributions across $x - Q^2$ bins for lead from targets 4 and 5.

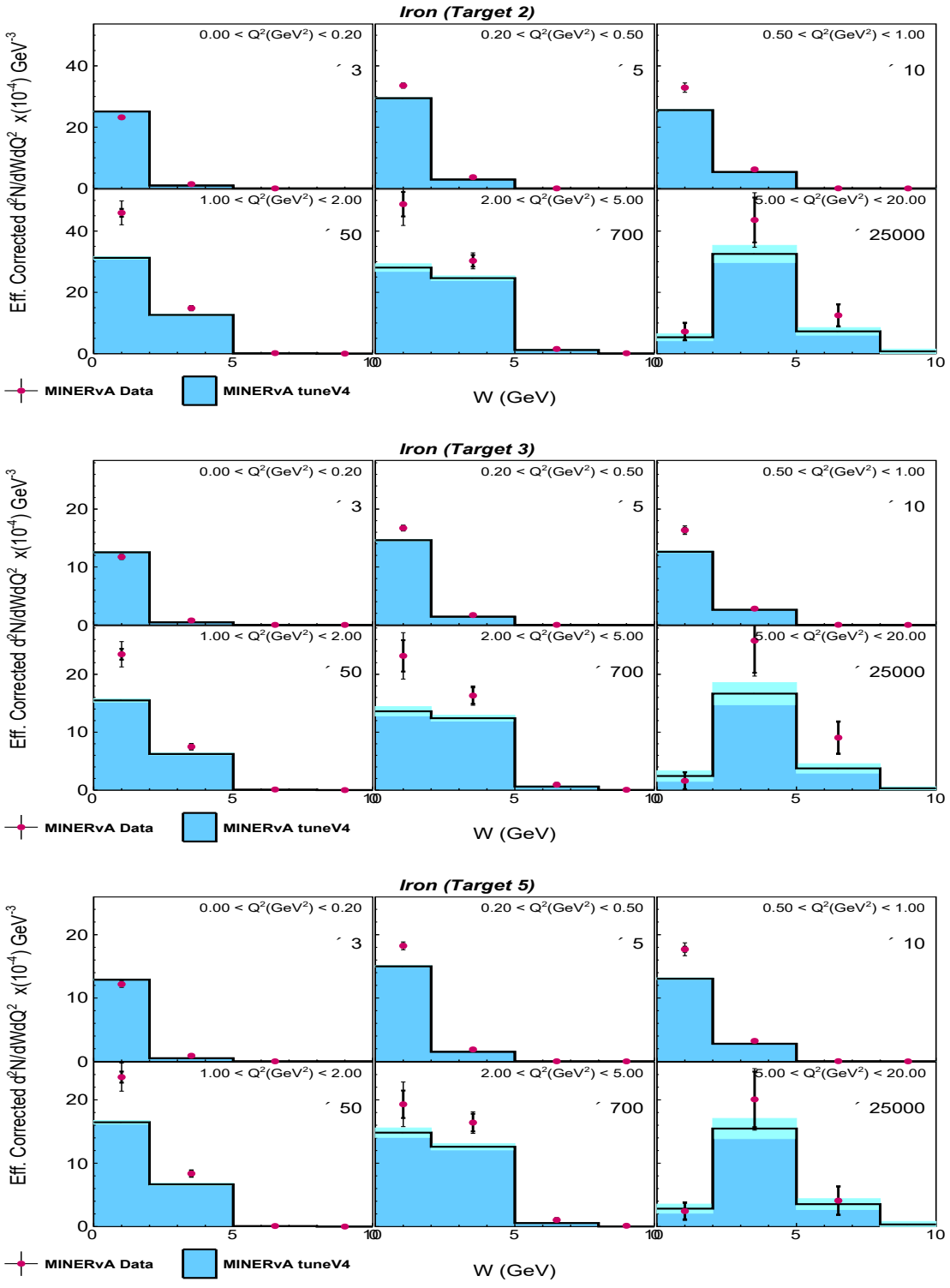

Figure G.14: Background subtracted, unfolded and efficiency corrected distributions across $W - Q^2$ bins for different iron targets.

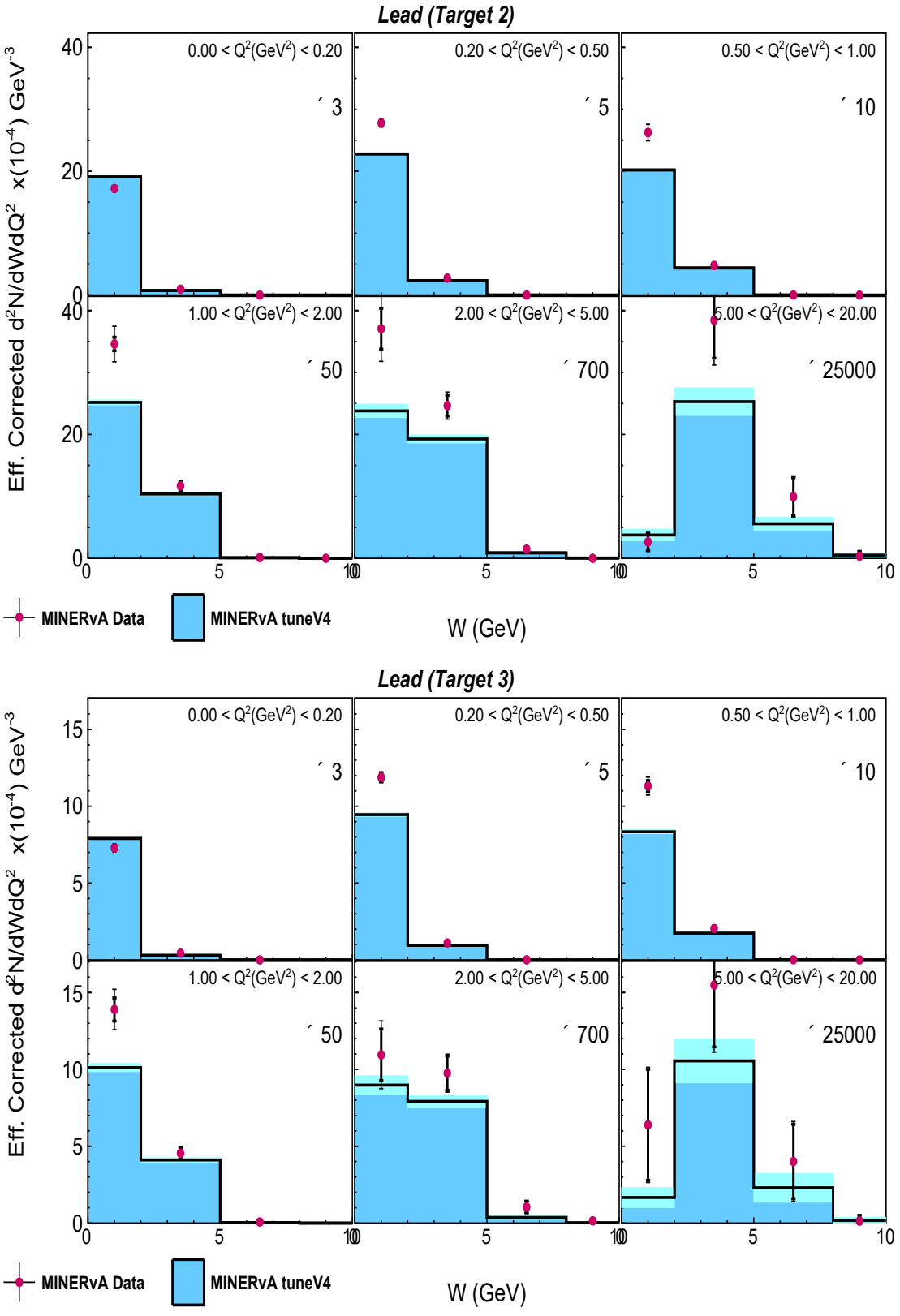

Figure G.15: Background subtracted, unfolded and efficiency corrected distributions across $W - Q^2$ bins for lead from targets 2 and 3.

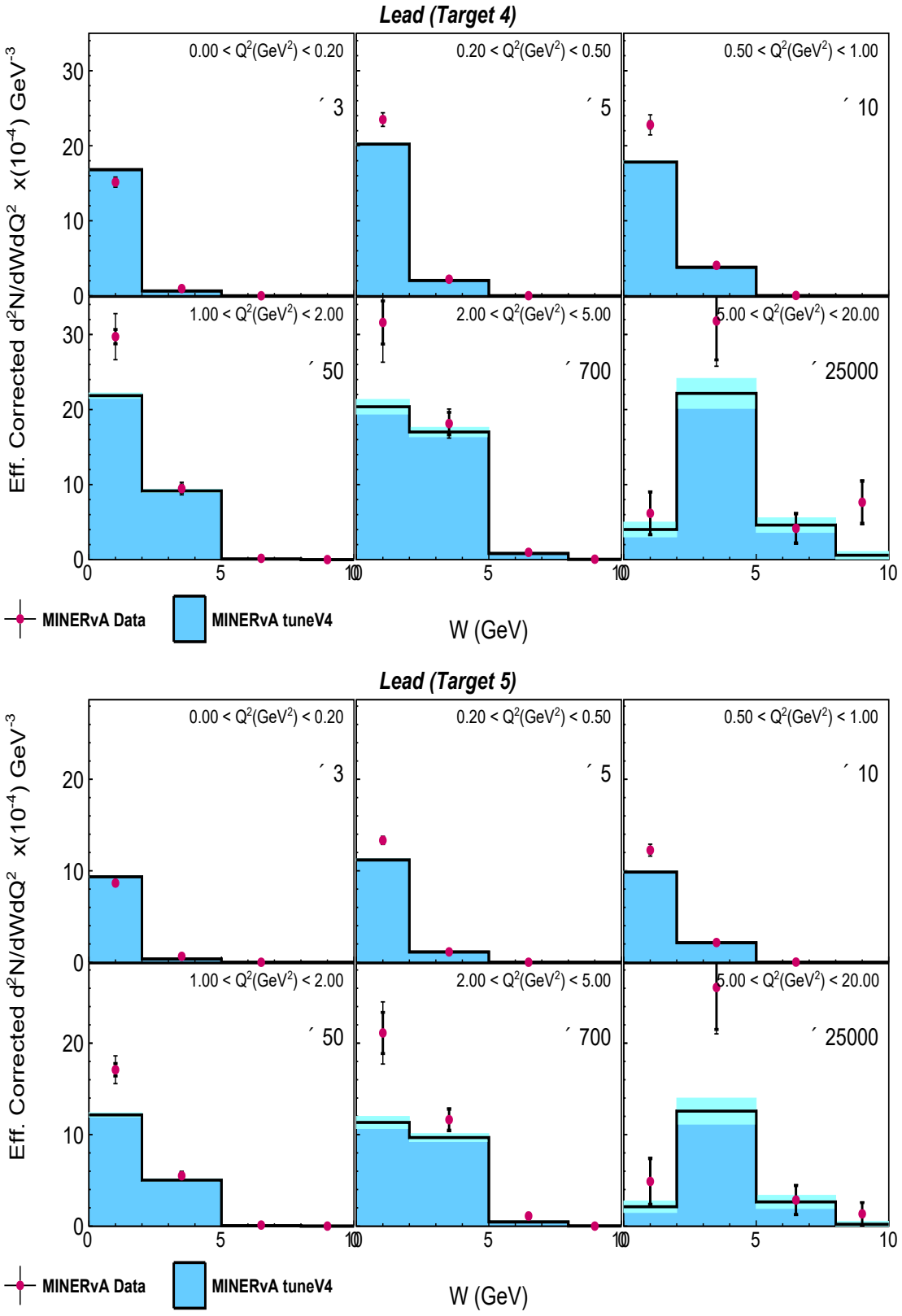

Figure G.16: Background subtracted, unfolded and efficiency corrected distributions across $W - Q^2$ bins for lead from targets 4 and 5.

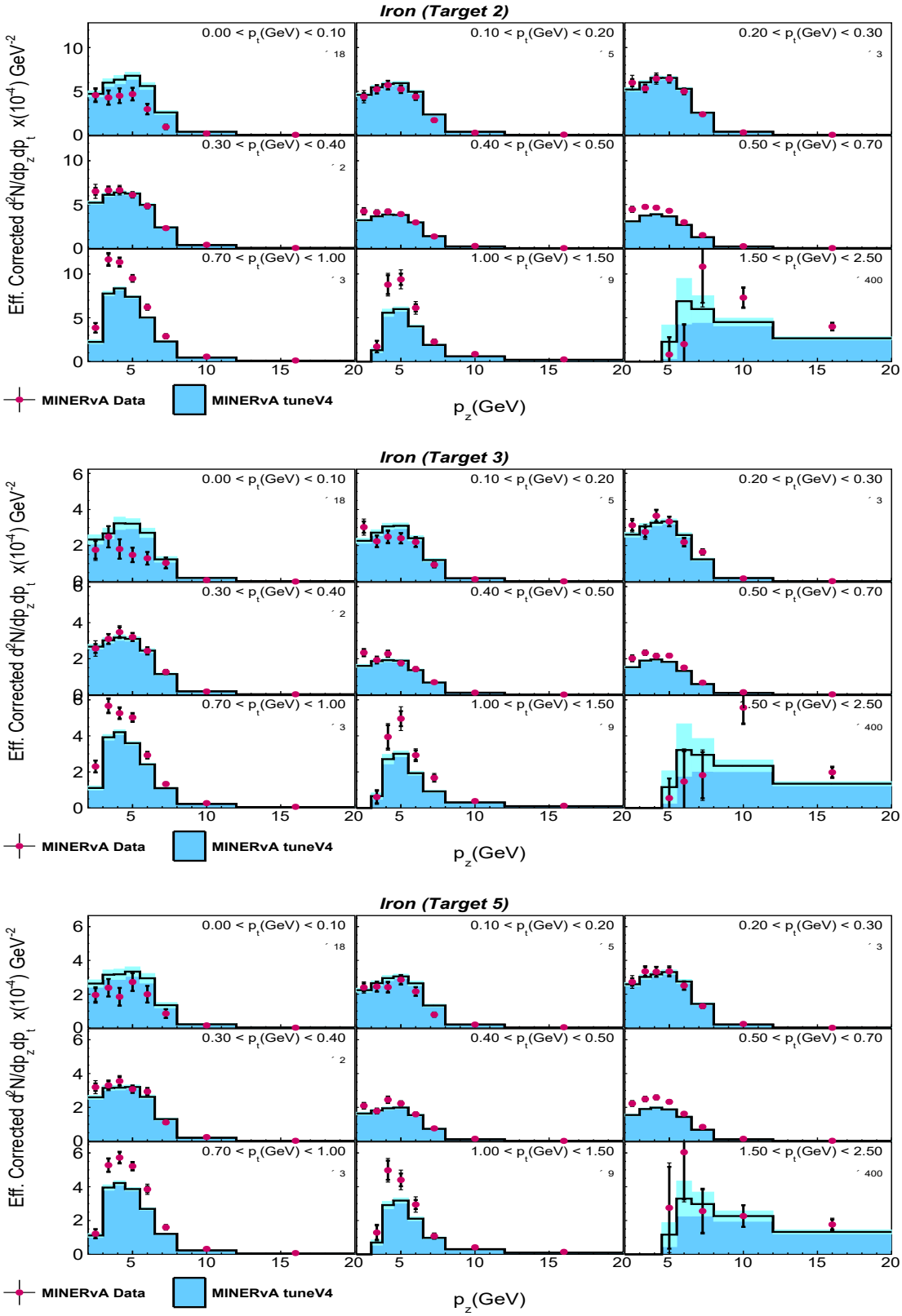

Figure G.17: Background subtracted, unfolded and efficiency corrected distributions across $p_z - p_t$ bins for different iron targets.

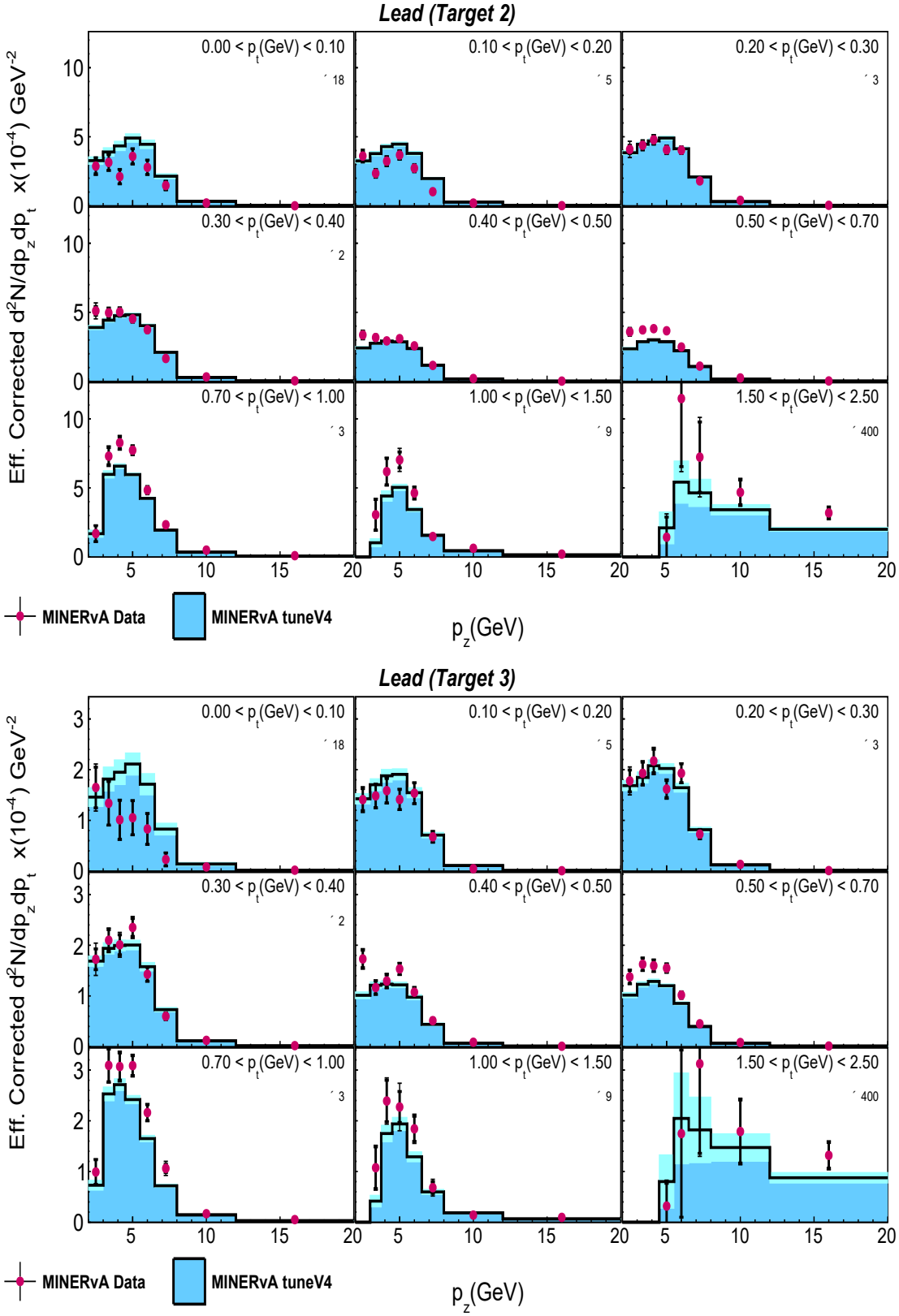

Figure G.18: Background subtracted, unfolded and efficiency corrected distributions across $p_z - p_t$ bins for lead from targets 2 and 3.

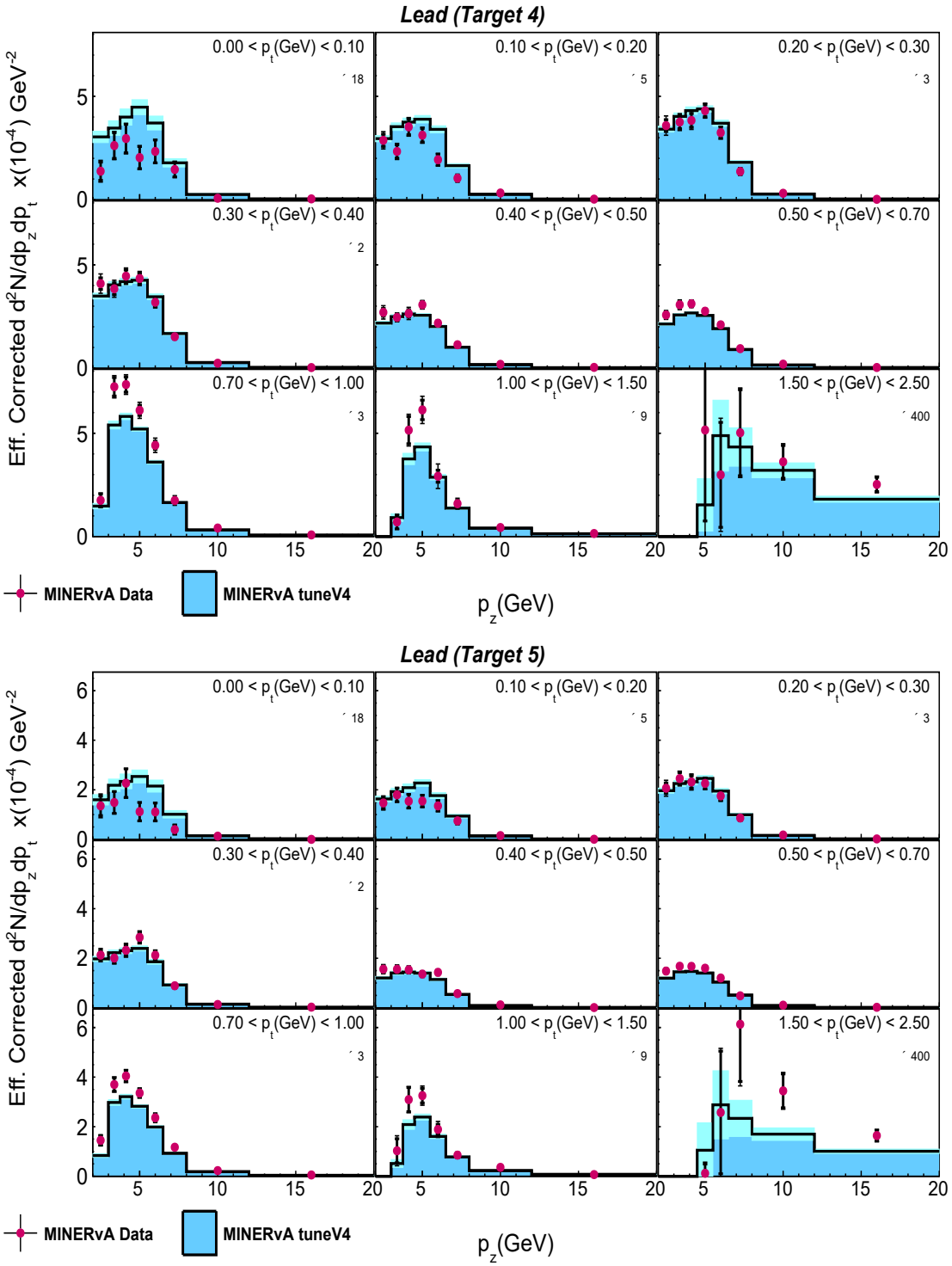

Figure G.19: Background subtracted, unfolded and efficiency corrected distributions across $p_z - p_t$ bins for lead from targets 4 and 5.